Transactions of the ASME, Journal of Heat Transfer (ISSN 0022-1481) is published monthly by The American Society of Mechanical Engineers, Three Park Avenue, New York, NY 10016. Periodicals postage paid at New York, NY and additional mailing offices. POSTMASTER: Send address changes to Transactions of the ASME, Journal of Heat Transfer, c/o THE AMERICAN SOCIETY OF MECHANICAL ENGINEERS, 22 Law Drive, Box 2300, Fairfield, NJ 07007-2300. **CHANGES OF ADDRESS** must be received at Society headquarters seven weeks before they are to be effective. Please send old label and new address.

Journal of Heat Transfer

Published Monthly by ASME

VOLUME 130 • NUMBER 12 • DECEMBER 2008 , pp. 121201-127001

RESEARCH PAPERS

(Contents continued on inside back cover)

This journal is printed on acid-free paper, which exceeds the ANSI Z39.48-1992 specification for permanence of paper and library materials. ♾™
♻ 85% recycled content, including 10% post-consumer fibers.

The ASME Journal of Heat Transfer is abstracted and indexed in the following:

Applied Science and Technology Index, Chemical Abstracts, Chemical Engineering and Biotechnology Abstracts (Electronic equivalent of Process and Chemical Engineering), Civil Engineering Abstracts, Compendex (The electronic equivalent of Engineering Index), Corrosion Abstracts, Current Contents, E & P Health, Safety, and Environment, Ei EncompassLit, Engineered Materials Abstracts, Engineering Index, Enviroline (The electronic equivalent of Environment Abstracts), Environment Abstracts, Environmental Engineering Abstracts, Environmental Science and Pollution Management, Fluidex, Fuel and Energy Abstracts, Index to Scientific Reviews, INSPEC, International Building Services Abstracts, Mechanical & Transportation Engineering Abstracts, Mechanical Engineering Abstracts, METADEX (The electronic equivalent of Metals Abstracts and Alloys Index), Petroleum Abstracts, Process and Chemical Engineering, Referativnyi Zhurnal, Science Citation Index, SciSearch (The electronic equivalent of Science Citation Index), Theoretical Chemical Engineering

Investigation of Thermal Accommodation Coefficients in Time-Resolved Laser-Induced Incandescence

K. J. Daun[1]
Department of Mechanical and Mechatronics Engineering,
University of Waterloo,
200 University Avenue West,
Waterloo, ON, N2L 3G1, Canada
e-mail: kjdaun@mme.uwaterloo.ca

G. J. Smallwood

F. Liu

Institute for Chemical Process and Environmental Technology,
National Research Council Canada,
1200 Montreal Road,
Ottawa, ON, K1A 0R6, Canada

Accurate particle sizing through time-resolved laser-induced incandescence (TR-LII) requires knowledge of the thermal accommodation coefficient, but the underlying physics of this parameter is poorly understood. If the particle size is known a priori, however, TR-LII data can instead be used to infer the thermal accommodation coefficient. Thermal accommodation coefficients measured between soot and different monatomic and polyatomic gases show that the accommodation coefficient increases with molecular mass for monatomic gases and is lower for polyatomic gases. This latter result indicates that surface energy is accommodated preferentially into translational modes over internal modes for these gases. [DOI: 10.1115/1.2977549]

Keywords: laser-induced incandescence, soot, accommodation coefficient, gas/surface scattering

Introduction

Research and development of novel nanoparticle sizing techniques is driven by several emerging applications. These tools are critical for assessing the impact of soot on human health and climate change, for example, which depend strongly on soot particle size [1–4]. Laser-based particle sizing is also used to understand how soot generated within combustion devices influences their operating efficiency [5], which is increasingly important in the context of climate change and high fuel costs [6]. Finally, accurate metrology techniques have recently been adopted to control the synthesis of engineered nanoparticles [7] such as carbon blacks. Laser-based diagnostics are well suited to these applications since, in contrast to direct sampling and transmission electron microscopy (TEM) analysis, they allow spatially and temporally resolved measurements of particles without perturbing the aerosol.

Although time-resolved laser-induced incandescence (TR-LII) was conceived as a tool for particle sizing over 20 years ago [8] only recently has it been adopted for carrying out particle sizing measurements in the above applications (e.g., see Refs. [9–20]). In this procedure a short laser pulse heats a sample of nanoparticles suspended in the carrier gas to incandescent temperatures, typically 3300–3600 K in low-fluence experiments. The spectral incandescence of the laser energized particles is measured as they return to thermal equilibrium with the gas, and a time-resolved temperature is usually defined pyrometrically using incandescence measurements made at two or more wavelengths. Since larger particles take longer to cool than smaller ones, the particle size distribution can, in principle, be recovered from the observed temperature decay.

When carrying out this measurement, it is critical to accurately model the heat transfer between the particle and the ambient gas during the cooling phase, which is almost entirely due to free-molecular heat conduction in experiments carried out at atmospheric pressure. In this regime gas molecules travel ballistically between the equilibrium gas and the particle surface without undergoing intermediate intermolecular collisions, so the overall conduction rate depends on the energy transferred when a gas molecule collides with the particle surface. This quantity is specified by the *thermal accommodation coefficient*; although this parameter was conceived by Maxwell [21], its quantitative definition is usually attributed to Knudsen [22],

$$\alpha = \frac{T_{g,o} - T_g}{T_s - T_g} = \frac{E_{g,o} - E_g}{E_s - E_g} \tag{1}$$

where T_s is the particle temperature, T_g and $T_{g,o}$ are the temperatures of the incident and scattered gas molecular streams, respectively, and E_s, E_g, and $E_{g,o}$ are the corresponding energy states. Clearly, accurate particle sizing is predicated on knowledge of α, and several recent studies [12,15,17,20,23,24] have found α values by comparing pyrometrically observed temperature decays from TR-LII experiments with particle morphologies measured by electron microscopy or light scattering with the intention of using these values to carry out TR-LII particle sizing under other experimental conditions. The majority of these studies report accommodation coefficients ranging from $\alpha=0.24$ [15] to $\alpha=0.44$ [17,24], although some studies [13,16] assume perfect accommodation in particle sizing studies. (Reference [15] originally reported $\alpha=0.07$ due to a calculation error and was subsequently corrected.) For the most part these results have done little to elucidate the underlying physics of the thermal accommodation coefficient, however, since the vast majority of these studies pertain to a single gas-particle combination carried out at a unique temperature and pressure. (Notable exceptions are Eremin et al. [17] and Gurentsov et al. [20], who reported α values between soot and Ar, CO, C_3O_2, and He.) Other types of accommodation coefficient measurements between graphite and various gases have been carried out (see, e.g., Refs. [25,26] and references therein), but these values are not directly applicable to laser-induced incandescence because α is generally a function of T_s, and the surface temperatures in these experiments are much lower than those encountered in LII. Due to the deficient knowledge of thermal accommodation, most LII researchers treat α more like a calibration constant than a physical parameter, and there is little consensus on what may constitute a reasonable value for this coefficient or how it may vary with experimental parameters such as gas composition.

[1]Corresponding author.

Contributed by the Heat Transfer Division of ASME for publication in the JOURNAL OF HEAT TRANSFER. Manuscript received January 25, 2008; final manuscript received May 12, 2008; published online September 25, 2008. Review conducted by Patrick E. Phelan.

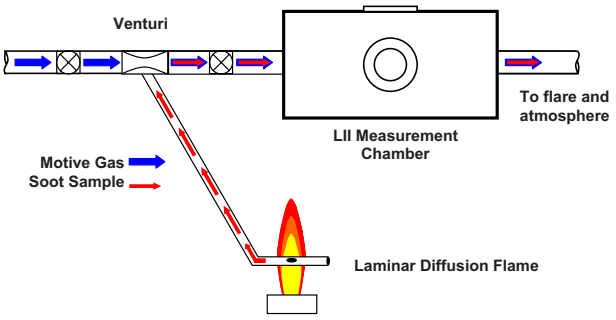

Fig. 1 Schematic of the experimental apparatus

These uncertainties severely limit confidence in particle sizes obtained by TR-LII.

This paper presents thermal accommodation coefficients between soot and different monatomic and polyatomic gases with the objective of identifying how gas molecular mass and structure influence thermal accommodation in LII experiments. The soot is extracted from an ethylene diffusion flame and entrained into a motive gas stream using a venturi-eductor. The gas/soot mixture then flows into a chamber where the LII measurement is carried out, and α is inferred from the observed temperature decay rate. The experimental results show that the thermal accommodation coefficient increases monotonically with molecular mass for the monatomic gas, and α becomes smaller as the structural complexity of the gas molecule increases for gases having similar molecular masses. The latter trend may be due to inefficient surface energy accommodation into the rotational and vibrational energy modes of the gas molecule compared to the translational modes, although further experimental and numerical studies are required to verify if this is indeed the case.

Experimental Apparatus

The experimental apparatus, shown in Fig. 1, consists of a LII sampling system that extracts soot from an ethylene laminar diffusion flame generated with a coflow burner operating under conditions described in Ref. [23]. Soot is sampled using a probe connected to the throat of a venturi having a 0.030 in. (0.762 mm) critical diameter. Motive gas flows through the venturi at 20 l/min, causing a pressure drop that induces soot from the flame centerline at a height of 52 mm above the burner into the motive gas stream. Although some gas from the flame and the surroundings is entrained into the sampling system with the soot, a large dilution ratio (>95% on a molar basis) ensures that it has a negligible influence on the experimental results. The motive gas and soot then enter the LII chamber, where the soot particles are energized with a pulsed Nd:YAG laser operating at 13.5 mJ/pulse at 20 Hz and 1064 nm. The pulse temporal width is about 7 ns, and relay imaging is used to obtain a near spatially uniform "top hat" beam profile as described in Ref. [27]. The laser heats the soot to a peak temperature of about 3600 K, and the resulting incandescence is imaged onto two photomultipliers equipped with narrowband interference filters centered at 397 nm (36 nm FWHM) and 782 nm (19 nm FWHM), respectively. (A more detailed description of the optics is provided in Ref. [27].) Transient signals from the photomultipliers are digitized and averaged over 100 shots to mitigate shot noise, resulting in a set of incandescence decay curves. These curves are used to derive an effective temperature, $T_s(t)$, using two-color pyrometry [27], which represents an average temperature of the primary particles biased toward the larger particles.

As noted above, inferring α from the observed LII cooling rate requires an independent measurement of the soot particle morphology as specified by the number of primary particles per aggregate, N_p, and the diameter of the primary particles, d_p. To a good approximation, the primary particle diameters can be treated as uniform while N_p usually obeys a log-normal distribution [28–30]. (The validity of these assumptions is discussed later in this paper.) In this analysis these parameters are inferred by transmission electron microscopy of soot particles sampled from the gas stream entering the LII chamber. The TEM grids are more sparse than those typical of in-flame sampling since the thermophoretic forces that drive soot particles onto the grid in the presence of a large temperature gradient are not present in this experiment. Nevertheless, images of 48 soot particles provide an adequate representation of those that enter the LII chamber. The images are analyzed using the projected area method [31] that computes the number of primary particles per aggregate based on the relationship

$$N_p = f_a (A_a / A_p)^{\varepsilon_a} \tag{2}$$

where A_a is the projected area of the aggregate calculated measured from the TEM image, while $A_p = \pi d_p^2/4$ is the projected area of a primary particle and f_a and ε_a are fractal parameters characteristic of soot aggregates. A primary particle diameter of 29 nm was sized manually from the TEM images, which is consistent with d_p values measured from soot sampled within the flame [32], and f_a and ε_a are set equal to 1.16 and 1.1, respectively, typical values for soot particles that are mass fractal in nature [33]. Figure 2 shows a histogram of the number of primary particles per aggregate, which indeed appears roughly log-normal in shape; the majority of aggregates contain between 100 and 300 primary particles, with an arithmetic mean of 179. Similar studies done on soot sampled near the extraction height within the ethylene diffusion flame [23,34] predict average values of N_p less than 100, which shows that while the primary particle diameter remains unchanged, some cluster-cluster aggregation occurs within the sampling manifold.

LII Data Analysis

The thermal accommodation coefficient is retrieved from the pyrometrically defined effective temperature, $T_s(t)$, based on a heat transfer model of the particle cooling rate [35]. Heat transfer in experiments carried out at low laser fluence and within the free-molecular regime is well understood, and although there is some uncertainty in the physical parameters of soot, in general there is widespread accord on best modeling practices for this type of experiment [36,37]. Furthermore, adsorbed surface contaminants that confound interpretations of α measurements on lower-temperature surfaces are unlikely to be present here due to the high energy of the soot particle relative to the potential well depths [38] formed by attractive van der Waals forces between the gas molecule and the surface atoms. Table 1 shows that the well depths, D, [39] are smaller than the characteristic surface energy at 3600 K, which prevents these gas species from adsorbing onto the soot particle surface.

In low-fluence LII experiments, the laser pulse is too weak to cause sublimation [40], which is the main source of uncertainty in LII modeling [36]. Furthermore radiation heat loss from the particles is negligible in experiments conducted in atmospheric pressure [35]. Consequently, after the laser pulse an energy balance on the soot particles reduces to

$$\rho_s c_s N_p \frac{\pi d_p^3}{6} \frac{dT_s}{dt} = -q_{\text{cond}}[T_s(t), T_g] \tag{3}$$

where ρ_s and c_s are the density and specific heat of soot and q_{cond} is the net heat transfer from the aggregate to the surrounding gas. The density and specific heat of soot are evaluated from Fried and Howard's correlations for graphite [41], while N_p and d_p are set equal to 200 nm and 29 nm based on TEM images of the extracted soot.

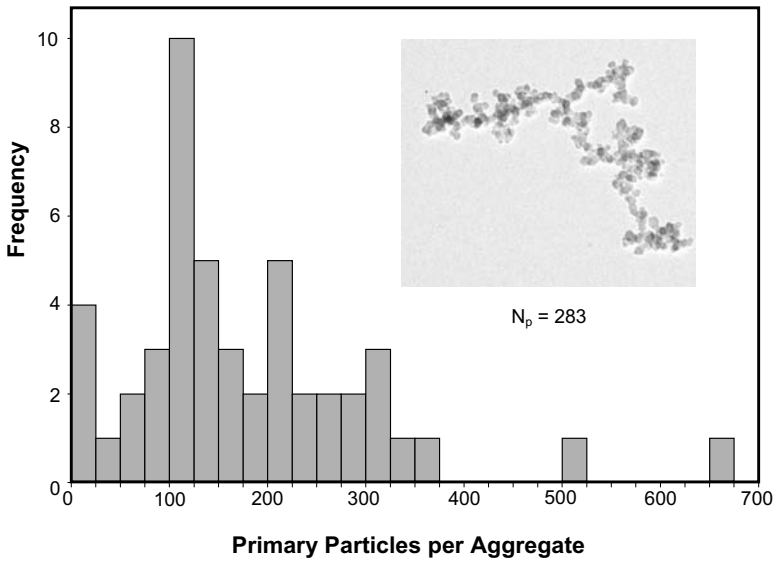

Fig. 2 Histogram of the number of primary particles per aggregate of soot sampled from the LII chamber. The inset shows a TEM image of a typical soot aggregate

Heat conduction in time-resolved LII experiments occurs in either the free-molecular regime or the transition regime [35] depending on the Knudsen number, $\mathrm{Kn}=2\lambda_{\mathrm{MFP}}/d_p$, where the Maxwell mean free path in the gas is

$$\lambda_{\mathrm{MFP}}(T_g)=\frac{k_{\mathrm{cond}}(T_g)}{f(T_g)P_g}[\gamma(T_g)-1]\sqrt{\frac{\pi m_g T_g}{2k_B}} \tag{4}$$

and the Eucken factor is $f(T_g)=k_{\mathrm{cond}}(T_g)/[\mu(T_g)c_v(T_g)]$. (Temperature dependent gas properties are found using correlations in Refs. [42–44].) Under the conditions of the present LII experiment, Kn ranges from 1 to 10 depending on the gas, so heat conduction from the primary particles occurs in the near free-molecular regime, as shown in Fig. 3. In this regime $q_{\mathrm{cond}}(T_s,T_g)=\alpha q_{\mathrm{cond,max}}(T_s,T_g)$, where $q_{\mathrm{cond,max}}(T_s,T_g)$ is the conduction heat transfer that would occur if every colliding gas molecule reached thermal equilibrium with the surface and is given by [45,46]

Table 1 Comparison of desorption energies between some gas species and graphite [46] and the surface energy at 3600 K

Species	D (meV) [46]	$D/(k_BT_s)$
He	16.6	0.05
Ar	96	0.31
N_2	104	0.34
CO	109.6	0.35
CH_4	130	0.42
Xe	162	0.52

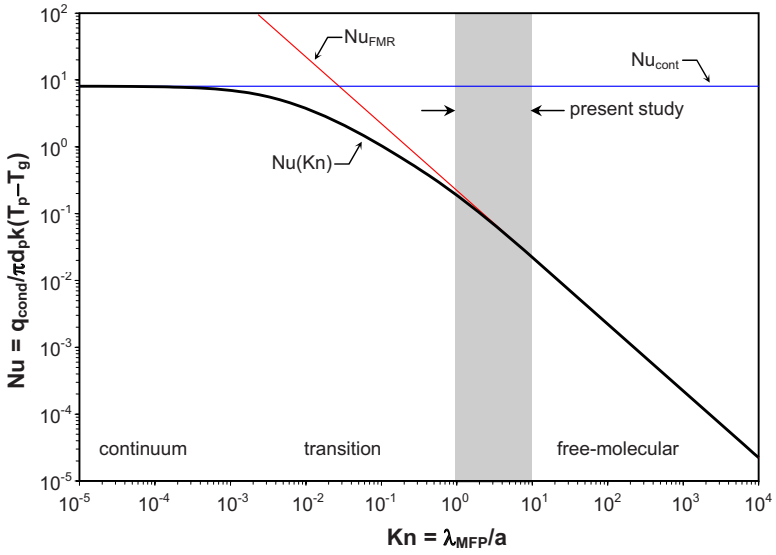

Fig. 3 Heat conduction between a primary particle and the surrounding gas takes place in the near-free-molecular regime

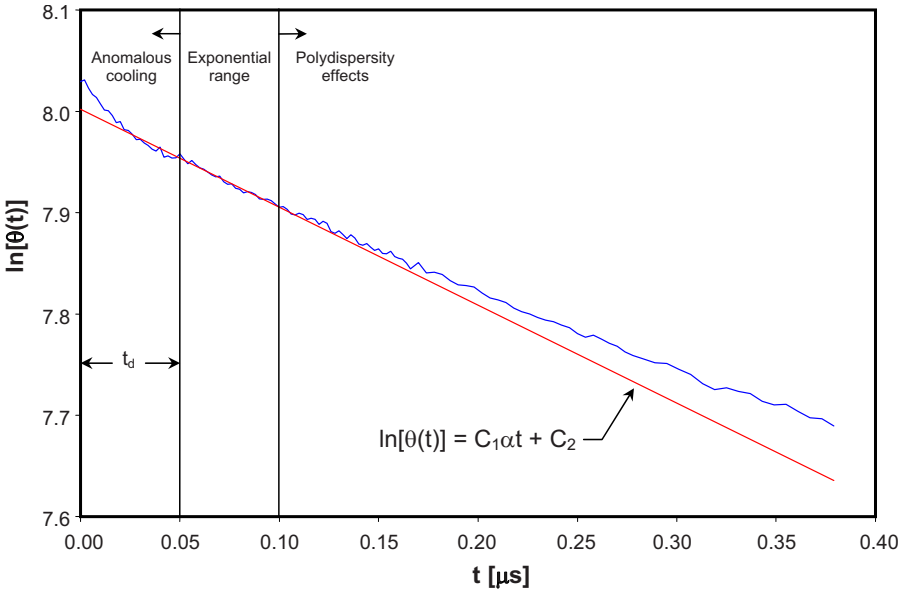

Fig. 4 Linear regression of the pyrometrically derived soot temperature

$$q_{\text{cond,max}}(T_s,T_g) = A_{\text{cond}} \frac{P_g c(T_g)}{8T_g} \frac{\gamma^*(T_g,T_s)+1}{\gamma^*(T_g,T_s)-1}[T_s(t)-T_g] \quad (5)$$

where $c(T_g)=(8k_BT_g/\pi m_g)^{1/2}$, $\gamma^*(T_g,T_s)$ is an average adiabatic constant,

$$\gamma^*(T_g,T_s) = \frac{1}{T_s-T_g}\int_{T_g}^{T_s} \frac{dT}{\gamma(T)-1} \quad (6)$$

and P_g and T_g are 101.3 kPa and 293 K, respectively. The effective heat transfer area of the soot aggregate, A_{cond}, is less than $N_p\pi d_p^2$ because primary particles on the aggregate exterior shield those on the interior from approaching gas molecules. In some previous studies [23,24], this was heuristically accounted for through an effective heat transfer area $A_{\text{cond}}=\pi D_a^2$ with a diameter derived from Eq. (2),

$$D_a = d_p(N_p/f_a)^{1/2\varepsilon_a} \quad (7)$$

based on the argument that at high Knudsen numbers an approaching gas molecule "sees" the projected area of the soot aggregate. This treatment was critically examined by Liu et al. [35], who performed discrete simulation Monte Carlo (DSMC) simulations of free-molecular heat transfer from a soot aggregate assuming a Maxwell scattering kernel. Their simulation showed that Eq. (7) underestimates A_{cond} because it does not consider gas molecules that reach the aggregate interior through scattering and partial accommodation with primary particles on the aggregate exterior, a process that depends on α. Instead, based on their DSMC simulation they recommend that Eq. (7) be used with

$$f_a = 1.04476 + 0.22329\alpha + 7.14286\times 10^{-3}\alpha^2 \quad (8)$$

and

$$2\varepsilon_a = 1.99345 + 0.30224\alpha - 0.11276\alpha^2 \quad (9)$$

which is the approach adopted here.

The thermal accommodation coefficient is found by first setting $\theta(t)=T_s(t)-T_g$ and then solving Eqs. (3) and (5) to get $\ln\theta(t)=-\alpha C_1 t+C_2$, where

$$C_1 = \frac{3}{4}\frac{A_{\text{cond}}}{\rho_s c_s N_p \pi d_p^3}\frac{P_g c(T_g)}{T_g}\frac{\gamma^*+1}{\gamma^*-1} \quad (10)$$

and C_2 is a constant of integration. The thermal accommodation coefficient is then found from a linear regression on $\ln\theta(t)$ with respect to cooling time, t, as shown in Fig. 4. (Note that defining $A_{\text{cond}}(\alpha)$ using Eqs. (7)–(9) makes this process nonlinear and iterative.)

When carrying out linear regression, one must account for the presence of a distinct nonexponential temperature decay lasting for 10–25 ns after the peak temperature that is particularly pronounced in LII experiments carried out at ambient temperatures. This commonly observed phenomenon, often referred to as "anomalous cooling," shows that particles lose sensible energy through mechanisms in addition to conduction that are not yet fully understood by the LII community. It is improper to calculate the accommodation coefficient using this data range since α defines the energy transfer by gas-surface scattering alone. After this brief period of nonexponential cooling, the effective temperature assumes an exponential decay characteristic of the Sauter mean primary particle diameter [18], indicating that the unknown heat transfer processes that cause anomalous cooling have ceased and the soot particles cool by conduction alone. At longer cooling times, however, the cooling rate becomes progressively nonexponential again due to nonuniform cooling of different-sized particles [18]. (This domain is used to determine the particle diameter distribution width in TR-LII sizing.) We avoid the nonexponential temperature decays caused by anomalous cooling and polydispersity by carrying out the linear interpolation on data sampled from 50 ns to 100 ns after the laser pulse.

Results and Discussion

The thermal accommodation coefficients are plotted in Fig. 5 as a function of the reduced mass, $\mu=m_g/m_s$, with error bars denoting three standard deviations of the mean. Molecules are classified as either monatomic, linear polyatomic, or nonlinear polyatomic; at gas temperatures in this experiment, the difference between successive rotational quanta is small enough that molecules of the latter two classes can be modeled as having two and three continuous rotational degrees of freedom, respectively.

The most prominent trend in the data is that α increases monotonically with μ for the monatomic gases, which has been observed in other types of accommodation coefficient experiments involving monatomic gases and different substrates at various temperatures including tungsten [47] (pp. 297–298) and graphite [25]. The seemingly predictable way that α varies with μ may lead one to seek a simple physical model to explain this trend, and

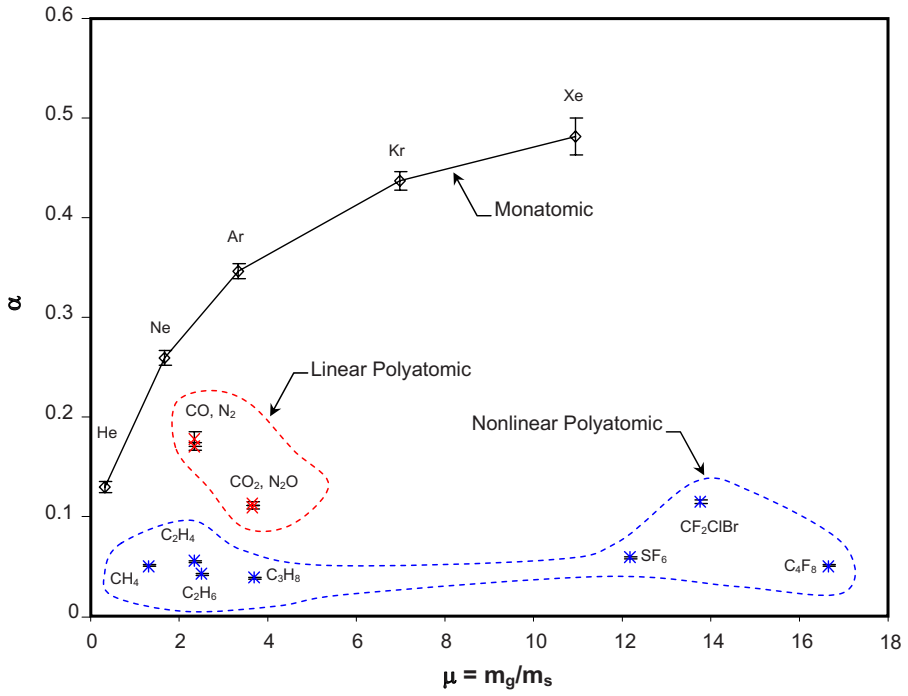

Fig. 5 Experimentally measured α_T values between soot and various gases

indeed the classical thermal accommodation literature (Refs. [47] (p. 322), [48,49]) postulates that the energy transfer efficiency in cases where $T_s \ll T_g$ and $\mu > 1$ is driven by the surface deformation rate, which in turn is a function of m_g through the gas molecular approach speed. It remains to be seen whether or not such a simple explanation applies to LII experiments involving monatomic gases.

Figure 5 also shows that α tends to decrease as the gas molecular structure becomes increasingly complex. This does not indicate less heat transfer from the soot particle; on the contrary, the additional rotational and vibrational modes of structurally complex molecules allow them to accommodate more surface energy compared to simpler molecules of similar mass, resulting in faster soot cooling. This is indicated by the product $C_1\alpha$, plotted in Fig. 6 for the different molecules; C_1 can be thought as a "thermal capacity" that depends on the specific heat of the gas and molecular collision rate with the soot surface, while α specifies the average energy transfer efficiency due to the collision dynamics. Following the definition of the thermal accommodation coefficient as it relates to free-molecular heat conduction (Refs. [45], [46] (Appen-

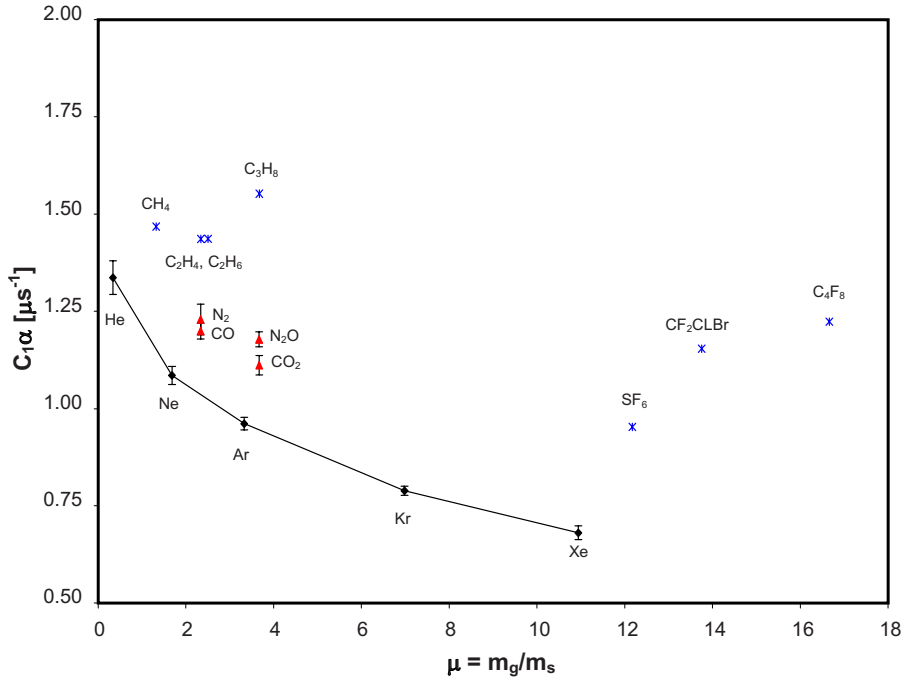

Fig. 6 Soot particle cooling rates in various gases specified by $C_1\alpha$

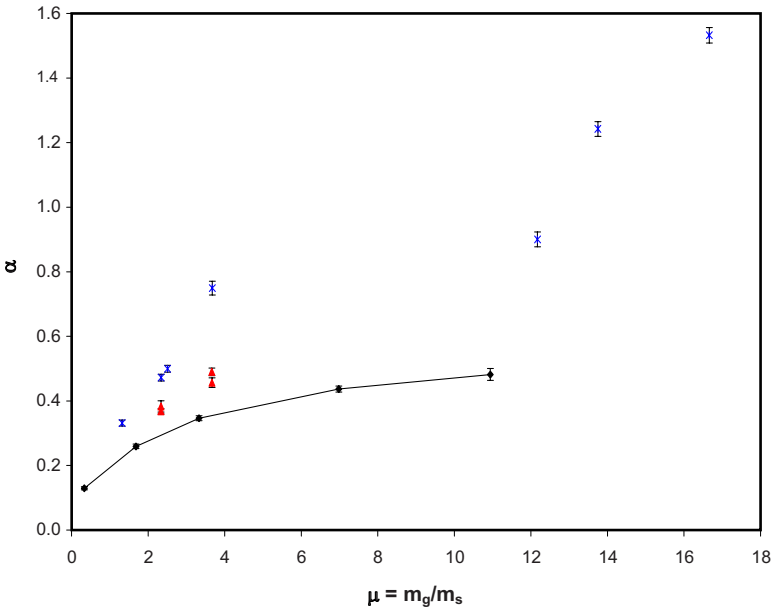

Fig. 7 Accommodation coefficients recalcuated by neglecting energy accommodation into internal energy modes (γ=5/3)

dix A), and [50]), lower α values indicate that the energy modes of the incident polyatomic molecule that should be available to accommodate surface energy as specified by $\gamma(T_g)$ or $\gamma^*(T_s,T_g)$ are not being filled as efficiently as those of the monatomic molecules. Since all gas molecules have three translational degrees of freedom and the number of internal degrees of freedom increases with increasingly complex molecular structure, a reasonable conjecture is that α is lower for the polyatomic molecules because surface energy is accommodated more readily into the translational modes over the internal modes of the incident gas molecule.

Interesting (but far from conclusive) support for this hypothesis comes from the trends of α values calculated assuming that only translational energy modes are available to accommodate surface energy, i.e., $c_v=3/2k_B$ (J/molecule K) and $\gamma=5/3$. As shown in Fig. 7 these modified accommodation coefficients lie above and generally follow the trend of $\alpha(\mu)$ observed for monatomic gases, which one would expect if the surface energy is accommodated preferentially into the translational mode of the gas molecule with a lesser amount going to the internal modes.

Preferential energy transfer to translational modes over internal modes has been measured experimentally in molecular beams of SF_6 [51] and CF_3Br [52] scattered by graphite sheets near 1000 K and predicted by a molecular dynamics simulation of a N_2 beam scattered by a platinum surface at 500 K [53]. It is also well known that energy is transferred less efficiently between the internal modes of colliding gas molecules (particularly vibrational modes) compared to translational modes, and equipartition in polyatomic gases occurs only after a large number of intermolecular collisions (see, e.g., Ref. [54]). Macroscopically this is manifested by vibrational relaxation; if the gas state is suddenly perturbed, by a shockwave for example, the vibrational temperature temporally lags behind the translational and rotational temperatures. Gas/surface scattering is another example of a potentially nonequilibrium process; one would expect equipartition to occur only if the incident gas molecules follow an adsorption/desorption channel and become "trapped" for an extended duration, whereas the well depths listed in Table 1 indicate that most incident molecules scatter after only a very brief encounter with the surface.

Thermal dissociation could complicate the interpretation of polyatomic species data, however, which happens when the vibrational modes of the gas molecule are excited by the surface atoms to the point where the gas molecule splits apart. High dissociation rates would strongly influence the energy transfer from the surface to the gas and the derived α values since these endothermic reactions would cool the soot surface. While thermal dissociation may occur to some extent given the large surface temperature, especially for the light hydrocarbons, the data suggest that this may not be happening for all gas species. In particular, the intermolecular bonds in the carbon dioxide molecule (532 kJ/mol) are much stronger than the weakest bond in nitrous oxide (167 kJ/mol), so if thermal dissociation was occurring, it would happen more frequently to N_2O molecules than to CO_2 molecules. Figure 5 shows that the α values for these two molecules are nearly equal, however, which would not be the case if thermal dissociation strongly influenced the heat conduction rate. Andersson and Pettersson [51] also concluded that thermal dissociation of SF_6 was negligible in their molecular beam experiment, albeit at a surface temperature of around 1000 K. Low dissociation rates are consistent with our hypothesis of inefficient vibrational accommodation since thermal dissociation occurs when sufficient surface energy is transferred to the vibrational modes of the gas atom to overcome the bond energy during the scattering process. (If the gas phase were in the continuum regime, on the other hand, gas molecules would be more prone to thermal dissociation due to repeated energetic intermolecular collisions near the particle surface.) Nevertheless, understanding how α may be affected by thermal dissociation requires further investigation.

Effect of Parametric Uncertainty on α

Laser-induced incandescence-based measurements of α are derived from a number of parameters, including the specific heat and density of the aerosol particle as well as its primary particle diameter, d_p, and the number of primary particles per aggregate, N_p, which both influence α through the heat transfer area, A_{cond}. Table 2 shows the normalized sensitivity of α to each of these variables for soot particles in nitrogen, expressed as $(x_0/\alpha_0)\cdot\partial\alpha/\partial x$, where x is the parameter of interest and α_0 and x_0 are the nominal values. Note that α is equally sensitive to uncertainties in ρ_s and c_s since these parameters appear together as a product in the denominator of Eq. (10); Starke et al. [13] found similar sensitivities in a LII particle sizing experiment.

Table 2 Influence of parametric uncertainty on α calculations (N_2)

Parameter	Nominal value	Normalized sensitivity	Parametric uncertainty	Uncertainty in α
ρ_s	2040 kg m^{-3}	1.179	±10% (±204 kg m^{-3})	±11.8% (±0.021)
c_s	1754 J kg^{-1} K^{-1}	1.179	±10% (±175 J kg^{-1} K^{-1})	±11.8% (±0.021)
d_p	29 nm	1.186	±20% (±5.8 nm)	±23.7% (±0.043)
N_p	200	0.025	−25%, +50% (−50, +100)	±1.3% (±0.002)
α_T	0.18			±48.6% (±0.087)

Table 2 shows that α is most sensitive to perturbations in ρ_s, c_s, and d_p. Uncertainties in these parameters are inevitable since they depend on the combustion reactants and the conditions under which the soot is formed. Given the range of values for ρ_s and c_s reported in combustion literature, we assign uncertainties of ±10% to these parameters. As noted above a detailed TEM analysis of soot sampled from the ethylene flame used in this study was performed by Tian et al. [32,34]. They found that d_p obeys an approximately normal distribution with σ=6.5 nm, so ±20% uncertainty in this variable is appropriate.

By far the most uncertain parameter is the number of primary particles per aggregate, N_p. Tian et al. [32,34] showed that N_p for in-flame soot particles is governed by a log-normal distribution, which is qualitatively consistent with Fig. 2, and the additional aggregation that the particles undergo as they travel from the flame to the LII chamber injects additional uncertainty. Fortunately, the effect of the uncertainty in N_p on α is very small, which was also noted in Kuhlmann et al. [24]. Assuming an uncertainty of ±100 primary particles per aggregate from Fig. 2 (although strictly speaking this uncertainty should be asymmetric for a log-normal distribution) results in a ±1.25% uncertainty in α. Summing these parametric uncertainties results in about ±50% uncertainty in the published α values, which is largely responsible for the wide range of LII-measured thermal accommodation coefficients reported in the literature.

Yet another major source of discrepancy between published values is how d_p and N_p are used to model A_{cond}. Almost all previous studies use the more conservative A_{cond} estimates based on the projected area, Eq. (7), which is partly why most published values are larger than those in the present work. Although we feel that accommodation coefficients obtained using Eqs. (7)–(9) more accurately reflect the energy transfer efficiency of a single scattering event compared to using the projected area, the overall trends shown in Fig. 5 apply regardless of how A_{cond} is calculated.

While some may argue that excluding anomalous cooling also introduces uncertainty into the calculated α values since it is not yet fully understood, the nonexponential temperature decay indicates heat transfer by a mechanism other than pure free-molecular conduction, so it must not be used to calculate α. Figure 8 shows that the calculated α values are affected by anomalous cooling if the entire cooling domain is used in the linear regression, but they become independent of delay time as t_d increases beyond 30 ns. Note that experimental precision also drops as t_d increases since fewer data are used in the linear regression.

These high levels of uncertainty contrast with other types of thermal accommodation coefficient experiments carried out under very controlled conditions. (It should also be noted, however, that at lower temperatures surface contamination by adsorbed gas species can be a complicating factor.) While it is impossible to replicate this level of control in a LII experiment, it would also be very difficult to obtain LII-like conditions using an experimental setup other than LII, and it is most certainly incorrect to apply accommodation coefficients obtained under different conditions (see Ref. [25], for example) directly to a LII analysis since α generally depends on T_s [26]. The most appropriate way to obtain thermal accommodation coefficients for time-resolved LII measurements is through LII.

Comparison to Previous Studies

To date there have been relatively few attempts to measure the thermal accommodation coefficient between aerosol particles and

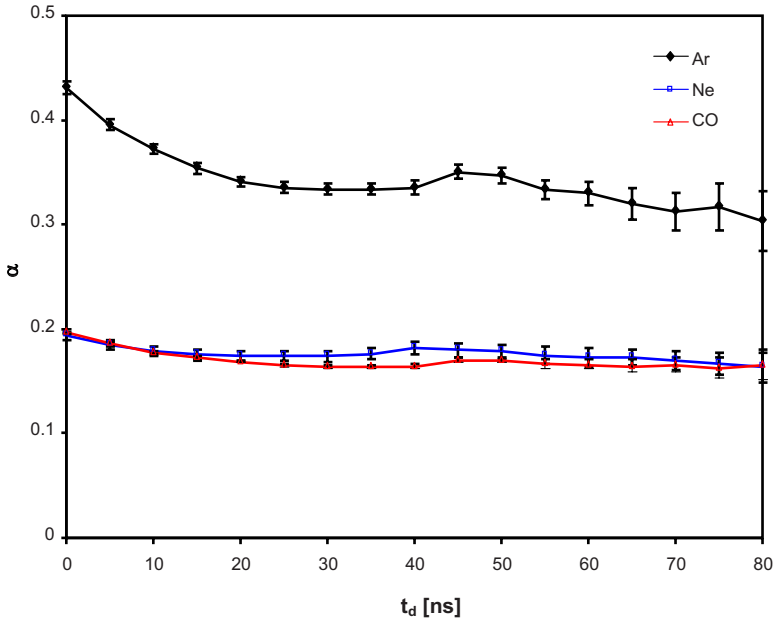

Fig. 8 Influence of delay time on measured α values

Table 3 Previously published thermal accommodation coefficients between soot/carbon black and various gases near room temperature [17,24]

Gas	α
He	0.1 [17]
Ar	0.44 [17]
CO	0.44 [17]
C_3O_2	0.51 [17]
N_2	0.43 [24]

the surrounding gas, and fewer still have been done on soot-laden aerosols at room temperature. Of particular note are studies by Eremin et al. [17], who measured α values between soot and various gases in a shock tube apparatus, and by Kuhlmann et al. [24], who found α for carbon blacks suspended in nitrogen at room temperature. The accommodation coefficients reported in these papers are reproduced in Table 3.

The results of the present study and those of Eremin et al. [17] are consistent in that they both find the thermal accommodation coefficients for argon to be three to four times that of helium. Furthermore, this study measured nearly identical accommodation coefficients for N_2 and CO, as did Kuhlmann et al. [24] and Eremin et al. [17].

On the other hand, the accommodation coefficients for polyatomic gases reported here are substantially lower than those found in these other studies. As noted above, this is partly because these studies use different density and specific heat values for soot and different definitions of A_{cond}. Kuhlman et al. [24] used a constant value of $\rho_s = 1850$ kg m^{-3} and a relationship for c_s that works out to 2039 J kg^{-1} K^{-1} at 3600 K, while the correlations of Fried and Howard [41] used here give corresponding values of 2058 kg m^{-3} and 1754 J kg^{-1} K^{-1} at the same temperature. Also, the heat transfer area by the method used by Kuhlmann et al. [24] is 31% smaller than predicted by Eqs. (7)–(9) for N_2 based on the α value found in this study. Adopting the parameters of Kuhlman et al. [24] to analyze data from this study increases α from 0.18 to 0.40 for nitrogen, which is much closer to the value of 0.44 reported in Ref. [24].

More perplexing is the fact that Eremin et al. [17] found the thermal accommodation coefficient of argon and carbon monoxide to be almost the same, while in this study α for Ar (0.36) is more than twice that for CO (0.17). This is because Eremin et al. [17] used the LII heat transfer model of Filippov et al. [55], which in turn is based on the conduction model of Williams and Loyalka [56]. This model neglects energy stored in the internal energy modes of gas molecules, however, and is only valid for monatomic gases. In using this technique to calculate α, Eremin et al. [17] found values for the polyatomic gases that are more like the ones shown in Fig. 6. If we assume $\gamma = 5/3$, then the revised accommodation coefficient for CO is now 0.35, which is very close to $\alpha_{\text{Ar}} = 0.36$. The similarity of these two values is in line with the results of Eremin et al. [17], but neglecting internal energy modes when calculating α is not consistent with the definition of the thermal accommodation coefficient given by Eq. (1).

Conclusions and Future Work

While the growing popularity of time-resolved LII is evidence of its potential attributes over other direct and laser-based particle sizing techniques, more must be known about the underlying physics of the thermal accommodation coefficient for this method to become a reliable tool for measuring size distributions in nanoparticle-laden aerosols. This is the first study to carry out LII-based α measurements for soot within a wide range of gases with the objective of inferring how gas molecular mass and structure influence thermal accommodation under these conditions. The results show that α increases monotonically with the gas molecular mass for monatomic gases and tends to be lower for more structurally complex molecules at similar molecular masses. The latter trend may be explained by preferential surface energy accommodation into the translational energy modes of the gas molecule over the internal energy modes.

While this theory seems consistent with the experimental data and the known physics of this gas/surface system, these data trends by themselves are inadequate to verify that our hypothesis is indeed correct. Ongoing research is focused on investigating thermal accommodation in LII through molecular dynamics simulations of gas/surface scattering from high-temperature graphite sheets. Preliminary results involving graphite and monatomic gases have replicated the trends and magnitudes of α in Fig. 5, and future simulations will measure how efficiently surface energy is accommodated into the rotational and vibrational modes of polyatomic gas molecules.

The most important conclusion of this work is that α varies in a predictable way with gas molecular mass and structure, which suggests that the underlying physics of gas/surface scattering for this system may become known after further study.

Acknowledgment

The authors wish to acknowledge Dr. Barry Stagg for suggesting the sampling apparatus, Reg Smith, Bob Sawchuk, and Dan Clavel for their technical support, and Dr. Dave Snelling, Patrick Mercier, Yvon Le Page, and other colleagues at the National Research Council Canada for their helpful discussions and support of this research.

Nomenclature

A_a = projected area of a soot aggregate
A_{cond} = particle heat transfer area
A_p = projected area of a primary particle
C_1 = inverse time constant, Eq. (10)
$c(T_g)$ = molecular speed
c_s = particle specific heat
D = potential well depth
d_p = primary particle diameter
F = Eucken factor
f_a = fractal prefactor
Kn = Knudsen number, $2\lambda_{\text{MFP}}/d_p$
k_B = Boltzmann's constant, 1.381×10^{-23} J molecule^{-1} K^{-1}
k_{cond} = thermal conductivity
m_g = gas molecular mass
m_s = particle atomic mass
N_p = number of primary particle per soot aggregate
Nu = Nusselt number, $q_{\text{cond}} \cdot [\pi d_p k_{\text{cond}}(T_p - T_g)]^{-1}$
P_g = gas pressure
q_{cond} = heat conduction rate
T_g = gas temperature
T_s = surface temperature
t = cooling time
t_d = sampling delay time
α = thermal accommodation coefficient
ε_a = fractal exponent
$\gamma(T)$ = adiabatic constant
$\gamma^*(T_s, T_g)$ = temperature-averaged adiabatic constant, Eq. (6)
λ_{MFP} = mean free path
μ = mass ratio, m_g/m_s
$\theta(t)$ = $T_s(t) - T_g$
ρ_s = particle density

References

[1] Jackobson, M. Z., 2004, "Climate Response of Fossil Fuel and Biofuel Soot, Accounting for Soot's Feedback to Snow and Sea Ice Albedo and Emissivity,"

J. Geophys. Res., **109**, p. D21201.
[2] Streets, D. G., Wu, Y., and Chin, M., 2006, "Two-Decadal Aerosol Trends as a Likely Explanation of the Global Dimming/Brightening Transition," Geophys. Res. Lett., **33**, pp. L15806.
[3] Maynard, A. D., and Kuempel, E. D., 2005, "Airborne Nanostructured Particles and Occupational Health," J. Nanopart. Res., **7**, pp. 587–614.
[4] Oberdörster, G., Oberdörster, E., and Oberdörster, J., 2005, "Nanotoxicology: An Emerging Discipline Evolving From Studies of Ultrafine Particles," Environ. Health Perspect., **113**, pp. 823–839.
[5] Baukal, C. E., Jr., 2000, *Heat Transfer in Industrial Combustion*, CRC, Boca Raton, FL.
[6] United States Department of Energy Office of Industrial Technologies, 2002, Industrial Combustion Technology Roadmap: A Technology Roadmap by and for the Industrial Combustion Community, U.S. DOE:OIT, Washington, DC.
[7] Grandqvist, C., Kish, L., and Marlow, W., 2004, *Gas Phase Nanoparticle Synthesis*, Kluwer, Dordrecht, The Netherlands.
[8] Melton, L. A., 1984, "Soot Diagnostics Based on Laser Heating," Appl. Opt., **13**, pp. 2201–2208.
[9] Will, S., Schraml, S., and Leipertz, A., 1995, "Two-Dimensional Soot-Particle Sizing by Time-Resolved Laser-Induced Incandescence," Opt. Lett., **20**, pp. 2342–2344.
[10] Filippov, A. V., and Roth, P., 1996, "In Situ Ultrafine Perticle Sizing by a Combination of Pulsed Laser Heatup and Particle Thermal Emission," J. Aerosol Sci., **27**, pp. 95–104.
[11] Mewes, B., and Seitzman, J. M., 1997, "Soot Volume Fraction and Particle Size Measurements With Laser-Induced Incandescence," Appl. Opt., **36**, pp. 709–717.
[12] Lehre, T., Jungfleisch, B., Suntz, R., and Bockhorn, H., 2003, "Size Distributions of Nanoscaled Particles and Gas Temperatures from Time-Resolved Laser-Induced-Incandescence Measurements," Appl. Opt., **42**, pp. 2021–2029.
[13] Starke, R., Kock, B., and Roth, P., 2003, "Nano-Particle Sizing by Laser-Induced Incandescence (LII) in a Shock Wave Reactor," Shock Waves, **12**, pp. 351–360.
[14] Dankers, S., and Leipertz, A., 2004, "Determination of Primary Particle Size Distributions From Time-Resolved Laser-Induced Incandescence Measurements," Appl. Opt., **43**, pp. 3726–3131.
[15] Kuhlmann, S.-A., Schumacher, J., Reimann, J., and Will, S., 2004, "Evaluation and Improvement of Laser-Induced Incandescence for Nanoparticle Sizing," *Proceedings of PARTEC*, Nuremburg, Germany, Mar 16–18.
[16] Kock, B. F., Kayan, C., Knipping, J., Orthner, H. R., and Roth, P., 2005, "Comparison of LII and TEM Sizing During Synthesis of Iron Particle Chains," Proc. Combust. Inst., **30**, pp. 1689–1697.
[17] Eremin, A. V., Gurentsov, E. V., Hofmann, M., Kock, B. F., and Schulz, C., 2006, "TR-LII for Sizing of Carbon Particles Forming at Room Temperature," Appl. Phys. B: Lasers Opt., **83**, pp. 449–454.
[18] Liu, F., Stagg, B. J., Snelling, D. R., and Smallwood, G. J., 2006, "Effects of Primary Soot Particle Size Distribution on the Temperature of Soot Particles Heated by a Nanosecond Pulsed Laser in an Atmospheric Laminar Diffusion Flame," Int. J. Heat Mass Transfer, **49**, pp. 777–788.
[19] Bougie, B., Ganippa, L. C., van Vilet, A. P., Meerts, W. L., Dam, N. J., and ter Meulen, J. J., 2007, "Soot Particulate Size Characterization in a Heavy-Duty Diesel Engine for Different Engine Loads by Laser-Induced Incandescence," Proc. Combust. Inst., **31**, pp. 685–691.
[20] Gurentsov, E., Eremin, A., and Schulz, C., 2007, "Formation of Carbon Nanoparticles by the Condensation of Supersaturated Atomic Vapor Obtained by the Laser Photolysis of C_3O_2," Kinetics and Catalysts, **48**, 194–203.
[21] Maxwell, J. C., 1879, "On Stresses in Rarefied Gases Arising from Inequalities of Temperature," Philos. Trans. R. Soc. London, **170**, pp. 231–256.
[22] Knudsen, M., 1911, "Die Molekulare Wärmeleitung der Gase und der Akkommodationskoeffizient," Ann. Phys., **339**(4), pp. 593–656.
[23] Snelling, D. R., Liu, F., Smallwood, G. J., and Gulder, O. L., 2004, "Determination of the Soot Absorption Function and Thermal Accommodation Coefficient Using Low-Fluence LII in a Laminar Coflow Ethylene Diffusion Flame," Combust. Flame, **136**, pp. 180–190.
[24] Kuhlmann, S.-A., Reimann, J., and Will, S., 2006, "On Heat Conduction Between Laser-Heated Nanoparticles and a Surrounding Gas," J. Aerosol Sci., **37**, pp. 1696–1716.
[25] Yasumoto, I., 1987, "Accommodation Coefficients of Helium, Neon, Argon, Hydrogen, and Deuterium on Graphitized Carbon," J. Phys. Chem., **91**, pp. 4298–4301.
[26] Saxena, S. C., and Joshi, R. K., 1981, *Thermal Accommodation and Adsorption Coefficients of Gases*, McGraw-Hill, New York.
[27] Snelling, D. R., Smallwood, G. J., Liu, F., Gülder, Ö. L., and Bachalo, W. D., 2005, "A Calibration-Independent Laser-Induced Incandescence Technique for Soot Measurement by Detecting Absolute Light Intensity," Appl. Opt., **44**, pp. 6773–6785.
[28] Köylü, Ü. Ö., and Faeth, G. M., 1992, "Structure of Overfire Soot in Buoyant Turbulent Diffusion Flames at Long Residence Times," Combust. Flame, **82**, pp. 140–156.
[29] Megaridis, C. M., and Dobbins, R. A., 1990, "Morphological Description of Flame-Generated Soot," Combust. Sci. Technol., **71**, pp. 95–109.
[30] Dobbins, R. A., and Megaridis, C. M., 1987, "Morphology of Flame-Generated Soot as Determined by Thermophoretic Sampling," Langmuir, **3**, pp. 254–259.
[31] Köylü, Ü. Ö., McEnally, C. S., Rosner, D. E., and Pfefferle, L. D., 1997, "Simultaneous Measurement of Soot Volume Fraction and Particle Size/Microstructure in Flames Using a Thermophoretic Sampling Technique," Combust. Flame, **110**, pp. 494–507.
[32] Tian, K., Thomson, K. A., Liu, F., Snelling, D. R., Smallwood, G. J., and Wang, D., 2004, "Distribution of the Number of Primary Particles of Soot Aggregates in a Nonpremixed Laminar Flame," Combust. Flame, **138**, pp. 195–198.
[33] Köylü, Ü. Ö., Faeth, G. M., Farias, T. L., and Carvalho, M. G., 1995, "Fractal and Projected Structure Properties of Soot Aggregates," Combust. Flame, **100**, pp. 621–633.
[34] Tian, K., Thomson, K. A., Liu, F., Snelling, D. R., Smallwood, G. J., and Wang, D., 2004, "Determination of the Morphology of Soot Aggregates Using the Relative Optical Density Method for the Analysis of TEM Images," Combust. Flame, **144**, pp. 782–791.
[35] Liu, F., Yang, M., Hill, F. A., Snelling, D. R., and Smallwood, G. J., 2006, "Influence of Polydisperse Distribution of Both Primary Particle and Aggregate Size on Soot Temperature in Low-Fluence LII," Appl. Phys. B: Lasers Opt., **83**, pp. 383–395.
[36] Michelsen, H. A., Liu, F., Kock, B. F., Blandh, H., Carwath, M., Drier, T., Hadef, R., Hofmann, M., Reimann, J. Will, S., Bengtsson, P.-E., Bockhorn, H., Foucher, F., Geigle, K.-P., Mounaïm-Rousselle, C., Schulz, C., Stirn, R., Tribalet, B., and Suntz, R., 2007, "Modeling Laser-Induced Incandescence of Soot: A Summary and Comparison of LII Models," Appl. Phys. B: Lasers Opt., **87**, pp. 503–521.
[37] Schulz, C., Kock, B. F., Hofmann, M., Michelsen, H., Will, S., Bougie, B., Suntz, R., and Smallwood, G., 2006, "Laser-Induced Incandescence: Recent Trends and Current Questions," Appl. Phys. B: Lasers Opt., **83**, pp. 333–354.
[38] Michelsen, H. A., 2003, "Understanding and Predicting the Temporal Response of Laser-Induced Incandescence From Carbonaceous Particles," J. Chem. Phys., **118**, pp. 7012–7045.
[39] Vidali, G., Ihm, G., Kim, H. Y., and Cole, M. W., 1991, "Potentials of Physical Adsorption," Surf. Sci. Rep., **12**, pp. 133–181.
[40] Yoder, G. D., Diwakar, P. K., and Hahn, D. W., 2005, "Assessment of Soot Particle Vaporization Effects During Laser-Induced Incandescence With Time-Resolved Light Scattering," Appl. Opt., **44**, pp. 4211–4219.
[41] Fried, L. E., and Howard, W. M., 2000, "Explicit Gibbs Free Energy Equation of State Applied to the Carbon Phase Diagram," Phys. Rev. B, **61**, pp. 8734–8743.
[42] McBride, B. J., Gordon, S., and Reno, M. A., 1993, "Coefficients for Calculating Thermodynamic and Transport Properties of Individual Species," NASA Office of Management, Washington, DC, NASA Technical Memorandum No. 4513.
[43] Burcat, A., and Ruscic, B., 2005, "Third Millennium Ideal Gas and Condensed Phase Thermochemical Database for Combustion With Updates From Active Thermochemical Tables," Argonne National Laboratory Report No. ANL-05-20 and Technion Report No. TAE 960.
[44] Keestin, J., Knierim, K., Mason, E. A., Najafi, B., Ro, S. T., and Waldman, M., 1984, "Equilibrium and Transport Properties of the Noble Gases and Their Mixtures at Low Density," J. Phys. Chem. Ref. Data, **13**, pp. 229–239.
[45] Filippov, A. V. and Rosner, D. E., 2000, "Energy Transfer Between an Aerosol Particle and Gas at High Temperature Ratios in the Knudsen Transition Regime," Int. J. Heat Mass Transfer, **43**, pp. 127–138.
[46] Liu, F., Daun, K. J., Snelling, D. R., and Smallwood, G. J., 2006, "Heat Conduction From a Spherical Nano-Particle: Status of Modeling Heat Conduction in Laser-Induced Incandescence," Appl. Phys. B: Lasers Opt., **83**, pp. 355–382.
[47] Goodman, F. O., 1974, "Thermal Accommodation," Prog. Surf. Sci., **5**, pp. 261–375.
[48] Gilbey, D. M., 1962, "A Re-Examination of Thermal Accommodation Coefficient Theory," J. Phys. Chem. Solids, **23**, pp. 1453–1461.
[49] Trilling, L. M., 1970, "The Interaction of Monatomic Inert Gas Molecules With a Continuous Elastic Solid," Surf. Sci., **21**, pp. 337–365.
[50] Kennard, E. H., 1938, *Kinetic Theory of Gases*, McGraw-Hill, New York, pp. 311–327.
[51] Andersson, M. B., and Pettersson, J. B. C., 1996, "Vibrational Excitation of SF_6 Scattering From Graphite," Chem. Phys. Lett., **250**, pp. 555–559.
[52] Andersson, M. B., Pettersson, J. B. C., and Marković, N., 1997, "Vibrational Excitation of CF_3Br Scattering From Graphite," Surf. Sci. Lett., **384**, pp. L880–L885.
[53] Blömer, J. and Beylich, A. E., 1999, "Molecular Dynamics Simulation of Energy Accommodation of Internal and Translational Degrees of Freedom at Gas-Surface Interfaces," Surf. Sci., **423**, pp. 127–133.
[54] Bird, G. A., 1994, *Molecular Gas Dynamics and the Direct Simulation of Gas Flows*, Oxford University Press, Oxford, UK, p. 28.
[55] Filippov, A. V., Markus, M. W., and Roth, P., 1999, "In-Situ Characterization of Ultrafine Particles by Laser-Induced Incandescence: Sizing and Particle Structure Determination," J. Aerosol Sci., **30**, pp. 71–87.
[56] Williams, M. M. R., and Loyalka, S. K., 1991, *Aerosol Science: Theory and Practice*, Permagon, Oxford, UK, pp. 308–309.

A Fixed-Angle Dynamic Heat Spreading Model for (An)Isotropic Rear-Cooled Substrates

Bjorn Vermeersch[1]
e-mail: bjorn.vermeersch@elis.ugent.be

Gilbert De Mey
e-mail: demey@elis.ugent.be

Department of Electronics and Information Systems,
Ghent University,
Sint Pietersnieuwstraat 41,
9000 Gent, Belgium

During a period of almost 40 years already, various fixed-angle heat spreading models have been developed in the literature. These models are commonly used by thermal engineers as approximations for the thermal steady-state resistance of a heat source on a rear-cooled substrate. In this paper, an extension of these models to dynamic (time-dependent) phenomena is proposed. The heat dissipated by a square source (side a) is assumed to spread out into the substrate (thickness b) under an angle ϕ. An analytical solution for the complex thermal impedance $Z_{th}(j\omega)$ in phasor notation is derived. The obtained expression, in which ϕ is used as a fitting parameter, is compared with accurate analytical results. A very good agreement is observed (average relative error less than 6%) for a wide range of the normalized thickness $\lambda = b/a$. A compact expression for the optimal heat spreading angle as a function of λ is given. Also the temperature response to a heat power step is investigated, and a simple formula for the thermal rise time is provided. Finally, the model can be easily extended to anisotropic media, which often appear in electronic packaging applications. Overall the proposed model allows a thermal designer to make quick yet accurate estimations about the dynamic behavior of the device. [DOI: 10.1115/1.2976557]

Keywords: thermal conduction, dynamic, heat spreading, fixed-angle model, microelectronics, anisotropy

1 Introduction

In early stages of the thermal design process, sophisticated simulators are—despite their high accuracy—often impractical. On the one hand, analytical methods based on infinite series require the summation of a large number of terms. Each of them can depend on the boundary conditions, leading to complicated expressions and substantial amounts of computer time. Finite element simulations, on the other hand, can be time-consuming as well and provide very little physical insight. It is, for instance, not straightforward to assess the impact of changing one or more design parameters (such as substrate material or its dimensions) on the thermal behavior.

To address this situation, various methods have been reported to approximate the thermal resistance of a power dissipating element on a rear-cooled substrate. One commonly used and well known approach is that of the fixed-angle heat spreading [1–10]. Such models provide quick estimations for the thermal resistance with an accuracy around 5–20%, which is reasonable for prototyping purposes. The key assumption is that the heat is spreading with a constant angle ϕ from the heat source. In other words, the heat flow is assumed to be confined into a pyramidal body. Early reports about this method go back to almost 40 years ago [1]. However, as stated in Ref. [10], no one seems to know the exact origin of the heat spreading angle concept. It seems to have started to live its own life among the engineering community. Progress has been continuously presented, even in more recent history [9].

Several variants of the model can be distinguished. A spreading angle ϕ=45 deg is the most common choice. This reflects the isotropy (as there is no preferential direction the heat should spread equally in vertical and lateral directions) and also leads to simple expressions. Nevertheless, a value of 32.5 deg is sometimes used as this provides the best overall fit [3,5]. Other authors proposed a spreading angle depending on the geometrical parameters to improve accuracy [6,8,9]. The analysis is usually carried out for square heat sources; however, also rectangular [6–8] and circular [4,8] shapes were taken into account. Further features include the modeling of laterally limited substrates [8,9], a stack of several substrate layers [2,4,9], and multiple heat sources [2,7].

Various other models, not using a fixed-angle approach, are also available to calculate the thermal spreading resistance. We have provided an exemplary but by no means exhaustive list of such works in the bibliography [11–15]. These models are more advanced than fixed-angle ones, in the sense that they pose substantially less restrictions concerning the boundary conditions and geometrical layout. Namely, they can easily account for convective cooling, and some of them allow to handle heat sources and substrates with nonunity aspect ratios [11–13].

The cited models, both fixed-angle and more advanced approaches, however all have a limitation in common. Namely, they are strictly limited to steady-state conditions; in other words, they provide just the thermal resistance. In the recent history, dynamic (time-dependent) thermal characterization is gaining more and more importance. This is particularly interesting with respect to the reliability of the devices [16]. As far as we are aware, only one paper related to a dynamic heat spreading model has been published [17]. The dynamic thermal behavior of an electronic package is hereby represented with a lumped equivalent network. The estimation of the thermal resistance and capacitance for each layer is based on a geometrical heat spreading model.

In this contribution, we will limit ourselves to a single substrate layer. In turn, however, more of the physics of the heat spreading can be included in the model, by means of analytical derivations

[1]Corresponding author.

Contributed by the Heat Transfer Division of ASME for publication in the JOURNAL OF HEAT TRANSFER. Manuscript received October 2, 2007; final manuscript received May 7, 2008; published online September 23, 2008. Review conducted by Roger Schmidt.

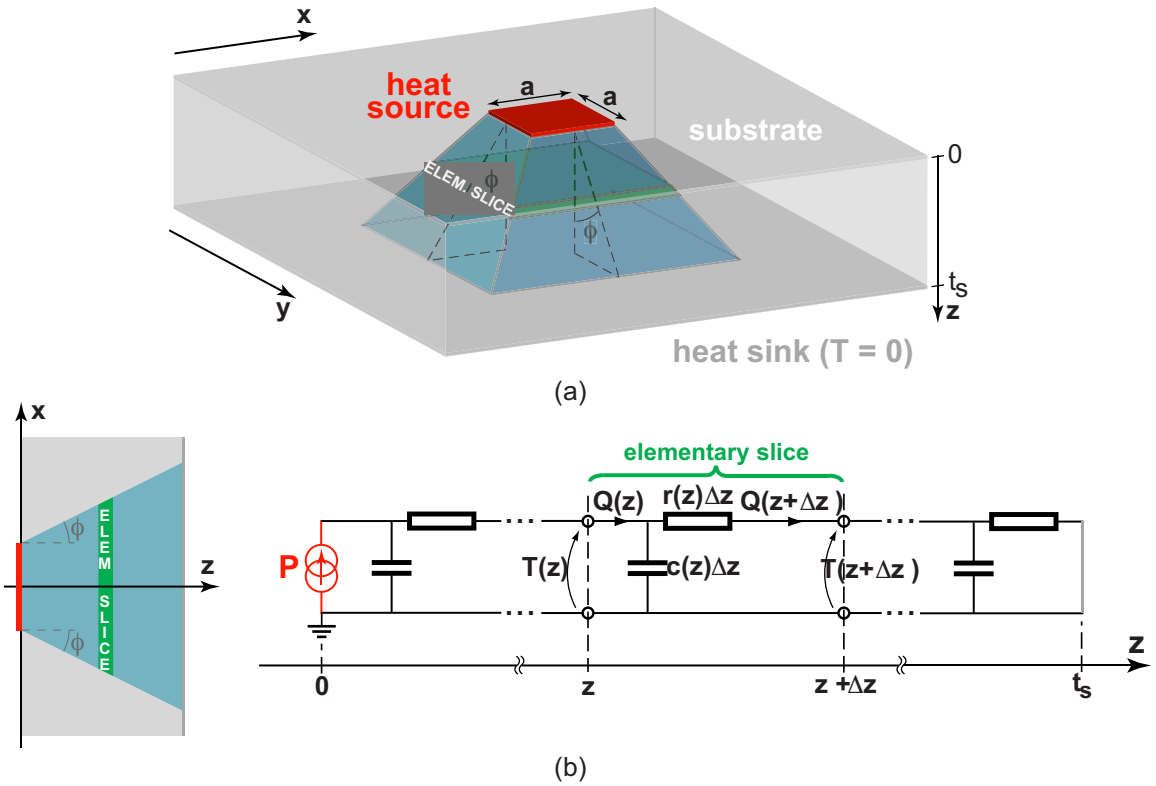

Fig. 1 Fixed-angle heat spreading model for a square heat source on a rear-cooled substrate: (*a*) geometry; (*b*) distributed network of the pyramidal body (phasor notation)

instead of an approximative *RC*-network. First, a closed form solution for the complex thermal impedance (in phasor notation) of the pyramidal body is derived. Comparison with accurate simulation results, based on infinite series expansion, shows a very good agreement. The optimum value for the spreading angle ϕ is given as a function of the normalized thickness of the substrate. The response to a heat power step (heating curve) is investigated, leading to a compact expression for the thermal rise time. It is demonstrated that the model performs significantly better compared with the lumped model approach found in literature. Finally, the model can be easily modified in order to handle anisotropic substrates. Cases where the thermal conductivity differs in vertical and lateral directions, typically occurring in heat spreader and sink applications, are investigated. With this extension, the model allows for rapid prototyping of the dynamic behavior of the substrate, even for advanced contemporary materials.

2 Model Definition

Let us consider a square heat source (side a), dissipating a power P, on a substrate with thickness b. The substrate material is characterized by a thermal conductivity k and a specific heat per unit volume C_v. The rear side of the substrate is perfectly cooled (ambient temperature $T=0$). Since we will establish a thermal characterization in the frequency domain, setting a nonzero isothermal boundary condition would correspond to an ambient whose temperature oscillates sinusoidally with the same frequency as the heat source. This being clearly nonphysical, only $T=0$ can be used. An arbitrary isothermal ambient $T=T_a$ is, however, easily accounted for by offsetting the temperature response in the time domain. We assume that while the heat is flowing in the z direction from the source to the sink, it spreads out under a fixed-angle ϕ in both the x and y directions (Fig. 1(*a*)).

It is well known that the time-dependent diffusion of heat can be modeled by a distributed *RC*-network. A representation of the pyramidal heat flow body together with the heat dissipation ("current source") and cold plate ("short circuit") is shown in Fig. 1(*b*). The analysis of the network will be carried out in the frequency domain using phasor notation: $\partial/\partial t \rightarrow j\omega$ with ω the angular frequency of the heat source. An elementary horizontal slice of the pyramid at depth z with thickness Δz is characterized by a capacitance $c(z)\Delta z$ and resistance $r(z)\Delta z$, in which

$$r(z) = \frac{1}{k \cdot A(z)}, \quad c(z) = C_v \cdot A(z) \tag{1}$$

where $A(z)$ is the local cross section area of the heat flow path

$$A(z) = (a + 2z \tan \phi)^2 \tag{2}$$

It should be noted that the total thermal impedance Z_{th} cannot be determined by direct integration, because the capacitances are grounded (thus not connected to the next slice). A differential equation will be used instead. For the sake of simplicity, we will introduce some short notations:

$$r_0 = \frac{1}{ka^2}, \quad c_0 = C_v a^2, \quad \alpha = \frac{2 \tan \phi}{a} \tag{3}$$

Equation (1) can now be written as

$$r(z) = \frac{r_0}{(1 + \alpha z)^2}, \quad c(z) = c_0(1 + \alpha z)^2 \tag{4}$$

Expressing the voltage and current laws for the elementary section marked in Fig. 1(*b*) and taking the limit $\Delta z \rightarrow 0$ yield differential equations for the heat flow and temperature distributions:

$$-\frac{dQ}{dz} = j\omega c(z)T(z) \quad \text{and} \quad -\frac{dT}{dz} = r(z)Q(z) \tag{5}$$

After some manipulation and using Eq. (4), this leads to

$$\frac{d^2T}{dz^2} + \frac{2\alpha}{1+\alpha z}\frac{dT}{dz} - \gamma T(z) = 0 \quad \text{with} \quad \gamma = \frac{j\omega C_v}{k} \tag{6}$$

We note here that for a rectangular heat source, the factor $(1+\alpha z)^2$ in Eq. (4) would be replaced by $(1+\alpha_1 z)(1+\alpha_2 z)$ with $\alpha_1 \neq \alpha_2$. The resulting differential equation does not take the form (6) and can no longer be solved analytically. For this reason, only a square shaped source is considered.

The general solution of Eq. (6) is found to be

$$T(z) = C_1 \frac{\cosh(\sqrt{\gamma}z)}{1+\alpha z} + C_2 \frac{\sinh(\sqrt{\gamma}z)}{1+\alpha z} \tag{7}$$

The coefficients C_1 and C_2 can be determined by applying the boundary conditions. The heat sink at the bottom $z=b$ and the power dissipation on the top $z=0$ imply, respectively,

$$T(z=b) = 0, \quad Q(z=0) = -\frac{1}{r(0)}\left.\frac{dT}{dz}\right|_{z=0} = P \tag{8}$$

By combination of Eq. (7) with Eq. (8), the temperature distribution is obtained. The thermal impedance is by definition nothing else than the source temperature divided by the dissipated power:

$$Z_{\text{th}} = \frac{T(z=0)}{P} = \frac{r_0}{\alpha + \sqrt{\gamma}\cdot \text{cotanh}(\sqrt{\gamma}b)} = \frac{1/ka^2}{\frac{2\tan\phi}{a} + \sqrt{\frac{j\omega C_v}{k}}\text{cotanh}\left(\sqrt{\frac{j\omega C_v}{k}}b\right)} \tag{9}$$

The steady-state resistance R_{th} is found by taking the limit $\omega \to 0$ and is given by

$$R_{\text{th}} = \frac{r_0 \cdot b}{1+\alpha b} \tag{10}$$

One can verify that this is the same result as obtained by direct integration of

$$dR_{\text{th}} = \frac{dz}{kA(z)} = \frac{dz}{k(a+2z\tan\phi)^2} \tag{11}$$

from $z=0$ to $z=b$.

In order to make further results generally applicable (not depending on the choice of substrate material), the impedance, as well as the frequency scale, is normalized. Introducing $\lambda = b/a$ finally gives

$$\tilde{Z}_{\text{th}} = \frac{Z_{\text{th}}}{r_0 b} = \frac{1}{2\lambda\tan\phi + \sqrt{j\tilde{\omega}}\cdot\text{cotanh}(\sqrt{j\tilde{\omega}})} \quad \text{with} \quad \tilde{\omega} = \frac{\omega}{\omega_0} \tag{12}$$

$$\omega_0 = \frac{k}{C_v b^2}$$

It is clear that the normalized impedance $\tilde{Z}_{\text{th}}$ is a function of the normalized frequency $\tilde{\omega}$. Apart from the normalized substrate thickness λ, no geometrical or material parameters are left in the normalized form $\tilde{Z}_{\text{th}}(\tilde{\omega})$. The spreading angle ϕ can be used as a fitting parameter, as shown later. The results for a specific substrate layout and material, obtained by denormalizing the model output, will obviously still be dependent on the particular values for k, C_v, and b, as can be seen from the expression for ω_0 in Eq. (12).

3 Exact Calculation of $Z_{\text{th}}(j\omega)$

In order to check whether the expression (12) provided by the fixed-angle model is a good approximation, accurate results for the thermal impedance are needed. The 3D heat equation (in phasor notation)

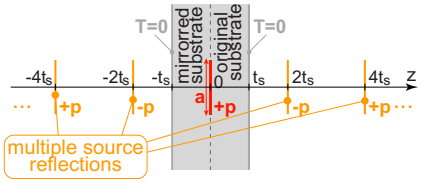

Fig. 2 Heat source sandwiched between two identical rear-cooled substrates for calculation of temperature distribution (cross section view)

$$k\nabla^2 T(\vec{r}) - j\omega C_v T(\vec{r}) = 0 \tag{13}$$

must be solved in the substrate. To achieve this, a slightly modified geometry is considered: The source is sandwiched between two identical rear-cooled substrates (Fig. 2, shaded area). For symmetrical reasons, the origin of the coordinate axes is chosen at the center of the heat source. Due to the symmetry in the z direction, the temperature distribution is exactly one-half as compared with the original problem.

For a point shaped source in $\vec{r}'$ dissipating 1 W in the free 3D space, the solution of Eq. (13) is known in closed form. This so called Green's function is given by [18]

$$G = \frac{1}{4\pi kR}\exp\left(-\sqrt{\frac{j\omega C_v}{k}}R\right) \quad \text{where} \quad R = \sqrt{(x-x')^2+(y-y')^2+(z-z')^2} \tag{14}$$

The temperature distribution generated by a distributed source can be obtained by integrating Green's function over the source area. In our case, we are, however, not dealing with free space: The geometry is limited by horizontal planes at $z=\pm b$, where $T=0$. These boundary conditions can be taken into account by introducing an infinite number of image sources (multiple reflection technique). The location (z coordinate) and sign of the image sources are as follows: $\pm 2b\ominus$, $\pm 4b\oplus$, $\pm 6b\ominus$, … (Fig. 2). The temperature in a point $(x,y,0)$ of the source is then given by

$$T(x,y,0) = 2\frac{P}{a^2}\int_{-a/2}^{a/2}\int_{-a/2}^{a/2} H(x,x',y,y')dx'dy' \tag{15}$$

where

$$H(x,x',y,y') = G(z-z'=0) + 2\sum_{n=1}^{\infty}(-1)^n G(z-z'=2nb) \tag{16}$$

The leading factor 2 in Eq. (15) is needed because (as mentioned before) the temperature for the original configuration is exactly twice the one found for the structure of Fig. 2.

Equation (15) provides an exact fully analytical expression for the temperature distribution in the heat source. Practical evaluation, however, requires truncation of the series (16), leading to an approximate value. Special care is taken to ensure convergence. The series was truncated when the relative iteration change of both real and imaginary parts of H was smaller than a preset value (10^{-9}). For thin substrates (small λ) and low frequencies, Green's function G is only weakly damped. In those cases, more than 2000 image sources were needed to obtain a convergent value for H. Precautions are also needed for numerical evaluation of the integral (15) because the first term in H has a singularity in the point $x=x', y=y'$. This can be treated analytically [7], but further details will be omitted here.

4 Results and Discussion

4.1 Thermal Impedance. A heat source ($a=100$ μm) on a silicon substrate ($k=160$ W/m K, $C_v=1.784\times10^6$ J/m^3 K) was

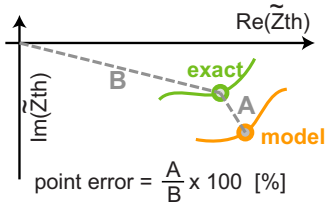

Fig. 3 Interpretation of the error function $e(\phi)$

divided into a 10×10 grid of identical squares. In each of the 100 center points, Eq. (15) was evaluated numerically yielding a detailed image of the temperature distribution inside the heat source. For the calculation of the thermal impedance, the average source temperature is used, as this is more representative for experimental measurements. The analysis was carried out over a large frequency range (with 10 points per decade) and for various substrate thicknesses ($\lambda=0.1,0.2,0.3,\ldots,0.9,1,2,5,$ and 10). The thermal impedance was normalized using the aforementioned r_0 and ω_0. Hence the fact that silicon parameters were used for the calculations is not a limiting factor: The normalized result is valid for any other substrate material.

These accurate calculation results can now be compared with the proposed fixed-angle heat spreading model (12), by means of the following error function:

$$e(\phi)=\frac{1}{N}\sum_{i=1}^{N}\frac{|\tilde{Z}_{\text{exact}}^{(i)}-\tilde{Z}_{\text{model}}^{(i)}(\phi)|}{|\tilde{Z}_{\text{exact}}^{(i)}|} \tag{17}$$

The superscript (i) denotes "evaluated in the ith frequency" and N is the number of calculated impedance points. Figure 3 shows a geometrical interpretation of the error function: e is a measure for the average relative deviation of each point between the model prediction ($\tilde{Z}_{\text{model}}$) and the actual value (calculation results $\tilde{Z}_{\text{exact}}$).

The error is clearly a function of the heat spreading angle ϕ hence the latter can be used as a fitting parameter. A computer program was written to sweep ϕ in steps of 0.1 deg and calculate the corresponding error $e(\phi)$. Some of the resulting error curves are shown in Fig. 4.

Each of the curves is showing a clear dip, indicating that there is an optimum value ϕ_{opt}, which minimizes the fitting error. The optimal heat spreading angle as a function of λ together with the corresponding error is presented in Fig. 5.

The proposed model is very suitable for thin substrates (error less than 3% for $\lambda\leq1$) but gives a good approximation for thicker substrates as well (largest error was observed for $\lambda=5$ and is only 5.39%). The ϕ_{opt} values can be fitted very well by

$$\phi_{\text{opt}}=\begin{cases}\lambda\leq1, & 5.86\ln(\lambda)+40.4\\ \lambda\geq1, & 46.45-6.048\lambda^{-0.969}\end{cases} \tag{18}$$

This function is also presented in Fig. 5 (solid line). The usefulness of Eq. (18) was tested by estimating ϕ_{opt} for $\lambda=0.14$, 1.4, and 7. The predicted and actual values are (28.9 deg, 28.9 deg), (42.1 deg, 41.9 deg), and (45.5 deg, 45.5 deg) respectively.

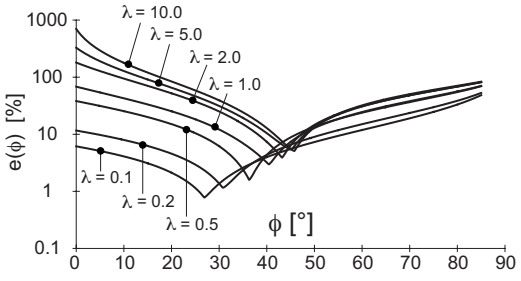

Fig. 4 Average relative fitting error as function of heat spreading angle ϕ for various substrate thicknesseses

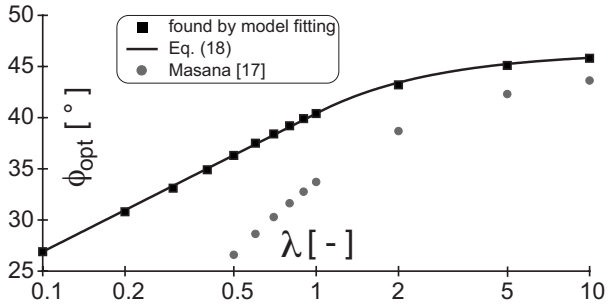

λ [-]	0.1	0.2	0.3	0.4	0.5	0.6	0.7
ϕ_{opt} [°]	26.9	30.8	33.1	34.9	36.3	37.5	38.4
$e(\phi_{\text{opt}})$ [%]	0.78	1.16	1.37	1.33	1.60	1.90	2.19

λ [-]	0.8	0.9	1	2	5	10
ϕ_{opt} [°]	39.2	39.9	40.4	43.2	45.1	45.8
$e(\phi_{\text{opt}})$ [%]	2.08	2.75	2.99	3.92	5.39	5.11

Fig. 5 Optimum heat spreading angle and corresponding average relative fitting error as function of normalized substrate thickness

A straightforward way to visualize the accuracy of the proposed model is to compare the normalized thermal impedance curves directly with those obtained by analytical calculation (see Fig. 6). A so called Nyquist representation was used, i.e., a plot of $\text{Im}(\tilde{Z}_{\text{th}}(j\tilde{\omega}))$ versus $\text{Re}(\tilde{Z}_{\text{th}}(j\tilde{\omega}))$ with $\tilde{\omega}$ as a parameter. Clearly, the agreement is very good. An increasing deviation is found for very thick substrates, as already observed before.

4.2 Step Response. Although the thermal impedance provides a compact and complete dynamic characterization, it is rather abstract because it is a frequency domain representation. Additional time domain information can provide more direct insight into the transient behavior and might be valuable for practical design. For this purpose, the response of the device is investigated when the heat source is suddenly switched on (power step). The resulting temperature as function of time can be determined by inverse Fourier transform. For a dissipation of P_0 watt, we have

$$T(t)=\int_{-\infty}^{\infty}Z_{\text{th}}(f)P(f)\exp(j2\pi ft)\text{d}f \quad \text{with} \quad P(f)=\frac{P_0}{2}\delta(f)+\frac{P_0}{j2\pi f} \tag{19}$$

in which $f=\omega/2\pi$ and δ is the Dirac impulse function. After some manipulation and using Eq. (12), we obtain

$$\tilde{T}(\tilde{t})=\frac{1}{2}+\frac{1+2\lambda\tan\phi}{\pi}\times\int_0^{\infty}\text{Im}\left[\frac{\exp(j2\pi\tilde{f}\tilde{t})}{\tilde{f}\cdot[2\lambda\tan\phi+\sqrt{j\tilde{f}}\cdot\text{cotanh}(\sqrt{j\tilde{f}})]}\right]d\tilde{f} \tag{20}$$

where both the temperature and time scales have been normalized:

$$\tilde{T}=\frac{T}{T_0},\quad \tilde{t}=\frac{t}{t_0},\quad T_0=\frac{P_0r_0b}{1+2\lambda\tan\phi},\quad t_0=\frac{2\pi C_vb^2}{k} \tag{21}$$

As can be seen from t_0, the time scale is inversely proportional to the ratio k/C_v (i.e., the diffusivity of the material), as could be expected. Equation (20) was evaluated numerically for various λ values, where each time $\phi=\phi_{\text{opt}}(\lambda)$ is introduced. Some of the

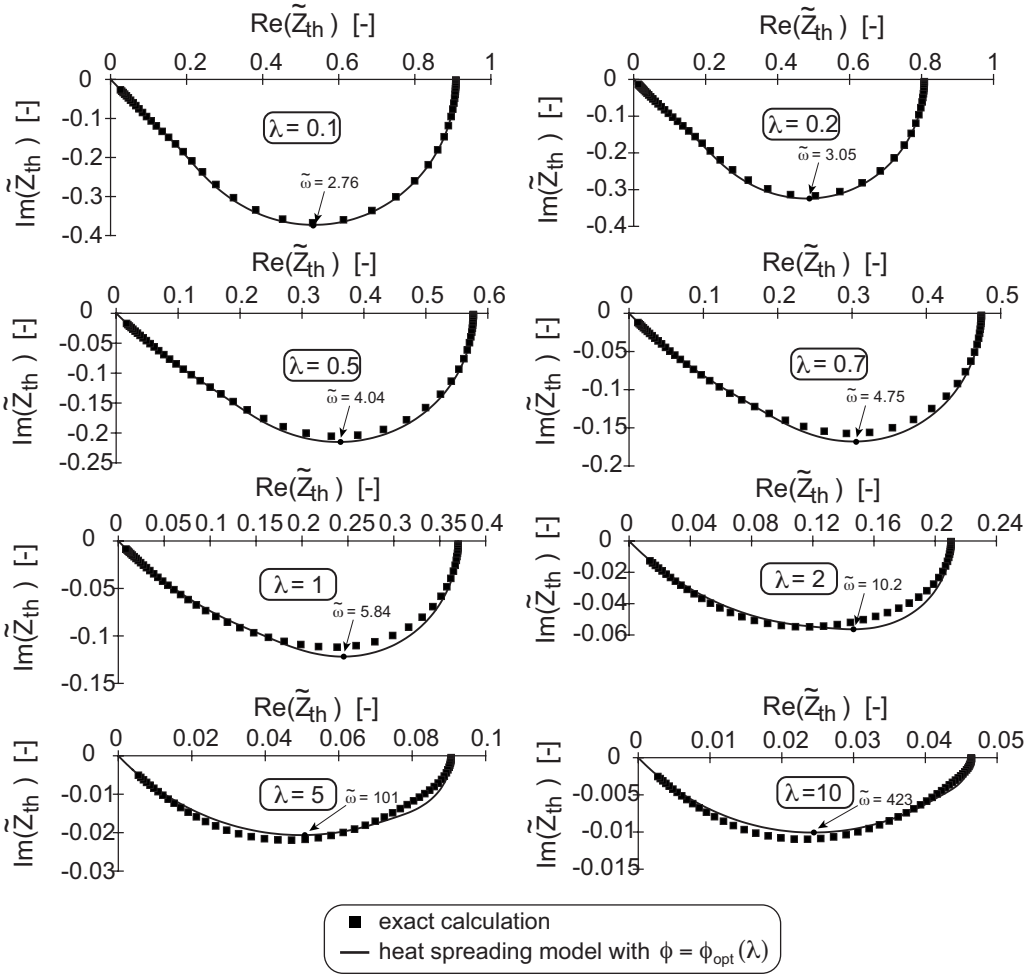

Fig. 6 Normalized thermal impedance curves for various substrate thicknesses

resulting heating curves are presented in Fig. 7. The accuracy of these curves was inspected for a very thin substrate ($\lambda=0.01$). In such a case, the temperature distribution is nearly one dimensional. Comparison between Eq. (20) and an analytical 1D solution resulted in a relative error less than 0.6% along the entire curve.

From the calculated step response, the thermal rise time was derived. This is the time the temperature takes to evolve from 10% to 90% of its final value ($\tilde{T}=0.1,\ldots,0.9$) and gives a good indication for the thermal "quickness of reaction" of the substrate. Figure 8 shows the normalized rise time as a function of λ.

In contrast to what can be expected, the response seems quicker if a thicker substrate is used. This is, however, not the case: The rise time is normalized to t_0, which is proportional to b^2. Plotting the graph without normalization produces a quickly increasing curve. The results can be approximated very well with the following function:

$$\tilde{t}_{rise} = 0.070 - 0.074\frac{\lambda - 0.687}{\lambda + 0.687} \tag{22}$$

which is also shown in Fig. 8. We note here the relative simple form of Eq. (22) should be regarded as merely coincidental. No obvious physical reason could be found explaining why λ would have +1 as exponent (and not, e.g., 0.9 or 1.1). The fitting was tested by estimating $\tilde{t}_{rise}$ for $\lambda=0.14$, 1.4, and 7. The predicted and

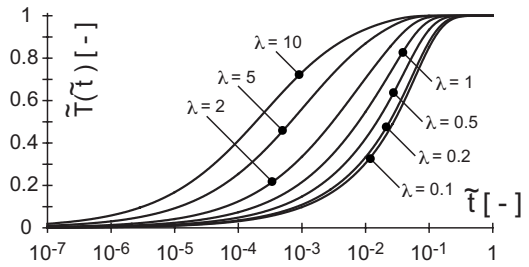

Fig. 7 Normalized response to a power step for various substrate thicknesses

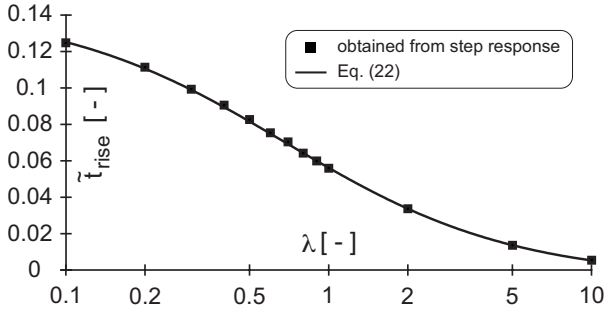

Fig. 8 Normalized rise time as function of normalized substrate thickness

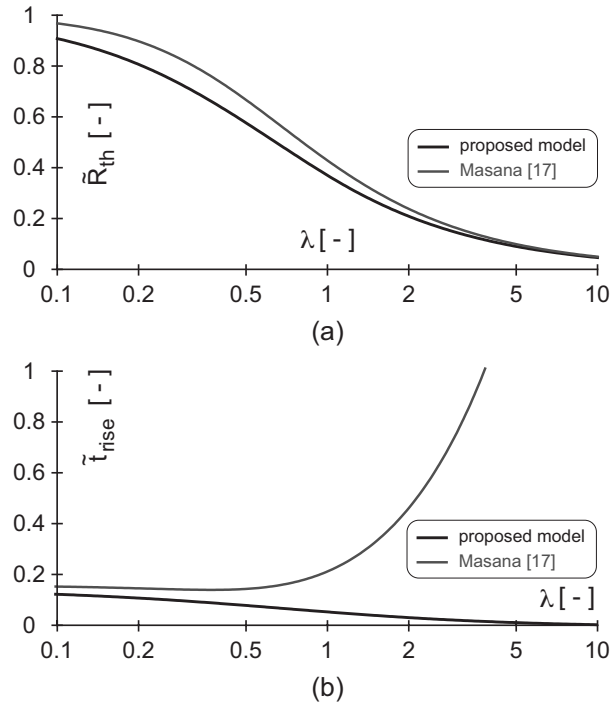

Fig. 9 Comparison between proposed analytical model and lumped network approximation: (*a*) thermal resistance; (*b*) thermal rise time

actual values are (0.119,0.119), (0.045,0.045), and (0.0092,0.0091) respectively.

4.3 Model Comparison. We will compare our results with those obtained by the multilayer model [17] of Masana, by means of the thermal resistance and rise time. With just these two values, one already obtains a good indication of the entire dynamic behavior. Since there is only one material layer, Masana's approach will lead to a single node network with one resistor and capacitor. Their values have been calculated using the spreading angle provided in Ref. [17]. As can be seen in Fig. 5, this ϕ_{opt} is clearly different from the one obtained here. Taking the limit of infinite lateral dimensions and normalizing lead to

$$\tilde{R}_{th,17} = \left(1 + \frac{4\lambda^2}{2\lambda + 1}\right)^{-1} \tag{23}$$

and

$$\tilde{t}_{rise,17} = \frac{1}{2\pi}\frac{1 + 2\lambda}{4\lambda^2 + 2\lambda + 1}\left(1 + \frac{\lambda^2}{2\lambda + 1} + \frac{16\lambda^4}{(2\lambda + 1)^2}\right) \tag{24}$$

These are compared with the results as obtained by our heat spreading model, which already proved to be quite accurate, in Fig. 9.

While the agreement for the thermal resistance is reasonable (Fig. 9(*a*)), Eq. (24) clearly gives a very poor estimation for the rise time, especially for thick substrates (Fig. 9(*b*)). This can be understood quite easily. Since there is only one node in the lumped network, it is as the entire material volume must be heated simultaneously. Charging such a large capacitor is much slower compared with the actual source temperature transient: In reality, the material is gradually heated as the heat spreads from source to sink. For thin substrates, this spreading effect is less pronounced, explaining why the deviation is smallest for small λ (see Fig. 9(*b*)).

By considering the thermal impedance, it can generally be expected that work in Ref. [17] will not provide satisfying results for the single-layer case. For a simple *RC*-stage, the Nyquist plot is a semicircle, with center point ($R_{th}/2$,0) on the real axis. As we clearly notice in Fig. 6, the actual behavior of the substrate is quite different. It must be noted that one could divide the substrate into several horizontal slices, each of them with the same thermal parameters. This will obviously improve the results of Masana's model [17], however, at a cost. To obtain the thermal impedance, an equivalent *RC*-network, with order equal to the number of layers, must be solved.

4.4 Discussion on Structure and Boundaries. Before turning to the anisotropic substrates, a few comments on the considered geometry and boundary conditions are appropriate. First of all, we considered a substrate, which is infinite in lateral (x and y) directions. Despite this approximation, the obtained results can still serve to be very accurate in practice, as long as certain geometrical and boundary conditions are met. We have performed numerical simulations for the case of adiabatic side edges. The results clearly show that the influence of the side walls is hardly noticeable, as long as the lateral substrate dimensions are a few times the base of the pyramidal flow path (the latter being approximately $(1+2\lambda)$ times the source size a). Additional requirements have to be fulfilled when edge cooling, i.e., a heat transfer coefficient h along the sides, is taken into account. Namely, this heat transfer coefficient should not exceed a certain maximal value and/or the substrate thickness should be small enough compared with the lateral substrate dimensions [12].

We also assumed the bottom of the substrate to be at a fixed reference temperature (cold plate or ideal heat sink). In practice various, other situations can occur, among which convective cooling may be of large interest. Poorer bottom cooling, i.e., a finite heat transfer coefficient h, will result in a wider heat spreading in order to utilize a larger contact area with the coolant. The model will therefore largely depend on the boundary conditions. For dynamic phenomena, as are studied here, an additional difficulty arises. At high frequencies, corresponding to early transitions in the step response, only the region close to the source is heated. In those cases, the boundary conditions at the substrate bottom (e.g., the value of h) do not play any role in the thermal behavior. As a consequence, the spreading angle becomes a function of three (normalized) parameters: $\phi_{opt} = \phi_{opt}(\lambda, \tilde{h}, \tilde{\omega})$. This makes, even in the steady-state limit, the model much more complicated and rather cumbersome to use. None of the considered papers [1–10,17], presenting a fixed-angle model, took convective or radiative cooling into account. In this context, we like, however, to point out again that a variety of models, not relying on a fixed-angle approach, do have the ability of tackling convection. Expressions accounting for single-sided (bottom) cooling [11–15], double-sided cooling [14], and edge cooling [11,12] are available in the literature. Nevertheless, many of these advanced models suffer from increased complexity due to the infinite series expansions, and, more importantly, each of them still only provides a steady-state analysis rather than a dynamic one as carried out here.

Next, we turn our attention to the analysis of multilayered structures. For a steady-state spreading model, a reasonable accuracy can be expected only if the materials have comparable thermal conductivities [4,9]. Flux lines are bent sharply as they approach the interface between a well and poorly conducting layer. This situation is very likely to occur in a typical electronic package, e.g., at the interface between the semiconductor die and an adhesive or soldering layer. For dynamic problems, more complications come into play. Since the size of the heated zone is frequency dependent, as explained earlier, the different layers will start to contribute gradually to the step response as time progresses. In addition, the total impedance of the stack is not simply given by the sum of the separate layer impedances, because the thermal capacitances are grounded. In these cases, a

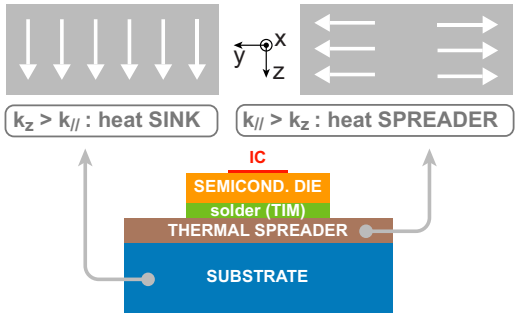

Fig. 10 Heat sink/spreader operation and typical occurrence in electronic package

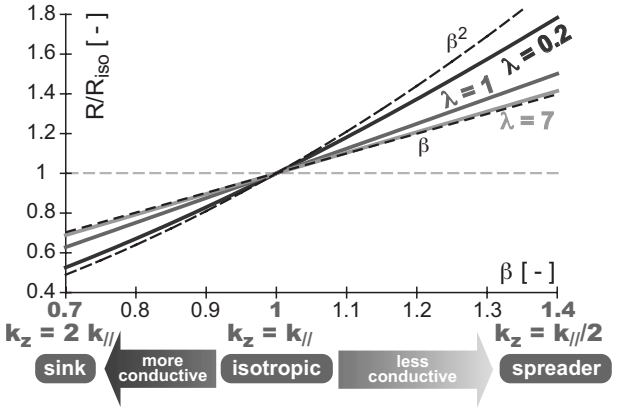

Fig. 11 Thermal resistance (as fraction of isotropic value) as function of anisotropy factor for various substrate thicknesses

closed form model such as proposed here would be highly impractical. A different approach such as the lumped network model of Masana [17] is more suitable.

5 Anisotropic Substrates

5.1 Background. In order to enhance or tune the thermal behavior of electronic chips, one may consider to use composite materials. These substrates can be produced by reinforcing a metal matrix with dispersion particles or fibers [19]. Carbon fiber reinforced copper and aluminum are typical examples used in electronics applications. For the resulting composite material, both the coefficient of thermal expansion (CTE) and thermal conductivity depend on the amount of fibers introduced [19,20]. This offers opportunities for a thermal designer. If the materials inside a chip package have CTEs that differ too much, a strong thermal stress is induced in the interface during every temperature cycle. In the end, this can lead to destruction of the package, e.g., by solder delamination. By using composites, however, one can tune the fiber content to optimize the CTE for a better thermal match and thereby reducing the thermal stresses.

Due to the production process, the fibers are typically orientated in parallel planes or along a preferential direction. This induces anisotropic behavior; the "in-plane" ($k_\parallel$, x, and y directions) and "through-thickness" (k_z) values for the thermal conductivity are different [20]. Note that such behavior also appears in some non-engineered materials, e.g., graphite, due to their microscopic structure. Depending on whether $k_\parallel$ is larger or smaller than k_z, the material is suitable as a heat spreader or heat sink, respectively (Fig. 10).

5.2 Model Modification. The heat Eq. (13) inside the substrate changes to

$$k_\parallel \frac{\partial^2 T}{\partial x^2} + k_\parallel \frac{\partial^2 T}{\partial y^2} + k_z \frac{\partial^2 T}{\partial z^2} - j\omega C_v T(x,y,z) = 0 \tag{25}$$

Let us introduce the following coordinate transformation:

$$z' = \beta z \tag{26}$$

If we now choose

$$\beta = \sqrt{\frac{k_\parallel}{k_z}} \tag{27}$$

we obtain

$$k_\parallel \nabla^2 T(x,y,z') - j\omega C_v T(x,y,z') = 0 \tag{28}$$

Scaling the z axis with the "anisotropy factor" β, Eq. (27) has thus lead to an isotropic heat equation for a medium with apparent conductivity $k_\parallel$. The boundary condition for the heat source transforms as

$$-k_z \left.\frac{\partial T(x,y,z)}{\partial z}\right|_0 = \frac{P}{a^2} \rightarrow -k_\parallel \left.\frac{\partial T(x,y,z')}{\partial z'}\right|_0 = \beta \frac{P}{a^2} \tag{29}$$

The cold plate condition $T(z=b)=0$ should simply be moved to the corresponding location $z'=\beta b$. Put into words, the combination of Eqs. (28) and (29) means that the temperature distribution in an anisotropic substrate $(k_\parallel, k_z)$ with thickness b is β times the temperature in an isotropic $(k_\parallel)$ substrate with thickness βb. The extension of our heat spreading model to anisotropic materials is then straightforward:

$$\tilde{Z}'_{\text{th}}(\lambda,\phi) = \beta \cdot \tilde{Z}_{\text{th}}(\beta\lambda,\phi') \quad \text{with} \quad \phi' = \phi_{\text{opt}}(\beta\lambda) \tag{30}$$

and

$$\tilde{t}'_{\text{rise}}(\lambda) = \tilde{t}_{\text{rise}}(\beta\lambda) \tag{31}$$

Obviously, the normalization values Z_0, ω_0, and t_0 should be changed accordingly as well. Note that the original model is verified only for a limited range of thicknesses, corresponding to $0.1 \le \beta\lambda \le 10$.

5.3 Results. Using the extended model (30) and (31), we will analyze the influence of anisotropy in the substrate. During the calculations, we keep b and $k_\parallel$ constant and consider a relative change of the through-thickness conductivity k_z. The ratios of the thermal resistance and rise time to their isotropic counterparts are investigated, allowing an easy interpretation of the results. Applying the model gives rise to

$$\frac{R}{R_{\text{iso}}} = \frac{R'_{\text{th}}}{R_{\text{th}}} = \beta^2 \frac{1 + 2\lambda \tan(\phi_{\text{opt}}(\lambda))}{1 + 2\beta\lambda \tan(\phi_{\text{opt}}(\beta\lambda))} \tag{32}$$

and

$$\frac{t}{t_{\text{iso}}} = \frac{t'_{\text{rise}}}{t_{\text{rise}}} = \beta^2 \frac{0.07 - 0.074\frac{\beta\lambda - 0.687}{\beta\lambda + 0.687}}{0.07 - 0.074\frac{\lambda - 0.687}{\lambda + 0.687}} \tag{33}$$

5.3.1 Thermal Resistance. We have plotted the ratio (32) as function of β, for a substrate with "small" ($\lambda=0.2$), "medium" ($\lambda=1$), and "large" ($\lambda=7$) thicknesses. The results are shown in Fig. 11.

The general tendency can be easily explained. If $\beta<1$ ($k_z > k_\parallel$), the average conductivity increases since we kept $k_\parallel$ constant; hence the resistance drops: $R/R_{\text{iso}}<1$. For $\beta>1$, we have the opposite situation. If we look more in details, we see that the alteration of the resistance depends on the thickness of the substrate.

For thin substrates, a behavior $R/R_{\text{iso}} \approx \beta^2$ is observed, and this

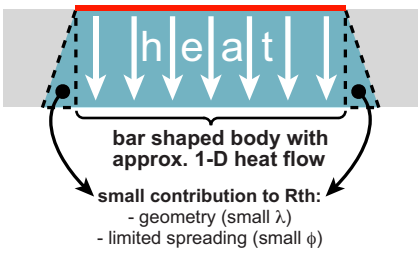

Fig. 12 Heat flow in thin substrates

approximation gets better as β is smaller. Mathematically, we can derive this by taking the limit of Eq. (32) for small λ values. We then can assume

$$2(\beta)\lambda \tan(\phi_{opt}) \ll 1 \tag{34}$$

which indeed leads to $R/R_{iso} \approx \beta^2$. As the condition (34) is better fulfilled for small β, the approximation for the resistance ratio holds better in that region as well. The results can also be explained in a physical way. For thin substrates, the heat is nearly one dimensional (flowing mainly vertically). As, in addition, the spreading angle ϕ_{opt} is relatively small for small λ, the pyramidal heat flow body is almost bar shaped (Fig. 12).

Taking these approximations into account produces

$$R \approx \frac{b}{k_z a^2}, \quad R_{iso} \approx \frac{b}{k_{\parallel} a^2} \quad \Rightarrow \quad \frac{R}{R_{iso}} \approx \frac{k_{\parallel}}{k_z} = \beta^2 \tag{35}$$

which confirms the earlier mathematical treatment. The approximation of a 1D heat flow gets better as k_z increases, again explaining the better fit for small β values.

For thick substrates, on the other hand, a resistance ratio $R/R_{iso} \approx \beta$ is observed, for the entire β range. Since λ is large, we now have

$$2(\beta)\lambda \tan(\phi_{opt}) \gg 1 \tag{36}$$

Taking into account that for thick substrates $\phi_{opt}(\beta\lambda) \approx \phi_{opt}(\lambda) \approx 45$ deg, the ratio (32) indeed will tend to $R/R_{iso} \approx \beta$. As λ is large, the condition (36) is fulfilled for every considered β value, explaining the good fit over the entire range. Once again a physical explanation can be given as well. We know that the source temperature for the anisotropic substrate with thickness b is β times the one for an isotropic case with thickness βb. For thick substrates, the base part of the heat flow pyramid only contributes very little to the resistance, because its cross section is much larger than the heat source. In combination with a nearly constant spreading angle, the geometrical scaling of the pyramid will hardly alter its resistance (Fig. 13). Only the factor β transforming the temperatures remains; hence we indeed have $R/R_{iso} \approx \beta$.

Not surprisingly, a gradual transition is noticed when moving from thin to thick substrates. The curve for $\lambda = 1$ lies between

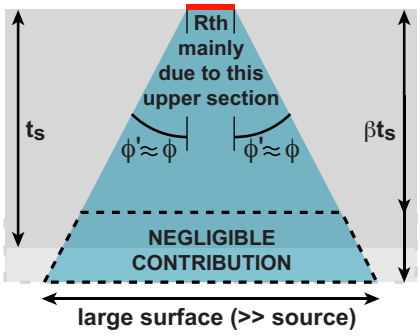

Fig. 13 Heat flow in thick substrates

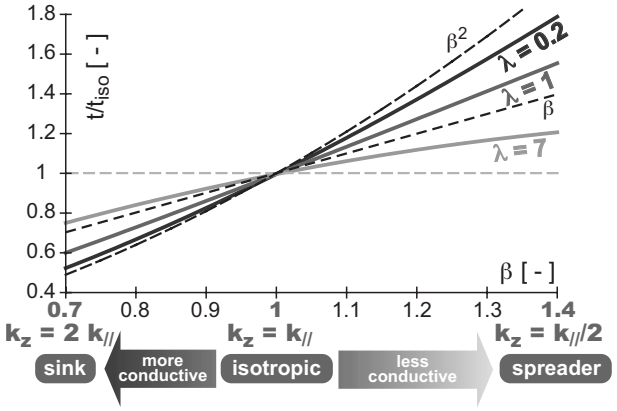

Fig. 14 Thermal rise time (as fraction of isotropic value) as function of anisotropy factor for various substrate thicknesses

those for $\lambda = 0.2$ and 7. Further investigation showed that a good fit could be obtained using $R/R_{iso} \approx \beta^{1.25}$, an exponent lying between 1 and 2 as expected.

5.3.2 Thermal Rise Time. The ratio (33) was plotted as function of β, again for a "thin" ($\lambda = 0.2$), medium ($\lambda = 1$), and thick ($\lambda = 7$) substrate (Fig. 14).

When the average conductivity of the substrate increases ($\beta < 1$), a quicker response is observed and vice versa for less conductive substrates ($\beta > 1$). This could be expected. As the capacitance is not changed, a smaller or bigger thermal resistance moves the time constant spectrum toward the smaller and larger values, respectively. By consequence, the rise time is shortened or extended as well. A different viewpoint would be to consider the transformation of the temperature distribution. The conductivity is hereby kept constant, while the thickness must be multiplied with a factor β. When $\beta > 1$, the heat path is longer, leading to an increase of both thermal resistance and capacitance. Overall, this will lead to a longer rise time. Analogously, a shorter rise time will be observed for $\beta < 1$.

Such argumentations should, however, be used with care. More detailed tendencies (such as the influence of the thickness) are not that clear, in contrast to the resistance ratio analyzed earlier. This is due to the complicated nature of the dynamic heat flow. The transient behavior is, in fact, characterized by a continuous spectrum of thermal time constants. The form of this spectrum eventually leads to a certain value for the rise time. Direct extraction of the time constants, however, is only possible from a Foster network but not from the Cauer network (Fig. 1) used to represent the heat diffusion. Geometrical reasoning as used for the resistance analysis is therefore not suitable to explain the behavior of the rise time.

6 Conclusions

We have proposed a fixed-angle heat spreading model for dynamic thermal characterization of a square heat source on a rear-cooled substrate. This extends the numerous works for steady-state conditions that can be found in the literature. The model allows a designer to obtain very quick but accurate estimations of the behavior, even for advanced materials. An analytic expression for the complex thermal impedance $Z_{th}(j\omega)$ was derived by means of an equivalent thermal RC-network. The model was then fitted to exact calculation results for a normalized thickness λ ranging from 0.1 to 10. If an appropriate spreading angle is chosen, an average error ≤5% can be obtained. A compact expression for the optimum angle ϕ_{opt} was provided. Some Nyquist plots of the thermal impedance were shown to illustrate the accurate estimation of the entire dynamic behavior. Next, we have investigated the thermal step response. Heating curves were presented and a

simple formula for the thermal rise time was derived. Comparison of our model with Masana's lumped network approach [17], the only paper related to the subject we have found, showed that the proposed method gives a much better estimation of the dynamic behavior, especially for thick substrates. Finally, an extension of the model to anisotropic substrates was provided. The influence of the anisotropy on the thermal behavior can be calculated almost straightforwardly. In particular, we have shown results for the resistance and rise time and explained them physically where possible.

Acknowledgment

Bjorn Vermeersch is preparing a Ph.D. as a Research Assistant for the Research Foundation–Flanders (FWO–Vlaanderen) and likes to thank FWO for supporting the presented work.

Nomenclature

Capital Letters

- CTE = coefficient of thermal expansion, m^{-1}
- C_v = specific heat per unit volume, J m^{-3} K^{-1}
- G = Green's function, K/W
- H = extended Green's function, K/W
- Q = heat flow, W
- P = power, W
- R = distance to coordinate origin $\|\vec{r}\|$, m
- R_{th} = steady-state thermal resistance $Z_{th}(j\omega=0)$, K/W
- T = temperature, K
- Z_{th} = thermal impedance, K/W

Lowercase Letters

- a = source dimension, m
- b = substrate thickness, m
- c = thermal capacitance per unit length, J K^{-1} m^{-1}
- $e(\phi)$ = relative error function
- f = frequency, Hz
- h = heat transfer coefficient, W m^{-2} K^{-1}
- j = complex unit $\sqrt{-1}$
- k = thermal conductivity, W m^{-1} K^{-1}
- r = thermal resistance per unit length, K W^{-1} m^{-1}
- $\vec{r}$ = 3D coordinate vector
- t = time, s
- t_{rise} = rise time, s
- $x/y/z$ = Cartesian 3D coordinates

Greek

- α = short notation for $2\tan(\phi)/a$, m^{-1}
- β = anisotropy factor
- γ = short notation for $j\omega C_v/k$, m^{-2}
- $\delta(f)$ = Dirac impulse, s
- λ = normalized substrate thickness b/a
- ∇ = gradient/divergence operator, m^{-1}
- ϕ = heat spreading angle, deg
- ω = angular frequency, rad/s

Subscripts and Superscripts

- $\sim$ = normalized
- $\|$ = in-plane
- 0 = reference
- iso = for isotropic substrate
- opt = optimal value
- Z = through-thickness

References

[1] Balents C., 1969, "Design Considerations for Power Hybrid Circuits," *Proceedings of the Internation Hybrid Microelectronics Symposium*, Dallas, TX, Oct. 29–30.
[2] Cook, K. B., Kerns, D. V., Nagle, H. T., Slagh, T. D., and Ruwe, V. W., 1976, "Computer-Aided Thermal Analysis of a Hybrid Multistage Active Bandpass Filter/Amplifier," IEEE Trans. Parts Hybrids Packag., **12**(4), pp. 344–350.
[3] David, R. F., 1977, "Computerized Thermal Analysis of Hybrid Circuits," IEEE Trans. Parts Hybrids Packag., **13**(3), pp. 283–290.
[4] Holway, L. H., and Adlerstein, M. G., 1977, "Approximate Formulas for the Thermal Resistance of Impatt Diodes Compared With Computer Calculations," IEEE Trans. Electron Devices, **24**(2), pp. 156–157.
[5] Zimmer, C. R., 1981, "Computer Simulation of Hybrid Integrated Circuits Including Combined Electrical and Thermal Effects," *Proceedings of the Third European Hybrid Microelectronics Conference*, Avignon, France, May 20, pp. 44–50.
[6] van Nie, A. G., 1983, "Accurate Fixed-Angle Models for Calculating the Temperature Rise of Rectangular Heat Sources in Hybrid Circuits," *Proceedings of the Fourth European Hybrid Microelectronics Conference*, Copenhagen, Denmark, May 17–20, pp. 523–530.
[7] Dean, D. J., 1985, *Thermal Design of Electronic Circuit Boards and Packages*, Electrochemical Society, Ayr, UK, pp. 75–90.
[8] Masana, F. N., 1996, "A Closed Form Solution of Junction to Substrate Thermal Resistance in Semiconductor Chips," IEEE Trans. Compon., Packag. Manuf. Technol., Part A, **19**(4), pp. 539–545.
[9] Masana, F. N., 1998, "Thermal Resistance Calculation in Multilayer Substrates," *Proceedings of the Fifth MIXDES*, Lodz, Poland, June 18–20, pp. 233–236.
[10] Guenin, B. M., 2003, "The 45° Heat Spreading Angle: An Urban Legend?" Electronics Cooling Magazine, **9**, pp. 10–12.
[11] Muzychka, Y. S., Yovanovich, M. M., and Culham, J. R., 2004, "Thermal Spreading Resistance in Compound and Orthotropic Systems," J. Thermophys. Heat Transfer, **18**(1), pp. 45–51.
[12] Muzychka, Y. S., Yovanovich, M. M., and Culham, J. R., 2006, "Influence of Geometry and Edge Cooling on Thermal Spreading Resistance," J. Thermophys. Heat Transfer, **20**(2), pp. 247–255.
[13] Ellison, G. N., 2003, "Maximum Thermal Spreading Resistance for Rectangular Sources and Plates With Nonunity Aspect Ratios," IEEE Trans. Compon. Packag. Technol., **26**(2), pp. 439–454.
[14] Fisher, T. S., Zell, F. A., Sikka, K. K., and Torrance, K. E., 1996, "Efficient Heat Transfer Approximation for the Chip-on-Substrate Problem," ASME J. Electron. Packag., **118**, pp. 271–279.
[15] Lee, S., Song, S., Au, V., and Moran, K. P., 1995, "Constriction/Spreading Resistance Model for Electronics Packaging," *Proceedings of the ASME/JSME Thermal Engineering Conference*, Maui, HI, March 19–24, 4, pp. 199–206.
[16] Székely, V., 2002, "Enhancing Reliability With Thermal Transient Testing," Microelectron. Reliab., **42**(4-5), pp. 629–640.
[17] Masana, F. N., 2001, "A New Approach to the Dynamic Thermal Modelling of Semiconductor Packages," Microelectron. Reliab., **41**, pp. 901–912.
[18] Vermeersch, B., and De Mey, G., 2007, "BEM Calculation of the Complex Thermal Impedance of Microelectronic Structures," Eng. Anal. Boundary Elem., **31**(4), pp. 289–298.
[19] Kaczmar, J. W., Pietrzak, K., and Wlosinski, W., 2000, "The Production and Application of Metal Matrix Composite Materials," J. Mater. Process. Technol., **106**, pp. 58–67.
[20] Wang, T. C., Fan, T. X., Zhang, D., Zhang, G. D., and Xiong, D. S., 2007, "Thermal Conductivity and Thermal Expansions of Aluminum/Carbon Composites Based on Wood Templates," Mater. Lett., **61**, pp. 1849–1854.

Single- and Dual-Phase-Lagging Heat Conduction Models in Moving Media

Lin Cheng

Mingtian Xu[1]
e-mail: mingtian@sdu.edu.cn

Institute of Thermal Science and Technology,
Shandong University,
P.O. Box 88,
Jing Shi Road 73,
Jinan,
Shandong Province 250061, P.R.C.

Liqiu Wang
Department of Mechanical Engineering,
University of Hong Kong,
Pokfalum Road, Hong Kong

*Motivated by the recent work of Christov and Jordan, ("Heat Conduction Paradox Involving Second-Sound Propagation in Moving Media," 2005, Phys. Rev. Lett., **94**, p. 154301), we examine the original single- and dual-phase-lagging heat conduction models without Taylor series approximation and their variants in moving media using the Galilean principle of relativity. It is found that the original single- and dual-phase-lagging heat conduction models are Galilean invariant and lead to a single governing equation even for the multidimensional media. However their variants violate the Galilean principle of relativity in the moving media. Although this paradox can be eliminated by replacing the partial time derivatives with the material derivatives, the resulting governing equations cannot be reduced to a single transport equation in the multidimensional media. Therefore we believe that the original single- and dual-phase-lagging heat conduction models are more advantageous in modeling the microscale heat conduction problems.* [DOI: 10.1115/1.2976787]

Keywords: single-phase-lagging heat conduction, dual-phase-lagging heat conduction, microscale heat conduction, Galilean principle of relativity

1 Introduction

We start with the classical Fourier law

$$\mathbf{q}(\mathbf{r},t) = -K\nabla T(\mathbf{r},t) \tag{1}$$

where the temperature gradient $\nabla T(\mathbf{r},t)$ is a vector function of the position vector $\mathbf{r}$ and the time variable t, $\mathbf{q}(\mathbf{r},t)$ is the heat flux, and K is the thermal conductivity of the isotropic thermally conducting material. This law has been widely and successfully applied in the conventional engineering heat conduction problems, in which the system has large spatial dimension and the emphasis is on the long time behavior. Nevertheless, this classical Fourier law suffers from an apparent drawback that it assumes the infinite speed of heat propagation [1–11]. In other words, Fourier's law has the unphysical property that it lacks inertial effects: if a sudden temperature perturbation is applied at one point in a heat conduction medium, it will be felt instantaneously and everywhere at distant points. Experimental observations of heat transport of the propagation of second sound, ballistic phonon propagation, and phonon hydrodynamics in solids at low temperatures depart fundamentally from the conventional Fourier law [3]. Recently, the validity of Eq. (1) has also been examined for the low-dimensional lattices [12–19]. The rapidly developing technology of the ultrafast pulse-laser heating, in which the nonequilibrium thermodynamic transition and the microstructural effect become significantly associated with the shortening of the response time, also challenges the classical Fourier law [3,20–22]. Furthermore, due to the wide application of microdevices and the rapid development of modern microfabrication technology, more and more microdevices with micro- and nanoscale dimensions emerge in various micromechanical systems. It is well known that the conventional Fourier law leads to an unaccepted result for these microdevices [11,23]. A better understanding of the heat transport in these tiny devices is required for a further development of nanotechnology [23].

Much effort has been devoted to the modification of the classical Fourier law. Several non-Fourier heat conduction models have been established. One of these is the Maxwell–Cattaneo (MC) model (also called the CV model),

$$\tau\frac{\partial \mathbf{q}}{\partial t} + \mathbf{q} = -K\nabla T \tag{2}$$

where τ is the time delay. This leads to a hyperbolic heat conduction equation. Therefore, the heat propagates like a wave with a finite speed [1–3,24], which has also been demonstrated experimentally [25–30]. Unfortunately it suffers from another paradox that the MC model does not comply with the Galileo's principle of relativity in the moving medium [24]. Although the extended MC model proposed in Ref. [24] resolves this paradox, it cannot yield a single governing equation of the heat transport in the multidimensional case.

The natural extension of the MC model (Eq. (2)) is

$$\mathbf{q}(\mathbf{r},t+\tau_q) = -K\nabla T(\mathbf{r},t) \tag{3}$$

which was proposed by Tzou [3] in a phenomenological manner. Apparently the original MC model can be recovered from the first order Taylor expansion of the left side of Eq. (3) with respect to time t. It was found that model (3) leads to the thermal vibration or the thermal wave phenomenon, which is the distinct feature of the single-phase-lagging heat conduction from the conventional Fourier heat conduction [31–33].

In Ref. [3], the non-Fourier model (3) was further extended to the following form:

$$\mathbf{q}(\mathbf{r},t+\tau_q) = -K\nabla T(\mathbf{r},t+\tau_T) \tag{4}$$

where τ_T and τ_q are the phase lags of the temperature gradient and the heat flux vector, respectively. The former is due to the microstructural interactions such as phonon scattering or phonon-electron interactions. The latter is, on the other hand, interpreted as the relaxation time accounting for the fast-transient effects of thermal inertia. In order to examine whether the heat conduction model (4) leads to the finite speed of heat propagation, the condi-

[1]Corresponding author.

Contributed by the Heat Transfer Division of ASME for publication in the JOURNAL OF HEAT TRANSFER. Manuscript received October 11, 2007; final manuscript received May 24, 2008; published online September 24, 2008. Review conducted by Ben Q Li.

tion for the occurrence of the thermal vibration phenomenon was explored in Ref. [31].

The first or second order Taylor expansions of Eqs. (3) and (4) give rise to the approximate single- or dual-phase-lagging heat conduction models,

$$\mathbf{q} + \tau_q \mathbf{q}_t = -K \nabla T \tag{5}$$

$$\mathbf{q} + \tau_q \mathbf{q}_t = -K(\nabla T + \tau_T \nabla T_t) \tag{6}$$

$$\mathbf{q} + \tau_q \mathbf{q}_t + \frac{\tau_q^2}{2}\mathbf{q}_{tt} = -K(\nabla T + \tau_T \nabla T_t) \tag{7}$$

$$\mathbf{q} + \tau_q \mathbf{q}_t = -K\left(\nabla T + \tau_T \nabla T_t + \frac{\tau_T^2}{2}\nabla T_{tt}\right) \tag{8}$$

$$\mathbf{q} + \tau_q \mathbf{q}_t + \frac{\tau_q^2}{2}\mathbf{q}_{tt} = -K\left(\nabla T + \tau_T \nabla T_t + \frac{\tau_T^2}{2}\nabla T_{tt}\right) \tag{9}$$

which lead to the following heat conduction governing equations [3]:

$$T_t + \tau_q T_{tt} = \alpha \Delta T \tag{10}$$

$$T_t + \tau_q T_{tt} = \alpha(\Delta T + \tau_T \Delta T_t) \tag{11}$$

$$T_t + \tau_q T_{tt} + \frac{\tau_q^2}{2}T_{ttt} = \alpha(\Delta T + \tau_T \Delta T_t) \tag{12}$$

$$T_t + \tau_q T_{tt} = \alpha\left(\Delta T + \tau_T \Delta T_t + \frac{\tau_T^2}{2}\Delta T_{tt}\right) \tag{13}$$

$$T_t + \tau_q T_{tt} + \frac{\tau_q^2}{2}T_{ttt} = \alpha\left(\Delta T + \tau_T \Delta T_t + \frac{\tau_T^2}{2}\Delta T_{tt}\right) \tag{14}$$

Among them, model (5) is nothing more than the CV model (2). Equation (11) forms a generalized, unified equation that reduces to the classical parabolic heat conduction equation when $\tau_T = \tau_q = 0$, to the hyperbolic heat conduction equation when $\tau_T = 0$ and $\tau_q = \tau$, with τ as the relaxation time defined in Ref. [34], to the energy equation in the phonon scattering model [1,35] when $\alpha = \tau_R c^2/3$, $\tau_T = (9/5)\tau_N$, and $\tau_q = \tau_R$, and to the energy equation in the phonon-electron interaction model [20,36] when $\alpha = k/(c_e + c_l)$, $\tau_T = c_l/G$, and $\tau_q = (1/G)[1/c_e + 1/c_l]^{-1}$. In the phonon scattering model, c is the average speed of phonons (sound speed), τ_R is the relaxation time for the umklapp process in which momentum is lost from the phonon system, and τ_N is the relaxation time for normal processes in which momentum is conserved in the phonon system. In the phonon-electron interaction model, k is the thermal conductivity of the electron gas, G is the phonon-electron coupling factor, and c_e and c_l are the heat capacity of the electron gas and the metal lattice, respectively. The approximate dual-phase-lagging heat conduction model [6]—with its wide applications in ultrafast pulse-laser heating, propagating of temperature pulses in superfluid liquid helium, nonhomogeneous lagging response in porous media, and thermal lagging in amorphous materials and with the effects of material defects and thermomechanical coupling—has aroused the tense research effort on its various aspects. The non-Fourier models (7)–(9) account for the second order effects of the lagging behavior for the microstructural interactions or the fast-transient effects of thermal inertia. For the details about models (5)–(9), please refer to Ref. [3].

In Ref. [31], we rederived the constitutive relation (4) from the Boltzmann transport equation. Based on Eq. (11), we addressed the conditions and features of thermal oscillation and resonance and their difference with those in the classical and hyperbolic heat conduction in particular [37]. The dual-phase-lagging heat conduction model was also proven to be well posed in a finite region under any linear boundary conditions [38,39]. Solutions of the single- or dual-phase-lagging heat conduction equations were obtained for some specific initial and boundary conditions [4,5,40–46]. Interestingly, Tzou [3] and Vadasz [47–50] developed an approximate equivalence between the heat conduction in porous media and the dual-phase-lagging heat conduction. The method and results in Ref. [37], thus, were applied to investigate the conditions of the occurrence of thermal oscillation in porous media.

Note that seven non-Fourier models (Eqs. (3)–(9)) are available for one microscale heat conduction problem. Different models usually lead to different results although their differences are quite small. In Refs. [51], the stabilities of heat conduction based on the non-Fourier models (6)–(9) were investigated, which resulted in the different stable regions of parameters τ_T and τ_q for different models. Therefore, a natural question is which model is more appropriate for describing the microscale heat conduction phenomena? That is, the constitutive relations (3)–(9) need to be assessed according to some criterion. The Galilean principle of relativity, the equivalence of inertial reference frames for all physical laws, may serve as a criterion for such a kind of assessment. Recently, Christov and Jordan [24] found that the MC model (2) of finite-speed heat conduction accidentally violates this principle; in order to eliminate this drawback, the material derivative was employed to replace the local partial time derivative and the improved MC model was proven to be invariant under the Galilean transformation. In the present work, we first attempt to examine other non-Fourier models by the Galilean principle of relativity. Then the methodology in Ref. [24] is employed to reformulate the non-Fourier models (6)–(9). Finally, we compare the original single- and dual-phase-lagging heat conduction models (3) and (4) with their variants (Eqs. (5)–(9)).

2 Examination of the Original and Approximate Single- and Dual-Phase-Lagging Conduction Models by the Galilean Principle of Relativity

We begin with establishing the governing equation of heat transport under the non-Fourier models (5)–(9). In order to do that, one needs the following balance equation of the internal energy:

$$\rho c_p\left(\frac{\partial T}{\partial t} + \mathbf{u} \cdot \nabla T\right) + \nabla \cdot \mathbf{q} = 0 \tag{15}$$

where ρ is the mass density, c_p is the specific heat at constant pressure, $\mathbf{u}$ is the velocity vector, and t is time. In the following the constant mass density is assumed. Then combining Eqs. (15) and (5)–(9) leads to the following governing equations of heat transport:

$$T_t + \mathbf{u} \cdot \nabla T + \tau_q(T_{tt} + (\mathbf{u} \cdot \nabla T)_t) = \alpha \Delta T \tag{16}$$

$$T_t + \mathbf{u} \cdot \nabla T + \tau_q(T_{tt} + (\mathbf{u} \cdot \nabla T)_t) = \alpha(\Delta T + \tau_T \Delta T_t) \tag{17}$$

$$T_t + \mathbf{u} \cdot \nabla T + \tau_q(T_{tt} + (\mathbf{u} \cdot \nabla T)_t) + \frac{\tau_q^2}{2}(T_{ttt} + (\mathbf{u} \cdot \nabla T)_{tt}) = \alpha(\Delta T + \tau_T \Delta T_t) \tag{18}$$

$$T_t + \mathbf{u} \cdot \nabla T + \tau_q(T_{tt} + (\mathbf{u} \cdot \nabla T)_t) = \alpha\left(\Delta T + \tau_T \Delta T_t + \frac{\tau_T^2}{2}\Delta T_{tt}\right) \tag{19}$$

$$T_t + \mathbf{u} \cdot \nabla T + \tau_q(T_{tt} + (\mathbf{u} \cdot \nabla T)_t) + \frac{\tau_q^2}{2}(T_{ttt} + (\mathbf{u} \cdot \nabla T)_{tt}) = \alpha\left(\Delta T + \tau_T \Delta T_t + \frac{\tau_T^2}{2}\Delta T_{tt}\right) \tag{20}$$

where $\alpha = K/(\rho c_p)$ is the thermal diffusivity, the subscript t indi-

cates the partial derivative with respect to time, and **u** is the velocity vector of the material point.

Classically, the physical law should not change its form under the following Galilean transformation:

$$\mathbf{r}' = \mathbf{r} - \mathbf{U}t, \quad t' = t \tag{21}$$

where **U** is the constant velocity between two inertial reference frames. Therefore if the heat conduction medium is moving with a constant speed **U**, an observer moving with the same speed should see the same heat conduction phenomena as the case when the heat conduction medium is at rest. More specifically, for different inertial frames, the heat propagation wave speed obtained according to Eqs. (16)–(20) should be the same. For simplicity and to avoid losing the generality, we only consider the following one-dimensional moving medium with constant speed U in the x-direction:

$$T_t + UT_x + \tau_q(T_{tt} + UT_{xt}) = \alpha T_{xx} \tag{22}$$

$$T_t + UT_x + \tau_q(T_{tt} + UT_{xt}) = \alpha(T_{xx} + \tau_T T_{xxt}) \tag{23}$$

$$T_t + UT_x + \tau_q(T_{tt} + UT_{xt}) + \frac{\tau_q^2}{2}(T_{ttt} + UT_{xtt}) = \alpha(T_{xx} + \tau_T T_{xxt}) \tag{24}$$

$$T_t + UT_x + \tau_q(T_{tt} + UT_{xt}) = \alpha\left(T_{xx} + \tau_T T_{xxt} + \frac{\tau_T^2}{2}T_{xxtt}\right) \tag{25}$$

$$T_t + UT_x + \tau_q(T_{tt} + UT_{xt}) + \frac{\tau_q^2}{2}(T_{ttt} + UT_{xtt}) = \alpha\left(T_{xx} + \tau_T T_{xxt} + \frac{\tau_T^2}{2}T_{xxtt}\right) \tag{26}$$

where x is the spatial coordinate and the subscript represents the partial derivative with respect to x.

By introducing the following Galilean transformation and notations:

$$y = x - Ut, \quad t = t, \quad \theta(y,t) = T(x,t) \tag{27}$$

Eqs. (22)–(26) become

$$\theta_t + \tau_q(\theta_{tt} - U\theta_{ty}) = \alpha\theta_{yy} \tag{28}$$

$$\theta_t + \tau_q(\theta_{tt} - U\theta_{ty}) = \alpha(\theta_{yy} + \tau_T\theta_{tyy} - \tau_T U\theta_{yyy}) \tag{29}$$

$$\theta_t + \tau_q(\theta_{tt} - U\theta_{ty}) + \frac{\tau_q^2}{2}(\theta_{ttt} - 2U\theta_{tty} + U^2\theta_{tyy}) = \alpha(\theta_{yy} + \tau_T\theta_{tyy} - \tau_T U\theta_{yyy}) \tag{30}$$

$$\theta_t + \tau_q(\theta_{tt} - U\theta_{ty}) = \alpha\left[\theta_{yy} + \tau_T\theta_{tyy} - \tau_T U\theta_{yyy} + \frac{\tau_T^2}{2}(\theta_{ttyy} - 2U\theta_{tyyy} + U^2\theta_{yyyy})\right] \tag{31}$$

$$\theta_t + \tau_q(\theta_{tt} - U\theta_{ty}) + \frac{\tau_q^2}{2}(\theta_{ttt} - 2U\theta_{tty} + U^2\theta_{tyy}) = \alpha\left[\theta_{yy} + \tau_T\theta_{tyy} - \tau_T U\theta_{yyy} + \frac{\tau_T^2}{2}(\theta_{ttyy} - 2U\theta_{tyyy} + U^2\theta_{yyyy})\right] \tag{32}$$

Obviously, all the above equations involve the constant speed U. Subsequently, an observer moving with the medium with the speed **U** may see a different heat conduction process from the case when the frame is at rest. This contradicts the Galilean principle of relativity, which may also be demonstrated by calculating the wave speeds for thermal disturbances in an infinite region based on Eqs. (22)–(24). When $U=0$, it is easy to show that the propagating speed of the heat wave is equal to $c=\sqrt{\alpha/\tau_q}$. When U is a nonzero constant, the propagating speed of the heat wave is given as $c_{1,2}=(1/2)(U\pm\sqrt{U^2+4c^2})$, which are nonlinear functions of U. Apparently $c_{1,2}$ is not the sum or difference of the frame velocity and thermal wave speed with the rest medium. Therefore it lacks physical meaning. From the previous analysis we can see that Eqs. (22)–(26) are obtained by the combination of the internal energy balance (Eq. (15)) and the non-Fourier models (5)–(9). It is easy to check that the internal energy balance equation is invariant under the Galilean transformation. Therefore we conclude that the non-Fourier models (5)–(9) must not comply with the Galilean principle of relativity. In order to prove this, we first introduce the following Galilean transformation and some notations:

$$\mathbf{r}' = \mathbf{r} - \mathbf{U}t, \quad t = t, \quad \theta(\mathbf{r}',t) = T(\mathbf{r}',t), \quad \mathbf{Q}(\mathbf{r}',t) = \mathbf{q}(\mathbf{r},t) \tag{33}$$

Applying these equations on Eqs. (5)–(9), we obtain

$$\mathbf{Q} + \tau_q(\mathbf{Q}_t - \mathbf{U}\cdot\nabla^{r'}\mathbf{Q}) = -K\nabla^{r'}\theta \tag{34}$$

$$\mathbf{Q} + \tau_q(\mathbf{Q}_t - \mathbf{U}\cdot\nabla^{r'}\mathbf{Q}) = -K[\nabla^{r'}\theta + \tau_T(\nabla^{r'}\theta_t - \mathbf{U}\cdot\nabla^{r'}\nabla^{r'}\theta)] \tag{35}$$

$$\mathbf{Q} + \tau_q(\mathbf{Q}_t - \mathbf{U}\cdot\nabla^{r'}\mathbf{Q}) + \frac{\tau_q^2}{2}[\mathbf{Q}_{tt} - 2\mathbf{U}\cdot\nabla^{r'}\mathbf{Q}_t + \mathbf{U}\cdot\nabla^{r'}(\mathbf{U}\cdot\nabla^{r'}\mathbf{Q})] = -K[\nabla^{r'}\theta + \tau_T(\nabla^{r'}\theta_t - \mathbf{U}\cdot\nabla^{r'}\nabla^{r'}\theta)] \tag{36}$$

$$\mathbf{Q} + \tau_q(\mathbf{Q} - \mathbf{U}\cdot\nabla^{r'}\mathbf{Q}) = -K\left[\nabla^{r'}\theta + \tau_T(\nabla^{r'}\theta_t - \mathbf{U}\cdot\nabla^{r'}\nabla^{r'}\theta) + \frac{\tau_T^2}{2}(\nabla^{r'}\theta_{tt} - 2\mathbf{U}\cdot\nabla^{r'}\nabla^{r'}\theta_t + \mathbf{U}\cdot\nabla^{r'}(\mathbf{U}\cdot\nabla^{r'}\nabla^{r'}\theta))\right] \tag{37}$$

$$\mathbf{Q} + \tau_q(\mathbf{Q}_t - \mathbf{U}\cdot\nabla^{r'}\mathbf{Q}) + \frac{\tau_q^2}{2}[\mathbf{Q}_{tt} - 2\mathbf{U}\cdot\nabla^{r'}\mathbf{Q}_t + \mathbf{U}\cdot\nabla^{r'}(\mathbf{U}\cdot\nabla^{r'}\mathbf{Q})] = -K\left[\nabla^{r'}\theta + \tau_T(\nabla^{r'}\theta_t - \mathbf{U}\cdot\nabla^{r'}\nabla^{r'}\theta) + \frac{\tau_T^2}{2}(\nabla^{r'}\theta_{tt} - 2\mathbf{U}\cdot\nabla^{r'}\nabla^{r'}\theta_t + \mathbf{U}\cdot\nabla^{r'}(\mathbf{U}\cdot\nabla^{r'}\nabla^{r'}\theta))\right] \tag{38}$$

One can see that all the above equations involve the speed of the moving frame. Therefore for different speeds of moving frames, the non-Fourier models (5)–(9) have different forms. This is in contradiction to the Galilean principle of relativity. However the original single-phase-lagging heat conduction model (3) and the dual-phase-lagging heat conduction model (4) obey the Galilean principle of relativity. This can be proven as follows.

The application of the Galilean transformation (33) on Eqs. (3) and (4) yields

$$Q(\mathbf{r}', t + \tau_q) = -K\nabla^{r'}\theta(\mathbf{r}', t)$$

$$Q(\mathbf{r}', t + \tau_q) = -K\nabla^{r'}\theta(\mathbf{r}', t + \tau_T)$$

The observation of these two equations shows that the single- and dual-phase-lagging heat conduction models keep the same form for all the inertial reference frames. Actually it is a trivial process to examine this because models (3) and (4) do not contain any time derivatives. Therefore the single-phase-lagging heat conduction model (3) is the simplest non-Fourier model, which is invariant under the Galilean transformation. Although the variants of the

original single- and dual-phase-lagging heat conduction models have not passed the test of the Galilean principle of relativity, they can still be used in the rest heat conduction media.

3 The Improved Non-Fourier Conduction Models

In Ref. [24], it is found that the classical MC model can be modified by using the material derivative instead of the partial time derivative, and the resulting improved MC model is invariant under the Galilean transformation. Applying the same strategy to the non-Fourier models (5)–(9) in the moving heat conduction medium with the constant speed **U**, we have

$$\mathbf{q} + \tau_q(\mathbf{q}_t + \mathbf{U}\cdot\nabla\mathbf{q}) = -K\nabla T \tag{39}$$

$$\mathbf{q} + \tau_q(\mathbf{q}_t + \mathbf{U}\cdot\nabla\mathbf{q}) = -K[\nabla T + \tau_T\nabla(T_t + \mathbf{U}\cdot\nabla T)] \tag{40}$$

$$\mathbf{q} + \tau_q(\mathbf{q}_t + \mathbf{U}\cdot\nabla\mathbf{q}) + \frac{\tau_q^2}{2}[\mathbf{q}_{tt} + 2\mathbf{U}\cdot\nabla\mathbf{q}_t + \mathbf{U}\cdot\nabla(\mathbf{U}\cdot\nabla\mathbf{q})] = -K[\nabla T + \tau_T\nabla(T_t + \mathbf{U}\cdot\nabla T)] \tag{41}$$

$$\mathbf{q} + \tau_q(\mathbf{q}_t + \mathbf{U}\cdot\nabla\mathbf{q}) = -K\left[\nabla T + \tau_T\nabla(T_t + \mathbf{U}\cdot\nabla T) + \frac{\tau_T^2}{2}\nabla(T_{tt} + 2\mathbf{U}\cdot\nabla T_t + \mathbf{U}\cdot\nabla(\mathbf{U}\cdot\nabla T))\right] \tag{42}$$

$$\mathbf{q} + \tau_q(\mathbf{q}_t + \mathbf{U}\cdot\nabla\mathbf{q}) + \frac{\tau_q^2}{2}[\mathbf{q}_{tt} + 2\mathbf{U}\cdot\nabla\mathbf{q}_t + \mathbf{U}\cdot\nabla(\mathbf{U}\cdot\nabla\mathbf{q})] = -K\left[\nabla T + \tau_T\nabla(T_t + \mathbf{U}\cdot\nabla T) + \frac{\tau_T^2}{2}\nabla(T_{tt} + 2\mathbf{U}\cdot\nabla T_t + \mathbf{U}\cdot\nabla(\mathbf{U}\cdot\nabla T))\right] \tag{43}$$

Introducing the Galilean transformation (33) in the above equations yields

$$\mathbf{Q} + \tau_q\mathbf{Q}_t = -K\nabla\theta \tag{44}$$

$$\mathbf{Q} + \tau_q\mathbf{Q}_t = -K(\nabla\theta + \tau_T\nabla\theta_t) \tag{45}$$

$$\mathbf{Q} + \tau_q\mathbf{Q}_t + \frac{\tau_q^2}{2}\mathbf{Q}_{tt} = -K(\nabla\theta + \tau_T\nabla\theta_t) \tag{46}$$

$$\mathbf{Q} + \tau_q\mathbf{Q}_t = -K\left(\nabla\theta + \tau_T\nabla\theta_t + \frac{\tau_T^2}{2}\nabla\theta_{tt}\right) \tag{47}$$

$$\mathbf{Q} + \tau_q\mathbf{Q}_t + \frac{\tau_q^2}{2}\mathbf{Q}_{tt} = -K\left(\nabla\theta + \tau_T\nabla\theta_t + \frac{\tau_T^2}{2}\nabla\theta_{tt}\right) \tag{48}$$

Obviously these equations do not involve the constant speed **U**. Furthermore, Eqs. (44)–(48) have the same form as Eqs. (5)–(9), respectively. Therefore, the improved non-Fourier models (39)–(43) give the same heat conduction phenomenon in different inertial frames; that is, they obey the Galilean principle of relativity. It also indicates that the non-Fourier models (5)–(9) are only applicable for the rest heat conduction medium, while the improved non-Fourier models (39)–(43) hold for both the rest and moving heat conduction media.

One of Eqs. (39)–(43) and the internal energy balance Eq. (15) compose the governing equation system of the microscale heat conduction in the moving medium. For two- or three-dimensional cases the heat flux vector **q** cannot be eliminated by these equations. Therefore the governing equations cannot be reduced to a single equation. Only for the one-dimensional case can a single governing equation be obtained, namely,

$$T_t + UT_x + \tau_q(T_{tt} + 2UT_{xt} + U^2T_{xx}) = \alpha T_{xx} \tag{49}$$

$$T_t + UT_x + \tau_q(T_{tt} + 2UT_{xt} + U^2T_{xx}) = \alpha(T_{xx} + \tau_T T_{txx} + \tau_T UT_{xxx}) \tag{50}$$

$$T_t + UT_x + \tau_q(T_{tt} + 2UT_{xt} + U^2T_{xx}) + \frac{\tau_q^2}{2}(T_{ttt} + 3UT_{ttx} + 3U^2T_{txx} + U^3T_{xxx}) = \alpha(T_{xx} + \tau_T T_{txx} + \tau_T UT_{xxx}) \tag{51}$$

$$T_t + UT_x + \tau_q(T_{tt} + 2UT_{xt} + U^2T_{xx}) = \alpha\left[T_{xx} + \tau_T(T_{txx} + UT_{xxx}) + \frac{\tau_T^2}{2}(T_{ttxx} + 2UT_{txxx} + U^2T_{xxxx})\right] \tag{52}$$

$$T_t + UT_x + \tau_q(T_{tt} + 2UT_{xt} + U^2T_{xx}) + \frac{\tau_q^2}{2}(T_{ttt} + 3UT_{ttx} + 3U^2T_{txx} + U^3T_{xxx}) = \alpha\left[T_{xx} + \tau_T(T_{txx} + UT_{xxx}) + \frac{\tau_T^2}{2}(T_{ttxx} + 2UT_{txxx} + U^2T_{xxxx})\right] \tag{53}$$

It is easy to show that the wave speeds of thermal disturbances with respect to the resting frame are now $c_{1,2} = U \pm c$, exactly as we would expect for a body moving with a constant speed U. In the material framework the improved non-Fourier models (39)–(43) can be further generalized as

$$\mathbf{q} + \tau_q\frac{D\mathbf{q}}{Dt} = -K\nabla T \tag{54}$$

$$\mathbf{q} + \tau_q\frac{D\mathbf{q}}{Dt} = -K\left(\nabla T + \tau_T\nabla\frac{DT}{Dt}\right) \tag{55}$$

$$\mathbf{q} + \tau_q\frac{D\mathbf{q}}{Dt} + \frac{\tau_q^2}{2}\frac{D^2\mathbf{q}}{Dt^2} = -K\left(\nabla T + \tau_T\nabla\frac{DT}{Dt}\right) \tag{56}$$

$$\mathbf{q} + \tau_q\frac{D\mathbf{q}}{Dt} = -K\left(\nabla T + \tau_T\nabla\frac{DT}{Dt} + \frac{\tau_T^2}{2}\nabla\frac{D^2T}{Dt^2}\right) \tag{57}$$

$$\mathbf{q} + \tau_q\frac{D\mathbf{q}}{Dt} + \frac{\tau_q^2}{2}\frac{D^2\mathbf{q}}{Dt^2} = -K\left(\nabla T + \tau_T\nabla\frac{DT}{Dt} + \frac{\tau_T^2}{2}\nabla\frac{D^2T}{Dt^2}\right) \tag{58}$$

where $D/Dt = \partial/\partial t + \mathbf{u}\cdot\nabla$. One of these equations and Eq. (15) compose a coupled system, which is the governing equation of the microscale heat conduction in a material continuum with velocity **u**. In a frame moving with constant velocity **U**, we introduce the following Galilean transformation and notations:

$$\mathbf{r}' = \mathbf{r} - \mathbf{U}t, \quad t = t, \quad \mathbf{u}(\mathbf{r},t) = \mathbf{U} + \mathbf{v}(\mathbf{r}',t)$$
$$\mathbf{q}(\mathbf{r},t) = \mathbf{Q}(\mathbf{r}',t), \quad T(\mathbf{r},t) = \theta(\mathbf{r}',t) \tag{59}$$

Note that **v** denotes the velocity relative to the moving frame. Then we obtain the following vector formulas relating the moving frame to the resting one:

$$\mathbf{q}_t = \mathbf{Q}_t - \mathbf{U}\cdot\nabla^{r'}\mathbf{Q}, \quad T_t = \theta_t - \mathbf{U}\cdot\nabla^{r'}\theta$$
$$\mathbf{u}\cdot\nabla^r = [\mathbf{U} + \mathbf{v}(\mathbf{r}',t)]\cdot\nabla^{r'} \tag{60}$$

where the superscripts on the gradient operators refer to the coordinates with respect to which they are taken. It is easy to verify that

$$\mathbf{q}_t + \mathbf{u}\cdot\nabla^r\mathbf{q} = \mathbf{Q}_t + \mathbf{v}(\mathbf{r}',t)\cdot\nabla^{r'}\mathbf{Q} \tag{61}$$

$$T_t + \mathbf{u} \cdot \nabla^r T = \theta_t + \mathbf{v}(\mathbf{r}', t) \cdot \nabla^{r'} \theta$$

Applying these equations on Eqs. (15) and (54)–(58) yields

$$\rho c_p \left(\frac{\partial \theta}{\partial t} + \mathbf{v} \cdot \nabla \theta \right) = -\nabla \cdot \mathbf{Q} \tag{62}$$

and

$$\mathbf{q} + \tau_q \left(\frac{\partial}{\partial t} + \mathbf{v} \cdot \nabla \right) \mathbf{Q} = -K \nabla T \tag{63}$$

$$\mathbf{q} + \tau_q \left(\frac{\partial}{\partial t} + \mathbf{v} \cdot \nabla \right) \mathbf{Q} = -K \left[\nabla T + \tau_T \nabla \left(\frac{\partial}{\partial t} + \mathbf{v} \cdot \nabla \right) \mathbf{T} \right] \tag{64}$$

$$\mathbf{q} + \tau_q \left(\frac{\partial}{\partial t} + \mathbf{v} \cdot \nabla \right) \mathbf{Q} + \frac{\tau_q^2}{2} \left(\frac{\partial}{\partial t} + \mathbf{v} \cdot \nabla \right) \left(\frac{\partial}{\partial t} + \mathbf{v} \cdot \nabla \right) \mathbf{Q} = -K \left[\nabla T + \tau_T \nabla \left(\frac{\partial}{\partial t} + \mathbf{v} \cdot \nabla \right) \mathbf{T} \right] \tag{65}$$

$$\mathbf{q} + \tau_q \left(\frac{\partial}{\partial t} + \mathbf{v} \cdot \nabla \right) \mathbf{Q} = -K \left[\nabla T + \tau_T \nabla \left(\frac{\partial}{\partial t} + \mathbf{v} \cdot \nabla \right) \mathbf{T} + \frac{\tau_T^2}{2} \nabla \left(\frac{\partial}{\partial t} + \mathbf{v} \cdot \nabla \right) \left(\frac{\partial}{\partial t} + \mathbf{v} \cdot \nabla \right) \mathbf{T} \right] \tag{66}$$

$$\mathbf{q} + \tau_q \left(\frac{\partial}{\partial t} + \mathbf{v} \cdot \nabla \right) \mathbf{Q} + \frac{\tau_q^2}{2} \left(\frac{\partial}{\partial t} + \mathbf{v} \cdot \nabla \right) \left(\frac{\partial}{\partial t} + \mathbf{v} \cdot \nabla \right) \mathbf{Q} = -K \left[\nabla T + \tau_T \nabla \left(\frac{\partial}{\partial t} + \mathbf{v} \cdot \nabla \right) \mathbf{T} + \frac{\tau_T^2}{2} \nabla \left(\frac{\partial}{\partial t} + \mathbf{v} \cdot \nabla \right) \left(\frac{\partial}{\partial t} + \mathbf{v} \cdot \nabla \right) \mathbf{T} \right] \tag{67}$$

where the superscripts are omitted without causing confusion. The energy balance (Eq. (15)) and one of Eqs. (63)–(67) compose the general governing equation of microscale heat transport in the moving frame. An observation shows that all these equations do not involve the constant velocity **U** of the moving frame. Therefore the improved non-Fourier models (54)–(58) are Galilean invariant.

3.1 The Original Single- and Dual-Phase-Lagging Heat Conduction Models. For the single- and dual-phase-lagging heat conduction models (3) and (4), we have mentioned that it is trivial to show that they comply with the Galilean principle of relativity because they do not involve any time derivative. The combination of Eq. (3) and the internal energy balance (Eq. (15)) leads to

$$\frac{\partial T(\mathbf{r}, t + \tau_q)}{\partial t} + \mathbf{u}(\mathbf{r}, t + \tau_q) \cdot \nabla T(\mathbf{r}, t + \tau_q) = \alpha \Delta T(\mathbf{r}, t) \tag{68}$$

This is the governing equation of microscale heat conduction under the single-phase-lagging model. Similarly, for the original dual-phase-lagging model (4), the governing equation of microscale heat conduction is written as

$$\frac{\partial T(\mathbf{r}, t + \tau_q)}{\partial t} + \mathbf{u}(\mathbf{r}, t + \tau_q) \cdot \nabla T(\mathbf{r}, t + \tau_q) = \alpha \Delta T(\mathbf{r}, t + \tau_T) \tag{69}$$

Apparently for the original single- and dual-phase-lagging models, the governing equation of microscale heat conduction in the moving medium is a single partial differential equation even for the two- and three-dimensional cases. Furthermore it has a quite simpler form compared with other models. Therefore the single- and dual-phase-lagging models demonstrate a big advantage in dealing with the microscale heat conduction in the moving medium.

4 Concluding Remarks

The original single- and dual-phase-lagging heat conduction models obey the Galilean principle of relativity and lead to a single governing equation of heat conduction in the moving medium even for two- and three-dimensional cases. Their variants, however, suffer from the violation of the Galilean principle of relativity. Although one can eliminate this paradox by replacing the local time derivative with the material derivative, the resulting governing equations cannot be reduced to a single equation in two- or three-dimensional cases. Therefore the original single- and dual-phase-lagging heat conduction models are preferable in dealing with the microscale heat conduction problems.

It is well known that the Boltzmann transport equation plays a central role in the study of the microscale and nanoscale heat conductions. The classical Fourier law and CV model for the one-dimensional case were established from the Boltzmann transport equation [11]. The phonon-electron interaction model was derived from the Boltzmann transport equation on a quantum mechanical and statistical basis [20]. Joshi and Majumdar [52] derived a phonon radiative transport equation between two parallel plates from the Boltzmann transport equation for the heat transport in dielectric solid films. Based on the Boltzmann transport equation, Chen [53,54] proposed ballistic-diffusive heat conduction equations of microscale heat transport in devices where the characteristic length is comparable to the mean free path of the energy carrier or the characteristic time is comparable to the relaxation time of the energy carrier. The original single- and dual-phase-lagging heat conduction models (3) and (4) were also established [31,33] from the Boltzmann transport equation. In addition, numerous numerical simulations based on the Boltzmann transport equation have emerged [55–64]. The findings of the present work as well as of Ref. [24] remind us that special attention should be given to the Galilean principle of relativity when the Boltzmann transport equation is employed to establish the microscale heat conduction models.

Acknowledgment

The support of our research program by National Basic Research Program of China (Project No. 2007CB206900) is greatly appreciated.

Nomenclature

- c = propagating speed of the heat wave in the rest frame
- c_p = specific heat at constant pressure
- K = thermal conductivity
- $\mathbf{q}$ = heat flux
- $\mathbf{r}$ = position vector
- $\mathbf{r}'$ = position vector
- t = time variable
- T = temperature field
- $\mathbf{U}$ = speed of the moving frame
- $\mathbf{v}$ = velocity vector
- x = spatial coordinate
- y = spatial coordinate

Greek Symbols

- α = thermal diffusivity
- θ = temperature field
- ρ = mass density
- τ = relaxation time
- τ_q = phase lag of the heat flux vector
- τ_T = phase lag of the temperature gradient

References

[1] Joseph, D. D., and Preziosi, L., 1989, "Heat Waves," Rev. Mod. Phys., **61**, pp. 41–73.

[2] Joseph, D. D., and Preziosi, L., 1990, "Addendum to the Paper 'Heat Waves' [Rev. Mod. Phys. 61, 41 (1989)]," Rev. Mod. Phys., **62**, pp. 375–391.

[3] Tzou, D. Y., 1996, *Macro- to Microscale Heat Transfer: The Lagging Behavior*, Taylor & Francis, Washington, DC.
[4] Tzou, D. Y., 1995, "A Unified Field Approach for Heat Conduction From Micro- to Macro-Scales," ASME J. Heat Transfer, **117**, pp. 8–16.
[5] Tzou, D. Y., and Zhang, Y. S., 1995, "An Analytical Study on the Fast-Transient Process in Small Scales," Int. J. Eng. Sci., **33**, pp. 1449–1463.
[6] Chandrasekharaiah, D. S., 1998, "Hyperbolic Thermoelasticity: A Review of Recent Literature," Appl. Mech. Rev., **51**, pp. 705–729.
[7] Chandrasekharaiah, D. S., 1986, "Thermoelasticity With Second Sound: A Review," Appl. Mech. Rev., **39**, pp. 355–376.
[8] Jou, D., Casas-Vázquez, J., and Lebon, G., 1999, "Extended Irreversible Thermodynamics Revisited (1988–98)," Rep. Prog. Phys., **62**, pp. 1035–1142.
[9] Onsager, L., 1931, "Reciprocal Relations in Irreversible Process. I," Phys. Rev., **37**, pp. 405–426.
[10] Jou, D., Casas-Vázquez, J., and Lebon, G., 2003, *Extended Irreversible Thermodynamics*, Springer, Berlin.
[11] Tien, C. L., Majumdar, A., and Gerner, F. M., 1998, *Microscale Energy Transport*, Taylor & Francis, Washington, DC.
[12] Lepri, S., Livi, R., and Politi, A., 2003, "Thermal Conduction in Classical Low-Dimensional Lattices," Phys. Rep., **377**, pp. 1–80.
[13] Li, B., and Wang, J., 2003, "Anomalous Heat Conduction and Anomalous Diffusion in One-Dimensional Systems," Phys. Rev. Lett., **91**, p. 044301.
[14] Li, B., Casati, G., Wang, J., and Prosen, T., 2004, "Fourier Law in the Alternate-Mass-Hard-Core Potential Chain," Phys. Rev. Lett., **92**, p. 254301.
[15] Narayan, O., and Ramaswamy, S., 2002, "Anomalous Heat Conduction in One-Dimensional Momentum-Conserving Systems," Phys. Rev. Lett., **89**, p. 200601.
[16] Savin, A. V., Tsironic, G. P., and Zolotaryuk, A. V., 2002, "Heat Conduction in One-Dimensional Systems With Hard-Point Interparticle Interactions," Phys. Rev. Lett., **88**, p. 154301.
[17] Dhar, A., 2001, "Heat Conduction in a One-Dimensional Gas of Elastically Colliding Particles of Unequal Masses," Phys. Rev. Lett., **86**, pp. 3554–3557.
[18] Prosen, T., and Campbell, D., 2000, "Momentum Conservation Implies Anomalous Energy Transport in 1D Classical Lattices," Phys. Rev. Lett., **84**, pp. 2857–2860.
[19] Giardiná, C., Livi, R., Politi, A., and Vassalli, M., 2000, "Finite Thermal Conductivity in 1D Lattices," Phys. Rev. Lett., **84**, pp. 2144–2147.
[20] Qiu, T. Q., and Tien, C. L., 1993, "Heat Transfer Mechanisms During Short-Pulse Laser Heating of Metals," ASME J. Heat Transfer, **115**, pp. 835–841.
[21] Tang, D. W., and Araki, N., 1999, "Wavy, Wavelike, Diffusive Thermal Responses of Finite Rigid Slabs to High-Speed Heating of Laser-Pulses," Int. J. Heat Mass Transfer, **42**, pp. 855–860.
[22] Han, P., Tang, D. W., and Zhou, L. P., 2006, "Numerical Analysis of Two-Dimensional Lagging Thermal Behavior Under Short-Pulse-Laser Heating on Surface," Int. J. Eng. Sci., **44**, pp. 1510–1519.
[23] Cahill, D. G., Ford, W. K., Goodson, K. E., Mahan, G. D., Majumdar, A., Maris, H. J., Merlin, R., and Phillpot, S. R., 2003, "Nanoscale Thermal Transport," J. Appl. Phys., **93**, pp. 793–818.
[24] Christov, C. I., and Jordan, P. M., 2005, "Heat Conduction Paradox Involving Second-Sound Propagation in Moving Media," Phys. Rev. Lett., **94**, p. 154301.
[25] Ackerman, C. C., Bertman, B., Fairbank, H. A., and Guyer, R. A., 1966, "Second Sound in Solid Helium," Phys. Rev. Lett., **16**, pp. 789–791.
[26] Jackson, H. E., Walker, C. T., and McNedlly, T. F., 1970, "Second Sound in NaF," Phys. Rev. Lett., **25**(1), pp. 26–28.
[27] Narayanamurti, V., and Dynes, R. C., 1972, "Observation of Second Sound in Bismuth," Phys. Rev. Lett., **28**(22), pp. 1461–1465.
[28] Kaminski, W., 1990, "Hyperbolic Heat Conduction Equation for Materials With a Nonhomogeneous Inner Structure," ASME J. Heat Transfer, **112**, pp. 555–560.
[29] Hehlen, B., Perou, A.-L., Courtens, E., and Vacher, R., 1995, "Observation of a Doublet in the Quasielastic Central Peak of Quantum-Paraelectric $SrTiO_3$," Phys. Rev. Lett., **75**, pp. 2416–2419.
[30] Roetzel, W., Putra, N., and Das, S. K., 2003, "Experiment and Analysis for Non-Fourier Conduction in Materials With Non-Homogeneous Inner Structure," Int. J. Therm. Sci., **42**, pp. 541–552.
[31] Xu, M. T., and Wang, L. Q., 2005, "Dual-Phase-Lagging Heat Conduction Based on Boltzmann Transport Equation," Int. J. Heat Mass Transfer, **48**, pp. 5616–5624.
[32] Cheng, L., Xu, M. T., and Wang, L. Q., 2008, "Thermal Vibration Phenomenon of Single Phase Lagging Heat Conduction and its Thermodynamic Basis," Chin. Sci. Bull., **53**(6), pp. 732–736, in Chinese.
[33] Cheng, L., Xu, M. T., and Wang, L. Q., 2008, "From Boltzmann Transport Equation to Single-Phase-Lagging Heat Conduction," Int. J. Heat Mass Transfer, doi:10.1016/j.ijheatmasstransfer.2008.04.004.
[34] Chester, M., 1963, "Second Sound in Solids," Phys. Rev., **131**, pp. 2013–2015.
[35] Guyer, R. A., and Krumhansi, J. A., 1966, "Solution of the Linearized Phonon Boltzmann Equation," Phys. Rev., **148**, pp. 766–778.
[36] Kaganov, M. I., Lifshitz, I. M., and Tanatarov, M. V., 1957, "Relaxation Between Electrons and the Crystalline Lattice," Sov. Phys. JETP, **4**, pp. 173–178.
[37] Xu, M. T., and Wang, L. Q., 2002, "Thermal Oscillation and Resonance in Dual-Phase-Lagging Heat Conduction," Int. J. Heat Mass Transfer, **45**, pp. 1055–1061.
[38] Wang, L. Q., Xu, M. T., and Zhou, X., 2001, "Well-Posedness and Solution Structure of Dual-Phase-Lagging Heat Conduction," Int. J. Heat Mass Transfer, **44**, pp. 1659–1669.
[39] Wang, L. Q., and Xu, M. T., 2002, "Well-Possedness of Dual-Phase-Lagging Heat Conduction Equation: Higher Dimensions," Int. J. Heat Mass Transfer, **45**, pp. 1165–1171.
[40] Antaki, P., 1998, "Solution for Non-Fourier Dual Phase Lag Heat Conduction in a Semi-Infinite Slab With Surface Heat Flux," Int. J. Heat Mass Transfer, **41**, pp. 2253–2258.
[41] Dai, W., and Nassar, R., 1999, "A Finite Difference Scheme for Solving the Heat Transport Equation at The Microscale," Numer. Methods Partial Differ. Equ., **15**, pp. 697–708.
[42] Dai, W., and Nassar, R., 2002, "An Approximate Analytic Method for Solving 1D Dual-Phase-Lagging Heat Transport Equations," Int. J. Heat Mass Transfer, **45**, pp. 1585–1593.
[43] Dai, W., Shen, L., Nassar, R., and Zhu, T., 2004, "A Stable and Convergent Three-Level Finite Difference Scheme for Solving a Dual-Phase-Lagging Heat Transport Equation in Spherical Coordinates," Int. J. Heat Mass Transfer, **47**, pp. 1817–1825.
[44] Lin, C. K., Husang, C. C., and Chang, Y. P., 1997, "The Unsteady Solution of a Unified Heat Conduction Solution of a Unified Heat Conduction Equation," Int. J. Heat Mass Transfer, **40**, pp. 1716–1719.
[45] Kulish, V. V., and Novozhilov, V. B., 2004, "An Integral Equation for the Dual-Lag Model of Heat Transfer," ASME J. Heat Transfer, **126**, pp. 805–808.
[46] Xu, Y. S., and Guo, Z. Y., 1995, "Heat Wave Phenomena in IC Chips," Int. J. Heat Mass Transfer, **38**, pp. 2919–2922.
[47] Vadasz, P., 2005, "Absence of Oscillations and Resonance in Porous Media Dual-Phase-Lagging Fourier Heat Conduction," ASME J. Heat Transfer, **127**, pp. 307–314.
[48] Vadasz, P., 2005, "Lack of Oscillations in Dual-Phase-Lagging Heat Conduction for a Porous Slab Subject to Imposed Heat Flux and Temperature," Int. J. Heat Mass Transfer, **48**, pp. 2822–2828.
[49] Vadasz, P., 2005, "Explicit Conditions for Local Thermal Equilibrium in Porous Media Heat Conduction," Transp. Porous Media, **59**, pp. 341–355.
[50] Vadasz, P., 2006, "Exclusion of Oscillations in Heterogeneous and Bi-Composite Media Thermal Conduction," Int. J. Heat Mass Transfer, **49**, pp. 4886–4892.
[51] Quintanilla, R., and Racke, R., 2006, "A Note on Stability in Dual-Phase-Lag Heat Conduction," Int. J. Heat Mass Transfer, **49**, pp. 1209–1213.
[52] Joshi, A. A., and Majumdar, A., 1993, "Transient Ballistic and Diffusive Phonon Heat Transport in Thin Films," J. Appl. Phys., **74**, pp. 31–39.
[53] Chen, G., 2001, "Ballistic-Diffusive Heat-Conduction Equations," Phys. Rev. Lett., **86**, pp. 2297–2300.
[54] Chen, G., 2002, "Ballistic-Diffusive Equations for Transient Heat Conduction From Nano To Macroscales," ASME J. Heat Transfer, **124**, pp. 320–328.
[55] Randrianalisoa, J., and Baillis, D., 2008, "Monte Carlo Simulation of Steady-State Microscale Phonon Heat Transport," ASME J. Heat Transfer, **130**, p. 072404.
[56] Jeng, M. S., Yang, R., Song, D. et al., 2008, "Modeling the Thermal Conductivity and Phonon Transport in Nanoparticle Composites Using Monte Carlo simulation," ASME J. Heat Transfer, **130**, p. 042410.
[57] Narumanchi, S. V. J., Murthy, J. Y., and Amon, C. H., 2005, "Comparison of Different Phonon Transport Models for Predicting Heat Conduction in Silicon-On-Insulator Transistors," ASME J. Heat Transfer, **127**, pp. 713–723.
[58] Narumanchi, S. V. J., Murthy, J. Y., and Amon, C. H., 2004, "Submicron Heat Transport Model in Silicon Accounting for Phonon Dispersion and Polarization," ASME J. Heat Transfer, **126**, pp. 946–955.
[59] Murthy, J. Y., and Mathur, S. R., 2003, "An Improved Computational Procedure for Sub-Micron Heat Conduction," ASME J. Heat Transfer, **125**, pp. 904–910.
[60] Narumanchi, S. V. J., Murthy, J. Y., and Amon, C. H., 2003, "Simulation of Unsteady Small Heat Source Effects in Sub-Micron Heat Conduction," ASME J. Heat Transfer, **125**, pp. 896–903.
[61] Murthy, J. Y., 2002, "Computation of Sub-Micron Thermal Transport Using an Unstructured Finite Volume Method," ASME J. Heat Transfer, **124**, pp. 1176–1181.
[62] Mazumder, S., and Majumdar, A., 2001, "Monte Carlo Study of Phonon Transport in Solid Thin Films Including Dispersion and Polarization," ASME J. Heat Transfer, **123**, pp. 749–759.
[63] Zeng, T., and Chen, G., 2001, "Phonon Heat Conduction in Thin Films: Impacts of Thermal Boundary Resistance and Internal Heat Generation," ASME J. Heat Transfer, **123**, pp. 340–347.
[64] Sverdrup, P. G., Ju, Y. S., and Goodson, K. E., 2001, "Sub-Continuum Simulations of Heat Conduction in Silicon-on-Insulator Transistors," ASME J. Heat Transfer, **123**, pp. 130–137.

Investigation of Heat Transfer and Pressure Drop of an Impinging Jet in a Cross-Flow for Cooling of a Heated Cube

D. Rundström
e-mail: drm@hig.se

B. Moshfegh
e-mail: bmh@hig.se

Division of Energy and Mechanical Engineering,
Department of Technology and Build Environment,
University of Gävle,
801 76 Gävle, Sweden;
Department of Mechanical Engineering,
Linköping University,
Linköping, Sweden

The objective of this study is to investigate the thermal performance and the cost measured in pressure drops of a targeted cooling system with use of an impinging jet in combination with a low-velocity channel flow on a heated wall-mounted cube. The effects of the Reynolds numbers of the impinging jet and the cross-flow, as well as the distance between the top and bottom plates, are investigated. A steady-state 3D computational fluid dynamics model was developed with use of a Reynolds stress model as turbulence model. The geometrical case is a channel with a heated cube in the middle of the base plate and two inlets, one horizontal channel flow and one vertical impinging jet. The numerical model was validated against experimental data with a similar geometrical setup. The velocity field was measured by particle image velocimetry and the surface temperature was measured by an infrared imaging system. This case results in a very complex flow structure where several flow-related phenomena influence the heat transfer rate and the pressure drops. The average heat transfer coefficients on each side of the cube and the pressure loss coefficients are presented; correlations for the average heat transfer coefficient on the cube and the pressure loss coefficients are created.
[DOI: 10.1115/1.2969266]

Keywords: electronics cooling, impinging jet, CFD, RSM

1 Introduction

Impinging jets are used for many industrial applications where high heat and mass transfer rates are required (e.g., drying paper and textiles, tempering glass, and cooling of electronic components). The current trend in electronic devices shows a steady increase in the dissipated heat from electronic components. Forced channel flow is frequently used as a cooling technique, see Refs. [1,2]. In combating the whole thermal load with forced channel flow, excessive flow rates will be required. In a typical electronic system, the printed circuit board (PCB) will contain one or a few high heat-dissipating components. One possible method to face this problem is to divide the channel flow in an impinging jet and a low-velocity cross-flow, see Ref. [3]. The impinging jet is placed over the high heat-dissipating component and provides a local region with high cooling performance, especially at the stagnation point. The cross-flow is important to ensure that well-distributed cooling performance is provided at the other parts of the PCBs, which require less cooling.

Impinging jets are also of great scientific interest. Extensive experimental and numerical research has been carried out to predict the flow and heat transfer characteristics in the stagnation region of an impinging jet. Most investigations have been focused on axisymmetric round jets impinging normally on a flat surface, cf. Ref. [4]. The case with an axisymmetric round jet impinging normally on a flat surface has also been simulated with different turbulence models to predict the heat transfer and flow configuration. The earlier investigation by Behnia et al. [5] has shown that the most common two-equation Reynolds averaged Navier–Stokes (RANS) models, e.g., the standard k-ε model, overpredict the heat transfer rate in the stagnation region by over 100%. Behnia et al. [5] also used the $\overline{v^2}$-f model to simulate the case, with satisfactory agreement with the experimental data. Other numerical investigations, such as the one by Abdon and Sundén [6], have used the expansion of the classical two-equation turbulence models (k-ε and k-ω) with realizable constraints. Craft et al. [7] used a low-Re model with the Yap correlation added to the ε-equation and three different Reynolds stress models (RSMs) to simulate the case.

The case with an impinging jet in a cross-flow has rarely been investigated earlier by means of computational code compared with confined and unconfined impinging jets as well as flows around bluff bodies. Two RANS-turbulence models, the $\overline{v^2}$-f model developed by Durbin [8] and a RSM with a two-layer model in the near-wall region, were used by Rundström and Moshfegh [9] in an earlier validation study of the turbulent flow from an impinging jet in a cross-flow on a wall-mounted cube. The models showed similar results near the walls and the RSM predicted the flow and turbulence characteristics better than the $\overline{v^2}$-f model in the free shear regions (i.e., far from the walls). The accuracy of the heat transfer prediction from the RSM was investigated by Rundström and Moshfegh [10] and the main features were well predicted by the model in all regions except in the stagnation region of the impinging jet, where the model seems to overpredict the heat transfer rate. The verified RSM from the previous studies is used in this study to investigate the influence of the velocities of the impinging jet and the cross-flow and the height of the channel on the heat transfer rate and on the pressure drops for the case with a single impinging jet in a cross-flow on a heated wall-mounted cube.

2 Computational Setup and Numerical Scheme

2.1 Geometrical Setup and Boundary Conditions. The computational domain is a rectangular channel with a heated cube in the middle of the bottom (see Fig. 1). The channel has two

Contributed by the Heat Transfer Division of ASME for publication in the JOURNAL OF HEAT TRANSFER. Manuscript received May 9, 2007; final manuscript received July 3, 2008; published September 22, 2008. Review conducted by Roger Schmidt.

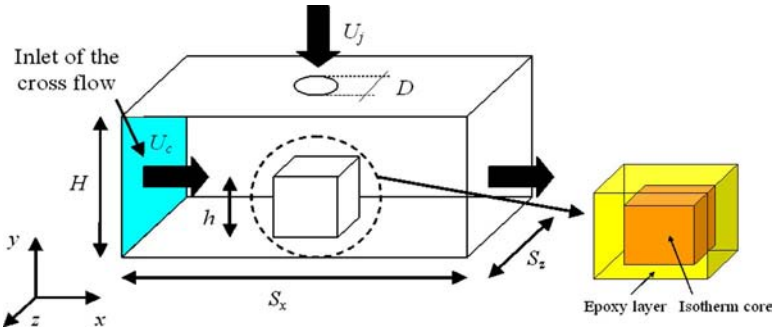

Fig. 1 Computational domain and a schematic sketch of the heated cube

inlets, one horizontal channel flow with a *low* velocity and one vertical impinging jet with a *high* velocity. The impinging jet enters through a circular nozzle at the middle of the top plate. The cube consists of an isothermal core of 70°C covered with an epoxy layer with low thermal conductivity and a thickness, δ_c, of 1.5 mm (see Fig. 1). The geometrical and flow details and the material properties are summarized in Tables 1 and 2. The cooling medium is air.

The following boundary conditions are used: The top and bottom walls are adiabatic with no-slip conditions. Symmetric boundary conditions are used for the sidewalls and zero gradient condition for the outflow (i.e., $\partial U/\partial x = \partial T/\partial x = 0$). The same temperatures of 20°C will be used for the cross-flow and the impinging jet. The mean velocities of cross-flow and the impinging jet are in the ranges of 1–2.8 m/s and 4–12 m/s, respectively. A fully developed channel flow profile is used for the cross-flow and a top-hat profile by Yu and Monkewitz [11] is used for the impinging jet, see Eq. (1).

$$V(d) = \frac{1}{1 + \sinh^{2n}(|d/D|\sinh^{-1}(1))} \tag{1}$$

where d is the diameter at the radial distance, D is the diameter of the nozzle, and $n=15$. The top-hat profile is normalized to fulfill the required mean velocity of the impinging jet. A turbulence intensity, I, of 10% and isotropic Reynolds stresses are assumed at the inlet of the impinging jet. The turbulent dissipation rate, ε, is estimated by

$$\varepsilon = C_\mu^{3/4}\frac{k^{3/2}}{l} \tag{2}$$

Table 1 Geometrical and flow details

D	12 mm
h	15 mm
H	$1.25h-2h=18.75-30$ mm
S_x, S_z	$4h=60$ mm
δ_c	1.5 mm
Re_j	4930–9860
Re_c	1284–5752

Table 2 Material properties

	Air	Epoxy layer
c_p	1006.43 J/kg K	1668.5 J/kg K
ρ	1.225 kg/m^3	1150.0 kg/m^3
λ	0.0242 W/m K	0.236 W/m K
μ	1.789×10^{-5} kg/m s	—

where C_μ is an empirical constant with a value of 0.09, k is the turbulent kinetic energy given by $k=0.5\overline{\mu_i'\mu_i'}$, and l is a length scale given by $l=0.07$ D. The top-hat profile was chosen because of the simplicity to create a more accurate velocity profile due to the vena contra phenomenon. The simplicity of Eq. (1) makes it suitable for practical application where the shape of the profile can be easily changed by adjusting the constant n.

2.2 Governing Equations. The steady-state, three-dimensional, incompressible continuity and Reynolds equations and the transport equation of energy are given by

$$\frac{\partial U_i}{\partial x_i} = 0 \tag{3}$$

$$\frac{\partial (U_j U_i)}{\partial x_j} = -\frac{1}{\rho}\frac{\partial p}{\partial x_i} + \frac{\partial}{\partial x_j}\left(\nu\frac{\partial U_i}{\partial x_j} - \overline{u_i' u_j'}\right) \tag{4}$$

$$\frac{\partial (U_j T)}{\partial x_j} = \frac{\partial}{\partial x_j}\left[\left(\alpha\frac{\partial T}{\partial x_j} - \overline{u_j' T'}\right)\right] \tag{5}$$

where U_i is the mean velocity and u_i' is the fluctuating velocity. The $-\overline{u_i' u_j'}$ and $-\overline{u_j' T'}$ are the modified Reynolds stresses and the modified turbulent heat fluxes and must be modeled in order to close the system equations. The transport equations of modified Reynolds stresses $-\overline{u_i' u_j'}$ can be written as

$$\underbrace{\frac{\partial}{\partial x_k}(U_k\overline{u_i' u_j'})}_{C_{ij}} = \underbrace{\frac{\partial}{\partial x_k}\left[-\overline{u_i' u_j' u_k'} - \overline{\frac{p'}{\rho}(\delta_{jk}u_i' + \delta_{ik}u_j')} + \nu\frac{\partial\overline{u_i' u_j'}}{\partial x_k}\right]}_{D_{ij}}$$

$$\underbrace{-\overline{u_i' u_k'}\frac{\partial U_j}{\partial x_k} - \overline{u_j' u_k'}\frac{\partial U_i}{\partial x_k}}_{P_{ij}} \underbrace{- 2\nu\overline{\frac{\partial u_i'}{\partial x_k}\frac{\partial u_j'}{\partial x_k}}}_{\varepsilon_{ij}}$$

$$\underbrace{+\overline{\frac{p'}{\rho}\left(\frac{\partial u_i'}{\partial x_j} + \frac{\partial u_j'}{\partial x_i}\right)}}_{\Phi_{ij}} \tag{6}$$

where C_{ij} is the convective part, P_{ij} is the production part, D_{ij} is the diffusion part, ε_{ij} is the dissipation part, and Φ_{ij} is the pressure-strain term. The modeled diffusion part, D_{ij}, is given by

$$D_{ij} = \frac{\partial}{\partial x_k}\left(\nu\frac{\partial\overline{u_i' u_j'}}{\partial x_k}\right) + \frac{\partial}{\partial x_k}\left(\frac{\nu_t}{\sigma_k}\frac{\partial\overline{u_i' u_j'}}{\partial x_k}\right) \tag{7}$$

The first term on the right-hand side of Eq. (7) is the molecular transport; the second term is the modeled version of turbulent transport proposed by Lien and Leschziner [12]. The turbulent viscosity, ν_t, is modeled as $\nu_t = C_\mu k^2/\varepsilon$, where k and ε are turbulent kinetic energy and dissipation rate of k. The kinetic energy is given by $k = 0.5\overline{u_i' u_i'}$ and the transport equation of turbulent dissipation rate is given by

$$\frac{\partial}{\partial x_j}(U_j\varepsilon) = \frac{\partial}{\partial x_j}\left[\left(\nu + \frac{\nu_t}{\sigma_\varepsilon}\right)\frac{\partial \varepsilon}{\partial x_j}\right] - C_{\varepsilon 1}\overline{u_i' u_j'}\frac{\partial U_i}{\partial x_j}\frac{\varepsilon}{k} - C_{\varepsilon 2}\frac{\varepsilon^2}{k} \quad (8)$$

The dissipation part, ε_{ij}, is modeled with the isotropic dissipation assumption as $\varepsilon_{ij} = (2/3)\delta_{ij}\varepsilon$, where δ_{ij} is the Kronecker delta. The pressure-strain term, Φ_{ij}, is modeled by a linear approach proposed by Launder and Shima [13].

The modified turbulent heat fluxes, $-\overline{u_j' T'}$, are modeled by the eddy-diffusivity hypothesis with constant turbulent Prandtl number, Pr_t, as

$$-\overline{u_j' T'} = \frac{\nu_t}{\mathrm{Pr}_t}\frac{\partial T}{\partial x_j} \quad (9)$$

The following constants have been used in the RSM: $C_\mu = 0.09$, $\sigma_k = 0.82$, $\sigma_\varepsilon = 1.0$, $C_{\varepsilon 1} = 1.44$, $C_{\varepsilon 2} = 1.92$, and $\mathrm{Pr}_t = 0.85$.

The near-wall region is completely resolved all the way through the viscous sublayer by a two-layer approach. The two-layer model is based on the one-equation model of Wolfshtein [14], with use of the turbulent length scales proposed by Chen and Patel [15]. Details about the modeling of the two-layer model can be found in the Fluent Manuals, see Ref. [16].

Table 3 Numerical scheme

Grid	Staggered grid
Pressure-velocity-coupling algorithm	SIMPLE
Discretization schema	
Nonlinear terms	Second-order upwind schema
Viscous terms	Second-order central scheme

2.3 Numerical Details. The finite-volume code FLUENT 6.2.16 was used to numerically solve the governing equations with a segregated scheme and the SIMPLE algorithm solved the pressure-velocity coupling, see Table 3.

Three different meshes are used in the study, one mesh for each geometrical case. The meshes consist of 651,524, 745,044, and 881,832 structured hexahedral cells for the cases with heights, H, of 18.75 mm, 22.5 mm, and 30 mm, respectively. There are 42 $\times$ 42 cells near the sidewalls of the cube. The top of the cube consists of a total of 5876 cells. The circular region under the inlet of the impinging jet consists of 2516 cells in the xz-plane. The mesh is refined enough near the solid walls ($y^+ \approx 1$) to solve the all-boundary layer with the two-layer model, see Fig. 2. There are five cells with identical spacing through the epoxy layer and there are 64,660 cells located in the epoxy layer. A grid independency study was performed by Rundström and Moshfegh [3] for the case of a height, H, of 30 mm and mean velocities of the impinging jet cross-flow of 10 m/s and 2.8 m/s, respectively.

3 Verification

3.1 Experimental Setup. The experimental setup is shown in Fig. 3. The experimental equipment consists of a wind tunnel with five cubes mounted in-line in the middle of the tunnel; only the

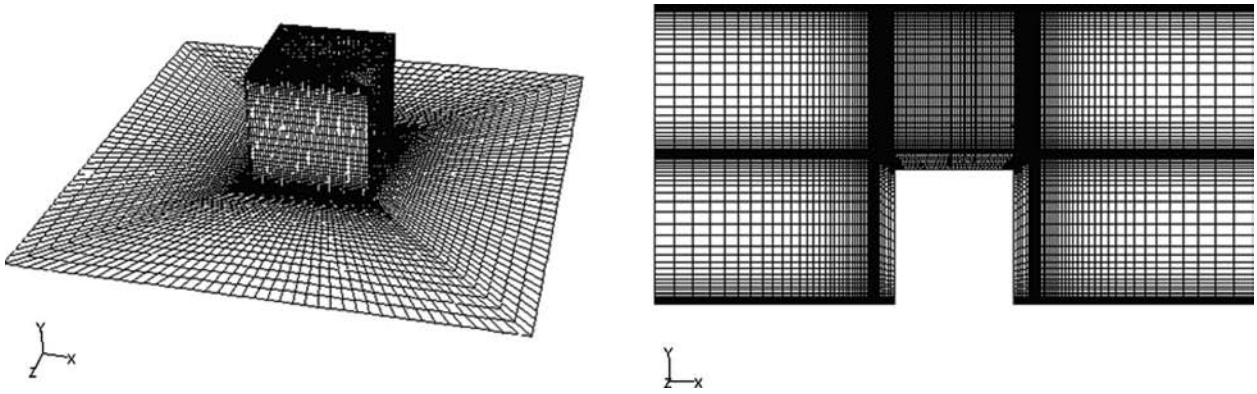

Fig. 2 Computational grid for the height, *H*, of 30 mm: perspective view (left) and side view (right)

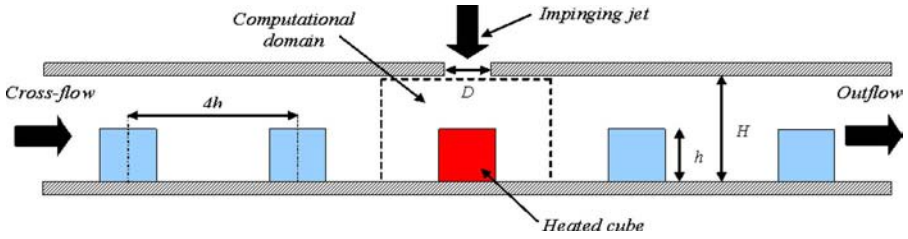

Fig. 3 Schematic sketch of the experimental setup

third cube is heated in the present study. The size of the cubes is 15 mm and the distance between each pair of cubes S_x is 60 mm. The tunnel has a height H of 30 mm and a width of 360 mm. One impinging jet is positioned above the third cube. The impinging jet is forced through a circular hole with a diameter, D, of 12 mm. The centers of the impinging jets and the third cube are identical. The impinging jet is provided with air from a separate channel placed above the top plate. All measurements are carried out at the third cube (see Fig. 3).

3.2 Measurements. The time-averaged velocity field and the Reynolds components were measured in the xy and xz planes with a particle image velocimetry (PIV) system. The PIV system included a double-pulsed Nd:YAG laser with a pulse energy of 25 mJ. The laser was used to produce an approximately 1 mm light sheet that illuminated the seed particles in the flow. A PCO Sensicam camera recorded the images of the seed particles in the light sheet. For each plane, 1000 image pairs were acquired. The commercial software VIDPIV ROWAN V4.0 was used to analyze the images. The PIV system used in this study with almost the same settings was used in Ref. [17]. In Ref. [17] the mean velocity and turbulence fluctuations were carried out both by the PIV system and a laser Doppler anemometry (LDA) system for a case with an axisymmetric round jet impinging normally on a flat surface and the results were compared. The maximum deviations observed between the two measurement systems were approximately 1% for the mean velocity components and 12% for the rms values of the fluctuating velocity components. The largest deviations were located in the near-wall region.

The time-averaged temperature distribution on the cube was measured by a low-wavelength (2–5.5 μm) infrared imaging system (Varioscan, Jenoptik). The Varioscan camera is equipped with a scanning mechanism to create images that are composed at 200 lines with 300 pixels. The relation between the pixel intensity and the temperature is established in an in situ calibration procedure in conjunction with an image restoration technique based on a Wiener filter, using the two-dimensional optical transfer function as described by Meinders et al. [18]. The maximum uncertainty in surface temperature measurement was estimated to be approximately 0.6°C near the edges, see Ref. [19]. These temperature and PIV measurements were carried out at the Department of Applied Physics, Delft University of Technology, Delft, The Netherlands, see Ref. [20] for more details.

3.3 Numerical Setup. The numerical and geometrical setup is identical with the description from Secs. 2.1 and 2.3 and the turbulence modeling is identical with the description from Sec. 2.2. The velocity profile and the turbulent properties at the inlet of the cross-flow (see Fig. 1) are predicted from a larger separate simulation with a row of wall-mounted cubes and the same geometrical configuration as in Fig. 3 under a fully developed channel flow. The boundary conditions for the impinging jet, that is, the velocity profile, turbulent kinetic energy, and turbulent dissipation rate, are derived from the measurements by Tummers et al. [20]. A curve fit from the velocity measurements is used to define the velocity profile, V. The turbulent kinetic energy, k, is calculated by assuming that the streamwise and spanwise Reynolds stresses, $\overline{u'^2}$ and $\overline{w'^2}$, are identical and the values for $\overline{u'^2}$ and $\overline{v'^2}$ are obtained from the above mentioned measurements. The turbulent dissipation rate, ε, is calculated by Eq. (2). It is worth mentioning that the mean velocities of cross-flow, U_c, and the impinging jet, U_j, are 1.73 m/s and 6.50 m/s, respectively.

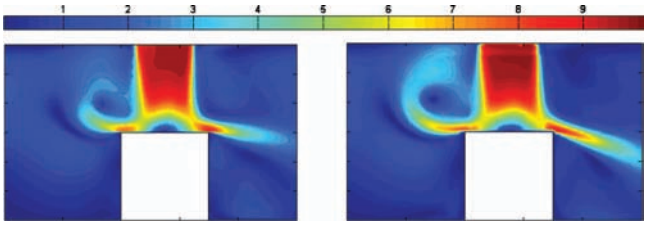

Fig. 4 Contours of velocity magnitude in the xy-plane, $z/h=0$: RSM (left) and PIV measurement (right)

3.4 Results From the Verification. The flow field shows a complex behavior (see Fig. 4). There are several flow-related phenomena that can affect cooling performance. For example, the position of the stagnation point on top of the cube is an important factor for the prediction of heat transfer rate on top of the cube, and the separation from the top of the cube has an important effect on the heat transfer mechanisms at the other four walls.

Figure 5 shows the normalized x-velocity component (U/U_j) as a function of the vertical distance (y/H) near the third cube. Each diagram represents different locations in the x-direction at the center of the cube. The first diagram represents the line at the distance $0.75h$ downstream from the center of the cube (i.e., $x/h=-0.75$); the four following diagrams represent the following x-positions: $x/h=-0.25$, $x/h=0.5$, $x/h=0.75$, and $x/h=1$, where the last three x-positions represent the distance upstream from the center of the cube.

The model shows good agreements with the PIV measurement

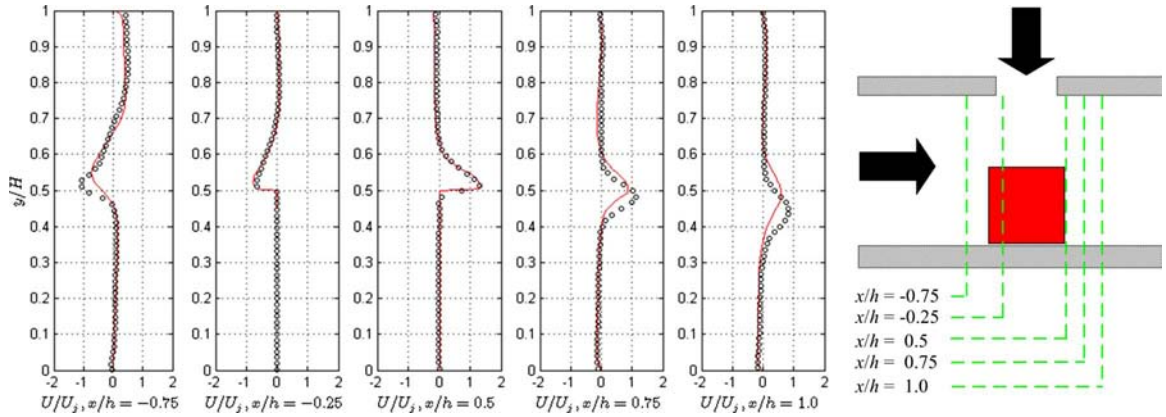

Fig. 5 x-velocity components (U/U_j) in the xy-plane, $z/h=0$: — represents RSM and ○ represents PIV measurement

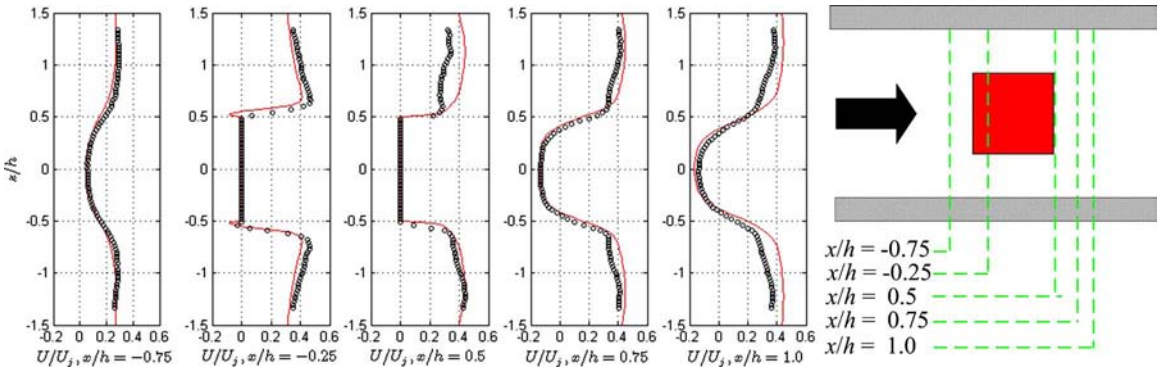

Fig. 6 ***x*-velocity components (U/U_j) in the *xz*-plane, $y/H=2/15$: — represents RSM and ○ represents measurement**

near the stagnation region (see the second and third diagrams from the left in Fig. 5). The recirculating region before the front side of the cube is in good agreement with the RSM and the PIV measurement (see the first diagram from the left in Fig. 5). The strong separation from the rear side is also well predicted by the model (see the third diagram from the left in Fig. 5), but the separated flow seems to be more forced against the bottom plate in the PIV measurement, which results in a lower position of the maximum in the PIV measurement than in the RSM (see the fourth and fifth diagrams from the left in Fig. 5). The peak also seems to decrease a little bit faster in size in the RSM than in the PIV measurement (see the fourth and fifth diagrams from the left in Fig. 5).

Figure 6 shows the normalized x-velocity component (U/U_j) as a function of the spanwise distance (z/h) at the vertical location of 4 mm (or $y/H=2/15$). Each diagram represents the same x-positions as in Fig. 6.

The blockage effect in front of the front side of the cube predicted by RSM is in good agreement with the PIV measurement (see the first diagram from the left in Fig. 6). The bypass flow is also in good agreement between the RSM and the PIV measurement, and the separated flows from the sidewalls are almost identical in the RSM and in the PIV measurement (see the second and third diagrams in Fig. 6). The agreement between the RSM and in the PIV measurement wake region behind the rear side is better close to the rear side than farther from the wall (see the fourth and fifth diagrams in Fig. 6). The recirculating flow near the centerline agrees well between the RSM and in the PIV measurement and the RSM seems to be less diffusive than the PIV measurement.

The diagrams in Fig. 7 show the temperature distribution along two paths on the surface of the cube.

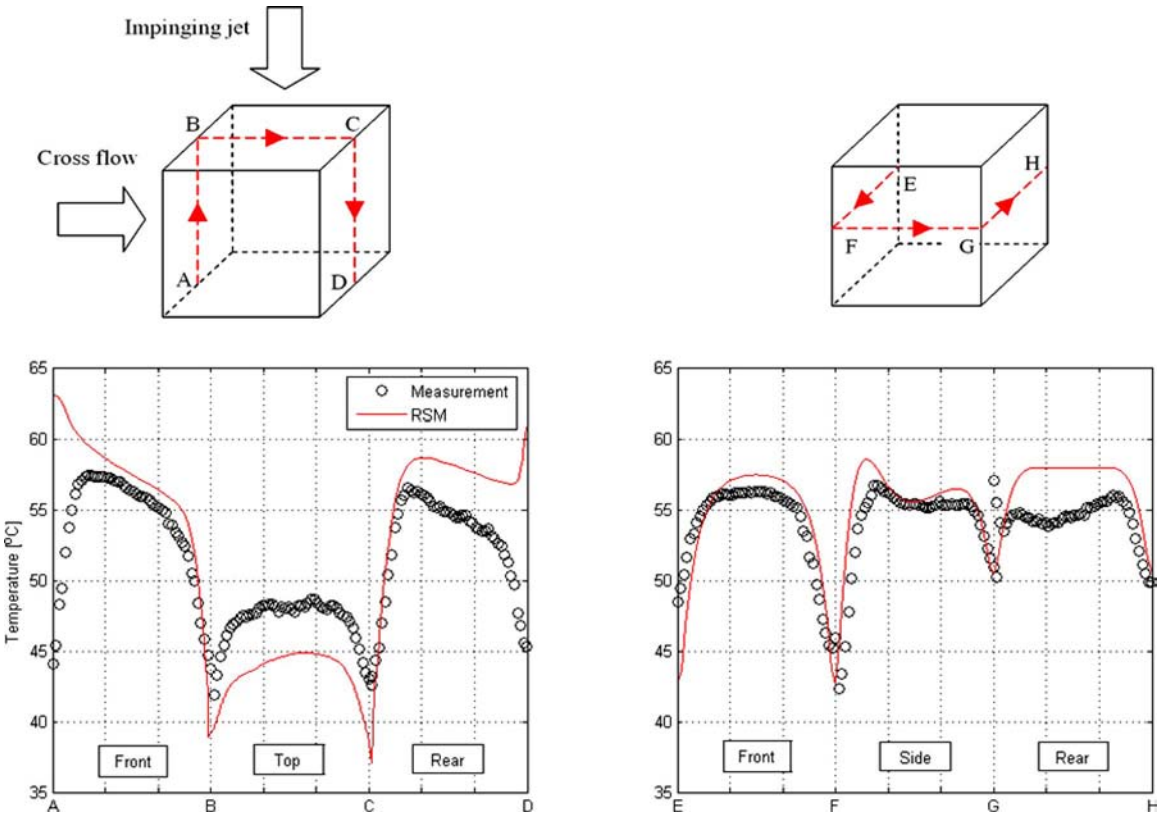

Fig. 7 Surface temperature in the *xy*-plane, $z/h=0$ (left) and in the *xz*-plane, $y/h=0.5$ (right)

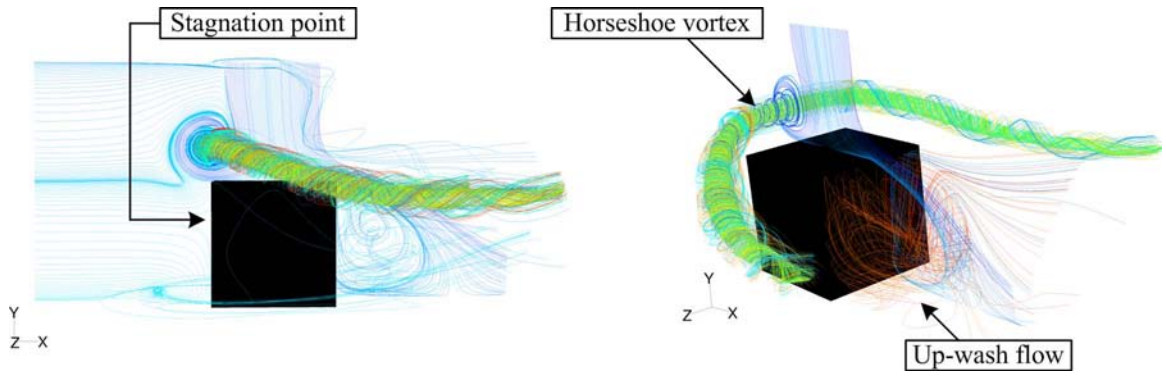

Fig. 8 Paths from the simulation with U_j/U_c=10/2.3 and H=30 mm

The best agreement between the model and measurement is observed on the front side of the cube. The rapidly decreasing temperatures near the corners are well predicted by the model. The heat transfer rate in the stagnation region seems to be a bit overpredicted by the model due to the lower temperature on the top of the cube. The opposite trend is observed on the rear side of the cube, where the predicted temperature is higher than the measured. The position of the maximum value is well predicted in the vertical direction (see the left diagram in Fig. 7) despite the fact that the temperature seems to be overpredicted. A minimum in the measured temperature in the spanwise direction can be observed on the rear side of the cube, where the model shows an almost constant temperature (see the right diagram in Fig. 7). The rapidly decreasing temperature in the measurement near the bottom plate can be explained by the heat losses through the base plate at the bottom of the cube (see the left diagram in Fig. 7), where the predicted temperature shows an increasing trend near the bottom plate due to the adiabatic boundary condition on the bottom plate. A similar trend was observed by Ničeno et al. [21] for a case with a single channel flow over a matrix of cubes where the experimental setup of the cubes was identical with the cube arrangement used in the present study. In Ref. [21] a comparison between a large eddy simulation (LES) with an adiabatic boundary condition on the bottom of the epoxy layer and measurements was presented and the same temperature discrepancies were observed. The predicted temperature agrees well with the measurement on the sidewall of the cube (see the right diagram in Fig. 7). A maximum value is observed in both measurement and in the predicted temperature near the front side on the sidewall where the recirculating occurs, and a minimum is observed at the middle of the sidewall at the reattachment point (see the right diagram in Fig. 7).

4 Results From the Parametric Study

The results from the parametric study, where the two mean velocities of the impinging jet, U_j, the cross-flow, U_c, vary with the distance, H, between the top and bottom plates, imply a significant change in the velocity field, which affects the pressure drops and the heat transfer rate on each side in different ways.

4.1 Flow Configuration. The cross-flow has several flow-related effects on the impinging jet and the separation from the top of the cube. Figure 8 shows the characteristic horseshoe shape when the streamlines from the cross-flow collide with the separated flow from the top of the front side, which results in a recirculating vortex flow around the cube. The region behind the rear side of the cube consists of two vertical recirculating vortices (perpendicular to the xz-plane) and one powerful horizontal vortex (perpendicular to the xy-plane) near the top of the cube. These three vortices occur due to the separations from the sharp edges of the rear side. The vortices result in a spiral-shaped upwash flow near the rear side (see Fig. 8).

The separation from the front side results in two small vertical vortices near each sidewall and the separated flow from the top creates an upwash flow near the sidewalls. The upwash flow is most significant near the reattachment points on the sidewalls, where the x-momentum is low and the separation from the top is most powerful. The cross-flow in the lower part of the channel curls around the front face of the cube. The position of the stagnation point at the front side is located at approximately $y \approx 0.77h$ (see Fig. 8). The flow configuration for the case with a height, H, of 22.5 mm and the same velocities is almost identical with the description above and is therefore not shown.

Figure 9 shows the paths from different locations to illustrate the flow configuration for the case with a height of 18.75 mm and where the velocities of the impinging jet and the cross-flow are 6 m/s and 1 m/s, respectively.

Figure 10 shows the paths from different locations to illustrate the flow configuration for the case with a height of 18.75 mm and where the velocities of the impinging jet and the cross-flow are 6 m/s and 2.3 m/s, respectively.

A comparison between Figs. 9 and 10 shows a significant change in the flow configuration when the mean velocity of the cross-flow increases from 1 m/s to 2.3 m/s. The case with a cross-flow velocity of 1 m/s results in a single horseshoe-shaped vortex flow around the cube when the cross-flow collides with the separations from the front side of the top of the cube, and a ring-shaped vortex structure is observed around the impinging jet (see Fig. 9). Two smaller horseshoe-shaped vortices are observed for the case with a cross-flow velocity of 2.3 m/s and the ring-shaped vortex is not observed for this case (see Fig. 10). The separations from the side parts of the top of the cube are forced over the horseshoe vertex and connect to the outer part of the horseshoe vortex for the case with a cross-flow velocity of 1 m/s (see Fig. 9). These separations pass through the cross-flow in curved lines and are not connected to the horseshoe vortices for the case with a cross-flow velocity of 2.3 m/s (see Fig. 10).

Two different types of flows are observed near the front side of the cube, where a larger amount of the cross-flow is forced up over the front side of the cube in the case with a cross-flow velocity of 1 m/s. The case with a cross-flow velocity of 2.3 m/s results in a clearer stagnation region at the front side of the cube and the path-lines in the xz-plane are more parallel with the sidewalls of the cube than for the case with a cross-flow velocity of 1 m/s (see Figs. 9 and 10). The separations from the edges between the front and the sidewalls of the cube are much stronger in the case with a cross-flow velocity of 2.3 m/s, which results in larger recirculation regions near the sidewalls. The weaker separations and the lower momentum in the x-direction in the case with a

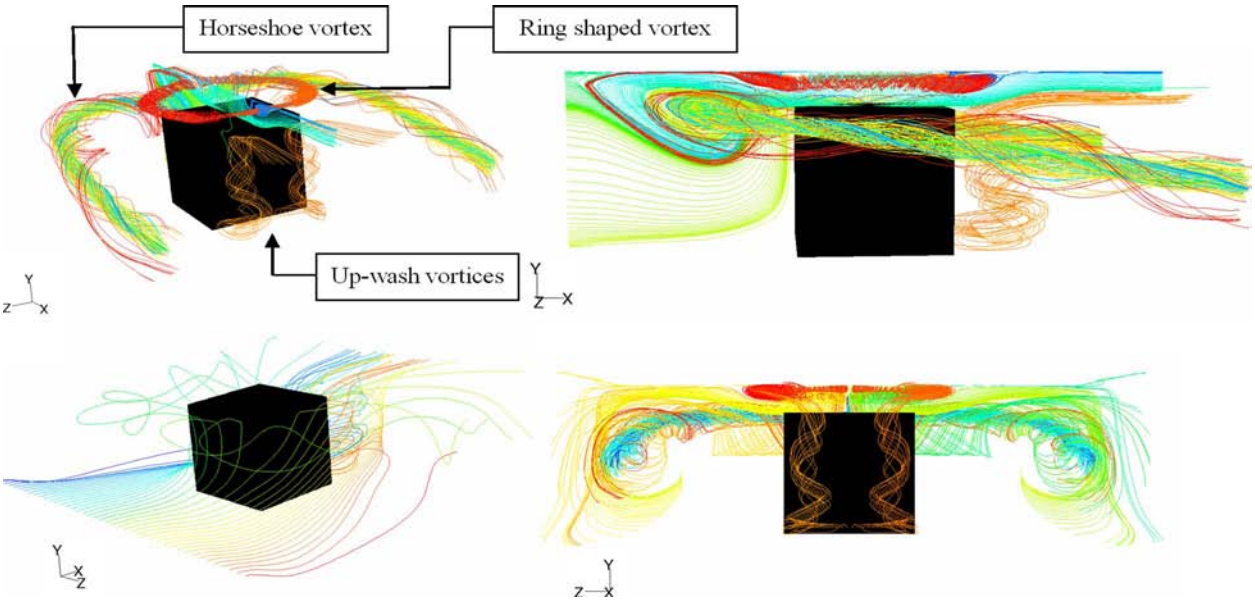

Fig. 9 Paths from the case with U_j/U_c=6/1 and H=18.75 mm

cross-flow velocity of 1 m/s result in a stronger upwash flow near the sidewalls and a larger amount of the cross-flow is forced against the cube (see Figs. 9 and 10). The horseshoe vortex seems also to contribute to the stronger upwash flow at the sidewalls for the case with a cross-flow velocity of 1 m/s (see Fig. 9).

4.2 Heat Transfer Rate. The diagrams in Fig. 11 show the average heat transfer coefficient on the sides, the average value, and a correlation for the average value as a function of the Reynolds number of the impinging jet, Re_j. The rows represent different distances, H, between the top and bottom plates; the columns represent different velocities of the cross-flow, U_c. The values of the heat transfer coefficients from Fig. 11 are also available in Tables 4–6 in the Appendix.

There are several mechanisms involved in the heat transfer rate on each side of the cube. The results show that the highest values of heat transfer coefficient occur on the top and the lowest values occur on the rear side of the cube in all cases. The heat transfer rate on the top of the cube is dominated by the stagnation region from the impinging jet. The variations of the average heat transfer coefficients on the top of the cube are in the range 83.8–241.9 W/m^2 K, which corresponds to heat fluxes in the range 2315–4124 W/m^2. The cross-flow has minor influence especially for higher Re numbers of the impinging jet and for lower distances between the top and bottom plates. The heat transfer coefficients on the top of the cube are approximately identical for different velocities of the cross-flow for each geometrical case when the Re numbers of the impinging jet are over 6000 (see Fig. 11 and Tables 4–6 in the Appendix). A significantly decreasing trend of the heat transfer coefficient on the top of the cube is observed when the cross-flow velocity increases for the cases with lower Re number of the impinging jet and with higher distances between the top and bottom plates (see the third row in Fig. 11

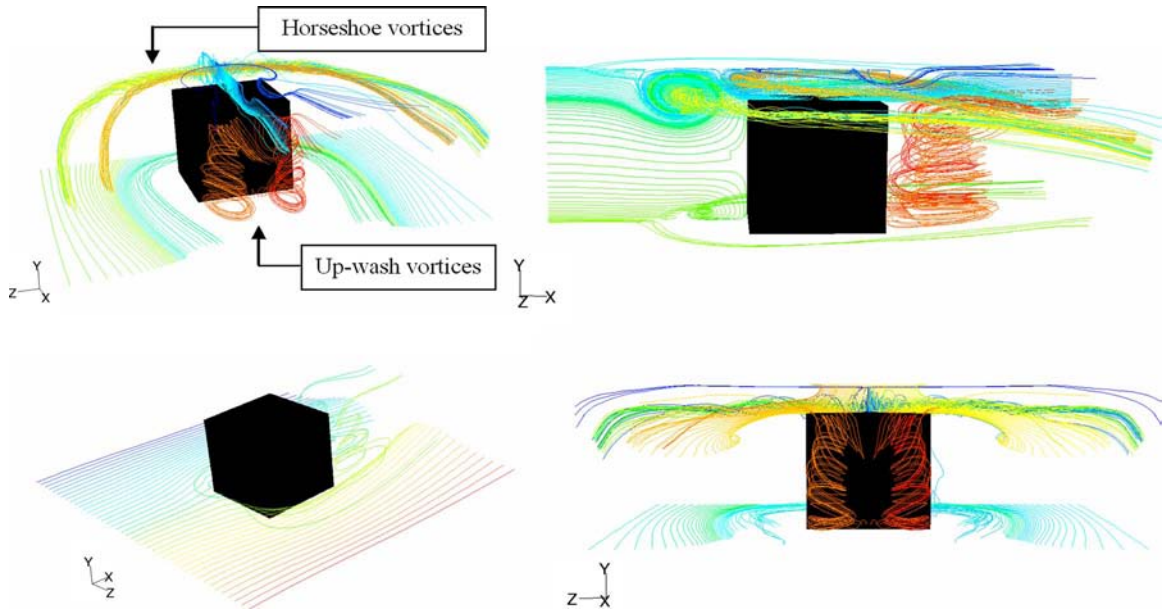

Fig. 10 Paths from the case with U_j/U_c=6/2.3 and H=18.75 mm

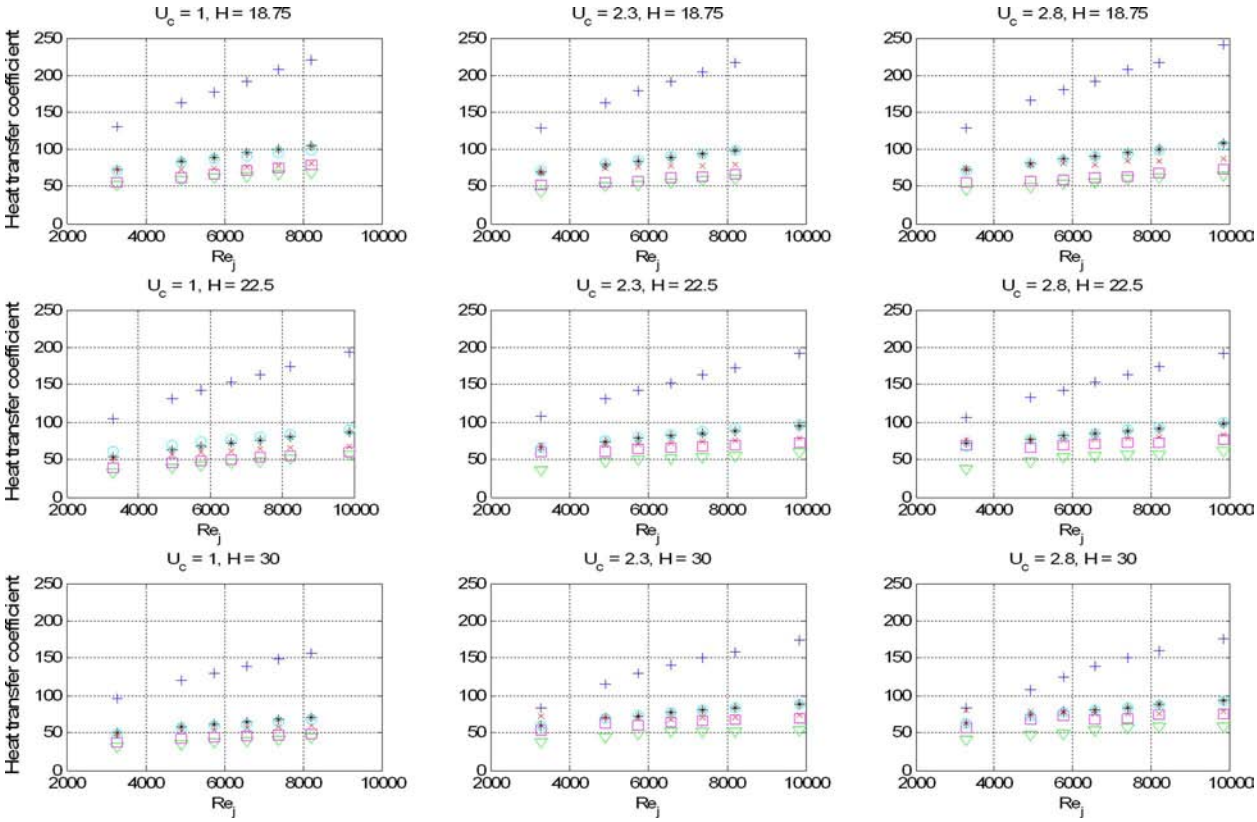

Fig. 11 Average heat transfer coefficient on the sides and the average value of all sides of the cube. ∗, average; +, top; ×, front; ▽, rear; □, sides; and ○, correlation.

and Table 6 in the Appendix). The stagnation point is moved downstream against the rear part of the top of the cube and an essential part of the impinging jet is missing the target under these circumstances.

There are two main flow mechanisms involved in the heat transfer coefficient on the front side of the cube: the effect of the cross-flow and the effect of the separation from the front part of the top of the cube. The cross-flow results in a stagnation region at the front side similar to that at the top of the cube when the cross-flow is strong, compared with the separation from the front part of the top of the cube. Increased velocity of the impinging jet results in stronger separation from the top of the cube, which in the first step results in a faster decrease in the cross-flow velocity; the stagnation effect decreases with decreased heat transfer rate as a consequence. A continuous increase in the velocity of the impinging jet will result in a successive transition from a stagnation flow to an upwash flow, where the position of the stagnation region dislocates against the bottom plate and where the strong separation from the top of the cube forces the flow over the front side of the cube. The separation from the top will have the main effect on the heat transfer rate on the front side after this transition. A further increase in the velocity of the impinging jet will increase the upwash flow and the heat transfer rate on the front side as a consequence. These effects seem to be controlled by the ratio of the Reynolds numbers of the impinging jet and the cross-flow, $\mathrm{Re}_j/\mathrm{Re}_c$, for all three channel heights. See Fig. 12 for an illustration of these effects.

This effect can be observed in the case with $H=30$ mm and $U_c=2.8$ m/s, where the heat transfer coefficient decreases when the velocity of the impinging jet increases from 4 m/s to 8 m/s and increases when the velocity of the impinging jet increases from m/s 8 to 12 m/s (see Fig. 11 and Table 6 in the Appendix). A minimum in the heat transfer rate on the front side is also observed for the cases with $H=30$ mm and $U_c=2.3$ m/s and for the cases with $H=22.5$ mm and $U_c=2.8$ m/s.

The heat transfer coefficient on the sidewalls increases when the cross-flow velocity increases in all cases except for those with a distance of 18.75 mm, where the heat transfer rate decreases when the cross-flow velocity increases from 1 m/s to 2.8 m/s with a minimum at 2.3 m/s (see Fig. 11 and Tables 4–6 in the Appendix). Possible explanations for the unexpected decrease are that a larger amount of the cross-flow is forced against the cube and a higher upwash flow is observed for these cases, as discussed

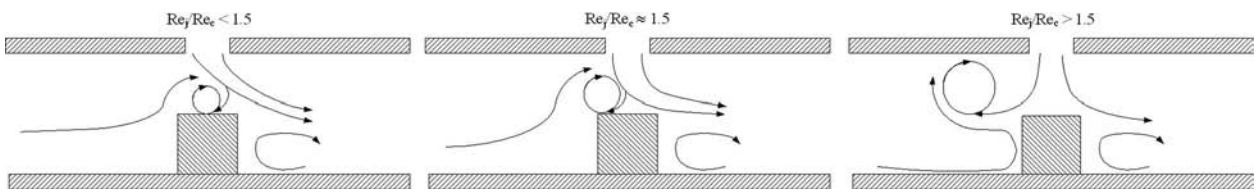

Fig. 12 Flow pattern for different ratios of the Reynolds numbers, $\mathrm{Re}_j/\mathrm{Re}_c$, for all three heights

above. The general influence of the impinging jet on the heat transfer coefficient on the sidewalls is that the heat transfer rate increases when the velocity of the impinging jet increases. Three exceptions can be observed where a decrease is observed between $U_j=4-6$ when $H=22.5$ mm and $U_c=2.8$ m/s, between $U_j=6-7$ when $H=30$ mm and $U_c=2.3$ m/s, and between $U_j=7-8$ when $H=30$ mm and $U_c=2.8$ m/s (see Fig. 11 and Tables 5 and 6 in the Appendix).

A similarity with the sidewalls is observed for the rear side of the cube, where a decrease in the heat transfer rate is observed for the cases with a distance of 18.75 mm when the cross-flow velocity increases from 1 m/s to 2.3 m/s (or from 1 m/s to 2.8 m/s) and where an increase is observed for the other cases when the cross-flow velocity increases (see Fig. 11 and Table 4 in the Appendix). Possible explanations for the unexpected decrease when the cross-flow increases from 1 m/s to 2.3 m/s for the cases with a distance of 18.75 mm are that a larger amount of the cross-flow is forced against the cube due to lower x-momentum, weaker separations from the edges between the front and the sidewalls, and the larger contribution from the horseshoe vortex, which results in a larger amount of the cross-flow being forced back into the wake region behind the rear side of the cube with a higher heat transfer as a consequence. The influence of the impinging jet on the heat transfer rate is that increased velocity results consistently in increased heat transfer rate.

The decreasing heat transfer rate on the sidewalls and on the rear side of the cube when the cross-flow velocity increases from 1 m/s to 2.3 m/s for the cases with a distance of 18.75 mm results in a decreasing average heat transfer coefficient over the whole cube; an increase is observed for the other cases when the cross-flow velocity increases (see Fig. 11 and Table 4 in the Appendix). Heat transfer also increases for all cases when the velocity of the impinging jet increases.

The values on the top and the average value of all sides increase significantly when the distance, H, decreases. An increasing trend is also observed on the sidewalls and on the rear side of the cube for the most part of the cases when the distance decreases.

There is a demand in the industry for quick-calculation methods such as correlations that can be used not only for quick estimation in an early phase of the design but also for optimization and strategic decisions. The significant connections between the distance, H, and the Reynolds numbers of the impinging jet, Re_j, and between the cross-flow, Re_c, and the average heat transfer coefficient make it possible to develop a correlation for the average heat transfer coefficient, h_{corr}. The correlation for the average heat transfer coefficient, $h_{\mathrm{corr}}=q''/(T_s-T_{\mathrm{in}})$, in Fig. 11 is based on the dimensionless distance, H/D, and the Reynolds numbers of the cross-flow, Re_c, and of the impinging jet, Re_j, and are given by

$$h_{\mathrm{corr}} = C_1\,\mathrm{Re}_c^{(C_5(H/D)^{C_6}+C_2)}\,\mathrm{Re}_j^{C_3}\left(\frac{H}{D}\right)^{C_4} \tag{10}$$

where $C_1=55.6398$, $C_2=4.5705$, $C_3=0.3529$, $C_4=-5.5056$, $C_5=-4.8792$, and $C_6=-0.1372$.

Figure 13 shows the evaluation of the correlations for the average heat transfer coefficient, h_{corr}, of all sides of the cube. All values from the correlation except 2 are within the region $\pm 10\%$ of the values from the simulations; the R^2-value is 0.952.

4.3 Pressure Loss Coefficients. Figure 14 shows the pressure loss coefficient for the cross-flow, i.e., the static pressure drop from the inlet, Δp_c, of the cross-flow to the outlet normalized by the dynamic pressure based on the mean velocity of the incoming cross-flow, $\rho U_c^2/2$.

All cases except for those with a mean cross-flow velocity of 1 m/s and a distance of 18.75 mm are well scaled by the ratios of the Reynolds numbers of the impinging jet, Re_j, and the cross-flow, Re_c, where the values from different cases with the same

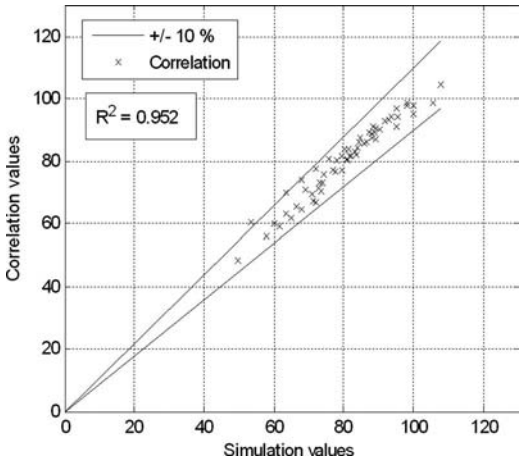

Fig. 13 Evaluation of the correlations for the average heat transfer coefficient, h_{corr}, of all sides of the cube

ratio between the Re numbers are located at approximately the same line (see Fig. 14). The decreasing slope in the region $\mathrm{Re}_j/\mathrm{Re}_c \approx 1.2-1.7$ occurs in the transition region, where an increase in the velocity of the impinging jet results in moving the recirculation vortex downstream so that the separations from the top of the cube dominate over the separations from the front side (see illustration in Fig. 12). It can also be interesting to note that it is approximately in this region where the minimum value for the heat transfer coefficient on the front side occurs (see Fig. 11). A positive slope is observed in the other regions, which means that the increased velocity of the impinging jet has a negative influence on the cross-flow in the form of an increased pressure drop for the cross-flow as a consequence. The pressure loss coefficient, C_c, is significantly lower for the cases with a cross-flow velocity of 1 m/s and a distance, H, of 18.75 mm (see Fig. 14) than for the other cases. A possible explanation for this behavior is that the separation from the top of the cube forces more against the top plate for these cases, which results in a faster decrease in the velocity of the separation from the front side of the top of the cube due to the near-wall effects, with decreasing pressure drop of the

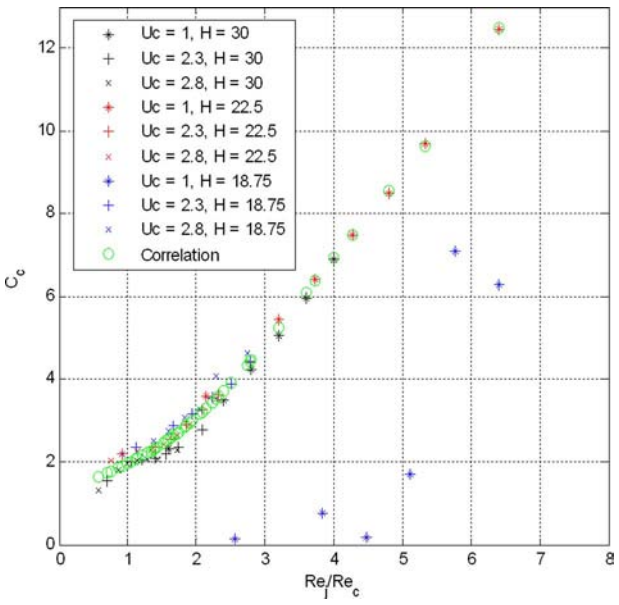

Fig. 14 Pressure loss coefficient, C_c, of the cross-flow

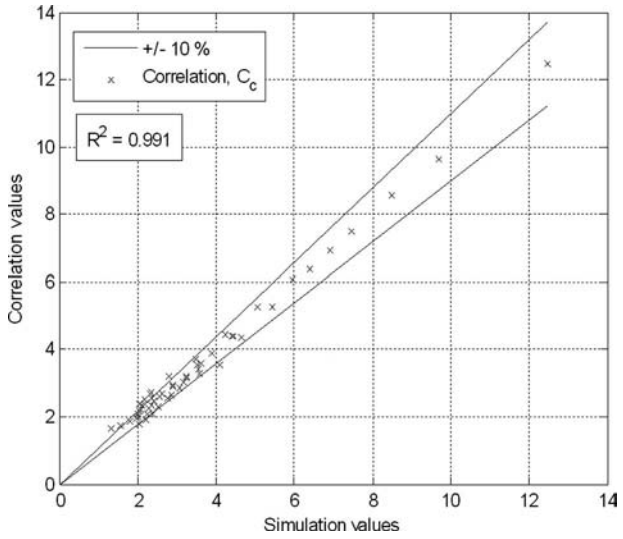

Fig. 15 Evaluation of the correlations for the pressure loss coefficient, C_c, of the cross-flow

cross-flow as a consequence.

The correlation for the pressure loss coefficient, C_c, of the cross-flow has been developed for all cases except the cases with a height of 18.75 mm and a cross-flow velocity of 1 m/s, which differ significantly from the other cases with the same ratio of the Reynolds numbers, $\mathrm{Re}_j/\mathrm{Re}_c$. The correlation is given by

$$C_c = \sum_{i=1}^{N} C_i \left(\frac{\mathrm{Re}_j}{\mathrm{Re}_c}\right)^{N-i} \tag{11}$$

where $N=6$, $C_1=0.0053$, $C_2=-0.0816$, $C_3=0.4142$, $C_4=-0.6007$, $C_5=1.0538$, and $C_6=1.1956$.

Figure 15 shows the evaluation of the correlations for the pressure loss coefficient, C_c, of the cross-flow. The higher values are better correlated than in the region around 2; the R^2-value is 0.991. A reason for the higher variation of the values around 2 is that several nonidentical values from different cases are located in this region, i.e., around this ratio of the Reynolds numbers, $\mathrm{Re}_j/\mathrm{Re}_c$ (see Fig. 14).

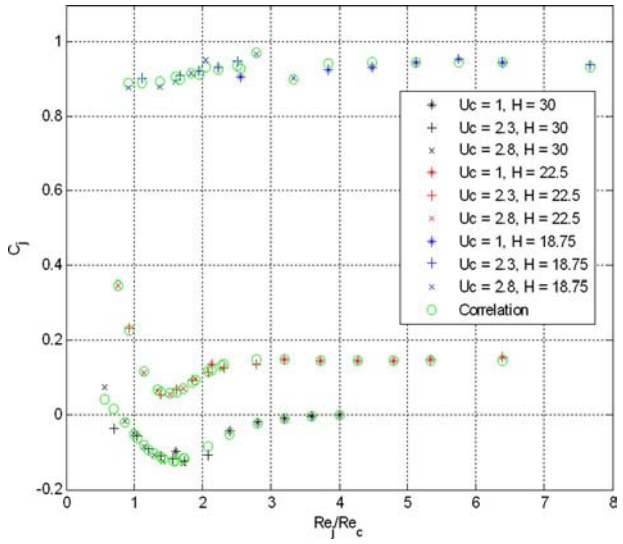

Fig. 16 Pressure loss coefficient, C_j, of the impinging jet

Figure 16 shows the pressure loss coefficient for the impinging jet, i.e., the static pressure drop from the inlet of the impinging jet, Δp_j, to the outlet normalized by the dynamic pressure based on the mean velocity of the impinging jet, $\rho U_j^2/2$.

All cases are well scaled by the ratios of the Reynolds numbers of the impinging jet, Re_j, and the cross-flow, Re_c, where the values from different cases with the same ratio between the Re numbers are located at approximately the same line for each distance, H (see Fig. 16). The values of the pressure loss coefficient, C_j, increase with decreasing distance, H, and a local minimum is observed for all distances at $\mathrm{Re}_j/\mathrm{Re}_c \approx 1.4-1.8$, an almost constant value when $3 < \mathrm{Re}_j/\mathrm{Re}_c$ and a negative slope when $\mathrm{Re}_j/\mathrm{Re}_c < 1.4$. It can be noted that the minimum values are observed at approximately the same $\mathrm{Re}_j/\mathrm{Re}_c$ ratio where the minimum values of the slopes for the pressure loss coefficient, C_c, of the cross-flow are observed (see Fig. 14).

A possible explanation for the negative slope when $\mathrm{Re}_j/\mathrm{Re}_c < 1.4$ is that the horseshoe vortex is located above the top of the cube, which forces the separations from the upper part of the front side of the cube and the attached part of the impinging jet more against the exit of the nozzle when the ratio $\mathrm{Re}_j/\mathrm{Re}_c$ is of lower magnitude (see Fig. 12). These blockage effects have negative influence on the impinging jet, which requires higher pressure at the outlet of the nozzle to force the impinging jet with the actual velocity. The horseshoe vortex and the stagnation point at the top of the cube move upstream when $\mathrm{Re}_j/\mathrm{Re}_c$ increases. The dislocation of the horseshoe vortex decreases the blockage effects, which decreases the required pressure at the exit of the nozzle at the same time when the pressure increases considerably in the stagnation region at the top of the cube when the stagnation point approaches the center of the cube. This high pressure region at the top of the cube acts as a resistance for the impinging jet, and the required pressure at the exit of the impinging jet increases when the stagnation effects increase. These two effects can explain the minimum value of the pressure loss coefficient, C_j, of the impinging jet at $\mathrm{Re}_j/\mathrm{Re}_c \approx 1.4-1.8$ when these two effects are involved. The stagnation effects have most influence on the required pressure at the exit of the nozzle when the ratio $\mathrm{Re}_j/\mathrm{Re}_c$ is higher than in the minimum value and the effects of the horseshoe vortex have a minor influence. The effects of the horseshoe vortex are negligible when $3 < \mathrm{Re}_j/\mathrm{Re}_c$, which results in a pure stagnation region and an almost constant value of the pressure loss coefficient, C_j, of the impinging jet. A range of negative values is observed when the distance, H, is 30 mm (see Fig. 16). These negative values occur due to the fact that the dynamic part of the total pressure is much lower at the outlet than at the inlet of the impinging jet and the exit of the nozzle is located above the high pressure region from the stagnation region.

The correlation for the pressure loss coefficient, C_j, of the impinging jet has been developed for all cases in the study where the pressure loss coefficient depends on the ratio of the Reynolds numbers $\mathrm{Re}_j/\mathrm{Re}_c$ and the dimensionless distance H/D. The correlation is given by

$$C_j = (1-\lambda)f + \lambda C_{12}\left(\frac{H}{D}\right)^{[C_{13}(H/D)+C_{14}]} \tag{12}$$

where λ and f are given by

$$\lambda = \frac{1}{2} + \frac{1}{2}\tanh\left[\frac{\left(\frac{\mathrm{Re}_j}{\mathrm{Re}_c}\right) + C_1}{C_2}\right] \tag{13}$$

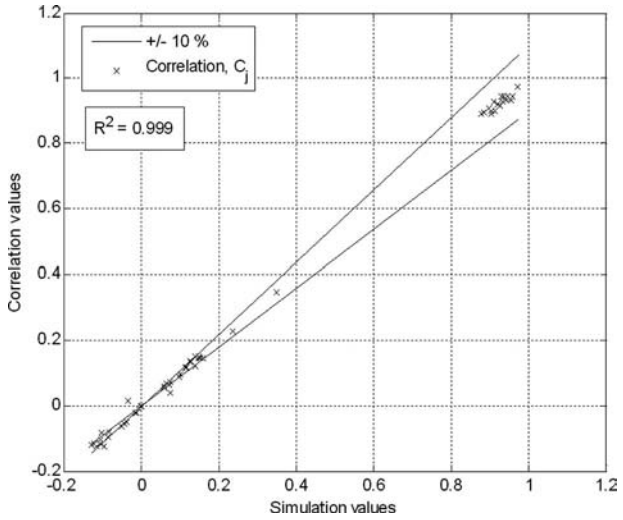

Fig. 17 Evaluation of the correlations for the pressure loss coefficient, C_j, of the impinging jet

$$f = \left[C_3\left(\frac{H}{D}\right)^2 + C_4\left(\frac{H}{D}\right) + C_5\right]\left(\frac{\mathrm{Re}_j}{\mathrm{Re}_c}\right)^2 + \left[C_6\left(\frac{H}{D}\right)^2 + C_7\left(\frac{H}{D}\right) + C_8\right]\left(\frac{\mathrm{Re}_j}{\mathrm{Re}_c}\right) + \left[C_9\left(\frac{H}{D}\right)^2 + C_{10}\left(\frac{H}{D}\right) + C_{11}\right] \quad (14)$$

where $C_1=-1.4748$, $C_2=0.7161$, $C_3=-2.6730$, $C_4=10.8303$, $C_5=-10.4920$, $C_6=7.9354$, $C_7=-32.4131$, $C_8=31.3714$, $C_9=-3.3016$, $C_{10}=12.5887$, $C_{11}=-10.7157$, $C_{12}=5.4567$, $C_{13}=-5.9109$, and $C_{14}=5.3130$.

Figure 17 shows the evaluation of the correlations for pressure loss coefficient, C_j, of the impinging jet. The higher values are better correlated than in the region around $\mathrm{Re}_j/\mathrm{Re}_c<0.2$ where several nonidentical values from different cases are located (see Fig. 16); the R^2-value is 0.999.

5 Conclusion and Discussion

The performance of a cooling technique with use of an impinging jet in a cross-flow on a heated wall-mounted cube was investigated numerically with use of a RSM that has been verified for both the velocity and the surface temperature. This case results in a very complex flow structure with several flow-related phenomena, such as stagnation points, separations, recirculating, and curvature effects, which have influence on the heat transfer rate. The investigation has pointed out the influence of the velocities of the impinging jet, U_j, and the cross-flow, U_c, and the distance, H, between the top and bottom plates on the heat transfer rate on the cube and on the pressure drops. The ratio between the Reynolds numbers of the impinging jet and the cross-flow, $\mathrm{Re}_j/\mathrm{Re}_c$, was shown to be an important parameter for the estimation of the pressure loss coefficients and a correlation for the pressure loss coefficient for the cross-flow, C_c, was developed with this ratio as the only input. The distance, H, was shown to have an important influence on the pressure loss coefficient of the impinging jet, C_j, and on the heat transfer rate of the cube. The dimensionless distance H/D was used as an input parameter together with the ratio of the Reynolds numbers, $\mathrm{Re}_j/\mathrm{Re}_c$, in the correlation for the pressure loss coefficient of the impinging jet, C_j. The dimensionless distance H/D was also used in the correlation for the average heat transfer coefficient on the cube, h_{corr}, together with the Reynolds numbers of the impinging jet, Re_j, and the cross-flow, Re_c. It can be noted that the average heat transfer coefficient on the cube increases considerably to a cost of higher pressure loss coefficients when the distance between the top and bottom plates decreases. The average heat transfer coefficient also increases when the velocity of the impinging jet, U_j, increases to a cost of a higher pressure loss coefficient of the cross-flow, C_c, and a higher pressure drop between the nozzle of the impinging jet and the outlet. This occurs despite the fact that the pressure loss coefficient of the impinging jet, C_j, decreases in some ranges when the velocity of the impinging jet, U_j, increases. The effect of decreasing the distance and increasing the velocity of the impinging jet, U_j, is most significant at the top of the cube, but these modifications have significant effects on the other four walls. The results of increasing the cross-flow velocity, U_c, are very complex and it is more difficult to predict the effects of the cross-flow on the heat transfer than it is for the other parameters. For example, the cross-flow can force the stagnation point from the impinging jet downstream to the rear part of the top of the cube when $\mathrm{Re}_j/\mathrm{Re}_c$ is low and an essential part of the impinging jet is missing the target, leading to a decreased heat transfer rate. Increased cross-flow velocity, U_c, results in an increased pressure drop over the channel despite the decrease in the pressure loss coefficient of the cross-flow, C_c.

This parametric study is in the early stage and the study should be extended to cover a wider range of the existing parameters and complemented with the influence of other parameters such as the size of the cube, position, size, angle, and geometry of the nozzle before the correlations for the heat transfer rate and the pressure drops are completed.

Acknowledgment

The authors gratefully acknowledge the funding received from the KK Foundations, Ericsson AB, Nokia AB, and University of Gävle in Sweden. The authors thank Dr. M. Tummers and Professor K. Hanjalić at Delft University of Technology for their help in the measurement part of the present study.

Nomenclature

C = pressure loss coefficient
c_p = specific heat (J/kg K)
D = nozzle diameter (m)
d = diameter at the radial distance (m)
H = channel height (m)
h = cube size (m) and heat transfer coefficient ($\mathrm{W/m^2\ K}$)
I = turbulence intensity (%)
k = turbulent kinetic energy ($\mathrm{m^2/s^2}$)
p = mean pressure (Pa)
p' = fluctuating pressure (Pa)
$\mathrm{Pr}=\nu/\alpha$ = Prandtl number
q'' = heat flux ($\mathrm{W/m^2}$)
$\mathrm{Re}_j=UD/\nu$ = Reynolds number based on the nozzle diameter and the jet velocity
$\mathrm{Re}_c=UH/\nu$ = Reynolds number based on the channel height and mean velocity in the channel
T = temperature (°C)
T' = fluctuating temperature (°C)
T_s = surface temperature (°C)
T_{in} = inlet air temperature (°C)

U = mean velocity (m/s)
u' = fluctuating velocity (m/s)
x,y,z = coordinate (m)

Greek Symbols

α = thermal diffusivity (m^2/s)
δ_{ij} = Kronecker delta
δ_c = thickness of the epoxy layer (m)
ε = dissipation of the turbulent kinetic energy (m^2/s^3)
λ = thermal conductivity (W/m K)
μ = dynamic viscosity (kg/m s)
ν = kinematic viscosity (m^2/s)
ρ = density (kg/m^3)
ω = turbulence frequency (1/s)

Subscripts

c = cross-flow
j = jet
t = turbulent

Appendix

Tables 4–6 are shown in this Appendix.

Table 4 Reynolds stress model, *H*=18.75

U_c/U_j	h_{front}	h_{top}	h_{rear}	h_{sides}	$h_{average}$	Δp_c	Δp_j
1/4	72.2	130.1	51.3	55.8	73.0	−0.09	−8.89
1/6	73.6	162.7	58.1	62.0	83.7	−0.47	−20.44
1/7	74.7	177.2	61.2	66.2	89.1	−0.1	−28.03
1/8	76.6	191.3	63.8	71.6	95.0	−1.05	−37.01
1/9	78.3	207.1	65.8	74.9	100.2	−4.34	−47.41
1/10	80.5	220.2	68.2	79.6	105.6	−3.86	−57.83
2.3/4	68.3	129.8	41.7	52.7	69.0	−7.68	−9.20
2.3/6	73.8	163.2	50.2	55.1	79.5	−9.28	−19.89
2.3/7	75.5	178.1	52.7	57.3	84.2	−10.30	−27.31
2.3/8	77.1	191.7	55.8	61.0	89.3	−11.49	−36.18
2.3/9	78.5	204.9	58.4	63.5	93.7	−12.63	−46.19
2.3/10	79.7	217.7	60.4	66.2	98.0	−14.39	−58.20
2.8/4	72.2	128.6	45.7	59.6	73.5	−10.6	−9.49
2.8/6	79.1	165.1	49.2	57.5	81.7	−12.17	−19.89
2.8/7	80.6	180.1	54.0	59.2	86.6	−13.21	−26.31
2.8/8	80.0	191.5	55.8	62.4	90.4	−14.7	−34.53
2.8/9	83.5	207.6	59.9	63.6	95.7	−15.64	−44.38
2.8/10	84.5	217.8	61.9	67.6	99.9	−19.64	−56.17
2.8/12	86.6	241.9	64.7	72.7	107.7	−22.26	−84.07

Table 5 Reynolds stress model, *H*=22.5

U_c/U_j	h_{front}	h_{top}	h_{rear}	h_{sides}	$h_{average}$	Δp_c	Δp_j
1/4	51.1	104.9	32.4	38.9	53.3	−2.20	−1.33
1/6	57.3	130.8	38.8	45.0	63.4	−3.34	−3.26
1/7	59.7	142.3	41.8	48.0	67.9	−3.93	−4.40
1/8	61.7	153.1	44.6	50.6	72.1	−4.58	−5.75
1/9	63.7	163.6	46.6	52.8	75.9	−5.21	−7.28
1/10	64.7	164.5	51.2	54.7	78.0	−5.94	−9.13
1/12	67.7	193.2	56.8	59.8	87.4	−7.64	−13.73
2.3/4	69.0	107.3	36.2	60.1	66.6	−7.12	−2.29
2.3/6	69.5	131.0	47.5	61.4	74.2	−7.59	−1.23
2.3/7	71.3	142.0	50.1	63.7	78.1	−8.31	−2.06
2.3/8	72.8	152.6	51.3	65.3	81.5	−9.40	−3.73
2.3/9	74.4	163.0	53.4	66.9	84.9	−10.55	−5.64
2.3/10	76.0	173.1	55.5	68.7	88.4	−11.75	−7.70
2.3/12	79.4	192.5	59.2	72.3	95.1	−14.32	−11.97
2.8/4	77.8	106.4	37.2	69.9	72.2	−9.79	−3.4
2.8/6	74.4	132.2	47.4	65.6	77.0	−10.83	−2.47
2.8/7	76.0	142.6	52.6	69.4	82.0	−11.01	−1.92
2.8/8	77.6	152.9	55.2	71.5	85.7	−11.65	−2.22
2.8/9	79.0	163.0	56.1	72.7	88.69	−12.64	−3.57
2.8/10	80.6	174.7	56.9	73.0	91.7	−13.89	−5.99
2.8/12	83.3	192.5	60.9	76.9	98.1	−16.89	−11.04

Table 6 Reynolds stress model, $H=30$

U_c/U_j	h_{front}	h_{top}	h_{rear}	h_{sides}	h_{average}	Δp_c	Δp_j
1/4	44.9	96.7	31.1	37.5	49.6	−1.43	0.96
1/6	51.0	119.7	34.9	42.5	58.1	−2.13	0.91
1/7	53.9	129.6	37.0	44.0	61.7	−2.59	0.58
1/8	56.3	139.0	39.0	45.2	64.9	−3.09	0.34
1/9	58.3	148.1	41.0	46.3	68.0	−3.65	0.17
1/10	59.6	157.0	43.3	48.3	71.3	−4.23	0.04
2.3/4	72.4	83.6	37.5	53.2	60.0	−5.03	0.35
2.3/6	70.3	115.5	44.1	62.9	71.1	−6.49	1.19
2.3/7	68.6	130.2	48.8	59.3	73.2	−6.66	2.69
2.3/8	68.3	140.9	51.3	64.0	77.7	−6.79	4.28
2.3/9	70.1	150.2	51.5	66.3	80.9	−7.07	5.82
2.3/10	71.2	158.6	52.4	67.0	83.2	−7.60	7.57
2.3/12	73.7	174.8	54.0	69.0	88.1	−9.05	9.37
2.8/4	80.8	83.8	41.1	55.8	63.4	−6.39	−0.72
2.8/6	79.2	107.1	46.4	68.4	73.9	−8.72	0.35
2.8/7	78.0	124.9	49.0	73.0	79.6	−9.51	1.44
2.8/8	76.3	139.6	53.1	67.9	81.0	−9.72	3.36
2.8/9	75.0	150.3	56.8	69.2	84.1	−9.91	5.29
2.8/10	76.2	159.6	57.4	73.6	88.1	−9.88	7.65
2.8/12	78.6	176.1	58.5	75.4	92.8	−11.04	11.47

References

[1] Jonsson, H., and Moshfegh, B., 2001, "Modeling of Thermal and Hydraulic Performance of Plate Fin Heat Sinks—Influence of Bypass," IEEE Trans. Compon. Packag. Technol., **24**(2), pp. 142–149.

[2] Meinders, E. R., and Hanjalić, K., 2002, "Experimental Study of the Convective Heat Transfer From In-Line and Staggered Configurations of Two Wall-Mounted Cubes," Int. J. Heat Fluid Flow, **46**, pp. 465–482.

[3] Rundström, D., and Moshfegh, B., 2006, "Investigation of Flow and Heat Transfer of an Impinging Jet in a Cross-Flow for Cooling of a Heated Cube," ASME J. Electron. Packag., **128**, pp. 150–156.

[4] Lee, J., and Lee, S. J., 1999, "Stagnation Region Heat Transfer of a Turbulent Axisymmetric Jet Impingement," Exp. Heat Transfer, **12**, pp. 137–156.

[5] Behnia, M., Parniex, S., and Durbin, P., 1999, "Numerical Study of Turbulent Heat Transfer in Confined and Unconfined Impinging Jets," Int. J. Heat Fluid Flow, **20**, pp. 1–9.

[6] Abdon, A., and Sundén, B., 2001, "Numerical Investigation of Impingement Heat Transfer Using Linear and Nonlinear Two-Equation Turbulence Models," Numer. Heat Transfer, Part A, **40**, pp. 563–578.

[7] Craft, T. J., Graham, L. J. W., and Launder, B. E., 1993, "Impinging Jet Studies for Turbulence Models Assessment II: An Examination of the Performance of Four Turbulence Models," Int. J. Heat Mass Transfer, **36**, pp. 2685–2697.

[8] Durbin, P., 1991, "Near-Wall Turbulence Closure Modelling Without Damping Function," Theor. Comput. Fluid Dyn., **3**, pp. 1–13.

[9] Rundström, D., and Moshfegh, B., 2005, "Numerical Investigation of Flow Behaviour of an Impinging Jet in a Cross Flow on a Wall-Mounted Cube Using RSM and v^2-f," *Proceedings of the Fourth International Symposium on Turbulence and Shear Flow Phenomenon*, Williamsburg, June 27–29.

[10] Rundström, D., and Moshfegh, B., 2006, "RSM Predictions of an Impinging Jet in a Cross Flow on a Wall-Mounted Cube, *Proceedings of the 13th International Heat Transfer Conference*, Sydney, Aug. 13–18.

[11] Yu, M. H., and Monkewitz, P. A., 1990, "The Effect on Nonuniform Density on the Absolute Instability of Two-Dimensional Inertial Jets and Wakes," Phys. Fluids A, **2**, pp. 1175–1181.

[12] Lien, F. S., and Leschziner, M. A., 1994, "Assessment of Turbulence Transport Models Including Non-Linear RNG Eddy-Viscosity Formulation and Second Moment Closure for Flow Over a Backward-Facing Step," Comput. Fluids, **23**, pp. 983–1004.

[13] Launder, B. E., and Shima, N., 1989, "Second-Moment Closure for Near-Wall Sublayer: Development and Application," AIAA J., **27**, pp. 1319–1325.

[14] Wolfshtein, M., 1969, "The Velocity and Temperature Distribution in One-Dimensional Flow With Turbulence Augmentation and Pressure Gradient," Int. J. Heat Mass Transfer, **12**, pp. 301–318.

[15] Chen, H. C., and Patel, V. C., 1988, "Near-Wall Turbulence Models for Complex Flows Including Separation," AIAA J., **26**, pp. 641–648.

[16] FLUENT 6.2, 2005, Fluent Manuals, Fluent Inc.

[17] Geers, L. F. G., Tummers, M. J., and Hanjalić, K., 2004, "Experimental Investigation of Impinging Jet Arrays," Exp. Fluids, **36**, pp. 946–958.

[18] Meinders, E. R., van der Meer, Th. H., and Hanjalić, K., 1996, "Application of Infrared Restoration Technique to Improve the Accuracy of Surface Temperature Measurements," *Proceedings of Quantitative Infrared Thermography III*, EUROTHERM No. 50, Stuttgart, Sept. 2–5.

[19] Meinders, E. R., van der Meer, Th. H., Hanjalić, K., and Lasance, C. J. M., 1997, "Application of Infrared Thermography to the Evaluation of Local Heat Transfer on Arrays of Cubical Protrusions," Int. J. Heat Fluid Flow, **18**, pp. 152–159.

[20] Tummers, M. J., Flikweert, M. A., Hanjalić, K., Rodink, R., and Moshfegh, B., 2005, "Impinging Jet Cooling of Wall-Mounted Cubes," *Proceedings of ERCOFTAC International Symposium on Engineering Turbulence Modelling and Measurements—ETMM6*, Sardinia, May 23–25.

[21] Ničeno, B., Dronkers, A. D. T., and Hanjalić, K., 2002, "Turbulent Heat Transfer From a Multi-Layered Wall-Mounted Cube Matrix: A Large Eddy Simulation," Int. J. Heat Fluid Flow, **23**, pp. 173–185.

Je-Young Chang
Intel Corporation,
5000 W. Chandler Boulevard,
CH5-157 Chandler, AZ 85226
e-mail: je-young.chang@intel.com

Ravi S. Prasher
Adjunct Professor
Department of Mechanical and Aerospace Engineering,
Arizona State University,
Tempe, AZ 85287;
and Intel Corporation,
5000 W. Chandler Boulevard,
CH5-157,
Chandler, AZ 85226
e-mail: ravi.s.prasher@intel.com

Suzana Prstic
Intel Corporation,
5000 W. Chandler Boulevard,
CH5-157 Chandler, AZ 85226

P. Cheng

H. B. Ma
e-mail: mah@missouri.edu

Department of Mechanical and Aerospace Engineering,
University of Missouri,
Columbia, MO 65211

Evaporative Thermal Performance of Vapor Chambers Under Nonuniform Heating Conditions

This paper reports the test results of vapor chambers using copper post heaters and silicon die heaters. Experiments were conducted to understand the effects of nonuniform heating conditions (hot spots) on the evaporative thermal performance of vapor chambers. In contrast to the copper post heater, which provides ideal heating, a silicon chip package was developed to replicate more realistic heat source boundary conditions of microprocessors. The vapor chambers were tested for hot spot heat fluxes as high as 746 W/cm^2. The experimental results show that evaporator thermal resistance is not sensitive to nonuniform heat conditions, i.e., it is the same as in the uniform heating case. In addition, a model was developed to predict the effective thickness of a sintered-wick layer saturated with water at the evaporator. The model assumes that the pore sizes in the sintered particle wick layer are distributed nonuniformly. With an increase of heat flux, liquid in the larger size pores are dried out first, followed by drying of smaller size pores. Statistical analysis of the pore size distribution is used to calculate the fraction of the pores that remain saturated with liquid at a given heat flux condition. The model successfully predicts the experimental results of evaporative thermal resistance of vapor chambers for both uniform and nonuniform heat fluxes. [DOI: 10.1115/1.2976786]

Keywords: heat pipe, vapor chamber, nonuniform heating, evaporative thermal performance, silicon die heater

1 Introduction

As integrated circuit (IC) technology evolves for microprocessors, components inside IC devices draw more power, thus generating more heat [1]. Furthermore, the heat generation is nonuniform with areas of high local heat fluxes at a few locations on the chip (die) [1,2], which are known as "hot spots." Trends [1] show an increase in thermal design power and an increase in both the average power density and the local power density. Over the past years, the increasing demands for more efficient heat removal from microprocessors have forced thermal engineers to take a closer look at every component of the thermal budget in order to remain in the air cooling mode. Use of heat pipes (or vapor chambers) is considered as one of the most promising technology options. The idea is to spread the heat over a much larger surface area to reduce the heat flux to a manageable level, an ability that can be attributed to the high effective thermal conductivity of a heat pipe [3–5].

In electronics cooling applications, heat is incident on a portion of the heat pipe surface (evaporator) where a silicon die is attached. For characterizing the thermal performance of a heat pipe, various heating methods at the evaporator have been used in the past. A close look at the literature reveals that previous experiments were conducted with a uniform heat source using a foil heater or a copper post heater [3–7]. Recently, DiStefano et al. [8] compared the copper post heater and silicon die heater methods, which impose uniform temperature and uniform heat flux boundary conditions, respectively; however, in their studies, heat was uniformly distributed across each heater area. Note that heat pipe/vapor chamber are interchangeably used in this paper.

In applications, a heat pipe is exposed to a concentrated nonuniform power source due to the presence of multiple hot spots on a silicon die [1,2], which is quite different from the uniform heat sources used by most of the previous researchers. The literature on the performance of heat pipes is comprehensive [3–5]; however, there is a lack of literature on the performance of heat pipes under hot spot (nonuniform) heating conditions. Therefore, a systematic study of the performance of heat pipes under hot spot heating conditions is desirable to answer the questions.

(1) Typically the burnout heat flux for commonly used commercial sintered-wick vapor chambers with water as the working fluid is known to be around 100 W/cm^2, whereas the local heat flux on the silicon die can be much higher than 300 W/cm^2 [1]. Therefore, the key question is whether or not the heat pipes can withstand very high heat fluxes from the hot spots without degradation in performance.
(2) The thermal resistance of a solid-based heat spreader such as copper increases due to the presence of hot spots [1,2] over that for a uniform heating condition. However, based on the existing literature, it is not known whether or not the

Contributed by the Heat Transfer Division of ASME for publication in the JOURNAL OF HEAT TRANSFER. Manuscript received October 10, 2007; final manuscript received June 3, 2008; published online September 23, 2008. Review conducted by Louis C. Burmeister. Paper presented at the 2005 International Electronic Packaging Technical Conference and Exhibition (IPACK2005), San Francisco, CA, July 15–22, 2005.

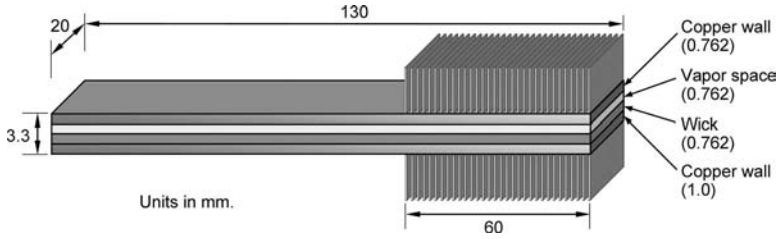

Fig. 1 Schematic of vapor chamber

thermal resistance of a heat-pipe-based heat spreader increases under hot spot heating conditions over that for a uniform heating condition.

(3) The thermal resistance of a heat pipe/vapor chamber also depends on the heat flux [9]. Particularly, the evaporator resistance decreases with increasing heat flux. However, it is not known if the evaporator resistance decreases with increasing heat flux in nonuniform heating conditions.

(4) Finally, there is a need to develop modeling schemes to perform design sensitivity studies on the performance of heat pipe/vapor chamber under nonuniform heating conditions.

The motivation behind the current work is to investigate the effects of nonuniform power sources on the thermal resistance of the evaporator of a vapor chamber and address some of the issues highlighted above. The focus is primarily on the thermal resistance of an evaporator, because nonuniformity of heat flux on the chip mainly affects the thermal resistance of the evaporator, which is in close proximity to the chip.

In the current investigation, we report the evaporative thermal performance of vapor chambers using copper post heaters and silicon die heaters, which were tested at various heat fluxes (power inputs). In contrast to the copper post heaters, which provide an ideal heating condition, the silicon chip packages replicate more realistic nonuniform heat source boundary conditions on the dies of microprocessor packages. The motivation to use the copper post heaters is discussed below. The silicon chip contains three metallic heaters: a 10×12 mm^2 heater in order to provide uniform heating, a 10×3 mm^2 heater in order to simulate a localized heating, and a 400×400 μm^2 heater in order to simulate the hot spots on actual microprocessors. In the experiment, the highest heat flux from the hot spot heaters was approximately 746 W/cm^2.

In order to predict the evaporative thermal performance of a vapor chamber as a function of heat flux, a model was developed to predict the effective wick thickness of a sintered-wick structure based on the statistical distribution of its particles. Experiments based on copper post heaters are ideal experiments to validate models, as they provide perfectly one-dimensional heat conduction through the copper posts. The model of effective wick thickness is first validated with the data obtained from the copper post heaters. Finally, this model is used to predict the thermal performance of a vapor chamber under nonuniform heating conditions. The predictions from the model are compared with the data obtained under nonuniform heating on the silicon die heaters.

2 Experimental Apparatus and Procedure

Experiments were conducted using vapor chambers with water as the working fluid. The schematic of the vapor chamber is shown in Fig. 1. As shown, the vapor chambers used in the study have a sandwich structure of lower copper wall, wick layer, vapor space, and upper copper wall. The sintered copper wick is at the bottom inside wall of the chamber container. Based on the microscopic images (not shown) of sintered particles for the vapor chambers, the porosity and the average radius of particles in the evaporator are approximately 53% and 32 μm, respectively. Also, for the present vapor chambers, approximately 100% of pore volume in the wick is charged with water. Overall the dimensions of the vapor chamber were 130 mm long, 20 mm wide, and 3.3 mm thick, and the details of the internal dimensions are shown in Fig. 1. The heat source (evaporator section) is at the bottom wall near the left end of the vapor chamber. A highly conductive thermal grease ($k\sim3.5$ W/m K) was applied at the interfaces of the heat sources and the vapor chambers. The lengths of the condenser sections that were covered with copper stacked fins on both sides of vapor chamber at the right end were approximately 60 mm, where the fins on both sides were cooled by air ducted to a blower (not shown).

Figure 2 shows the two different sets of test heaters that are used for testing vapor chambers: a copper post heater and a silicon die heater. The copper post heater setup is shown in Fig. 2(*a*). An electric heater was attached at the bottom of the copper post, and the three thermocouples (TCs) were evenly spaced along the copper post in order to establish the power delivered from the heater to the vapor chamber. In the current study, two different sizes (5×5 mm^2 and 10×10 mm^2) of copper post heaters were used for evaluating the effect of heater size on vapor chamber performance. The silicon die heater setup is shown in Fig. 2(*b*), where a silicon die with electric heaters was used as the heating source. A schematic of the electronic package with a silicon die heater is shown in Fig. 3(*a*). As shown in Fig. 3, the micropin grid array (μPGA) package includes a silicon die ($\sim$750 um thick) with metallic heaters fabricated at the bottom. The whole package was mounted on a test board through a socket. Figure 3(*b*) shows the dimensions and locations of the main heater (10×12 mm^2), the strip heater (10×3 mm^2), and the hot spot heater (400×400 μm^2) in the silicon die, all of which were centered on the die. These heaters were designed to replicate the source boundary conditions on the dies of microprocessor packages. Specifically, the two heater sizes (10×3 mm^2 and 10×12 mm^2) were selected to closely match the test conditions of copper post heater sizes (5×5 mm^2 and 10×10 mm^2), where the ratio of heater sizes is equal to 4. Another reason to have a strip heater of this size was to mimic the actual microprocessor conditions. In a real microprocessor, most of the heat dissipated from the core rather than from the cache area [2]. Depending on the microprocessor architecture, the core area can be much smaller than the whole area of the die. Therefore, the strip heat mimics the core area on a chip. Similarly, the hot spot heater mimics the localized hot spots in actual microprocessors. Hot spot heat fluxes in excess of 300 W/cm^2 are expected for future microprocessors [1]. In the present study, the heat flux on the hot spot was varied from 256 W/cm^2 to 746 W/cm^2.

Details of the fabrication processes of the heaters can be found in the paper by Prasher et al. [10]. The test board facilitated proper connections to the heaters on the die. In this setup, direct current was supplied to the heating element by a dc power supply, and the power was estimated from the voltage drop across the test heater.

As shown in Figs. 2(*a*) and 2(*b*), two thermocouples (T/C2 and T/C3) were attached on the top wall of each vapor chamber with a thermally conductive epoxy. T/C2 was located 5 mm away from the center of the evaporator section (heat source area) toward the

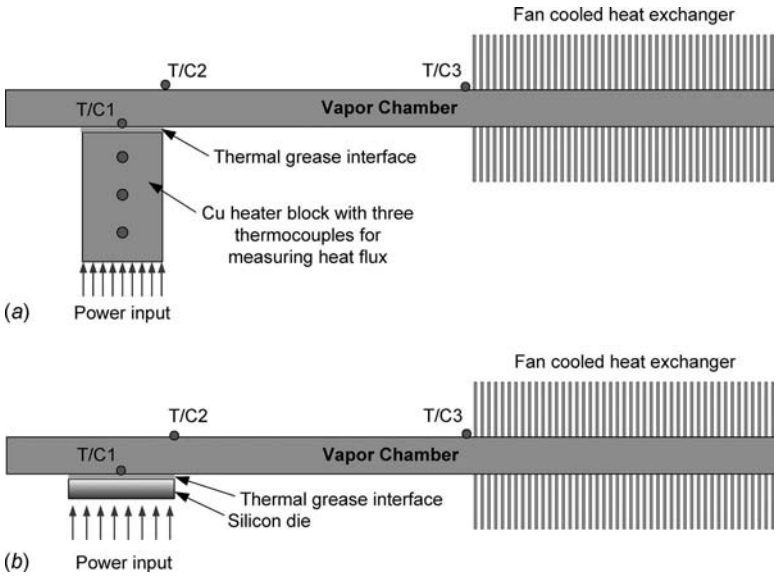

Fig. 2 Schematics of two heater test setups: (*a*) copper post heater setup and (*b*) silicon die heater setup

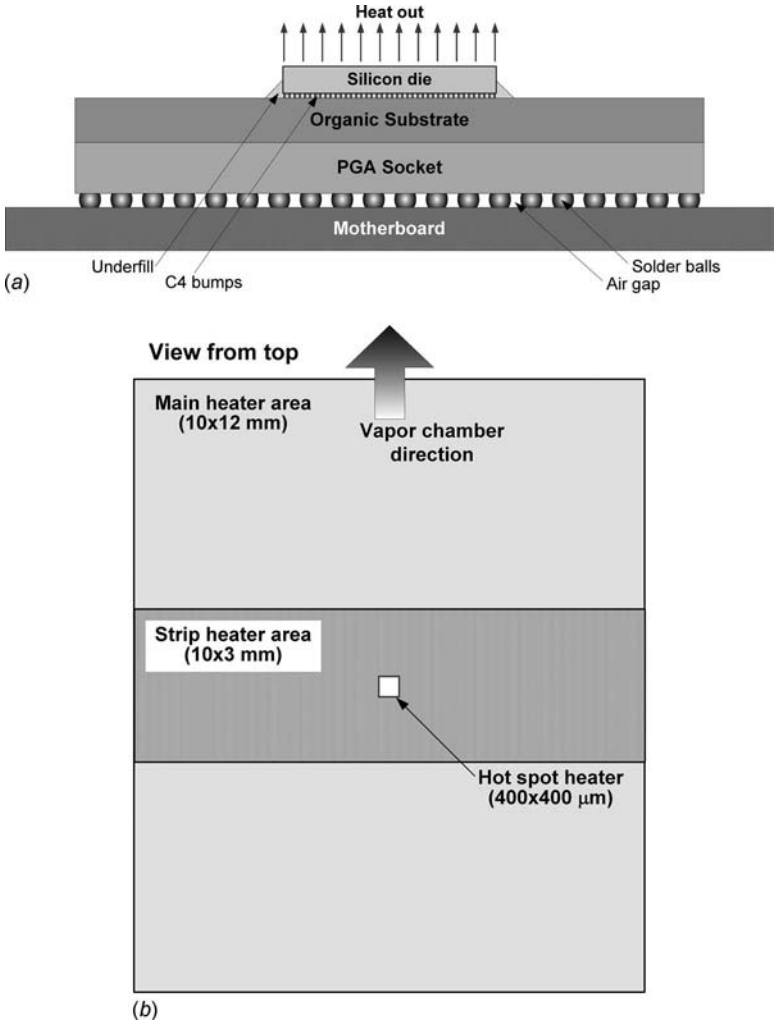

Fig. 3 Schematic of package based heaters: (*a*) schematic of package with silicon die heaters and (*b*) locations of heaters at the back side of silicon die

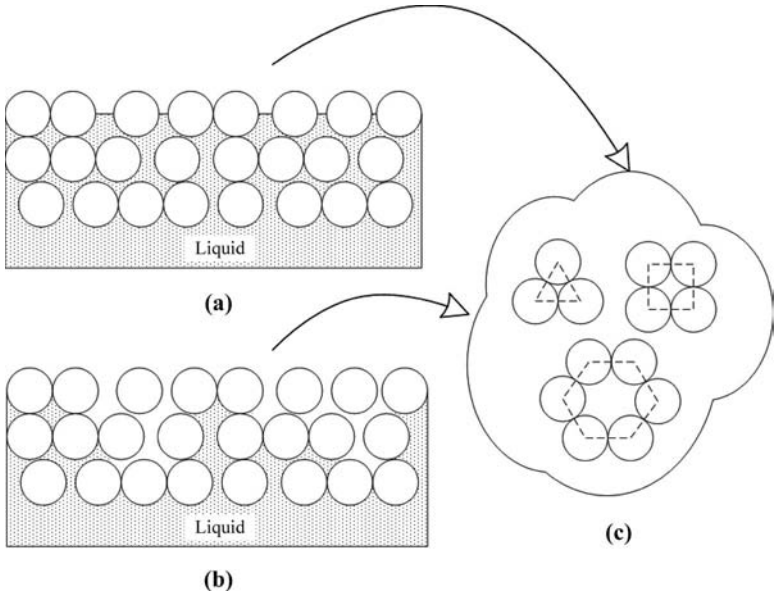

Fig. 4 Receding process of liquid in wick and possible particle structures

condenser section, and T/C3 was located just before the first fin in the condenser section. Also, the vapor chamber had a thermocouple hole (0.4 mm diameter and 5 mm depth) in the copper wall (1 mm thickness) on the heater side. The hole was drilled into the center of the evaporator from one edge. The gap between the hole and the bottom surface of the vapor chamber was approximately 0.05 mm. A metal-sheathed thermocouple (0.25 mm diameter) was inserted in the hole with a conductive thermal grease ($k \sim 3.5$ W/m K) to provide temperature measurement (T/C1) at the bottom surface of the vapor chamber. For a given test condition, the three temperature readings (T/C1, T/C2, and T/C3) at steady state are used to calculate the evaporator resistance and the adiabatic resistance, which are defined, respectively, as

$$\theta_{\text{evap}} = \frac{T_1 - T_2}{q} \tag{1}$$

$$\theta_{\text{adia}} = \frac{T_2 - T_3}{q} \tag{2}$$

where T_1, T_2, and T_3 are the temperature readings of T/C1, T/C2, and T/C3, respectively, and q is the power delivered from heater to vapor chamber, as shown in Fig. 2. For the test setups in Figs. 2(*a*) and 2(*b*), the vapor chamber was insulated between the evaporator and the condenser with multiple layers of foam to avoid heat loss through the top and the bottom sides of the vapor chamber.

During the experiment, the condenser temperature (T/C3) was maintained at a desired point (45°C) by adjusting the fan flow rate to the fins at the condenser section. This emulated the typical operation conditions of vapor chambers in electronic thermal management applications. Differences between the T/C2 and T/C3 temperatures were small ($\theta_{\text{adia}} \sim 0.05$°C/W) due to the high thermal conductance of the vapor space [9,11].

The experimental uncertainties in evaporator resistances θ_{evap} were estimated using Kline and McClintock [12] methodology. The uncertainty in temperature measurement was estimated considering the measurement resolution of thermocouples, which was estimated to be ±0.4°C at all power input conditions. For the silicon die heater setups, the substrate conduction loss through the motherboard was estimated to be less than 1% based on the previous analysis of Prasher et al. [10]. The low conduction loss is due to the low thermal conductivities of the components on the motherboard side (C4 bumps, substrate, socket, solder balls, and test board). Based on the uncertainties in the temperatures and the heat fluxes, the overall uncertainty estimates in the evaporator resistances were 16% and 10% for heat fluxes between 30 W/cm^2 and 70 W/cm^2, respectively. The uncertainty values of the copper post heater setup were estimated to be comparable to the values given above.

3 Modeling of Effective Wick Thickness

In order to predict the temperature drop occurring in the vapor chamber, the thermal resistances occurring in the evaporator and condenser must be determined. When heat is added on the evaporator section, heat is transferred from the heat pipe wall, through the wick saturated with the working fluid, and to the liquid-vapor-solid interface, where thin film evaporation occurs. The vapor flows from the evaporator, through the adiabatic section, and to the condensing section, where the vapor condenses and releases the latent heat. The heat is transferred from the condensation film, through the wick saturated with the condensate, and to the heat pipe wall, where the heat is removed by forced flow of air. During this heat transfer process, thermal resistance in the wick plays an important role in determining the total temperature drop in the heat pipe, in particular, for a high heat flux application. Prasher [9] developed a heat conduction model to predict the temperature drop occurring in the wick. This model, however, cannot predict the temperature response as the power input is varied. The primary reason for this is that the model does not consider the heat flux (power input) effects on the liquid level in the wick.

When the power input in the evaporator is increased, the flow rate of working fluid in the flow path increases, thereby increasing the total pressure drop. In order to overcome the pressure drop, the driving pressure occurring in the wick must increase. The increase of the capillary pressure is directly related to the meniscus radius of the liquid-vapor interface in the sintered wick. The capillary pressure occurring in the heat pipe can be expressed as

$$\Delta P_{\text{cap}} = 2\sigma\left(\frac{1}{r_{\text{evap}}} - \frac{1}{r_{\text{cond}}}\right) \tag{3}$$

where r_{evap} and r_{cond} are the meniscus radii at the liquid-vapor interface in the evaporator and condenser sections, respectively. For the vapor chamber investigated herein, r_{cond} can be assumed to be close to infinity. The capillary pressure in the heat pipe will

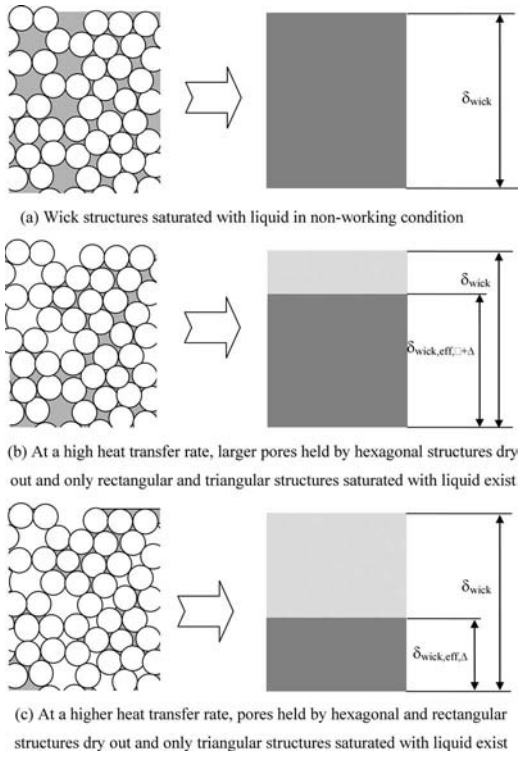

Fig. 5 Schematic of wick structure and effective thickness

only depend on the meniscus radius of the sintered wick in the evaporator. Cheng and Ma [13] showed that if the wick consists of sintered particles with a uniform radius, the possible arrangements formed in the wick are triangular, rectangular, and hexagonal structures, as shown in Fig. 4. Viewed from one particle, there are several structures formed around this particle. By listing all possible arrangements of these structures and considering that each group of those structures has the same possibility, the percentage of each structure can be determined, i.e., the percentages for the triangular, rectangular, and hexagonal structures are 45%, 28%, and 27%, respectively. The minimum meniscus radius is defined as

$$r_{\min} = \frac{2A_{\text{gap}}}{P_{\text{gap}}} \tag{4}$$

where A_{gap} is the minimum area trapped by particles and P_{gap} is the perimeter of the trapped area. The minimum meniscus radii of the triangular, rectangular, and hexagonal structures are calculated to be $0.103r_p$, $0.273r_p$, and $0.654r_p$, respectively, where r_p is the particle radius. As a reference case, the average minimum meniscus radius $r_{\min}$ for the sintered particles with a uniform radius is calculated to be $r_{\min}=0.443r_p$, which agrees well with the one cited by Ferrell and Alleavitch [14] and most heat pipe textbooks [3–5], providing confidence in the current estimates.

With an increase of power input, the liquid in large pore sizes cannot be held anymore and recedes to fill smaller pore sizes. There are two factors determining the thermal resistance of the wick thickness: one is the expanded liquid-vapor interface and the other is the effective thickness of wick saturated with working fluid. Due to a high heat transfer coefficient for thin film evaporation, the thermal resistance at the expanded liquid-vapor-solid interfaces is much smaller than the thermal resistance of a wick saturated with the working fluid, so the thermal resistance R in the wick can be approximately determined by the effective thickness of a wick saturated with working fluid, i.e.,

$$R = \frac{\delta_{\text{wick,eff}}}{k_{\text{wick,eff}}} \tag{5}$$

where $\delta_{\text{wick,eff}}$ is the effective thickness of a wick saturated with working fluid, and $k_{\text{wick,eff}}$ is the effective thermal conductivity of a wick.

When the power input to the heat pipe is zero, the liquid level in the evaporator will not recede into the wick, so the effective thickness $\delta_{\text{wick,eff}}$ of a wick is equal to the total thickness δ_{wick} of a wick in the evaporator, as illustrated in Fig. 5(*a*). As the power input to the evaporator is increased, the liquid level recedes into the wick to produce the meniscus radius and the capillary pressure to overcome the liquid pressure drop occurring in the flow path, i.e.,

$$\Delta p_{\text{cap}} = \Delta p_l + \Delta p_v + \Delta p_g \tag{6}$$

The pumping head Δp_{cap} due to the capillary pressure can be determined by Eq. (3). The pressure drop Δp_g due to gravity can be neglected, if the vapor chamber is tested in a horizontal position. The liquid pressure drop Δp_l is the result of the combined effect of both viscous and inertial forces. If the flow rate in the wick is very small, the effect of inertial force can be neglected, and the pressure difference in the liquid phase is caused only by the frictional forces at the liquid-solid interface and the liquid-vapor interface due to the vapor flow effect. The total liquid pressure drop can be determined by integrating the pressure gradient over the length of the flow passage as

$$\Delta p_l(x) = -\int_0^x \frac{dp_l}{dx} dx \tag{7}$$

where the limits of integration are from the evaporator end ($x=0$) to the condenser end ($x=L$), and dp_l/dx is the gradient of the liquid pressure resulting from the frictional forces from the solid wick, wall, and vapor flow at the liquid-vapor interface, which can be written as [5]

$$\frac{dp_l}{dx} = \left(\frac{\mu_l}{KA_w\rho_l}\right)\dot{m}_l \tag{8}$$

where $\dot{m}_l$ is the local mass flow rate in the wick, and K is the permeability of the sintered particle wick, which can be expressed as [5]

$$K = \frac{r_s^2\varepsilon^3}{37.5(1-\varepsilon)^2} \tag{9}$$

where r_s is the average radius of the sintered particles. For uniform heat addition and rejection, Eq. (7) can be expressed as

$$\Delta p_l = \left(\frac{\mu_l}{KA_w\rho_l h_{\text{fg}}}\right)L_{\text{eff}}q \tag{10}$$

where $q=\dot{m}_l h_{\text{fg}}$ and the effective heat pipe length L_{eff} can be defined as

$$L_{\text{eff}} = 0.5L_{\text{evap}} + L_{\text{adia}} + 0.5L_{\text{cond}} \tag{11}$$

If the heat pipe is charged with an appropriate amount of working fluid and the wetting point occurs at the cap end of the condenser, the vapor pressure drop can be calculated by the approach recommended by Peterson [5] and Dunn and Reay [3]. Based on the one-dimensional vapor flow approximation, the vapor pressure drop can be determined by

$$\Delta p_v = \left(\frac{(f_v\,\text{Re}_v)\mu_v}{2r_{h,v}^2A_v\rho_v h_{\text{fg}}}\right)L_{\text{eff}}q \tag{12}$$

where the product of the frictional factor and Reynolds number $f_v\,\text{Re}_v$ depends only on the cross-sectional shape, if the flow is laminar.

As the power input to the evaporator is increased, the meniscus radius decreases, as determined by Eqs. (3), (6), (10), and (12). If

the meniscus radius is between ∞ and $0.654r_p$, the receding of liquid level will occur in the relatively larger pores, i.e., in the hexagonal structure. When the power input is increased further, the wick structure with larger pores cannot hold liquid and the wick structure with larger pores such as hexagonal structures will dry out, as illustrated in Fig. 5(*b*). In this condition, the thermal resistance in the wick is due to the rectangular and triangular structures saturated with liquid because the vapor generated at the liquid-vapor interface can easily escape from the opened hexagonal structures, as shown in Fig. 5(*b*). The thermal resistance can be expressed as

$$R = \frac{\delta_{\text{wick,eff},\square+\Delta}}{k_{\text{wick,eff}}} \tag{13}$$

where $\delta_{\text{wick,eff},\square+\Delta}$ is the effective thickness of the wick consisting of the rectangular and triangular structures saturated with liquid, which can be found by the percentages of the wick structures, i.e.,

$$\delta_{\text{wick,eff},\square+\Delta} = 0.73\delta_{\text{wick}} \tag{14}$$

As the power input to the evaporator continues to increase, the liquid level will recede into relatively smaller pores. If the meniscus radius is smaller than $0.654r_p$, which corresponds to the situation shown in Fig. 5(*b*), the liquid-vapor interface will vary in the rectangular structures of the wick. When the power input is higher than that corresponding to the meniscus radius of $0.273r_p$, as illustrated in Fig. 5(*c*), the wick structure with the rectangular structures cannot hold the liquid and will dry out. If this situation occurs, the thermal resistance in the wick is primarily attributed to the triangular structures saturated with liquid, because the vapor generated at the liquid-vapor interface can easily escape from the opened hexagonal and rectangular structures, as shown in Fig. 5(*c*). In this condition, the thermal resistance can be expressed as

$$R = \frac{\delta_{\text{wick,eff},\Delta}}{k_{\text{wick,eff}}} \tag{15}$$

where $\delta_{\text{wick,eff},\Delta}$ is the effective thickness of the wick consisting of the triangular structures saturated with liquid, which can be found by the percentages of the wick structures, i.e.,

$$\delta_{\text{wick,eff},\Delta} = 0.45\delta_{\text{wick}} \tag{16}$$

If the power input to the evaporator is increased further, the liquid-vapor interface will further recede and the meniscus radius falls between $0.273r_p$ and $0.103r_p$, which represents the pore size range of the triangular structure. When the power input is higher than that corresponding to the minimum meniscus radius of $0.103r_p$, the whole heat pipe dries out and reaches the capillary limitation.

Clearly, the thermal resistance in the wick in the evaporator is directly dependent on the power input, which determines the meniscus radius variation and liquid distribution in the wick. For a given power input, the meniscus radius can be calculated, and the percentages of hexagonal, rectangular, and/or triangular structures in the wick saturated with liquid can be obtained. As the effective thickness of the wick saturated with liquid can be determined, the temperature difference across the wick in the evaporator can be calculated. Based on the calculation procedures discussed above, the thermal resistance of the wick per unit area in the evaporator can be expressed as

$$R = C_1 \frac{2\sigma/r_{\text{eff}}}{L_{\text{eff}}\left(\dfrac{\mu_l}{\text{KA}_w\rho_l h_{\text{fg}}} + \dfrac{C(f_v\,\text{Re}_v)\mu_v}{2r_{h,v}^2 A_v \rho_v h_{\text{fg}}}\right)} + C_2 \tag{17}$$

where constants C_1 and C_2 depend on the particle size and the meniscus radius at the liquid-vapor interface in the evaporator.

The quantity of liquid decreases in the evaporator, as heat flux increases, resulting in an increase of the liquid in the condenser. However, the surface area in the condenser is much larger than that in the evaporator, so the effect of liquid level on the thermal resistance in the condenser can be neglected.

Table 1 Test conditions used for copper post heater setup

No. of vapor chambers tested	10
Heater size (mm^2)	10×10 and 5×5
Heat flux (W/cm^2)	30, 50, and 70
Condenser temperature[a] (°C)	45

[a]Represents TC3 reading in Fig. 2.

4 Results and Discussion

Experiments were conducted to estimate the evaporative resistance θ_{evap} of vapor chamber. Tables 1 and 2 summarize the test conditions under which the vapor chambers were tested. The effective wick thickness model was validated by comparing θ_{evap} data obtained on the copper post heaters. Finally, a numerical model very similar to that of Prasher [9] combined with the effective wick thickness model for $\delta_{\text{wick,eff}}$ as a function of heat flux was used to calculate the evaporative resistance of the vapor chambers under nonuniform heating conditions using the silicon die heaters.

4.1 Tests With Copper Post Heaters. In the first set of experiments, two different sizes (10×10 mm^2 and 5×5 mm^2) of copper post heaters were used. For each copper post heater, ten

Table 2 Test conditions used for silicon die heater setup

	Case 1	Case 2	Case 3	
No. of vapor chambers tested	3	3	1	
Heater option[a]	Main	Strip	Main	Hot spot
Power input (W)	30–70	30–70	30	0.37–1.1
			50	0.37–1.1
			70	0.37–1.1
Condenser temperature[b] (°C)		45		

[a]See Fig. 3 for heater dimensions and locations on the silicon die.
[b]Represents TC3 reading in Fig. 2.

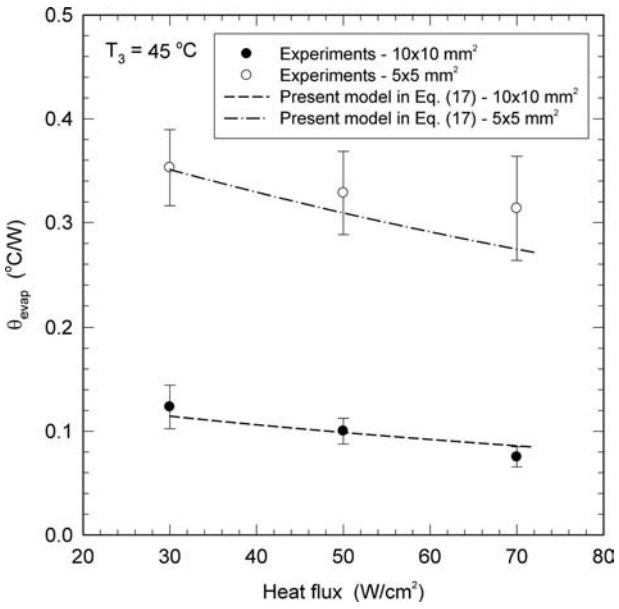

Fig. 6 Comparisons of model predictions with experimental data of copper post heaters

different vapor chambers were tested at three different heat fluxes (30 W/cm^2, 50 W/cm^2, and 70 W/cm^2) and a fixed condenser temperature of 45°C, which represent the typical operating ranges of vapor chambers used for electronic thermal management applications. Figure 6 shows the mean values and standard deviations of θ_{evap} data of ten vapor chambers. As shown, the deviations of 5×5 mm^2 heater data are greater than those of 10×10 mm^2 heater data, which can be attributed to the fact that a slight misalignment between the copper post heater and the thermocouple (TC1 in Fig. 2(*a*)) can affect the variations of θ_{evap} measurements, more for the smaller size heater than for the larger size.

Figure 6 shows that θ_{evap} is dependent on the heater size. The 5×5 mm^2 heater yielded almost three times higher θ_{evap} values than the 10×10 mm^2 heater, which is smaller than the ratio (4) of heater sizes. This can be explained by the heat diffusion in the bottom copper wall of vapor chamber, which should affect θ_{evap} data, more for the smaller size heater than for the larger size. Prasher [9] also observed similar data trends and proposed a conduction-based model (assuming that θ_{evap} is independent of heat flux), which successfully captured the trend of dependency of evaporative resistance on heater size. However, the present test results also show that θ_{evap} decreases with increasing heat flux for both of the test heaters. The θ_{evap} value continued to decrease, until the wick in the evaporator nearly reached the dryout point (not shown). While a conduction type phenomenon plays a key role in the evaporator section, the dependence of θ_{evap} on heat flux indicates that the conduction-based model needs to be improved to capture this physical phenomenon and, as discussed before, the change in evaporative resistance should be attributed to the change of vapor fraction in the wick at different heat fluxes.

As discussed before, θ_{evap} is directly dependent on the meniscus radius variation and liquid distribution in the wick, which are directly affected by heat flux (power input). At a given power input, the meniscus radius in the evaporator was determined, and the percentages of hexagonal, rectangular, and/or triangular structures in the wick saturated with liquid were determined. The effective thickness $\delta_{wick,eff}$ of wick saturated with liquid was calculated and the thermal resistance across the wick in the evaporator was found. As discussed before, the porosity and the average radius of sintered particles in the evaporator of vapor chambers are approximately 53% and 32 μm, respectively, for which the constants C_1 and C_2 in Eq. (17) can be readily calculated. The thermal conductivity $k_{wick,eff}$ of the wick was obtained by calibrating the model with the experimental data at 30 W/cm^2 for the 10×10 mm^2 copper post heater. This thermal conductivity was kept constant for generating the modeling curves in Fig. 6.

In Fig. 6, the model predictions of θ_{evap} are compared with the experimental data of copper post heaters. As shown, the model predictions agree well with the experimental data, and the model also successfully captures the dependency of θ_{evap} on heat flux (power input). As discussed before, when the heat flux (power input) increases, the liquid level in the wick recedes and the effective thickness $\delta_{wick,eff}$ of wick saturated with liquid decreases, thereby resulting in the reduction of θ_{evap} in the wick. The pore size determined by the particle structure directly affects the receding of liquid in the sintered particles. Figure 6 shows that the current modeling approach is adequate to assess the evaporative thermal performance of a heat pipe/vapor chamber.

Copper post heaters are ideal in providing one-dimensional heat conduction conditions, with which the current modeling approach with effective wick thickness $\delta_{wick,eff}$ was validated. Due to nonuniform heating and spreading in the silicon die heaters, a numerical model will be needed for capturing the physical behaviors. Therefore, the evaporator model validated on the ideal case (copper post heater) is combined with a numerical heat conduction model to predict the evaporative performance of the vapor chambers on the silicon die heaters.

4.2 Tests With Silicon Die Heaters. In the second set of experiments, silicon die heaters were used as the heat sources. Based on the previous test results in Fig. 6, three vapor chambers were selected, which represent the average θ_{evap} performance. Therefore, part-to-part variations of θ_{evap} measurements are minimized and the trend of θ_{evap} performance can be more clearly determined, while testing with silicon die heaters. For the selected vapor chambers, the power input was varied from 30 W to 70 W, while the condenser temperature was maintained at 45°C. As shown in Table 2, three different power profiles were used: Case 1: the silicon die was uniformly heated using the main heater (10×12 mm^2); Case 2: only the strip heater (10×3 mm^2) was powered up on the die; Case 3: both the main heater and the hot spot heater (400×400 μm^2) were powered up together. In this experiment, the highest heat flux from the hot spot heater was approximately 746 W/cm^2 in Case 3 (1.1 W over the 400×400 μm^2 hot spot area plus 70 W background heating over the 10×12 mm^2 die area).

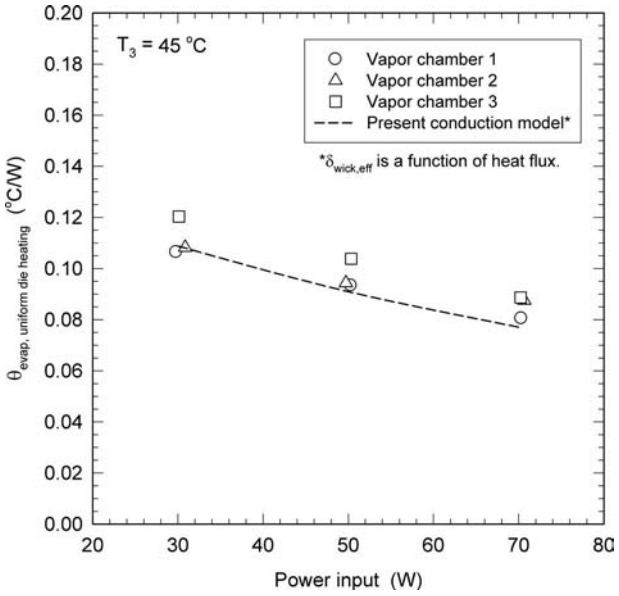

Fig. 7 Test results of vapor chambers with silicon die heaters under uniform die heating conditions

Figure 7 shows the θ_{evap} data of three vapor chambers tested under uniform heating condition (Case 1). It also shows a similar dependence of θ_{evap} data on power input to the 10×10 mm^2 copper post heater data in Fig. 6. Although for the uniform heating case, the heater area of the silicon die heaters was 20% larger than for the 10×10 mm^2 copper post heater, the two evaporator thermal resistances are comparable. This is because the effective wick thickness depends on the heat flux. This shows that there is not much difference between the constant temperature boundary condition and the constant heat flux boundary condition.

Figures 8(*a*) and 8(*b*) show the θ_{evap} data of vapor chambers tested under nonuniform heating conditions, that is, Cases 2 and 3 in Table 2, respectively. Three vapor chambers were tested in Fig. 8(*a*), and one vapor chamber was tested with three different hot spot power conditions in Fig. 8(*b*). As shown in Figs. 8(*a*) and 8(*b*), θ_{evap} data are made dimensionless by division by the corresponding θ_{evap} data of uniform heating conditions for the respective vapor chambers shown in Fig. 7. Figures 8(*a*) and 8(*b*) show that the ratio of $\theta_{evap,nonuniform}$ to $\theta_{evap,uniform}$ is close to 1, i.e., there is no difference between $\theta_{evap,nonuniform}$ and $\theta_{evap,uniform}$. Specifically in Fig. 8(*a*), the data trend for different heater sizes seems to be the opposite to that obtained with the copper post heaters in Fig. 6, although the ratios of the heater sizes are the same (equal to 4). This can be explained by the difference in the heat fluxes of copper post heater and the silicon die strip heater. The heat flux on

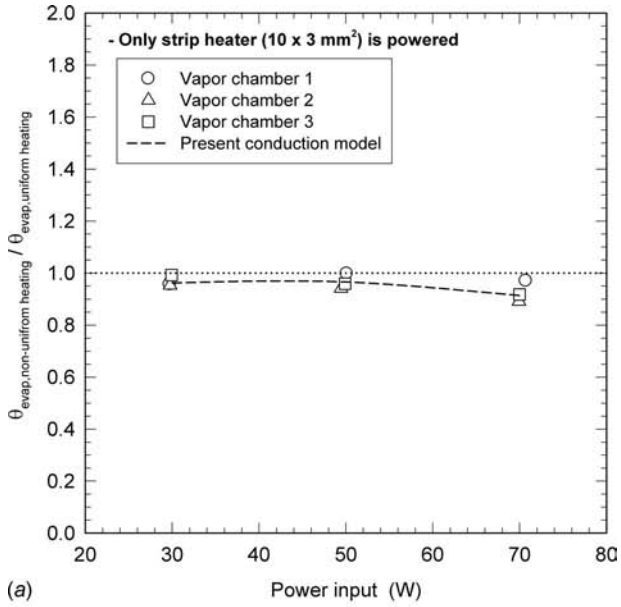

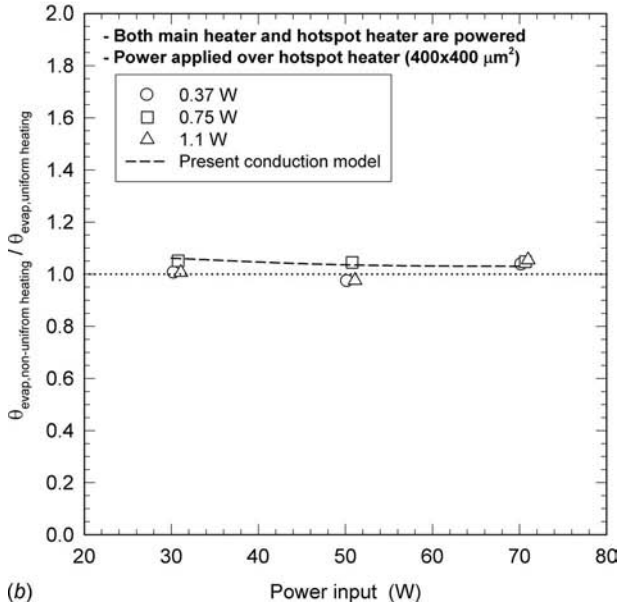

Fig. 8 Test results of vapor chambers with silicon die heaters under nonuniform die heating conditions: (*a*) Only strip heater is powered; (*b*) both main heater and hot spot heater are powered

the copper post heater ranges from 30 W/cm^2 to 70 W/cm^2 for both the 10×10 mm^2 and the 5×5 mm^2 sizes. The heat flux on the uniform silicon heater ranges from 25 W/cm^2 to 58.3 W/cm^2, whereas the heat flux on the strip heater ranges from 100 W/cm^2 to 233.3 W/cm^2, i.e., it is four times larger than the uniform heater. As discussed earlier, the effective thickness $\theta_{wick,eff}$ of the wick is a decreasing function of the heat flux. To understand the physics, if the spreading of the heat is neglected, the thermal resistance in the wick can be approximately written as

$$\theta_{evap} \sim \frac{\delta_{wick,eff}}{k_{wick,eff}A_e} \tag{18}$$

For estimating the wick thicknesses at various heat flux conditions, a curve fit of the previous analytical modeling results validated on the copper post heater (Fig. 6) shows that

$$\frac{\delta_{wick,eff}}{\delta_{wick}} = 12.71q''^{-0.755} \tag{19}$$

where q'' is the average heat flux from a heater surface. Based on Eq. (19), the ratio of effective wick thickness of uniform heater to that of strip heater at the same power input can be estimated as

$$\frac{\delta_{wick,eff,strip}}{\delta_{wick,eff,uniform}} = 0.35 \tag{20}$$

Therefore,

$$\frac{\theta_{evap,strip}}{\theta_{evap,uniform}} \sim \left(\frac{\delta_{wick,eff}}{A_e}\right)_{strip} \Big/ \left(\frac{\delta_{wick,eff}}{A_e}\right)_{uniform} = 0.35 \times 4 = 1.4 \tag{21}$$

This one-dimensional analysis shows why the evaporator resistance of the strip heater is similar to that of the uniform heater. In Fig. 8(*a*), $\theta_{evap,strip}$ and $\theta_{evap,uniform}$ are almost the same because the heat spreading in the silicon die and copper wall should affect θ_{evap} data, more for the smaller size heater than for the larger size. In Sec. 4.3, the model for $\delta_{wick,eff}$ (Eq. (19)) is combined with a numerical heat conduction model to more accurately model θ_{evap} for different cases by capturing the effect of heat spreading through the silicon die and the copper walls of the vapor chamber.

As shown in Fig. 8(*b*), the impact of hot spot heating on θ_{evap} data is small. This could be attributed to the fact that the bottom copper wall (1 mm thickness) of vapor chamber was efficient in reducing the nonuniformity of temperature profiles from the silicon die heater.

4.3 Comparisons With Conduction Based Model. A conduction model was constructed, which is similar to that of Prasher [9] except that $\delta_{wick,eff}$ is a function of heat flux. Prasher [9] assumed a constant $\delta_{wick,eff}$. In the conduction model, all the components of the vapor chamber in Fig. 1 were modeled as solid components using ICEPAK™. The fins at the condenser section were modeled as an effective heat transfer coefficient, which was adjusted to match the test condition of T/C3~45 °C. The thermal interface material was described as an effective thermal resistance of ~0.13 K cm^2/W. The effective thermal conductivity $k_{vapor,eff}$ of the vapor was calculated to match the experimental data of $\theta_{adia}\sim0.05$ °C/W between the two monitoring points of T/C2 and T/C3 in Fig. 2, which gave a $k_{vapor,eff}$ value of 6.5×10^4 W/m K. This value is high due to the high thermal conductance of the vapor space [9,11]. Therefore, it does not play a significant role in determining θ_{evap}.

The next steps were to determine both the effective thermal conductivity $k_{wick,eff}$ and the effective thickness $\delta_{wick,eff}$ of the wick. Using Eq. (19), a $\delta_{wick,eff}$ value was estimated for each of the experimental conditions in Figs. 7, 8(*a*), and 8(*b*), and the wick thickness in the conduction model was adjusted accordingly for calculating the corresponding θ_{evap} value.

The calculated θ_{evap} values are plotted in Figs. 7, 8(*a*), and 8(*b*), for comparisons with the experimental data. As shown in all of these, the conduction-based model captures the trends of experimental data for the silicon die heaters. Note that the effective wick thickness model was validated on the copper post heaters, which resemble the constant temperature boundary conditions, whereas the silicon die heaters resemble the constant heat flux boundary conditions. This shows that there is not much difference between the constant temperature boundary condition and the constant heat flux boundary condition.

Finally, although the local heat flux on hot spots can be very large, the vapor chamber still functions. Similarly, the results showing that evaporator resistance is not sensitive to the presence of hot spots are important because solid-based heat spreaders are used in most desktop and workstation processors [1,2]. The thermal resistance of the spreaders increases due to the presence of hot spots and nonuniform heating whereas that of the vapor cham-

ber does not depend on nonuniform heating, i.e., a vapor chamber can be a better spreader of heat even under nonuniform heating conditions. Therefore, the experimental results are novel and useful for development of electronics cooling solutions.

5 Conclusions

Vapor chambers with water as the working fluid were tested using the copper post heaters and silicon die heaters. The silicon die heaters were developed to replicate nonuniform heating conditions of microprocessor packages. The key objective of the experiments was to understand the effects of nonuniform power distribution at the heating source on the evaporative thermal performance of vapor chambers. Based on the statistical distribution of particles, an analytical model developed to predict the effect of heat flux on the liquid distribution in the sintered particle wick in the evaporator was able to predict θ_{evap}. The model predictions were in good agreement with experimental data for both uniform and nonuniform heating conditions. The experimental results show that evaporator thermal resistance is not sensitive to nonuniform heat conditions, i.e., it is the same as in the uniform heating case.

Nomenclature

A = area, m^2
C_1, C_2 = constants defined in Eq. (17)
d = diameter, m
f = friction factor
g = gravitational acceleration, m/s^2
h_{fg} = latent heat, J/kg
k = thermal conductivity, W/m K
K = permeability, m^{-2}
L = length, m
$\dot{m}$ = mass flow rate, kg/s
P = perimeter, m
p = pressure, N/m^2
q = power input, W
q'' = heat flux, N/cm^2
r = radius, m
R = thermal resistance, °C m^2/W
Re = Reynolds number
T = temperature, °C
x = coordinate, m

Greek Symbols

δ = thickness, m
μ = dynamic viscosity, N s/m^2
θ_{adia} = adiabatic thermal resistance, °C/W
θ_{evap} = evaporator thermal resistance, °C/W
ρ = mass density, kg/m^3
σ = surface tension, N/m
Δp = pressure drop, N/m^2

Subscripts

adia = adiabatic
cond = condenser
cap = capillary
evap = evaporator
eff = effective
g = gravity
gap = pore gap trapped by particles
h = hydraulic
l = liquid
min = minimum
p = particle
s = solid
v = vapor

References

[1] Mahajan, R., Chiu, C.-P., and Chrysler, G., 2006, "Cooling a Microprocessor Chip," Proc. IEEE, **94**(8), pp. 1476–1486.
[2] Watwe, A., and Viswanath, R., 2003, "Thermal Implications of Non-Uniform Die Power and CPU Performance," *Proceedings of the InterPack '03 Conference*, Maui, HI, July 6–11, Paper No. IPACK 2003-35044.
[3] Dunn, P. D., and Reay, D. A., 1994, *Heat Pipes*, 4th ed., Pergamon, New York/Elsevier Science, New York.
[4] Faghri, A., 1995, *Heat Pipe Science and Technology*, Taylor & Francis, Washington, DC.
[5] Peterson, G. P., 1994, *An Introduction to Heat Pipe*, Wiley, New York.
[6] Wang, Y., and Peterson, G. P., 2005, "Investigation of a Novel Flat Heat Pipe," ASME J. Heat Transfer, **127**, pp. 165–170.
[7] Vadakkan, U., Garimella, S. V., and Murthy, J. Y., 2004, "Transport in Flat Heat Pipes at High Heat Fluxes From Multiple Discrete Sources," ASME J. Heat Transfer, **126**, pp. 347–354.
[8] DiStefano, E., Pokharna, H., and Machiroutu, S. V., 2004, "Raising the Bar for Heat Pipes in Notebook Cooling," *Proceedings of the 13th International Heat Pipe Conference*, Shanghai, China, Sept. 21–25.
[9] Prasher, R. S., 2003, "A Simplified Conduction Based Modeling Scheme for Design Sensitivity Study of Thermal Solution Utilizing Heat Pipe and Vapor Chamber Technology," ASME J. Electron. Packag., **125**(3), pp. 378–385.
[10] Prasher, R. S., Dirner, J., Chang, J.-Y., Myers, A., Chau, D., He, D., and Prstic, S., 2007, "Nusselt Number and Friction Factor of Staggered Arrays of Low Aspect Ratio Micro Pin Fins Under Cross Flow for Water as Fluid," ASME J. Heat Transfer, **129**(2), pp. 141–153.
[11] Avenas, Y., Gillot, C., Bricard, A., and Schaeffer, C., 2002, "On the Use of Flat Heat Pipes as Thermal Spreaders in Power Electronics Cooling," *Proceedings of the IEEE 33rd Annual Power Electronics Specialists Conference*, Vol. 2, Cairns, Australia, June, pp. 753–757.
[12] Kline, S. J., and McClintock, F. A., 1953, "Describing Uncertainties in Single-Sample Experiments," Mech. Eng. (Am. Soc. Mech. Eng.), **75**, pp. 3–8.
[13] Cheng, P., and Ma, H. B., 2007, "A Mathematical Model Predicting the Minimum Meniscus Radius Occurring in Mix Particles," ASME J. Heat Transfer, **129**(3), pp. 391–394.
[14] Ferrell, J. K., and Alleavitch, J., 1970, "Vaporization Heat Transfer in Capillary Wick Structures," Chem. Eng. Prog., Symp. Ser., **66**(102), pp. 82–91.

Analytic Solution of Three-Dimensional Viscous Flow and Heat Transfer Over a Stretching Flat Surface by Homotopy Analysis Method

Ahmer Mehmood[1]
Department of Mathematics,
Quaid-i-Azam University,
45320 Islamabad 44000, Pakistan;
Department of Mathematics (FBAS),
International Islamic University,
Islamabad 44000, Pakistan
e-mail: ahmerqau@yahoo.co.uk

Asif Ali
Department of Mathematics,
Quaid-i-Azam University,
45320 Islamabad 44000, Pakistan

In this paper heat transfer in an electrically conducting fluid bonded by two parallel plates is studied in the presence of viscous dissipation. The plates and the fluid rotate with constant angular velocity about a same axis of rotation where the lower plate is a stretching sheet and the upper plate is a porous plate subject to constant injection. The governing partial differential equations are transformed to a system of ordinary differential equations with the help of similarity transformation. Homotopy analysis method is used to get complete analytic solution for velocity and temperature profiles. The effects of different parameters are discussed through graphs. [DOI: 10.1115/1.2969753]

Keywords: three-dimensional flow, heat transfer, MHD, homotopy analysis method, analytic solution

1 Introduction

In recent years the study of viscous flows over a stretching flat surface has grown considerably. This is due to their important industrial applications such as in metallurgy and chemical process industries. Sakiadis [1] initiated the study of boundary layer flows over a continuous solid surface that moves with a constant velocity. Crane [2] considered the same problem for the case when the surface velocity varies linearly with the distance x measured from the origin and presented a closed form solution to it. The interesting aspect of Crane's problem is that it is still possible to obtain a closed form solution even when numerous other physical features have been taken into account such as suction, magnetic field, viscoelasticity of the fluid, etc. (see Refs. [3–5]). The study of flows over stretching surfaces has been further extended in different directions by number of researchers [6–15].

Industrially, the study of heat transfer problems of a viscous incompressible fluid over a plane surface moving in an ambient fluid is important in several engineering applications such as materials manufactured by extrusion processes and heated materials traveling between a feed roll and a wind up roll or on a conveyer belt. During the manufacture of polymer sheets, the melt issues from a slit and is subsequently stretched to achieve the desired thickness. The achievement of the desired characteristics by the final product depends strictly on the stretching rate and the rate of cooling in the process. In this regard the heat transfer analysis of such types of flows is very much important. Keeping this fact in mind, Dutta et al. [16] studied the temperature field in the flow over a stretching surface subject to uniform heat flux. Andersson et al. [17] investigated the unsteady two dimensional non-Newtonian flow of a power-law fluid past a stretching surface. Bujurke et al. [18] and Dandapat and Gupta [19] examined the temperature distribution in the steady boundary layers of a second grade fluid near a stretching surface.

Industrially, magnetohydrodynamic (MHD) fluids have become very much important in the processes of heat transfer. For example, in metallurgical industry many metallurgical processes involve the cooling of continuous strips and filaments by drawing them through a coolant. In these processes the properties of the final product depend largely on the rate of cooling. To get the final product of desired characteristics it is necessary to control the rate of cooling. The rate of cooling is controlled by drawing the strips and filaments in an electrically conducting fluid subject to a magnetic field. Heat transfer analysis of MHD fluid over a uniformly stretching sheet was investigated by Chakrabarti and Gupta [10]; Dandapat and Gupta [19] studied flow and heat transfer phenomenon in a viscoelastic fluid over a stretching sheet. Chamkha [12] studied three dimensional free convection on a vertical stretching surface with heat generation and absorption. Further studies could be seen in Refs. [20–25].

In all above mentioned studies the authors have considered unbounded domain. There are very few studies in which authors have considered the channel flow. In 1983 Borkakoti and Bharali [26] studied the two dimensional channel flow with heat transfer analysis of a hydromagnetic fluid where the lower plate was a stretching sheet. The flow between two rotating disks has important technical applications such as in lubrication. Keeping this fact in mind Vajravelu and Kumar [27] studied the effect of rotation on the two dimensional channel flow. In Ref. [27] the authors solved the governing equations analytically and numerically. In the present work we study the heat transfer phenomenon in the channel flow considered in Ref. [27]. We present analytic solution to both the momentum equations and the energy equation. Homotopy analysis method (HAM) [28] has been used to get accurate and purely analytic solution of the governing equations.

Recently, Liao [28] introduced an analytic technique for highly nonlinear problems in science and engineering. The technique has successfully been applied to many nonlinear problems such as nonlinear water waves [29], similarity boundary layer flows [30], Cheng–Chang equation [31], unsteady boundary layers [13,32,33], nonhomogeneous Blasius problem [34], and so on (for further applications of the method the reader is referred to see Refs. [35–42]). All of these verify the validity of the homotopy analysis method.

[1]Corresponding author.

Contributed by the Heat Transfer Division of ASME for publication in the JOURNAL OF HEAT TRANSFER. Manuscript received June 23, 2007; final manuscript received April 11, 2008; published online September 16, 2008. Review conducted by Sai C. Lau.

This paper is organized into five sections. In Sec. 2 mathematical description of the problem and its analytic solution is presented. Section 3 contains heat transfer analysis of the problem and analytic solution to it. Graphical representation of results and their discussion is also given in Sec. 4. Some concluding remarks are given in Sec. 5. At the end some constants appearing in solution expressions are defined in the Appendix.

2 Flow Analysis

2.1 Governing Equations. We consider a fully developed hydromagnetic flow of an incompressible viscous fluid between two parallel plates. One is situated at $y=0$ and the other is situated at $y=h$. The upper plate is a porous plate subjected to uniform injection and the lower plate is stretched by two equal and opposite forces along the x-axis. A magnetic field of strength B_0 is applied perpendicular to the plates along the y-axis. The upper plate is subjected to a uniform injection. The plates and the fluid rotate in unison about the y-axis with an angular velocity Ω. Therefore, the governing equations and boundary conditions for this case in dimensionless form are given by [27]

$$f^{iv} - R(f'f'' - ff''') - 2Kg' - Mf'' = 0 \tag{1}$$

$$g'' - R(f'g - fg') + 2Kf' - Mg = 0 \tag{2}$$

subject to the boundary conditions

$$\begin{aligned} &f = 0, \quad f' = 1, \quad g = 0 \quad \text{at } \eta = 0 \\ &f = \lambda, \quad f' = 0, \quad g = 0 \quad \text{at } \eta = 1 \end{aligned} \tag{3a}$$

where $'$ denotes the differentiation with respect to η and the dimensionless quantities are defined through

$$\begin{aligned} &\eta = \frac{y}{h}, \quad u = axf'(\eta), \quad v = -ahf(\eta), \quad w = axg(\eta) \\ &R = \frac{ah^2}{\nu}, \quad M = \frac{\sigma B_0{}^2 h^2}{\rho\nu}, \quad K = \frac{\Omega h^2}{\nu} \end{aligned} \tag{3b}$$

in which R is the viscosity parameter, M is the magnetic parameter, and K is the rotation parameter.

2.2 Analytic Solution by HAM. We use HAM to solve the nonlinear system ((1), (2), and (3a)) analytically. It is also possible to solve the system ((1), (2), and (3a)) numerically by using fourth-order Runge–Kutta scheme (say). In this method one needs to select some suitable numerical initial guess approximations for which the solution converges. Our experience shows that it is very difficult to choose such suitable approximations blindly without any information. In this situation HAM is observed to be very useful. Due to the boundary conditions ((3a) and (3b)) it is reasonable to choose the initial approximations of the form [28]

$$f_0 = (1 - 2\lambda)\eta^3 + (3\lambda - 2)\eta^2 + \eta \tag{4}$$

$$g_0 = 0 \tag{5}$$

where the initial approximations are required to satisfy the boundary data ((3a) and (3b)). The corresponding linear operators are given by

$$L_1[F(\eta;p)] = \frac{d^4F}{d\eta^4} \tag{6}$$

$$L_2[G(\eta;p)] = \frac{d^2G}{d\eta^2} \tag{7}$$

which satisfy the properties

$$L_1[C_1 + C_2\eta + C_3\eta^2 + C_4\eta^3] = 0 \tag{8}$$

$$L_2[C_5 + C_6\eta] = 0 \tag{9}$$

where $C_i, i=1,\ldots,6$, are arbitrary constants.

We construct the so-called zero-order deformation equations [28]

$$(1-p)L_1[F(\eta;p) - f_0(\eta)] = p\hbar N_1[F(\eta;p), G(\eta;p)] \tag{10}$$

$$(1-p)L_1[G(\eta;p) - g_0(\eta)] = p\hbar N_2[F(\eta;p), G(\eta;p)] \tag{11}$$

with boundary conditions

$$\begin{aligned} &F(\eta;p) = 0, \quad \frac{\partial F(\eta;p)}{\partial\eta} = 1, \quad G(\eta;p) = 0 \quad \text{at } \eta = 0 \\ &F(\eta;p) = \lambda, \quad \frac{\partial F(\eta;p)}{\partial\eta} = 0, \quad G(\eta;p) = 0 \quad \text{at } \eta = 1 \end{aligned} \tag{12}$$

where $p \in [0,1]$ is the embedding parameter, $\hbar$ is the nonzero auxiliary parameter, and the nonlinear operators N_1 and N_2 are, respectively, defined by

$$N_1[F(\eta;p), G(\eta;p)] = \frac{\partial^4 F}{\partial\eta^4} - R\left(\frac{\partial F}{\partial\eta}\frac{\partial^2 F}{\partial\eta^2} - F\frac{\partial^3 F}{\partial\eta^3}\right) - 2K\frac{\partial G}{\partial\eta} - M\frac{\partial^2 F}{\partial\eta^2} \tag{13}$$

$$N_2[F(\eta;p), G(\eta;p)] = \frac{\partial^2 G}{\partial\eta^2} - R\left(\frac{\partial F}{\partial\eta}G - F\frac{\partial G}{\partial\eta}\right) + 2K\frac{\partial F}{\partial\eta} - MG \tag{14}$$

Notice that for $p=0$ and $p=1$ we, respectively, have

$$F(\eta;0) = f_0(\eta), \quad G(\eta;0) = g_0(\eta) \tag{15}$$

and

$$F(\eta;1) = f(\eta), \quad G(\eta;1) = g(\eta) \tag{16}$$

So, as p varies from 0 to 1, $F(\eta;p)$ and $G(\eta;p)$ move from initial guess approximations $f_0(\eta)$ and $g_0(\eta)$ to the final solution $f(\eta)$ and $g(\eta)$, respectively. By Taylor's theorem and Eq. (15), we have

$$F(\eta;p) = f_0(\eta) + \sum_{m=1}^{+\infty} f_m(\eta)p^m \tag{17}$$

$$G(\eta;p) = g_0(\eta) + \sum_{m=1}^{+\infty} g_m(\eta)p^m \tag{18}$$

where

$$f_m(\eta) = \frac{1}{m!}\left.\frac{\partial^m F(\eta;p)}{\partial p^m}\right|_{p=0}, \quad g_m(\eta) = \frac{1}{m!}\left.\frac{\partial^m G(\eta;p)}{\partial p^m}\right|_{p=0} \tag{19}$$

We assume that series (17) and (18) are convergent at $p=1$, then we have from Eq. (16) that

$$F(\eta) = f_0(\eta) + \sum_{m=1}^{\infty} f_m(\eta) \tag{20}$$

$$G(\eta) = g_0(\eta) + \sum_{m=1}^{\infty} g_m(\eta) \tag{21}$$

Differentiating the zero-order deformation equations (10)–(12) m-times ($m=1,2,3,\cdots$) with respect to p at $p=0$ and then dividing the resulting expressions by $m!$, we get the mth-order deformation equations

$$L_1[f_m(\eta) - \chi_m f_{m-1}(\eta)] = \hbar P_m(\eta) \tag{22}$$

$$L_2[g_m(\eta) - \chi_m g_{m-1}(\eta)] = \hbar Q_m(\eta) \tag{23}$$

with boundary conditions

$$f_m = f'_m = g_m = 0 \quad \text{at } \eta = 0$$
$$f_m = f'_m = g_m = 0 \quad \text{at } \eta = 1 \tag{24}$$

where

$$P_m = f'''_{m-1} - 2Kg'_{m-1} - Mf''_{m-1} - R\sum_{k=0}^{m-1}[f'_{m-1-k}f''_k - f_{m-1-k}f'''_k] \tag{25}$$

$$Q_m = g''_{m-1} + 2Kf'_{m-1} - Mg_{m-1} - R\sum_{k=0}^{m-1}[f'_{m-1-k}g_k - f_{m-1-k}g'_k] \tag{26}$$

and

$$\chi_m = \begin{cases} 0 & \text{for } m \le 1 \\ 1 & \text{for } m > 1 \end{cases} \tag{27}$$

We use the symbolic computation software MATHEMATICA to solve first few deformation equations and find that the solution expressions for $f(\eta)$ and $g(\eta)$ are of the form

$$f_m(\eta) = \sum_{n=0}^{4m+4} a_{m,n}\eta^n \tag{28}$$

$$g_m(\eta) = \sum_{n=0}^{4m+4} b_{m,n}\eta^n \tag{29}$$

where $a_{m,n}$ and $b_{m,n}$ are constant coefficients that can be determined by using the following recurrence formulas for $m \ge 1$ (for detail the reader is referred to Ref. [36]):

$$a_{m,0} = \chi_m\chi_{4m+2}a_{m-1,0} + \sum_{k=0}^{4m+4} \varsigma_k\Gamma_{m,k}\mu_k\left(\frac{k-2}{4}\right) \tag{30}$$

$$a_{m,1} = \chi_m\chi_{4m+1}a_{m-1,1} + \sum_{k=0}^{4m+4} \varsigma_{k+1}\Gamma_{m,k}\mu_k\left(\frac{k+1}{2}\right) \tag{31}$$

$$a_{m,2} = \chi_m\chi_{4m}a_{m-1,2} - \sum_{k=0}^{4m+4} \varsigma_k\Gamma_{m,k}\mu_k\left(\frac{k+4}{2}\right) \tag{32}$$

$$a_{m,3} = \chi_m\chi_{4m-1}a_{m-1,3} - \sum_{k=0}^{4m+4} \varsigma_{k+1}\Gamma_{m,k}\mu_k\left(\frac{k+3}{2}\right) \tag{33}$$

$$a_{m,n} = \chi_m\chi_{4m+2-n}a_{m-1,n} + \Gamma_{m,n-4}\mu_{n-4}, \quad 4 \le n \le 4m+4 \tag{34}$$

Similarly,

$$b_{m,0} = \chi_m\chi_{4m+2}b_{m-1,0} - \sum_{k=0}^{4m+4} \varsigma_k\Delta_{m,k}\nu_k \tag{35}$$

$$b_{m,1} = \chi_m\chi_{4m+1}b_{m-1,1} - \sum_{k=0}^{4m+4} \varsigma_{k+1}\Delta_{m,k}\nu_k \tag{36}$$

$$b_{m,n} = \chi_m\chi_{4m+2-n}b_{m-1,n} + \Delta_{m,n-2}\nu_{n-2}, \quad 2 \le n \le 4m+4 \tag{37}$$

where the different constants appearing in Eqs. (30)–(37) are defined in the Appendix. Hence by using the above recurrence formulas one can easily find for any m the $f_m(\eta)$ and $g_m(\eta)$ from Eqs. (28) and (29), respectively, with the knowledge of following first few

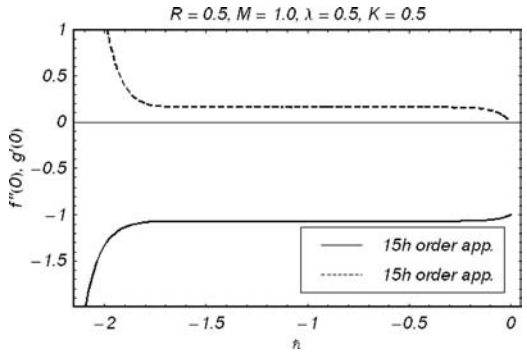

Fig. 1 $\hbar$**–curves for** $f(\eta)$ **and** $g(\eta)$ **at 15th order approximation**

$$a_{0,0} = 0, \quad a_{0,1} = 1, \quad a_{0,2} = (3\lambda - 2), \quad a_{0,3} = (1 - 2\lambda), \quad a_{0,4} = 0 \tag{38}$$

and

$$b_{0,i} = 0 \quad \text{for } i = 0, \ldots, 4 \tag{39}$$

Therefore, the complete solution can be written as

$$f(\eta) = f_0(\eta) + \sum_{m=1}^{+\infty} f_m(\eta) \tag{40}$$

$$g(\eta) = g_0(\eta) + \sum_{m=1}^{+\infty} g_m(\eta) \tag{41}$$

As mentioned by Liao [28], whenever the solution series converges it will be one of the solutions of the considered problem. The convergence of the solution series is strongly dependent on the choice of the auxiliary parameter $\hbar$. The values of $\hbar$ for which the solution series converges are determined by drawing the so-called $\hbar$-curves. In our problem, to find the values of $\hbar$ for which the solution series (40) and (41) converge, we have plotted the $\hbar$-curves for both $f(\eta)$ and $g(\eta)$ in Fig. 1. The portion on $\hbar$-axis for which the $\hbar$-curves are parallel to the $\hbar$-axis is recognized as the set of suitable values of $\hbar$ for which the solution series (40) and (41) will converge. Notice that Eqs. (40) and (41) are infinite series and for their convergence it is necessary that the contribution of the higher order terms must be negligible. The convergence of the solution series is proved with the help of Table 1.

3 Heat Transfer Analysis

3.1 Energy Equation. The energy equation for the present problem with viscous dissipation in dimensionless form is given by

$$T'' + \Pr[RfT' + \mathrm{Ec}(4f'^2 + g^2) + \mathrm{Ec}_x(f''^2 + g'^2)] = 0 \tag{42}$$

subject to the boundary conditions

$$T(0) = 1, \quad T(1) = 0 \tag{43}$$

where $\Pr = \mu C_p/k$ is the Prandtl number, $\mathrm{Ec} = a^2h^2/C_p(\theta_0 - \theta_h)$ is the Eckert number, $\mathrm{Ec}_x = a^2x^2/C_p(\theta_0 - \theta_h)$ is the local Eckert number, and the dimensionless temperature is defined as

Table 1 HAM solution at different orders

$\Pr=0.7$, $M=0.1$, $K=0.5$, $R=2.0$, $\lambda=\mathrm{Ec}_x=\mathrm{Ec}=0.5$			
Order of app.	$f''(0)$	$g'(0)$	$T'(0)$
5th order	−1.178060	0.144786	−0.658585
10th order	−1.178080	0.144798	−0.658474
15th order	−1.178080	0.144798	−0.658474

$$T(\eta) = \frac{\theta - \theta_h}{\theta_0 - \theta_h} \tag{44}$$

where θ_0 and θ_h are temperatures at the lower and upper plates, respectively.

3.2 HAM Solution. To find the analytic solution of Eq. (42) subjected to the boundary conditions (43), we follow the same procedure as performed in Sec. 2.2. To avoid the repetition, we will omit the details of the method. Due to the boundary conditions (43) we choose the initial approximation

$$T_0(\eta) = 1 - \eta \tag{45}$$

with linear operator

$$L_3[\tau(\eta;p)] = \frac{\partial^2 \tau}{\partial \eta^2} \tag{46}$$

which satisfy the property

$$L_3[C_7 + C_8\eta] = 0 \tag{47}$$

where C_7, and C_8 are constants.

The zero-order deformation equation is then given by

$$(1-p)L_3[\tau(\eta;p) - T_0(\eta)] = p\hbar N_3[F(\eta;p), G(\eta;p), \tau(\eta;p)] \tag{48}$$

with subjected boundary conditions

$$\tau(0;p) = 1, \quad \tau(1;p) = 0 \tag{49}$$

where the nonlinear differential operator N_3 is defined through

$$N_3[F(\eta;p), G(\eta;p), \tau(\eta;p)] = \frac{\partial^2 \tau}{\partial \eta^2} + \mathrm{Pr}\left[RF\frac{\partial \tau}{\partial \eta} + \mathrm{Ec}\left\{4\left(\frac{\partial F}{\partial \eta}\right)^2 + G^2\right\} + \mathrm{Ec}_x\left\{\left(\frac{\partial^2 F}{\partial \eta^2}\right)^2 + \left(\frac{\partial G}{\partial \eta}\right)^2\right\}\right] \tag{50}$$

For $p=0$ and $p=1$ we, respectively, have

$$\tau(\eta,0) = T_0(\eta) \quad \text{and} \quad \tau(\eta,1) = T(\eta) \tag{51}$$

Using Taylor's theorem and Eq. (51) we have

$$T(\eta) = T_0(\eta) + \sum_{m=1}^{+\infty} T_m(\eta) \tag{52}$$

where

$$T_m(\eta) = \left.\frac{1}{m!}\frac{\partial^m \tau(\eta;p)}{\partial p^m}\right|_{p=0} \tag{53}$$

Therefore, the mth-order deformation equation is then given by

$$L_3[T_m(\eta) - \chi_m T_{m-1}] = \hbar R_m(\eta) \tag{54}$$

subject to the boundary conditions

$$T_m(0) = 0, \quad T_m(1) = 0 \tag{55}$$

where

$$R_m(\eta) = T''_{m-1} + \mathrm{Pr}\sum_{k=0}^{m-1}\left[Rf_{m-1-k}T'_k + \mathrm{Ec}(4f'_{m-1-k}f'_k + g_{m-1-k}g_k) + \mathrm{Ec}_x(f''_{m-1-k}f''_k + g'_{m-1-k}g'_k)\right] \tag{56}$$

By solving first few deformation equations we find that the solution expression for $T(\eta)$ can in general be written as

$$T(\eta) = \sum_{n=0}^{4m+4} d_{m,n}\eta^n \tag{57}$$

where $d_{m,n}$ denotes the constant coefficients that can be determined by using the following recurrence formulas for $m \geq 1$:

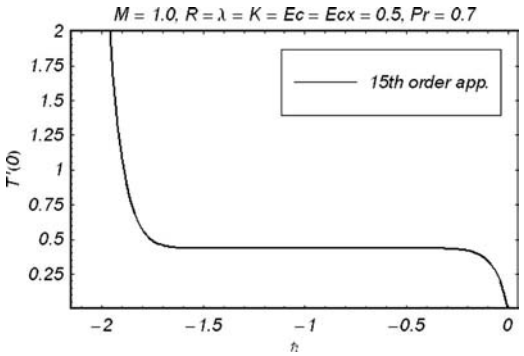

Fig. 2 $\hbar$–curve for $T(\eta)$ at 15th order approximation

$$d_{m,0} = \chi_m\chi_{4m+2}d_{m-1,0} - \sum_{k=0}^{4m+4} \mathrm{s}_k\Lambda_{m,k}\nu_k \tag{58}$$

$$d_{m,1} = \chi_m\chi_{4m+1}d_{m-1,1} - \sum_{k=0}^{4m+4} \mathrm{s}_{k+1}\Lambda_{m,k}\nu_k \tag{59}$$

$$d_{m,n} = \chi_m\chi_{4m+2-n}d_{m-1,n} + \Lambda_{m,n-2}\nu_{n-2}, \quad 2 \leq n \leq 4m+4 \tag{60}$$

where the constants involved in above expressions are defined in the Appendix. Note that by using the above recurrence relations one can easily find all $d_{m,n}$ with the knowledge of the following first few:

$$d_{0,0} = 1, \quad d_{0,1} = -1, \quad d_{0,2} = d_{0,3} = d_{0,4} = 0 \tag{61}$$

Therefore, the complete solution for temperature distribution across the channel can be written as

$$T(\eta) = T_0(\eta) + \sum_{m=1}^{+\infty} T_m(\eta) \tag{62}$$

To find the suitable values of $\hbar$ for which the solution series (62) converges, we have plotted the $\hbar$-curve (see Fig. 2). The interval on $\hbar$-axis for which the $\hbar$-curve is parallel to the $\hbar$-axis contains the admissible values of $\hbar$. The convergence of the solution series (62) is shown through Table 1. In Table 1 it is shown that the contribution of the higher order terms $T_m(\eta)$ (for $m \geq 15$) is negligible, which proves the convergence of the series (62).

4 Graphical Results and Discussion

The flow analysis of the present problem has been performed by Vajravelu and Kumar [27] in which the authors have discussed in detail the effect of different parameters on the velocity profile. In the present analysis we study the heat transfer characteristics in the fluid. To see the effects of different parameters on temperature distribution across the channel we have plotted the temperature T against η for different sets of values of the involved parameters (Table 2). The effects of the parameter λ, which corresponds to the constant injection at the upper plate, are shown graphically in Fig. 3. It is observed that by increasing the injection at the wall the temperature increases and this increase is maximum near the stretching wall. In Fig. 4 the effects of the rotation parameter K are shown. Obviously, by increasing K the temperature increases and again this increase is maximum near the stretching plate. Figure 5 demonstrates the effects of the viscosity parameter R in the presence of wall injection. It is shown that the temperature decreases by increasing the values of R. The effects of the Prandtl number Pr on temperature profiles in the presence of viscous dissipation are shown in Fig. 6. Clearly, by increasing Pr the temperature increases near the stretching wall. However, in the absence of the viscous dissipation ($\mathrm{Ec}=\mathrm{Ec}_x=0$) the effect of the Prandtl number is to decrease the temperature, as shown in Fig. 7.

Table 2 Numerical values of some important physical quantities

15th order HAM solution at $R=2.0$, $\hbar=-0.8$						
Pr	Ec_x	Ec	λ	K	M	$T'(0)$
1.0	0.5	0.5	0.5	0.5	1.0	−0.5153790
2.0	0.5	0.5	0.5	0.5	1.0	−0.0539821
0.7	1.0	0.5	0.5	0.5	1.0	−0.4802890
0.7	2.0	0.5	0.5	0.5	1.0	−0.1239200
0.7	0.5	1.0	0.5	0.5	1.0	−0.3178090
0.7	0.5	0.5	0.5	0.5	2.0	−0.6614910
0.7	0.5	0.5	0.5	0.5	3.0	−0.6597170
0.7	0.5	0.5	0.5	1.0	1.0	−0.6453420
0.7	0.5	0.5	0.5	2.0	1.0	−0.4375950

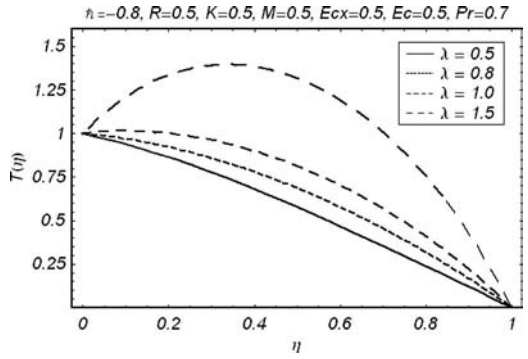

Fig. 3 Temperature distribution at different values of the injection parameter

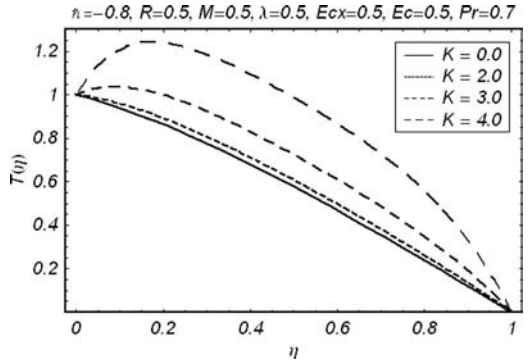

Fig. 4 Effect of rotation parameter *K* on temperature profile

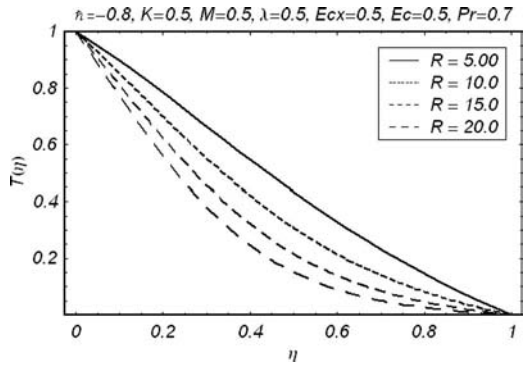

Fig. 5 Temperature profiles at different *R*

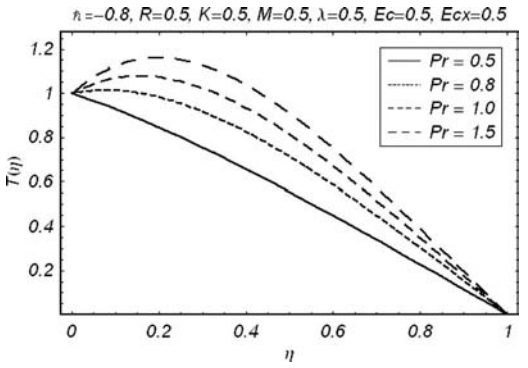

Fig. 6 Influence of the Prandtl number on temperature distribution

The effects of viscous dissipation for which the Eckert number Ec and the local Eckert number Ec_x are responsible are shown in Figs. 8 and 9. It is clear from the graphs that by increasing Ec and Ec_x the temperature near the stretching wall increases. This is due to the fact that heat energy is stored in the fluid due to the frictional heating. The effect of the magnetic field on temperature is shown in Fig. 10. From this figure it is clear that by increasing the magnetic field strength the temperature decreases across the channel.

5 Concluding Remarks

Heat transfer in a rotating electrically conducting fluid bounded by two parallel plates is studied. The upper plate is a porous plate and the lower plate is a stretching sheet. Analytic solution to velocity and temperature distribution is given by a purely analytic technique, namely, homotopy analysis method. The convergence of the solution series is shown by giving HAM solutions at dif-

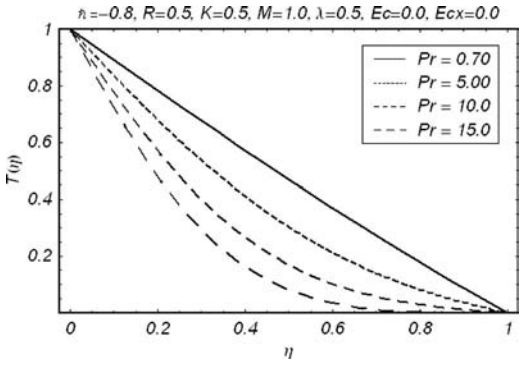

Fig. 7 $T(\eta)$ plotted at different local Eckert numbers

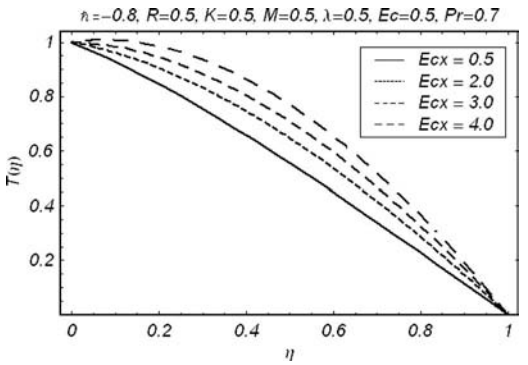

Fig. 8 Effect of the Eckert number on $T(\eta)$

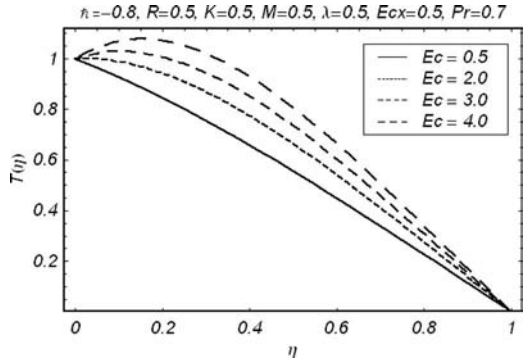

Fig. 9 Effect of Prandtl number on $T(\eta)$ in the absence of viscous dissipation

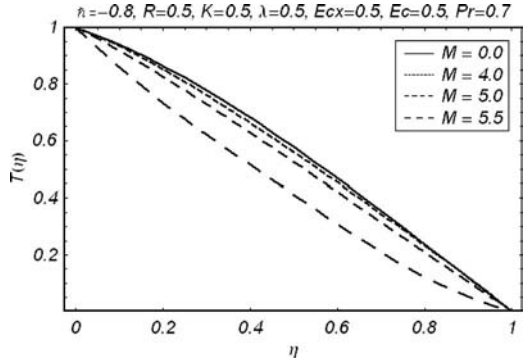

Fig. 10 Influence of magnetic field on temperature distribution

ferent orders. It is observed that injection at the upper plate causes to increase the temperature in the flow regime and the magnetic field decreases the temperature across the flow field. It is also observed that in the presence of viscous dissipation the Prandtl number causes to enhance the temperature whereas in the absence of viscous dissipation an increase in the Prandtl number causes to decrease the temperature across the channel. Furthermore an increase in the angular velocity of the system results in increasing the heat transfer near the heated plate.

Appendix

The constants involved in solution expressions (in previous sections) are defined as follows:

$$\Gamma_{m,n} = \hbar[\chi_{4m+2-n}(D_{m-1,n} - 2KE_{m-1,n} - MB_{m-1,n}) - R(\alpha_{m,n} - \beta_{m,n})] \tag{A1}$$

$$\Delta_{m,n} = \hbar[\chi_{4m+2-n}(H_{m-1,n} + 2KA_{m-1,n} - Mb_{m-1,n}) - R(\gamma_{m,n} - \delta_{m,n})] \tag{A2}$$

$$\Lambda_{m,n} = \hbar[\chi_{4m+2-n}J_{m-1,n} + \Pr\{R\omega_{m,n} + \mathrm{Ec}(4\tau_{m,n} + \sigma_{m,n}) + \mathrm{Ec}_x(\Omega_{m,n} + \Theta_{m,n})\}] \tag{A3}$$

$$\alpha_{m,n} = \sum_{k=0}^{4m+4} \sum_{j=\max\{0,n-4m+4k\}}^{\min\{n,4k+4\}} B_{k,j}A_{m-1-k,n-j} \tag{A4}$$

$$\beta_{m,n} = \sum_{k=0}^{4m+4} \sum_{j=\max\{0,n-4m+4k\}}^{\min\{n,4k+4\}} C_{k,j}a_{m-1-k,n-j} \tag{A5}$$

$$\gamma_{m,n} = \sum_{k=0}^{4m+4} \sum_{j=\max\{0,n-4m+4k\}}^{\min\{n,4k+4\}} b_{k,j}A_{m-1-k,n-j} \tag{A6}$$

$$\delta_{m,n} = \sum_{k=0}^{4m+4} \sum_{j=\max\{0,n-4m+4k\}}^{\min\{n,4k+4\}} E_{k,j}a_{m-1-k,n-j} \tag{A7}$$

$$\omega_{m,n} = \sum_{k=0}^{4m+4} \sum_{j=\max\{0,n-4m+4k\}}^{\min\{n,4k+4\}} I_{k,j}a_{m-1-k,n-j} \tag{A8}$$

$$\tau_{m,n} = \sum_{k=0}^{4m+4} \sum_{j=\max\{0,n-4m+4k\}}^{\min\{n,4k+4\}} A_{k,j}A_{m-1-k,n-j} \tag{A9}$$

$$\sigma_{m,n} = \sum_{k=0}^{4m+4} \sum_{j=\max\{0,n-4m+4k\}}^{\min\{n,4k+4\}} b_{k,j}b_{m-1-k,n-j} \tag{A10}$$

$$\Omega_{m,n} = \sum_{k=0}^{4m+4} \sum_{j=\max\{0,n-4m+4k\}}^{\min\{n,4k+4\}} B_{k,j}B_{m-1-k,n-j} \tag{A11}$$

$$\Theta_{m,n} = \sum_{k=0}^{4m+4} \sum_{j=\max\{0,n-4m+4k\}}^{\min\{n,4k+4\}} E_{k,j}E_{m-1-k,n-j} \tag{A12}$$

$$A_{m,n} = (n+1)a_{m,n+1} \tag{A13}$$

$$B_{m,n} = (n+1)A_{m,n+1} \tag{A14}$$

$$C_{m,n} = (n+1)B_{m,n+1} \tag{A15}$$

$$D_{m,n} = (n+1)C_{m,n+1} \tag{A16}$$

$$E_{m,n} = (n+1)b_{m,n+1} \tag{A17}$$

$$H_{m,n} = (n+1)E_{m,n+1} \tag{A18}$$

$$I_{m,n} = (n+1)d_{m,n+1} \tag{A19}$$

$$J_{m,n} = (n+1)I_{m,n+1} \tag{A20}$$

$$\mu_n = \frac{1}{(n+1)(n+2)(n+3)(n+4)} \tag{A21}$$

$$\nu_n = \frac{1}{(n+1)(n+2)} \tag{A22}$$

$$\varsigma_k = \begin{cases} 0 & \text{if } k \text{ is odd} \\ 1 & \text{if } k \text{ is even} \end{cases} \tag{A23}$$

References

[1] Sakiadis, B. C., 1961, "Boundary Layer Behavior on Continuous Solid Surface. I Boundary Layer Equations for Two-Dimensional and Axisymmetric Flow," AIChE J., **7**, pp. 26–28.

[2] Crane, L. J.,1970, "Flow Past a Stretching Plate," Z. Angew. Math. Phys., **21**, pp. 645–647.

[3] Andersson, H. I., 1992, "MHD Flow of a Viscoelastic Fluid Past a Stretching Surface," Acta Mech., **95**, pp. 227–230.

[4] Troy, W. C., Overman, II, E. A., Eremont-Rout, G. B., and Keener, J. P., 1987, "Uniqueness of Flow of Second Order Fluid Past a Stretching Sheet," Q. Appl. Math., **44**, pp. 753–755.

[5] Ariel, P. D.,1994, "MHD Flow of a Viscoelastic Fluid Past a Stretching Sheet With Suction," Acta Mech., **105**, pp. 49–56.

[6] Jacobi, A. M.,1993, "A Scale Analysis Approach to the Correlation of Continuous Moving Sheet, (Backward Boundary Layer) Forced Convective Heat Transfer," ASME J. Heat Transfer, **115**, pp. 1058–1061.

[7] Banks, W. H. H., 1983, "Similarity Solutions of the Boundary-Layer Equations for a Stretching Wall," J. Mec. Theor. Appl., **2**, pp. 375–392.

[8] Banks, W. H. H., and Zaturska, M. B., 1986, "Eigensolutions in Boundary

Layer Flow Adjacent to a Stretching Wall," IMA J. Appl. Math., **36**, pp. 263–273.
[9] Rajagopal, K. R., 1987, "A Non Similar Boundary Layer on a Stretching Sheet in a Non-Newtonian Fluid With Uniform Stream," J. Mathematical and Physical Sciences, **21**, pp. 189–200.
[10] Chakrabarti, A., and Gupta, A. S., 1979, "Hydromagnetic Flow and Heat Transfer Over a Stretching Sheet," Q. Appl. Math., **37**, pp. 756–755.
[11] Chaudhary, M. A., Merkin, J. H., and Pop, I., 1995, "Similarity Solutions in the Free Convection Boundary-Layer Flows Adjacent to Vertical Permeable Surface in Porous Media," Eur. J. Mech. B/Fluids, **14**, pp. 217–237.
[12] Chamkha, A. J., 1999, "Hydromagnetic Three-Dimensional Free Convection on a Vertical Stretching Surface With Heat Generation or Absorption," Int. J. Heat Fluid Flow, **20**, pp. 84–92.
[13] Xu, H., and Liao, S. J., 2005, "Series Solution of Unsteady Magnetohydrodynamic Flows of Non-Newtonian Fluids Cause by an Impulsively Stretching Plate," J. Non-Newtonian Fluid Mech., **129**, pp. 46–55.
[14] Vajravelu, K., 1986, "Hydromagnetic Flow and Heat Transfer Over a Continuous, Moving Porous Flat Surface," Acta Mech., **64**, pp. 179–185.
[15] Zakaria, M., 2004, "Magnetohydrodynamic Viscoelastic Boundary Layer Flow Past a Stretching Plate and Heat Transfer," Appl. Math. Comput., **155**, pp. 165–177.
[16] Dutta, B. K., Roy, P., and Gupta, A. S., 1985, "Temperature Field in Flow Over a Stretching Surface With Uniform Heat Flux," Int. Commun. Heat Mass Transfer, **12**, pp. 89–94.
[17] Andersson, H. I., Aarseth, J. B., Braud, N., and Dandapat, B. S., 1996, "Flow of a Power-Law Fluid Film on an Unsteady Stretching Surface," J. Non-Newtonian Fluid Mech., **62**(1), pp. 1–8.
[18] Bujurke, N. M., Biradar, S. N., and Hiremath, P. S., 1987, "2nd-Order Fluid-Flow Past a Stretching Sheet With Heat-Transfer," ZAMP, **38**(4), pp. 653–657.
[19] Dandapat, B. S., and Gupta, A. S., 1989, "Flow and Heat Transfer in a Viscoelastic Fluid Over a Stretching Sheet," Int. J. Non-Linear Mech., **24** pp. 215–219.
[20] Mehmood, A., and Ali, A., "An Explicit Analytic Solution of Steady Three-Dimensional Stagnation Point Flow of Second Grade Fluid Towards a Heated Plate," ASME J. Appl. Mech., to be published.
[21] Mehmood, A., and Ali, A., 2006, "Analytic Solution of Generalized Three-Dimensional Flow and Heat Transfer Over a Stretching Plane Wall," Int. Commun. Heat Mass Transfer, **33**, pp. 1243–1252.
[22] Chen, C. K., and Chen, M. I., 1988, "Heat and Mass Transfer of a Continuous Stretching Surface With Suction or Blowing," J. Math. Anal. Appl., **135**, pp. 568–580.
[23] Gupta, P. S., and Gupta, A. S., 1977, "Heat and Mass Transfer on a Stretching Sheet With Suction or Blowing," Can. J. Chem. Eng., **55**, pp. 744–746.
[24] Ali, M. E., 1994, "Heat Transfer Characteristics of a Continuous Stretching Surface," Waerme- Stoffuebertrag., **29**, pp. 227–234.
[25] Mehmood, A., Ali, A., and Shah, T., 2008, "Heat Transfer Analysis of Unsteady Boundary Layer Flow by Homotopy Analysis Method," Commun. Nonlinear Sci. Numer. Simul., **13**(5), pp. 902–912.
[26] Borkakoti, A. K., and Bharali, A., 1983, "Hydromagnetic Flow and Heat Transfer Between Two Horizontal Plates, the Lower Plate Being a Stretching Sheet," Q. Appl. Math., **41**, pp. 461–467.
[27] Vajravelu, K., and Kumar, B. V. R., 2004, "Analytic and Numerical Solutions of Coupled Nonlinear System Arising in Three-Dimensional Rotating Flow," Int. J. Non-Linear Mech., **39**, pp. 13–24
[28] Liao, S. J., 2003, *Beyond Perturbation: Introduction to Homotopy Analysis Method*, CRC, Boca Raton, FL.
[29] Liao, S. J., and Cheung, K. F., 2003, "Homotopy Analysis of Nonlinear Progressive Waves in Deep Water," J. Eng. Math., **45**, pp. 105–116.
[30] Liao, S. J., and Pop, I., 2004, "Explicit Analytic Solution for Similarity Boundary Layer Equations," Int. J. Heat Mass Transfer, **47**(1), pp. 75–85.
[31] Wang, C., Zhu, J. M., Liao, S. J., and Pop, I., 2003, "On the Explicit Analytic Solutions of Cheng-Chang Equations," Int. J. Heat Mass Transfer, **46**(10), pp. 1855–1860.
[32] Liao, S. J., 2006, "An Analytic Solution of Unsteady Boundary Layer Flows Caused by Impulsively Stretching Plate," Commun. Nonlinear Sci. Numer. Simul., **11**, pp. 326–339.
[33] Ali, A., and Mehmood, A., 2008, "Homotopy Analysis of Unsteady Boundary Layer Flow Adjacent to Permeable Stretching Surface in a Porous Medium," Commun. Nonlinear Sci. Numer. Simul., **13**, pp. 340–349.
[34] Allan, F. M., and Syam, M. I., 2005, "On Analytic Solution of the Non-Homogeneous Blasius Problem," J. Comput. Appl. Math., **182**, pp. 355–365.
[35] Liao, S. J., 2005, "A New Branch of Solution of Boundary Layer Flows Over an Impermeable Stretched Plate," Int. J. Heat Mass Transfer, **48**, pp. 2529–2539.
[36] Liao, S. J., 1999, "A Uniformly Valid Analytical Solution of 2D Viscous Flow Past a Semi Infinite Flat Plate," J. Fluid Mech., **385**, pp. 101–128.
[37] Liao, S. J., 1999, "An Explicit, Totally Analytic Approximate Solution for Blasius Viscous Flow Problems," Int. J. Non-Linear Mech., **34**, pp. 759–778.
[38] Mehmood, A., and Ali, A., 2007, "Unsteady Boundary Layer Flow Due to an Impulsively Started Moving Plate," Proc. Inst. Mech. Eng., Part G: J. Aero. Engr., **221**, pp. 385–390.
[39] Liao, S. J., and Campo, A., 2002, "Analytic Solutions of the Temperature Distribution in Blasius Viscous Flow Problems," J. Fluid Mech., **453**, pp. 411–425.
[40] Yang, C., andLiao, S. J., 2006, "On the Explicit, Purely Analytic Solution of Von Karman Swirling Viscous Flow," Commun. Nonlinear Sci. Numer. Simul., **11**(1), pp. 83–93.
[41] Liao, S. J., 2003, "On the Analytic Solution of Magnetohydrodynamic Flows of Non-Newtonian Fluids Over a Stretching Sheet," J. Fluid Mech., **488**, pp. 189–212.
[42] Liao, S. J., 2004, "On Homotopy Analysis Method for Nonlinear Problems," Appl. Math. Comput., **147**, pp. 499–513.

Estimating the Wall Heat Flux of Unsteady Conjugated Forced Convection Between Two Corotating Disks Using an Inverse Solution Scheme

David T. W. Lin[1]
Associate Professor
Insitute of Engineering Technology,
National University of Tainan,
Tainan City 700, Taiwan, R.O.C.
e-mail: david@mail.nutn.edu.tw

Hung Yi Li

Wei Mon Yan

Department of Mechatronic Engineering,
Huafan University,
Shih Ting, Taipei 223, Taiwan, R.O.C.

An inverse solution scheme based on the conjugate gradient method with the minimization of the object function is presented for estimating the unknown wall heat flux of conjugated forced convection flows between two corotating disks from temperature measurements acquired within the flow field. The validity of the proposed approach is demonstrated via the estimation of three time- and space-dependent heat flux profiles. A good agreement is observed between the estimated results and the exact solution in every case. In general, the accuracy of the estimated results is found to improve as the temperature sensors are moved closer to the unknown boundary surface and the error in the measured temperature data is reduced. [DOI: 10.1115/1.2976788]

Keywords: inverse solution, conjugated forced convection, conjugate gradient method, corotating disks

1 Introduction

The problem of fluid flow and heat transfer in radial flows between two corotating disks is of practical significance in many engineering applications. In many cases, the fluid flow and heat transfer characteristics are unsteady. However, in conjugated heat transfer problems involving corotating disks, it is frequently difficult, if not impossible, to measure the heat flux or temperature at the rotating disk surface. Therefore, the use of some form of inverse technique is generally required. However, such inverse problems are ill-posed, and hence the estimated solutions are highly sensitive to errors in the measured input data. Various researchers have proposed methods for overcoming the inherent instability of inverse solution schemes [1–4].

Moutsoglou [5] considered the problem of steady-state forced convection between parallel flat plates and used a straight inversion scheme and the whole domain regularization technique to estimate the unknown heat flux at the upper plate surface from temperature data measured at the lower plate. Colaco and Orlande [6] investigated the inverse problem of predicting two boundary heat fluxes in irregularly shaped channels containing a forced convection flow. Huang and Ozisik [7] determined the spacewise variation of the heat flux along a parallel plate duct containing a laminar flow stream from temperature measurements acquired at various locations within the flow field. Liu and Ozisik [8] employed the conjugate gradient method and an adjoint equation to conduct an inverse analysis of the timewise variation of the wall heat flux for the case of transient turbulent forced convection within a parallel plate duct. Raghunath [9], Bokar and Ozisik [10], and Liu and Ozisik [11] considered the inverse convection problem of determining the inlet temperature of a thermally developing hydrodynamically developed laminar flow between parallel plates from temperature measurements taken downstream of the entrance region. Machado and Orlande [12] applied the conjugate gradient method with an adjoint equation to estimate the timewise and spacewise variations of the wall heat flux of a parallel plate channel containing a laminar forced convection flow. Park and Lee [13] derived the space-dependent wall heat flux of a duct containing laminar flow using the Karhunen–Loeve Galerkin procedure. Fic [14] presented an inverse solution scheme for estimating the boundary velocity in steady-state convection-diffusion heat transfer problems with a potential fluid flow. Li and Yan considered the inverse problem of estimating the space- and time-dependent wall heat flux distributions for an unsteady forced convection within a parallel plate duct [15,16] and an annular duct [17], respectively. In a more recent study, Chen et al. [18,19] considered the equivalent problem in a parallel annular duct.

Due to their practical significance, the fluid flow and heat transfer characteristics of flow systems involving rotating bodies have attracted considerable attention. For example, Attia [20] considered the unsteady flow of an incompressible viscous non-Newtonian fluid above an infinite rotating disk. Seghir-Ouali et al. [21] employed an experimental approach to investigate the problem of convective heat transfer within a rotating cylinder with an axial air flow. Siddiqui et al. [22] obtained numerical solutions for the effects of the hall current and heat transfer on the magnetohydrodynamic (MHD) flow of a Burger's fluid induced by the pull of eccentric rotating disks. Aus der Wiesche [23] performed large-eddy simulations to establish the heat transfer characteristics of a pair of corotating disks in a parallel air crossflow.

In unsteady conjugated heat transfer problems, the heat capacity of the wall has a significant effect on the transient characteristics of the forced convection heat transfer performance. The effects of wall conduction on the characteristics of mixed convection channel flows in the direct solver were studied by Lee and Yan [24] and Yan and Lee [25], and the results indicated that both the conduction in the wall and the wall heat capacity play an important role in unsteady conjugated mixed convection channel flow. Yan and Lee [26] also examined the characteristics of unsteady conjugated mixed convection flow and the heat transfer between two corotating disks. In Ref. [27], Luna et al. applied the energy equation and the integral boundary layer technique to per-

[1]Corresponding author.

Contributed by the Heat Transfer Division of ASME for publication in the JOURNAL OF HEAT TRANSFER. Manuscript received October 24, 2007; final manuscript received April 21, 2008; published online September 24, 2008. Review conducted by Peter Vadasz.

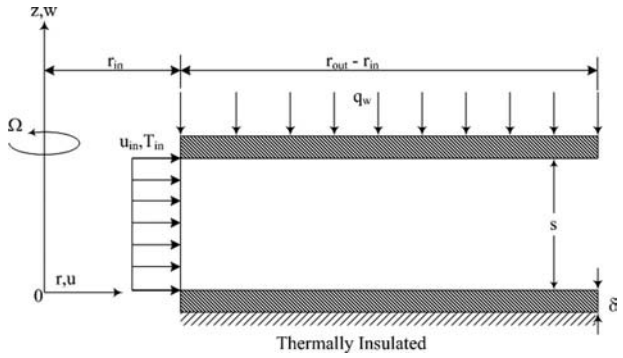

Fig. 1 Geometry and coordinate system

form a transient analysis of the conjugated heat transfer process in the thermal entrance region of a circular duct containing a fully developed laminar power-law fluid flow. Indinger and Shevchuk [28] presented numerical solutions for the transient laminar heat transfer characteristics of a rotating disk heated to a constant temperature and then suddenly subjected to unsteady cooling in still air. Ozar et al. [29] and Basu and Cetegen [30,31] observed heat transfer phenomena in a thin liquid film flowing over a rotating disk by the experiment and numerical method, separately. In a later study, Shevchuk [32] examined the unsteady conjugated heat transfer problem of a nonuniformly heated rotating disk. Lallave et al. [33] investigated the conjugate heat transfer characteristics of a rotating uniformly heated solid disk of finite thickness and radius under the impingement of a confined liquid jet. Although the conjugated mixed convection problem with the rotating system was the concern of those previous researchers, the direct solution was used in most of these studies. Sladek et al. [34] combined the Stehfest algorithm, the Laplace inversion, and the meshless local Petrov–Galerkin method to solve the inverse heat conduction problem of fluid flows within 3-D axisymmetric rotating bodies.

Reviewing literature, it is found that the problem of the unsteady forced convection flow between two corotating disks has received relatively little attention. However, the heat transfer characteristics of radial flows between corotating disks are of practical significance in many engineering applications and therefore merit a detailed investigation. In general, most previous studies of conjugated mixed convection in rotating systems employed direct numerical approaches. However, in such systems, it is generally impractical to measure the heat flux or temperature at the rotating surface, and hence some form of inverse technique is required. Accordingly, the current study develops an inverse scheme to investigate the heat transfer characteristics of the unsteady laminar forced convection flow between two corotating disks. In the proposed approach, a conjugate gradient method is used to estimate the space- and time-dependent wall heat fluxes acting on the surface of the upper disk from temperature data acquired from various locations within the flow field.

2 Analysis

2.1 Direct Problem. Figure 1 presents a schematic of the problem considered in the present analysis. As shown, the parallel disks corotate at an angular speed Ω and have an opening of $2r_{in}$ at the center, a wall thickness of δ, and a separation of s. The geometry of the rotating disks is described using a cylindrical coordinate system (r,z). The inlet coolant fluid flows radially outwards through the annular space between the two disks at a uniform velocity u_{in} and a uniform temperature T_{in}. Initially, the entire system, i.e., the flowing fluid and the two disk walls, have a uniform temperature T_{in}. However, at time $t=0$, the upper disk wall is subjected to a wall heat flux q_w, which varies as a function of the time, t, or as a function of both the time and the radial position, r. As shown, the lower disk wall is thermally insulated.

The aim of the current inverse analysis is to estimate the heat flux profile along the surface of the upper disk based on temperature measurements acquired at different locations within the coolant fluid flow. To simplify the analysis, the following assumptions are made. (1) The flow is steady, incompressible, and axisymmetric. (2) The fluid is laminar and is a boundary layer flow. (3) The flow has a high Peclet number and thus conduction in the radial direction of the fluid is negligible. (4) The heat conducted in the radial direction of the wall is sufficiently small to be neglected. The following dimensionless quantities are introduced to nondimensionalize the governing equations:

$$R=\frac{r}{s},\quad Z=\frac{z}{s},\quad R_{\text{in}}=\frac{r_{\text{in}}}{s},\quad R'=R-R_{\text{in}},\quad \theta(R,Z,\tau)=\frac{T-T_{\text{in}}}{\Delta T_c}$$

$$\text{Pe}=\frac{u_{\text{in}}s}{\alpha_f},\quad \text{Re}=\frac{u_{\text{in}}}{s\nu},\quad \text{Ro}=\frac{\Omega s}{u_{\text{in}}},\quad Q=\frac{q_w}{q_{\text{ref}}}$$

$$U=\frac{u}{u_{\text{in}}},\quad V=\frac{v}{u_{\text{in}}},\quad W=\frac{w}{u_{\text{in}}},\quad P'=\frac{p'}{(\rho u_{\text{in}}^2)} \tag{1}$$

$$\tau=\frac{\alpha f^t}{s^2},\quad K=\frac{k_w}{k_f},\quad \lambda=\frac{\delta}{s},\quad A=\frac{\alpha_w}{\alpha_f}$$

where k_w and k_f are the thermal conductivities of the plate and the fluid, respectively, α_w and α_f are the thermal diffusivities of the plate and the fluid, separately, T is the temperature, q_w is the heat flux applied to the wall, and q_{ref} is the reference heat flux. In this paper, the heat transfer to the wall is assumed positive.

The dimensionless governing equations describing the problem shown in Fig. 1 have the following form.

For the continuity equation,

$$\frac{\partial(RU)}{\partial R}+R\frac{\partial W}{\partial Z}=0 \tag{2a}$$

For the radial momentum equation,

$$U\frac{\partial U}{\partial R}+W\frac{\partial U}{\partial Z}-\frac{V^2}{R}=-\frac{dP'}{dR}+\left(\frac{1}{\text{Re}}\right)\frac{\partial^2 U}{\partial Z^2}+2\text{Ro}V \tag{2b}$$

For the tangential momentum equation,

$$U\frac{\partial V}{\partial R}+W\frac{\partial V}{\partial Z}+\frac{UV}{R}=\left(\frac{1}{\text{Re}}\right)\frac{\partial^2 V}{\partial Z^2}-2\text{Ro}U \tag{2c}$$

For the energy equation,

$$\text{Fluid}\quad \left(\frac{1}{\text{Pe}}\right)\frac{\partial\theta_f}{\partial\tau}+U\frac{\partial\theta_f}{\partial R}+W\frac{\partial\theta_f}{\partial Z}=\left(\frac{1}{\text{Pe}}\right)\frac{\partial^2\theta_f}{\partial Z^2} \tag{2d}$$

$$\text{Plate}\quad \frac{\partial\theta_w}{\partial\tau}=A\frac{\partial^2\theta_w}{\partial Z^2} \tag{2e}$$

The corresponding initial conditions and boundary conditions are as follows:

$$\tau=0:\quad \theta_f=\theta_w=0 \tag{2f}$$

$$\tau>0:\quad R=R_{\text{in}}:\quad U-1=V=W=0,\quad \theta_f=\theta_w=0 \tag{2g}$$

$$Z=-\lambda:\quad \frac{\partial\theta_w(R,-\lambda,\tau)}{\partial Z}=0 \tag{2h}$$

$$Z=0:\quad U=V=W=0,\quad \theta_f=\theta_w,\quad K\frac{\partial\theta_w(R,0,\tau)}{\partial Z}=\frac{\partial\theta_f(R,0,\tau)}{\partial Z} \tag{2i}$$

$$Z=1: \quad U=V=W=0, \quad \theta_f=\theta_w, \quad K\frac{\partial\theta_w(R,1,\tau)}{\partial Z}=\frac{\partial\theta_f(R,1,\tau)}{\partial Z} \tag{2j}$$

$$Z=1+\lambda: \quad K\frac{\partial\theta_w(R,1+\lambda,\tau)}{\partial Z}=Q(R,\tau) \tag{2k}$$

In the direct problem, the heat flux applied to the surface of the upper disk is known, and the objective is to compute the dimensionless temperature distribution in the fluid flow between the two disks. In the direct solution procedure, the governing equations are transformed into finite difference equations using a fully implicit numerical scheme in which the r-direction convection term is approximated by the upstream difference method, the z-direction diffusion term by the central difference scheme, and the unsteady term by the backward difference scheme. Note that the full details of the numerical procedure are presented in Ref. [35] and are therefore omitted here. The resulting system of equations forms a tridiagonal matrix, which can then be solved using the Thomas algorithm [36].

2.2 Inverse Problem. In the direct problem described above, the velocity distribution, initial conditions, and boundary conditions are all known, and thus the temperature distribution in the flow field and the upper disk is easily derived. However, in the inverse problem, the dimensionless heat flux $Q(R,\tau)$ acting on the surface of the upper disk is not known and must be estimated from temperature data acquired using sensors located within the fluid stream. Essentially, the problem of estimating the wall heat flux from the measured temperature data involves minimizing the following objective function:

$$J=\sum_{i=1}^{M}\sum_{k=1}^{N}(\theta_{f,i,k}-\Theta_{i,k})^2 \tag{3}$$

where $\theta_{f,i,k}=\theta_f(R_i,Z_1,\tau_k)$ is the calculated dimensionless temperature corresponding to an estimated $Q(R,\tau)$ and $\Theta_{i,k}=\Theta(R_i,Z_1,\tau_k)$ is the measured dimensionless temperature. Note that $Z_1=0$ indicates that the temperature sensors are located at the interface between the fluid and the lower disk wall. Similarly, $0<Z_1<1$ implies that the sensors are positioned at some vertical height within the fluid stream, while $Z_1=1$ indicates that the temperature measurements are acquired at the interface between the fluid and the upper disk wall. Finally, M and N indicate the number of measurement data in the R and τ dimensions, respectively.

In the inverse solution procedure performed in this study, the conjugate gradient method [37] is used to determine the unknown wall heat flux $Q(R,\tau)$ by minimizing the objective function J. The iterative process employed to do so can be expressed as

$$Q_{m,n}^{p+1}=Q_{m,n}^{p}-\beta^p d_{m,n}^{p} \tag{4}$$

where $Q_{m,n}=Q(R_m,\tau_n)$, β^p is the step size, and $d_{m,n}^{p}$ is the direction of descent and is determined from

$$d_{m,n}^{p}=\left(\frac{\partial J}{\partial Q_{m,n}}\right)^p+\gamma^p d_{m,n}^{p-1} \tag{5}$$

in which the conjugate coefficient γ^p is calculated as

$$\gamma^p=\frac{\sum_{m=1}^{M}\sum_{n=1}^{N}\left[\left(\frac{\partial J}{\partial Q_{m,n}}\right)^p\right]^2}{\sum_{m=1}^{M}\sum_{n=1}^{N}\left[\left(\frac{\partial J}{\partial Q_{m,n}}\right)^{p-1}\right]^2} \quad \text{with} \quad \gamma^0=0 \tag{6}$$

In Eq. (6), $\partial J/\partial Q_{m,n}$ represents the gradient of the objective function. The step size β^p in Eq. (4) is determined from

$$\beta^p=\frac{\sum_{i=1}^{M}\sum_{k=1}^{N}(\theta_{f,i,k}^{p}-\Theta_{i,k})\sum_{m=1}^{M}\sum_{n=1}^{N}\left(\frac{\partial\theta_{f,i,k}}{\partial Q_{m,n}}\right)^p d_{m,n}^{p}}{\sum_{i=1}^{M}\sum_{k=1}^{N}\left[\sum_{m=1}^{M}\sum_{n=1}^{N}\left(\frac{\partial\theta_{f,i,k}}{\partial Q_{m,n}}\right)^p d_{m,n}^{p}\right]^2} \tag{7}$$

where $\partial\theta_{f,i,k}/\partial Q_{m,n}$ is the sensitivity coefficient. This coefficient can be obtained by differentiating the direct problem with respect to $Q_{m,n}$, i.e.,

$$\left(\frac{1}{\mathrm{Pe}}\right)\frac{\partial}{\partial\tau}\left(\frac{\partial\theta_f}{\partial Q_{m,n}}\right)+U\frac{\partial}{\partial R}\left(\frac{\partial\theta_f}{\partial Q_{m,n}}\right)+W\frac{\partial}{\partial Z}\left(\frac{\partial\theta_f}{\partial Q_{m,n}}\right)=\left(\frac{1}{\mathrm{Pe}}\right)\frac{\partial^2}{\partial Z^2}\left(\frac{\partial\theta_f}{\partial Q_{m,n}}\right) \tag{8a}$$

$$\frac{\partial}{\partial\tau}\left(\frac{\partial\theta_w}{\partial Q_{m,n}}\right)=A\frac{\partial^2}{\partial Z^2}\left(\frac{\partial\theta_w}{\partial Q_{m,n}}\right) \tag{8b}$$

$$\tau=0: \quad \frac{\partial\theta_f(R,Z,0)}{\partial Q_{m,n}}=\frac{\partial\theta_w(R,Z,0)}{\partial Q_{m,n}}=0 \tag{8c}$$

$$\tau>0: \quad R=R_{\mathrm{in}}: \quad \frac{\partial\theta_f(R_{\mathrm{in}},Z,\tau)}{\partial Q_{m,n}}=\frac{\partial\theta_w(R_{\mathrm{in}},Z,\tau)}{\partial Q_{m,n}}=0 \tag{8d}$$

$$Z=-\lambda: \quad \frac{\partial}{\partial Z}\left(\frac{\partial\theta_w(R,-\lambda,\tau)}{\partial Q_{m,n}}\right)=0 \tag{8e}$$

$$Z=0: \quad \frac{\partial\theta_f(R,0,\tau)}{\partial Q_{m,n}}=\frac{\partial\theta_w(R,0,\tau)}{\partial Q_{m,n}}=0 \tag{8f}$$

$$K\frac{\partial}{\partial Z}\left(\frac{\partial\theta_w(R,0,\tau)}{\partial Q_{m,n}}\right)=\frac{\partial}{\partial Z}\left(\frac{\partial\theta_f(R,0,\tau)}{\partial Q_{m,n}}\right) \tag{8g}$$

$$Z=1: \quad \frac{\partial\theta_f(R,1,\tau)}{\partial Q_{m,n}}=\frac{\partial\theta_w(R,1,\tau)}{\partial Q_{m,n}}=0 \tag{8h}$$

$$K\frac{\partial}{\partial Z}\left(\frac{\partial\theta_w(R,1,\tau)}{\partial Q_{m,n}}\right)=\frac{\partial}{\partial Z}\left(\frac{\partial\theta_f(R,1,\tau)}{\partial Q_{m,n}}\right) \tag{8i}$$

$$Z=1+\lambda: \quad K\frac{\partial}{\partial Z}\left(\frac{\partial\theta_w(R,1+\lambda,\tau)}{\partial Q_{m,n}}\right)=\hat{u}(R-R_m,\tau-\tau_n) \tag{8j}$$

for $m=1,2,\ldots,M$ and $n=1,2,\ldots,N$, where

$$\hat{u}(R-R_m,\tau-\tau_n)=\begin{cases}1 & \text{if } R=R_m, \quad \tau=\tau_n\\ 0 & \text{otherwise}\end{cases} \tag{8k}$$

The gradient of the objective function, $\partial J/\partial Q_{m,n}$, is determined by differentiating Eq. (3) with respect to $Q_{m,n}$, i.e.,

$$\frac{\partial J}{\partial Q_{m,n}}=2\sum_{i=1}^{M}\sum_{k=1}^{N}(\theta_{i,k}-\Theta_{i,k})\frac{\partial\theta_{f,i,k}}{\partial Q_{m,n}} \tag{9}$$

In general, if the inverse problem contains no measurement errors, the condition

$$J(Q_{m,n}^{p})<\varphi \tag{10}$$

can be used as a termination criterion for the iterative process, where φ is a small specified positive number. However, in the current case, the measured temperature data inevitably contain a degree of error. Accordingly, the termination criterion is specified using the discrepancy principle [38], i.e.,

$$J(Q_{m,n}^{p})<MN\sigma^2 \tag{11}$$

where σ is the standard deviation of the measurement error.

The computational procedure employed to solve the current inverse convection problem can be summarized as follows.

Step 1. Solve the sensitivity problem to calculate the sensitivity coefficient $\partial\theta_{f,i,k}/\partial Q_{m,n}$.

Step 2. Make an initial guess of the dimensionless heat flux $Q^0_{m,n}$ and set the iteration step number to $p=0$.

Step 3. Solve the direct problem to compute $\theta_{f,i,k}$.

Step 4. Calculate the objective function. Terminate the iteration process if the specified criterion is satisfied; otherwise go to Step 5.

Step 5. Knowing $\partial\theta_{f,i,k}/\partial Q_{m,n}$, $\theta_{f,i,k}$, and $\Theta_{i,k}$, compute the gradient of the objective function, $\partial J/\partial Q_{m,n}$.

Step 6. Knowing $\partial J/\partial Q_{m,n}$, compute γ^p and $d^p_{m,n}$.

Step 7. Knowing $\partial\theta_{f,i,k}/\partial Q_{m,n}$, $\theta_{f,i,k}$, $\Theta_{i,k}$, and $d^p_{m,n}$, compute for β^p.

Step 8. Knowing β^p and $d^p_{m,n}$, compute $Q^{p+1}_{m,n}$. Set $p=p+1$ and return to Step 3.

3 Results and Discussions

As described above, the aim of the current inverse analysis is to estimate the unknown heat flux acting on the surface of the upper disk in the corotating pair from temperature measurements taken within the flow field or at the interface between the flow field and the upper or lower disks. As shown in Fig. 1, three types of boundary are applied on the corotating disks, i.e., the interface between the disk wall and the fluid, the quantity of the heat flux entering the upper disk surface, and the adiabatic boundary on the lower disk wall. In practice, such temperature measurements inevitably contain a certain degree of error. To reflect this, the temperature data, Θ, used in the present simulations as the basis for estimating the unknown boundary conditions, are computed by adding a random error to the exact temperature solutions, θ, obtained by solving the direct problem, i.e.,

$$\Theta = \theta + \sigma\zeta \tag{12}$$

where σ is the standard deviation of the measurement data and ζ is a random variable with a normal distribution, a zero mean, and a unit standard deviation. The value of ζ is calculated using the IMSL subroutine DRNNOR [39] and is specified within the range $-2.576<\zeta<2.576$, which represents the 99% confidence bound for the measured temperature.

The validity and applicability of the proposed inverse solution procedure are demonstrated by considering three different heat flux profiles.

In Case 1,

$$Q(\tau) = 0.01\tau, \quad \tau \le 500 \tag{13a}$$

$$Q(\tau) = 0.01(1000-\tau), \quad \tau > 500 \tag{13b}$$

In Case 2,

$$Q(\tau) = 5\ \sin(\pi\tau/1000) \tag{13c}$$

In Case 3,

$$Q(R,\tau) = 0.125R'\ \sin(\pi\tau/1000) \tag{13d}$$

As can be seen, the heat flux profiles in Cases 1 and 2 have the form of simple time-dependent triangular and sinusoidal functions, respectively, whereas Case 3 considers the rather more complicated scenario of a wall heat flux that varies both in time and space. In performing the simulations, the dimensionless thickness of the disk wall, λ, is assumed to be 0.1, and 41 equally spaced measurements are taken in the ranges $0\le R'\le 40$ and $0\le\tau\le 1000$, respectively. These data are then used as input data to reconstruct the unknown wall heat flux in the inverse problem. The simulations consider an air stream (Pr=0.7) flowing between two corotating disks with carbon steel walls ($K=2000$ and $A=0.65$). The opening radius, R_{in}, and the through-flow Reynolds number, Re, are assumed to be 20 and 500, respectively.

To evaluate the robustness of the proposed inverse solution procedure, the three heat flux profiles described in Eqs. (13*a*)–(13*d*) are estimated under the assumptions of measurement errors of $\sigma=0$, 0.03, 0.06, or 0.09, respectively, and sensor positions of $Z_1=0-0.9$. The accuracy of the estimated results is quantified using the following absolute average error index:

$$\varepsilon = \frac{1}{n_t}\sum_{j=1}^{n_t}|f-f_0| \tag{14}$$

where f is the estimated result with measurement errors, f_0 is the exact result, and n_t is the number of temporal steps. Clearly, a smaller value of ε indicates a better estimation result, and vice versa.

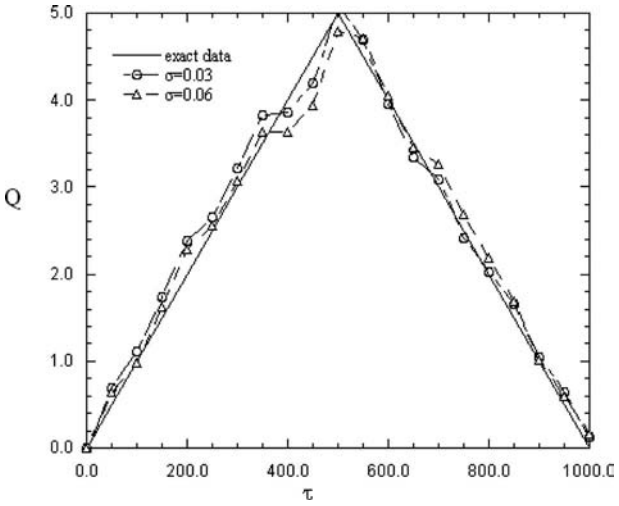

Fig. 2 Comparison of the exact result and inverse results ($\sigma=0.03$ and $\sigma=0.06$) for the Case 1 heat flux profile ($Z_1=0.9$)

Figure 2 compares the exact solution of the Case 1 heat flux profile with the estimated results obtained under the assumption of temperature measurement errors of $\sigma=0.03$ and $\sigma=0.06$, respectively. Note that in both cases, the temperature sensor is assumed to be located at $Z_1=0.9$. In general, when the temperature measurements are error-free, the estimated heat flux profile virtually coincides with the exact solutions. Furthermore, a good general agreement exists between the exact result and the inverse solutions even when the temperature measurements include an error component. Thus, the robustness of the proposed inverse solution scheme is confirmed. From inspection, the absolute average errors of the estimated dimensionless heat fluxes are found to be 0.144 and 0.174 for measurement errors of $\sigma=0.03$ and $\sigma=0.06$, respectively. In addition, the corresponding relative errors are computed to be around 2.88% and 3.48%, respectively, where the relative error is defined as the absolute average error divided by the maximum wall heat flux.

Figure 3(*a*) illustrates the variation of the absolute average error of the estimated results with the temperature measurement error as a function of the sensor location under various conditions in which σ ranges from 0.0 to 0.09 at $Z_1=0.0$, 0.3, 0.6, or 0.9, separately. In general, large measuring errors make the estimated results diverge from the error-free solutions. It is observed that the absolute average error increases with an increasing measurement error, but decreases with an increasing value of Z_1, i.e., the sensors are moved closer toward the upper disk. For convenience, the data presented in Fig. 3(*a*) are also tabulated in Table 1. It is noted in Table 1 that the absolute average errors are relatively amplified when σ is increased from 0.03 to 0.06, compared with that when σ is changed from 0.06 to 0.09, especially $Z_1=0.0$ and 0.3. From inspection, it is found that the absolute average error is highly sensitive to input data errors over the range $\sigma=0.03-0.06$, particularly when the sensors are located further from the unknown boundary surface, i.e., at $Z_1=0.0$ or $Z_1=0.3$, respectively. Figure

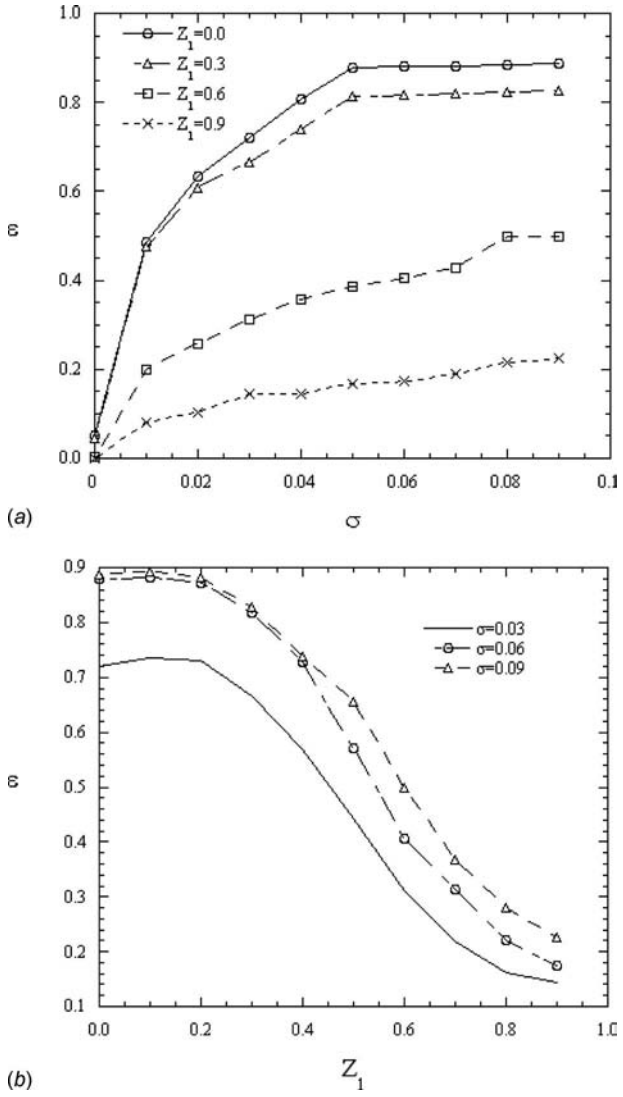

Fig. 3 Variation of the absolute average error with the (*a*) measurement error as a function of sensor location and (*b*) the sensor location as a function of the measurement error for the Case 1 heat flux profile

3(*b*) illustrates the variation of the absolute average error with the sensor location as a function of the temperature measurement error. It is apparent that irrespective of the magnitude of the measurement error, the absolute average error reduces significantly as the value of Z_1 increases beyond 0.2. In other words, an improved estimation performance is obtained as the sensors are moved closer to the unknown boundary of interest. Overall, the results show that the accuracy of the inverse solution scheme improves as the error in the temperature measurement data decreases or the distance between the temperature sensors and the upper boundary surface reduces.

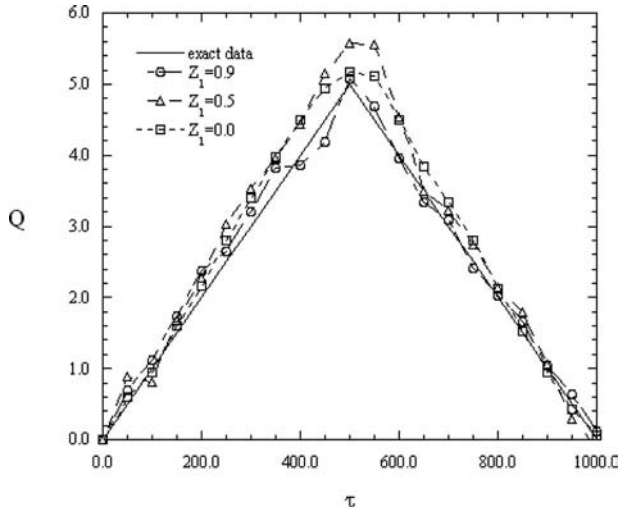

Fig. 4 Comparison of the exact result and inverse results (σ =0.03) for the Case 1 heat flux profile as a function of the sensor location

To evaluate the effect of the sensor location on the estimation performance of the proposed scheme, Fig. 4 compares the estimated and exact solutions for the Case 1 heat flux profile for a constant temperature measurement error of σ=0.03 and sensor locations of Z_1=0.0, 0.5, and 0.9, respectively. In general, it is seen that the deviation between the estimated results and the exact solution increases as the value of Z_1 decreases. In other words, the accuracy of the estimated heat flux reduces as the sensors are moved further from the unknown boundary surface.

To verify the applicability of the inverse solution scheme to the estimation of unknown time-dependent heat flux profiles of various forms, the simulation procedure described above was repeated for the second heat flux boundary condition, i.e., the time-dependent sinusoidal profile given in Eq. (13*c*). Figure 5(*a*) compares the exact solution with the estimated results obtained using input data with measurement errors of σ=0.03 and σ=0.06, respectively, and the sensor location is Z_1=0.9. As in Fig. 2, it can be seen that a good agreement is obtained between the exact result and the estimated solutions as the value of the measurement error is reduced. Figure 5(*b*) shows the effect of the sensor location on the accuracy of the estimated results given a constant measurement error of σ=0.03. As in the previous example, the deviation between the estimated result and the exact solution increases as the sensor is moved further from the upper wall. Figure 6 plots the variation of the absolute average error with the sensor location as a function of the measurement error. It is evident that the accuracy of the estimated results improves as the error in the measurement data decreases or the sensor is moved closer to the upper wall surface.

Finally, the wall heating condition of Case 3, which is a function of space (R') and time (τ), is tested. Figure 7 shows the estimated heat fluxes at R'=8, 20, and 32 under different measurement errors (σ=0.03 and σ=0.06) for wall heating conditions

Table 1 The absolute average errors at different σ and Z_1 for the wall heating condition of Case 1

σ	0.0	0.01	0.02	0.03	0.04	0.05	0.06	0.07	0.08	0.09
Z_1=0.0	0.05	0.485	0.633	0.719	0.806	0.877	0.88	0.882	0.885	0.887
Z_1=0.3	0.04	0.475	0.608	0.665	0.739	0.814	0.817	0.82	0.823	0.827
Z_1=0.6	0.004	0.199	0.258	0.312	0.357	0.388	0.406	0.429	0.5	0.5
Z_1=0.9	0.0	0.081	0.104	0.144	0.144	0.169	0.174	0.191	0.215	0.226

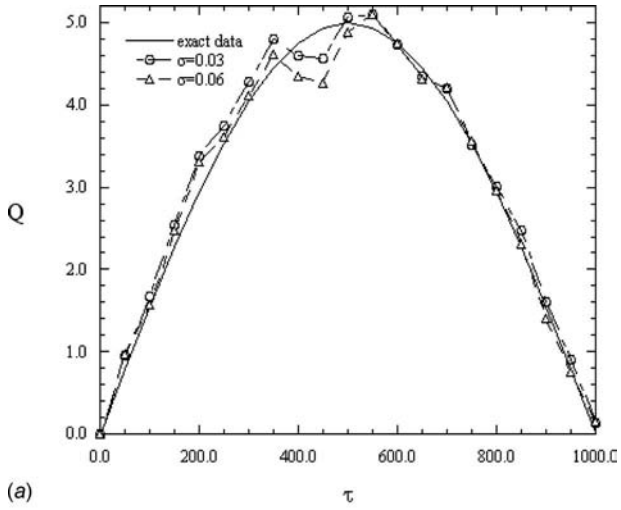

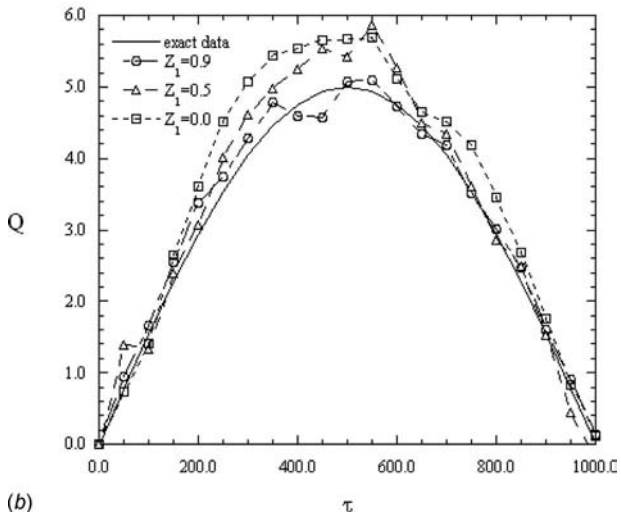

Fig. 5 Comparison of the exact result and inverse results for the Case 2 heat flux profile: (*a*) $\sigma=0.03$ and $\sigma=0.06$ ($Z_1=0.9$) and (*b*) $Z_1=0.0$, $Z_1=0.5$, and $Z_1=0.9$ ($\sigma=0.03$)

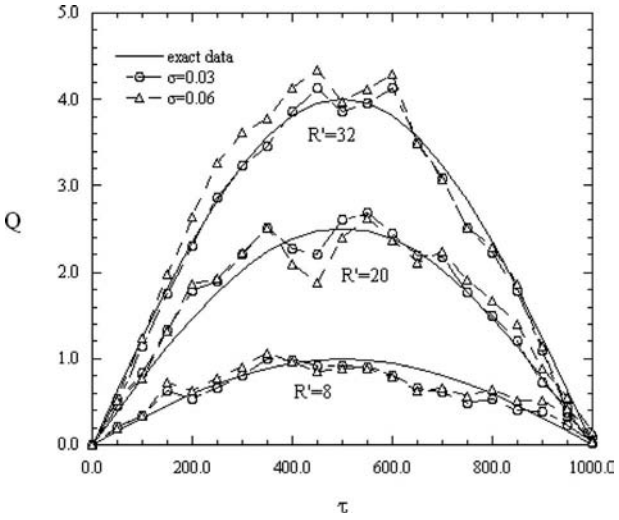

Fig. 7 Comparison of the exact result and inverse results ($\sigma=0.03$ and $\sigma=0.06$) for the Case 3 heat flux profile ($Z_1=0.9$)

of Case 3 and compared with the exact data; the sensor location is $Z_1=0.9$. As shown, the heat flux considered in this example is both time- and space-dependent. In general, it can be seen that the absolute value of the heat flux increases with an increasing value of R'. Finally, it is noted that for a given value of R', the accuracy of the estimated results improves as the measurement error reduces. Figure 8 shows the variation of the absolute average error with the sensor location as a function of the measurement error. As in previous examples, it can be seen that the accuracy of the estimated results improves as the sensor is moved toward the unknown boundary surface or as the measurement error is reduced. Table 2 summarizes the variation of the absolute average error as a function of both the measurement error and the sensor location. The results show that the accuracy of the estimated results reduces when the sensor is positioned closer to the lower wall. For example, given a constant measurement error of $\sigma=0.09$, the estimation errors corresponding to sensor locations of $Z_1=0.0$, 0.3, 0.6, and 0.9 are found to be 1.055, 1.017, 0.436, and 0.246, re-

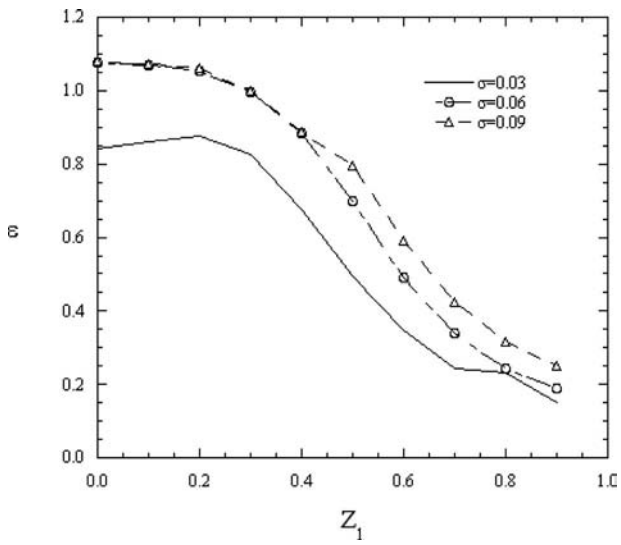

Fig. 6 Variation of the absolute average error with the sensor location as a function of the measurement error for the Case 2 heat flux profile

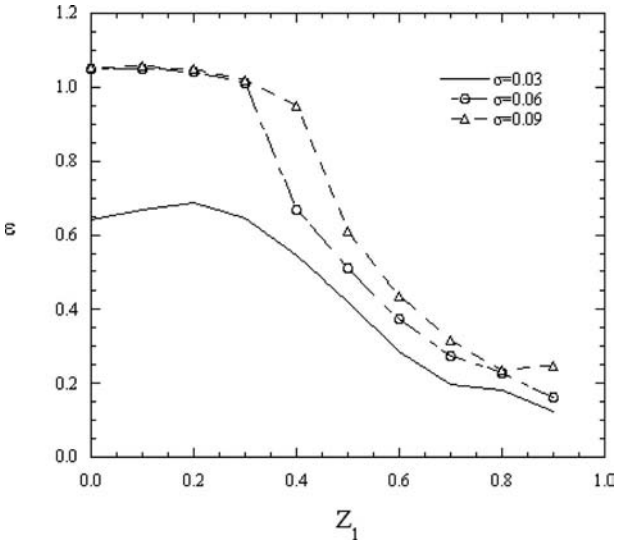

Fig. 8 Variation of the absolute average error with the sensor location as a function of the measurement error for the Case 3 heat flux profile

Table 2 The absolute average errors at different σ and Z_1 for the wall heating condition of Case 3

Z_1	0.0	0.1	0.2	0.3	0.4	0.5	0.6	0.7	0.8	0.9
σ=0.0	0.071	0.07	0.068	0.034	0.028	0.008	0.004	0.001	0.0	0.0
σ=0.03	0.642	0.668	0.687	0.645	0.544	0.422	0.285	0.195	0.181	0.125
σ=0.06	1.049	1.049	1.043	1.01	0.669	0.511	0.373	0.273	0.227	0.162
σ=0.09	1.055	1.056	1.05	1.017	0.948	0.611	0.436	0.317	0.234	0.246

spectively. However, it is apparent that the effect of the sensor location on the accuracy of the estimated results becomes less pronounced as the measurement error reduces.

In general, the results presented in this section of the paper confirm the ability of the proposed inverse solution scheme to estimate surface heat flux profiles of various forms given knowledge of the corresponding temperature distribution within the fluid field. Overall, the results demonstrate that the accuracy of the estimated solutions is enhanced as the temperature sensors are moved toward the unknown boundary surface or the precision of the measured temperature data is improved.

4 Conclusions

This study has presented an inverse scheme based on the conjugate gradient method to estimate the space- and time-dependent wall heat flux in the problem of unsteady conjugated forced convection between two parallel corotating disks. The validity of the proposed approach has been demonstrated by considering three different heat flux profiles. In general, the results have shown that the solution scheme yields satisfactory results for all three profiles. It has also been shown that the accuracy of the estimated results can be enhanced by suppressing the error in the measurement data or by locating the temperature sensors closer to the unknown boundary surface.

Acknowledgment

The financial support provided to this study by the National Science Council of the Republic of China under Contract No. NSC 96-2221-E-269-007 is gratefully acknowledged.

Nomenclature

A = dimensionless thermal diffusivity
d = direction of descent
f = estimated result with measurement errors
f_0 = exact result
h = heat transfer coefficient
J = objective function
K = dimensionless thermal conductivity
k = thermal conductivity
M = number of the measured data in the R direction
N = number of the measured data in the τ direction
n_t = number of temporal steps
P', p' = dimensionless and dimensional pressure departures
Pe = Peclet number
Q = dimensionless wall heat flux
q_w = wall heat flux
q_{ref} = reference heat flux
R, r = dimensionless and dimensional radial coordinates
R = dimensionless relative radial position
$R_{\text{in}}, r_{\text{in}}$ = dimensionless and dimensional radius openings
Re = Reynolds number
Ro = rotation number
s = disk spacing
T = temperature
T_{in} = inlet temperature
t = time
U, V, W = dimensionless velocity
u_{in} = inlet velocity
u, v, w = velocity
Z_1 = Z-coordinate position of temperature sensors
Θ = measured dimensionless temperature data

Greek Symbols

α = thermal diffusivity
β = step size
δ = disk wall thickness
ε = absolute average error
γ = conjugate coefficient
Ω = angular speed of corotating disks
φ = specified positive number
λ = dimensionless disk wall thickness
ν = kinematic viscosity
θ = dimensionless temperature
σ = standard deviation
τ = dimensionless time
ζ = random variable

Superscript

p = pth iteration

Subscripts

f = fluid
w = wall

References

[1] Beck, J. V., Blackwell, B., and Clair, C. R., 1985, *Inverse Heat Conduction: Ill-Posed Problems*, Wiley, New York.
[2] Alifanov, O. M., 1994, *Inverse Heat Transfer Problems*, Springer-Verlag, New York.
[3] Kurpisz, K., and Nowak, A. J., 1995, *Inverse Thermal Problems*, Computational Mechanics, Southampton.
[4] Ozisik, M. N., and Orlande, H. R. B., 2000, *Inverse Heat Transfer*, Taylor & Francis, New York.
[5] Moutsoglou, A., 1990, "Solution of an Elliptic Inverse Convection Problem Using a Whole Domain Regularization Technique," J. Thermophys. Heat Transfer, **4**(3), pp. 341–349.
[6] Colaco, M. J., and Orlande, H. R. B., 2001, "Inverse Forced Convection Problem of Simultaneous Estimation of Two Boundary Heat Fluxes in Irregularly Shaped Channels," Numer. Heat Transfer, Part A, **39**(7), pp. 737–760.
[7] Huang, C. H., and Ozisik, M. N., 1992, "Inverse Problem of Determining Unknown Wall Heat Flux in Laminar Flow Through a Parallel Plate Duct," Numer. Heat Transfer, Part A, **21**(1), pp. 55–70.
[8] Liu, F. B., and Ozisik, M. N., 1996, "Inverse Analysis of Transient Turbulent Forced Convection Inside Parallel−Plate Ducts," Int. J. Heat Mass Transfer, **39**(12), pp. 2615–2618.
[9] Raghunath, R., 1993, "Determining Entrance Conditions From Downstream Measurements," Int. Commun. Heat Mass Transfer, **20**, pp. 173–183.
[10] Bokar, J. C., and Ozisik, M. N., 1995, "An Inverse Analysis for Estimating the Time-Varying Inlet Temperature in Laminar Flow Inside a Parallel Plate Duct," Int. J. Heat Mass Transfer, **38**, pp. 39–45.
[11] Liu, F. B., and Ozisik, M. N., 1996, "Estimation of Inlet Temperature Profile in Laminar Duct Flow," Inverse Probl. Eng., **3**, pp. 131–143.
[12] Machado, H. A., and Orlande, H. R. B., 1997, "Inverse Analysis for Estimating the Timewise and Spacewise Variation of the Heat Flux in a Parallel Plate Channel," Int. J. Numer. Methods Heat Fluid Flow, **7**, pp. 696–710.
[13] Park, H. M., and Lee, J. H., 1998, "A Method of Solving Inverse Convection Problem by Means of Mode Reduction," Chem. Eng. Sci., **53**, pp. 1731–1744.
[14] Fic, A., 2004, "A Study of the Steady-State Inverse Heat Transfer Problem of Estimating the Boundary Velocity," Numer. Heat Transfer, Part A, **45**(2), pp. 153–170.

[15] Li, H. Y., and Yan, W. M., 1999, "Estimation of Space and Time Dependent Wall Heat Flux in an Inverse Convection Problem," J. Thermophys. Heat Transfer, **13**(3), pp. 394–396.
[16] Li, H. Y., and Yan, W. M., 2003, "Identification of Wall Heat Flux for Turbulent Forced Convection by Inverse Analysis," Int. J. Heat Mass Transfer, **46**, pp. 1041–1048.
[17] Li, H. Y., and Yan, W. M., 2000, "Inverse Convection Problem for Determining Wall Heat Flux in Annular Duct Flow," ASME J. Heat Transfer, **122**(3), pp. 460–464.
[18] Chen, C. K., Wu, L. W., and Yang, Y. T., 2006, "Comparison of Whole-Domain and Sequential Algorithms for Function Specification Method in the Inverse Heat Transfer Problem of Laminar Convective Pipe Flow," Numer. Heat Transfer, Part A, **50**(10), pp. 927–947.
[19] Chen, C. K., Wu, L. W., and Yang, Y. T., 2008, "Proposed Modification to Whole Domain Function Specification Method to Improve Accuracy of Its Estimations," ASME J. Heat Transfer, **130**, pp. 051702.
[20] Attia, H. A., 2003, "Unsteady Flow of a Non-Newtonian Fluid Above a Rotating Disk With Heat Transfer," Int. J. Heat Mass Transfer, **46**, pp. 2695–2700.
[21] Seghir-Ouali, S., Saury, D., Harmand, S., Phillipart, O., and Laloy, D., 2006, "Convective Heat Transfer Inside a Rotating Cylinder With an Axial Air Flow," Int. J. Therm. Sci., **45**, pp. 1166–1178.
[22] Siddquiddi, A. M., Rana, M. A., and Ahmed, N., 2008, "Effects of Hall Current and Heat Transfer on MHD Flow of a Burger's Fluid Due to a Pull of Eccentric Rotating Disks," Commun. Nonlinear Sci. Numer. Simul., **13**, pp. 1554–1570.
[23] Aus der Wiesche, S., 2007, "Heat Transfer From a Rotating Disk in a Parallel Air Crossflow," Int. J. Therm. Sci., **46**, pp. 745–754.
[24] Lee, K. T., and Yan, W. M., 1994, "Numerical Study of Transient Conjugated Mixed Convection in a Vertical Pipe," Numer. Heat Transfer, **26**, pp. 161–179.
[25] Yan, W. M., and Lee, K. T., 1995, "Unsteady Conjugated Mixed Convection in a Vertical Channel," ASME J. Heat Transfer, **117**, pp. 234–238.
[26] Yan, W. M., and Lee, K. T., 1996, "Unsteady Conjugated Mixed Convection Flow and Heat Transfer Between Two Co-Rotating Discs," Int. J. Heat Mass Transfer, **40**, pp. 2975–2988.
[27] Luna, N., Méndez, F., and Mar, E., 2003, "Transient Analysis of the Conjugated Heat Transfer in Circular Ducts With a Power Law Fluid," J. Non-Newtonian Fluid Mech., **111**, pp. 69–85.
[28] Indinger, T., and Shevchuk, I. V., 2004, "Transient Laminar Conjugate Heat Transfer of a Rotating Disk: Theory and Numerical Simulations," Int. J. Heat Mass Transfer, **47**, pp. 3577–3581.
[29] Ozar, B., Cetegen, B. M., and Faghri, A., 2004, "Experiments on Heat Transfer in a Thin Liquid Film Flowing Over a Rotating Disk," ASME J. Heat Transfer, **126**, pp. 184–192.
[30] Basu, S., and Cetegen, B. M., 2006, "Analysis of Hydrodynamics and Heat Transfer in a Thin Liquid Film Flowing Over a Rotating Disk by the Integral Method," ASME J. Heat Transfer, **128**, pp. 217–225.
[31] Basu, S., and Cetegen, B. M., 2007, "Effect of Hydraulic Jump on Hydrodynamics and Heat Transfer in a Thin Liquid Film Flowing Over a Rotating Disk Analyzed by Integral Method," ASME J. Heat Transfer, **129**, pp. 657–663.
[32] Shevchuk, I. V., 2006, "Unsteady Conjugate Laminar Heat Transfer of a Rotating Non-Uniformly Heated Disk: Application to the Transient Experimental Technique," Int. J. Heat Mass Transfer, **49**, pp. 3530–3537.
[33] Lallave, J. C., Rahman, M. M., and Kumar, A., 2007, "Numerical Analysis of Heat Transfer on a Rotating Disk Surface Under Confined Liquid Jet Impingement," Int. J. Heat Fluid Flow, **28**, pp. 720–734.
[34] Sladek, J., Sladek, V., and Hon, Y. C., 2006, "Inverse Heat Conduction Problems by Meshless Local Petrov–Galerkin Method," Eng. Anal. Boundary Elem., **30**, pp. 250–261.
[35] Yan, W. M., Tsay, Y. L., and Lin, T. F., 1989, "Transient Conjugated Heat Transfer in Laminar Pipe Flows," Int. J. Heat Mass Transfer, **32**, pp. 775–777.
[36] Patankar, S. V., 1980, *Numerical Heat Transfer and Fluid Flow*, Hemisphere, Washington, DC.
[37] Hestenes, M. R., 1980, *Conjugate Direction Methods in Optimization*, Springer-Verlag, New York, Chap. 4.
[38] Alifanov, O. M., 1974, "Solution of an Inverse Problem of Heat Conduction by Iteration Methods," J. Eng. Phys., **26**(4), pp. 471–476.
[39] 1987, User's Manual, Math Library Version 1.0, IMSL Library Edition 10.0, IMSL, Houston, TX.

Computational Analysis of Surface Curvature Effect on Mist Film-Cooling Performance

Xianchang Li[1]
Department of Mechanical Engineering,
Lamar University,
Beaumont, TX 77710
e-mail: xianchang.li@lamar.edu

Ting Wang
Energy Conversion & Conservation Center,
University of New Orleans,
New Orleans, LA 70148-2220

Air-film cooling has been widely employed to cool gas turbine hot components, such as combustor liners, combustor transition pieces, turbine vanes, and blades. Studies with flat surfaces show that significant enhancement of air-film cooling can be achieved by injecting water droplets with diameters of 5–10 μm into the coolant airflow. The mist/air-film cooling on curved surfaces needs to be studied further. Numerical simulation is adopted to investigate the curvature effect on mist/air-film cooling, specifically the film cooling near the leading edge and on the curved surfaces. Water droplets are injected as dispersed phase into the coolant air and thus exchange mass, momentum, and energy with the airflow. Simulations are conducted for both 2D and 3D settings at low laboratory and high operating conditions. With a nominal blowing ratio of 1.33, air-only adiabatic film-cooling effectiveness on the curved surface is lower than on a flat surface. The concave (pressure) surface has a better cooling effectiveness than the convex (suction) surface, and the leading-edge film cooling has the lowest performance due to the main flow impinging against the coolant injection. By adding 2% (weight) mist, film-cooling effectiveness can be enhanced approximately 40% at the leading edge, 60% on the concave surface, and 30% on the convex surface. The leading edge film cooling can be significantly affected by changing of the incident angle due to startup or part-load operation. The film cooling coverage could switch from the suction side to the pressure side and leave the surface of the other part unprotected by the cooling film. Under real gas turbine operating conditions at high temperature, pressure, and velocity, mist-cooling enhancement could reach up to 20% and provide a wall cooling of approximately 180 K. [DOI: 10.1115/1.2970071]

Keywords: film cooling, surface curvature, mist cooling, heat transfer enhancement

1 Introduction

Cooling of gas turbine (GT) hot components is a critical task because these components such as combustor liners, combustor transition pieces, turbine vanes (nozzles), and blades (buckets) need to be protected from the flue gas at extremely high temperature. External air-film cooling, as well as internal cooling, has been successfully used in protecting turbine airfoils for the last half-century [1,2] with a continuous research effort striving to make the cooling more effective.

Film cooling. In film cooling, there are many flow and geometric parameters that affect the cooling performance, such as jet hole shape, coolant injection angle, blowing ratio, inlet velocity profile, turbulence intensity, and coolant-supply plenum configuration. In general, cooling can be optimized with a comprehensive study on the effect of all these factors. For example, Jia et al. [3] investigated a slot jet film cooling by using numerical simulations together with experiments. Kwak and Han [4,5] measured the heat transfer coefficients and film-cooling effectiveness on a gas turbine blade tip. Wang et al. [6] conducted an experimental study focusing on the flow mixing behavior inside the slots. Bell et al. [7] studied film cooling from shaped holes and measured the local and averaged adiabatic film-cooling effectiveness. Brittingham and Leylek [8] performed the numerical simulation on film cooling with compound-angle shaped holes. Colban et al. [9] compared the cylindrical and fan-shaped film cooling on a vane endwall at low and high free-stream turbulence levels. Suryanarayanan et al. [10] measured the film-cooling effectiveness under rotation on the rotor blade platform.

Curvature effect on film cooling. Most of the above studies used flat surfaces and supplied a main flow. In the real gas turbine application, the film-cooling flow in the leading-edge area is subject to impingement from the main flow (shower-head cooling), which possesses very different flow mechanism from those further downstream where the main flow is basically parallel to the surface. The coolant flow structure will also be affected by the strong curvature near the leading edge. The strong leading-edge curvature is further demarcated into concave and convex curvatures on the suction surface and pressure surface, respectively. Nicolas and Le Meur [11] compared the performance of film cooling with curved walls to that with a flat plate. The performance was improved for the concave wall with relatively high mass flow rate ratios, while the cooling efficiency on the convex wall was less than that on the plate. Mayle et al. [12] also compared film cooling with a slot jet on curved surfaces to that on a flat surface. Convex curvature was found to increase the adiabatic wall effectiveness whereas concave curvature was found to be detrimental. The finding of Mayle et al. seems to be opposite to the Nicolas and Le Meur's study. Ito et al. [13] measured the local film cooling with a row of jets on a gas turbine blade. The static pressure force around the jet on the convex wall produced a higher effectiveness than that on a flat wall when the momentum flux ratio was small. At a large momentum flux ratio, the inertia of the jet forced the jet to move away from the wall and the cooling effectiveness became smaller. The effect of curvature on the concave side was the reverse of those for the convex surface. Later, Schwarz et al. [14] showed that the opposite performance might be caused by different coolant injection rates. At low blowing

[1]Corresponding author.

Contributed by the Heat Transfer Division of ASME for publication in the JOURNAL OF HEAT TRANSFER. Manuscript received August 29, 2007, final manuscript received April 16, 2008; published online September 15, 2008. Review conducted by Minking Chyu.

rates, film cooling was more effective on the convex surface than on a flat or a concave surface. As the injection rate increased, the normal and tangential jet momenta promoted lift-off from the convex surface, thereby lowered the performance. Jiang and Han [15] studied the effect of film hole row location on local film-cooling effectiveness distribution on a turbine blade model. Results indicated that injection from a different film hole row location provided a different effectiveness distribution on pressure and suction surfaces depending on local mainstream velocity and blade curvature. Berhe and Patankar [16] conducted a numerical study to investigate the effect of surface curvature on cooling effectiveness. For the low blowing ratios considered, the convex surface resulted in a higher cooling effectiveness than both the flat and concave surfaces. On the concave surface, the mixing between the coolant jet and the mainstream was strong, so the cooling effectiveness degraded. To enhance the film-cooling performance in the vicinity of the turbine blade leading edge, Kim et al. [17] investigated the flow characteristics of the film-cooled turbine blade using a cylindrical body model. Their results showed that the blowing ratio had a strong effect on film-cooling effectiveness as well as the coolant trajectory.

Mist cooling. As the working gas temperature continuously increases to augment thermal efficiency, new cooling techniques are needed to surpass incremental improvements of convectional gas turbine cooling technologies. A promising technology to enhance film cooling is to inject water mist (small droplet) into the coolant flow. Each droplet acts as a cooling sink and flies over a distance before it completely vaporizes. This "distributed cooling" characteristic allows controlled cooling by manipulating different sizes of injected water droplets. Another important merit of employing mist film cooling is that some larger droplets can fly longer and evaporate farther into the downstream region where single-phase air-film cooling becomes less effective. Li and Wang [18,19] simulated air/mist film cooling and showed that a small amount of mist injection (2% of the coolant mass flow rate) could increase the adiabatic cooling effectiveness about 30–50% under low temperature, velocity, and pressure conditions similar to those in the laboratory. Under the GT operating conditions with high temperature and high pressures (Wang and Li [20]), the cooling enhancement was found less attractive in terms of "enhancement percentage" (10–20%) than the cases with low pressure, velocity, and temperature conditions. However, due to high surface temperature in the real gas turbine condition, relatively smaller percentage of cooling enhancement can result in larger wall temperature reduction, which is critical to significantly extend the life expectancy of gas turbine airfoils. Li and Wang [21] presented the air/mist film cooling heat transfer coefficient under nonadiabatic wall condition including conjugate condition employing internal channel cooling.

Enhancing heat transfer by injecting tiny water droplets is not a new concept. Related applications have been developed and research has been conducted. One example is gas turbine inlet cooling [22]. Furthermore, fog overspray is used to provide cooling in the compressor. Petr [23] performed a thermodynamic analysis of the gas turbine cycle with wet compression. Nirmalan et al. [24] conducted an experimental study of turbine vane heat transfer with water-air mist cooling. The authors' research group conducted a series of mist/steam cooling experimental studies [25–28] for application in the *H*-type gas turbine using a closed-loop steam cooling scheme.

The previous mist/air-film-cooling simulations were conducted on flat surfaces with the main flow parallel to the surface [18–21]. This paper will focus on investigating the shower-head film cooling near the leading edge and the subsequent curved surface effects on mist film cooling. The flow fields over the curved surfaces are expected to create a body force exerted on the water droplet by the cross-stream pressure gradient. It is interesting to see how these effects would alter the water droplet dynamics and lead to different film-cooling performances from that on a flat surface.

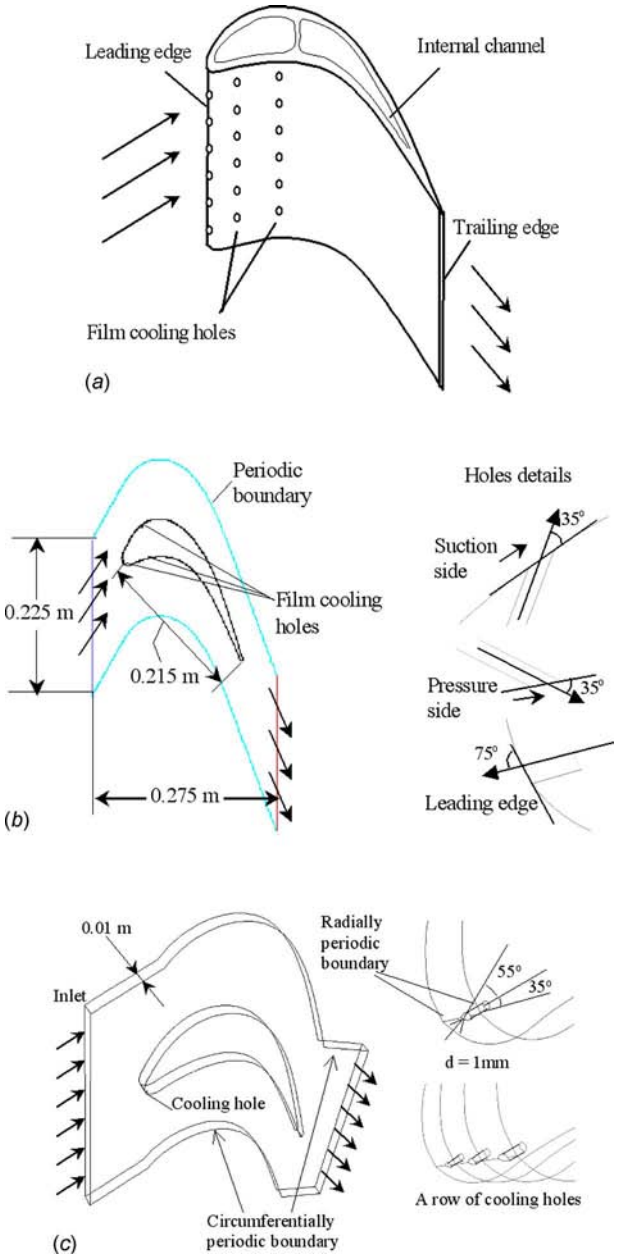

Fig. 1 Schematic of film cooling and computational domain: (*a*) film-cooling concept, (*b*) 2D cases, and (*c*) 3D cases

2 Numerical Model

2.1 Airfoil and Cooling Hole Configurations. While the configuration of the internal channel and jet holes in real gas turbine airfoil can be complicated, a simplified schematic of turbine blade with film-cooling holes is shown in Fig. 1(*a*). In general, the coolant air enters the cooling channel from the blade root and then is injected through the holes at locations of leading edge, side surfaces, and trailing edge. The complete cooling process is a combination of external film cooling and internal convective cooling.

Figure 1(*b*) shows the periodic computational domain for the 2D cases and the injection holes (slots). The blade has a chord length of 0.215 m, and the distance between the two blades is 0.225 m. There are a total of 30 blades with a hub diameter of 2.15 m. The injection angle for both pressure and suction sides is 35 deg, while the injection angle at the leading edge is 75 deg. The size of all the holes is about 1 mm. The jet hole is located at

30 mm downstream from the leading edge on the suction side and 20 mm on the pressure side. For the 3D case shown in Fig. 1(*c*), the flow is approximated as periodic in the radial direction so that only one of the holes in a row is considered. The hole with a diameter of 1 mm lies in the plane of the main inlet velocity vector and the leading edge with an angle of 55 deg to the main flow. The center-to-center distance between the two adjacent holes is 10 mm.

2.2 Numerical Method. To simulate film cooling with mist, it is feasible to consider the droplets as a discrete phase since the volume fraction of the liquid is usually small (<1%). The droplets are tracked in a Lagrangian frame of reference, and the mass, momentum, and heat transfer are computed between the discrete phase and the continuous flow. The effect of droplets on the continuous phase is incorporated as a source term to the governing equations. This method has been used in many studies such as dispersion of postdryout dispersed flow [29], evaporating droplets in a swirling jet [30], and evaporating spray in turbulent gas flow [31]. The Lagrangian method has also been used in the studies of mist film cooling with a flat surface by the authors [18–21].

To apply the discrete phase model to mist film cooling, the time-averaged steady-state Navier–Stokes equations, as well as equations for mass, energy and species transport, are solved. The Reynolds number (Re) of the main flow (based on the duct height and the inlet condition) is over 90,000. Therefore, a turbulence model has to be considered. In this study, the standard $k-\varepsilon$ model is employed. Since the standard k-ε model is mainly valid for high Reynolds number fully turbulent flow, an enhanced wall function is used for the region close to the wall. Basically, the whole domain is separated into a viscosity-affected region and a fully turbulent region by defining a turbulent Reynolds number. The standard k-ε model is used in the fully turbulent region, and the one-equation model of Wolfstein [32] is used in the viscosity-affected region. The turbulent viscosities calculated from these two regions are blended to smooth the transition. The constants in turbulence equations are consistent with Ref. [33]. More details on the governing equations, as well as the turbulence model, were documented in Refs. [18,19]. An extended discussion on the turbulence model is given later in this paper.

Stochastic Particle Tracking. The standard k-ε turbulence model is based on the time-averaged equations. Using this flow velocity to trace the droplet will result in an averaged trajectory. In the real flow, the instantaneous velocity fluctuation would make the droplet dance around this average track. However, the instantaneous velocity is not calculated in the current approach as the time-averaged Navier–Stokes equations are solved. One way to simulate the effect of instantaneous turbulence on droplet dispersion is to use the stochastic tracking scheme [34]. Basically, the droplet trajectories are calculated by using the instantaneous flow velocity ($\bar{u}+u'$) rather than the average velocity ($\bar{u}$). The velocity fluctuation is then given as

$$u' = \zeta(\overline{u'^2})^{0.5} = \zeta(2k/3)^{0.5} \tag{1}$$

where ζ is the normally distributed random number. This velocity will apply during a characteristic lifetime of the eddy (t_e), given from the turbulence kinetic energy and dissipation rate. After this time period, the instantaneous velocity will be updated with a new ζ value until a full trajectory is obtained. When the stochastic tracking is applied, the basic interaction between the droplets and the continuous phase remains the same, accounted for by the source terms in the conservation equations. The source terms are not directly but rather indirectly affected by the stochastic method. For example, the drag force between the droplets and the airflow depends on the slip velocity calculated by the averaged Navier–Stokes equations if without the stochastic tracking. With the stochastic tracking, a random velocity fluctuation is imposed at an instant of time, and the drag force and additional convective heat transfer will be calculated based on this instantaneous slip velocity. The source terms associated with this instantaneous drag force and convective heat transfer enter the momentum and energy equations without any additional formulation. For a steady-state calculation, the "instant of time" means "each iteration step." Therefore, the averaged momentum equation will not be affected by the stochastic tracking scheme, rather the trajectory of the droplet will reflect the effect of the imposed instantaneous perturbation.

2.3 Boundary Condition Setup

Airflow. Two sets of operating conditions are considered. The first set is for a typical laboratory condition featured with low temperature, velocity, and pressure. The main flow is assumed to be dry air (zero humidity). The uniform velocity (10 m/s) and the temperature (400 K) are assigned to the mainstream inlet. Coolant flow is assigned as saturated air (100% relative humidity). The jet inlet velocity is 10 m/s, and the temperature is 300 K. The blowing ratio, which is defined as $M=(\rho v)_{\text{jet}}/(\rho v)_{\text{main}}$, is 1.33 in this case. The inlet condition of the turbulence is specified by the turbulence intensity and the hydraulic diameter to calculate the turbulence length scale. The turbulent intensity is 3% at the mainstream inlet and 1% at the coolant flow inlet. The flow exit (outlet) of the main computational domain is assumed to be at a constant pressure of 1 atm. All the walls in the computational domain are adiabatic and have a no-slip velocity boundary condition. Note that the above assigned temperature and velocity conditions are referenced in several previous studies of air-film cooling, for example, in Refs. [7,8].

The second set of parameters is associated with practical gas turbine operating conditions, featured with high temperature, velocity, and pressure. The main flow in this case has a temperature of 1561 K and a velocity of 128 m/s, while the jet flow has a temperature of 644 K and a velocity of 106 m/s. These parameters give a blowing ratio of 2 and a Reynolds number of 1.61×10^6, based on a chord length of 0.215 m. The operational pressure is 15 atm. These settings are not selected to match any specific commercial model but they are a realistic representation of typical gas turbine operating conditions.

Droplet injection. The droplet is uniformly given as either 5 μm or 10 μm in diameter. The mass ratio of mist over the cooling airflow is 2% for lower operating conditions, which is about 7.0×10^{-4} kg/s for the 2D slot with a width of 1 mm and a unit depth of 1 m. For the high operating condition, the mist concentration is 10% because more heat needs to be absorbed in this case due to the large temperature difference. Mist is injected at ten locations uniformly distributed along the 2D jet inlet. The 3D case is run at low operating conditions, and the number of injection locations is 41. The trajectory number for stochastic tracking is chosen to be 25. The trajectory number is the number of droplet paths tracked from each injection location by using different turbulence fluctuating velocity. The boundary condition of droplets at walls is assigned as "reflect," which means the droplets elastically rebound off once reaching the wall. At the outlet, the droplets just simply flee/escape from the computational domain.

2.4 Meshing and Simulation Procedures. To conduct numerical simulation, the computational domain is meshed with a proper setup on the boundary conditions. As shown in Fig. 2, unstructured and nonuniform grids are constructed in this study, and the basic element is triangles for the 2D case. The grids near the blade surface as well as the cooling holes are denser than the other areas. Furthermore, the near-wall grid is adapted twice (four times finer) to capture the wall effect on calculated results for both single-phase and mist film-cooling cases. The total number of the cells for the 2D domain is 62,800, while the 3D domain has a total mesh of 337,000 (not shown in the figure).

The commercial software package FLUENT (version 6.2.16) from Fluent, Inc. (Lebanon, NH) is adopted. The simulation uses the segregated solver, which employs an implicit pressure-

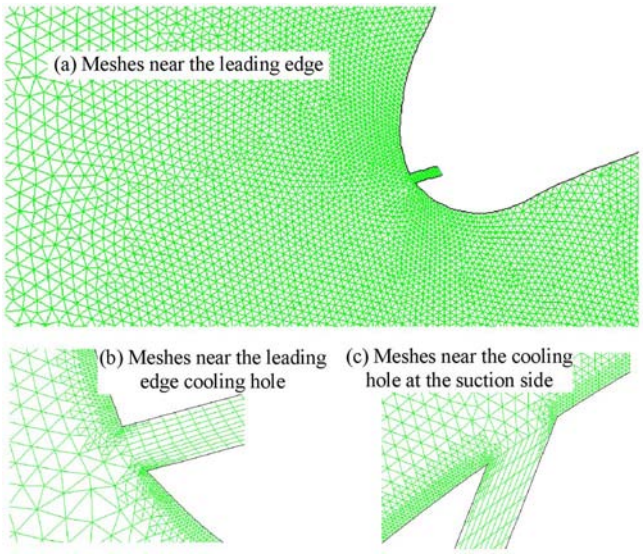

Fig. 2 Meshes of partial domain and details near injection holes (with grid adaptation)

correction scheme [34]. The SIMPLE algorithm is used to couple the pressure and velocity. Second order upwind scheme is selected for spatial discretization of the convective terms and species. After obtaining an approximate flow field of the airflow, the droplet trajectories are calculated by using Lagrangian trajectory calculations. At the same time, the drag, heat, and mass transfer between the droplets and the airflow are calculated. Iteration proceeds alternatively between the continuous and discrete phases. Ten iterations in the continuous phase are conducted between the two iterations in the discrete phase. Converged results are obtained after the residuals are less than the specified values. A converged result renders a mass residual of 10^{-4}, an energy residual of 10^{-6}, and momentum and turbulence kinetic energy residuals of 10^{-5}. These residuals are the summation of the imbalance for each cell, scaled by a representative of the flow rate. Typically, 2000–4000 iterations are needed to obtain a converged result, which takes about 4–5 h physical time on a 2.8 GHz Pentium 4 personal computer for a 2D case and five to ten times longer for the 3D cases.

2.5 Discussion of the Modeling. The flow near the leading edge of a turbine blade actually impinges on the surface and creates a strong streamwise pressure gradient near the stagnation region. The presence of the high-pressure gradient field usually suppresses any turbulence production and could even relaminarize the flow in the boundary layer. Therefore, appropriate handling of laminar-turbulent transition downstream of the leading edge is also important despite the laminar flow in the gas turbine environment being more of "disturbed" nature attributed to high freestream turbulence and unsteady disturbance. These phenomena further complicate prediction and modeling of the flow field. In this study, no attempt has been made to tackle the complexity of the above issues.

Note that the constants adopted in the turbulence model may not be the most appropriate values for mist film-cooling flow, especially on the flow near the leading edge. Usually these constants need to be "tuned" for different flow physics such as impingement flow, accelerated flow, decelerated flow, separated flow, low-Reynolds number flow, curved flow, and rotating flow. A better knowledge is needed on what values these turbulence constants should be for a mist film-cooling flow. Furthermore, the main purpose of this study is to investigate the effect of adding mist to the air flow on film-cooling effectiveness rather than to study how turbulence models should be modified to predict mist film-cooling flow more accurately under the influence of curvature. Therefore, using the same values of these turbulence constants for both the air-only flow and the air/mist flow provides a controlled condition for a meaningful comparison of the results. Again, the detailed turbulence model and associated constants were documented in Refs. [18,19].

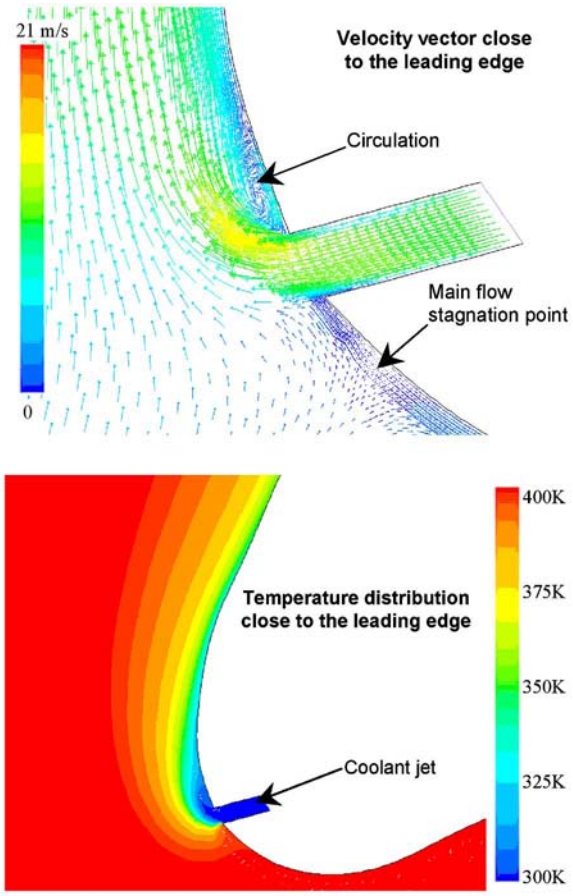

Fig. 3 Flow pattern and temperature distribution

3 Results and Discussion

3.1 Film Cooling Near Turbine Blade Leading Edge (2D Slot)

3.1.1 Air-Only Film Cooling at Low Operating Conditions. Figure 3 shows the velocity vector and temperature distribution close to the leading edge. The inlet velocity for both jet and main flow is 10 m/s and the inlet temperature is 400 K for the main flow and 300 K for the jet flow, respectively. The coolant injection is located slightly above the stagnation point of the main flow. Near the leading edge, the main gas flow essentially impinges to the surface. The local hot gas flow has only a small velocity component parallel to the cooling surface and the injection momentum is retarded by the opposing momentum of the impinging main flow. Both phenomena are different from film-cooling mechanism over a flat surface. Therefore, the local blowing ratio (or effective blowing ratio) at the leading edge will have a different value although the nominal blowing ratio is 1.33 in this case.

As discussed earlier, the blowing angle at the leading edge is 75 deg rather than a smaller value (30–35 deg) optimized for a flat surface due to the specific position of the leading edge versus the main flow. There is a relatively strong circulation due to the flow separation close to the jet exit, which will generally lower the cooling effectiveness. The temperature profile and the adiabatic cooling effectiveness along the cooling surface are given in Fig. 4. Note that $s/2b$ in the figure is the dimensionless distance on the

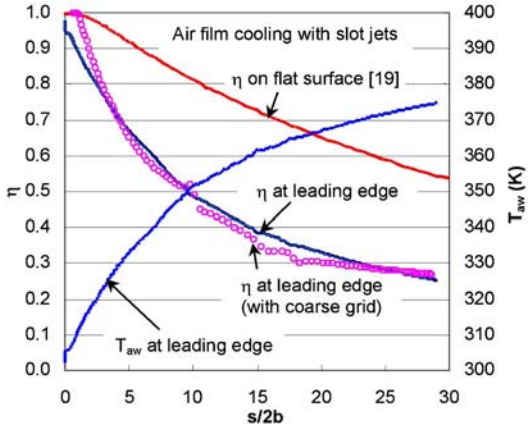

Fig. 4 Comparison of air-only leading-edge adiabatic cooling effectiveness with that on a flat surface with the same nominal blowing ratio of 1.33

specified surface and b is the slot width. The result of film cooling with a flat surface is also given for comparison. The adiabatic cooling effectiveness (η) is defined as

$$\eta = (T_g - T_{aw})/(T_g - T_c) \tag{2}$$

where T_g is the mainstream gas temperature, T_c is the temperature of the coolant (jet), and T_{aw} is the adiabatic wall temperature. The value of η ranges from 0 (no cooling) to 1 (perfect cooling), which usually serves as an indicator to examine the performance of film cooling.

Figure 4 shows that on both leading edge and flat surface, the adiabatic cooling effectiveness decreases with the distance away from the injection hole; however, the adiabatic cooling effectiveness is lower near the leading edge than on a flat surface. Besides the difference due to geometry and flow fields, the lower velocity parallel to the wall makes the penetration in the normal direction relatively stronger than that in the tangential direction, especially when the injection angle is big. The effect of surface curvature is another reason for the low cooling effectiveness. Furthermore, the strong circulation close to jet injection results in a higher mixing and lower adiabatic cooling effectiveness immediately downstream of the hole ($s/2b<1$). On the other hand, different lines for the adiabatic cooling effectiveness in Fig. 4 summarize the grid sensitivity study. When the grid becomes finer (for example, adapted close to the wall), the results collapse to the same curve (two lines for η at the leading edge), which indicates the independence of simulation results on grid systems.

3.1.2 Mist Film Cooling at Low Operating Conditions. As seen in previous studies [18–21], injecting mist into the coolant airflow can improve the performance of air-film cooling. The tiny water droplets will stay close to the coolant jet and will absorb heat via evaporation to keep the coolant temperature low. Figure 5 shows the droplets' trajectories for the case of leading-edge cooling. The droplets have a diameter of 5 μm in this figure. The droplets roughly follow the coolant streamlines, adhere to the wall area, and quickly vaporize. However, some of the droplets do penetrate through the coolant zone and move into the main flow. This means the strayed droplets lower the temperature of the main flow rather than the coolant flow, which makes the cooling enhancement lower than the case on a flat surface.

Figure 6 gives the cooling effectiveness with 2% mist (by mass) and 5 μm droplet. Compared with air-only film cooling, η increases from 0.28 to 0.38 at $s/2b=25$. Also shown in Fig. 6 is the ratio of adiabatic cooling effectiveness with and without mist, η_{mist}/η_0. By defining the enhancement as $[(\eta_{mist}/\eta_0)-1]$, the maximum enhancement can reach 44% at a location downstream from $s/2b=14$ to 22. The average cooling enhancement is 25

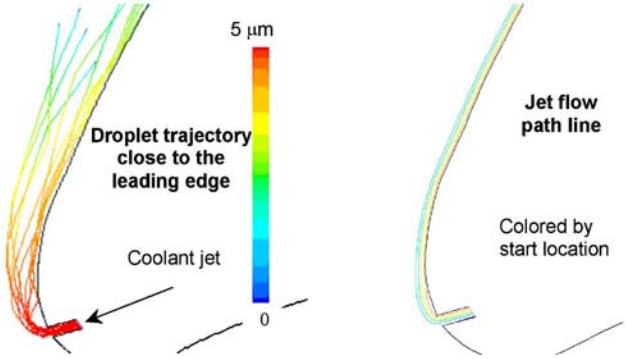

Fig. 5 Droplet trajectories versus jet flow pathlines for leading-edge mist cooling

–30%. Comparing the current results with the findings over flat surfaces in Ref. [18], the enhancement ratio of mist cooling at the leading edge is higher at $s/2b=5-20$, which is partially due to the lower air-film cooling at the leading edge (see Fig. 4). The cooling enhancement ratio becomes smaller farther downstream on the concave wall, whereas the enhancement on the flat surface maintains a high value of 44% downstream of $s/2b=25$. This is caused by the concave surface effect to be discussed in detail later.

Note that mist film cooling itself can be improved by using different droplet sizes and concentrations. Figure 7 shows the cooling effectiveness and enhancement ratio when different droplet sizes and mist concentration are employed. As expected, larger droplets make the enhancement lower due to their stronger penetration into the main flow and smaller surface to the volume ratio, while higher concentration enhances air-film cooling more significantly due to more available latent heat. For example, the enhancement at $s/2b=25$ increases from 10% to 20% when the mist concentration increases from 2% to 5%. On the other hand, when the droplet size increases from 5 μm to 10 μm, the enhancement becomes small (5% in average). Certainly, in a real application, the droplets will have a distributed size, and the cooling performance will be a combination of the results with different sizes of uniform droplets.

3.1.3 Effect of Incident Angle on Cooling of the Leading Edge. In the case of startup or partial load, the incident angle of main flow will change. The effect of the incident angle on leading-edge film-cooling performance is examined. Figure 8 shows the flow pattern as well as the temperature distribution with a new angle,

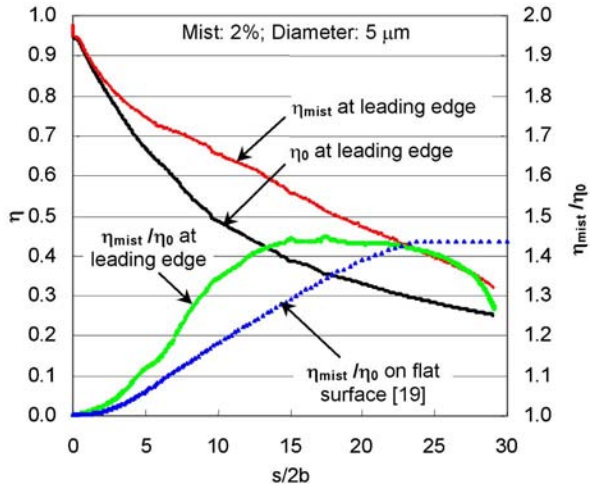

Fig. 6 Enhancement of adiabatic cooling effectiveness by injecting mist with the nominal blowing ratio of 1.33

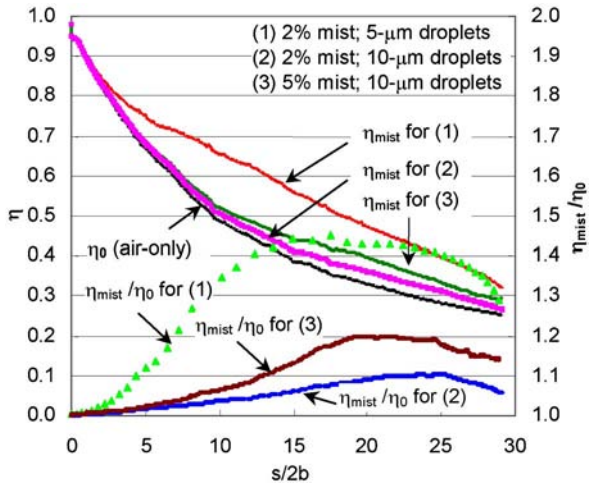

Fig. 7 Effects of the droplet size and mist concentration on film-cooling enhancement at the leading edge

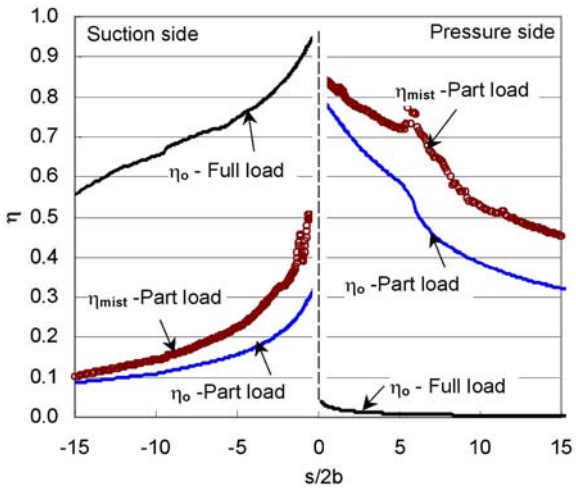

Fig. 9 Effect of the main flow incident angle on adiabatic film-cooling effectiveness near the leading edge

which is 15 deg smaller than that in Secs. 3.1.1 and 3.1.2. The coolant flow is significantly affected by the incident angle. Since the stagnation point of the main flow moves to a location above the injection hole, most of the coolant flow turns down to the pressure side rather than to the suction side as in the previous cases. This movement of stagnation point makes the film protection on the pressure side better but the suction side undesirable. The coolant jet is quickly bent and pushed toward the wall by the incoming main flow; hence the cooling film does not travel too far downstream and results in a quickly degraded cooling effectiveness from 0.8 to 0.3 within a distance of 30 slot widths on the pressure side, as shown in Fig. 9. Although some cooling also prevails on the suction side, the cooling effectiveness is lower than 0.3. When mist is injected during the partial load condition, cooling enhancement is observed in both sides with an enhancement of 30–50%.

3.1.4 Mist Film Cooling at High Operating Conditions. All the cases in Secs. 3.1.1–3.1.3 are conducted at low operating conditions to be comparable with other studies in the public literature. These cases can be used to show the fundamental phenomena of film cooling with and without mist injection. However, gas turbines are usually operated at very high pressure, temperature, and velocity. The performance of air-film cooling and mist film cooling could be different. To simulate a typical gas turbine operating condition, the main flow has a temperature of 1561 K and a velocity of 128 m/s, and the jet flow has a temperature of 644 K and a velocity of 106 m/s. These parameters give a blowing ratio of 2 and a Reynolds number of 1.61×10^6 (based on the length scale of 0.215 m). The operating pressure is 15 atm. Figure 10 shows that the enhancement is relatively low, even with a high mist concentration (10%). This is because the large temperature difference ($T_g - T_j = 1561\ \text{K} - 644\ \text{K} = 917\ \text{K}$) in high operating conditions needs larger wall temperature drop to reach the same unit percentage of cooling effectiveness, whereas this temperature difference is 100 K (400 K–300 K) under the low temperature and pressure conditions. For example, a 30 K wall temperature reduction will contribute to 30 percentage points of η value (based on $T_g - T_j = 400\ \text{K} - 300\ \text{K}$) under low pressure and temperature conditions, whereas the same 30 K wall temperature reduction will only harness 3.3 percentage of η enhancement under elevated GT operating conditions. The highest cooling enhancement ratio with a mist of 10% (weight) is about 20%. The relatively low cooling enhancement under GT operating conditions was also reported in Ref. [20], which revealed that the performance can be improved by employing different injection angles as well as blowing ratios. Note that cooling enhancement should be evaluated differently under different operating conditions when the absolute surface temperature reduction is important. For example, a 20% cooling effectiveness enhancement can result in a decent 180 K reduction in wall temperature under the elevated GT operating conditions.

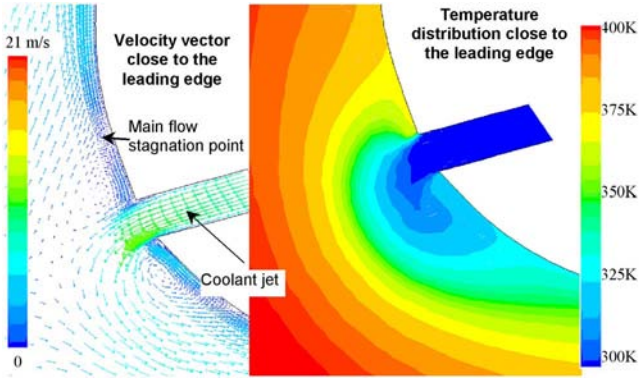

Fig. 8 Effect of the main flow incident angle on flow and temperature distribution close to the leading edge

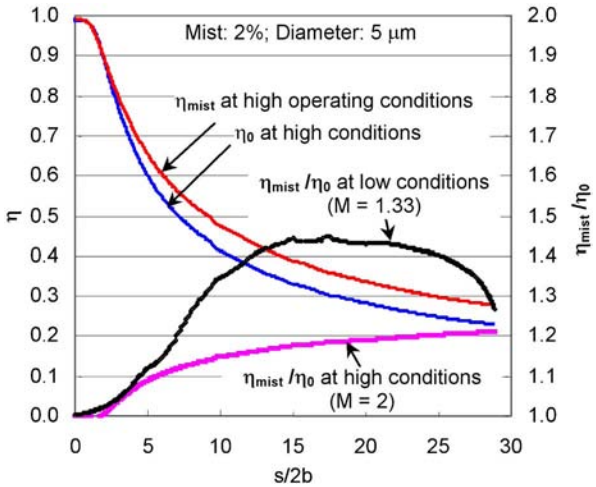

Fig. 10 Effect of elevated operating conditions on mist film-cooling performance of the turbine blade leading edge

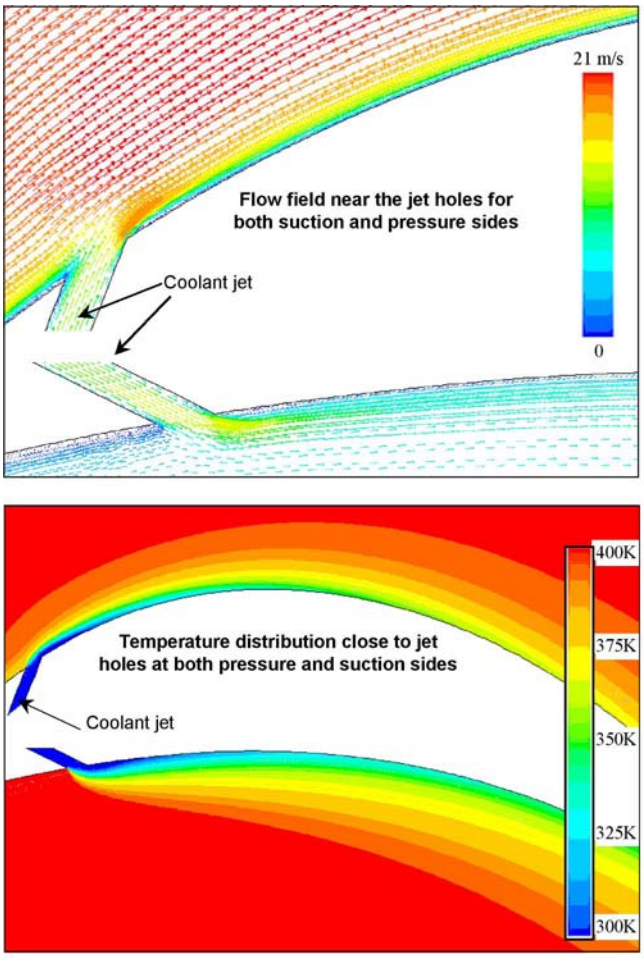

Fig. 11 Flow pattern and temperature distribution of film cooling under the curvature effect on the pressure and suction sides

3.2 Mist Film Cooling With Curvature Effect on Pressure and Suction Sides (2D Slot)

3.2.1 Air-Only Film Cooling on Pressure and Suction Sides. Since the flow fields over the curved surfaces are expected to create a body force exerted on the water droplet by the cross-stream pressure gradient, it is essential to examine the behavior of mist film cooling with the downstream curvature on both pressure and suction sides. To realize the effect of curvature on mist film cooling, the air-film cooling is simulated first as a base line for comparison. The injection angles for both sides are the same, 35 deg, and the injection momentums are also the same. Figure 11 shows that the suction side has a higher flow velocity (or cross-flow) than the pressure side, which results in a smaller effective blowing ratio in the suction side. A small recirculation (separation) region occurs in both sides immediately downstream of the injection hole. To optimize the mist film-cooling performance, the injection velocity and the angle need to be designed differently for these two sides.

Figure 12 shows the adiabatic cooling effectiveness of air-film cooling for both suction and pressure sides. The η values for both curved surfaces are lower than that over a flat surface but higher than the case at the leading edge. The poor performance at the leading edge is caused by the impingement of main flow against the injection coolant and less cross-flow near the leading edge to sweep the coolant jet downstream.

At the 2D settings in this study, the pressure (concave) side shows a higher cooling effectiveness than the suction (convex)

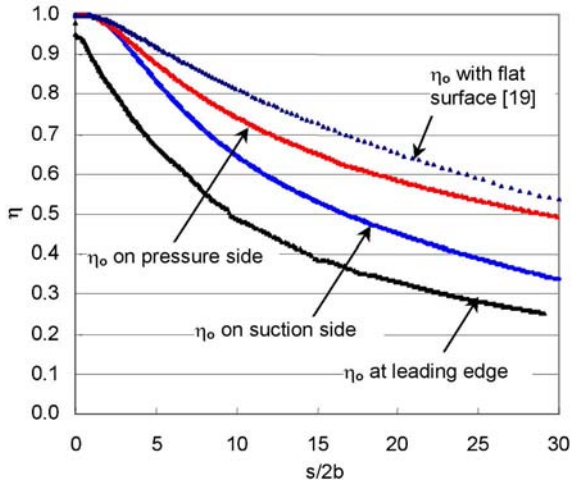

Fig. 12 Comparison of air-only film-cooling effectiveness on flat and curved surfaces with a nominal blowing ratio of 1.33

side. This is consistent with the results of Nicolas and Le Meur [11] and the high blowing ratio results of Schwarz et al. [14] but contrary to the results of Mayle et al. [12] and Berhe and Patankar [16]. When comparison is made between the flat surface and the curved surface, Mayle et al. [12] and Berhe and Patankar [16] reported that η values are higher on the convex surfaces than on the flat surfaces. Schwarz et al. [14] also observed that η values are higher on the convex surfaces than on the flat surfaces for low blowing ratio cases. The inconsistent results from previous studies [12–16] imply that the effect of curvature on film cooling is closely related to the geometrical settings (such as the hole configuration and injection angles) and flow parameters (such as the blowing ratio and main flow characteristics). The comparison will not be conclusive unless all the setting conditions are consistent. Irrespective of the inconsistency in the results of air-only film cooling on curved surfaces, the focus in this study is on investigating the potential cooling enhancement by injecting mist into the coolant. By using the current approach, the thermodynamic, heat transfer, and major flow characteristics of the mist flow are expected to be adequately simulated.

3.2.2 Mist Enhancement on Film Cooling With Curved Surface. Figure 13 shows the cooling effectiveness of mist film cooling with curved surfaces. The mist concentration is 2%, and

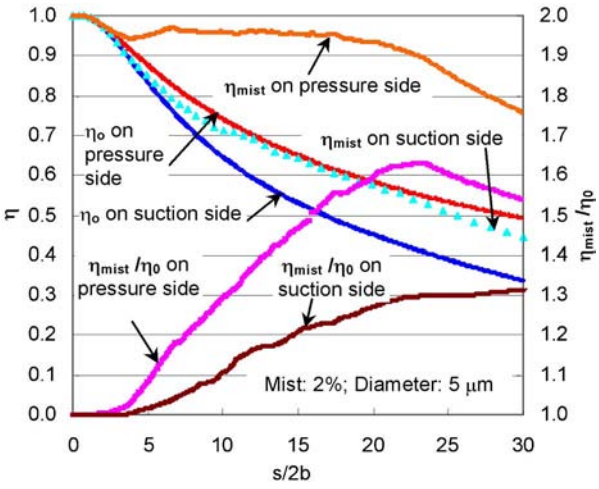

Fig. 13 Enhancement of film cooling with mist injection on concave and convex surfaces

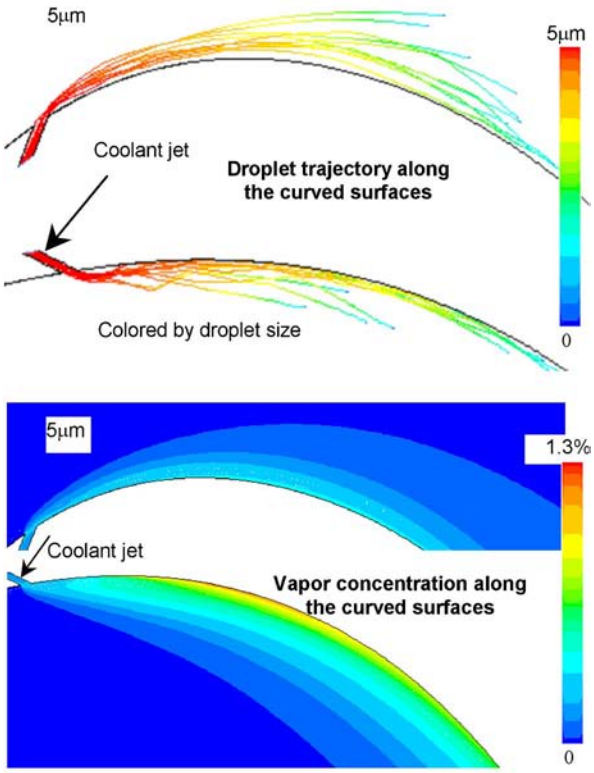

Fig. 14 2D droplet trajectories and vapor concentration in mist film cooling with concave and convex surfaces

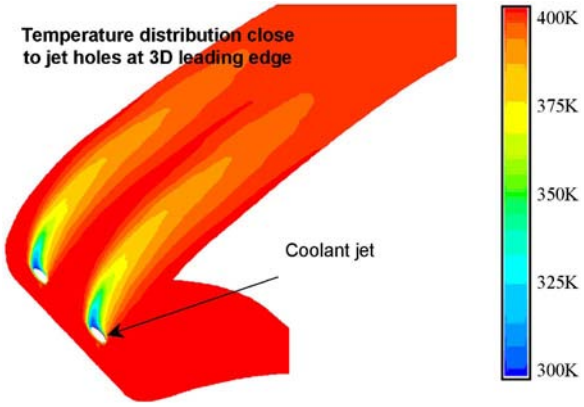

Fig. 15 Temperature distribution of air-film cooling on 3D leading-edge surface

the droplet size is 5 μm. The enhancement ratio on the pressure side is observed higher than on the suction side with the maximum enhancement of 61% on the pressure side and 31% on the suction side. It is believed that the difference in cooling enhancement is solely a consequence of the droplet thermal-fluid dynamics under the influence of curvature because the comparison reference is the air-only film cooling of each individual case.

To help investigate the droplet dynamics, the droplet trajectories are traced and given in Fig. 14. It is observed from this figure that the droplets in the convex side migrate away from the surface, and the droplets on the concave side tend to adhere closely to the wall. Other than the injection inertia, these phenomena can be simply explained as the centrifugal force driving droplets away from the convex wall and the centrifugal force pushing droplets toward the concave wall. Hence mist-cooling enhancement is more pronounced on the pressure surface than on the suction surface. This seemingly easy explanation is actually contrary to the boundary layer induced flow stability on the convex surface and instability on the concave surface.

As early as 1917, Rayleigh [35] deduced the instability criterion for axisymmetrical circular flow, which was later employed to explain "Streamwise convex curvature has a stabilizing effect on the boundary layer flow and concave curvature destabilizes the boundary layer flow." This statement would not be true if the flow was inviscid and no boundary layer would be present. The inviscid flow theory gives a flow field with the velocity increasing with the radius away from the concave surface and decreasing with the radius away from the convex surface. The boundary layer actually disturbs this potential flow fields and presents a velocity deficit on both surfaces. This means that if the droplets were in the boundary layers, the droplets would migrate toward the convex wall and move away from the concave surface.

The contrary phenomenon shown in Fig. 14 can be explained as that the initial injection momentum of the coolant flow penetrates through the boundary layer and brings the droplets into the inviscid flow field. Therefore, the droplets are not subject to the instability of the boundary layer flow over the curved surfaces, rather, before they reach equilibrium, the droplets are subjected to the local cross-stream pressure gradient that generates centrifugal body force which pushes the droplets toward the concave surface and away from the convex surface. When the boundary layer grows thicker, some of the droplets were entrained into the boundary layer and move toward the convex surface further downstream on the convex surface, as shown in Fig. 14. In a 3D flow, the droplet dynamics can be further complicated by the secondary flows induced by the coolant jet. If the blowing ratio is different, the global phenomena could be changed and the film-cooling effectiveness could even be reversed, but the fundamental mechanisms should be invariant. The droplet dynamics in Fig. 14 does not involve the complexity of the secondary flow because only the 2D flow field is simulated.

The concentration of vapor due to droplet evaporation is also presented in Fig. 14. The concentration on the pressure side is higher than that on the suction side, which is consistent with the high cooling enhancement on the pressure side. The primary reasons are the droplet dynamics discussed earlier and the low average velocity of the freestream close to the pressure surface.

3.3 Film Cooling of 3D Leading Edge. The results shown in Secs. 3.1 and 3.2 are for the cases of two-dimensional slot jet. Although 2D cases can be used to investigate the basic mechanism of mist film cooling under the influence of curvature, the real applications are usually 3D with complicated injection geometries and flow parameters, which are subject to effects of endwall and of rotation. To simplify the real applications, only a row of holes at the leading edge is considered. Furthermore, the effect of endwalls is ignored, so the row of holes can be simplified as a single hole that periodically appears in the radial direction from the hub to the tip. The distance between the periodic boundaries is 10 mm in the radial direction. The hole has a diameter of 1 mm. The injection angle is 55 deg to the main flow direction or 35 deg to the surface tangent (see Fig. 1(c)). Figure 15 shows the temperature distribution on the blade surface. The surface temperature is low at the region immediate downstream of the cooling jet, and the cooling effect gradually becomes negligible. For the case shown in the figure, the jet primarily flows to the suction surface. Adjusting the incident angle or the cooling jet location can significantly change the areas covered by the cooling film. Multiple rows of cooling hole arrangement can mitigate the problems of changing loads or incident angles.

Figure 16 shows the adiabatic film-cooling effectiveness along the centerline of the injection hole in the 3D domain. Compared with the 2D case (see Fig. 4), the coolant coverage is weaker for the 3D case due to the strong mixing and secondary flow folding between the jet and the main flows. A peak value of η (0.9) is

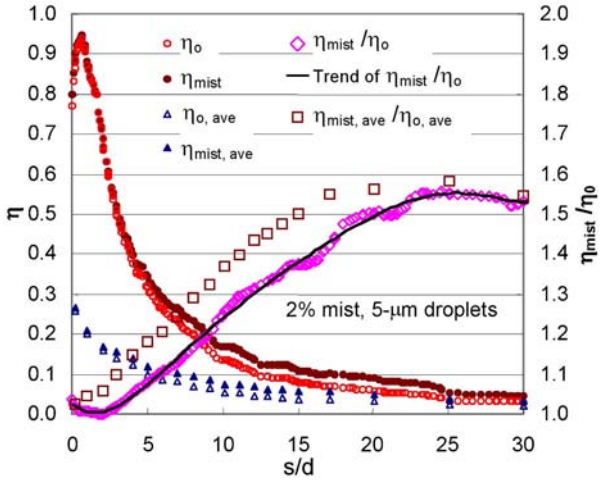

Fig. 16 Adiabatic cooling effectiveness of 3D leading-edge film cooling and its enhancement with mist injection

observed around $s/d=1.5$ with relatively low cooling effectiveness ($\eta<0.9$) in the proximity of the injection hole ($s/d<1.5$). This is different from the monotonically decreasing η value shown in the 2D cases in Fig. 4. Figure 16 further indicates a sharp drop of η to a very low level within a short distance downstream. For instance, η drops to 20% at $s/d=8$ and further down to 10% at $s/b=12$. With a 2% mist injection, the cooling effectiveness increases, although it is still low. The cooling enhancement is noticeable with the highest enhancement of 55% at $s/d=25$. Note that the jiggles on the curves are mostly caused by the numerical iteration method used with the stochastic droplet tracking [19]. A solid line fairing through the jiggled points represents more realistic cooling enhancement values. The span-averaged value is also given in the figure. Although the span-averaged value is low, the mist enhancement is even more significant with a maximum level of 56%. At the same location (s/d), the average enhancement ratio is higher than that along the centerline.

3.4 Validation of Simulation Results. It is important to verify any numerical solution with experimental data. However, there are not yet any experimental data available in the public literature for mist film cooling, either with simple or complicated geometries. The general methodology, modeling, and the numerical algorithm employed in this study are based on the validations established by the authors in previous studies [18,19]. Before the simulated results are validated with the experimental data, the results of this study can be fairly treated as qualitative descriptions of mist film-cooling performance under the effects of various studied parameters.

4 Conclusions

This paper studies the mist film-cooling effectiveness near the leading edge of a turbine blade and on the blade surfaces subject to curvature effect. In general, injection of mist into the coolant flow can increase the adiabatic film-cooling effectiveness (η) at the leading edge and on the curved sidewalls. Smaller droplets achieve better cooling enhancement. The major findings are as follows.

- In the 2D settings of this study, air-only adiabatic film-cooling effectiveness (η) degrades under the effect of curvature in the following descending order: flat surface > concave (pressure) surface > convex (suction) surface > leading edge. These results are consistent with some published studies while inconsistent with others due to the sensitivity of the results to the different parameters, such as blowing ratio, injection angle, and strength of the curvature.
- The leading-edge film cooling can be significantly affected by changing the incident angle due to the startup or part load operations. The film-cooling coverage could switch from the suction side to the pressure side and leaves the surface of the other part unprotected by the cooling film.
- 2D mist film cooling achieves higher enhancement on the pressure side than on the suction side. The maximum mist-cooling enhancement is approximately 60% on the pressure side and 30% on the suction side.
- The water droplet traces show that the centrifugal force pushes the droplets toward the concave wall and drives the droplets away from the convex wall, hence mist-cooling enhancement is more pronounced on the pressure surface than on the suction surface. This observation is contrary to the boundary layer induced flow stability on the convex surface and instability on the concave surface. A hypothetical explanation is given as that most of the droplets are outside the boundary layer after being injected into the main stream and before they reach equilibrium with the local pressure field, the local cross-stream pressure gradient generates centrifugal body force over both the concave and convex surfaces.
- 3D simulation of the leading-edge film cooling shows along the centerline a relatively low η near the hole and a peak η at $s/d=1.5$. Adding 2% mist (weight) can achieve an average of 30% cooling enhancement with the highest local enhancement reaching 55% at $s/d=25$. Although the span-average cooling effectiveness is low, the mist enhancement is higher than that along the centerline.
- Under real gas turbine operating conditions at high pressure, temperature, and velocity, the enhancement of mist cooling achieves 20%, which seems lower than under low *T-P-V* condition. However, a decent wall cooling of 180 K can be achieved by 20% enhancement in contrast to 50 K wall temperature reduction with 50% cooling enhancement under low *T-P-V* conditions.

Acknowledgment

This study is partially supported by the Louisiana Governor's Energy Initiative via the Clean Power and Energy Research Consortium (CPERC) and administrated by the Louisiana Board of Regents.

Nomenclature

b = slot width (m)
d = diameter (m)
k = turbulence kinetic energy (m^2/s^2)
M = blowing ratio $(\rho u)_c/(\rho u)_g$
Re = Reynolds number, ud/ν
s = distance along a surface
T = temperature (K, °F)
u = streamwise velocity component (m/s)
v = spanwise velocity component (m/s)
x,y,z = coordinates

Greek Symbols

ε = turbulence dissipation rate (m^2/s^3)
η = adiabatic film-cooling effectiveness $(T_g-T_{aw})/(T_g-T_c)$
ν = kinematic viscosity (m^2/s)
ρ = density (kg/m^3)

Subscript

aw = adiabatic wall
c = coolant or jet flow
g = hot gas/air
0 = air-only film cooling

References

[1] Eriksen, V. L., and Goldstein, R. J., 1974, "Heat Transfer and Film Cooling Following Injection Through Inclined Tubes," ASME J. Heat Transfer, **96**, pp. 239–245.

[2] Goldstein, R. J., Eckert, E. R. G., and Burggraf, F., 1974, "Effects of Hole Geometry and Density on Three-Dimensional Film Cooling," Int. J. Heat Mass Transfer, **17**, pp. 595–607.

[3] Jia, R., Sunden, B., Miron, P., and Leger, B., 2005, "A Numerical and Experimental Study of the Slot Film Cooling Jet With Various Angles," ASME J. Turbomach., **127**, pp. 635–645.

[4] Kwak, J. S., and Han, J. C., 2003, "Heat Transfer Coefficients and Film-Cooling Effectiveness on a Gas Turbine Blade Tip," ASME J. Heat Transfer, **125**, pp. 494–502.

[5] Kwak, J. S., and Han, J. C., 2003, "Heat Transfer Coefficients and Film Cooling Effectiveness on the Squealer Tip of a Gas Turbine Blade," ASME J. Turbomach., **125**, pp. 648–657.

[6] Wang, T., Chintalapati, S., Bunker, R. S., and Lee, C. P., 2000, "Jet Mixing in a Slot," Exp. Therm. Fluid Sci., **22**, pp. 1–17.

[7] Bell, C. M., Hamakawa1, H., and Ligrani, P. M., 2000, "Film Cooling From Shaped Holes," ASME J. Heat Transfer **122**, pp. 224–232.

[8] Brittingham, R. A., and Leylek, J. H., 2000, "A Detailed Analysis of Film Cooling Physics: Part IV: Compound-Angle Injection With Shaped Holes," ASME J. Turbomach., **122**, pp. 133–145.

[9] Colban, W., Thole, K. A., and Haendler, M., 2006, "A Comparison of Cylindrical and Fan-Shaped Film Cooling on a Vane Endwall at Low and High Free Stream Turbulence Levels," ASME Paper No. 2006-90021.

[10] Suryanarayanan, A., Mhetras, S. P., Schobeiri, M. T., and Han, J. C., 2006, "Film-Cooling Effectiveness on a Rotating Blade Platform," ASME Paper No. 2006-90034.

[11] Nicolas, J. and Le Meur, A., 1974, "Curvature Effects on Turbine Blade Cooling Film," ASME Paper No. 74-GT-156.

[12] Mayle, R. E., Kopper, F. C., Blair, M. F., and Bailey, D. A., 1977, "Effect of Streamline Curvature on Film Cooling," ASME J. Eng. Power, **99**, pp. 77–82.

[13] Ito, S., Goldstein, R. J., and Eckert, E. R. G., 1978, "Film Cooling of a Gas Turbine Blade," ASME J. Eng. Power, **100**, pp. 476–481.

[14] Schwarz, S. G., Goldstein, R. J., and Eckert, E. R. G., 1991, "Influence of Curvature on Film Cooling Performance," ASME J. Turbomach., **113**, pp. 472–478.

[15] Jiang, H. W., and Han, J.-C., 1996, "Effect of Film Hole Row Location on Film Effectiveness on a Gas Turbine Blade," ASME J. Heat Transfer, **118**, pp. 327–333.

[16] Berhe, M. K., and Patankar, S. V., 1999, "Curvature Effects on Discrete-hole Film Cooling," ASME J. Turbomach., **121**, pp. 781–791.

[17] Kim, K.-S., Kim, Y. J., and Kim, S.-M., 2006, "Enhancement of Film Cooling Performance at the Leading Edge of Turbine Blade," ASME Paper No. 2006-90321.

[18] Li, X., and Wang, T., 2006, "Simulation of Film Cooling Enhancement with Mist Injection," ASME J. Heat Transfer, **128**, pp. 509–519.

[19] Li, X., and Wang, T., 2007, "Effects of Various Modeling Schemes on Mist Film Cooling," ASME J. Heat Transfer, **129**, pp. 472–482.

[20] Wang, T. and Li, X., 2006, "Simulation of Mist Film Cooling at Gas Turbine Operating Conditions," Proceedings of the ASME Turbo Expo 2006, Barcelona, Spain, May 8–11.

[21] Li, X., and Wang, T., 2006, "Two-Phase Flow Simulation of Mist Film Cooling With Different Wall Heating Conditions," Proceedings of the 13th International Heat Transfer Conference, Sydney, Australia, August 13–18.

[22] Chaker, M., Meher-Homji, C. B., and Mee, M., 2004, "Inlet Fogging of Gas Turbine Engines—Part I: Fog Droplet Thermodynamics, Heat Transfer and Practical Considerations," ASME J. Eng. Gas Turbines Power, **126**, pp. 545–558.

[23] Petr, V., 2003, "Analysis of Wet Compression in GT's," Proceedings of the International Conference on Energy and the Environment, Shanghai, China, Dec. 11–13, Vol. 1, pp. 489–494.

[24] Nirmalan, N. V., Weaver, J. A., and Hylton, L. D., 1998, "An Experimental Study of Turbine Vane Heat Transfer With Water-Air Cooling," ASME J. Turbomach., **120**(1), pp. 50–62.

[25] Guo, T., Wang, T., and Gaddis, J. L., 2000, "Mist/Steam Cooling in a Heated Horizontal Tube, Part I: Experimental System, Part II: Results and Modeling," ASME J. Turbomach., **122**, pp. 360–374.

[26] Guo, T., Wang, T., and Gaddis, J. L., 2000, "Mist/Steam Cooling in a 180° Tube Bend," ASME J. Heat Transfer, **122**, pp. 749–756.

[27] Li, X., Gaddis, J. L., and Wang, T., 2003, "Mist/Steam Cooling by a Row of Impinging Jets," Int. J. Heat Mass Transfer, **46**, pp. 2279–2290.

[28] Li, X., Gaddis, J. L., and Wang, T., 2003, "Mist/Steam Heat Transfer With Jet Impingement Onto a Concave Surface," ASME J. Heat Transfer, **125**, pp. 438–446.

[29] Wang, M. J., and Mayinger, F., 1995, "Post-Dryout Dispersed Flow in Circular Bends," Int. J. Multiphase Flow, **21**, pp. 437–454.

[30] Aggarwal, S. K., and Park, T. W., 1999, "Dispersion of Evaporating Droplets in a Swirling Axisymmetric Jet," AIAA J., **37**, pp. 1578–1587.

[31] Chen, X.-Q., and Pereira, J. C. F., 1995, "Prediction of Evaporating Spray in Anisotropically Turbulent Gas Flow," Numer. Heat Transfer, Part A, **27**, pp. 143–162.

[32] Wolfshtein, M., 1969, "The Velocity and Temperature Distribution of One-Dimensional Flow With Turbulence Augmentation and Pressure Gradient," Int. J. Heat Mass Transfer, **12**, pp. 301–318.

[33] Launder, B. E., and Spalding, D. B., 1972, *Lectures in Mathematical Models of Turbulence*, Academic, London, England.

[34] Fluent Manual, Version 6.2.16, 2005, Fluent, Inc.

[35] Rayleigh, J. W. S., 1917, "On the Dynamics of Revolving Fluids," Proc. R. Soc. London, Ser. A, **93**, pp. 148–154.

Stable/Unstable Stratification in Thermosolutal Convection in a Square Cavity

D. K. Maiti[1]
Department of Mathematics,
Birla Institute of Technology and Science,
Pilani 333031, India
e-mail: d_iitkgp@yahoo.com

A. S. Gupta

S. Bhattacharyya

Department of Mathematics,
Indian Institute of Technology,
Kharagpur 721302, India

A numerical study is made of double-diffusive convection in a square cavity with a sliding top lid in the presence of combined vertical temperature and concentration gradients. The bottom lid and other two walls are kept fixed. The side walls are adiabatic and impermeable to solute while the top and bottom lids are kept at constant but distinct temperature and concentration. The governing unsteady Navier–Stokes equations combined with the heat and mass transport equations are solved numerically through a finite volume method on a staggered grid system using QUICK scheme for convective terms. The resulting equations are then solved by an implicit, time-marching, pressure correction-based algorithm. The flow configuration is classified into four cases depending on positive/negative values of thermal Grashof number and solutal Grashof number. A detailed comparison of the four flow configurations is made in this paper. In conclusion, these four flow configurations can be brought to either stably or unstably stratified field. Furthermore, the possibility of salt-fingering and double-diffusive instability in the absence of the top lid motion is explored and the effect of the lid motion is clearly exhibited. The dependence of the average rates of heat and mass transfer from the top and bottom lids on the flow parameters is also investigated in the presence of top lid motion.
[DOI: 10.1115/1.2969757]

Keywords: binary mixture, presence and absence of lid motion, stable/unstable stratification, thermal and solutal buoyancy forces, upwind scheme, heat and mass transfer

1 Introduction

A number of practical situations involve convective heat transfer, which is neither forced nor free in nature. Such flow known as mixed convection arises when a fluid is forced over a heated surface at a rather low velocity. The term double-diffusive convection refers to a process involving simultaneous thermal and concentration gradients. The effects of thermal and solutal buoyancy forces in natural or mixed convection lead to complex flow structures and the understanding of their influence on heat and mass transfer is relevant in many fields, such as vulcanology, oceanography, materials processing, drying chambers, etc. Excellent overview of this field, its relevance in understanding many natural systems, and its wide variety of engineering applications were documented by Gebhart and Pera [1] and Turner [2].

The problem of flow with moving surfaces, accompanied by heat and mass transfer, belongs to the family of lid-driven cavity problems. Flow in a lid-driven cavity accompanied by heat transfer was studied thoroughly by Moallemi and Jang [3], Iwatsu et al. [4], and Monsour and Viskanta [5]. Iwatsu et al. [4] investigated mixed convection in a cavity with a stable vertical temperature gradient and with a moving upper lid of the cavity. Owing to the stable stratification of the fluid, the primary recirculation of the flow driven by the upper lid is confined to the upper region, whereas in the lower region heat transfer is dominated by conduction. Monsour and Viskanta [5] studied experimentally and numerically the mixed convection flow in a narrow vertical cavity. Moallemi and Jang [3] studied the mixed convection in a lid-driven cavity.

Configurations involving heat and mass transfer in a lid-driven cavity filled with a mixture of vapor and a noncondensable gas have relevance to several industrial processes such as drying technology and natural gas storage tank. Alleborn et al. [6] investigated the steady two-dimensional flow accompanied by heat and mass transfer in a shallow lid-driven cavity with a moving heated bottom lid and a cooled top lid moving with a different constant velocity. However in their analysis density change with concentration was neglected. The cavity was assumed to be filled with a binary mixture of vapor and a noncondensable gas. Steady two-dimensional mixed convection in a square lid-driven cavity under combined effects of thermal and solutal buoyancy was studied by Al-Amiri et al. [7]. However, in their analysis the bottom lid of the cavity is always held at a higher temperature and concentration than that of the upper lid. Furthermore they studied the effects of thermal Richardson number for given values of thermal and solutal Grashof number under cooperating buoyancy forces only. These results have applications to the problem of disposal of a pollutant by a cold conveyor belt (sliding top lid) through condensation.

In this paper we study heat and mass transfer in a square cavity with sliding top lid filled with a mixture of a noncondensable gas and vapor. Here the flow is governed by two mechanisms: shear force due to the sliding top lid and buoyancy forces due to vertical temperature and concentration gradients for different combinations of temperature and concentration at the top/bottom lid. The side walls are assumed to be thermally insulated and impermeable to solute. Dufour effect and Soret effect are neglected. Four flow configurations are considered depending on the negative/positive value of thermal and solutal Grashof number. Our specific aim is to investigate the influence of thermal and solutal buoyancy as well as the shearing of the top lid on each of the four cases mentioned above. Extensive numerical calculations are made in these cases to determine flow pattern in the absence of lid motion. In this manner the effect of the top lid motion is clearly demon-

[1]Corresponding author.

Contributed by the Heat Transfer Division of ASME for publication in the JOURNAL OF HEAT TRANSFER. Manuscript received July 4, 2007; final manuscript received June 6, 2008; published online September 19, 2008. Review conducted by Cholik Chan.

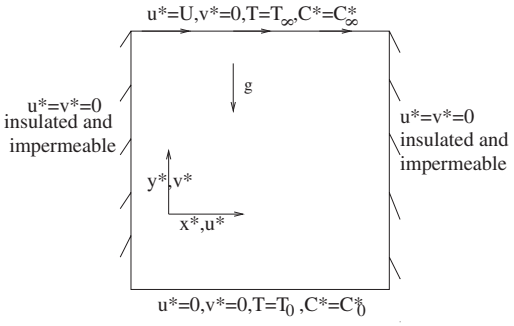

Fig. 1 Schematic of the flow configuration of the cavity with boundary conditions

strated. The investigation is completed by documenting the heat and mass transfer in the form of average Nusselt and Sherwood number over a range of parameter values in the presence of lid motion.

These results are likely to have engineering applications in the study of flow, heat, and mass transfer in a lid-driven cavity, particularly for low lid-Reynolds numbers.

2 Problem Formulation and Numerical Method

2.1 Physical Configuration. We consider the flow within a closed square cavity of length L filled with a binary mixture of vapor and a noncondensable gas. The flow is assumed to be laminar and two dimensional and the fluid is assumed to be incompressible and viscous. In Cartesian coordinates (x^*, y^*), the x^*-axis is taken along the bottom lid, which is horizontal, and the y^*-axis is along the left wall of the cavity. The top lid is maintained at temperature T_∞ with concentration C^*_∞ and the bottom lid is at concentration C^*_0 with temperature T_0. Thus the horizontal lids impose vertical temperature and concentration gradients on the flow. The side walls are thermally insulated and impermeable to solute. For the case of lid-driven cavity, the top lid is assumed to be sliding horizontally from left to right at constant speed U while the bottom lid and other two walls are kept fixed, as shown in Fig. 1. In the absence of lid motion, the top lid is also kept fixed.

2.2 Model Equations With Boundary Conditions. The binary fluid is assumed to be Newtonian. The variation of density ρ with temperature and concentration is given by (see Ref. [1])

$$\rho(T, C^*) = \rho_1[1 - \beta_T(T - T_\infty) - \beta_C(C^* - C^*_\infty)] \tag{1}$$

where ρ_1 is a reference density, $\beta_T = -1/\rho(\partial\rho/\partial T)_{C^*}$, and $\beta_C = -1/\rho(\partial\rho/\partial C^*)_T$. Furthermore T is the temperature of the fluid and C^* is the concentration of vapor.

The case of lid-driven cavity. The governing Navier–Stokes equations together with the equation of continuity, heat, and mass transport equations in nondimensional form are given by

$$\nabla \cdot \mathbf{V} = 0 \tag{2}$$

$$\frac{\partial \mathbf{V}}{\partial t} + (\mathbf{V} \cdot \nabla)\mathbf{V} = -\nabla p + \frac{1}{\mathrm{Re}}\nabla^2 \mathbf{V} + (\theta \cdot \mathrm{Ri}_T + C \cdot \mathrm{Ri}_C)\mathbf{j} \tag{3}$$

$$\frac{\partial \theta}{\partial t} + (\mathbf{V} \cdot \nabla)\theta = \frac{1}{\mathrm{Re} \cdot \mathrm{Pr}}\nabla^2 \theta \tag{4}$$

$$\frac{\partial C}{\partial t} + (\mathbf{V} \cdot \nabla)C = \frac{1}{\mathrm{Re} \cdot \mathrm{Sc}}\nabla^2 C \tag{5}$$

where $\mathbf{j}$ is the unit vector in the y-direction. The characteristic length scale and velocity scale are considered as L and U, respectively, with $\theta = (T - T_\infty)/\Delta T$, $C = (C^* - C^*_\infty)/\Delta C^*$, where $\Delta T = T_0 - T_\infty$ and $\Delta C^* = C^*_0 - C^*_\infty$. The nondimensional quantities $\mathbf{V} = (u, v)$, p, and t denote the velocity, pressure, and time, respectively. The variables with asterisk denote dimensional variables. Note that in writing the vertical component of the momentum equation given by Eq. (3), use is made of the usual Boussinesq approximation of treating density as constant except when accounting for the buoyancy force terms given by the last two terms.

The flow field is characterized by five nondimensional parameters: (i) Prandtl number Pr, (ii) Schmidt number Sc, (iii) Reynolds number Re, (iv) thermal Grashof number Gr_T, and (v) solutal Grashof number Gr_C, which are defined, respectively, by

$$\mathrm{Pr} = \frac{\nu}{\alpha}, \quad \mathrm{Sc} = \frac{\nu}{D}, \quad \mathrm{Re} = \frac{UL}{\nu}, \quad \mathrm{Gr}_T = \frac{g\beta_T \Delta T L^3}{\nu^2}$$

$$\mathrm{Gr}_C = \frac{g\beta_C \Delta C^* L^3}{\nu^2} \tag{6}$$

Here ν, α, and D denote the kinematic viscosity, thermal diffusivity, and mass diffusivity of the fluid, respectively, while g stands for the gravitational acceleration. Note that in Eq. (3), $\mathrm{Ri}_T = \mathrm{Gr}_T/\mathrm{Re}^2$ and $\mathrm{Ri}_C = \mathrm{Gr}_C/\mathrm{Re}^2$ stand for thermal and solutal Richardson numbers, respectively. Furthermore one may define buoyancy forces ratio $B = \beta_C \Delta C^*/\beta_T \Delta T = \mathrm{Gr}_C/\mathrm{Gr}_T$.

The boundary conditions for $t > 0$ are given by

$$u = v = 0, \quad \frac{\partial \theta}{\partial x} = \frac{\partial C}{\partial x} = 0 \quad \text{on the side walls } (x = 0, x = 1)$$

$$u = v = 0, \quad \theta = 1, \quad C = 1 \quad \text{on the bottom wall } (y = 0) \tag{7}$$

$$u = 1, \quad v = 0, \quad \theta = 0, \quad C = 0 \quad \text{on the top wall } (y = 1)$$

Absence of lid motion. The governing equations are made dimensionless using the same length, temperature, and concentration scales as in the case of lid motion except the velocity scale, which is taken as $(g\beta_T|\Delta T|L)^{1/2}$. Therefore in this natural convection case, the thermal Grashof number is defined as $\mathrm{Gr}^N_T = g\beta_T|\Delta T|L^3/\nu^2$ and hence $\mathrm{Gr}_T = (\Delta T/|\Delta T|) \cdot \mathrm{Gr}^N_T$. Except the buoyancy terms, here the governing equations are the same as in the case of lid motion with $\mathrm{Re} = (\mathrm{Gr}^N_T)^{1/2}$. Here the buoyancy terms are

$$\theta \cdot \frac{\Delta T}{|\Delta T|} + C \cdot B \cdot \frac{\Delta T}{|\Delta T|} \tag{8}$$

The only difference in the boundary conditions here from those in the presence of the top lid motion is that $u = 0$ on the top lid.

For the sake of numerical calculation, both the problems (in the presence and absence of the top lid motion) are considered as time dependent. Initial conditions are taken arbitrarily. Typically, the fluid is considered to be at rest with uniform temperature T_∞ and concentration C^*_∞ for smaller values of parameters. To facilitate the convergence of solution for given set of parameters, the converged solution of a case with smaller values of parameters is used as the initial guess. Through the sensitivity test, it is observed that the final flows are always steady and the same final flow is obtained using different initial data.

2.3 Studied Configurations. Now $\beta_T = -1/\rho(\partial\rho/\partial T)_{C^*}$ is generally positive since density decreases with increase in temperature. This is, of course, not generally true. In the range of 0–4 °C, the density of water increases with increasing temperature (maximum density anomaly) so that β_T is then negative. However, $\beta_C = -1/\rho(\partial\rho/\partial C^*)_T$ may be either positive or negative. However, with an increase in concentration C^* of the vapor, the density of the fluid increases so that β_C is negative. Of course there is exception to this statement. In fact, humid air with water vapor is less dense than dry air because molecular weight of water is smaller than that of diatomic oxygen and diatomic nitrogen.

Thus for air and water vapor, increasing vapor concentration will reduce density. It is clear from Eq. (1) that the two buoyant mechanisms, viz., thermal and solutal buoyancy forces, reinforce each other when the quantities $\beta_T \Delta T$ and $\beta_C \Delta C^*$ have the same sign and oppose each other when they have opposite sign. Therefore B is positive when the above two mechanisms aid each other and negative when these mechanisms conflict with each other.

For cooperating buoyancy forces $B(=\beta_C \Delta C^*/\beta_T \Delta T) > 0$, which implies either

$$(C_0^* - C_\infty^*) > 0 \quad \text{and } (T_0 - T_\infty) < 0 \quad \text{(Case-IA)}$$

or

$$(C_0^* - C_\infty^*) < 0 \quad \text{and } (T_0 - T_\infty) > 0 \quad \text{(Case-IB)}$$

For opposing buoyancy forces $B < 0$, which implies either

$$(C_0^* - C_\infty^*) < 0 \quad \text{and } (T_0 - T_\infty) < 0 \quad \text{(Case-IIA)}$$

or

$$(C_0^* - C_\infty^*) > 0 \quad \text{and } (T_0 - T_\infty) > 0 \quad \text{(Case-IIB)}$$

In terms of Gr_C and Gr_T, the above four cases can be summarized as follows: Case-IA-$\mathrm{Gr}_T < 0$, $\mathrm{Gr}_C < 0$; Case-IB-$\mathrm{Gr}_T > 0$, $\mathrm{Gr}_C > 0$; Case-IIA-$\mathrm{Gr}_T < 0$, $\mathrm{Gr}_C > 0$, and Case-IIB-$\mathrm{Gr}_T > 0$, $\mathrm{Gr}_C < 0$.

2.4 The Numerical Method. The pressure correction-based iterative algorithm SIMPLE [8] is used for solving the governing equations with the boundary conditions specified previously. The computational domain is divided into Cartesian cells. Staggered grid is used for arrangement of the physical variables. A three-level fully implicit scheme is used for discretization of time derivatives. A third-order accurate QUICK [9] is employed to discretize the convective terms in the Navier–Stokes equations. A detailed discussion of the upwind scheme and SIMPLE method used here was given in our paper [10]. The time-dependent equations are marched in time until the solution becomes independent of time. The convergence criterion is employed in the form

$$|\phi_{i,j}^{n+1} - \phi_{i,j}^{n}|_{\max} < \epsilon, \quad \left|1.0 - \frac{\overline{\mathrm{Nu}_t}}{\overline{\mathrm{Nu}_b}}\right| < \delta_\theta \quad \text{and} \quad \left|1.0 - \frac{\overline{\mathrm{Sh}_t}}{\overline{\mathrm{Sh}_b}}\right| < \delta_C \tag{9}$$

Here i and j denote the cell indices, n is the time level, ϕ stands for u, v, θ or C, $\overline{\mathrm{Nu}_t}$ and $\overline{\mathrm{Nu}_b}$ are area-averaged Nusselt numbers on the top and bottom lids, respectively, and $\overline{\mathrm{Sh}_t}$ and $\overline{\mathrm{Sh}_b}$ are area-averaged Sherwood numbers on the top and bottom lids, respectively. The values of ϵ, δ_θ, and δ_C are considered to be 10^{-4}, 10^{-3} and 10^{-3}, respectively.

A comparison of the u-velocity and temperature profiles along the vertical midsection of the cavity (Fig. 9 of Ref. [7]) between the present results and those of Al-Amiri et al. [7] is made. The maximum percentage difference of the computed u-velocity, which is 0.5%, from those of Al-Amiri et al. [7] occurs at $y = 0.9$ for $B = -25$. Table 1 presents the comparison with the results of Janssen and Henkes [11] for the cavity without lid motion in the case of no species diffusion. Here Ra is the Rayleigh number and S is the gradient of stratification in the center of the cavity, which are defined by $\mathrm{Ra} = \mathrm{Gr}_T * \mathrm{Pr}$ and $S = \partial\theta/\partial y$, respectively. Table 1 shows that the present results are in excellent agreement with those of Janssen and Henkes [11].

The grid independence tests are conducted by varying the grid sizes from 50×50 to 250×250 in the absence of top lid motion and also compared with those of Janssen and Henkes [11] (see Table 1). Our results agree well with those of Janssen and Henkes [11] for all grids. Agarwal [12] found steady-state solution for lid-driven cavity for $\mathrm{Re} = 7500$ with 121×121 grids using third-order-accurate upwind scheme. Therefore the finest grids 125×125 and 250×250 are used in the present calculation for the flows with and without lid motion, respectively.

Table 1 Comparison of $\overline{\mathrm{Nu}}\mathrm{Ra}^{-1/4}$ and gradient of stratification S with those of Janssen and Henkes for different grids at $\mathrm{Ra} = 10^6$

	$\overline{\mathrm{Nu}}\mathrm{Ra}^{-1/4}$		S	
Grids	Present	Janssen and Henkes	Present	Janssen and Henkes
60×60		0.2789		0.9190
50×50	0.2760		0.928	
120×120		0.2790		0.9144
125×125	0.2803		0.9120	
240×240		0.2791		0.9132
250×250	0.2786		0.9102	

3 Results and Discussion

As pointed out earlier, the parameters governing the flow are Re, Gr_T, Gr_C, Sc, and Pr. In our study, we choose $\mathrm{Pr} = 0.72$ and $\mathrm{Sc} = 0.56$. It may be noted that in a gaseous mixture, the Sc varies up to 10 [1]. Numerical solutions for the four flow configurations as described in Sec. 2.3 are presented for different values of Gr_C, Gr_T, and Re.

3.1 Fluid Flow Analysis. Dense fluid tends to sink and less dense fluid tends to rise. This results in a tendency for the upper regions of a fluid to be composed of lower density material than the lower regions. By definition, a layer of binary fluid having a thermal and solutal distribution is said to be unstable if either the temperature or solute or both have statically unstable stratification. Thus an unstable layer shows a tendency to overturn and mix. On the other hand a binary fluid layer is said to be stable if the quiescent layer does not have any tendency to overturn. Our specific aim is to investigate the variation of solutal and thermal buoyancy forces and the effect of Reynolds number (which is the measure of shear forces) on the four flow configurations.

3.1.1 Influence of Solutal Buoyancy. We now discuss the influence of solutal buoyancy force on the flow characteristics by varying Gr_C for negative and positive values of Gr_T when $\mathrm{Re} = 700$.

We first take $\mathrm{Gr}_T = -10^6$ so that $\mathrm{Ri}_T = -10^6/700^2 < 0$. The flow configurations of Case-IA and Case-IIA are clearly the same for no species diffusion ($B = 0$). It is clear that the flow is stable in Case-IA in the absence of the top lid motion ($\mathrm{Re} = 0$) since the fluid at the bottom lid is kept at a higher concentration than that of the upper one while the temperature of the fluid at the lower lid is smaller than that of the upper one. However, the flow in Case-IIA is unstable when the solutal buoyancy force dominates over the thermal buoyancy force. Just the reverse is true (i.e., the flow is stable) when thermal buoyancy dominates over the solutal buoyancy and this will be considered in Sec. 3.1.2. Figure 2(*a*) shows that the lower part of the cavity is almost stagnant in the case of no solutal diffusion ($\mathrm{Gr}_C = 0$). Due to the stabilizing influence of thermal buoyancy, the flows are motionless in the bulk of the interior cavity and the heat transfer is primarily due to thermal conduction in this region and this can be seen in the isothermal lines in Fig. 2(*b*). Figure 3(*a*) displays the streamlines in the case of flow with aiding buoyancy forces for $\mathrm{Gr}_C = -10^6$. As mentioned earlier, this corresponds to the Case-IA, which is a stable configuration when $\mathrm{Re} = 0$. With an increase in $|\mathrm{Gr}_C|$, more and more of the fluid in the lower part of the cavity becomes stagnant owing to a decrease in the strength of both the eddies. As $|\mathrm{Gr}_C|$ increases, the fluid near the lower lid becomes heavier than that at the upper

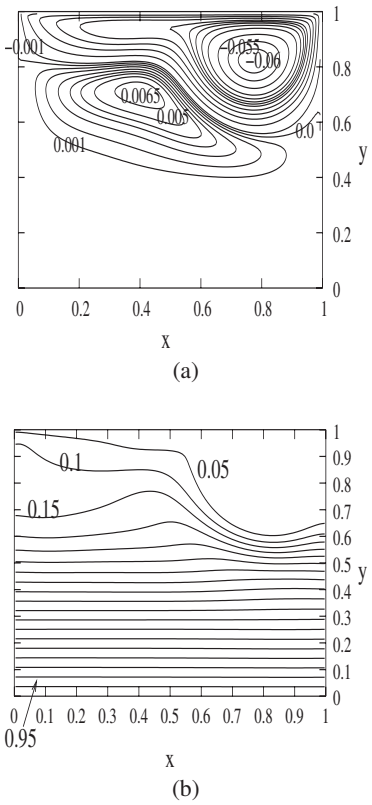

Fig. 2 Contour plots for $Gr_C=0$ when $Gr_T=-10^6$ ($B=0$) at Re =700: (a) streamlines and (*b*) isotherms

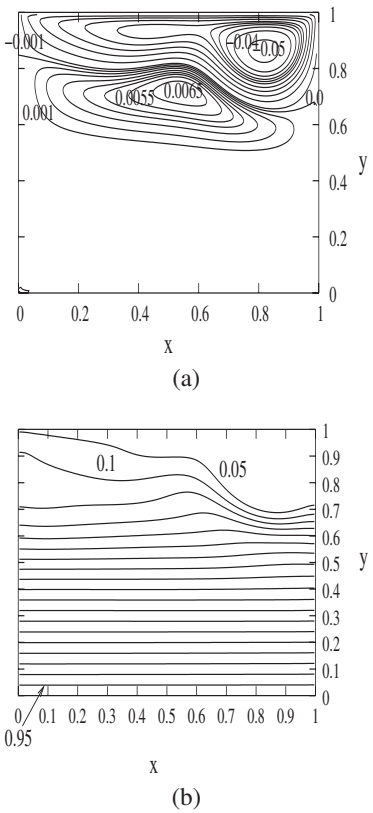

Fig. 3 Contour plots for $Gr_C=-10^6$ when $Gr_T=-10^6$ ($B=1$) at Re=700 (Case-IA): (*a*) streamlines, (*b*) isotherms, and (*c*) isohalines

lid for a constant temperature difference. The corresponding isotherms and isohalines for the above stable case approach linear profile, as displayed in Figs. 3(*b*) and 3(*c*).

We next consider the case of flow with opposing buoyancy forces ($B<0$) with $Gr_C>0$ for the above combination of Gr_T and Re. Figure 4(*a*) displays the streamlines for the case with $Gr_C=10^6$. It is interesting to note that here due to cancellation of almost equal and opposite thermal and solutal buoyancy forces, there is a large primary eddy due to shearing of the top lid. Figure 5(*a*) shows the streamlines for the case of $Gr_C=5\times10^6$. The vertical overturning and mixing of the fluid forming a secondary eddy at the lower part of the cavity can be seen here. With an increase in Gr_C, the solutal buoyancy gains noticeable influence compared with the thermal buoyancy. As a result, the heavier fluid from the top lid flows down along the right-vertical wall toward the bottom lid due to the movement of the top lid from left to right. Apparently, the downward heavier fluid accompanied by the primary eddy forms this counterclockwise eddy at the lower part. Therefore, the dominant solutal buoyancy over thermal buoyancy forms this secondary eddy in the presence of top lid motion. Further increase in solutal gradient leads to an increase in the strength of both eddies. The corresponding isothermal and isosolutal lines are shown in Figs. 4(*b*) and 4(*c*) for $Gr_C=10^6$ and in Figs. 5(*b*) and 5(*c*) for $Gr_C=5\times10^6$. Figures 4(*b*) and 4(*c*) suggest that the temperature and concentration are well distributed in the bulk of the interior cavity with high temperature and concentration. It can be seen from Figs. 5(*b*) and 5(*c*) that the well-mixed zone is divided into two zones in such a way that the fluid in the upper part is with high temperature and concentration whereas the lower part contains fluid with low temperature and concentration. For a pure buoyancy flow without top lid motion, a large primary eddy would be expected; this is shown in Fig. 6(*a*) for $B=-5$ with $Gr_C=5\times10^6$. In this case the main source of convective activity is the domination of solutal buoyancy over thermal buoyancy. Here the temperature is the stabilizing component but the solute is the destabilizing component because the fluid (rich in solute) is heavier near the upper lid whose temperature is higher than that of the lower lid. In this study, Sc/Pr $(=\alpha/D)=7/9$ so that the thermal diffusivity is less than the mass diffusivity. One would, therefore, expect that salt-fingering [13] does not take place. Figure 6 clearly shows this. Physically it can be explained as follows. Imagine that a blob of fluid is pushed upward. In the new position, the blob will be richer in solute compared with that in the original position in the presence of the prevailing positive vertical solute gradient because solute diffuses faster into the blob than heat (owing to $D>\alpha$). At the same time, in the displaced position, the blob will remain almost as cold as that in the original position due to smaller diffusion of heat. Consequently in the new position, the blob becomes heavier than the surrounding warm fluid and tends to drop down. So salt-fingering does not occur. Figures 6(*b*) and 6(*c*) show that only one well-mixed zone is observed, which has

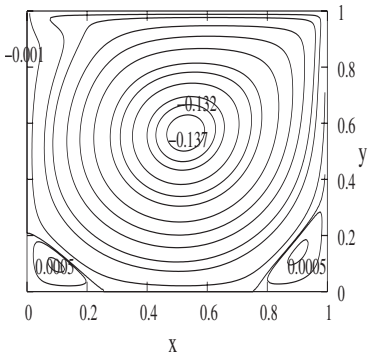

Fig. 4 Contour plots for $Gr_C=10^6$ when $Gr_T=-10^6$ ($B=-1$) at Re=700 (Case-IIA): (*a*) streamlines, (*b*) isotherms, and (*c*) isohalines

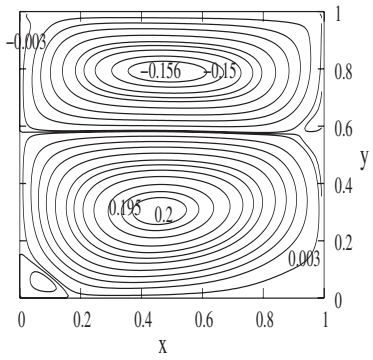

Fig. 5 Contour plots for $Gr_C=5\times10^6$ when $Gr_T=-10^6$ ($B=-5$) at Re=700 (Case-IIA): (*a*) streamlines, (*b*) isotherms, and (*c*) isohalines

similar characteristics as the lower zone of Figs. 5(*b*) and 5(*c*).

We now take $Gr_T=10^6$ so that $Ri_T=10^6/700^2>0$. Here Case-IB and Case-IIB are the same for $B=0$ and the positive value of B leads to Case-IB whereas the negative B leads to Case-IIB. The absence of species diffusion ($Gr_C=0$) leads to an unstable configuration with overturning of the fluid near the lower part of the cavity due to only thermal buoyancy, as shown in Fig. 7(*a*). This is due to the fact that less dense fluid near the hot bottom tends to rise as in the case of Benard convection. Thus a primary eddy near the top due to the shearing of the top lid and a secondary eddy along with a small tertiary eddy at the left bottom corner are formed. Heat transfer in the lower part of the cavity is due to thermal buoyancy-driven convection and the corresponding isotherms are presented in Fig. 7(*b*). The streamlines at $Gr_C=10^6$ ($B=1$) are similar to those in Fig. 5(*a*) with $\Psi_{min}=-0.115$ for upper eddy and $\Psi_{max}=0.14$ for lower eddy. It is interesting to note that in the presence of cooperating buoyancy forces $B=1$, the behavior of the unstable stratification remains unstable. Furthermore it may be noted that both the eddies are strengthened with an increase in Gr_C. This can be explained by pointing out that as Gr_C increases, more fluid flows down from the top lid toward the bottom in the presence of the top lid motion. As in the case of Figs. 5(*b*) and 5(*c*), there exists also a two well-mixed zone for $B=1$. However, here the upper zone contains fluid of low temperature with high concentration and at the lower zone, fluid is with high temperature and low concentration. In the absence of top lid motion, the flow field would consist of two convective states corresponding to two possible directions of rotation of the single cell as the destabilizing components are both the temperature and concentration. This is depicted in Fig. 8(*a*) at $Gr_C=5\times10^6$ ($B=5$). It is interesting to note that the directions of both the eddies in Fig. 8(*a*) are opposite to those in the presence of lid motion. As a result, the temperature of the two zones, as displayed in Figs. 8(*b*) and 8(*c*), is slightly increased whereas concentration is decreased compared to the case of top lid motion at the same temperature and concentration gradients.

However, for opposing buoyancy forces (Case-IIB) with $B=-5$, the overturning of the flow near the bottom is halted and it

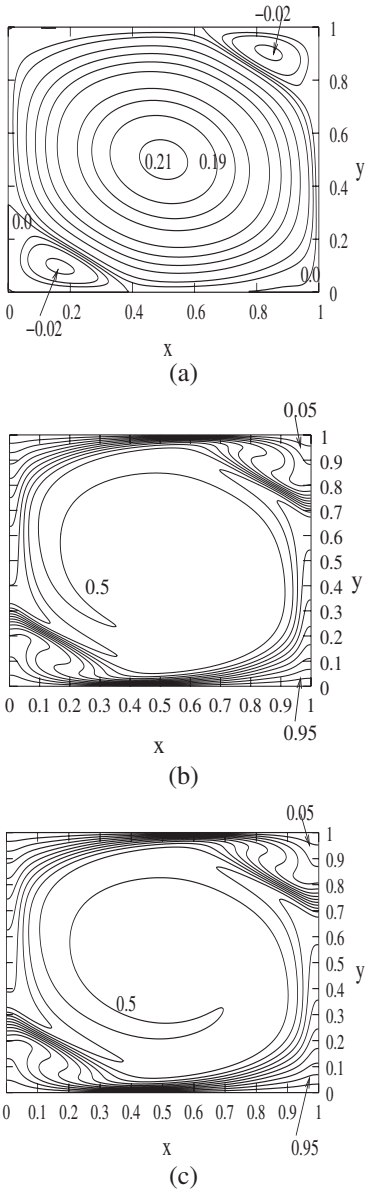

Fig. 6 Contour plots for $B=-5$ ($Gr_T=-10^6$ and $Gr_C=5\times10^6$) (Case-IIA: in the absence of top lid motion): (*a*) streamlines, (*b*) isotherms, and (*c*) isohalines

becomes practically stagnant there owing to statically stable stratification (which has similar flow characteristics as those of Fig. 3(*a*)). Note that here the effect of the large solutal gradient ($B=-5$) is opposite to that in Case-IIA. For relatively small value of solutal gradient ($B=-1$), the stratification is shown in Fig. 9(*a*). It is interesting to note that despite $B=-1$ in both Cases IIA and IIB, there is a lot of difference in the disposition of streamlines (see Figs. 4(*a*) and 9(*a*)). This stems from the fact that whereas the shear force and solutal buoyancy force reinforce each other in Case-IIA, they are in opposition in Case-IIB.

3.1.2 Influence of Thermal Buoyancy. In order to find the influence of thermal buoyancy force on the flow inside cavity, Gr_T is varied for positive and negative values of Gr_C when $Re=700$.

We first consider $Gr_C=-10^6$ so that $Ri_C=-10^6/700^2<0$. For the case of no thermal gradient ($Gr_T=0$), the heavier fluid tends to remain near the bottom. The flow features due to this stable solutal gradient with no thermal gradient are similar to those of Fig. 2(*a*). Now under the cooperating buoyancy forces with $Gr_T<0$

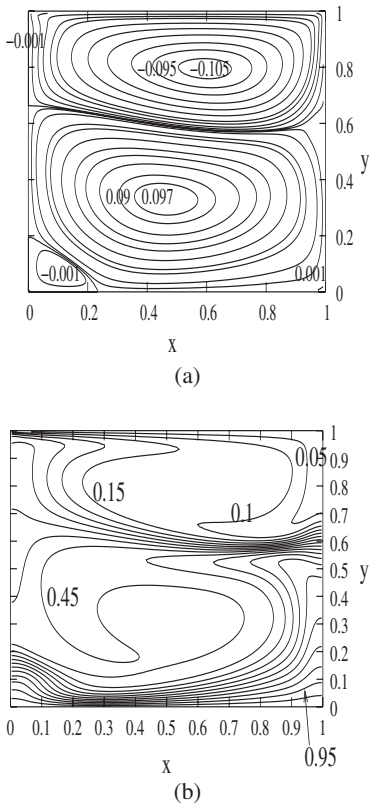

Fig. 7 Contour plots for $Gr_C=0$ when $Gr_T=10^6$ ($B=0$) at Re =700: (*a*) streamlines and (*b*) isotherms

(Case-IA), the stratification remains statically stable as discussed in the previous section (see Fig. 3(*a*)). An increase in thermal gradient leads to more stable configuration since the more heated fluid near the top tends to remain near the top.

On the other hand, reverse flow characteristics leading to statically unstable stratification are observed for the case of opposing buoyancy forces with $Gr_T>0$ (Case-IIB). This can be seen in Fig. 9 for $Gr_T=10^6$. Therefore the effect of thermal gradient in Case-IIB is opposite to that of Case-IA. An increase in thermal gradient leads to more unstable stratification at the lower part of the cavity as the fluid near the bottom becomes more heated (the flow features at $Gr_T=5\times10^6$ are almost similar to those of Fig. 5(*a*) (Case-IIA)). Furthermore the effect of thermal gradient is opposite to the effect of solutal gradient in Case-IIB as the two buoyancy forces compete with each other here. It is to be observed that at $Gr_T=5\times10^6$ (Case-IIB), there exist two well-mixed zones also as in the cases of Figs. 5(*b*) and 5(*c*) (Case-IIA) with almost the same nondimensional temperature and concentration distribution. However, the fluid characteristics of the two zones of Case-IIB are opposite to those in the case of Case-IIA, which means that the upper zone contains the fluid of low temperature with low concentration and the fluid of high temperature and concentration is in the lower zone. This is not surprising since the direction of gradients of temperature and concentration in Case-IIA is opposite to that of Case-IIB. In the absence of lid motion for the configuration Case-IIB (when temperature is the driving component and concentration is the stabilizing component), the streamlines are shown in Fig. 10(*a*) at $Gr_T=5\times10^6$ with $B=-0.2$. Here the directions of rotation of eddies are opposite to those in the case of lid motion. Figures 10(*b*) and 10(*c*) suggest that both the temperature and concentration of two well-mixed zones are increased in the absence of lid motion compared with those in the presence of lid motion.

Let us next consider the case of $Gr_C=10^6$ so that Ri_C

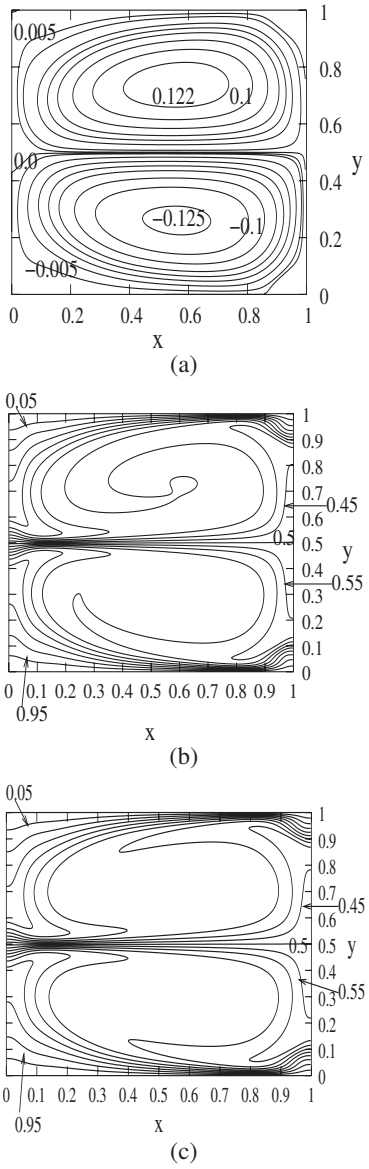

Fig. 8 Contour plots for $Gr_C=5\times10^6$ when $Gr_T=10^6$ ($B=5$) (Case-IB: in the absence of top lid motion): (*a*) streamlines, (*b*) isotherms, and (*c*) isohalines

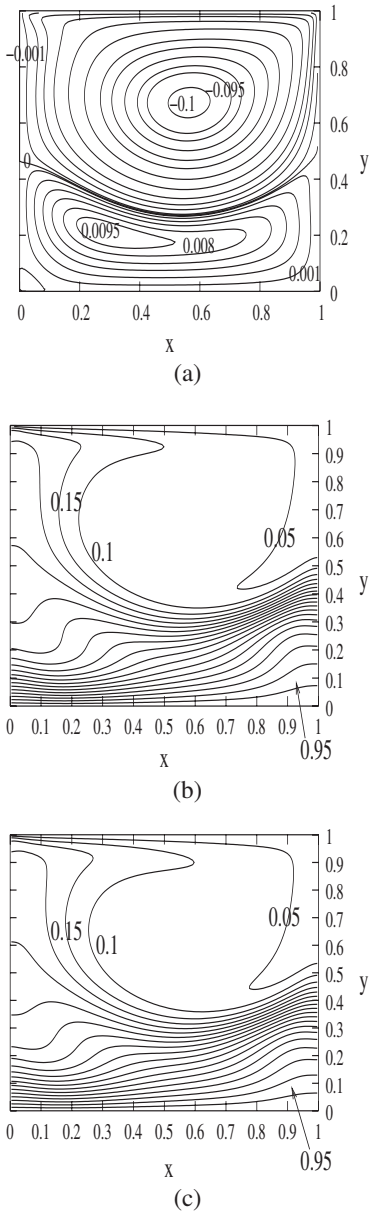

Fig. 9 Contour plots for $Gr_C=-10^6$ when $Gr_T=10^6$ ($B=-1$) at Re=700 (Case-IIB): (*a*) streamlines, (*b*) isotherms and (*c*) isohalines

$=10^6/700^2>0$. For no thermal gradient ($Gr_T=0$), the flow characteristics with $Gr_C=10^6$ are opposite to those of the previous case of $Gr_C=-10^6$ but similar to those shown in Fig. 7 with two eddies. Using similar argument given in the previous section for Fig. 5(*a*), the appearance of the secondary eddy at the lower part is due to the solutal gradient in the absence of thermal gradient. As discussed in the previous section, under the cooperating buoyancy forces $B(=1)$ with $Gr_T=10^6$ (Case-IB), the flow remains statically unstable. For $Gr_T=5\times10^6$, the thermal buoyancy has similar effect (leading to more unstable stratification) as the solutal buoyancy on the flow characteristics of Case-IB since both the buoyancy forces reinforce each other. As in the case of solutal buoyancy effects in the absence of lid motion, here also there are two eddies with the same directions of rotation at $Gr_T=5\times10^6$ with $B=0.2$. The absolute value of maximum strength of both the eddies is 0.0525 at these values of parameters. Here the characteristics of well-mixed zones are similar to those of Figs. 8(*b*) and 8(*c*).

However, for the case of opposing buoyancy forces with $Gr_T<0$ (Case-IIA), the statically unstable stratification is converted to a stable one. In fact, upon increasing $|Gr_T|$, the stratification becomes more and more stable (which has similar flow characteristics as those of Fig. 3) since the fluid near the top lid becomes more and more heated compared with that near the bottom lid. Therefore, the influence of thermal buoyancy on the flow of Case-IIA is opposite to that of the solutal buoyancy, as illustrated in the previous section (see Figs. 4 and 5).

A novel result of the analysis is that when Le=1 (i.e., Pr=Sc), the equations for heat transport and mass transport given by Eqs. (4) and (5) become identical for a given velocity distribution. Now since the boundary conditions for θ and C are identical (see Eq. (7)), it follows from the uniqueness property of differential equation that $\theta=C$. Hence it is clear from Eq. (3) that the two buoyancy force terms exactly cancel each other when $Gr_T=-Gr_C$ (i.e., when $B=-1$). Therefore in this case the momentum equations are decoupled from the transport equations. The streamlines in this case are unaffected by the thermal or solutal buoyancy forces. These are sketched in Fig. 11.

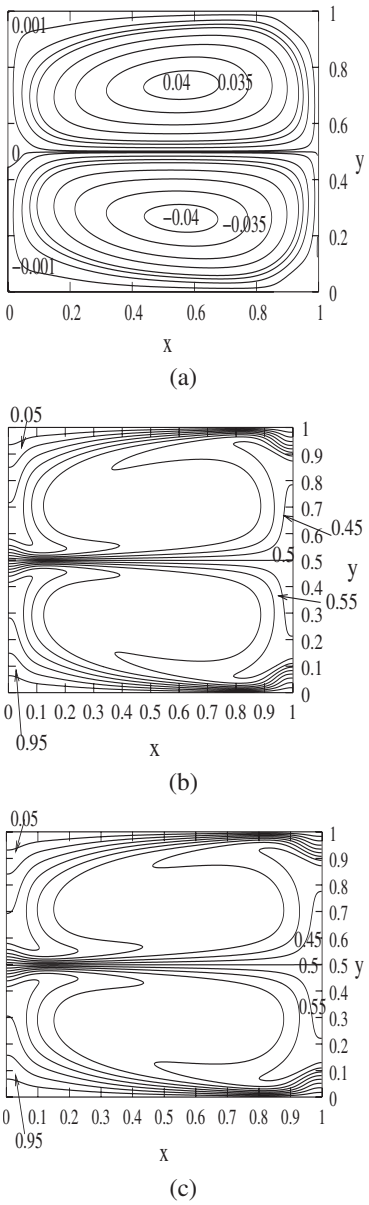

Fig. 10 Contour plots for $Gr_T=5\times10^6$ when $Gr_C=-10^6$ ($B=-0.2$) (Case-IIB: in the absence of top lid motion): (*a*) streamlines, (*b*) isotherms, and (*c*) concentration

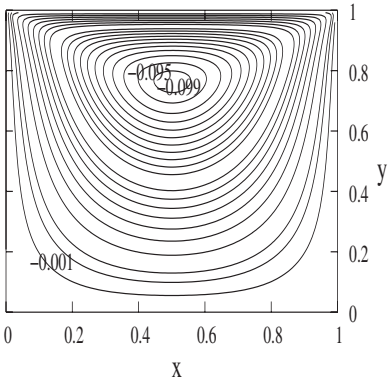

Fig. 11 Contour plots of streamlines for $B=-1$ ($Gr_T=-10^6$, $Gr_C=10^6$) at Re=1 with Le=1 (Pr=Sc=0.72)

3.1.3 Effect of Reynolds Number. From the foregoing discussion it is clear that Case-IA and Case-IB lead to the case of stable and unstable stratifications, respectively, for any positive value of B when Re=0. However, the Case-IIA and Case-IIB would be either stable or unstable depending on the negative values of B at Re=0. Here we consider $B=-5$ with $|Gr_T|=10^6$ so that Case-IIA and Case-IIB correspond to unstable and stable cases, respectively, at small Re. Also we consider the case of $B=-0.2$ with $|Gr_C|=10^6$ so that Case-IIA and Case-IIB refer to stable and unstable cases, respectively, at small Re. Now we study the effect of Reynolds number on two main configurations: statically stable and unstable stratifications.

For statically stable stratification. As Re increases from 700 to 5000, the primary eddy tends to fill up the entire cavity in Case-IA for cooperating buoyancy forces ($B>0$). When Re=5000, the flow features are similar to those of Fig. 4(*a*) (lid-driven cavity flow in a nonstratified fluid) with three tertiary eddies. Reynolds number has also a significant effect on the flow under opposing buoyancy forces ($B<0$). This corresponds to Case-IIA with $B=-0.2$, $Gr_C=-10^6$ and to Case-IIB with $B=-5$, $Gr_T=10^6$ (flow characteristics for Case-IIA and Case-IIB at Re=5000 are almost similar to those of Fig. 4(*a*)). It is clear that for fixed values of B, with an increase in Re, the shear-induced primary eddy caused by the sliding top lid progressively increases and occupies practically the entire cavity. Due to the shearing of the top lid, as Re increases the primary eddy gains in strength and brings the fluid near the top lid to the interior of the cavity so that the fluid in the interior is with high temperature and low concentration in Case-IA. Using the same argument one can say that in Case-IIA, the fluid in the interior cavity is with high temperature and high concentration whereas interior cavity in Case-IIB contains fluid with low temperature and concentration. Hence the Reynolds number has a vital role in mixing of fluids in the interior cavity irrespective of aiding or opposing buoyancy forces.

For statically unstable stratification. For Case-IB, the primary eddy becomes stronger with increased size as Re increases. At Re=5000, the flow characteristics are almost similar to those of Fig. 4(*a*). Thus we find that for large Re, the shear forces dominate over the buoyancy forces leading to a larger and larger primary eddy. This result is also true for opposing buoyancy forces for $B=-5$ with $Gr_T=-10^6$ (Case-IIA) and for $B=-0.2$ with $Gr_C=-10^6$ (Case-IIB). At higher Re, the major part of the interior cavity from the upper side contains fluid with low temperature and high concentration for Case-IB. Furthermore it is clear that the mixing for Case-IIA and Case-IIB has similar characteristics as in the case of stable stratification for large Re.

3.2 Heat and Mass Transfer Analysis. The effect of solutal buoyancy on the average Nusselt number $\overline{Nu}$ and average Sherwood number $\overline{Sh}$ is depicted in Fig. 12. Figure 12(*a*) reveals that $\overline{Nu}$ and $\overline{Sh}$ from both the lids decrease with an increase in $|Gr_C|$ (for fixed $Gr_T<0$) in Case-IA. Physically this stems from the fact that in the presence of cooperating buoyancy forces ($B>0$), the flow becomes almost stagnant with no significant convection and this stagnant region of the fluid occupies the greater portion of the cavity from the lower side as $|Gr_C|$ increases. Thus in this case heat transfer is mainly due to thermal conduction while mass transfer is practically due to molecular diffusion with no significant role of convection. On the other hand in the case of opposing buoyancy forces ($B<0$, Case-IIA), both $\overline{Nu}$ and $\overline{Sh}$ increase as $|Gr_C|$ increases for given $Gr_T<0$. This can be explained by pointing out that the convective activities inside the cavity intensify due to the increased strength of primary eddy and secondary eddy by increasing the solutal gradient in presence of the upper lid motion.

As in the case of $Gr_T<0$, $\overline{Nu}$ and $\overline{Sh}$ increase for unstable stratification (Case-IB) and decrease for stable stratification (Case-IIB) with an increase in $|Gr_C|$ for the case of $Gr_T>0$. This is shown in Fig. 12(*b*). Using the same argument for Case-IIA in

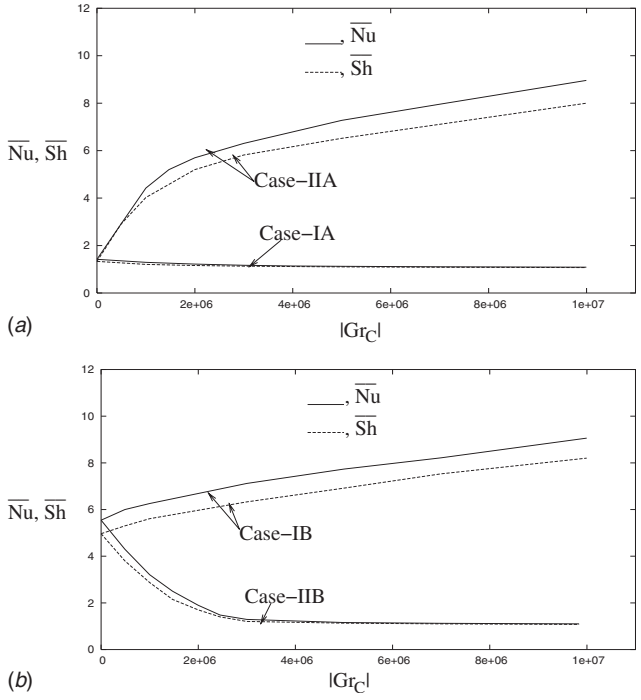

Fig. 12 The average Nusselt number ($\overline{Nu}$) and Sherwood number ($\overline{Sh}$) versus solutal Grashof number (Gr_C): (*a*) $Ri_T = -10^6/700^2$ and (*b*) $Ri_T = 10^6/700^2$

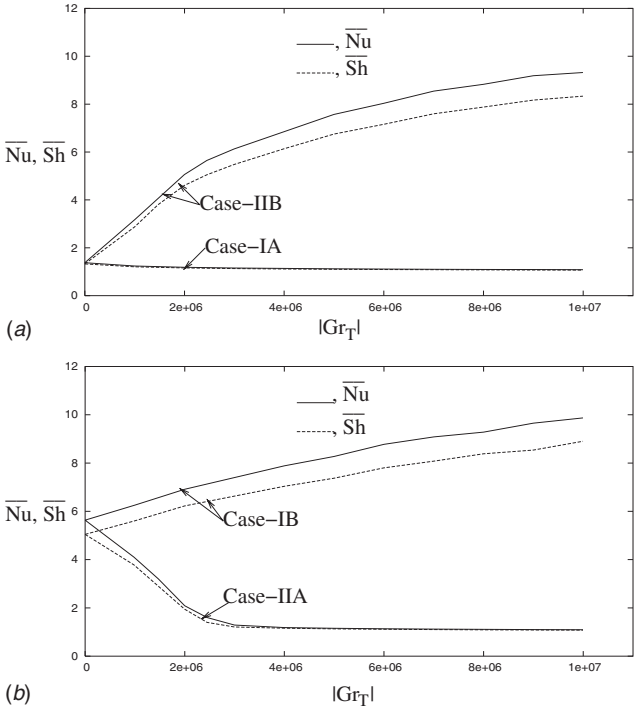

Fig. 13 The average Nusselt number ($\overline{Nu}$) and Sherwood number ($\overline{Sh}$) versus thermal Grashof number (Gr_T): (*a*) $Ri_C = -10^6/700^2$ and (*b*) $Ri_C = 10^6/700^2$

Fig. 12(*a*), heavier fluid from the upper lid tends to fall toward the interior in the presence of top lid motion at higher solutal gradient in Case-IB. However, in Case-IIB, the heavier fluid at the bottom tends to remain in the lower part of the cavity owing to the flow becoming more and more stagnant there and hence the heat flow is more and more conduction dominated.

Figure 13 suggests that thermal buoyancy has also similar effects as solutal buoyancy on $\overline{Nu}$ and $\overline{Sh}$ for Case-IA and Case-IB. Note that for $B>0$, buoyancy activities intensify inside the cavity by increasing either thermal or solutal gradients. However, thermal buoyancy has reverse effects on $\overline{Nu}$ and $\overline{Sh}$ to those for the solutal buoyancy for the Case-IIA and Case-IIB. Basically under competing B, the tendency of thermal/solutal buoyancy is to bring Case-IIA to a statically stable/unstable state and Case-IIB to a statically unstable/stable state. Therefore beyond a certain value of B, near -1 (not equal to -1) as $\mathrm{Le}=\mathrm{Sc}/\mathrm{Pr}\neq 1$, the thermal/solutal buoyancy is overwhelmed by solutal/thermal buoyancy owing to either conduction or convection-controlled situation for each of two Cases IIA and IIB at small Re.

It can be seen from Fig. 14 that as Re increases, both $\overline{Nu}$ and $\overline{Sh}$ increase for both statically stable and unstable stratifications. The convective activities are enhanced by increasing Re. Furthermore it is clear from Fig. 14(*a*) that for given Re, $\overline{Nu}$ and $\overline{Sh}$ under opposing buoyancy forces are more than the corresponding values for the case under cooperating buoyancy forces.

From Figs. 12 and 13, it is clear that the heat flux is more than the mass flux. This is due to the fact that for the fluid we have considered, $D>\alpha$. Hence the thermal boundary layer is thinner than the solutal boundary layer so that the heat flux is more than the mass flux.

4 Conclusions

A numerical study of combined heat and mass transfer in a square cavity with a sliding top lid in the presence of vertical temperature and concentration gradients is presented. Four flow configurations are classified depending on positive/negative value of Gr_C and Gr_T. The influence of solutal buoyancy and thermal

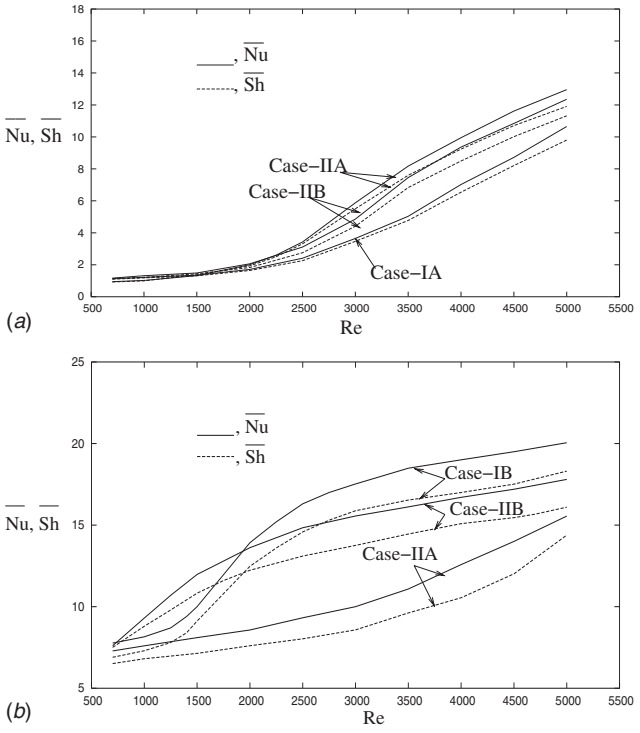

Fig. 14 The average Nusselt number ($\overline{Nu}$) and Sherwood number ($\overline{Sh}$) versus Reynolds number: (*a*) stable stratification (Case-IA ($B=5$, $Gr_T=-10^6$), Case-IIA ($B=-0.2$, $Gr_T=-5\times10^6$) and Case-IIB ($B=-5$, $Gr_T=10^6$)) and (*b*) unstable stratification (Case-IB ($B=5$, $Gr_T=10^6$), Case-IIA ($B=-5$, $Gr_T=-10^6$) and Case-IIB ($B=-0.2$, $Gr_T=5\times10^6$))

buoyancy on flow configurations is studied in two situations: (a) in the presence of top lid motion from left to right and (b) in the absence of top lid motion. Effect of shearing of the top lid is also investigated in situation (a). Based on this, we conclude the following in situation (a):

(i) Under the cooperating buoyancy forces, the statically stable/unstable configuration remains statically stable/unstable by increasing thermal and solutal gradients. However, under opposing buoyancy forces, the stable and unstable configurations with no solutal/thermal gradient are converted to unstable and stable states, respectively, by imposing nonzero solutal/thermal gradient.
(ii) The studied four flow configurations can be brought to two main flow configurations, viz., statically stable and unstable stratifications in thermosolutal convection at small Re.
(iii) Under opposing buoyancy forces, more energy and species can be carried away from the top/bottom lid toward the bottom/top lid even at very small Re for values of B near -1. However, for $\mathrm{Le}=\mathrm{Sc}/\mathrm{Pr}=1$ and $B=-1$, the buoyancy terms in momentum equation vanish identically. This implies that the buoyancy forces have no effect on the flow, which will then consist of a single eddy due to shearing of the top lid only.
(iv) The Reynolds number has significant effect on the flow inside the cavity for both statically stable and unstable configurations.
(v) The average rates of heat and mass transfer increase for the case of unstable stratification whereas they decrease for stable stratification with an increase in thermal/solutal gradients for both $B>0$ and $B<0$. However, the average rates of heat and mass transfer increase as Re increases for both stable and unstable stratifications.

Detailed numerical calculations reveal that in the absence of top lid motion (situation (b)), the flow characteristics vary significantly from those of situation (a) in the following cases only.

(i) The case when the fluid at the top lid has higher temperature and concentration compared to those of the bottom lid: for a value of B (say, $B=-5$), in the presence of top lid motion there are two well-mixed zones. However, in the absence of lid motion there is only one well-mixed zone having similar characteristics as those of the lower zone in the presence of lid motion.
(ii) The case when the temperature and concentration of the bottom lid are higher than those of the top lid: for a value of B (say, $B=-0.2$), both the temperature and concentration rise in the two well-mixed zones in the absence of lid motion as compared with the corresponding values in the presence of lid motion.
(iii) The case when the fluid at the top lid has higher concentration with lower temperature than those at the bottom lid: in the absence of lid motion, the concentration in both the well-mixed zones decreases whereas temperature increases in comparison with the corresponding values (of $B>1$ and $B<1$) in the presence of lid motion.

Acknowledgment

The authors thank the referees for their valuable comments, which enabled them to present an improved version of the paper. One of the authors (A.S.G) acknowledges financial assistance of Indian National Science Academy for carrying out this work.

Nomenclature

B = buoyancy forces ratio, $\beta_C(C_0^*-C_\infty^*)/\beta_T(T_0-T_\infty)$
C = nondimensional vapor concentration, $(C^*-C_\infty^*)/(C_0^*-C_\infty^*)$
Gr_C = solutal Grashof number, $g\beta_C(C_0^*-C_\infty^*)L^3/\nu^2$
Gr_T = thermal Grashof number, $g\beta_T(T_0-T_\infty)L^3/\nu^2$
Gr_T^N = thermal Grashof number in natural convection, $g\beta_T|T_0-T_\infty|L^3/\nu^2$
$\overline{\mathrm{Nu}}$ = area-averaged Nusselt number, $\int_0^1(-(\partial\theta/\partial y)_{\mathrm{lid}})dx$
p = nondimensionless pressure, $p^*/\rho U^2$
Pr = Prandtl number, ν/α
Re = Reynolds number, UL/ν
Sc = Schmidt number, ν/D
$\overline{\mathrm{Sh}}$ = area-averaged Sherwood number, $\int_0^1(-(\partial C/\partial y)_{\mathrm{lid}})dx$
T = dimensional temperature (K)

Greek Symbols

β_C = coefficient of solute expansion (K^{-1})
β_T = coefficient of thermal expansion (K^{-1})
Ψ = stream function, $u=\delta\Psi/\delta y$
θ = dimensionless temperature, $(T-T_\infty)/(T_0-T_\infty)$

Subscripts

0 = value at the bottom lid
∞ = value at the top lid
max = maximum value
min = minimum value

References

[1] Gebhart, B., and Pera, L., 1971, "The Nature of Vertical Natural Convection Flows Resulting From the Combined Buoyancy Effect of Thermal and Mass Diffusion," Int. J. Heat Mass Transfer, **14**, pp. 2025–2050.
[2] Turner, J. S., 1974, "Double-Diffusive Phenomena," Annu. Rev. Fluid Mech., **6**, pp. 37–56.
[3] Moallemi, M. K., and Jang, K. S., 1992, "Prandtl Number Effects on Laminar Mixed Convection Heat Transfer in a Lid-Driven Cavity," Int. J. Heat Mass Transfer, **35**, pp. 1881–1892.
[4] Iwatsu, R., Hyun, J. M., and Kuwahara, K., 1993, "Mixed Convection in a Driven Cavity With Stable Vertical Temperature Gradient," Int. J. Heat Mass Transfer, **36**(6), pp. 1601–1608.
[5] Monsour, R. B., and Viskanta, R., 1994, "Shear-Opposed Mixed-Convection Flow and Heat Transfer In a Narrow, Vertical Cavity," Int. J. Heat Fluid Flow, **15**(6), pp. 462–469.
[6] Alleborn, N., Raszillier, H., and Durst, F., 1999, "Lid-Driven Cavity With Heat and Mass Transport," Int. J. Heat Mass Transfer, **42**, pp. 833–853.
[7] Al-Amiri, A. M., Khanafer, K. M., and Pop, I., 2007, "Numerical Simulation of Combined Thermal and Mass Transport in a Square Lid-Driven Cavity," Int. J. Therm. Sci., **46**(7), pp. 662–671.
[8] Patankar, S. V., 1980, *Numerical Heat Transfer and Fluid Flow*, Hemisphere, New York.
[9] Leonard, B. P., 1979, "A Stable and Accurate Convective Modelling Procedure Based on Quadratic Upstream Interpolation," Comput. Methods Appl. Mech. Eng., **19**, pp. 59–98.
[10] Bhattacharyya, S., Maiti, D. K., and Dhinakaran, S., 2006, "Influence of Buoyancy on Vortex Shedding and Heat Transfer From a Square Cylinder in Wall Proximity," Numer. Heat Transfer, Part A, **50**, pp. 585–606.
[11] Janssen, R. J. A., and Henkes, R. A. W. M., 1993, "Accuracy of Finite Volume Discretizations for the Bifurcating Natural-Convection Flow in a Square Cavity," Numer. Heat Transfer, Part B, **24**, pp. 191–207.
[12] Agarwal, R. K., 1981, "A Third-Order-Accurate Upwind Scheme for Navier-Stokes Solutions at High Reynolds Numbers," AIAA Paper No. 81–0112.
[13] Turner, J. S., 1979, *Buoyancy Effects in Fluids*, Cambridge University Press, Cambridge.

Effect of Nonuniform Stack Compression on Proton Exchange Membrane Fuel Cell Temperature Distributions

N. Fekrazad

T. L. Bergman[1]
e-mail: tberg@engr.uconn.edu

Department of Mechanical Engineering,
The University of Connecticut,
Storrs, CT 06268

A three-dimensional model is used to predict the power output and internal temperature distribution of a small proton exchange membrane fuel cell stack. Of particular interest is the influence of nonuniform stack compression on thermal conditions inside the fuel cell. A dimensionless membrane isothermality is correlated with a dimensionless compressive load distribution, suggesting that similar relationships may be developed for other fuel cell geometries. Fuel cell performance, in terms of minimizing temperature variations inside the device, can be enhanced by application of nonuniform stack compression.
[DOI: 10.1115/1.2970066]

Keywords: fuel cell, contact resistance, temperature distribution

Introduction

Computational models of fuel cell behavior can be used to predict the influence of various parameters that are difficult to measure. Information gleaned from the predictions might assist in the design and optimization of the fuel cell stack geometry and operating conditions. A recent review of fuel cell modeling is provided elsewhere [1] and will not be repeated here.

A topic that has received little attention is the effect of the compressive force used to assemble a proton exchange membrane (PEM) fuel cell stack that is composed of many individual fuel cells sandwiched in series electrically. For example, one would expect the thermal and electrical contact resistances that evolve between various planar components of the stack to be sensitive to the compressive force applied to the stack. In addition, the transport properties within the porous gas diffusion layers (GDLs) might change in response to the compressive force applied to these delicate porous materials. Thermal and/or electrical contact resistances relevant to the bipolar plate (BP)-GDL interface have been measured recently as a function of the applied compressive forces [2–4].The effect of compressive loading on fuel cell stack power output has been discussed to a limited degree [4–8].

Building upon recently reported contact resistance and transport property measurements of relevant fuel cell materials [2], the influence of different compressive loads on (i) the measured and predicted fuel cell power output, (ii) the predicted maximum temperatures that develop within the membrane electrode assemblies (MEAs), and (iii) the predicted temperature distributions within the membranes has been reported [9,10]. Studies based on a 2D modeling approach [10] have shown that thermal conditions within the fuel cell membrane may be made more uniform through application of optimal clamping pressures to the fuel cell stack. Enhanced thermal uniformity (and, in turn, enhanced uniformity of humidity conditions within the fuel cell and proton concentrations in the membrane) is desirable since it is expected to increase the durability of the membranes used in PEM fuel cells, leading to decreased cost and increased service life of such devices. In particular, increased uniformity of internal conditions may reduce formation of hot spots within the membranes, which would, in turn, promote local membrane humidification and subsequently reduce or eliminate membrane damage. Structural damage to any single membrane within an entire stack, such as the formation of small pinholes, allows the mixing of the cathode and anode gases and promotes the gradual deterioration of fuel cell performance [11–13].

In this study, an existing 2D model [10] is extended to include 3D effects in order to account for (for example) the influence of feed gas stoichiometry, defined as the ratio of the amount of gas supplied to the fuel cell to the amount of gas consumed in the electrochemical reactions within the fuel cell [14]. However, the unique aspect is to consider a new approach to fuel cell stack assembly, specifically, to simulate the fuel cell's response to *spatially nonuniform* compressive loads. As will become evident, the results suggest that such an approach could be exploited to promote more isothermal conditions within a fuel cell, while having negligible impact on the power output of the fuel cell. Correlation of a dimensionless membrane isothermality to a dimensionless clamping pressure distribution is achieved, suggesting that similar fuel cell stack geometry-specific relationships could be developed to assist in the realization of more durable fuel cells. Nonuniform pressure distributions applied to fuel cell stack components would be trivial to implement in practice and could be done at no cost.

Mathematical Model

A section of a PEM fuel cell, arbitrarily showing three anode (H_2) channels and three cathode (Air) channels, is illustrated in Fig. 1(*a*). Additional channels would typically exist in the $\pm y$ directions. During operation, the water vapor-saturated hydrogen that is fed to the anode channels is partially transferred through the top GDL (Fig. 1(*b*)) to the adjacent catalyst layer where it is decomposed into electrons and protons by an electrochemical reaction. The electrons flow through the electrically conducting bipolar plates to an external load (not shown) to provide electrical power. Meanwhile, protons migrate through the non-electrically-conducting membrane toward the cathode side of the fuel cell. The oxygen contained in the air of the cathode channels is transferred through the bottom GDL upward to the adjacent catalyst layer and combines with the protons from the membrane and electrons from the external load to form liquid water.

A fuel cell *stack* consists of many individual fuel cells sandwiched together in series. Therefore, within a stack with coflow-

[1]Corresponding author.

Contributed by the Heat Transfer Division of ASME for publication in the JOURNAL OF HEAT TRANSFER. Manuscript received August 23, 2007; final manuscript received June 19, 2008; published September 19, 2008. Review conducted by Ben Q. Li.

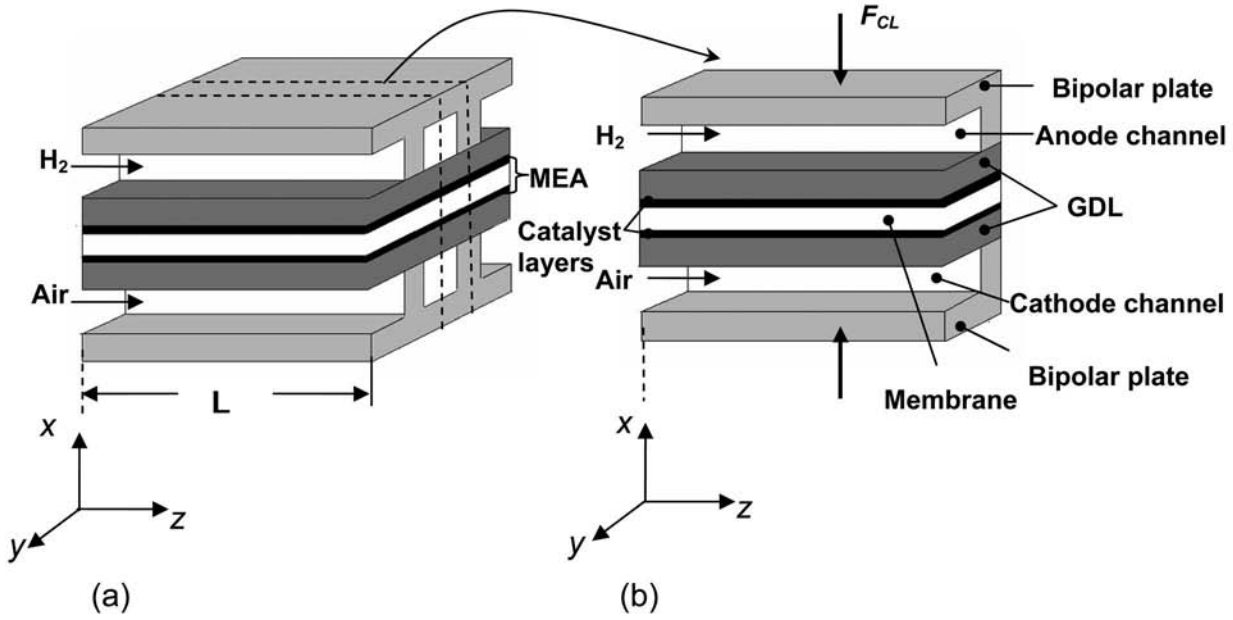

Fig. 1 Schematic of (*a*) a repeating section of the fuel cell stack and (*b*) the computational domain

ing gas streams, the top boundary of Fig. 1(*a*) corresponds to the centerline of a bipolar plate equipped with anode gas channels on its bottom side (shown) and cathode channels on its top side (not shown) and is characterized by periodic conditions in the x-direction. For coflowing fuel (H_2) and oxidant (air), x-z planes of symmetry also occur in the y-direction, and a magnification of the dashed control volume of Fig. 1(*a*) (that is subject to symmetry boundary conditions and extends from the centerline of a flow channel to the centerline of a bipolar plate land) is shown in Fig. 1(*b*).

The computational domain of Fig. 1(*b*) is selected to take advantage of both symmetry and periodicity. For very high stoichiometric ratios (gas flow rates) and fully developed conditions, transport occurs across the MEA (which consists of the membrane and thin catalyst layers) and variability also occurs in the y-direction. However, variation in the z-direction would be small. Hence, the 3D response at very high stoichiometry is expected to be similar to the response that would be predicted using a 2D (x,y) modeling approach. Using 2D modeling [10] the effect of various *uniform* clamping forces (Fig. 1(*b*)) has been considered. In this study, 3D effects that emerge due to (i) the fuel cell being operated at low stoichiometric ratios, (ii) the gases in the channels experiencing entrance effects, and (iii) *spatially nonuniform* clamping forces along the channel length (z-direction) are considered. Counterflowing or cross-flowing anode and cathode gases are not considered here, but could be investigated with appropriate revisions to the model.

To develop a tractable 3D model, it is necessary to implement a number of assumptions beyond those pertaining to the periodicity of the stack geometry. Consistent with the 2D model described in detail elsewhere [9,10], the following assumptions are made. First, steady-state behavior is assumed. Although transient effects, such as high frequency fluctuations due to the motion of water droplets [10], may affect the durability of the membrane, such events are random and cannot be predicted with any model. Air and hydrogen obey the ideal gas law and are assumed to be fully saturated with water vapor at the channel inlets. All flows are assumed to be laminar because of the small dimensions of the gas channels (0.5×0.8 mm^2) and the low gas velocities. Water is assumed to exist in the liquid and vapor phases within the entire MEA, and in the vapor phase within other regions of the computational domain (excluding the impermeable bipolar plates). The proton concentration within the membrane is assumed to be spatially uniform and equal to the distribution of sulfonic acid groups that are embedded in the membrane's architecture. Variable properties are accounted for, except as noted in Ref. [10]. Despite not accounting for detailed two-phase flow effects, the 2D model [10] that is extended to the 3D model in this study is capable of predicting the experimentally determined influence of various uniform compressive forces that are applied to a single MEA fuel cell operating at high stoichiometry on the fuel cell power output as well as the predictions of the results reported by other authors. The 3D model reported here is based on use of Sigracet® GDLs with measured properties and contact resistances as reported in Ref. [2]. As noted in the previous 2D modeling effort [10], the variation of the BP-GDL electrical contact resistance is the dominant factor in changing the fuel cell power output at various uniform compressive loads.

First, the 3D model is generated by extending the extensive set of 2D governing equations [10] to the appropriate 3D forms in a straightforward manner. The governing equations describe the conservation of mass, momentum, thermal energy, ionic charge, electronic charge, and species. They are very lengthy and cannot be repeated here due to space limitation. Boundary and coupling conditions are also very lengthy and are straightforward extensions of the extensive set of conditions used in the 2D model and reported in detail elsewhere [10]. Second, the 3D equations (extensions of the existing 2D equations) are then linked to new 3D equations applied to the gas channels as follows.

Gas Channel Governing Equation. Neither evaporation nor condensation of water is accounted for within the anode or cathode flow channels (the water phase change occurs within the MEA and is accounted for there). However, conditions do change within the gas channels in the z-direction in response to flow development and the phase change processes. For example, the total mass flux at the individual channel inlets is not the same as the total mass flux at the individual channel outlets because of the exchange of mass associated with the electrochemical processes and, specifically, the exchange of water with the adjoining GDLs. In the absence of phase change *within* the channels, the 3D mass conservation equation is

$$\frac{\partial}{\partial x}(\rho u) + \frac{\partial}{\partial y}(\rho v) + \frac{\partial}{\partial z}(\rho w) = 0 \quad (1)$$

The channel flow field is obtained by solving the steady-state Navier–Stokes equations, which express the momentum conservation as

$$u\frac{\partial u}{\partial x} + v\frac{\partial u}{\partial y} + w\frac{\partial u}{\partial z} = -\frac{1}{\rho}\frac{\partial p}{\partial x} + \nu_f\left(\frac{\partial^2 u}{\partial x^2} + \frac{\partial^2 u}{\partial y^2} + \frac{\partial^2 u}{\partial z^2}\right) \quad (2)$$

$$u\frac{\partial v}{\partial x} + v\frac{\partial v}{\partial y} + w\frac{\partial v}{\partial z} = -\frac{1}{\rho}\frac{\partial p}{\partial y} + \nu_f\left(\frac{\partial^2 v}{\partial x^2} + \frac{\partial^2 v}{\partial y^2} + \frac{\partial^2 v}{\partial z^2}\right) \quad (3)$$

$$u\frac{\partial w}{\partial x} + v\frac{\partial w}{\partial y} + w\frac{\partial w}{\partial z} = -\frac{1}{\rho}\frac{\partial p}{\partial z} + \nu_f\left(\frac{\partial^2 w}{\partial x^2} + \frac{\partial^2 w}{\partial y^2} + \frac{\partial^2 w}{\partial z^2}\right) \quad (4)$$

where $\nu_f = x_{O_2}\nu_{O_2} + x_{N_2}\nu_{N_2} + x_{H_2O}\nu_{H_2O}$ with the individual species viscosities evaluated based on the local temperature.

The temperature distribution in the channels is obtained by solving the energy equation

$$\rho c_p\left(u\frac{\partial T}{\partial x} + v\frac{\partial T}{\partial y} + w\frac{\partial T}{\partial z}\right) = k_f\left(\frac{\partial^2 T}{\partial x^2} + \frac{\partial^2 T}{\partial y^2} + \frac{\partial^2 T}{\partial z^2}\right) \quad (5)$$

where $k_f = x_{O_2}k_{O_2} + x_{N_2}k_{N_2} + x_{H_2O}k_{H_2O}$ and the species thermal conductivities are evaluated based on the local temperature. No chemical reactions occur in the flow channels, and the species distributions evolve in response to the combined effects of diffusion and advection as follows:

$$u\left(\frac{\partial x_i}{\partial x}\right) + v\left(\frac{\partial x_i}{\partial y}\right) + w\left(\frac{\partial x_i}{\partial z}\right) = D_i\left(\frac{\partial^2 x_i}{\partial x^2} + \frac{\partial^2 x_i}{\partial y^2} + \frac{\partial^2 x_i}{\partial z^2}\right) \quad (6)$$

where $D_i = D_{0,i}(T/T_0)^{3/2}(p_0/p)$ using values of $D_{0,i}$, T_0, and p_0 reported elsewhere [15].

Boundary and Coupling Conditions. Boundary and coupling conditions are applied to solve the governing equations and determine $T(x,y,z)$, $\varphi_i(x,y,z)$, $\varphi_e(x,y,z)$, $x_{O_2}(x,y,z)$, $x_{H_2}(x,y,z)$, $x_W(x,y,z)$, $u(x,y,z)$, $v(x,y,z)$, $w(x,y,z)$, and $p(x,y,z)$ throughout the entire computational domain.

For the mass conservation and momentum equations, the velocities of the gases at the inlets of the anode and the cathode channels are prescribed ($u=v=0, w=w_{in}$). At the outlets of the flow channels, the pressure is prescribed using values that are consistent with typical operating conditions within fuel cells ($2 \le p(x,y,z=L) \le 3$ bars). New boundary and coupling conditions are developed to link Eqs. (1)–(6) with the 3D extensions of the existing 2D model equations. Specifically, at the interface between the anode and cathode flow channels and adjacent GDLs, the boundary conditions for the Navier–Stokes equations (2)–(4) are specified such that the mass flow rate and momentum transfer across the GDL-channel interface is conserved. The boundary condition for Darcy's equation that is applied within the GDLs [10] is represented by pressure continuity across the interface. No-slip impermeable conditions are applied at the gas-BP and GDL-BP interfaces. The vertical centerline of each flow channel is subject to no shear conditions with zero mass flux, reflecting the symmetry of the problem.

For temperature and species conservation equations, the inlet values of the anode and the cathode flow channels are prescribed; $T(x,y,z=0)=T_{in}, x_i(x,y,z=0)=x_{i,in}$. At the channel outlets, the gradients of the temperature and the species concentrations are assumed to be zero. Temperature and species variables, and their associated fluxes, are continuous across the interface between the channels and GDLs. The bipolar plates are impermeable but thermally and electrically conducting. The centerline of the flow channel is characterized by zero-flux conditions, reflecting the symmetry of the problem.

To mimic the behavior of the entire stack, periodic thermal conditions (identical local temperatures and local heat fluxes in the x-direction) are applied at the top and bottom boundaries of the control volume shown in Fig. 1(*b*). Zero velocity and zero temperature, species, and ionic and electronic potential gradients are specified at the symmetry x-z planes indicated by dashed lines in Fig. 1(*a*). The vertical surfaces at the inlet and outlet of the fuel cell are insulated from the thermal, electrical, and ionic perspectives. All predictions are based on a cell voltage (voltage difference between the top and bottom of the computational domain) of 0.6 V, which is a typical operating condition.

Clamping Pressure Influence on Contact Resistances and GDL Permeability. Extensive discussion regarding the effect of thermal and electrical contact resistances at the interface between the GDLs and the BPs on fuel cell behavior can be found in Ref. [10]. Specifically, the sensitivity of (i) the thermal and electrical contact resistances and (ii) the GDL permeability to the compressive pressure for different GDLs have been recently reported, and the following expressions are curve fits to the Sigracet®-based experimental data of Ref. [2].

$$R_{T,c} = (-2.1p_{cl}^2 + 86p_{cl} + 407)^{-1} \quad (7)$$

$$R_{e,c} = (-2.1 \times 10^3 p_{cl}^2 + 9.7 \times 10^4 p_{cl} + 10^5)^{-1} \quad (8)$$

Units of the various constants are not included in the preceding expressions but are consistent in order to use, as input, the clamping pressure in bars, yielding contact resistances with the units reported in the Nomenclature. A curve fit to the reported data for the in-plane GDL permeability is

$$K_p = -2 \times 10^{-13} p_{cl}^2 - 9 \times 10^{-13} p_{cl} + 2.1 \times 10^{-11} \quad (9)$$

while the ratio of the in-plane to the through-plane permeability is 66 [2].

Numerical Solver. The governing equations, subject to the numerous boundary and coupling conditions, were solved using a finite element method. In the solution of the 3D equations applied to the flow channels, a combination of second-order elements for the velocity components and linear elements for the pressure (the default element for the incompressible Navier–Stokes application mode in the commercial code FEMLAB) is used. Due to the large number of coupled equations that needs to be solved, the total number of elements was limited to approximately 32,000. A grid-size sensitivity study was performed by reducing the number of elements by approximately 10% (Grid A), 20% (Grid B), and 40% (Grid C) from values associated with the finest mesh. Deviations in predicted local temperatures (relative to predictions using the finest mesh) are 0.006 K for Grid A, 0.03 K for Grid B, and 0.08 K for Grid C. The predicted fuel cell power output for typical cases agreed to within six figures of the predictions associated with the finest grid for Grid A, and the discrepancy increased to 0.04% and 0.21% agreement for Grids B and C, respectively. Hence, the results reported here, which are all generated with the finest mesh, are considered to be grid-size independent.

Quantitatively, the results were generated using $15 \times 18 \times 20$ elements in each BP, $10 \times 10 \times 20$ elements in each gas flow channel, $10 \times 18 \times 20$ elements in each GDL, $10 \times 18 \times 20$ elements in each catalyst layer, and $8 \times 18 \times 20$ elements in the membrane in x-, y-, and z-direction, respectively. The required CPU time on a 3 GHz Pentium 4 computer was approximately 2 h per simulation when predictions associated with similar operating conditions were used as initial conditions for the new case of interest. Predictions based on arbitrary initial conditions typically require approximately 10 h CPU time to converge.

Results and Discussion

The results were obtained using the thermophysical property values reported in Table 2 of Ref. [10] along with the base case parameters listed in Table 1. Note that the fuel cell is short relative to most PEM devices. Specification of a small length is necessary

Table 1 Base case parameters and properties

Parameter	Value
Channel depth (x-direction)	0.5 mm
Channel half-width (y-direction)	0.4 mm
Channel length (z-direction)	10 mm
BP land half-width (y-direction)	0.3 mm
BP half-thickness (x-direction)	1.5 mm
Air inlet temperature	353 K
Air outlet pressure	3 bars
Oxygen/nitrogen ratio in air at inlet	0.21/0.79
Hydrogen inlet temperature	353 K
Hydrogen outlet pressure	3 bars
Oxygen stoichiometric ratio	2.08
Air to hydrogen stoichiometric ratio	1.5

due to computational constraints associated with the large number of governing equations that are included in the physical description of the device, and the need to report grid-independent predictions. As a result, temperature differences are quite small. Nonetheless, the predictions are useful in that they suggest a novel way to potentially improve the uniformity of thermal and humidity conditions regardless of the size of the fuel cell, as will become evident.

Base Case 3D Predictions: Uniform Clamping Pressure. The model was checked by comparing the 3D predictions to the 2D predictions [10] for limiting case conditions. (Note that, in turn, the benchmark 2D predictions were validated by comparison to experimental results in terms of the sensitivity of the predicted and measured fuel cell power output to the applied uniform compressive loading of the cell.)

To facilitate discussion, a magnified view (not to scale) of the membrane of Fig. 1(b) is shown in Fig. 2 in which locations associated with subsequent discussion are identified. For example, to consider typical membrane temperatures, results will be reported for the shaded *interrogation plane* that is located midway through the thickness of the membrane ($x=t/2$).

The effect of stoichiometry on the predicted temperature differences ($\Delta T \equiv T_{\max} - T_{\min}$) that evolve in the interrogation plane of Fig. 2 for uniform clamping pressures of $p_{cl}=1$ bar and 3 bars is shown in Figs. 3 and 4.

In Fig. 3, the solid lines represent ΔT_y at three different streamwise locations within the interrogation plane of the membrane (see Fig. 2). The two dashed lines of Fig. 3 correspond to the 2D predictions [10]. As evident in Figs. 3(a) and 3(b), the 2D and 3D predictions are in relatively good agreement at the highest stoichiometric ratios, as expected since the 2D results are, in effect, associated with infinite gas flow rates. The small deviation between the 2D and 3D predictions evident at the highest stoichiometric ratio may be attributed to, for example, the developing flows in the channels that are captured by the 3D simulation. Regardless of the stoichiometry, the 2D and 3D predictions are in remarkable agreement at $z=L/2$ (middle). This good agreement is

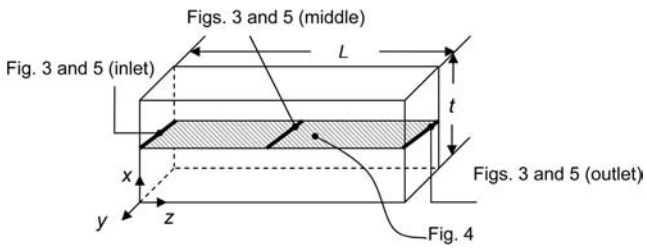

Fig. 2 Magnified view of the membrane with a shaded interrogation plane

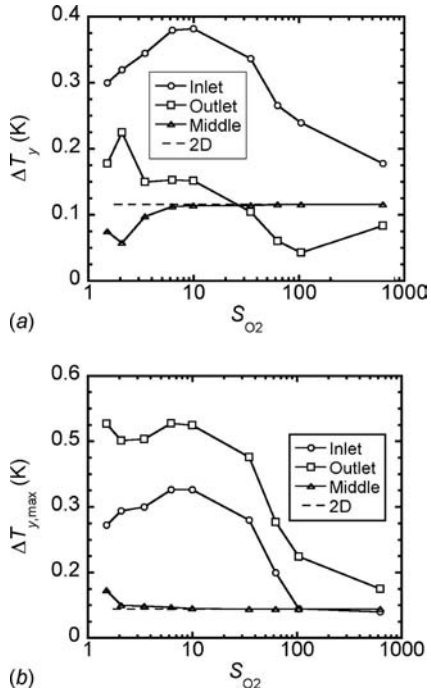

Fig. 3 Temperature difference in the y-direction at different locations within the membrane as a function of O_2 stoichiometric ratio with uniform clamping pressure. (a) $p_{cl}=1$ bar and (b) $p_{cl}=3$ bars.

partially explained by the fact that the 2D model corresponds to fully developed channel flow conditions, and the inlet gas conditions of the 3D model are identical to the mean conditions specified in the 2D model. Hence, heat and mass transfer rates at the flow channel-GDL interface, near the inlet ($z=0$) of the 3D channel, will exceed those predicted with the 2D model (due to entrance effects). On the other hand, at the outlet ($z=L$) of the 3D channel, heat and mass transfer rates will be less than those predicted with the 2D model due to the streamwise variation of the gas temperature and humidity. Therefore, at some intermediate distance along the channel, these effects will offset one another, leading to relatively good agreement between the two models. Note that at $p_{cl}=1$ bar (Fig. 3(a)) the maximum temperature difference in the y-direction is located at the inlet, while $\Delta T_{y,\max}$ switches to the channel outlet as the uniform clamping pressure is increased to 3 bars (Fig. 3(b)). This behavior will be exploited later.

Maximum temperature differences in the z-direction (these values are determined by first finding a set of data containing the

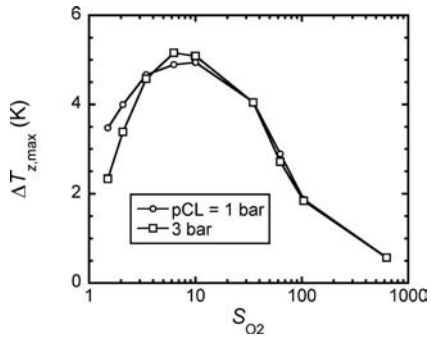

Fig. 4 Maximum temperature differences in the z-direction (along lines of constant y in the interrogation plane) as a function of O_2 stoichiometric ratio for uniform $p_{cl}=1$ bar and 3 bars

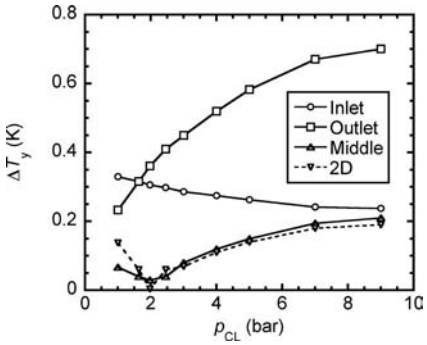

Fig. 5 Temperature differences in the *y*-direction at different locations along the flow channels as a function of uniform clamping pressure, $S_{O_2}=2.08$

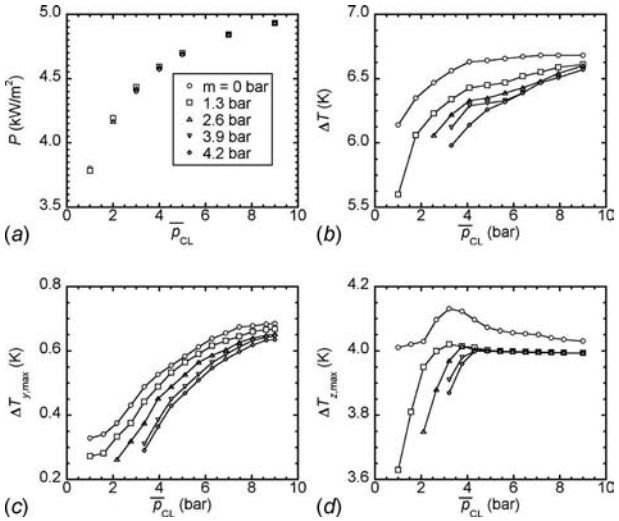

Fig. 6 (*a*) Power density, (*b*) difference between maximum and minimum temperatures of the membrane, (*c*) maximum temperature difference along the membrane (*y*-direction), and (*d*) maximum temperature difference along the membrane (*z*-direction) as a function of the nonuniform clamping pressure distribution. Gas pressure is $p=3$ bars.

maximum temperature differences along *each* line of constant y within the membrane, then comparing these values and reporting the largest single value in the data set) are shown in Fig. 4. At the highest stoichiometric ratios, variations in the z-direction are expected to be small since streamwise advection dominates diffusion in the gas channels. Therefore, $\Delta T_{z,\max}$ is expected to approach zero as the stoichiometric ratio increases, and this trend is evident for both clamping pressures. Conversely, at zero stoichiometric ratio the fuel cell cannot produce power and $\Delta T_{z,\max}$ must be zero. This asymptotic behavior is also evident in Fig. 4. Overall temperature differences in the z-direction are approximately 5°C at moderate stoichiometric ratios and are significantly larger than the temperature differences spanning across the membrane in the y-direction, as reported in Fig. 3.

Base Case 3D Predictions: Nonuniform Clamping Pressure. Thermal uniformity within the membrane is desirable because high temperatures or large temperature gradients can cause damage. Uniform temperatures will correspond to enhanced uniformity of the moisture distribution within the fuel cell, which is also desirable to promote fuel cell durability and reduces the need for detailed two-phase flow and heat transfer modeling [4,10]. For example, maximum local temperatures must be kept below the softening temperature of a Nafion® membrane, 119°C [13], while large spatial temperature differences may lead to highly nonuniform moisture conditions and, in turn, local drying and burnout of the membrane. In addition to temperature and humidity differences, high thermal or moisture gradients may also adversely affect membrane durability. In general, spatial gradients in the spanwise (y) direction exceed those in the flow (z) direction. In Ref. [10], an optimum uniform clamping pressure ($p_{\mathrm{cl}}\approx 2$ bars) to maximize thermal uniformity was found to exist for a very wide range of operating conditions and fuel cell geometries for various GDL materials. However, that conclusion, based on 2D modeling, may be valid only at high stoichiometric ratios for the 3D fuel cell of Fig. 1.

The effect of various uniform ($m=0$) clamping pressures on temperature differences ($\Delta T \equiv T_{\max}-T_{\min}$) in the y-direction at different locations along the flow channels (see Fig. 2) is reported in Fig. 5. Note that the particular stoichiometric ratio used ($S_{O_2}=2.08$) is somewhat arbitrary but typical of fuel cell operating conditions. The dashed line in Fig. 5 corresponds to the 2D results associated with infinite stoichiometry [10]. As evident, the temperature variations in the y-direction are very sensitive to the clamping pressure and the z-location of interrogation. At $z=L/2$ (middle), the value of ΔT_y is minimized at $p_{\mathrm{cl}}\approx 2$ bars and exhibits a sensitivity to the clamping pressure that is in remarkable agreement with the 2D results. At the inlet ($z=0$) and outlet ($z=L$), temperature differences within the membrane are minimized at high and low clamping pressures, respectively. Regardless of the clamping pressure, temperature differences at $z=L/2$ are always smaller than temperature differences at the entrance or exit of the flow channels.

The results of Fig. 5 suggest that *if* small clamping pressures are applied near the channel outlets and large clamping pressures are applied in the vicinity of the channel inlet, reduced temperature variations within the membrane might be achieved. Hence, application of nonuniform clamping pressure distributions is now considered.

In the following discussion, the local clamping pressure is assumed to have a linear distribution described by

$$p_{\mathrm{cl}}(m,z) = \bar{p}_{\mathrm{cl}} + m\left(\frac{1}{2} - \frac{z}{L}\right) \tag{10}$$

Note that large values of m are avoided to ensure specification of a compressive load at all z-locations. Such a distribution would result if the compressible materials (GDLs and MEAs) within the fuel cell stack exhibit elastic behavior and different compressive forces are applied along the fuel cell in the z-direction. In practice, a fuel cell stack is compressed by a series of all-threaded rods equipped with springs and/or Belville washers, and application of a linear clamping pressure distribution is readily achievable.

Pertinent results using various clamping pressure distributions are shown in Fig. 6. The effect of $\bar{p}_{\mathrm{cl}}$ on the fuel cell's power density over the entire range of nonuniformity ($m=0$ bar, 1.3 bars, 2.6 bars, 3.9 bars, and 4.2 bars) is shown in Fig. 6(*a*). As evident, the power output increases with the *average* clamping pressure but application of a *nonuniform* clamping pressure has a negligible impact. The results reported elsewhere [16] for the same conditions show that local maximum MEA temperatures (at the interface between the cathode catalyst layer and the membrane) are also unaffected by the nonuniformity of the clamping pressure distribution but increase with the average clamping pressure. Hence, nonuniformity of the clamping pressure has neither a beneficial nor a detrimental effect on either the power output or maximum membrane temperatures for the fuel cell of Fig. 1 operating under the conditions considered here.

Thermal uniformity within the MEA is, however, beneficially affected by application of nonuniform clamping pressures, and the results are shown Fig. 6(*b*). Note that ΔT represents the difference between the absolute maximum and minimum temperatures any-

Table 2 Slope of the clamping pressure distribution, *m* (bar), for various average clamping and gas pressures for Fig. 7

p(bar)	$\bar{p}_{cl}$ (bar) 1	2	3	4	5	7	9
2	1.1, 1.3	1.3, 2.6	2.6, 3.9 4.2	2.6, 3.9, 4.2	3.9, 4.2	1.3, 2.6, 3.9, 4.2	1.3, 2.6, 3.9, 4.2
2.1	1.3	2.6, 3.0, 3.9	1.3, 2.6, 3.9, 4.2	1.3, 2.6, 3.9	2.6	1.3, 2.6	2.6, 4.2
2.25	1.3	1.3, 2.6, 3.0, 3.9	1.3, 2.6, 3.9, 4.2	2.6, 3.9, 4.2	2.6, 4.2	1.3, 2.6	-
2.5	1.3	1.3, 2.6, 3.0	1.3, 2.6, 3.9, 4.2	1.3, 2.6, 3.9, 4.2	2.6	1.3, 3.9	-
3	1.1, 1.3, 1.5	1.3, 2.6, 3.0	1.3, 2.6, 3.9, 4.2	1.3, 2.6, 3.9, 4.2	1.3, 2.6, 3.9, 4.2	1.3, 2.6, 3.9, 4.2	1.3, 2.6, 3.9, 4.2

where in the MEA, and the locations of the maximum and minimum values change as the clamping pressure and its distribution are adjusted [9,16]. Thermal uniformity is enhanced because minimum local MEA temperatures (at the interface between the anode-side GDL and the adjacent catalyst layer) increase as nonuniform clamping pressure distributions are applied. Humidity and proton concentration conditions would, likewise, be made more uniform. The values of $\Delta T_{y,\max}$ and $\Delta T_{z,\max}$, shown in Figs. 6(*c*) and 6(*d*) (the temperature differences are defined in the same manner as in the discussion of Figs. 3 and 4), are in general reduced with incorporation of the nonuniform clamping pressure scheme, presumably reducing stresses within the membrane and enhancing fuel cell durability. Detailed temperature distributions within the MEA and flow channels are reported elsewhere [9,16].

3D Parametric Simulations: Correlation of Results. In the discussion so far, a particular fuel cell operating under base case conditions with various uniform and nonuniform applied compressive forces has been examined. Consideration of all possible operating conditions, all possible BP geometries, all possible fuel cell materials, and all possible flow channel configurations is impossible. In the discussion to follow, the results are correlated for the particular fuel cell configuration considered here under a broader range of operating conditions. As will be shown, correlation of results reported in terms of various dimensionless temperature distributions is possible, and the correlation shows that nonuniform clamping pressure distributions can be beneficial but must be applied judiciously.

Approximately 90 simulations were performed using the properties of a Sigracet® GDL, and the parameters of Table 1, for various average clamping pressures and values of m, as listed in Table 2. As evident, a range of anode and cathode gas pressures, $2 \le p \le 3$ bars, is considered and $m=0$ is not included.

A dimensionless uniformity of the membrane temperature, $B \equiv (T_{\max}-T_{\min})/T_{in}$, is reported in Fig. 7 as a function of a dimensionless compression pressure distribution of the form $A \equiv (m/\bar{p}_{cl})\cdot(p/\bar{p}_{cl})^{0.55}$. The results of individual simulations are shown as data points, while the solid lines are shown as curve fits of the predictions.

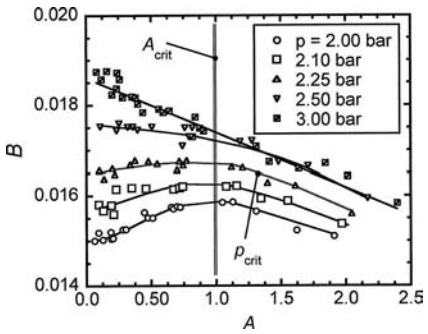

Fig. 7 Relationship between the dimensionless thermal uniformity (*B*) and the dimensionless compression pressure distribution (*A*)

For constant (nonzero) m, if $\bar{p}_{cl}=0$, $A \to \infty$ and no power is generated due to the infinite electrical contact resistances. Therefore, no temperature gradients can exist within the fuel cell and $B \to 0$. Generally, one would not operate at high A conditions. Also for constant (nonzero) m, if the gas operating pressure goes to zero, $A \to \infty$, no power is generated, and $B \to 0$. At high gas operating pressures, power is increased and the temperature differences approach zero at a slower rate as $A \to \infty$ (the approach to $B=0$ for $p=3$ bars is not evident in Fig. 7). Note that inclusion of m in the definition of A explicitly incorporates the effects of the clamping pressure nonuniformity on the isothermality of the membrane, and results in the correlation of otherwise scattered data.

The exponent of A (0.55) was determined by first considering the base case results associated with an operating gas pressure of $p=3$ bars, resulting in the nearly linear dependence of B on A, as evident in Fig. 7. In short, at $p=3$ bars, thermal conditions within the membrane can be made more uniform by increasing the dimensionless nonuniformity of the applied clamping pressure distribution.

Above a critical gas pressure of $p_{crit} \approx 2.25$ bars, increasing the nonuniformity of the clamping pressure distribution will enhance the thermal uniformity of the membrane. However, below the critical clamping pressure ($p \le 2.1$ bars), application of a nonuniform clamping pressure distribution will initially increase the temperature differences within the membrane, prior to reducing the temperature differences. The transition occurs at a dimensionless clamping pressure distribution of $A_{crit} \approx 1$. For the lowest gas pressures ($p \approx 2$ bars), optimal conditions, in terms of membrane thermal uniformity, exist for uniform clamping pressures ($m=A=0$). Hence, application of nonuniform clamping pressure distributions can either enhance or reduce the fuel cell thermal (and humidity) uniformity, depending on the operating conditions of the fuel cell.

Summary and Conclusions

A 3D model of a PEM fuel cell stack has been developed. The model accounts for the variation of thermal and electrical contact resistances at the BP-GDL interface as well as changes in the permeability of the GDLs in response to changes in the compressive load applied to the stack. The model was validated by comparing its predictions at high stoichiometric ratio with existing experimentally validated 2D model.

The temperature distribution within the membrane is highly dependent on the clamping pressure distribution. Maximum tem-

perature differences within the membrane at different locations along the flow channels are minimized at different values of p_{cl}. A novel approach to fuel cell stack assembly, application of nonuniform clamping pressure distributions, is proposed and the predictions suggest that thermal conditions within the stack can become more uniform with negligible impact on the fuel cell power output or maximum membrane temperature. Although some of the effects reported here may appear to be minor (that is, the change in the difference between local maximum and local minimum temperatures as a function of the clamping pressure is less than 1 °C), the effects would be amplified if a larger fuel cell were to be considered.

Dimensionless parameters describing the clamping pressure distribution as well as the nonuniformity of thermal conditions within the membrane have been introduced. The two parameters can be correlated, and the results show that the potential benefits of applying a nonuniform clamping pressure distribution are dependent on the operating conditions of the particular fuel cell considered here and, due to creep or strain-related fatigue, optimal compressive forces may change with time. Hence, general recommendations regarding an optimal nonuniform clamping pressure distribution cannot be made. Despite these limitations, the concept of improving fuel cell durability through application of nonuniform compressive forces in stack assembly appears to be of value. Assembly of fuel cell stacks with nonuniform clamping pressures is an inexpensive alternative to other strategies aimed at improving fuel cell durability and, in turn, potentially reducing fuel cell cost.

Nomenclature

A = dimensionless thermal uniformity
B = dimensionless compression pressure distribution
D_i = species diffusivity, m^2/s
F = force, N
K_p = hydraulic permeability of the porous media, m^2
L = channel length, m
P = power density, W/m^2
$R_{e,c}$ = electric contact resistance, $\Omega\ m^2$
$R_{T,c}$ = thermal contact resistance, $m^2\ K/W$
S = stoichiometric ratio
T = temperature, K
k = thermal conductivity, W/m K
m = slope of local pressure distribution, bar
c_p = specific heat, J/kg K
p = gas pressure, Pa or bar
p_{cl} = clamping pressure, bar
$\bar{p}_{cl}$ = average clamping pressure, bar
t = membrane thickness, m
u, v, and w = velocity components, m/s
x, y, and z = coordinate directions
x_i = mole fraction of the ith component

Greek Symbols

ν = kinematic viscosity, m^2/s
φ_i = ionic potential, V
φ_e = electronic potential, V
ρ = density, kg/m^3

Subscripts

cl = clamping
H_2 = hydrogen
O_2 = oxygen
W = water
crit = critical
f = fluid
in = inlet
max = maximum
min = minimum
0 = reference value
y = y-direction

References

[1] Faghri, A., and Guo, Z., 2005, "Challenges and Opportunities of Thermal Management Issues Related to Fuel Cell Technology and Modeling," Int. J. Heat Mass Transfer, **48**, pp. 3891–3920.
[2] Ihonen, J., Mikkola, M., and Lindbergh, G., 2004, "Flooding of Gas Diffusion Backing in PEFCs," J. Electrochem. Soc., **151**(8), pp. A1152–A1161.
[3] Mishra, V., Yang, F., and Pitchumani, R., 2004, "Measurement and Prediction of Electrical Contact Resistance Between Gas Diffusion Layers and Bipolar Plate for Applications to PEM Fuel Cells," ASME J. Fuel Cell Sci. Technol., **1**, pp. 2–9.
[4] Khandelwal, M., and Mench, M. M., 2006, "Direct Measurement of Through-Plane Thermal Conductivity and Contact Resistance in Fuel Cell Materials," J. Power Sources, **161**, pp. 1106–1115.
[5] Barbir, F., Braun, J., and Neutzler, J., 1999, "Properties of Molded Graphite Bi-Polar Plates for PEM Fuel Cell Stacks," J. New Mater. Electrochem. Syst., **2**, pp. 197–200.
[6] Mathias, M. F., Roth, J., Fleming, J., and Lehnert, W., 2003, "Diffusion Media Materials and Characterisation," *Handbook of Fuel Cells: Fundamentals, Technology and Applications*, Vol. 3, Wiley, New York, pp. 517–537.
[7] Birgersson, E., Noponen, M., and Vynnycky, M., 2005, "Analysis of a Two-Phase Non-Isothermal Model for a PEFC," J. Electrochem. Soc., **152**(5), pp. A1021–A1034.
[8] Ge, J., Higier, A., and Liu, H., 2006, "Effect of Gas Diffusion Layer Compression on PEM Fuel Cell Performance," J. Power Sources, **159**, pp. 922–927.
[9] Fekrazad, N., 2007, "The Effect of Compressive Load on PEM Fuel Cell Stack Performance and Behavior," Ph.D. thesis, University of Connecticut, Storrs, CT.
[10] Fekrazad, N., and Bergman, T. L., 2007, "The Effect of Compressive Load on Proton Exchange Membrane Fuel Cell Stack Performance and Behavior," ASME J. Heat Transfer, **129**, pp. 1004–1013.
[11] Stanic, V., and Hoberecht, M., 2004, "Mechanism of Pin-Hole Formation in Membrane Electrode Assemblies for PEM Fuel Cells," *Proceedings of the Fourth International Symposium on Proton Conducting Membrane Fuel Cells*, J. VanZee, S. R. Narayanan, and M. Murthy, eds., The Electrochemical Society, Pennington, NJ, Abstract No. W1-1891.
[12] Liu, D., and Case, S., 2006, "Durability Study of Proton Exchange Fuel Cells Under Dynamic Testing Conditions With Cyclic Current Profile," J. Power Sources, **162**(1), pp. 521–531.
[13] Uan-Zo-Li, J. T., 2001, "The Effects of Structure, Humidity and Aging on the Mechanical Properties of Polymeric Ionomers for Fuel Cell Applications," M.S. thesis, The Virginia Polytechnic Institute and State University, Blacksburg, VA.
[14] Barbir, F., 2005, *PEM Fuel Cells: Theory and Practice*, Elsevier, New York, Chaps. 3 and 5.
[15] Um, S., Wang, C.-Y., and Chen, K. S., 2000, "Computational Fluid Dynamics Modeling of Proton Exchange Membrane Fuel Cells," J. Electrochem. Soc., **147**(12), pp. 4485–4493.
[16] Fekrazad, N., and Bergman, T. L., 2007, "Effect of Non-Uniform Clamping Pressure on PEM Fuel Cell Stack Performance," *Proceedings of the 2007 ASME-JSME Thermal Engineering Summer Heat Transfer Conference*, K. Okazaki et al., eds., ASME, New York, Paper No. HT2007-32076.

Time-Resolved Micro-Raman Thermometry for Microsystems in Motion

Justin R. Serrano

Sean P. Kearney

Engineering Sciences Center,
Sandia National Laboratories,
Albuquerque, NM 87185-0346

Micro-Raman thermometry has been demonstrated to be a feasible technique for obtaining surface temperatures with micron-scale spatial resolution for microelectronic and microelectromechanical systems (MEMSs). However, the intensity of the Raman signal emerging from the probed device is very low and imposes a requirement of prolonged data collection times in order to obtain reliable temperature information. This characteristic currently limits Raman thermometry to steady-state conditions and thereby prevents temperature measurements of transient and fast time-scale events. In this paper, we discuss the extension of the micro-Raman thermometry diagnostic technique to obtain transient temperature measurements on microelectromechanical devices with 100 μs temporal resolution. Through the use of a phase-locked technique we are able to obtain temperature measurements on electrically powered MEMS actuators powered with a periodic signal. Furthermore, we demonstrate a way of obtaining reliable temperature measurements on micron-scale devices that undergo mechanical movement during the device operation. [DOI: 10.1115/1.2976552]

Keywords: Raman spectroscopy, thermometry, MEMS, thermal actuators

1 Introduction

Temperature diagnostics are essential tools for the evaluation and design of microelectronics devices and microelectromechanical systems (MEMSs). The length scale of these devices necessitates a thermometry technique with micron- and sub-micron-scale spatial resolutions. Typical thermometry tools, such as IR thermography [1,2], lack sufficient spatial resolution to provide reliable temperature information to be used in device design, development, and evaluation. Moreover, the Raman technique provides temperature data that are free from bias errors associated with incomplete knowledge of device emissivity, which plague IR techniques.

In recent years, micro-Raman spectroscopy has surfaced as a versatile tool for obtaining localized temperature measurements on active electronic and mechanical systems [3–11]. For MEMS devices, Raman thermometry has been successfully used as a tool for evaluating and validating thermal models of electrically and optically powered thermal actuators [6–8]. Although this technique can achieve micron-scale spatial resolution in the temperature measurement due to the tight focusing of a probe-laser beam, the long photon collection times (on the order of tens of seconds to a few minutes) required to accurately determine surface temperatures impose the requirement of steady-state thermal conditions within the device under test. This limitation currently impedes the measurement of transient thermal phenomena with micro-Raman thermometry.

Recently, Kuball et al. [5] developed a technique whereby time-resolved temperature measurements were obtained with Raman thermometry on AlGaN/GaN transistors [5]. Their technique employs a pulsed device powering scheme and a Raman probe-laser beam that is modulated in and out of alignment with the microscope in a phase-locked manner relative to the cyclic device forcing to "map" the device temperature in time. While the method used by Kuball and co-workers can be applied effectively to microelectronic devices that do not undergo any in-plane displacement, it is not effective for measurements in moving MEMS devices, such as electrically powered thermal actuators.

In this paper, we discuss the implementation of a phase-locked, time-resolved Raman thermometry technique similar to that of Kuball et al. [5]. Our system overcomes the limitation of a fixed sample surface and, therefore, can be applied to actuators in operation and in motion. By using a system with paired cylindrical optics, micron-scale spatial resolution can be maintained along the axis of long, thin MEMS actuators, while still obtaining reliable data from the moving actuator surfaces. In addition, our system utilizes liquid-crystal shutters to modulate the probe-laser beam. These shutters are less expensive than the acousto-optic modulators used by Kuball et al. [5] and are effective for MEMS forced to kilohertz rates. The obtained temperature measurements are then compared with numerical simulations of the devices.

2 Experimental Details

2.1 Device Description. Two different types of electrically powered thermal actuators were used in this study. Both actuator styles were fabricated using Sandia National Laboratories' SUMMiT-V™ (Sandia's ultraplanar multilevel MEMS technology) five layer polysilicon surface-micromachining process [12]. This process utilizes a polysilicon base plane (Poly0) and four structural polysilicon layers (Poly1–Poly4) separated by sacrificial oxide layers. After the final deposition, the oxide layers are etched away to release the polysilicon structures.

The first type of device was a standard chevron-style electrothermal actuator (Fig. 1(*a*)), which has a 20 μm wide central shuttle and four 3 μm wide $\times$ 300 μm long legs. The actuator was fabricated from a laminate of the bottom three structural layers of SUMMiT, Poly1, Poly2, and Poly3, with an overall thickness of 6.75 μm and a nominal actuator-to-substrate distance of 2.3 μm. The offset of the legs was 12 μm.

The second style of actuator tested was an optothermal actuator (Fig. 1(*b*)) [13], which was configured to operate electrically. The actuator design has two 3 μm wide $\times$ 300 μm long legs and a large 150 μm diameter center shuttle. The offset angle of the legs

Contributed by the Heat Transfer Division of ASME for publication in the JOURNAL OF HEAT TRANSFER. Manuscript received August 13, 2007; final manuscript received June 10, 2008; published online September 16, 2008. Review conducted by Minking Chyu. Paper presented at the 2007 ASME International Mechanical Engineering Congress (IMECE2007), Seattle, WA, November 10–16, 2007.

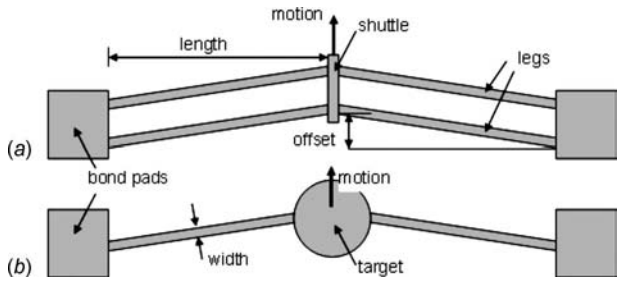

Fig. 1 Schematics of (*a*) chevron-style electrothermal actuator and (*b*) optothermal actuator tested in this study

is 6 deg. These actuators were fabricated from a laminate of the top two layers in SUMMiT, Poly3 and Poly4, for a thickness of 4.5 μm and a 6.5 μm gap to the substrate. In operation, for both designs, the current flowing through the device causes Joule heating and subsequent thermal expansion of the legs. Due to the offset in the legs, the center shuttle undergoes a linear displacement, as indicated in Fig. 1.

2.2 Phase-Locked Raman Thermometry. For thermometry measurements we used a Renishaw in-Via Raman microscope with a 180° backscattering geometry that uses a 488 nm Ar^+ laser as the probe source. A schematic of the Raman system is presented in Fig. 2. The Raman signal is collected with a back-illuminated charge-coupled device (CCD) camera, which, when coupled to the Raman system, gives a spectral dispersion of 0.59 cm^{-1}/pixel and improved quantum efficiency. By using a back-illuminated CCD (quantum efficiency (QE) at 500 nm >95%) we are able to obtain comparable signal-to-noise ratios (SNRs) to the stock CCD camera (QE at 500 nm ~ 12%) over much shorter acquisition times. The spatial resolution of the instrument is determined by the 100× magnification, 0.75 numerical aperture (NA) objective lens, which provides a laser spot size smaller than 500 nm. Additional defocusing of the laser beam within the sample results in a lateral spatial resolution of ~1.2 μm [8].

In the Raman process, the interaction of the incident photons with the optical phonon modes of the sample leads to inelastic scattering of the laser light. The inelastically scattered photons are either higher (anti-Stokes) or lower (Stokes) in frequency than the incident photon. In silicon, the Raman light results from the triply degenerate optical phonon at the Brillouin zone center and therefore the Raman spectrum has a single peak at approximately 520 cm^{-1} from the laser-line frequency at room temperature.

For thermometry in silicon, various temperature-induced

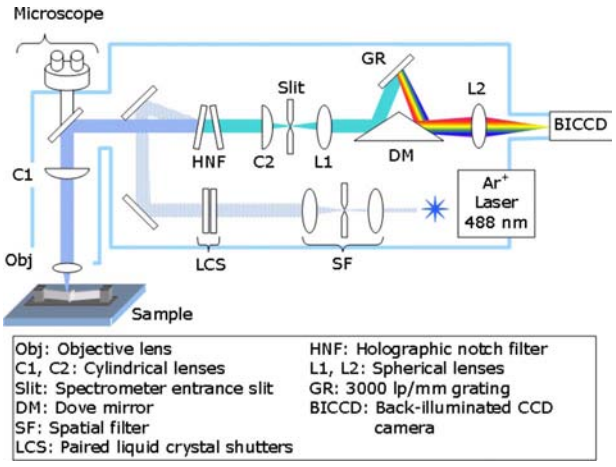

Fig. 2 Schematic of micro-Raman system

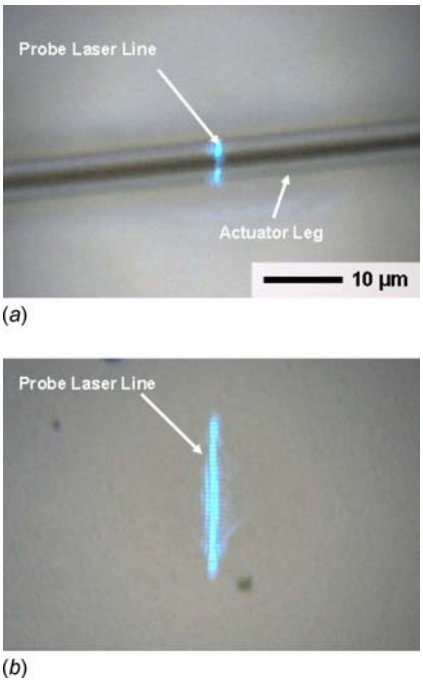

Fig. 3 (*a*) Image of probe-laser line obtained with cylindrical optics in Raman system with laser incident on leg of chevron-style actuator. (*b*) Probe-laser line incident on a flat surface to show full extent of probe-laser line. During the experiments, the laser is used as shown in (*a*).

changes in the Raman spectra from the surface can be used, including the peak position and peak width, as well as the ratio of the intensities of the Stokes and anti-Stokes peaks, with examples of temperature-dependent Raman spectra provided in Refs. [3,14,15]. However, in the absence of evolving stress in the sample, the location of the Stokes peak has been demonstrated to be a robust indicator of surface temperature [6–8]. For polysilicon, the center of the Stokes peak, Ω, decreases linearly in frequency with increased temperature, as determined through Raman measurements of a sample in a temperature-controlled hot stage [8]. Temperature can then be obtained by the expression

$$T = T_0 + \left(\frac{d\Omega}{dT}\right)^{-1}(\Omega - \Omega_0) \tag{1}$$

where $d\Omega/dT = -0.024$ $cm^{-1}/°C$ is the slope of the peak position versus temperature calibration, and Ω_0 is the peak position at the initial temperature, T_0. The uncertainty in the measurement obtained with this temperature method is typically better than ±5 °C.

A drawback of the conventional point-based micro-Raman thermometry technique is that it is not feasible for moving samples since the surface under the probe beam is continuously changing. To overcome this limitation, the beam delivery optics have been modified to use a cylindrical lens (C1 in Fig. 2), such that, at the sample, the probe laser is focused to a line ~20 μm long as shown in Fig. 3. To obtain signal from a moving actuator leg, we focus the probe-laser line onto the leg such that it is oriented perpendicular to the axis of the actuator leg motion. In this manner, the probe laser is always positioned on the same axial location on the leg, even during the motion of the actuator, and a Raman signal originates from the moving intersection of the probe-laser line and the actuator leg. We avoid introducing a temperature bias in the measurement through inadvertent sample heating with the probe laser by reducing the laser power density at the sample to 20 $\mu W/\mu m^2$, at which the maximum laser-induced temperature rise was determined to be less than 1 °C for the chevron-style

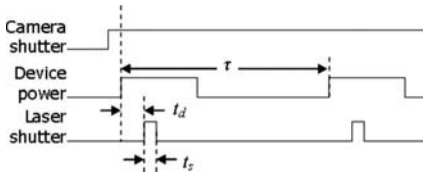

Fig. 4 Timing diagram for phase-locked, time-resolved Raman thermometry

actuator leg geometry [8].

The signal from the sample surface is filtered with a holographic notch filter (HNF), which blocks out the intense elastically scattered light at the laser-line frequency. A second cylindrical lens (C2) is then used to focus the signal onto the entrance slit of the spectrometer. This cylindrical lens focuses in the dimension perpendicular to the axis of the laser line only so that any positional information along the laser line is maintained. The signal is dispersed by a 3000 lines/mm grating and focused onto the back-illuminated CCD camera by a 250 mm lens (L2). Since the actuator/probe-beam intersection is dynamic, the signal from the surface appears on different regions of the CCD chip at different delay times.

To carry out the spectroscopic measurement, the Raman signal from the surface is binned along the direction of the probe-laser line using a region of interest (ROI) on the CCD. Because the signal along the laser-line direction is not spatially resolved, the temperature under the laser line must be uniform and cannot have temperature gradients. For structures, such as the thermal actuator legs studied here, this condition is fully met.

To account for the motion of the actuator at different delay times, the ROI is adjusted after several measurements. This ensures capturing the signal arising only from the actuator leg and minimizes the amount of background signal collected during each measurement, thereby improving SNR. Adjustment of the location of the ROI is optional, as a larger ROI will permit acquisition throughout the full range of operation of the device at the expense of increased accumulation of background signal and lower SNR; a smaller ROI improves the SNR but requires repeated adjustment to ensure capturing the signal from the device. For the test discussed here, the imaged line of Raman signal from the surface was ~7 pixels tall and is displaced by ~8 pixels at the full stroke of motion of the devices. Therefore, a 10 pixel-tall ROI, adjusted two or three times during the measurement, resulted in a reasonable SNR (SNR[1] >40) using peak Raman intensity) with minimal background collection.

Improved temporal resolution is achieved by modulating the probe laser in a phase-locked manner relative to the cyclic electrical forcing of the device under test. A timing diagram showing the relation between the various modulation signals is shown in Fig. 4. Modulation of the laser beam is achieved with a pair of liquid-crystal shutters (DisplayTech LV1300P) mounted in series to provide a contrast ratio of 10^6:1 of the laser beam when the shutters are off. The minimum open time, t_s, is 100 μs and establishes the maximum temporal resolution of the technique, which is sufficient for mapping temperature in devices operated up to 1 kHz. Because the Raman signal from the sample is very weak, the signal must be accumulated over multiple periods to get sufficient signal to accurately determine the peak position. By varying the time delay, t_d, between the activation of the device and the opening of the liquid-crystal shutters, the Raman signal can be captured for different 100 μs intervals along the operating period of the device. During the measurement, the mechanical shutter on the camera is left open and the Raman signal is time-integrated on the CCD chip. Because a Raman signal is built up from multiple laser pulses, the temperature calibration curves used for steady-state thermometry are still valid and Eq. (1) can be used.

[1]The SNR for shot-noise-limited detection is $\mathrm{SNR}=I_{\mathrm{Raman}}/\sqrt{I_{\mathrm{Raman}}+I_{\mathrm{background}}}$, where I indicates peak intensity.

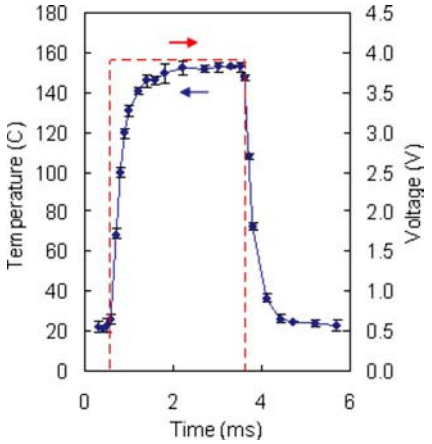

Fig. 5 Temperature profile of a standard electrothermal actuator operated at 3.9 V. The time axis has been shifted by 0.7 ms. The dashed line indicates the applied voltage signal (3.9 V, 100 Hz, and 30% duty cycle).

The actuators were powered with a square voltage pulse train at 100 Hz (10 ms period) with a duty cycle of 30% or 50% (3 or 5 ms on-time). Since the devices were powered over many cycles, the long off-time ensured that they properly cooled down during each cycle and that no overheating took place. For each time delay setting, three different Raman temperature measurements were taken and then averaged. To obtain enough Raman signal to properly extract temperature information for a steady-state measurement requires an integration time of 2–5 s with the probe laser present on the sample. However, modulation of the probe laser to 100 μs "on-times" at 100 Hz increases the total imaging time to 200–500 s or 20,000–50,000 device cycles. To map out an entire cycle of operation in a device requires approximately 5 h per power setting. The benefit of the increased quantum efficiency of the back-illuminated camera is evident in these times since taking the same measurements with the lower quantum efficiency stock front-illuminated CCD camera from Renishaw would require integration times nearly twice as long for the same peak signal intensity.

3 Results and Discussion

The temperature of the moving actuators was measured at the point with the highest temperature along the actuator legs. For the standard four-legged electrothermal actuators shown in Fig. 1(*a*), this point is 200 μm from the bond pad as discussed previously [8] and verified for this study. For the optothermal actuators, the temperature profile along the legs is almost symmetric and the highest temperature occurs at the midpoint along the leg, 150 μm from the bond pads.

Figure 5 shows the temperature profile obtained from a standard electrothermal actuator powered at 3.9 V. Upon activating the device, the temperature rises slowly up to the peak temperature of ~150°C. After approximately 2 ms the temperature has stabilized and plateaus. Once the signal is turned off the temperature cools within ~1.5 ms. At this power level, the motion of the actuator leg at the measurement location was just over 1.5 μm, sufficient to make a point-based measurement nearly impossible without tedious repositioning of the probe-laser spot. Higher driving voltages result in even greater displacements.

For the electrically powered optothermal actuators powered at 3.66 V the temperature rise occurs quickly upon turning the device on, as shown in Fig. 6. Although the increased thermal mass of the center target in the device would suggest that the increase in

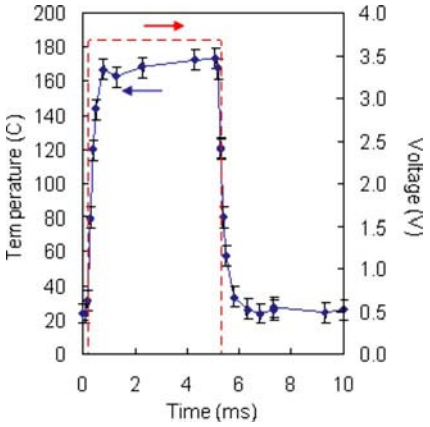

Fig. 6 Temperature of an electrically powered optothermal actuator operated at 3.66 V. The time axis has been shifted by 0.25 ms. The dashed line indicates the applied voltage signal (3.66 V, 100 Hz, and 50% duty cycle).

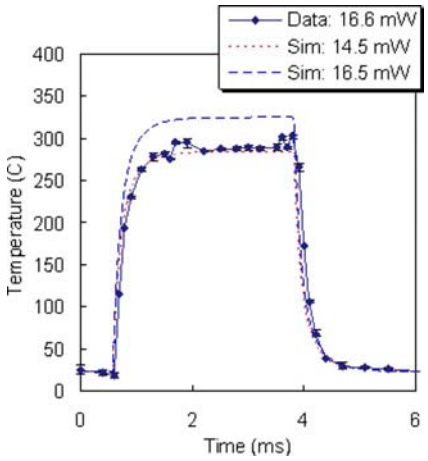

Fig. 7 Temporal evolution of the temperature on the leg of a standard electrothermal actuator operated at 6.0 V. The dotted and dashed lines indicate temperatures obtained from numerical simulations.

temperature should be slow, the data indicate a very fast increase in temperature within the first millisecond of operation. This fast response points to the large central target acting as a heat sink, which causes the actuator legs to behave thermally as individual 300 μm long structures, rather than as a single long structure as is the case for the standard electrothermal actuator. On the cooling portion of the thermal profile, the increased thermal conductivity of the surrounding air [16] also contributes to the fast response.

The time dependence of the leg temperature on the electrothermal actuator of Fig. 1(*a*) was compared with predicted temperatures obtained from numerical simulations. The simulations were carried out using an explicit one-dimensional finite-difference calculation of the heat transfer along one of the actuator legs, and taking into consideration the actuator dimensions and the temperature dependence of the thermal conductivity and resistivity of SUMMiT polysilicon [7]. The model only considers electrical and thermal transports along one leg of a standard actuator and assumes that (i) all dimensions are equal to nominal device dimensions, (ii) symmetry exists across the central shuttle, and (iii) all legs are identical. Additionally, the heat loss to the surrounding air is considered as purely conductive, as the Rayleigh number based on the device cross section is on the order of 10^{-2}, below the limit for convective heat transfer to take place.

For the standard electrothermal actuator operated at 6.0 V and a power dissipation of 16.6 mW along the leg, the simulations predict a temperature of 323°C, which occurs within 2 ms of the device activation. Measurements on the device indicate a plateau temperature of ~288°C. The discrepancy between the measured and modeled temperatures is likely due to the assumptions taken in the model, such as the device dimensions, which are known to have significant variation due to the device processing [7] and can vary by as much as 15% in the widths and 5% in the heights. The temporal behavior, however, agrees qualitatively with that obtained in the measurements, and the measured and predicted rise times are in good agreement. If the power dissipated across the leg is reduced to 14.5 mW the agreement between the model and the data is greatly improved, as indicated by the dotted line in Fig. 7. The reduced dissipation is the result of changing the device dimensions within the known range of device dimensions.

4 Conclusions

Micro-Raman thermometry is a tool that can reliably measure the temperature excursion incurred by electrically powered MEMS devices. Until recently, measurements were limited to steady-state thermal conditions. Using a pulsed-powering scheme together with a phase-locked modulated probe-laser beam, the time evolution of the device temperature during the operating cycle can be measured. A temporal resolution of 100 μs was achieved with the aid of inexpensive liquid-crystal shutters to modulate the probe-laser beam. This resolution easily permits determining temperature events into the kilohertz range.

Moreover, by using beam delivery optics that allow for a probe line instead of a circular spot, the Raman signal from the surface was collected even if the sample surface is in motion. Time-resolved temperatures have been obtained on electrically powered thermal actuators powered with square voltage pulses. Accurate temperature measurements were obtained with an uncertainty of less than 5°C even with device motion being to the actuator leg width and as much as several microns across the plane of detection of the microscope.

Acknowledgment

Sandia is a multiprogram laboratory operated by Sandia Corporation, a Lockheed Martin Co., for the United States Department of Energy's National Nuclear Security Administration under Contract No. DE-AC04-94AL85000.

References

[1] Trigg, A., 2003, "Applications of Infrared Microscopy to IC and MEMS Packaging," IEEE Trans. Electron. Packag. Manuf., **26**, pp. 232–238.
[2] Zhang, Z. M., 2000, "Surface Temperature Measurements Using Optical Techniques," Annu. Rev. Heat Transfer, **11**, pp. 351–411.
[3] Abel, M. R., Graham, S., Serrano, J. R., Kearney, S. P., and Phinney, L. M., 2007, "Raman Thermometry of Polysilicon Microelectromechanical Systems in the Presence of an Evolving Stress," ASME J. Heat Transfer, **129**, pp. 329–334.
[4] Beechem, T., Graham, S., Kearney, S. P., Phinney, L. M., and Serrano, J. R., 2007, "Invited Article: Simultaneous Mapping of Temperature and Stress in Microdevices Using Micro-Raman Spectroscopy," Rev. Sci. Instrum., **78**, p. 061301.
[5] Kuball, M., Reidel, G. J., Pomeroy, J. W., Sarua, A., Uren, M. J., Martin, T., Milton, K. P., Maclean, J. O., and Wallis, D. J., 2007, "Time-Resolved Temperature Measurement of AlGaN/GaN Electronic Devices Using Micro-Raman Thermometry," IEEE Electron Device Lett., **28**, pp. 86–89.
[6] Serrano, J. R., and Phinney, L. M., 2007, "Micro-Raman Thermometry of Laser Heated Surfaces," IPACK2007-33571: Proceedings of the InterPACK 2007, Vancouver, BC, Canada, July 8–12, pp. 1–7.
[7] Serrano, J. R., Phinney, L. M., and Kearney, S. P., 2006, "Micro-Raman Thermometry of Thermal Flexure Actuators," J. Micromech. Microeng., **16**, pp. 1128–1134.
[8] Kearney, S. P., Phinney, L. M., and Baker, M. S., 2006, "Spatially Resolved Temperature Mapping of Electrothermal Actuators by Surface Raman Scattering," J. Microelectromech. Syst., **15**, pp. 314–321.
[9] Abel, M. R., Wright, T. L., Sunden, E. O., Graham, S., King, W. P., and Lance, M. J., 2005, "Thermal Metrology of Silicon Microstructures Using Raman Microscopy," Proceedings of the Semi-Therm Symposium, San Jose, CA, Mar. 15–17, pp. 235–242.
[10] Kuball, M., Hayes, J. M., Uren, M. J., Martin, T., Birbeck, J. C. H., and

Balmer, R. B. T. H., 2002, "Measurements of Temperature in Active High-Power AlGaN/GaN HFETs Using Raman Spectroscopy," IEEE Electron Device Lett., **23**, pp. 7–9.
[11] Ostermeir, R., Brunner, K., Absteiter, G., and Weber, W., 1992, "Temperature Distribution in Si-MOSFETs Studied by Micro Raman Spectroscopy," IEEE Trans. Electron Devices, **39**, pp. 858–863.
[12] Sniegowski, J. J., and de Boer, M. P., 2000, "IC-Compatible Polysilicon Surface Micromachining," Annu. Rev. Mater. Sci., **30**, pp. 299–333.
[13] Serrano, J. R., Phinney, L. M., and Brooks, C. F., 2005, "Laser-Induced Damage of Polycrystalline Silicon Optically Powered MEMS Actuators," IPACK2005-73322: Proceedings of the InterPACK'05, San Francisco, CA, July 17–22, pp. 1–6.
[14] Balkanski, M., Wallis, R. F., and Haro, E., 1983, "Anharmonic Effects in Light Scattering Due to Optical Phonons in Silicon," Phys. Rev. B, **28**, pp. 1928–1934.
[15] Tsu, R., and Hernandez, J. G., 1982, "Temperature Dependence of Silicon Raman Lines," Appl. Phys. Lett., **41**, pp. 1016–1018.
[16] Lide, D. R., 2008, *CRC Handbook of Chemistry and Physics*, 88th ed., CRC Press, Boca Raton, FL.

Liquid Single-Phase Flow in an Array of Micro-Pin-Fins—Part I: Heat Transfer Characteristics

Weilin Qu[1]
e-mail: qu@hawaii.edu

Abel Siu-Ho

Department of Mechanical Engineering,
University of Hawaii at Manoa,
Honolulu, HI 96822

This is Paper I of a two-part study concerning thermal and hydrodynamic characteristics of liquid single-phase flow in an array of micro-pin-fins. This paper reports the heat transfer results of the study. An array of 1950 staggered square micro-pin-fins with 200×200 μm^2 *cross-section by 670* μm *height were fabricated into a copper test section. De-ionized water was used as the cooling liquid. Two coolant inlet temperatures of* $30\,^{\circ}C$ *and* $60\,^{\circ}C$ *and six maximum mass velocities for each inlet temperature ranging from 183 to 420* $kg/m^2\,s$ *were tested. The corresponding inlet Reynolds number ranged from 45.9 to 179.6. General characteristics of average and local heat transfer were described. Six previous conventional long and intermediate pin-fin correlations and two micro-pin-fin correlations were examined and were found to overpredict the average Nusselt number data. Two new heat transfer correlations were proposed for the average heat transfer based on the present data, in which the average Nusselt number is correlated with the average Reynolds number by power law. Values of the exponent m of the Reynolds number for the two new correlations are fairly close to those for the two previous micro-pin-fin correlations but substantially higher than those for the previous conventional pin-fin correlations, indicating a stronger dependence of the Nusselt number on the Reynolds number in micro-pin-fin arrays. The correlations developed for the average Nusselt number can adequately predict the local Nusselt number data.*
[DOI: 10.1115/1.2970080]

Keywords: micro-pin-fins, heat sink, liquid cooling, single phase, heat transfer

1 Introduction

Breakthrough in many cutting-edge technologies is increasingly dependent on the availability of highly efficient cooling techniques that are capable of dissipating a large amount of heat from small areas. Single-phase liquid-cooled miniature heat sinks, which incorporate internal heat transfer enhancement structures that are tens to hundreds of micrometers in size, have emerged as one solution to these cooling challenges. Among a large variety of possible microscale enhancement structures, parallel microchannels have received the most attention so far [1–5].

Recent advancement in microfabrication techniques, however, allows more complex microscale geometries to be fabricated directly into high-thermal-conductivity solid substrates at low cost, which makes it possible to explore alternative enhancement structures that may be more effective than microchannels. A promising configuration is staggered or aligned microscale pin-fin arrays [6–12]. Important features of micro-pin-fin arrays that are intended for miniature heat sink applications as discussed in the previous studies [6–12] include the following: (a) liquid such as water or refrigerant is the coolant of choice in order to achieve better cooling performance; (b) heat is transferred to a micro-pin-fin array from one endwall only (base endwall); (c) pin-fins span the full distance between the base endwall and the cover endwall, and there is no clearance gap between the cover endwall and pin-fin tips; (d) pin-fin height-to-diameter ratio H_{fin}/d is in the intermediate range of 0.5–8 due to fabrication limitation, and endwalls have a considerable effect on overall array thermal and hydrodynamic characteristics; and (e) the low coolant flow rate and small characteristic dimension of pin-fins usually yield a low Reynolds number of less than 1000. The flow is therefore in a laminar or a transitional regime.

An effective design and a performance assessment of micro-pin-fin heat sinks require a fundamental understanding and an accurate description of virtually all thermal and hydrodynamic aspects of micro-pin-fin arrays. While interest in microscale pin-fins is fairly recent, arrays of conventional-sized pin-fins that are several millimeters or larger in diameter have been used as heat transfer enhancement structures in a wide variety of engineering applications, and their heat transfer and pressure drop characteristics have been studied quite extensively in the past. Both long pin-fins ($H_{fin}/d > 8$) [13–19] and intermediate pin-fins ($0.5 \le H_{fin}/d \le 8$) [20–27] were examined in the previous studies. Arrays of long pin-fins or tube banks are used mostly in heat exchanger applications [13–19]. Their heat transfer and pressure drop performance is dominated by pin-fins, and the endwall effect is negligible. In addition, available experimental data for low Reynolds number flow, i.e., $Re < 1000$, is rather limited. Arrays of intermediate pin-fins are common heat transfer enhancement structures in turbine cooling applications [20–27]. In these applications, gases are generally used as the coolant, and a high flow rate produces a high Reynolds number of at least several thousands.

While fluid flow and heat transfer conditions and/or pin-fin geometry in most previous conventional-sized pin-fin studies differ considerably from those of micro-pin-fins, there are a few studies that are quite relevant, in which heat transfer and pressure drop associated with low Reynolds number ($Re < 1000$) single-phase flow in arrays of intermediate pin-fins were investigated [28–30]. In a two-part paper, Short et al. [28,29] experimentally studied pressure drop and heat transfer of air flow in 44 arrays of staggered circular pin-fins having diameters d of 1.57–3.18 mm and

[1]Corresponding author.

Contributed by the Heat Transfer Division of ASME for publication in the JOURNAL OF HEAT TRANSFER. Manuscript received September 11, 2007; final manuscript received March 4, 2008; published online September 17, 2008. Review conducted by Yogendra Joshi. Paper presented at the 2007 ASME International Mechanical Engineering Congress (IMECE 2007), Seattle, WA, November 10–16, 2007.

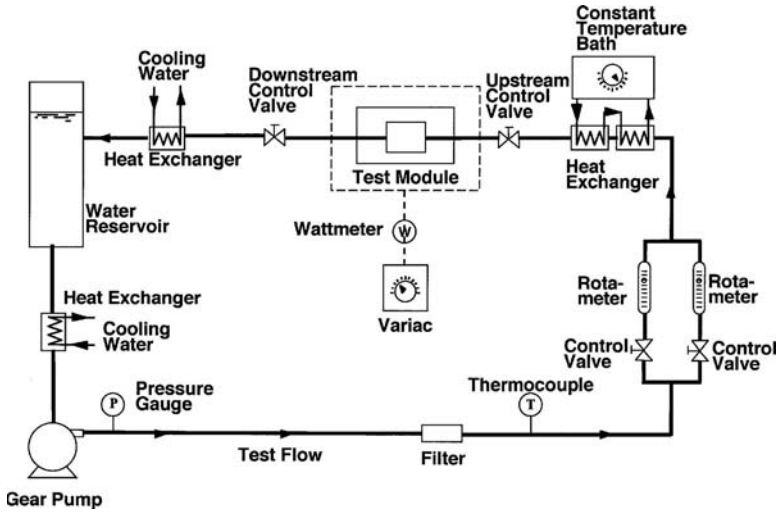

Fig. 1 Schematic of the flow loop

pin-fin height-to-diameter ratios H_{fin}/d of 1.88–7.25. New empirical correlations for the friction factor and heat transfer were proposed for two flow regimes of low Reynolds numbers ($175 < Re < 1000$) and high Reynolds numbers ($Re < 1000$). Moores and Joshi [30] conducted an experimental study of water pressure drop and heat transfer in three arrays of staggered circular pin-fins with d of 3.67–3.84 mm and H_{fin}/d of 0.52–1.09. They also proposed new friction factor and heat transfer correlations for the two flow regimes of $200 < Re < 1000$ and $Re > 1000$.

A limited number of studies have recently been carried out on liquid single-phase pressure drop and heat transfer in micro-pin-fin arrays. Koşar et al. [6] studied water pressure drop across four arrays of staggered and aligned circular and diamond shaped micro-pin-fins having d of 50 and 100 μm and H_{fin}/d of 1 and 2. The Reynolds number ranged from 5 to 128. Existing conventional scale correlations were not able to predict their pressure drop data. New friction factor correlations were proposed. Peles et al. [7] provided a theoretical analysis of heat transfer in micro-pin-fin arrays using a conventional long pin-fin correlation. Effects of geometrical and thermohydraulic parameters on the thermal resistance were discussed. Koşar and Peles [8] studied water pressure drop and heat transfer in an array of staggered circular pin-fins with d of 99.5 μm and H_{fin}/d of 2.44. The Reynolds number ranged from 14 to 112. Existing macroscale correlations overpredicted the Nu data by more than a factor of 2 at low Re and provided a moderate agreement at high Re. The dependence of Nu on Re was more notable than that for long tube correlations. Koşar and Peles [9] studied refrigerant R-123 heat transfer in an array of staggered circular pin-fins having d of 99.5 μm and H_{fin}/d of 2.44. It was again found that the existing macroscale correlations overpredicted the Nu data at low Re and provided a good prediction at high Re. A new heat transfer correlation was proposed based on the R-123 data as well as the water data from their previous study [8]. Koşar et al. [10] studied water pressure drop and heat transfer in an array of hydrofoil pin-fins with a chord thickness of 100 μm and a height of 243 μm. The Reynolds number ranged from 15 to 720. A new heat transfer correlation was proposed based on the experimental data. Prasher et al. [11] experimentally studied water pressure drop and heat transfer in five arrays of staggered circular and square micro-pin-fins having d of 55–153 μm and H_{fin}/d of 1.3–2.8. The Reynolds number ranged from 15 to 720. A transition in heat transfer and friction factor behavior was identified at around $Re = 100$. Previous conventional as well as micro-pin-fin correlations could not predict their heat transfer data. New heat transfer correlations were proposed. Siu-Ho et al. [12] studied water pressure drop and heat transfer in an array of staggered square pin-fins having equivalent d_e of 200 μm and H_{fin}/d_e of 3.35. The Reynolds number ranged from 93 to 634. Previous conventional as well as microscale pin-fin correlations could not predict their heat transfer data.

Due to the complex nature of the fluid flow and heat transfer in micro-pin-fin arrays, analytical or numerical models have not been developed. Most existing studies are empirical in nature. Even though these previous studies provided valuable insight into the transport characteristics of the single-phase fluid flow and heat transfer in micro-pin-fin arrays, findings remain inconclusive, especially when comparing experimental results from different sources with correlation predictions. In addition, available experimental data remain very limited. Detailed experimental measurements are still needed in order to obtain a fundamental understanding of the thermal and hydrodynamic aspects of micro-pin-fin arrays and to develop accurate predictive tools.

The present study expands on the aforementioned micro-pin-fin studies by investigating water heat transfer and pressure drop in an array of staggered square micro-pin-fins with an equivalent diameters of 200 μm and heights of 670 μm. The objectives of the present study are as follows: (1) to provide new heat transfer and pressure drop data for liquid single-phase flow in a micro-pin-fin array, (2) to assess the accuracy of previous correlations in describing the thermal and hydrodynamic characteristics of the present micro-pin-fin array, (3) to reveal the important parametric trends, and (4) to develop new correlations for the micro-pin-fin array. The presentation of the results is made in two parts. The first part, presented in this paper, reports the heat transfer results of the study. The second part, documented in Paper II [31], reports the pressure drop results.

2 Experimental Apparatus

2.1 Flow Loop. A flow loop was constructed to adjust the liquid coolant, de-ionized water, to the desired operating conditions. Figure 1 shows a schematic of the flow loop. Water was circulated using a gear pump. A compact heat exchanger was used to bring the water to a temperature of approximately 19°C before it entered the pump. After leaving the pump, the water flowed through a filter with a 40 μm pore size to prevent solid particles from clogging microsize flow passages in the heat sink. The water then passed through one of two rotameters for mass flow rate measurement. The rotameters were calibrated using the standard weighting method. The accuracy of the mass flow rate measurement was better than 4% of the readings. Afterward, the water flowed through a second heat exchanger that was connected to a

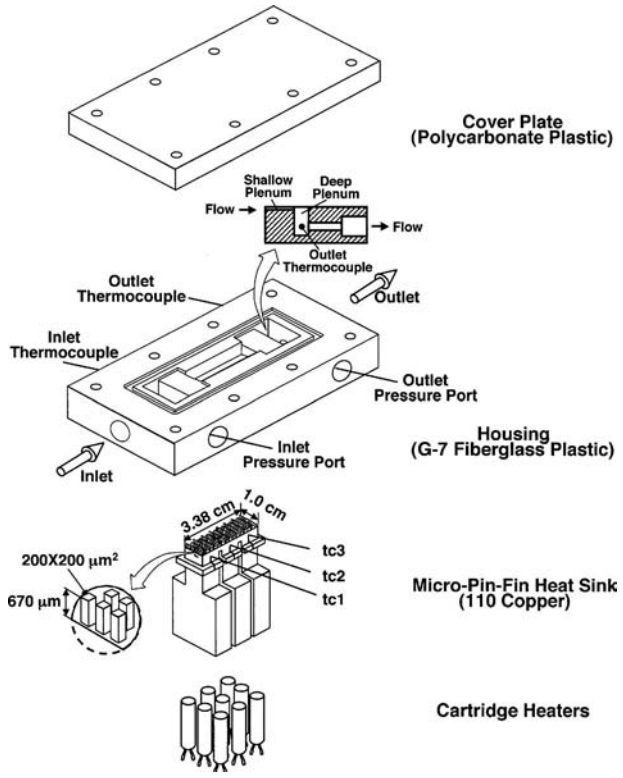

Fig. 2 Test module construction

constant temperature bath, where water was brought to the desired test module inlet temperature. The water then entered the test module. The water exiting the test module flowed through a third heat exchanger to lower its temperature before it returned to the reservoir.

2.2 Test Module. Figure 2 shows the construction of the test module. The test module was composed of a 110 copper micro-pin-fin heat sink, a G-7 fiberglass plastic housing, a polycarbonate plastic (Lexan) cover plate, and nine cartridge heaters. The micro-pin-fin heat sink had a platform (top) area of 3.38 cm (length) by 1.0 cm (width), which is also the total area of the micro-pin-fin array base endwall. An array of 1950 staggered micro-pin-fins with 200×200 μm^2 cross-section ($W_{fin}\times L_{fin}$) by 670 μm height (H_{fin}) were milled out of the top surface. A top view of the micro-pin-fin array, together with key dimensions, is shown in Fig. 3. The micro-pin-fins were machined using a microend mill. The uncertainty in the micro-pin-fin cross-sectional dimension $W_{fin}\times L_{fin}$ was estimated to be 5 μm, and the uncertainty in the pin-fin height H_{fin} was 10 μm. Below the heat sink top surface, three type-K thermocouples were inserted along the center plane to measure the streamwise temperature distribution in the heat sink and are indicated in Fig. 2 as tc1–tc3 from upstream to downstream. The streamwise distances of the three thermocouples from the heat sink inlet, z_{tc1}, z_{tc3}, and z_{tc3}, are 5 mm, 16.6 mm, and 28.2 mm, respectively. Three narrow slots were cut from the bottom surface up through most of the heat sink's height to reduce streamwise heat conduction within the heat sink. Nine holes were drilled into the bottom surface of the heat sink to accommodate the cartridge heaters that were connected in parallel and powered by a Variac. The total electrical power input to the nine cartridge heaters P_W was measured by a 0.5% accuracy wattmeter.

The central portion of the housing was removed where the micro-pin-fin heat sink was inserted. A room temperature vulcanizing (RTV) silicone rubber was applied along the interface between the housing and the heat sink to prevent leakage. The housing contained plenums both upstream and downstream of the micro-pin-fin arrays. Each plenum had a deep portion leading to a shallow portion to ensure an even distribution of flow. An absolute pressure transducer was connected to the inlet deep plenum via a pressure tap to measure the inlet pressure. A differential pressure transducer was connected to the inlet and outlet deep plenums to measure the pressure drop across the heat sink. Uncertainty in the pressure drop measurements was estimated to be less than 0.25% of the readings. Also located in the inlet and outlet deep plenums are two Type-K thermocouples, one in the inlet and the other in the outlet, to measure the inlet and exit temperatures, respectively. To eliminate the thermal stratification effect, the thermocouples were located close to the inlet and outlet flow channels in the housing, respectively, as illustrated in Fig. 2. Uncertainty in all thermocouple measurements was less than $\pm0.3^\circ$C. The readings of pressure transducers and thermocouples were recorded using an HP data acquisition/control system that was interfaced to a PC.

The cover plate was bolted atop the housing, as shown in Fig. 2. The cover plate and the heat sink top surface containing the micro-pin-fin array formed a closed flow passage for the water. A shallow groove was machined into the housing around the heat sink top surface and was filled with a RTV silicone rubber to create a leak-proof seal. After the test module was assembled, multiple layers of ceramic fiber were wrapped around the heat sink for thermal insulation to reduce the heat loss to the ambient.

2.3 Test Procedure. Prior to conducting a heat transfer test, the flow loop components were first adjusted to yield the desired test module inlet temperature T_{in} and the total mass flow rate $\dot{m}$. Table 1 summarizes the operating conditions in the present study. G_{max} in Table 1 indicates the maximum water mass velocity in the micro-pin-fin array and is defined as

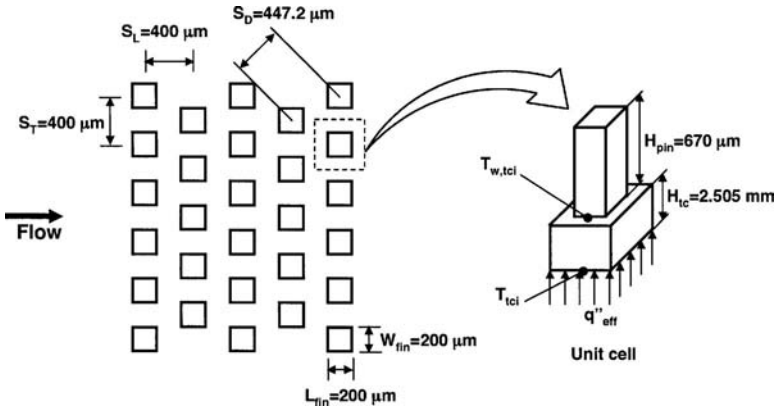

Fig. 3 Top view of the micro-pin-fin array and schematic of the unit cell

Table 1 Operating conditions for the present study

Coolant	Inlet temperature, T_{in} (°C)	Mass flow rate, $\dot{m}$ (g/s)	Maximum mass velocity, G_{max} (kg/m^2 s)	Inlet Reynolds number, Re_{in}
De-ionized water	30	0.611–1.408	183–420	45.9–105.9
	60	0.611–1.398	183–417	78.6–179.6

$$G_{\max} = \frac{\dot{m}}{A_{\min}} \tag{1}$$

where $A_{\min}$ is the minimum transverse flow area of the micro-pin-fin array,

$$A_{\min} = W_{hs} H_{fin}\left(1 - \frac{W_{fin}}{S_T}\right) \tag{2}$$

The definition of the Reynolds number in the present study follows that commonly employed in previous studies of micro-pin-fins [6–12],

$$\mathrm{Re} = \frac{\rho_f u_{\max} d_e}{\mu_f} \tag{3}$$

where $u_{\max}$ indicates the maximum water velocity in the micro-pin-fin array,

$$u_{\max} = \frac{G_{\max}}{\rho_f} \tag{4}$$

Re_{in} in Table 1 represents the inlet Reynolds number with all water properties evaluated at T_{in}. d_e represents an equivalent diameter of the square micro-pin-fins, corresponding to the diameter of circular pin-fins d,

$$d_e = \frac{4A_c}{P_{fin}} \tag{5}$$

where A_c is the cross-sectional area of a single micro-pin-fin,

$$A_c = W_{fin} L_{fin} \tag{6}$$

and P_{fin} is the cross-section perimeter of a single micro-pin-fin,

$$P_{fin} = 2(W_{fin} + L_{fin}) \tag{7}$$

After the flow became stable, the heater power was set to a low level where the reading from the downstream thermocouple tc3 inside the heat sink, which was the highest among those from the three thermocouples tc1–tc3, was about 50°C for T_{in}=30°C and about 70°C for T_{in}=60°C. The power was then increased in small increments as the flow loop components were constantly adjusted to maintain the desired inlet temperature and mass flow rate, as given in Table 1. At each heater power level, the heat sink was allowed to reach steady state conditions. Once at steady state, readings from the pressure transducers and thermocouples were recorded at 0.5 s intervals for 3 min. The pressure and temperature data reported in this paper are obtained by time-averaging the aforementioned readings over the 3 min measurement period. Readings from the rotameter and wattmeter were recorded manually. The present study concerns only water single-phase flow in the micro-pin-fin array, where the tc3 reading at each flow rate was less than 90°C.

Heat loss from the test module was evaluated from the difference between the total electrical power input measured by the wattmeter P_W and the measured enthalpy change of the water flow $\dot{m}c_{p,f}(T_{out}-T_{in})$,

$$Q_{loss} = P_W - \dot{m}c_{p,f}(T_{out} - T_{in}) \tag{8}$$

Even though effort was made to reduce the heat loss from the test module to the ambience, it has been found that Q_{loss} ranged from 3% to 15% of P_W for T_{in}=30°C and from 6% to 34% for T_{in}=60°C. Higher heat loss occurred at lower water flow rate. In the present study, the amount of heat that was transferred to the micro-pin-fin array was calculated from

$$Q_{fin} = P_W - Q_{loss} \tag{9}$$

The level of heat flux that is removed from the micro-pin-fin array by water flow is represented by an effective heat flux q''_{eff}, defined based on the total area of the micro-pin-fin array base endwall, A_t=3.38×1.0 cm^2,

$$q''_{eff} = \frac{Q_{fin}}{A_t} \tag{10}$$

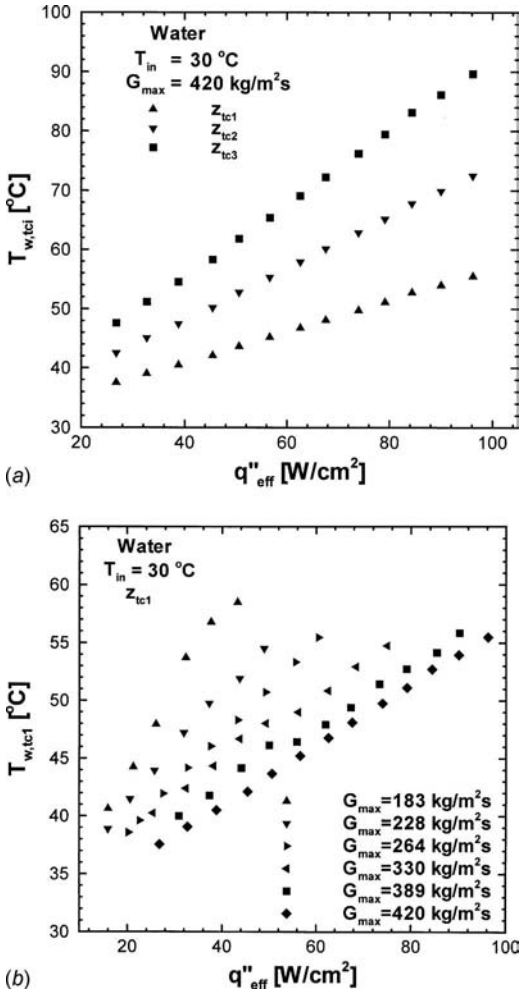

Fig. 4 Variation of the measured micro-pin-fin base temperature with input heat flux (*a*) at $z_{tc1}-z_{tc3}$ for T_{in}=30°C and G_{max} =420 kg/m^2 s and (*b*) at z_{tc1} for T_{in}=30°C and all six G_{max}

3 Results and Discussion

3.1 Temperature Measurement Results. Figures 4(*a*) and 4(*b*) plot the measured micro-pin-fin base temperature $T_{w,tci}$ versus the input heat flux q''_{eff}. Figure 4(*a*) shows the variation of $T_{w,tci}$ with q''_{eff} at the three z_{tci} for T_{in}=30°C and G_{max} =420 kg/m^2 s. Assuming a one-dimensional heat conduction between the thermocouple location and the micro-pin-fin base, as shown in Fig. 3, $T_{w,tci}$ is evaluated from

$$T_{w,\mathrm{tc}i} = T_{\mathrm{tc}i} - \frac{q''_{\mathrm{eff}} H_w}{k_s} \tag{11}$$

where $T_{\mathrm{tc}i}$ represents the readings from the thermocouples. At each $z_{\mathrm{tc}i}$, Fig. 4(*a*) shows that $T_{w,\mathrm{tc}i}$ increases with increasing q''_{eff}. For the same q''_{eff}, $T_{w,\mathrm{tc}i}$ increases along the flow direction from z_{tc1} to z_{tc3}. Figure 4(*b*) shows $T_{w,\mathrm{tc}i}$ at z_{tc1} versus q''_{eff} for $T_{\mathrm{in}} = 30\,^{\circ}\mathrm{C}$ and all six $G_{\max}$. $T_{w,\mathrm{tc1}}$ decreases with increasing $G_{\max}$ for a given q''_{eff}. The overall trend in the measured micro-pin-fin base temperature is typical of a single-phase heat transfer system.

3.2 Average Heat Transfer Characteristics. An average heat transfer coefficient for an entire micro-pin-fin array has been employed by most previous micro-pin-fin heat transfer studies [7–11] to represent the performance of the micro-pin-fin array as a heat transfer enhancement structure. In the present study, the average heat transfer coefficient for the micro-pin-fin array h_{ave} is evaluated from

$$q''_{\mathrm{eff}} A_t = h_{\mathrm{ave}} (T_{w,\mathrm{ave}} - T_{f,\mathrm{ave}}) [(A_t - N_t A_c) + \eta_{\mathrm{fin}} N_t A_{\mathrm{fin}}] \tag{12}$$

Equation (12) is derived from a simple energy balance: the left-hand side represents the heat input to the micro-pin-fin array, and the right-hand side represents the heat removal from the pin-fin array by water flow. In Eq. (12), N_t indicates the total number of pin-fins in the array ($N_t = 1950$) and A_{fin} is the wetted surface area of a single pin-fin,

$$A_{\mathrm{fin}} = P_{\mathrm{fin}} H_{\mathrm{fin}} \tag{13}$$

The term $A_t - N_t A_c$ in Eq. (12) therefore represents the wetted area of the micro-pin-fin array base endwall, and $N_t A_{\mathrm{fin}}$ is the total wetted surface area of micro-pin-fins. h_{fin} represents the fin efficiency,

$$\eta_{\mathrm{fin}} = \frac{\tanh(m_{\mathrm{fin}} H_{\mathrm{fin}})}{m_{\mathrm{fin}} H_{\mathrm{fin}}} \tag{14}$$

where m_{fin} is the fin parameter,

$$m_{\mathrm{fin}} = \sqrt{\frac{h_{\mathrm{ave}} P_{\mathrm{fin}}}{k_s A_c}} \tag{15}$$

$T_{w,\mathrm{ave}}$ and $T_{f,\mathrm{ave}}$ represent the average micro-pin-fin base temperature and the average water bulk temperature, respectively. $T_{w,\mathrm{ave}}$ is obtained by averaging the measured micro-pin-fin base temperature at the three thermocouple locations $T_{w,\mathrm{tc}i}$,

$$T_{w,\mathrm{ave}} = \frac{T_{w,\mathrm{tc1}} + T_{w,\mathrm{tc2}} + T_{w,\mathrm{tc3}}}{3} \tag{16}$$

$T_{f,\mathrm{ave}}$ is taken as the average of the measured water inlet and outlet temperatures,

$$T_{f,\mathrm{ave}} = \frac{T_{\mathrm{in}} + T_{\mathrm{out}}}{2} \tag{17}$$

Once $T_{w,\mathrm{ave}}$ and $T_{f,\mathrm{ave}}$ are determined from Eqs. (16) and (17), respectively, the value of h_{ave} for the entire micro-pin-fin array can be calculated iteratively from Eq. (12). The uncertainty in h_{ave} is calculated using the method developed by Kline and McClintock [32]. The uncertainty ranges from 5.7% to 19.3%, with an average of 8.3%.

Figures 5(*a*) and 5(*b*) plot the variation of h_{ave} with q''_{eff} for $T_{\mathrm{in}} = 30\,^{\circ}\mathrm{C}$ and $T_{\mathrm{in}} = 60\,^{\circ}\mathrm{C}$, respectively, and for all $G_{\max}$ that were tested. Figures 5(*a*) and 5(*b*) show that h_{ave} increases appreciably with increasing $G_{\max}$ for a given q''_{eff}. For a constant $G_{\max}$, h_{ave} remains fairly constant or increases only slightly with increasing q''_{eff}. The observed trend is consistent with that reported in previous micro-pin-fin studies [8–10]. The slight increase in h_{ave} value with increasing q''_{eff} may be attributed to the increase in the average Reynolds number $\mathrm{Re}_{\mathrm{ave}}$ defined as

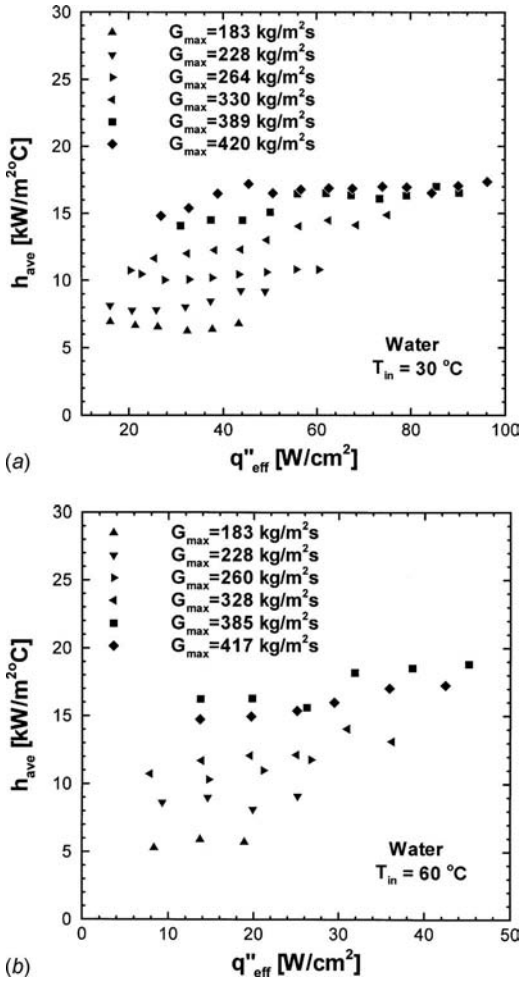

Fig. 5 Variation in average heat transfer coefficient with input heat flux: (*a*) $T_{\mathrm{in}} = 30\,^{\circ}\mathrm{C}$ and (b) $T_{\mathrm{in}} = 60\,^{\circ}\mathrm{C}$

$$\mathrm{Re}_{\mathrm{ave}} = \frac{\rho_{f,\mathrm{ave}} u_{\max,\mathrm{ave}} d_e}{\mu_{f,\mathrm{ave}}} \tag{18}$$

where water properties are evaluated at $T_{f,\mathrm{ave}}$. This is because a high $T_{f,\mathrm{ave}}$ corresponding to a high q''_{eff} led to reduced water density and viscosity.

Figure 6 plots the variation in the average Nusselt number $\mathrm{Nu}_{\mathrm{ave}}$ with the average Reynolds number $\mathrm{Re}_{\mathrm{ave}}$ on a log-log scale. $\mathrm{Nu}_{\mathrm{ave}}$ is evaluated from

$$\mathrm{Nu}_{\mathrm{ave}} = \frac{\mathrm{h}_{\mathrm{ave}} d_e}{k_{f,\mathrm{ave}}} \tag{19}$$

The uncertainty in $\mathrm{Re}_{\mathrm{ave}}$ is about 5.8%. The uncertainty in $\mathrm{Nu}_{\mathrm{ave}}$ ranges from 5.6% to 19.2%, with an average of 8.1%. Despite the scatter in the data, Fig. 6 shows that $\mathrm{Nu}_{\mathrm{ave}}$ increases with increasing $\mathrm{Re}_{\mathrm{ave}}$ in a fairly linear fashion for both inlet temperatures. The large scatter in the data may be attributed to the uncertainties in $\mathrm{Nu}_{\mathrm{ave}}$ and $\mathrm{Re}_{\mathrm{ave}}$ as well as to the variations in water properties due to temperature change. Nevertheless, the observed trend indicates that the relationship between $\mathrm{Nu}_{\mathrm{ave}}$ and $\mathrm{Re}_{\mathrm{ave}}$ may be described by power law ($\mathrm{Nu}_{\mathrm{ave}} \propto \mathrm{Re}_{\mathrm{ave}}^{m}$).

3.3 Assessment of Previous Heat Transfer Correlations. Eight previous correlations for low Reynolds number ($\mathrm{Re} < 1000$) single-phase heat transfer in pin-fin arrays are selected and summarized in Table 2. Among the eight correlations, the first four (correlations 1–4) were based on heat transfer experimental data for conventional long pin-fin arrays ($H_{\mathrm{fin}}/d > 8$), the next two

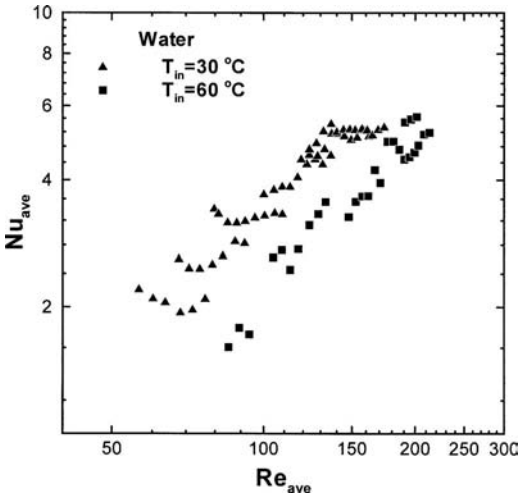

Fig. 6 Variation in the average Nusselt number with the average Reynolds number

(correlations 5 and 6) for conventional intermediate pin-fin arrays ($0.5 \leq H_{\text{fin}}/d \leq 8$), and the last two (correlations 7 and 8) for micro-pin-fin arrays. It should be noted that most correlations were developed for circular pin-fins.

A close examination of the correlations listed in Table 2 reveals that most previous pin-fin heat transfer correlations adopted either one of the following two functional forms to correlate the experimental data:

$$\text{Nu}_{\text{ave}} = c\ \text{Re}_{\text{ave}}^{m}\text{Pr}_{f,\text{ave}}^{n} \tag{20}$$

and

$$\text{Nu}_{\text{ave}} = c\ \text{Re}_{\text{ave}}^{m}\text{Pr}_{f,\text{ave}}^{n}\left(\frac{\text{Pr}_{f,\text{ave}}}{\text{Pr}_{w,\text{ave}}}\right)^{l} \tag{21}$$

$\text{Pr}_{f,\text{ave}}$ in Eqs. (20) and (21) is the water Prandtl number at $T_{f,\text{ave}}$, and $\text{Pr}_{w,\text{ave}}$ in Eq. (21) is the water Prandtl number at $T_{w,\text{ave}}$. The term $(\text{Pr}_{f,\text{ave}}/\text{Pr}_{w,\text{ave}})^{l}$ in Eq. (21) represents a property correction factor to account for the effect of fluid property variation on heat transfer. $(\mu_{f,\text{ave}}/\mu_{w,\text{ave}})^{l}$ was used instead of $(\text{Pr}_{f,\text{ave}}/\text{Pr}_{w,\text{ave}})^{l}$ in the correlations by Whitaker [15] (correlation 2) and Hwang and Yao [17] (correlation 3). While the exponents m, n, and l are usually constants in the correlations, the coefficient c is often correlated as a function of geometric parameters of pin-fin arrays, such as d, H_{fin}, S_L, and S_T, to account for the effect of geometric parameters on heat transfer.

The values of the exponent m of Re_{ave} in the eight correlations are provided in Table 2. Table 2 shows that m in the conventional long pin-fin correlations (correlations 1–4) has lower values between 1/3 and 0.5. On the other hand, m in the two micro-pin-fin correlations (correlations 7 and 8) has higher values of 0.99 and 0.84, which indicate a stronger dependence of Nu_{ave} on Re_{ave} in micro-pin-fin arrays as compared with that in conventional long pin-fin arrays. No clear trend could be identified in the m values for the two conventional intermediate pin-fin correlations (correlations 5 and 6): an m value of 0.33 for the Short et al. [29] correlation (correlation 5) is at the low end of those for the conventional long pin-fin correlations, and an m value of 0.64 for the Moores and Joshi correlation (correlation 6) is higher than those for the conventional long pin-fin correlations.

Figures 7(*a*)–7(*f*) compare the predictions of the six previous conventional pin-fin correlations (correlations 1–6) with the present data. Similarly, Figs. 8(*a*) and 8(*b*) compare the predictions of the two previous micro-pin-fin correlations (correlations 7

Table 2 Correlations for heat transfer in pin-fin arrays

Correlation	Reference	Average Nusselt number, Nu_{ave}	Exponent, m	MAE (%)
1	Zukauskas [13]	$\text{Nu}_{\text{ave}}=0.9\text{Re}_{\text{ave}}^{0.4}\text{Pr}_{f,\text{ave}}^{0.36}(\text{Pr}_{f,\text{ave}}/\text{Pr}_{w,\text{ave}})^{0.25}$	0.36	168.5
2	Whitaker [15]	$\text{Nu}_{\text{ave}}=2\text{Re}_{\text{ave}}^{1/3}\text{Pr}_{f,\text{ave}}^{1/3}(\mu_{f,\text{ave}}/\mu_{w,\text{ave}})^{0.14}$	1/3	314.3
3	Hwang and Yao [17]	$\text{Nu}_{\text{ave}}=0.83\lambda^{1/3}\text{Re}_{\text{ave}}^{1/3}\text{Pr}_{f,\text{ave}}^{1/3}(\mu_{f,\text{ave}}/\mu_{w,\text{ave}})^{0.14}$ $\lambda=\beta^4-1/(1+\beta^4)\ln(\beta^2)+(1-\beta^4)$ $\beta=(1/1-\varepsilon)^{1/2},\ \varepsilon=S_TS_L-W_{\text{fin}}L_{\text{fin}}/S_TS_L$	1/3	107.2
4	Khan et al. [18,19]	$\text{Nu}_{\text{ave}}=0.61(S_T/d_e)^{0.591}(S_L/d_e)^{0.053}/[(S_T/d_e)-1]^{0.5}$ $\times\{1-2\ \exp[-1.09(S_L/d_e)]\}\text{Re}_{\text{ave}}^{1/2}\text{Pr}_{f,\text{ave}}^{1/3}$	0.5	453.2
5	Short et al. [29]	For $\text{Re}_{\text{ave}}<1000$, $\text{Nu}_{\text{ave}}=0.76(S_L/d_e)^{0.16}(S_T/d_e)^{0.2}(H_{\text{fin}}/d_e)^{-0.11}\text{Re}_{\text{ave}}^{0.33}\text{Pr}_{f,\text{ave}}^{1/3}$	0.33	71.1
6	Moores and Joshi [30]	For $\text{Re}_{\text{ave}}<1000$, $\text{Nu}_{\text{ave}}=h_{\text{ave}}d_e/k_{f,\text{ave}}$, $h_{\text{ave}}/\eta_{\text{fin}}=h_{c6},\ h_{c6}=\text{Nu}_{c6}k_{f,\text{ave}}/d_e$ $\text{Nu}_{c6}=0.64(H_{\text{fin}}/d_e)^{0.36}\text{Re}_{\text{ave}}^{0.64}\text{Pr}_{f,\text{ave}}^{0.36}$	0.64	497.0
7	Koşar and Peles [9]	$\text{Nu}_{\text{ave}}=0.0423\text{Re}_{\text{ave}}^{0.99}\text{Pr}_{f,\text{ave}}^{0.21}(\text{Pr}_{f,\text{ave}}/\text{Pr}_{w,\text{ave}})^{0.25}$	0.99	77.7
8	Prasher et al. [11]	For $\text{Re}_{\text{ave}}<100$, $\text{Nu}_{\text{ave}}=0.132(S_L-d_e/d_e)^{-0.256}\text{Re}_{\text{ave}}^{0.84}$	0.84	104.2
9	Present study	$\text{Nu}_{\text{ave}}=0.0285\text{Re}_{\text{ave}}^{0.932}\text{Pr}_{f,\text{ave}}^{1/3}$	0.932	11.7
10	Present study	$\text{Nu}_{\text{ave}}=0.0241\text{Re}_{\text{ave}}^{0.953}\text{Pr}_{f,\text{ave}}^{0.36}(\text{Pr}_{f,\text{ave}}/\text{Pr}_{w,\text{ave}})^{0.25}$	0.953	10.7

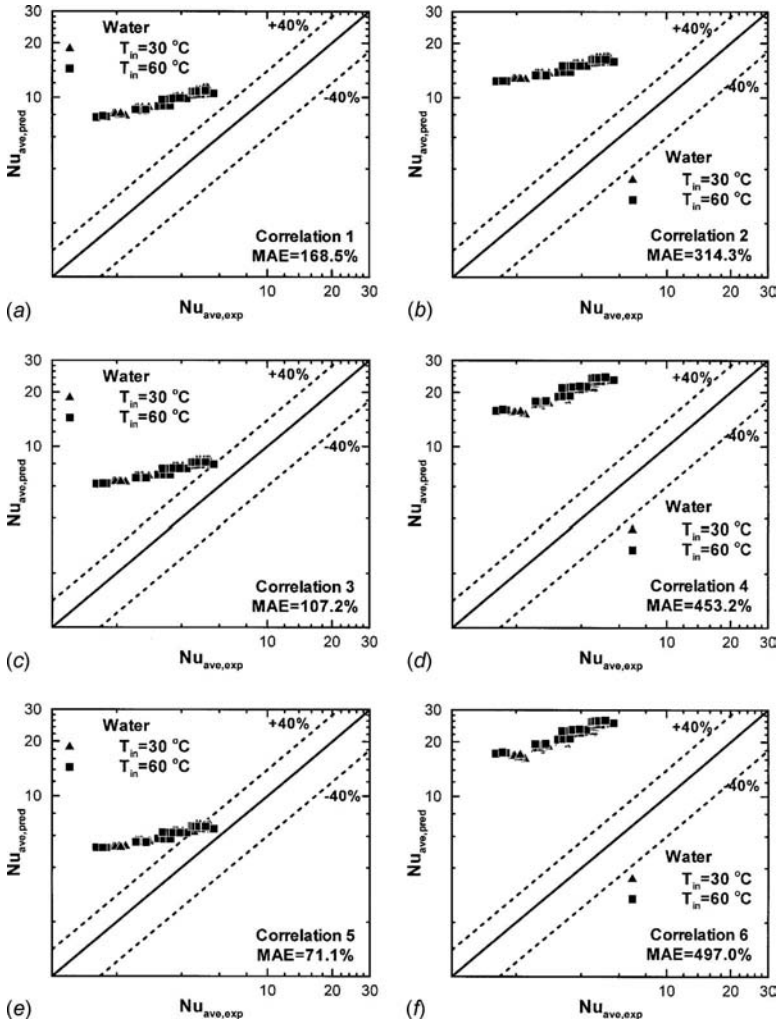

Fig. 7 Comparison of the average Nusselt number data with predictions of (*a*) correlation 1, (*b*) correlation 2, (*c*) correlation 3, (*d*) correlation 4, (*e*) correlation 5, and (*f*) correlation 6

and 8) with the data. Also included in these figures as well as in Table 2 for each correlation is the mean absolute error (MAE), defined as

$$\mathrm{MAE} = \frac{1}{M}\sum \frac{|\mathrm{Nu}_{\mathrm{ave,exp}} - \mathrm{Nu}_{\mathrm{ave,pred}}|}{\mathrm{Nu}_{\mathrm{ave,exp}}} \times 100\% \qquad (22)$$

where M is the number of data points.

Figures 7(*a*)–7(*f*) show that the previous conventional long and intermediate pin-fin correlations overpredict the present $\mathrm{Nu}_{\mathrm{ave}}$ data. The deviation is larger at low $\mathrm{Nu}_{\mathrm{ave,exp}}$ and decreases with increasing $\mathrm{Nu}_{\mathrm{ave,exp}}$. Figures 8(*a*) and 8(*b*) show that the previous micro-pin-fin correlations also overpredict the present $\mathrm{Nu}_{\mathrm{ave}}$ data by fairly large margins. However, the deviation is fairly constant throughout the entire $\mathrm{Nu}_{\mathrm{ave,exp}}$ range.

The comparisons suggest that the previous heat transfer correlations may not be able to describe heat transfer in the present

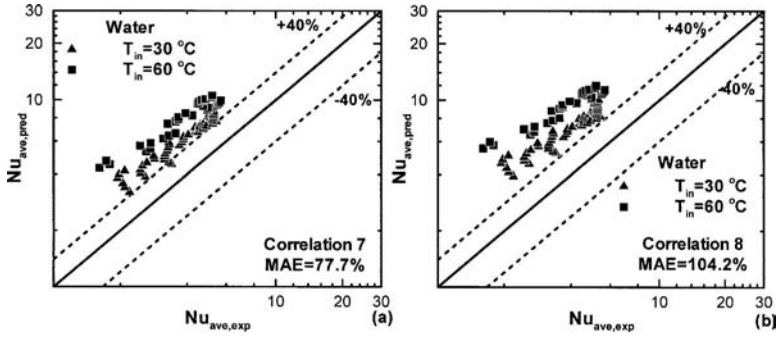

Fig. 8 Comparison of the average Nusselt number data with predictions of (*a*) correlation 7 and (*b*) correlation 8

micro-pin-fin array with sufficient accuracy. It is important to emphasize that the discrepancy between the previous correlation predictions and present data is not necessarily related to weaknesses in the correlations themselves but more to the geometric parameters and operating conditions of the present micro-pin-fin arrays falling outside the recommended application range for these previous correlations. Extrapolating a correlation to geometrical parameters and operating conditions beyond those for which the correlation was originally developed can lead to appreciable errors.

3.4 New Heat Transfer Correlations. Deviations in the predictions of previous correlations from the present data point to the need to develop new correlations that can yield more accurate predictions. Two new heat transfer correlations are proposed based on the two common functional forms given by Eqs. (20) and (21). It should be noted that a correlation based on Eq. (20) without accounting for the property variation effect may lead to less accurate predictions when there exists a high temperature difference between micro-pin-fin base and liquid coolant. The functional form is nevertheless adopted as the resulting correlation is much easier to use, and no prior knowledge of $T_{w,\mathrm{ave}}$ is needed in order to calculate $\mathrm{Nu}_{\mathrm{ave}}$.

Since only water was tested as a cooling liquid, the range of the Prandtl number is not wide enough to allow the exponents n and l in Eqs. (20) and (21) to be correlated from the present data. The values that were used in the previous correlations are therefore adopted in the new correlations: the exponent n of $\mathrm{Pr}_{f,\mathrm{ave}}$ in Eq. (20) is assumed to be 1/3 [4,5], and the exponent n of $\mathrm{Pr}_{f,\mathrm{ave}}$ and exponent l of $\mathrm{Pr}_{f,\mathrm{ave}}/\mathrm{Pr}_{f,\mathrm{ave}}$ in Eq. (21) are assumed to be 0.36 and 0.25, respectively [1]. The two correlations can then be expressed as

$$\mathrm{Nu}_{\mathrm{ave}} = c\mathrm{Re}_{\mathrm{ave}}^{m}\mathrm{Pr}_{f,\mathrm{ave}}^{1/3} \tag{23}$$

and

$$\mathrm{Nu}_{\mathrm{ave}} = c\mathrm{Re}_{\mathrm{ave}}^{m}\mathrm{Pr}_{f,\mathrm{ave}}^{0.36}\left(\frac{\mathrm{Pr}_{f,\mathrm{ave}}}{\mathrm{Pr}_{w,\mathrm{ave}}}\right)^{0.25} \tag{24}$$

A linear regression analysis is performed to determine the values of the coefficient c and exponent m for the above two correlations. The final correlations are

$$\mathrm{Nu}_{\mathrm{ave}} = 0.0285\mathrm{Re}_{\mathrm{ave}}^{0.932}\mathrm{Pr}_{f,\mathrm{ave}}^{1/3} \tag{25}$$

and

$$\mathrm{Nu}_{\mathrm{ave}} = 0.0241\mathrm{Re}_{\mathrm{ave}}^{0.953}\mathrm{Pr}_{f,\mathrm{ave}}^{0.36}\left(\frac{\mathrm{Pr}_{f,\mathrm{ave}}}{\mathrm{Pr}_{w,\mathrm{ave}}}\right)^{0.25} \tag{26}$$

The two correlations are listed in Table 2 as correlations 9 and 10, respectively.

Figures 9(*a*) and 9(*b*) compare the predictions of correlations 9 and 10 with the present data, respectively. The overall MAE values of 11.7% and 10.7% for the two new heat transfer correlations demonstrate their excellent predictive capability.

The exponent m in correlations 9 and 10 has values of 0.932 and 0.953, respectively. The values are fairly close to those for the two previous micro-pin-fin correlations (0.99 for correlation 7 and 0.84 for correlation 8) and are substantially higher than those for the previous conventional long and intermediate pin-fin correlations (form 0.33 to 0.64), which confirms a stronger dependence of $\mathrm{Nu}_{\mathrm{ave}}$ on $\mathrm{Re}_{\mathrm{ave}}$ in micro-pin-fin arrays. Koşar and Peles [8] attributed the stronger dependence of $\mathrm{Nu}_{\mathrm{ave}}$ on $\mathrm{Re}_{\mathrm{ave}}$ in micro-pin-fin arrays to the endwall effects. According to Koşar and Peles [8], a thicker boundary layer would be formed in the vicinity of the wall-pin intersection at lower Re, which might result in a reduced heat transfer coefficient. In addition, the presence of endwalls might delay flow separation to higher Re, which might also lead to a weaker heat transfer at lower Re. To quantitatively explain the observed trend, a three-dimensional numerical analysis of heat transfer in the micro-pin-fin array is currently being pursued by the authors.

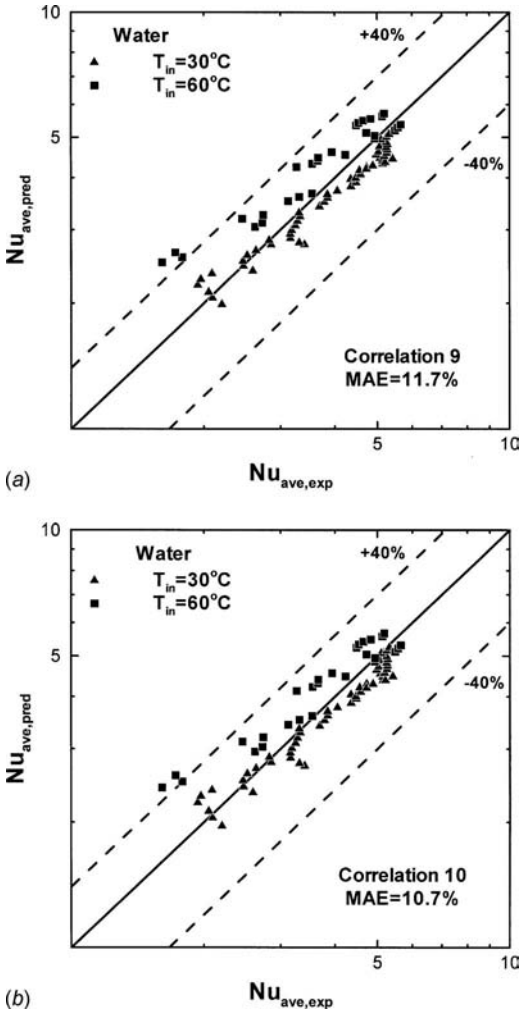

Fig. 9 Comparison of the average Nusselt number data with predictions of (*a*) correlation 9 and (*b*) correlation 10

The coefficients c in correlations 9 and 10 are assumed as constants and have values of 0.0285 and 0.0241, respectively. Most previous studies on heat transfer in pin-fin arrays indicated that the c value is affected by pin-fin geometric parameters, such as d, H_{fin}, S_L, and S_T. A common approach to account for the effect, which has been adopted in developing correlations 3–6 and 8, is to correlate c as a function of these geometric parameters. However, as the interest in using micro-pin-fin arrays as heat transfer enhancement structures is fairly recent, only a limited number of micro-pin-fin geometries have been tested so far, which makes it difficult to develop such a general correlation for c.

3.5 Local Heat Transfer Characteristics. The present test section design allows the local heat transfer coefficient averaged over the four surfaces (upstream, downstream, and sides) of a single micro-pin-fin $h_{\mathrm{tc}i}$ at the three $z_{\mathrm{tc}i}$ to be evaluated. Taking advantage of symmetry, a unit cell containing a single micro-pin-fin is examined at each $z_{\mathrm{tc}i}$, as shown in Fig. 3. $T_{w,\mathrm{tc}i}$ is evaluated from Eq. (11). Assuming a linear increase in water temperature along the flow direction, the water bulk temperature at $z_{\mathrm{tc}i}$, $T_{f,\mathrm{tc}i}$, can be determined from

$$T_{f,\mathrm{tc}i} = T_{\mathrm{in}} + (T_{\mathrm{out}} - T_{\mathrm{in}})\frac{z_{\mathrm{tc}i}}{L_{hs}} \tag{27}$$

The following energy balance can be written for the unit cell:

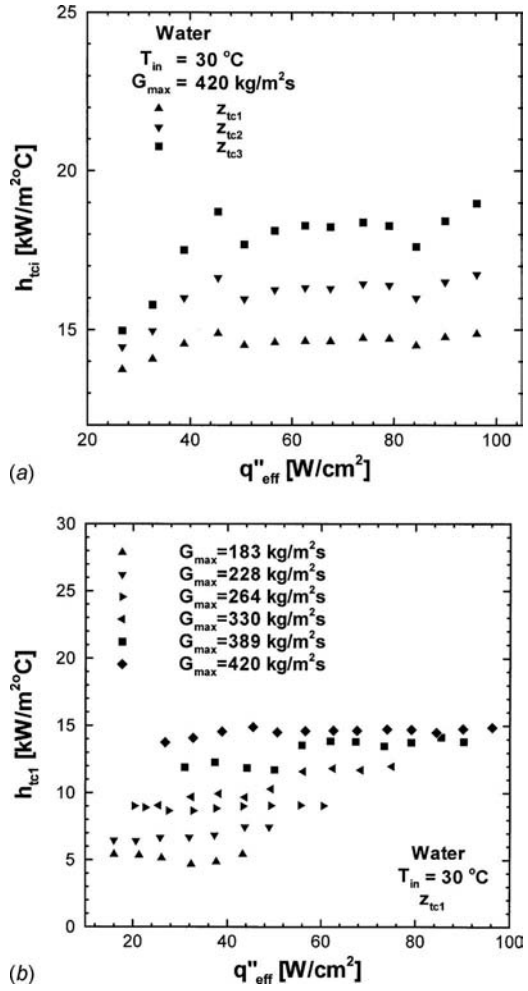

Fig. 10 Variation in local heat transfer coefficient with input heat flux (*a*) at z_{tc1}–z_{tc3} for T_{in}=30°C and G_{max}=420 kg/m² s and (*b*) at z_{tc1} for T_{in}=30°C and all six G_{max}

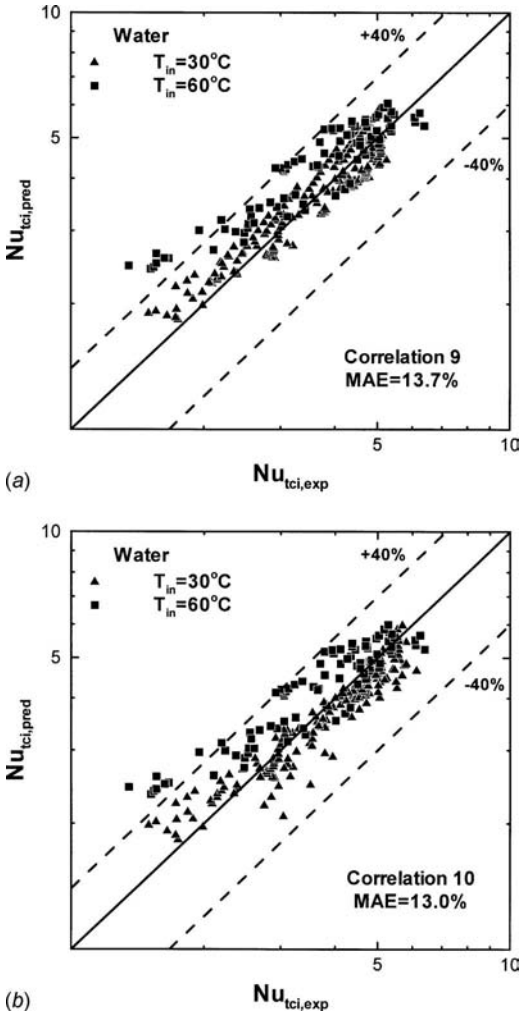

Fig. 11 Comparison of the local Nusselt number data with predictions of (*a*) correlation 9 and (*b*) correlation 10

$$q''_{\text{eff}} A_{\text{cell}} = h_{\text{tc}i}(T_{w,\text{tc}i} - T_{f,\text{tc}i})[(A_{\text{cell}} - A_c) + \eta_{\text{fin}} A_{\text{fin}}] \tag{28}$$

where A_{cell} is the area of the unit cell base endwall,

$$A_{\text{cell}} = S_L S_T \tag{29}$$

Once $T_{w,\text{tc}i}$ and $T_{f,\text{tc}i}$ are determined from Eqs. (11) and (27), respectively, the value of $h_{\text{tc}i}$ can be calculated iteratively from Eq. (28).

Figure 10(*a*) shows the variation in $h_{\text{tc}i}$ with q''_{eff} for T_{in} =30°C and G_{max}=420 kg/m² s. At each $z_{\text{tc}i}$, $h_{\text{tc}i}$ increases slightly with increasing q''_{eff}. For a given q''_{eff}, $h_{\text{tc}i}$ increases appreciably along the flow direction. The higher value of $h_{\text{tc}i}$ downstream of the micro-pin-fin array may be caused by the increase in the Reynolds number along the streamwise direction. This is because the higher downstream water temperature led to a reduced water density and viscosity. Figure 10(*b*) shows $h_{\text{tc}i}$ at z_{tc1} versus q''_{eff} for T_{in}=30°C and all six G_{max}. h_{tc1} increases appreciably with increasing G_{max} for a given q''_{eff}. For a constant G_{max}, h_{tc1} remains fairly constant or increases only slightly with increasing q''_{eff}. The observed trend is consistent with that found in h_{ave}, as shown in Figs. 5(*a*) and 5(*b*).

Once $h_{\text{tc}i}$ is calculated, the local Nusselt number $\text{Nu}_{\text{tc}i}$ can be evaluated from

$$\text{Nu}_{\text{tc}i} = \frac{h_{\text{tc}i} d_e}{k_{f,\text{tc}i}} \tag{30}$$

Figures 11(*a*) and 11(*b*) compare the $\text{Nu}_{\text{tc}i}$ data with the predictions of correlations 9 and 10, respectively. The overall MAE values of 13.7% and 13.0% for the two correlations demonstrate that the correlations developed for the average Nusselt number can adequately describe the local heat transfer characteristics.

4 Conclusions

This is Paper I of a two-part study devoted to thermal and hydrodynamic characteristics of water single-phase flow in an array of staggered square micro-pin-fins. This paper reports the heat transfer results of the study. In this paper, new average and local heat transfer data were presented, complemented by an identification of unique parametric trends and an assessment of the suitability of previous correlations to predicting the present experimental results. Two new heat transfer correlations were developed based on the average heat transfer data. Key findings from the study are as follows:

(1) The average Nusselt number increases with increasing average Reynolds number. The relationship can be described by power law.
(2) Six previous heat transfer correlations for low Reynolds number (Re < 1000) single-phase flow in conventional long and intermediate pin-fin arrays were examined in predicting

the average Nusselt number data. All previous correlations overpredicted the data. The deviation in the predictions from the data is larger at the low Nusselt number and decreases with increasing Nusselt number.

(3) Two previous micro-pin-fin correlations, that of Koşar and Peles [9] and that of Prasher et al. [11], were also examined and found to overpredict the data. The deviation in the predictions from the data is fairly constant throughout the entire Nusselt number range.

(4) Two new correlations were proposed for the average Nusselt number based on the present data, in which the average Nusselt number is correlated with the average Reynolds number by power law. Values of the exponent m of the Reynolds number in the two new correlations are fairly close to those for the previous micro-pin-fin correlations (the correlations of Koşar and Peles [9] and Prasher et al. [11]) but substantially higher than those for the previous conventional long and intermediate pin-fin correlations. The results indicate a stronger Nusselt number dependence on the Reynolds number in micro-pin-fin arrays.

(5) The correlations developed for the average Nusselt number can adequately predict the local Nusselt number data.

Acknowledgment

The authors are grateful for the support of the National Science Foundation (Award No. CBET07-30315). The micro-pin-fin heat sink test section was fabricated at the Laser-Assisted Multi-scale Manufacturing Laboratory, University of Wisconsin-Madison. The assistance of Professor Frank Pfefferkorn and Yongho Jeon in fabricating the heat sink test section was greatly appreciated.

Nomenclature

A_c = cross-sectional area of a micro-pin-fin
A_{cell} = area of the unit cell base endwall
A_{fin} = wetted surface area of a micro-pin-fin
$A_{\min}$ = minimum transverse flow area of a micro-pin-fin array
A_t = total area of the micro-pin-fin array base endwall
c = coefficient in heat transfer correlation
c_p = specific heat
d = diameter of a circular pin-fin
d_e = equivalent diameter of a square micro-pin-fin
$G_{\max}$ = maximum mass velocity
h = heat transfer coefficient
h_{ave} = average heat transfer coefficient for the entire micro-pin-fin array
$h_{\text{tc}i}$ = local heat transfer coefficient at the thermocouple streamwise location
H_{fin} = height of a pin-fin
H_w = distance from thermocouple to micro-pin-fin base
k = thermal conductivity
l = exponent of the Prandtl number ratio or viscosity ratio
L_{fin} = length of a micro-pin-fin
L_{hs} = length of the micro-pin-fin array base endwall
m = exponent of the Reynolds number
m_{fin} = fin parameter
$\dot{m}$ = total mass flow rate
M = number of data points
n = exponent of the Prandtl number
N_t = total number of micro-pin-fins in array
Nu = Nusselt number
Nu_{ave} = average Nusselt number
$\text{Nu}_{\text{tc}i}$ = local Nusselt number at the thermocouple streamwise location
P_{fin} = cross-section perimeter of a micro-pin-fin
P_w = total power input
Pr = Prandtl number
$\text{Pr}_{f,\text{ave}}$ = Prandtl number at $T_{f,\text{ave}}$
$\text{Pr}_{w,\text{ave}}$ = Prandtl number at $T_{w,\text{ave}}$
q''_{eff} = heat flux based on the total area of the micro-pin-fin array base endwall
Q_{fin} = heat transferred to a micro-pin-fin array
Q_{loss} = heat loss
S_D = diagonal pitch
S_L = longitudinal pitch
S_T = transverse pitch
Re = Reynolds number based on d or d_e
Re_{ave} = average Reynolds number
T = temperature
$T_{f,\text{ave}}$ = average water bulk temperature
$T_{f,\text{tc}i}$ = water bulk temperature at the thermocouple streamwise location
T_{in} = inlet temperature
T_{out} = outlet temperature
$T_{\text{tc}i}$ = thermocouple reading
$T_{w,\text{ave}}$ = average micro-pin-fin base temperature
$T_{w,\text{tc}i}$ = micro-pin-fin base temperature at the thermocouple streamwise location
$u_{\max}$ = maximum velocity
W_{fin} = width of a micro-pin-fin
W_{hs} = width of the micro-pin-fin array base endwall
$z_{\text{tc}i}$ = streamwise location of thermocouple ($i=1-3$)

Greek Symbols

β = geometric parameter in the Hwang and Yao correlation (correlation 3)
η_{fin} = fin efficiency
λ = geometric parameter in the Hwang and Yao correlation (correlation 3)
μ = viscosity
ρ = density

Subscripts

ave = average
$c6$ = Moores and Joshi correlation (correlation 6)
exp = experimental (measured)
f = liquid (water) bulk
in = inlet
out = outlet
pred = predicted
$p1$ = deep plenum
$p2$ = shallow plenum
s = solid (copper)
$\text{tc}i$ = thermocouple ($i=1-3$)
w = base endwall

References

[1] Tuckerman, D. B., and Pease, R. F. W., 1981, "High-Performance Heat Sinking for VLSI," IEEE Electron Device Lett., **EDL-2**(5), pp. 126–129.
[2] Kawano, K., Minakami, K., Iwasaki, H., and Ishizuka, M., 1998, "Micro Channel Heat Exchanger for Cooling Electrical Equipment," ASME Paper No. HTD-361-3/PID-3.
[3] Harms, T. M., Kazmierczak, M. J., and Cerner, F. M., 1999, "Developing Convective Heat Transfer in Deep Rectangular Microchannels," Int. J. Heat Fluid Flow, **20**(2), pp. 149–157.
[4] Qu, W., and Mudawar, I., 2002, "Experimental and Numerical Study of Pressure Drop and Heat Transfer in a Single-Phase Micro-Channel Heat Sink," Int. J. Heat Mass Transfer, **45**(12), pp. 2549–2565.
[5] Lee, P. S., Garimella, S. V., and Liu, D., 2005, "Investigation of Heat Transfer in Rectangular Microchannels," Int. J. Heat Mass Transfer, **48**(9), pp. 1688–1704.
[6] Koşar, A., Mishra, C., and Peles, Y., 2005, "Laminar Flow Across a Bank of Low Aspect Ratio Micro Pin Fins," ASME J. Fluids Eng., **127**(3), pp. 419–430.
[7] Peles, Y., Koşar, A., Mishra, C., Kuo, C.-J., and Schneider, B., 2005, "Forced Convective Heat Transfer Across a Pin Fin Micro Heat Sink," Int. J. Heat Mass Transfer, **48**(17), pp. 3615–3627.

[8] Koşar, A., and Peles, Y., 2006, "Thermal-Hydraulic Performance of MEMS-Based Pin Fin Heat Sink," ASME J. Heat Transfer, **128**(2), pp. 121–131.
[9] Koşar, A., and Peles, Y., 2006, "Convective Flow of Refrigerant (R-123) Across a Bank of Micro Pin Fins," Int. J. Heat Mass Transfer, **49**(17-18), pp. 3142–3155.
[10] Koşar, A., Kuo, C., and Peles, Y., 2006, "Hydoroil-Based Micro Pin Fin Heat Sink," ASME Paper No. IMECE2006-13257.
[11] Prasher, R. S., Dirner, J., Chang, J. Y., Myers, A., Chau, D., He, D., and Prstic, S., 2007, "Nusselt Number and Friction Factor of Staggered Arrays of Low Aspect Ratio Micro-Pin-Fins Under Cross Flow for Water As Fluid," ASME J. Heat Transfer, **129**(2), pp. 141–153.
[12] Siu-Ho, A., Qu, W., and Pfefferkorn, F., 2007, "Experimental Study of Pressure Drop and Heat Transfer in a Single-Phase Micro-Pin-Fin Heat Sink," ASME J. Electron. Packag., **129**(4), pp. 479–487.
[13] Zukauskas, A., 1972, "Heat Transfer From Tubes in Crossflow," *Advances in Heat Transfer*, Vol. 8, Academic, New York, pp. 93–160.
[14] Gunter, A. Y., and Shaw, W. A., 1945, "A General Correlation of Friction Factor for Various Types of Surfaces in Crossflow," Trans. ASME, **67**, pp. 643–660.
[15] Whitaker, S., 1972, "Forced Convection Heat Transfer Correlations for Flow in Pipes, Past Flat Plates, Single Cylinders, Single Spheres, and for Flow in Packed Beds and Tube Bundles," AIChE J., **18**(2), pp. 361–371.
[16] Gaddis, E. S., and Gnielinski, V., 1985, "Pressure Drop in Cross Flow Across Tube Bundles," Int. Chem. Eng., **25**(1), pp. 1–14.
[17] Hwang, T. H., and Yao, S. C., 1986, "Crossflow Heat Transfer in Tube Bundles at Low Reynolds Numbers," ASME J. Heat Transfer, **108**(3), pp. 697–700.
[18] Khan, W. A., 2004, "Modeling of Fluid Flow and Heat Transfer for Optimization of Pin-Fin Heat Sinks," Ph.D. thesis, University of Waterloo, Waterloo, Canada.
[19] Khan, W. A., Culham, J. R., and Yovanovich, M. M., 2006, "Convection Heat Transfer from Tube Banks in Crossflow: Analytical Approach," Int. J. Heat Mass Transfer, **49**(25–26), pp. 4831–4838.
[20] Metzger, D. E., Berry, R. A., and Benson, J. P., 1982, "Developing Heat Transfer in Rectangular Ducts With Staggered Arrays of Short Pin Fins," ASME J. Heat Transfer, **104**(4), pp. 700–706.
[21] Simoneau, R. J., and VanFossen, G. J., Jr., 1984, "Effect of Location in an Array on Heat Transfer to a Short Cylinder in Crossflow," ASME J. Heat Transfer, **106**(1), pp. 42–48.
[22] Armstrong, J., and Winstanley, D., 1988, "A Review of Staggered Array Pin Fin Heat Transfer for Turbine Cooling Applications," ASME J. Turbomach., **110**(1), pp. 94–103.
[23] Chyu, M. K., 1990, "Heat Transfer and Pressure Drop for Short Pin-Fin Arrays With Pin-Endwall Fillet," ASME J. Heat Transfer, **112**(4), pp. 926–932.
[24] Chyu, M. K., Hsing, Y. C., and Natarajan, V., 1998, "Convective Heat Transfer of Cubic Fin Arrays in a Narrow Channel," ASME J. Turbomach., **120**(2), pp. 362–367.
[25] Chyu, M. K., Hsing, Y. C., Shih, T. I.-P., and Natarajan, V., 1999, "Heat Transfer Contributions of Pins and Endwall in Pin-Fin Arrays: Effects of Thermal Boundary Condition Modeling," ASME J. Turbomach., **121**(2), pp. 257–263.
[26] Hwang, J. J., Lai, D. Y., and Tsia, Y. P., 1999, "Heat Transfer and Pressure Drop in Pin Fin Trapezoidal Ducts," ASME J. Turbomach., **121**(2), pp. 264–271.
[27] Marques, C., and Kelly, K. W., 2004, "Fabrication and Performance of a Pin Fin Micro Heat Exchanger," ASME J. Heat Transfer, **126**(3), pp. 434–444.
[28] Short, B. E., Jr., Raad, P. E., and Price, D. C., 2002, "Performance of Pin Fin Cast Aluminum Coldwalls, Part I: Friction Factor Correlation," J. Thermophys. Heat Transfer, **16**(3), pp. 389–396.
[29] Short, B. E., Jr., Raad, P. E., and Price, D. C., 2002, "Performance of Pin Fin Cast Aluminum Coldwalls, Part II: Colburn j-Factor Correlations," J. Thermophys. Heat Transfer, **16**(3), pp. 397–403.
[30] Moores, K. A., and Joshi, Y. K., 2003, "Effect of Tip Clearance on the Thermal and Hydrodynamic Performance of a Shrouded Pin Fin Array," ASME J. Heat Transfer, **125**(6), pp. 999–1006.
[31] Qu, W., and Siu-Ho, A., 2008, "Liquid Single-Phase Flow in an Array of Micro-Pin-Fins: Part-II Pressure Drop Characteristics," ASME J. Heat Transfer, **130**, p. 124501.
[32] Kline, S. J., and McClintock, F. A., 1953, "Describing Uncertainties in Single-Sample Experiments," Mech. Eng. (Am. Soc. Mech. Eng.), **75**(1), pp. 3–8.

Ab Initio Molecular Dynamics Study of Nanoscale Thermal Energy Transport

Tengfei Luo
Department of Mechanical Engineering,
Michigan State University,
2555 Engineering Building,
East Lansing, MI 48824
e-mail: luotengf@msu.edu

John R. Lloyd
Department of Mechanical and Astronautical Engineering,
Naval Postgraduate School,
333 Watkins Hall,
Monterey, CA 93943
e-mail: lloyd@egr.msu.edu

Ab initio molecular dynamics, which employs density functional theory, is used to study thermal energy transport phenomena in nanoscale structures. Thermal equilibration in multiple thin layer structures with thicknesses less than 1 nm per layer is simulated. Different types of layer combinations are investigated. Periodic boundary conditions in all directions are used in all cases. Two neighboring layers are first set to different temperatures using Nosé–Hoover thermostats, and then the process of energy equilibration is simulated with a "free run" (without any thermostat controlling the temperatures). The temperature evolutions in the two neighboring layers are computed. The atomic vibration power spectra are calculated and used to explain the phenomena observed in the simulation. [DOI: 10.1115/1.2976562]

Keywords: ab initio, molecular dynamics, thermal energy transport, nanoscale

1 Introduction

Moore's law predicted that the number of transistors on a chip will double about every two years. This anticipated trend toward miniaturization of electronic devices has led to device features in the nanometer range. Silicon integration suppliers are now producing 65 nm CPUs, 45 nm silicon is on-target for delivery in 2007 [1], and 28 nm silicon-on-insulator transistors are predicted to reach a gate length of 28 nm by the year 2009 [2]. Together with the trend of miniaturization are the ultrafast transportation phenomena. The time scales of interest in nanoengineering range from femtoseconds to nanoseconds. In such confined geometrical structures and at ultrasmall time scales, charge transport and mass transport have been studied extensively for many years. On the other hand, nanoscale thermal energy transport, which has great influence on the performance of many miniaturized systems such as CPU chips and semiconductor lasers, has not gained as much attention as other transport phenomena. In some areas, especially in nanoscale electronic devices, thermal transport issues have become a bottleneck or barrier to their further development. As a result, understanding and predicting thermal transport become essential to further the advance of nanoengineering.

In general, there exist two kinds of heat carriers in solid state thermal transport: phonons and electrons. Phonons are the quanta of the lattice vibrational field [3]. Phonons dominate the energy transport in semiconductors and insulators. While in metals, electrons are the main energy transporters.

There are many different approaches to study nanoscale thermal transport. Among them, classical molecular dynamics (MD) has the potential to simulate ultrasmall and ultrafast transport phenomena [4–8]. Classical MD is a computational method that simulates the real motion of every single atom involved in thermal energy transport by using a "predefined" empirical potential and then solving Newton's equation of motion. After a trajectory of the atoms' motion is obtained through the simulation, properties of the system can be calculated. Thus, if one can find an empirical potential field model accurate enough to describe the interaction of the atoms in the system of interest, any property related to the motion or transport of the atoms can be predicted through a MD simulation. Such empirical potential functions are often determined by fitting parameters to reproduce one or several properties of a certain system under prescribed conditions. When these fitted potential functions are used to calculate other properties or when the simulation is carried out on different conditions, the results become questionable [9,10]. Not only does classical MD suffer from this transferability problem but it also fails to take electrons into consideration because the predefined potential has already integrated out the electronic degrees of freedom. This feature prevents its application on thermal energy or electronic transport simulation in metallic materials where the electrons play an important role in transport phenomena.

The reign of traditional molecular dynamics and electronic structure methods was greatly extended by the family of techniques that is called "ab initio molecular dynamics." The basic idea underlying this ab initio molecular dynamics method is to compute the forces acting on the nuclei from electronic structure calculations that are performed "on-the-fly" as the molecular dynamics trajectory is generated [11]. In this method, both electronic and nuclear degrees of freedom are considered, and any system consisting of any atom can be simulated without suffering from the transferability problem. We are not aware of any previous work using ab initio molecular dynamics to model thermal energy transport directly.

In the current work, an ab initio molecular dynamics approach employing density functional theory (DFT) is used to simulate the thermal energy equilibration in different types of multi-thin-layers in different temperatures. This should be considered the first step toward the use of the ab initio method to model lattice thermal energy transport (phonon transport). Our work did not involve explicit electron transport properties, which can be calculated using the ab initio method separately by calculating the electronic structure of a system. We expect to model phonon transport, electron transport, and phonon-electron interaction in future work within the reign of the ab initio method. The results show reasonable physics and thus suggest the possibility that the ab initio molecular dynamics simulation is appropriate for the simulation of nanoscale thermal energy transport.

2 Theory and Modeling

2.1 Theory. As we know, any material can be described as consisting of nuclei and electrons. Because the electrons travel

Contributed by the Heat Transfer Division of ASME for publication in the JOURNAL OF HEAT TRANSFER. Manuscript received October 8, 2007; final manuscript received June 5, 2008; published online September 18, 2008. Review conducted by Jayathi Murthy. Paper presented at the Second Energy Nanotechnology International Conference (ENIC2007), Santa Clara, CA, September 5–7, 2007.

thousands of times faster than nuclei, they can follow any nuclear motions with infinitesimal time elapse. As a result, we can decouple the electronic and nuclear motions and say that the electrons respond "instantaneously" to any change in nuclear coordinates. This approximation allows us to rewrite the full electron-nucleus many-body wave function as the product of a nuclear and an electronic wave function. Since the electronic wave function only depends on the instantaneous nuclear configuration, not on time, we can describe its behavior with the time-independent Schrödinger equation. On the other hand, the nuclei are massive enough to be treated as classical particles and can be simulated as if they respond to the electronic forces according to Newton's laws [11]. This semiclassical approximation, coupled with separation of electronic and nuclear variables, is called the Born–Oppenheimer approximation [12]. The molecular dynamics method that utilizes this approximation and solves the static electronic structure problem in each molecular dynamics step given the set of "fixed" nuclear positions at the instant of time is called Born–Oppenheimer MD (BOMD). When BOMD is used, although the electrons are taken into consideration, a simulation can still proceed in a time scale given by the atomic motion due to the fact that the electronic structure problem is calculated at each MD step. BOMD has been demonstrated to be a very accurate and useful method in chemistry, biology, and many other areas. However, in BOMD the electronic structure problem has to be solved self-consistently at each MD step, which introduces a relatively high computational workload and prevents its use in large systems and large time simulations.

An approach to cut down the computational expenses of BOMD, which includes the electrons in a single state, was proposed by Car and Parrinello in 1985 [13]. It is called the Car–Parrinello MD (CPMD) approach. The CPMD approach takes intrinsic advantage of the smooth time-evolution of the dynamically evolving electronic subsystem as much as possible while it makes an acceptable compromise concerning the size of the time step, which is at the nuclear motion time scale. Essentially, the difference between CPMD and BOMD is that the electronic wave function is kept automatically minimized to its ground-state as the nuclei are propagated rather than being solved self-consistently at each molecular dynamics step. The basic idea of the Car–Parrinello approach can be viewed as a way to exploit the quantum-mechanical adiabatic time-scale separation of fast electronic and slow nuclear motions by transforming that separation into a classical-mechanical adiabatic energy-scale separation in the framework of dynamics theory [11]. Car–Parrinello proposed a universal Lagrangian for the electron-nucleus system [13]

$$L_{\mathrm{CP}} = \underbrace{\sum_I \frac{1}{2} M_I \dot{\boldsymbol{r}}_{n,I}^2 + \sum_i \frac{1}{2} \mu_i \langle \dot{\varphi}_i | \dot{\varphi}_i \rangle}_{\text{kinetic energy}} - \underbrace{\langle \psi_o | H_e | \psi_o \rangle}_{\text{potential energy}} + \text{constraints} \tag{1}$$

Here M_I is the atomic mass, $\dot{\boldsymbol{r}}_{n,I}$ is the nuclear degree of freedom, φ_i is the electronic one-particle orbital, ψ_o is the electronic wave function at the ground-state, H_e is the Hamiltonian of the electron subsystem, and μ_i is the "fictitious mass" assigned to the orbital degrees of freedom. The first two terms include nuclear kinetic energy and the fictitious kinetic energy of the electronic degrees of freedom. The third term, in the classical mechanics point of view, is the potential energy. In addition, possible constraints within the set of electron wave functions must be imposed, such as orthonormality.

In classical mechanics the force on the nuclei is obtained from the derivative of the Lagrangian with respect to the nuclear positions. This suggests that a functional derivative with respect to the orbitals, which are interpreted as classical fields, might yield the force on the orbitals, given the Lagrangian in Eq. (1). The corresponding Lagrange equations of motion for both nuclear positions and the orbitals are

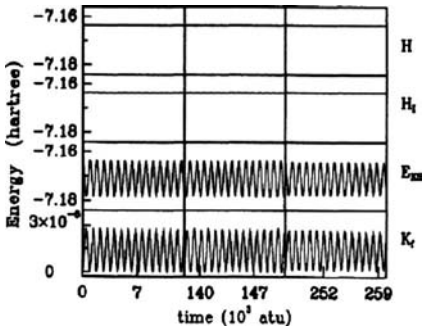

Fig. 1 Typical energies in a CPMD run

$$M_I \ddot{\boldsymbol{r}}_{n,I}(t) = -\frac{\partial}{\partial \boldsymbol{r}_{n,I}} \langle \psi_o | H_e | \psi_o \rangle + \frac{\partial}{\partial \boldsymbol{r}_{n,I}} \{\text{constraints}\} \tag{2}$$

$$\mu_i \ddot{\varphi}_i(t) = -\frac{\delta}{\delta \varphi_i^*} \langle \psi_o | H_e | \psi_o \rangle + \frac{\delta}{\delta \varphi_i^*} \{\text{constraints}\} \tag{3}$$

According to the Car–Parrinello equation of motion above, the nuclei evolve in time at a certain (instantaneous) physical temperature $\propto \Sigma_I M_I \dot{\boldsymbol{r}}_{n,I}^2$, whereas a "fictitious temperature" $\propto \Sigma_i \mu_i \langle \dot{\varphi}_i | \dot{\varphi}_i \rangle$ is associated with the electronic degrees of freedom. During a CPMD run, the electrons are kept at a much lower "electronic temperature" when compared with the "nuclear temperature." In this terminology, low electronic temperature means that the electronic subsystem is close to its instantaneous minimum energy $\min_{\psi_o} \langle \psi_o | H_e | \psi_o \rangle$, i.e., close to the exact Born–Oppenheimer surface [14], see Fig. 1.

Thus, a ground-state wave function optimized for the initial configuration of the nuclei will stay close to its ground-state during time-evolution if it is kept at a sufficiently low temperature.

The total ground-state energy of the interacting system of electrons with classical nuclei fixed at positions $\{\boldsymbol{r}_{n,I}\}$ can be obtained through the minimization of the Kohn–Sham energy

$$\min_{\psi_o} \{\langle \psi_o | H_e | \psi_o \rangle\} = \min_{\{\varphi_i\}} E^{\mathrm{KS}}[\{\varphi_i\}] \tag{4}$$

where the Kohn–Sham energy E^{KS} is given by [15]

$$E^{\mathrm{KS}}[\{\varphi_i\}] = T_s[\{\varphi_i\}] + \int d\boldsymbol{r} V_{\mathrm{ext}}(\boldsymbol{r}) n(\boldsymbol{r}) + \frac{1}{2} \int d\boldsymbol{r} V_H(\boldsymbol{r}) n(\boldsymbol{r}) + E_{\mathrm{xc}}[n] \tag{5}$$

The first term is the kinetic energy of a noninteracting reference system consisting of the same number of electrons exposed to the same external potential as in the fully interacting system. The second term comes from the fixed external potential. The third term is the classical electrostatic energy of two charge clouds, which stem from the electronic density. The last term is the contribution from the exchange-correlation function. We can see from Eq. (5) that the Kohn–Sham energy is an explicit functional of the set of auxiliary functions $\{\varphi_i(\boldsymbol{r})\}$ that satisfy the orthonormality relation $\langle \varphi_i | \varphi_j \rangle = \delta_{ij}$. This is a dramatic simplification since the minimization with respect to all possible many-body wave functions $\{\psi\}$ is replaced by a minimization with respect to a set of orthonormal one-particle functions, the Kohn–Sham orbitals $\{\varphi_i\}$. In the DFT framework, the associated electronic one-body density or charge density

$$n(\boldsymbol{r}) = \sum_i^{\mathrm{occ}} f_i |\varphi_i(\boldsymbol{r})|^2 \tag{6}$$

is obtained from a single Slater determinant built from the occupied orbitals, where $\{f_i\}$ are integer occupation numbers.

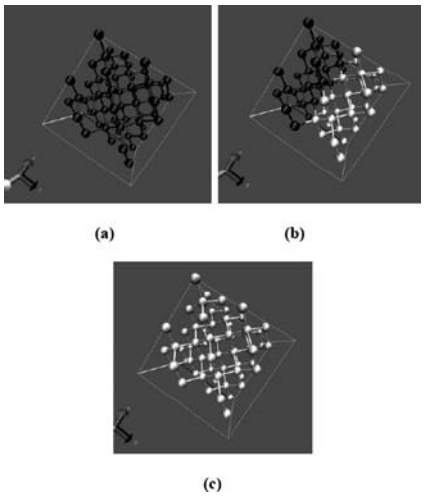

Fig. 2 Material combinations of thin layers ((a) Si–Si, (b) Si–Ge, and (c) Ge–Ge)

In many current density functional theory codes, plane waves are used as the basic set in order to represent the periodic part of the orbitals, φ_i. Such a method makes use of the reality that the periodicity of the lattice produces a periodic potential and thus imposes the same periodicity on the density.

In order to minimize the size of the plane wave basis necessary for the calculation, core electrons are replaced by pseudopotentials. Pseudopotentials are thus required to correctly represent the long range interactions of the core and to produce pseudo-wave-function solutions that approach the full wave function outside a core radius, r_c. Inside this radius the pseudopotential and the wave function should be as smooth as possible in order to allow for a small plane wave cutoff. In addition, it is desired that a pseudopotential is transferable. This means that the same pseudopotential can be used in calculations for different systems under different conditions with comparable accuracy.

2.2 System and Modeling. In the current research project, we use the CPMD package version 3.11 [16]. This CPMD program is a plane wave/pseudopotential implementation of density functional theory, particularly designed for ab initio molecular dynamics. Visual molecular dynamics (VMD) [17] is used to visualize the structure of systems.

In the thermal energy transport simulation, different systems were studied. The simulated systems contain 64 atoms. In terms of material, silicon-silicon (Si–Si) with a lattice constant of 5.431 Å, germanium-germanium (Ge–Ge) with a lattice constant of 5.658 Å, and silicon-germanium (Si–Ge) thin layer combinations were studied. For the Si–Ge system, the simulation cell size was chosen as twice the germanium lattice constant (i.e., 11.316 Å), in which case the silicon density is slightly larger than its bulk density, and the germanium density is the same as its bulk density. A geometry optimization with periodic boundary condition showed that such a structure is stable. The reasons we chose silicon and germanium for simulation are as follows: (1) They have similar crystal structure and (2) they are semiconductors that have well defined band gaps. Thus we do not need to consider excited states that would result in substantially greater computational time. Examples of the thin layer structures are shown in Fig. 2.

Because both bulk silicon and germanium have face-centered-cubic (fcc) crystal structures, the three different combinations of materials were set as fcc lattices. Geometric optimizations were performed and showed that fcc crystal arrangements are stable in these three combinations.

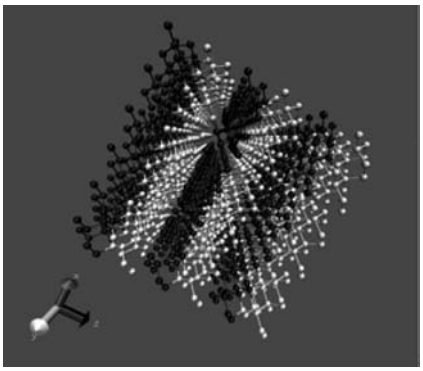

Fig. 3 Periodic boundary condition in the Si–Ge system

Periodic boundary conditions were employed in both systems and in all three (x-,y-,z-) directions, as seen in Fig. 3. The system's periodicity in the z-direction suggests that each layer would have thermal communication with the neighboring two layers.

The pseudopotential used for silicon was the Trouiller–Martins norm-conserving pseudopotential [18]. A norm-conserving pseudopotential means that outside the core, the real and pseudo-wave-functions generate the same charge density. For germanium, the Stumpf–Gonze–Schaeffler pseudopotential, which is also norm-conserving, was used. The reason why we chose these two pseudopotentials is that they are well established and give adequate accuracy while requiring a very demanding calculation time. To deal with the exchange-correlation function in the Kohn–Sham energy, see Eq. (5), the local density approximation (LDA) [19] was employed for both materials.

The procedure of the simulation is as follows. First, the neighboring two layers are set to different temperatures using Nosé–Hoover thermostats [20,21]. Then, all the thermostats are removed to let the thermal energy equilibrate. Finally, the temperature evolutions of the two layers are visualized, and the vibration power spectra are calculated. One thing worth mentioning is that the temperature here is defined according to the kinetic theory:

$$T = \frac{2\bar{E}_K}{3k_B}$$

where $\bar{E}_K$ is the mean kinetic energy over all the atoms, and thus temperature T is used as a label indicating how much kinetic energy does the system has.

3 Results and Discussion

3.1 64-Atom Silicon-Silicon. For this system, the contacting silicon thin layers, as shown in Fig. 2(a), are set to 100 K and 50 K in case (a), 300 K and 100 K in case (b), and 400 K and 100 K in case (c), and the temperatures of the two layers are maintained by thermostats for 10,000, 25,000, and 30,000 time steps, respectively. Then, thermostats are released to allow the energy to equilibrate, see Fig. 4. Then the vibration power spectra of the two layers are calculated, as seen in Fig. 5.

For this system that contains 64 silicon atoms, there is no material mismatch. The thermal energy transport is as would be expected in the bulk material. The equilibration time required was very short (around 2000 step $\approx$ 200 fs). The final temperatures of each layer were equal to the average set temperatures. From the vibration coupling point of view, see Fig. 6, the vibration spectra of the two thin layers overlapped almost perfectly, which resulted in fast thermal communication and thus short equilibration time.

In silicon, phonons are the thermal carriers. The thicknesses of the layers are around 0.5 nm, which is much less than the phonon

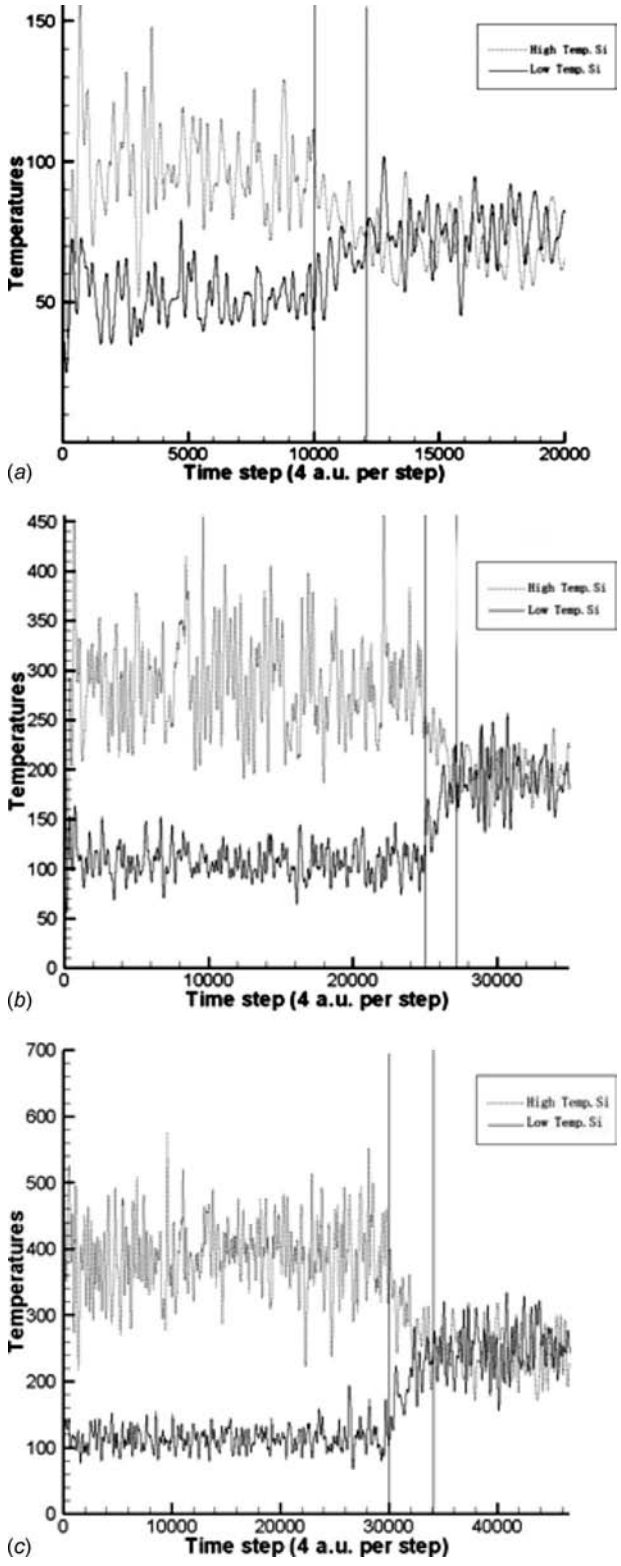

Fig. 4 Temperature evolutions in the two contacting thin layers (Si–Si): (a) 100 K versus 50 K, (b) 300 K versus 100 K, and (c) 400 K versus 100 K

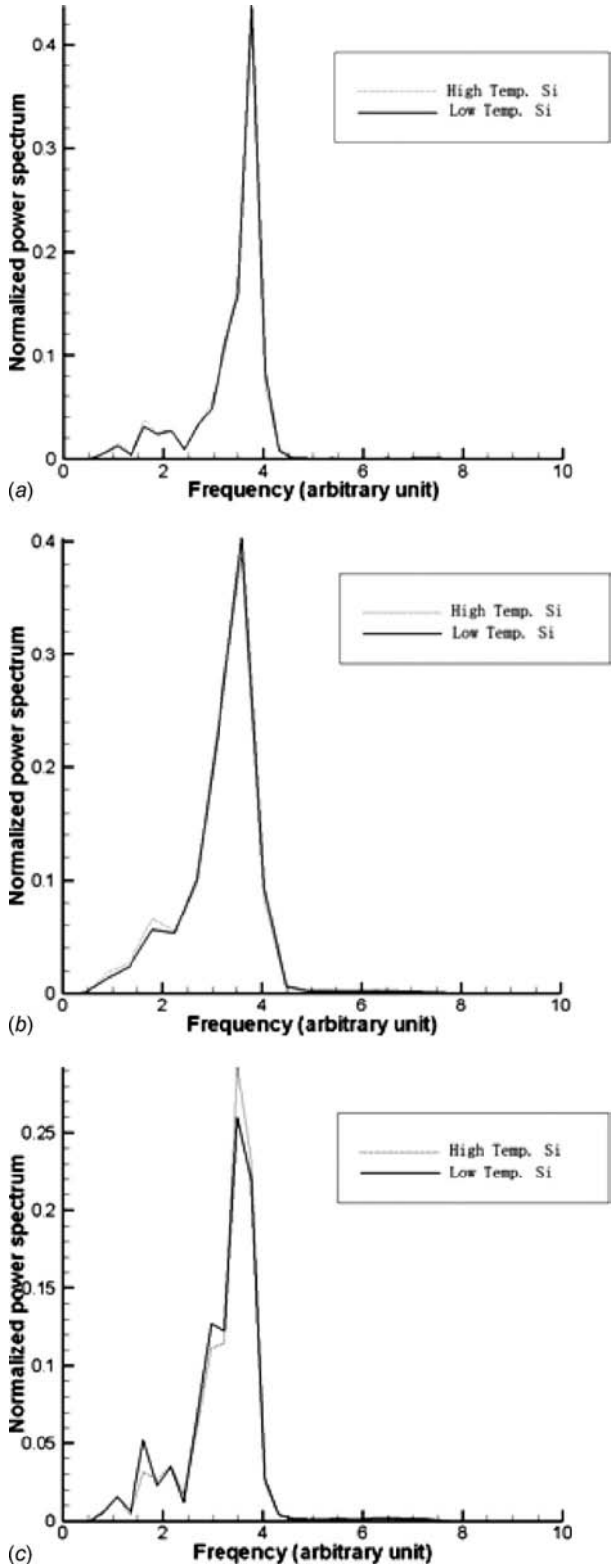

Fig. 5 Atomic vibration power spectra (Si–Si): (a) 100 K versus 50 K, (b) 300 K versus 100 K, and (c) 400 K versus 100 K

mean free path. Phonons travel ballistically from one layer to another. We see that the time required to transport different amounts of thermal energy is almost the same. This verifies the ballistic transport of the phonons.

Another phenomenon worth discussing is that of the temperature oscillation. The magnitude of the oscillation should be inversely proportional to the square root of the number of atoms included in the calculation of the mean temperature of the ensemble. This can be expressed as

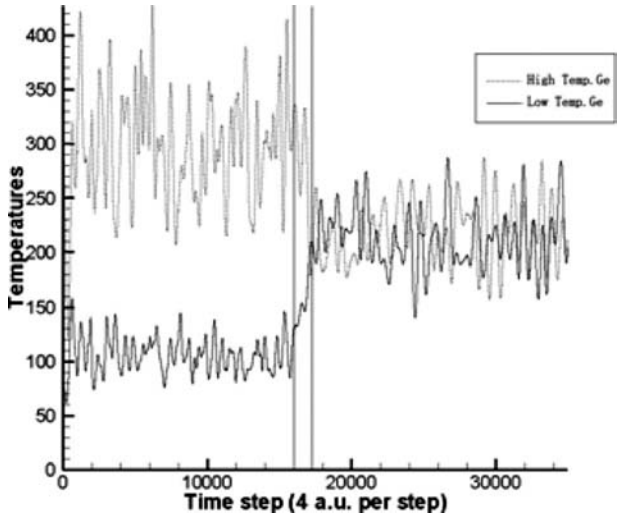

Fig. 6 Temperature evolutions in contacting thin layers (Ge–Ge)

$$\Delta T_{\text{osc}} = \sqrt{\frac{2}{3N}} \times T_{\text{mean}} \tag{7}$$

This expression explains why the temperature oscillations in the high temperature layers are larger than in the low temperature layers.

3.2 64-Atom Germanium-Germanium. This system consists of pure germanium atoms, as seen in Fig. 2(*c*). Two contacting layers are set to 300 K and 100 K separately at the beginning, and the temperature difference is maintained by thermostats for 16,000 steps. Then the thermostats are released to allow energy transport (Fig. 6). The vibration power spectra plot is presented in Fig. 7.

From Fig. 6, we see that the equilibration time required is very short (around 1000 step≈100 fs). As seen in the pure silicon cases, the vibration coupling is very strong according to the power spectra plot. The very strong vibration coupling is determined by the identical properties, such as bond strength and atomic weight, of the two layers.

3.3 64-Atom Silicon-Germanium. This system consists of 32 silicon atoms and 32 germanium atoms, see Fig. 2(*b*). The

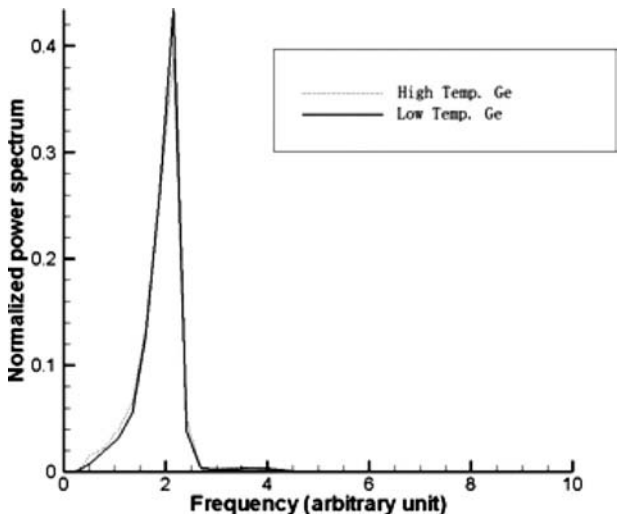

Fig. 7 Atomic vibration power spectra (Ge–Ge)

silicon layer and the germanium layer were first set to (a) 100 K versus 50 K, (b) 50 K versus 100 K, (c) 700 K versus 450 K, and (d) 1000 K versus 500 K in the four simulations. The time steps, during which the temperatures are controlled in these three cases, are 10,000, 8000, 8000 and 10,000, respectively. The thermostats were then removed and the thermal energy equilibration process began. Figure 8 shows the computed temperature profiles. The vibration power spectra were calculated and are shown in Fig. 9.

In Fig. 8(*a*), the temperatures do not converge to a uniform temperature, as was observed in pure materials. This suggests that the two neighboring layers have little communication from a thermal energy transport point of view, although they have different temperatures. From the vibration point of view, due to the mass difference and the low temperatures, as we can see from Fig. 9(*a*), there is little spectra overlap between the two contacting layers. Also, from the phonon point of view, at such low temperatures only the low-lying phonons were excited, which also suggested the small overlap of the power spectra. In these ultrathin structures, only phonons with wavelength shorter than the structure dimensions are captured. These phonons should be acoustic phonons, which can have smaller wavelengths.

In case (b), we switched the set temperature for the two thin layers. After a comparatively very long time (more than 20 ps) equilibration, the temperature came to a uniform value. We examined the vibration spectrum and found that the overlap was greater than case (a). From the above two cases, it is believed that in such ultrathin layer junctions, thermal energy transport across the interface is affected by how the temperature difference is applied. Such behavior is similar to a *P-N* junction in electron transport.

In Figs. 8(*c*) and 8(*d*), which correspond to 700 K versus 450 K and 1000 K versus 500 K, respectively, the temperatures in the two neighboring layers, after long time of equilibration, reached a uniform value. In case (c), the time required to reach the equilibrium state is about 140,000 steps (~14 ps), while in case (d), the time required is 50,000 steps (~5 ps). From the power spectra plots, Figs. 9(*c*) and 9(*d*), we see that the overlap in (d) is greater than that in (c), which suggests a more significant vibration coupling in (d) than in (c). The spectra overlaps of these two cases are greater than in case (a). However, the vibration couplings in cases (c) and (d) are much less than in the pure material cases, which explains why a long equilibration time is required. Also, because the materials are different, there is an acoustic mismatch. Thus when acoustic phonons travel from one side to another side, there will be scattering at the interface, and only a small part of the carrier's energy is delivered to the other side of the interface. Apparently, the strength of the interface scattering depends on temperature.

4 Summary and Conclusion

The current work simulated the thermal energy transport from high temperature nanometer thin layers to low temperature nanometer thin layers. The transport behaviors in the different cases studied differ from each other. The temperature range effect and material combination effect are observed. When there is no material mismatch, which is seen in the cases in Secs. 3.1 and 3.2, the vibrations in the two layers coupled to each other, and the thermal energy was transported without impedance. However, in the cases where the two layers are made of different types of materials, the energy transport becomes quite difficult due to the weak coupling of the atomic vibrations in the two layers. In the very low temperature case (a) (Sec. 3.3), due to the rare overlap of vibration power spectra of the neighboring layers, the energy transport across the interface is barely observed. However, such insulation behavior also depends on how the temperature differences are applied. In case (b) (Sec. 3.3), where the temperature differences were applied in a way that the phonon spectra have more overlap, thermal communication happened more readily, although it was a very slow process. At very high temperatures, cases (c) and (d) (Sec. 3.3), the vibration resonance becomes greater than that in

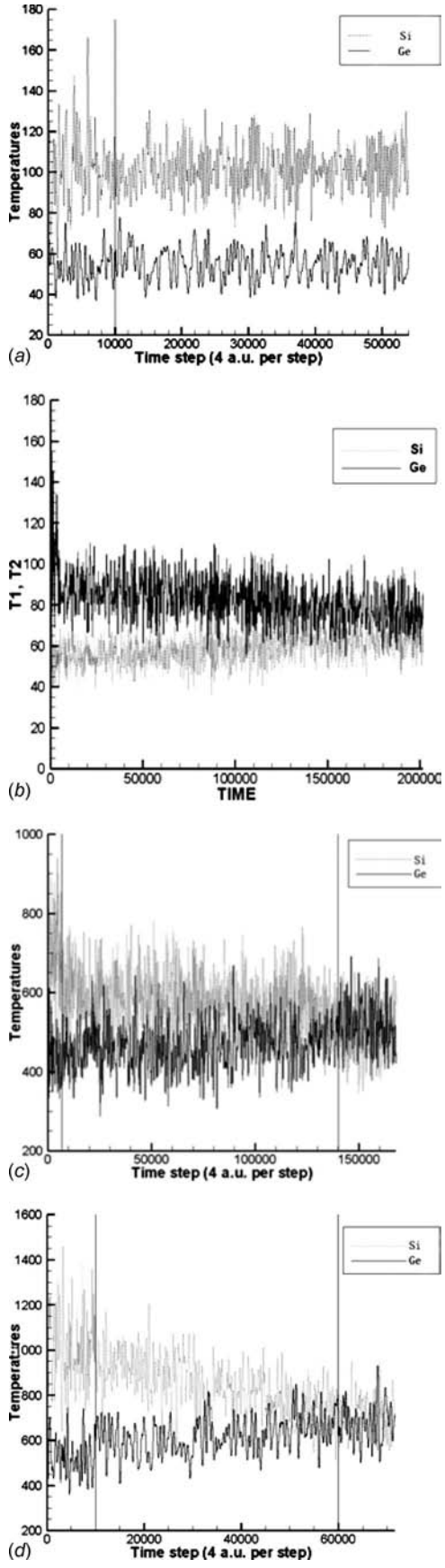

Fig. 8 Temperature evolutions in the two contacting thin layers (Si–Ge): (a) 100 K versus 50 K, (b) 50 K versus 100 K, (c) 700 K versus 450 K, and (d) 1000 K versus 500 K

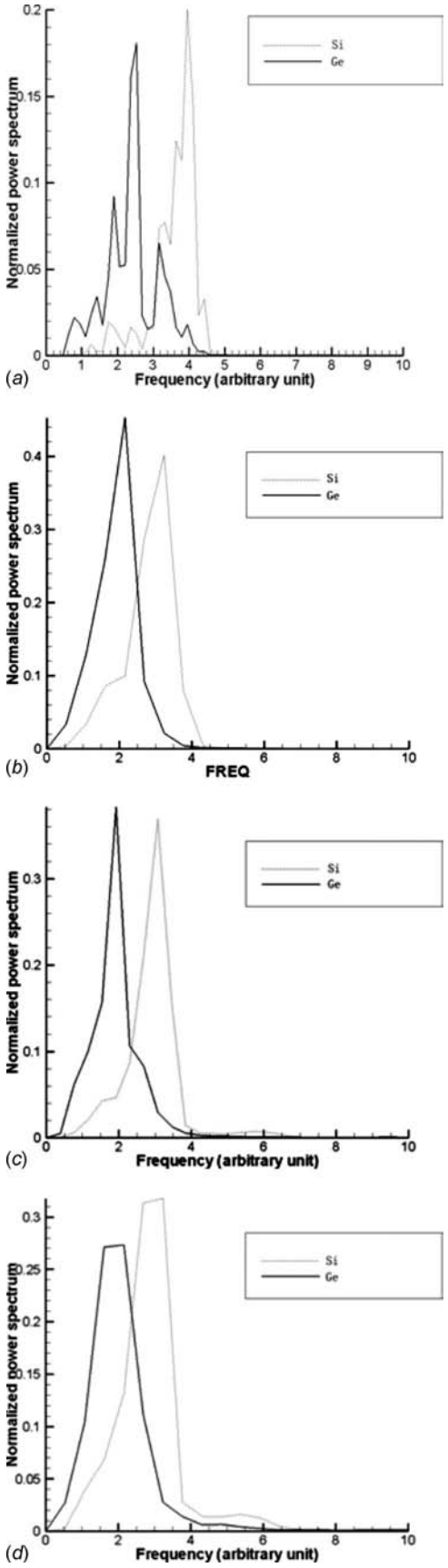

Fig. 9 Atomic vibration power spectra (Si–Ge): (a) 100 K versus 50 K, (b) 50 K versus 100 K, (c) 700 K versus 450 K, and (d) 1000 K versus 500 K

the low temperature situation, and the thermal energy is successfully transported from the high temperature side to the low temperature side, although such processes were shown to be very slow compared with the pure material case. From the phononic point of view, the acoustic mismatch, which is a result of the material mismatch at the material interface, scatters the phonon wave packet and thus leads to large transport impedance. This is another explanation for the slow or even zero energy transport.

From this work, we can see that the DFT-MD simulation reflected physically reasonable thermal transport phenomena in nanoscale structures. It also demonstrated its ability of "on-the-fly" calculation, that is, no empirical potential was needed. It is promising that the DFT-MD can handle more complicated thermal transport problems than the classical MD is able to handle due to the empirical potential function limitation. Also, with the application of DFT-MD, it is possible to include the electrons in the simulation of thermal transport, which will help solve the long-standing problem of classical MD in simulating metallic materials.

Acknowledgment

The authors gratefully acknowledge the support of NSF Grant Award (Contract No. 0522594) to enable this work to be performed. They also wish to thank Professor Arun Majumdar for his valuable comments on this study.

Nomenclature

E_{xc} = exchange-correlation function
E^{KS} = Kohn–Sham energy
$\bar{E}_K$ = mean kinetic energy over atoms
f_i = occupation numbers
H_e = Hamiltonian of the electron subsystem
i,I = subscripts of the ith and Ith degrees of freedom
L_{CP} = Car–Parrinello Lagrangian
M = atomic mass
N = total number of atoms in an ensemble
n = electron density
$\boldsymbol{r}_{e,i}, \boldsymbol{r}_{n,I}$ = electronic and nuclear degrees of freedom
$\boldsymbol{r}$ = position vector
T_{mean} = mean temperature of an ensemble
T_s = kinetic energy of a noninteracting electron system
V_{ext} = external potential
V_H = hartree potential
ΔT_{osc} = magnitude of the temperature oscillation
μ_i = "fictitious masses" assigned to the orbital degrees of freedom
φ = electronic one-particle orbital
ψ = electronic wave function at ground-state

References

[1] Moore's Law, 2007, http://www.intel.com.
[2] International Technology Roadmap for Semiconductors, 2005, http://public.itrs.net.
[3] Ziman, J. M., 1960, *Electrons and Phonons*, Oxford University Press, New York.
[4] Volz, S., Saulnier, J. B., Lallemand, M., Perrin, B., Depondt, P., and Mareschal, M., 1996, "Transient Fourier-Law Deviation by Molecular Dynamics in Solid Argon," Phys. Rev. B, **54**, pp. 340–347.
[5] Poetzsch, R. H. H., and Böttger, H., 1994, "Interplay of Disorder and Anharmonicity in Heat Conduction: Molecular Dynamics Study," Phys. Rev. B, **50**, pp. 15757–15763.
[6] Lukes, J. R., and Zhong, H., 2007, "Thermal Conductivity of Individual Single-Wall Carbon Nanotubes," ASME J. Heat Transfer, **129**, pp. 705–716.
[7] Lukes, J. R., Liang, X.-G., and Tien, C.-L., 2000, "Molecular Dynamics Study of Solid Thin-Film Thermal Conductivity," ASME J. Heat Transfer, **122**, pp. 536–543.
[8] Wang, X., and Xu, X., 2002, "Molecular Dynamics Simulation of Heat Transfer and Phase Change During Laser Material Interaction," ASME J. Heat Transfer, **124**, pp. 265–274.
[9] Broido, D. A., and Ward, A., 2005, "Lattice Thermal Conductivity of Silicon From Empirical Interatomic Potentials," Phys. Rev. B, **72**, p. 014308.
[10] Gomes, C. J., Madrid, M., Goicochea, J. V., and Amon, C. H., 2006, "In-Plane and Out-of-Plane Thermal Conductivity of Silicon Thin Films Predicted by Molecular Dynamics," ASME J. Heat Transfer, **128**, pp. 1114–1121.
[11] Marx, D., and Hutter, J., 2000. "Ab Initio Molecular Dynamics: Theory and Implementation," *Modern Methods and Algorithms of Quantum Chemistry* (NIC Series Vol. 1), pp. 301–449.
[12] Born, M., and Oppenheimer, R., 1927, "Zur Quantentheorie der Molekeln," Ann. Phys., **84**, pp. 457–484.
[13] Car, R., and Parrinello, M., 1985, "Unified Approach for Molecular Dynamics and Density-Functional Theory," Phys. Rev. Lett., **55**(22), pp. 2471–2474.
[14] Pastore, G., Smargiassi, E., and Buda, F., 1991, "Theory of *Ab-Initio* Molecular-Dynamics Calculations," Phys. Rev. A, **44**, pp. 6334–6347.
[15] Kohn, W., and Sham, L. J., 1965, "Self-Consistent Equations Including Exchange and Correlation Effects," Phys. Rev., **140**, pp. A1133–A1138.
[16] CPMD, Copyright IBM Corp., 1990–2006, Copyright MPI fur Festkorperforschung Stuttgart, 1997–2001.
[17] Humphrey, W., Dalke, A., and Schulten, K., 1996, "VMD: Visual Molecular Dynamics," J. Mol. Graphics, **14**, pp. 33–38.
[18] Troullier, N., and Martins, J. L., 1991, "Efficient Pseudopotentials for Plane-Wave Calculations," Phys. Rev. B, **43**, pp. 1993–2006.
[19] Perdew, J. P., and Zunger, A., 1981, "Self-Interaction Correction to Density-Functional Approximations for Many-Electron System," Phys. Rev. B, **23**, pp. 5048–5079.
[20] Nosé, S., 1984, "A Unified Formulation of the Constant Temperature Molecular Dynamics Methods," J. Chem. Phys., **81**, pp. 511–519.
[21] Hoover, W. G., 1985, "Canonical Dynamics: Equilibrium Phase-Space Distributions," Phys. Rev. A, **31**, pp. 1695–1697.

Numerical Investigation of the Linear Stability of a Free Convection Boundary Layer Flow Using a Thermal Disturbance With a Slowly Increasing Frequency

Manosh C. Paul
Department of Mechanical Engineering,
University of Glasgow,
Glasgow G12 8QQ, UK
e-mail: m.paul@mech.gla.ac.uk

D. Andrew S. Rees
Department of Mechanical Engineering,
University of Bath,
Bath BA2 7AY, UK

Numerical simulations are performed to investigate the linear stability of a two-dimensional incompressible free convection flow induced by a vertical semi-infinite heated flat plate. A small-amplitude local temperature disturbance with a slowly increasing frequency is introduced on the surface near to the leading edge in order to generate disturbance waves within the boundary layer. The aim is to compare the response of the thermal boundary layer with that obtained by selecting discrete disturbance frequencies. In the present study, air is considered to be the working fluid for which the value of the Prandtl number is taken to be $Pr=0.7$. The computational results show that the disturbance decays initially until it reaches a critical distance, which depends on the current frequency of the disturbance. Thereafter the disturbance grows, but the growth rate also depends on the effective frequency of the disturbance. Comparisons with previous work using constant disturbance frequencies are given, and it is shown that the sine-sweep technique is an effective method for analyzing the instability of convectively unstable boundary layers. [DOI: 10.1115/1.2976554]

Keywords: numerical simulation, free convection, linear stability, receptivity, sine sweep

1 Introduction

In the free convection boundary layer flow over a vertical surface, the primary mode of instability takes the form of two-dimensional waves, which travel in the streamwise direction. This is well known to be a hydrodynamic instability [1,2] even though the basic state is generated by buoyancy forces and the flow is advectively unstable as opposed to being absolutely unstable.

Goldstein [3] in the study of evolution of Tollmien–Schlichting waves recognized that near the leading edge, but not so near that the fully elliptic equations have to be considered, the boundary layer is fairly thin and grows rapidly in the downstream direction compared with the situation further downstream. In this region the parallel flow assumption is inaccurate. On the other hand, at greater distances from the leading edge, the parallel flow approximation holds and the linear stability properties of the flow can be fairly accurately predicted by the thermal equivalent of the Orr–Sommerfeld equation. In the free convection boundary layer flow, Paul [4] and Paul et al. [5] also showed that the linear stability results based on the parallel flow approximation (Paul et al. [6]) agree well with the results obtained from full unsteady 2D simulations at large downstream distances, but that there is poor agreement near the leading edge region. It was concluded that it is necessary to solve the full unsteady 2D equations in order to obtain accurate predictions of the stability characteristics near the base of the neutral curve rather than to use the parallel flow approximation.

In Refs. [4,5], the stability of the free convection thermal boundary layer flow from a vertical flat plate was studied by introducing the following thermal disturbances: (i) an isolated internal disturbance at one point in time and (ii) a time-periodic local variation in the surface temperature near the leading edge of the flat plate. When the point thermal disturbance was introduced, it was found that, as time progresses, the disturbance diffuses and travels downstream, leaving behind an undisturbed flow. The spatial wavelength of the traveling cells also increases, which is consistent with the fact that the base flow accelerates in the streamwise direction. In addition, the variation of the surface rate of heat transfer with time showed a distinctive time scale or frequency associated with the evolving disturbance. The latter disturbance may be regarded as being of similar type to the suction strip approach of Fasel and Konzelmann [7], the oscillating heat source of Brooker et al. [8], and the vibrating ribbon experiments of Dietz [9]. Such thermal disturbances produce instability waves of Tollmien–Schlichting type into the otherwise steady flow, and then the magnitude of the waves either grows or decays roughly in accordance with linear stability theory analysis such as was performed by Paul et al. [6] using the parallel flow approximation.

In addition, for the time-periodic thermal oscillation [4,5], sinusoidal thermal disturbances of fixed frequency were introduced near the leading edge of a flat plate to generate wavelike instabilities in order to study the stability and thermal receptivity of the boundary layer flow. A large range of different frequencies were introduced in order to trace out a neutral stability curve based on the full elliptic system of equations. The main purpose of the present paper is to revisit this stability problem by using thermal disturbances with a gradually increasing frequency. In other engineering contexts this procedure is referred as a sine-sweep. If the sine-sweep method were shown to be able to reproduce the sta-

Contributed by the Heat Transfer Division of ASME for publication in the JOURNAL OF HEAT TRANSFER. Manuscript received September 19, 2007; final manuscript received May 22, 2008; published online September 18, 2008. Review conducted by Cholik Chan.

bility characteristics of the boundary layer accurately, then it could be used to replace a very large number of simulations with one albeit lengthy simulation. In our application of the sine-sweep idea a slow variation of the effective frequency is used, and the stability properties of the boundary layer are compared with those obtained in Refs. [5,6] in order to determine the applicability of the sine-sweep idea.

The sine-sweep idea may also be applied to experimental setups in order to determine the stability characteristics of the boundary layer. This would also yield important information such as neutral curves and local growth rates relatively quickly.

2 Governing Equations and Boundary Conditions

We consider the two-dimensional incompressible free convection boundary layer flow over a vertical infinite span heated plate where x is the streamwise coordinate and y is the wall-normal coordinate. A detailed schematic of the flow configuration may be found in Ref. [5]. The equations of motion of the free convective boundary layer flow are taken to be the incompressible Navier–Stokes and energy transport equations. For unsteady two-dimensional flow this system, subject to the Oberbeck–Boussinesq approximation, may be written in nondimensional stream function (ψ), vorticity (ω), and temperature (θ) form [5] as

$$\frac{\partial^2 \psi}{\partial x^2} + \frac{\partial^2 \psi}{\partial y^2} = \omega \tag{1}$$

$$\frac{\partial \omega}{\partial t} = \frac{\partial^2 \omega}{\partial x^2} + \frac{\partial^2 \omega}{\partial y^2} + \frac{\partial \psi}{\partial x}\frac{\partial \omega}{\partial y} - \frac{\partial \psi}{\partial y}\frac{\partial \omega}{\partial x} + \frac{\partial \theta}{\partial y} \tag{2}$$

$$\frac{\partial \theta}{\partial t} = \frac{1}{\mathrm{Pr}}\left(\frac{\partial^2 \theta}{\partial x^2} + \frac{\partial^2 \theta}{\partial y^2}\right) + \frac{\partial \psi}{\partial x}\frac{\partial \theta}{\partial y} - \frac{\partial \psi}{\partial y}\frac{\partial \theta}{\partial x} \tag{3}$$

where the stream function (ψ) is defined such that $u=\psi_y$ and $v=-\psi_x$. Here u and v are the nondimensional velocity components along the x and y coordinate directions, respectively. The constant Pr is the fluid Prandtl number. The detailed nondimensionalizations of the full governing equations are given in Refs. [4,5]. We note that the length scale used is a natural one based on the properties of the fluid and the temperature drop. Therefore no Grashof number appears in the equations, as Gr=1 defines this natural length scale. The boundary layer approximation is now equivalent to $x \gg 1$.

On applying the Schwartz–Christoffel transformation $3(\xi+i\eta) = [4(x+iy)]^{3/4}$ into Eqs. (1)–(3) and introducing a small disturbance into the steady flow for which we set

$$\psi(\xi,\eta,t) = \bar{\psi}(\xi,\eta) + \delta\hat{\psi}(\xi,\eta,t) \tag{4}$$

$$\omega(\xi,\eta,t) = \bar{\omega}(\xi,\eta) + \delta\hat{\omega}(\xi,\eta,t) \tag{5}$$

$$\theta(\xi,\eta,t) = \bar{\theta}(\xi,\eta) + \delta\hat{\theta}(\xi,\eta,t) \tag{6}$$

the following linearized perturbation equations are obtained:

$$\frac{\partial^2 \hat{\psi}}{\partial \xi^2} + \frac{\partial^2 \hat{\psi}}{\partial \eta^2} = A\hat{\omega} \tag{7}$$

$$A\frac{\partial \hat{\omega}}{\partial t} = \frac{\partial^2 \hat{\omega}}{\partial \xi^2} + \frac{\partial^2 \hat{\omega}}{\partial \eta^2} + A^{1/2}\left(\frac{\partial \hat{\theta}}{\partial \xi}\sin\frac{1}{4}\phi + \frac{\partial \hat{\theta}}{\partial \eta}\cos\frac{1}{4}\phi\right) + \left(\frac{\partial \bar{\omega}}{\partial \eta}\frac{\partial \hat{\psi}}{\partial \xi} - \frac{\partial \bar{\omega}}{\partial \xi}\frac{\partial \hat{\psi}}{\partial \eta}\right) + \left(\frac{\partial \bar{\psi}}{\partial \xi}\frac{\partial \hat{\omega}}{\partial \eta} - \frac{\partial \bar{\psi}}{\partial \eta}\frac{\partial \hat{\omega}}{\partial \xi}\right) \tag{8}$$

$$A\frac{\partial \hat{\theta}}{\partial t} = \frac{1}{\mathrm{Pr}}\left(\frac{\partial^2 \hat{\theta}}{\partial \xi^2} + \frac{\partial^2 \hat{\theta}}{\partial \eta^2}\right) + \left(\frac{\partial \bar{\psi}}{\partial \xi}\frac{\partial \hat{\theta}}{\partial \eta} - \frac{\partial \bar{\psi}}{\partial \eta}\frac{\partial \hat{\theta}}{\partial \xi}\right) + \left(\frac{\partial \bar{\theta}}{\partial \eta}\frac{\partial \hat{\psi}}{\partial \xi} - \frac{\partial \bar{\theta}}{\partial \xi}\frac{\partial \hat{\psi}}{\partial \eta}\right) \tag{9}$$

where δ in Eqs. (4)–(6) represents a small quantity, and therefore powers of δ have been neglected when deriving Eqs. (7)–(9). Furthermore, the overbar indicates the steady state base flow quantities while the hat (circumflex) denotes the perturbation variables. The quantity ϕ, which appears in Eq. (8), is the polar angle from the heated surface, while the function A is defined according to $A^3=(\frac{3}{4})^2(\xi^2+\eta^2)^2$.

The corresponding boundary conditions that are needed to solve Eqs. (7)–(9) are

$$\hat{\psi} = \hat{\psi}_\eta = 0, \quad \hat{\theta} = 0 \quad \text{on} \quad \eta = \eta_{\min} = 0 \tag{10}$$

$$\hat{\psi} = \hat{\psi}_\xi = 0, \quad \hat{\theta}_\xi = 0 \quad \text{on} \quad \xi = \xi_{\min} \tag{11}$$

$$\hat{\psi}_\eta = 0, \quad \hat{\omega} = 0, \quad \hat{\theta} = 0 \quad \text{as} \quad \eta = \eta_{\max} \tag{12}$$

while at the outflow ($\xi_{\max}$) we apply a buffer domain function in order to dampen down disturbances and to prevent unphysical reflections. Further details of the use of a buffer function are given in Sec. 3. It should be noted here that the leading edge of the heated surface was taken to be at $\xi_{\min}=20$, which corresponds to $x \simeq 37$ in Cartesian coordinates. The origin of the coordinate system is outside of the computational domain and therefore we define the new variable $x^*=x-37$, which is the distance to the leading edge. The parallel flow investigations (PFIs) [6] were carried out for the same x^*.

After solving for the basic state, $(\bar{\psi},\bar{\omega},\bar{\theta})$, using the procedure outlined in Sec. 3, a thermal disturbance is introduced by changing the surface temperature near the leading edge. Therefore we solve the linearized disturbance equations (7)–(9) subject to the no-slip condition on the surface and the thermal boundary condition

$$\hat{\theta} = e^{-a(\xi-\xi_0)^2}\sin(ct^2) \quad \text{at} \quad \eta = 0 \tag{13}$$

where $\lambda=2ct$ is defined as the temporal frequency, which is a slowly varying function of time t. In Eq. (13) $\xi_0=20$ is the center of the region where the thermal disturbance is introduced. This region is located well upstream of where the boundary layer becomes unstable. In addition, $a=0.1$ was chosen such that the thermal disturbance region was well resolved on the computational grid but is still located fully upstream of the neutral point.

3 Numerical Method

Finite difference techniques are used to solve the system of nonlinear equations (1)–(3) and the system of linear equations (7)–(9). The overall accuracy of the numerical scheme is second order in both time and space.

The time-dependent equations are discretized using central differences and the DuFort–Frankel method for the time-derivative and diffusion terms. The Jacobian terms are approximated using the Arakawa [10] formulation, which was designed to be particularly suitable for unsteady flows. Derivative boundary conditions are approximated using a standard ghost point approach, which has a smaller discretization error than a one-sided first-order approximation.

The Poisson equation (7) was solved using a multigrid correction scheme algorithm to accelerate iterative convergence. It incorporates a V-cycle algorithm involving the line Gauss–Seidel relaxation procedure. The method is based on the pointwise method described in Ref. [11] but adopts two line relaxations per coordinate direction on each multigrid level.

The buffer domain technique of the outflow boundary follows the methodology introduced by Kloker et al. [12]. The naive im-

position of boundary conditions involving either the first or second derivatives of the dependent variables results in the progressive upstream propagation of spatially pointwise oscillations, which eventually degrade the evolving solution. Kloker et al. [12] discussed at length six different strategies for dealing with outflow conditions and concluded that, for the Blasius boundary layer at least, a very satisfactory method is to use an absorbing buffer region. Such a region is used to damp out disturbances to the basic flow and is sometimes called a relaminarization region. The method has also been used very satisfactorily in other flows; see Refs. [13,14], for example. For the present problem the concept of a buffer region translates into setting

$$\chi_{\text{dist}}^{\text{new}} = F(\xi) \times \chi_{\text{dist}}^{\text{old}} \tag{14}$$

at each time step. Here χ represents either the vorticity or temperature, χ^{old} is the computed value of χ obtained using the DuFort–Frankel method subject to the boundary condition $\partial\chi/\partial\xi=0$ at $\xi=\xi_{\max}$, and χ^{new} is the value of χ, which is used to compute χ at subsequent time steps. The buffer function $F(\xi)$ takes the value of 1 in most of the computational domain and is a fifth-order polynomial in ξ, which decreases from 1 at the start of the buffer region to 0 at outflow. At both the beginning ($\xi=\xi_{b1}$) and the end ($\xi=\xi_{b2}$) of the buffer region the function has zero first and second derivatives. In more detail, the buffer function used was

$$F(\xi) = 1, \quad \xi < \xi_{b1}$$

$$F(\xi) = 1 - 10\gamma^3 + 15\gamma^4 - 6\gamma^5, \quad \xi_{b1} < \xi < \xi_{b2} \tag{15}$$

$$F(\xi) = 0, \quad \xi > \xi_{b2}$$

where $\gamma=(\xi-\xi_{b1})/(\xi_{b2}-\xi_{b1})$. For nonlinear problems, such as those involving the computation of the basic steady flow, the outflow formula (14) translates into the following form, which is suitable for solving for the true variables rather than for disturbances:

$$\chi^{\text{new}} = F(\xi) \times \chi^{\text{old}} + [1 - F(\xi)] \times \chi^{\text{basic}} \tag{16}$$

where χ^{basic} represents the basic boundary layer solutions of the corresponding variable (vorticity or temperature), which is obtained from the steady solutions of Eqs. (1)–(3).

In the simulation, $\xi_{\max}=620$ was chosen and the buffer region started from $\xi_{b1}=520$. A series of simulations was undertaken changing the position of the start of the buffer region, and the test results show that there was no effect on the solutions in the unbuffered region.

Initially, a total of 480 nodes were used in the ξ-direction with a uniform distribution of the mesh size of $d\xi=1.25$. In the y-direction we used 48 nodes and the domain extends to $\eta_{\max}=12$. In order to show grid independence test of our stability results, the above grid size was doubled, i.e., we used 960 nodes in the x-direction and 96 nodes in the y-direction. We have $\delta\xi=5\delta\eta$, which yields a cell aspect ratio of 5, and therefore a line relaxation method is essential. We were able to take five multigrid levels and each V-cycle was comprised of two relaxation sweeps in each coordinate direction for each grid. At each time step the vorticity and temperature fields are updated for the new time level, followed by the solution of the Poisson equation for the stream function, and finally the boundary vorticity is computed using the ghost point approach.

4 Results and Discussion

We have run simulations for three different values of the parameter c in Eq. (13): $c=10^{-4}$, $c=5\times10^{-5}$, and $c=2.5\times10^{-5}$, with a constant time step of $\delta t=0.01$. In Sec. 4.1, some computed results of the linear stability are presented for $c=5\times10^{-5}$, and a detailed comparison of the stability characteristics for the other values of c with the fixed frequency simulation of Ref. [5] is presented in Sec. 4.2.

In order to generate results up to the maximum effective frequency of $\lambda_{\max}=0.8$, for which the corresponding nondimensional time is $t_{\max}=8000$, we used a total of 4×10^5 time steps for $c=10^{-4}$. When the value of c is reduced to half of its original value, i.e., for $c=5\times10^{-5}$, the computational cost doubles and we required 8×10^5 time steps to achieve results up to $\lambda_{\max}=0.8$ or $t_{\max}=8000$. Similarly, we required 16×10^5 time steps for $c=2.5\times10^{-5}$.

We note that the value of δt is very small compared with the physical time scales over which variations of interest take place. In addition, the magnitude of c is chosen such that the frequency variation is slow enough that the transient results obtained for any frequency are very close to the results that were obtained when the flow was perturbed with a fixed frequency. This sine-sweep approach has often been used in other engineering contexts to determine, for example, the resonance characteristics of mechanical systems or the acoustic properties of cavities. It is, to our knowledge, the first time that it has been used to assess the stability characteristics of a thermal boundary layer.

4.1 Stability Results for $c=5\times10^{-5}$. Given that the effective temporal frequency in the sine-sweep disturbance (13) is a function of time (viz., $\lambda=2ct$), it is now possible to trace out the evolution of the thermal disturbance inside the boundary layer with respect to either time or frequency. In this regard we have plotted some isocontours of the temperature disturbance, $\hat{\theta}$, in Fig. 1 for $c=5\times10^{-5}$. The contour levels in each frame are set at $\pm10^{-n}\max_{x^*,y}|\hat{\theta}|$ for $n=1,2,\ldots,5$, and it must be noted that the wall-normal coordinate, y, has been stretched substantially in order to see the patterns clearly. The dashed contours correspond to negative values of $\hat{\theta}$ while the solid lines correspond to positive values of $\hat{\theta}$. The results in Fig. 1 are for various values of the disturbance frequency λ. The results shown in the lowest frame are for $\lambda=0.1$, which corresponds to the nondimensional time of $t=1000$, while the top frame is for $\lambda=0.75$ for which the corresponding time is $t=7500$.

The numerical values corresponding to the contour plots show that, for all values of λ, the thermal disturbances decay initially with x^* near the leading edge of the surface and then grow with x^*; this feature is easily seen in Fig. 1 for $\lambda>0.55$, and for $\lambda<0.55$ it is clearer in Fig. 3. The x^* locations where the disturbance begin to be amplified (i.e., the neutral location) depend on the forcing frequency λ. We find that, when $\lambda>0.5$, the initial decay of the thermal disturbances is substantial and that the neutral location moves downstream as λ increases. The neutral point location is indicated by the black triangles for $\lambda\geq0.5$.

In Fig. 1 we can also see that the length of the thermal cells increases with distance from the leading edge, thereby confirming that the basic flow accelerates, the streamwise velocity being roughly proportional to $x^{1/2}$. As time progresses, which corresponds to increasing the disturbance frequencies, the wavelength decreases. The effects of the buffer function used in the buffer region near the outflow at $x^*=3565$ are also noticeable, where the damping of the disturbances is clearly evident. Also it should be noted that the largest positive thermal wave located at the upstream of the start of the buffer domain takes a total of 136 spatial nodes when $\lambda=0.1$, while it is 26 when $\lambda=0.4$

The time evolution of the surface rate of heat transfer, $H(t)$, which was computed using the following relation:

$$H(x^*,t) = \left(\frac{\partial\hat{\theta}}{\partial\eta}\right)_{\eta=0} \tag{17}$$

has been plotted in Fig. 2 at (a) $x^*=16$ and (b) $x^*=207$ for the same value of c, i.e., $c=5\times10^{-5}$. Figure 2(*a*) shows that the mag-

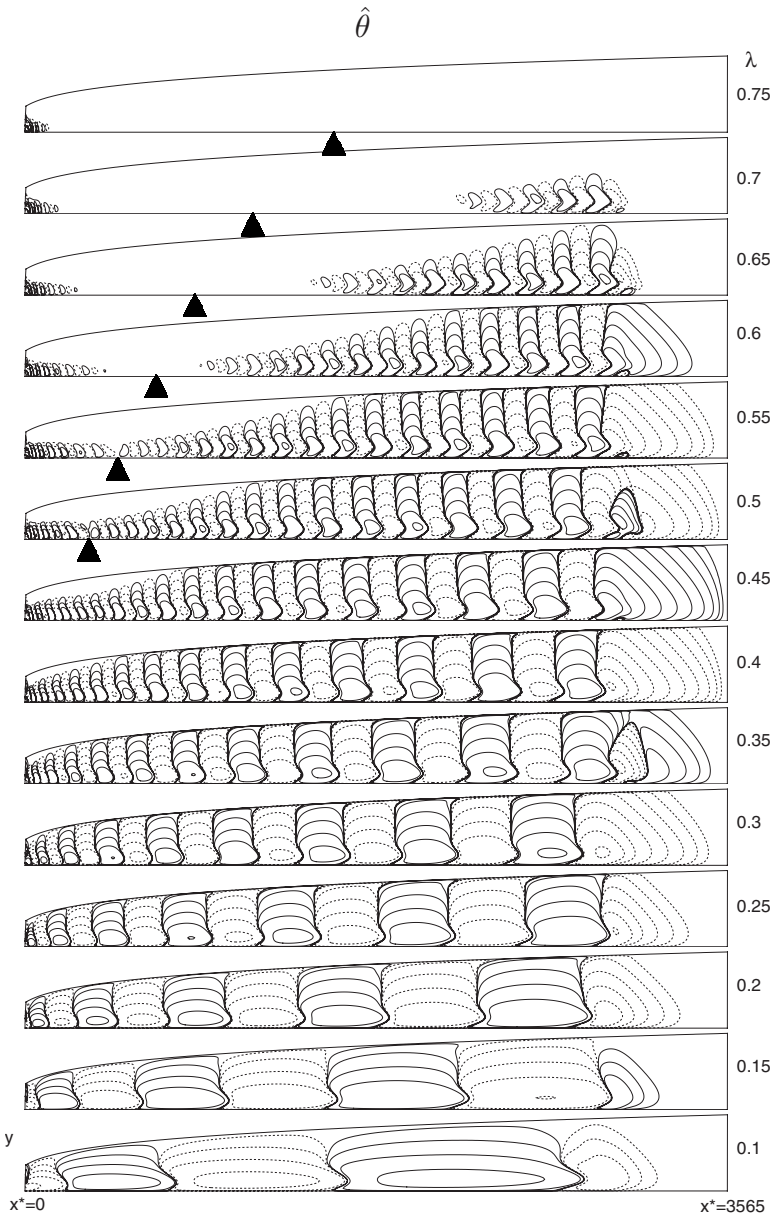

Fig. 1 Contours of $\hat{\theta}$ recorded at various values of the temporal frequency, λ, for $c=5\times10^{-5}$. Here ten contour levels are plotted based on the global extrema within each frame (see the text of the paper). The dashed contour lines represent negative values of $\hat{\theta}$ while the solid lines represent positive $\hat{\theta}$.

nitude of the disturbance decays for all time as this location is close to the leading edge of the vertical surface and well upstream of the neutral location, $x^*=147$, determined by Paul et al. [6]. On the other hand, Fig. 2(*b*) shows that the disturbance grows until t is just below 3000 and then decays, as this distance is well above downstream of the neutral location. The dashed lines in both frames indicate the envelope of the local maximum responses; and for the other x^* locations, these envelopes are plotted in Fig. 3 using a log scale.

In Fig. 3 the envelopes of the maximum response of the thermal disturbance in terms of the surface rate of heat transfer are displayed against time t for a selection of locations along the boundary layer. The results are calculated at various locations along the heated surface using the following relation:

$$Q(x^*,t)=\text{envelope}\left\{\log_{10}\left|\left(\frac{\partial\hat{\theta}}{\partial\eta}\right)_{\eta=0}\right|\right\} \tag{18}$$

This equation defines a surface in (x^*,t)-space or equivalently in (x^*,λ)-space.

The variation of Q at $x^*=16$ (i.e., at $x=53$) shows that Q decays for all time, which is not surprising, and it is, indeed, expected, since this location is very close to the leading edge of the surface and it lies well below the critical/neutral distance ($x^*=147$) of the neutral curve obtained by Paul et al. [6]. The next four curves in Fig. 3 are at $x^*=34$ (i.e., at $x=71$), $x^*=52$ (i.e., at $x=89$), $x^*=72$ (i.e., at $x=109$), and $x^*=93$ (i.e., at $x=130$), respectively, and since these are also below the critical distance no growth of the

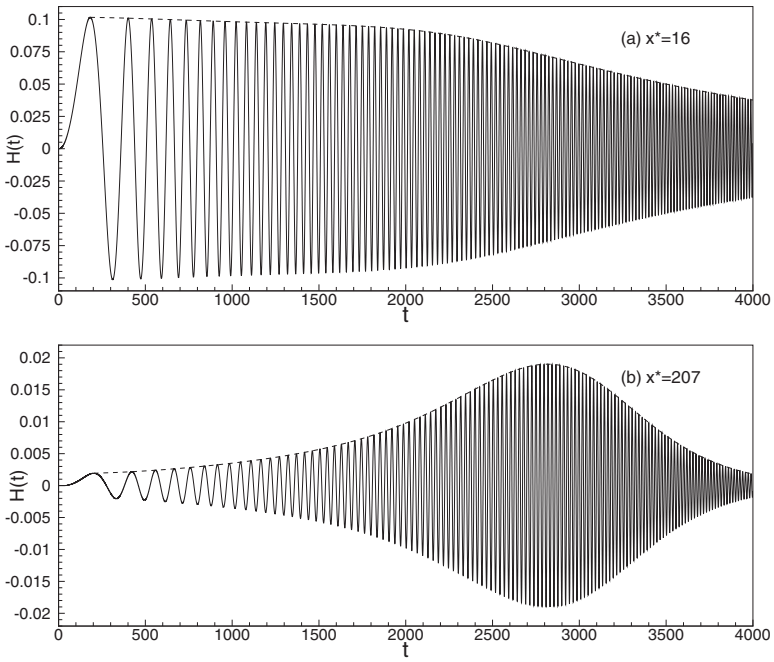

Fig. 2 Time variation of the surface rate of heat transfer recorded at (*a*) $x^*=16$ and (*b*) $x^*=207$ where $c=5\times10^{-5}$

thermal disturbance is observed. Thus the results obtained from the elliptic calculations approximately coincide with the results from the parallel flow analysis of Paul et al. [6]. At larger values of x^*, the corresponding curves show that there is a frequency interval within which the disturbances grow. The frequencies of maximum disturbance amplification for any given distance, x^*, which are plotted as a dotted line in the figure, show clearly that the disturbances also grow in space for any given frequency—this aspect will be looked at more closely in Figs. 4–7 and summarized later.

The uppermost curve in Fig. 3 corresponds to $x^*=2813$ (i.e., $x=2850$), which is just upstream of the buffer region, and this is the location where the disturbances are expected to reach their largest values. In the buffer zone no growth of the disturbances is achieved as its purpose is to dampen down the disturbances and remove unphysical reflections near the outflow boundary.

While Fig. 3 shows the variation of the disturbance amplitude with time, t, for a set of values of x^*, Fig. 4 shows its variation with x^* at chosen times or, equivalently, at chosen effective frequencies, λ. From this figure we can see that the disturbance amplitude decays for all frequencies when x^* is sufficiently close to the leading edge. As mentioned before, this region is within the stable region of the neutral curve. The curve corresponding to $\lambda=0.1$ is almost horizontal after the initial decay, indicating that disturbances of this frequency are almost neutral, i.e., they neither grow nor decay. However, when λ takes larger values we see very evident regions of decay and growth. Neutral locations correspond to minima in these curves, which are denoted by circles.

The frequency for which the largest disturbance amplitude is obtained at a given downstream location depends on x^*; this is

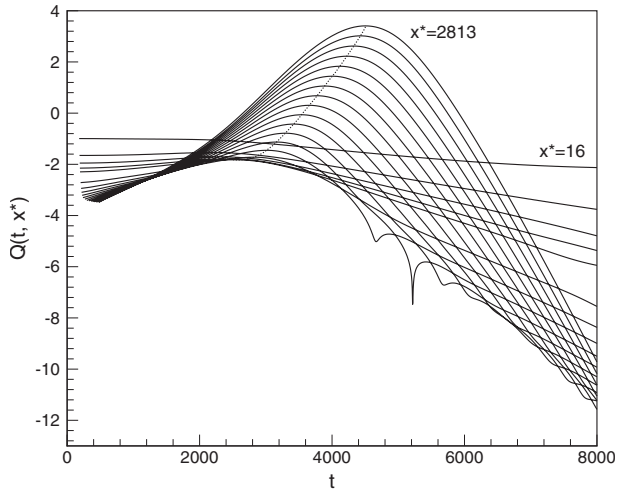

Fig. 3 Envelope of the maximum heat transfer response, *Q*, against time for various locations along the heated surface where $c=5\times10^{-5}$

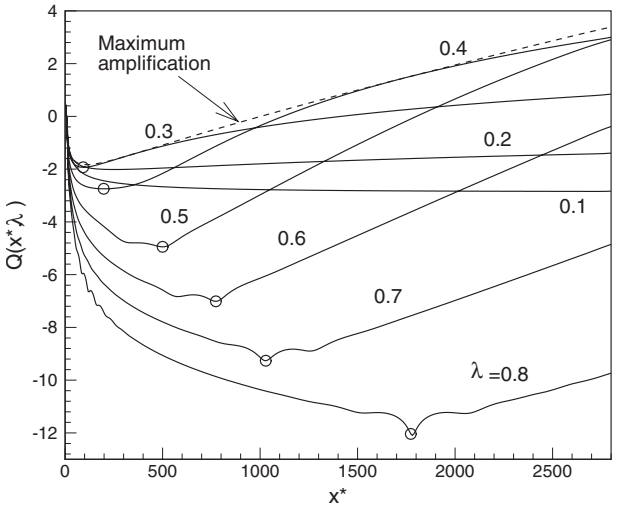

Fig. 4 Envelope of the maximum heat transfer response, *Q*, against distance for various disturbance frequencies, where $c=5\times10^{-5}$

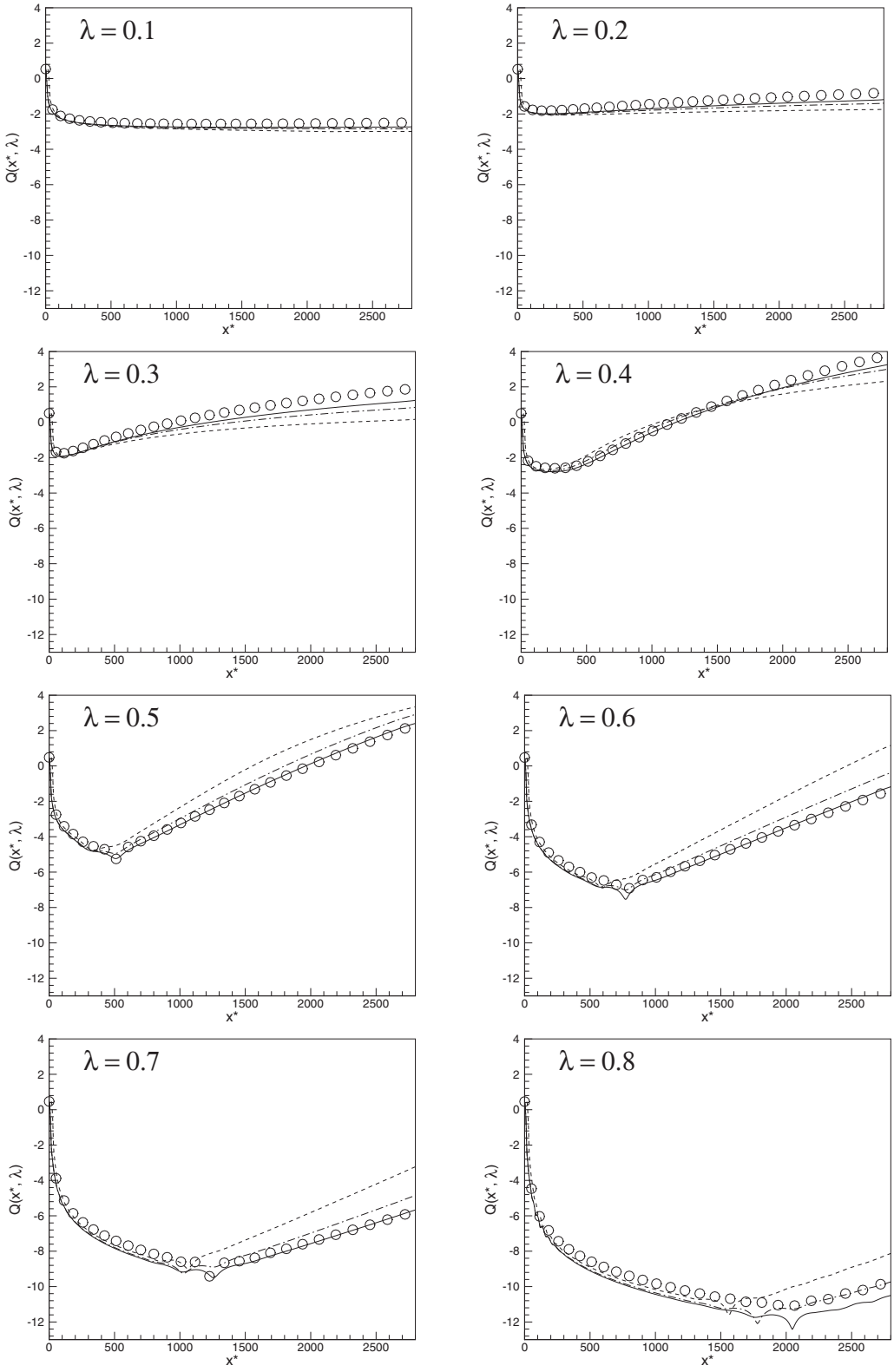

Fig. 5 Comparison of Q for the three different values of c and the discrete frequency [5]. The dashed lines are for $c=10^{-4}$, the dashed-dotted lines are for $c=5\times10^{-5}$, the solid lines are for $c=2.5\times10^{-5}$, and the circles are for the discrete frequency results.

illustrated clearly in Fig. 4 by the dashed line. For example, near to $x^*=500$, the frequency $\lambda=0.3$ gives the maximum amplitude, while near the buffer domain, values of λ that are closer to 0.4 yield the greatest response.

4.2 Results for the Different Values of c. In this section we summarize the stability results that have been presented in Sec. 4.1 and we also give a detailed comparison of those obtained for the other values of the parameter c with the discrete frequency [5].

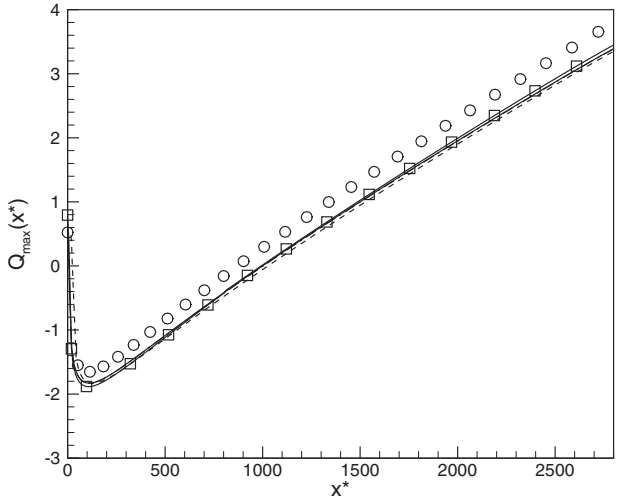

Fig. 6 The envelope of the curves presented in Figs. 4 and 5. For legends, see Fig. 5. The solid line with square symbols denotes the results for $c=2.5\times10^{-5}$ obtained by the finer grid, 960×96.

With this in mind, the envelope of the maximum surface heat transfer rate, $Q(x^*,\lambda)$, has been computed for the other two values of c, namely, $c=10^{-4}$ and $c=2.5\times10^{-5}$, and these are plotted in Fig. 5 along with the results for $c=5\times10^{-5}$ and the fixed frequency results.

The circles in each frame of Fig. 5 represent the results obtained by Paul et al. [5], which were obtained with constant frequency forcing. The sine-sweep simulation results are plotted as

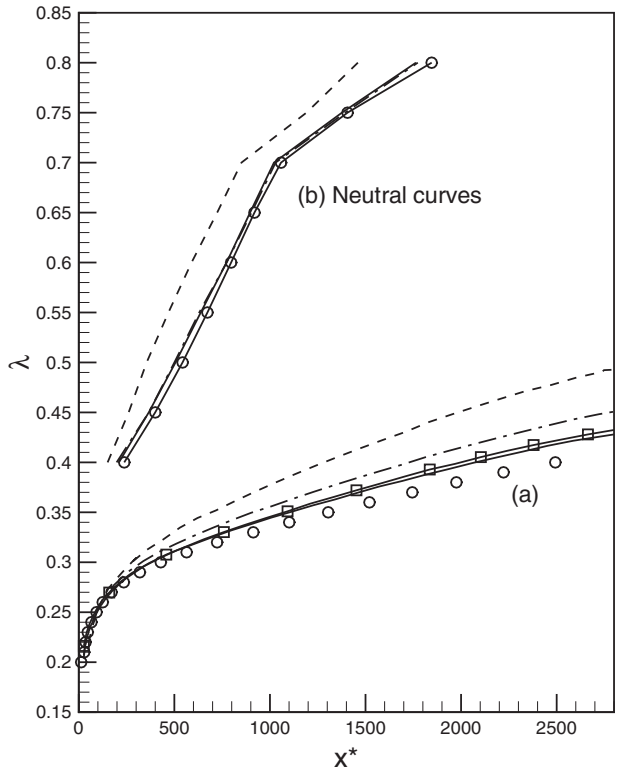

Fig. 7 (*a*) The values of λ, which correspond to $Q_{max}(x^*)$ shown in Fig. 6. These curves show which frequency corresponds to the most amplified disturbance at each value of x^*. (*b*) Neutral curves. The solid line with square symbols denotes the results for $c=2.5\times10^{-5}$ obtained by the finer grid, 960×96.

Table 1 Computed values of the neutral locations, (*A*) $c=10^{-4}$, (*B*) $c=5\times10^{-5}$, and (*C*) $c=2.5\times10^{-5}$, and comparison with Paul et al. [5]

	Neutral locations, x_c^*			
λ	*A*	*B*	*C*	Ref. [5]
0.5	355	500	506	543
0.55	469	630	638	673
0.6	590	773	773	797
0.65	724	903	896	919
0.7	851	1029	1021	1058
0.75	1191	1393	1377	1406

the dashed lines for $c=10^{-4}$, while the dashed-dotted lines are the results for $c=5\times10^{-5}$ and the solid lines are for $c=2.5\times10^{-5}$. This figure shows clearly that the qualitative agreement of the sine-sweep results with the fixed frequency results is very good. The results of $c=2.5\times10^{-5}$ have also an excellent quantitative agreement with the fixed frequency for $0.5<\lambda<0.7$, but when $\lambda=0.8$, it appears that the results of $c=5\times10^{-5}$ show better agreement with the fixed frequency results. In the first three frames, when $\lambda<0.4$, the $c=2.5\times10^{-5}$ results deviate slightly from the fixed frequency results in the downstream section of the boundary layer.

Table 1 shows the computed values of the neutral location against the disturbance frequency, λ, for the different values of c, where the corresponding values obtained by Paul et al. [5] are also shown. The results show that the neutral locations obtained using our sine-sweep simulations agree well with Ref. [5] especially for $c=5\times10^{-5}$ and $c=2.5\times10^{-5}$.

Figure 6 now displays the upper envelope of the curves shown in Figs. 4 and 5, where the envelope is defined as

$$Q_{\max}(x^*)=\max_{0.2\le\lambda\le0.45}Q(x^*,\lambda) \tag{19}$$

Thus $Q_{\max}(x^*)$ represents the maximum possible response of the boundary layer to thermal disturbances at each streamwise station. The values of the frequencies, which maximize Q and which are denoted by λ_{opt}, are shown in Fig. 7(*a*)—it is this figure that shows for which disturbance frequency, the largest disturbance amplitude, is obtained at a given downstream location.

The circles in Fig. 6 correspond to the previous computational results of Ref. [5] for disturbances of fixed frequency, while the dashed lines correspond to the results for $c=10^{-4}$, the dashed-dotted lines correspond to the results for $c=5\times10^{-5}$, and the solid lines correspond to the results for $c=2.5\times10^{-5}$. In addition, the solid line with square symbols in Figs. 6 and 7(*a*) corresponds to the results for $c=2.5\times10^{-5}$, which are obtained by the second grid setup, 960×96. It is clearly seen from these figures that the stability results obtained by both grid arrangements agree quite well and they are well resolved in the simulations.

The curves of $Q_{\max}$ obtained by the sine-sweep simulations lie slightly below the fixed frequency results [5]. The distance from the leading edge at which $Q_{\max}$ obtains its minimum values (Fig. 6) also varies with c (Table 2). This distance x^*, which disturbances are not amplified at all and which we refer to as "neutral distance" or "neutral point," decreases as c decreases; for ex-

Table 2 Distance from the leading edge at which Q_{max} obtains its minima (Fig. 6) and error relative to fixed frequency results

c	x^*	λ_{opt}	Error (%)
10^{-4}	126	0.262	4.4
5×10^{-5}	114	0.261	3.6
2.5×10^{-5}	109	0.255	1.2

ample, we have found that the neutral distance for $c=10^{-4}$ is $x^*=126$, while it is $x^*=114$ for $c=5\times10^{-5}$ and $x^*=109$ for $c=2.5\times10^{-5}$. The computations of Ref. [5] yield a value of the neutral distance of $x^*=105$, which clearly agrees quite well with the sine-sweep result for $c=2.5\times10^{-5}$. The corresponding values of the frequency at the neutral point obtained with the present method are about $\lambda=0.263$ for $c=10^{-4}$, $\lambda=0.261$ for $c=5\times10^{-5}$, and $\lambda=0.255$ for $c=2.5\times10^{-5}$, while the value obtained by Ref. [5] was about $\lambda=0.252$. So, the frequency result for $c=2.5\times10^{-5}$ also agrees quite well with the previous fixed frequency simulation.

The neutral curves for the different values of c are also presented in Fig. 7(*b*) against the disturbance frequency, and these are compared with those of the fixed frequency simulation [5], where again quite good agreement is found for $c=5\times10^{-5}$ and $c=2.5\times10^{-5}$ with Ref. [5].

The PFIs of Ref. [6] showed that the value of λ at the neutral point was about $\lambda=0.264$. Although the present result is closer to that of the PFI than to the constant frequency computation, our aim here is to see whether the sine-sweep computation can reproduce the constant frequency results sufficiently accurately using just one numerical simulation. Table 2 shows that the errors in the present computations are roughly 4.4% for $c=10^{-4}$, 3.6% for $c=5\times10^{-5}$, and 1.2% for $c=2.5\times10^{-5}$. Therefore, we conclude that the sine-sweep technique with a sufficiently small value of c (in this case, $c=2.5\times10^{-5}$) gives excellent results.

From the computational point of view, the total wall-clock time required to perform the sine-sweep code is much less than the constant frequency code. The total work done is proportional to the number of time steps taken in each code, as the amount of work done per time step is the same for the sine-sweep code and the fixed frequency code. It is likely that one requires simulations from more than 100 cases to achieve a well resolved neutral curve as shown in Ref. [6]. In the previous simulations of Ref. [5] with the selected discrete frequency we required about 10^5 time steps to achieve a periodic solution after the transient. We had to run the fixed frequency code 100 times to find the solutions for 100 frequencies. On the other hand, the present sine-sweep code with $c=2.5\times10^{-5}$ has saved about 86% of computational time compared with the fixed frequency code. The savings are even larger for the two larger values of c. We saved 92% of computational time with $c=5\times10^{-5}$ and 96% with $c=10^{-4}$. To conclude, the present sine-sweep code was found to not only accurately reproduce the fixed frequency code results but also results in significant computational time savings.

5 Conclusion

In this paper, we have reported on a numerical investigation in order to study the linear stability of a two-dimensional incompressible free convection boundary layer flow over a heated semi-infinite flat plate. A small-amplitude local temperature disturbance with slowly increasing frequency was introduced on the surface near the leading edge in order to generate disturbance waves inside the boundary layer. We have compared the stability characteristics obtained from the sine-sweep computations with those of the fixed frequency computations of Paul et al. [5] and with the PFI of Paul et al. [6].

As far as we are aware, this has been the first study where the sine-sweep technique has been used to assess the stability characteristics of a thermal boundary layer. It has been shown that this technique is an effective method for analyzing the stability of an advectively unstable boundary layer. Even larger savings can be expected from simulations with an entire frequency spectrum perturbed simultaneously as, e.g., by a pulse disturbance. This approach is possible as the problem studied here is linear and disturbance waves may be linearly superimposed.

Acknowledgment

The authors thank the anonymous referees for their valuable comments on the earlier version of this paper, which have served to improve the manuscript.

References

[1] Nachtsheim, P. R., 1963, "Stability of Free Convection Boundary Layer Flows," NASA Technical Report No. TN D-2089.
[2] Hieber, C. A., and Gebhart, B., 1971, "Stability of Vertical Natural Convection Boundary Layers," J. Fluid Mech., **48**, pp. 625–646.
[3] Goldstein, M. E., 1983, "The Evolution of Tollmien-Schlichting Waves Near a Leading Edge," J. Fluid Mech., **127**, pp. 59–81.
[4] Paul, M. C., 2002, "The Stability of Free Convective Boundary Layer Flows," Ph.D. thesis, University of Bath, UK.
[5] Paul, M. C., Rees, D. A. S., and Wilson, M., 2007, "Thermal Receptivity of Free Convective Flow From a Heated Vertical Surface: Linear Waves," Int. J. Therm. Sci., **47**, pp. 1382–1392.
[6] Paul, M. C., Rees, D. A. S., and Wilson, M., 2005, "The Influence of Higher Order Effects on the Linear Wave Instability of Vertical Free Convective Boundary Layer Flow," Int. J. Heat Mass Transfer, **48**, pp. 809–817.
[7] Fasel, H., and Konzelmann, U., 1990, "Non-Parallel Stability of a Flat-Plate Boundary Layer Using the Complete Navier-Stokes Equations," J. Fluid Mech., **221**, pp. 311–347.
[8] Brooker, A. M. H., Patterson, J. C., and Armfield, S. W., 1997, "Non-Parallel Linear Stability Analysis of the Vertical Boundary Layer in a Differentially Heated Cavity," J. Fluid Mech., **352**, pp. 265–281.
[9] Dietz, A. J., 1999, "Local Boundary-Layer Receptivity to a Convected Free-Stream Disturbance," J. Fluid Mech., **378**, pp. 291–317.
[10] Arakawa, A., 1966, "Computational Design of Long-Term Numerical Integration of the Equations of Fluid Motion: I. Two Dimensional Incompressible Flow," J. Comput. Phys., **1**, pp. 119–143.
[11] Briggs, W., 1987, *A Multigrid Tutorial*, S.I.A.M., Philadelphia.
[12] Kloker, M., Konzelmann, U., and Fasel, H., 1993, "Outflow Boundary Conditions for Spatial Navier-Stokes Simulations of Transitional Boundary Layers," AIAA J., **31**, pp. 620–628.
[13] Stemmer, C., Kloker, M., and Wagner, S., 2000, "Navier-Stokes Simulation of Harmonic Point Disturbances in an Airfoil Boundary Layer," AIAA J., **38**, pp. 1369–1376.
[14] Bake, S., Meyer, G., and Rist, U., 2002, "Turbulence Mechanism in Klebanoff Transition: A Quantitative Comparison of Experiment and Direct Numerical Simulation," J. Fluid Mech., **459**, pp. 217–243.

Natural Convection Heat Transfer Enhancements From a Cylinder Using Porous Carbon Foam: Experimental Study

Yorwearth L. Jamin

A. A. Mohamad
e-mail: mohamad@ucalgary.ca

Department of Mechanical and Manufacturing Engineering,
Schulich School of Engineering,
CEERE, University of Calgary,
Calgary, AB, T2N 1N4, Canada

The main objective of this experimental study is to quantify and compare the heat transfer enhancement of carbon foam and aluminum fins in natural convection. The study measures steady state heat transfer from a heated vertical pipe, with and without porous medium. The largest increase in Nusselt number was achieved by a solid carbon foam sleeve, which was about 2.5 times greater than a bare copper pipe.
[DOI: 10.1115/1.2977606]

Keywords: natural convection, porous media, heat exchangers, heat transfer enhancements

1 Introduction

In most natural convection heat exchangers the thermal resistance is highest at the fluid/solid interface, especially if the fluid has a Prandtl number order of 1 (i.e., air). Porous mediums have been identified as a means to reduce the thermal resistance at the gas/solid interface and enhance heat transfer rates. Vafai and Kim [1] investigated a thin porous layer attached to a flat plate in a forced convection environment. They noted that enhanced heat transfer could be achieved when the effective conductivity of the porous layer was higher than that of the fluid. Angirasa [2] conducted an experimental investigation of forced air convection enhancement with metallic fibrous materials with porosities of 0.93 and 0.97. When a porous layer was attached to a flat plate he observed an increase in Nusselt number up to four times relative to a bare plate. However, natural convection enhancement due to a thin porous layer attached to an external surface is not a well studied phenomenon, and experimental characterization of the momentum and thermal boundary layers is not readily available.

The objective of the present study is to experimentally quantify the heat transfer enhancement of carbon foam, compare results to a bare and aluminum finned pipe, and consequently provide a basis for evaluating the suitability of carbon foam for industrial applications. The study investigates steady state heat transfer from a heated vertical pipe, with and without a thin porous medium attached to the external surface, in a natural convection environment. Heat transfer performance results of four carbon foam cases are compared to a bare copper pipe and an aluminum finned pipe.

2 Porous Carbon Foam

The porous medium under investigation is high thermal conductivity (HTC) carbon foam, which is commercially produced by Poco Graphics Inc. The production of the HTC foam is based on a process developed at the Oak Ridge National Laboratory, which turns mesophase pitch into carbon foam. The end product is composed of uniformly shaped bubbles with even distribution set within carbon ligaments. The z-direction has different thermal properties than the x-y direction, which results in a nonisotropic material. That is, there is less resistance to heat transfer and therefore a higher thermal conductivity in the z-plane [3]. It should also be noted that thermal conductivities decrease with increasing temperature. Material properties published by Poco Graphics Inc. are presented in Table 1.

3 Experimental Setup and Procedure

The vertical pipe and data acquisition system are illustrated in Fig. 1 with the vertical pipe located at the center of the test section (dimensions of 50 cm long, 35 cm wide, and 25 cm high). Small gaps in two sides of the test chamber walls (1) allow for ambient temperature air supply to enter the chamber with minimal disturbance to the natural convection currents. Increases in pipe surface temperature cause natural convection to occur along its vertical surface. A heating cartridge with a rated wattage of 50 W (Omega CIR-3051/120 V) is inserted into the pipe (2) and connected to a variable current power supply (3), which provides a uniform heat flux. Power supplied to the heating cartridge (41.14 Ω) is measured with a rectifier (4) and is calculated using the formula $P = Vs^2/R$, where Vs is the measured voltage and R is the heater resistance. Variation in Rayleigh number is achieved by increasing the power supplied to the heating cartridge. The propagated uncertainty associated with power measurement is ± 0.2 W. Six type-K thermocouples (Omega TT-K-36) soldered into the pipe wall (5) provide temperature measurements. The maximum propagated uncertainty associated with mean surface temperature is ± 1.8°C. A single type-K thermocouple measures ambient air temperature inside the test section (6). The pipe assembly is mounted inside a chamber on two Teflon rods (7) and is illustrated in Fig. 2. Teflon is used to mount the pipe in order to minimize heat losses. The HTC foam is press fitted onto the pipe with Dow 340 thermal grease applied to the interface between the pipe and the HTC foam to reduce thermal contact resistance. Thermocouple and power wires are routed through the hollow bottom Teflon rod to a FieldPoint (FP) data acquisition system (8).

A National Instruments, FieldPoint, PC-based, distributed input/output (I/O) data acquisition system is used for this investigation. The FP system is connected to a laptop and LABVIEW 6.1 via a serial port. dc signals generated by the sensors are transmitted to the FieldPoint I/O modules. The I/O modules filter, digitize, calibrate, and scale raw sensor signals to engineering units. The LABVIEW application queries the FieldPoint network interface at a sampling rate equal to the slowest I/O module sampling rate (i.e., 0.88 Hz). The parameters measured with corresponding sensors,

Contributed by the Heat Transfer Division of ASME for publication in the JOURNAL OF HEAT TRANSFER. Manuscript received October 26, 2007; final manuscript received March 17, 2008; published online September 24, 2008. Review conducted by Yutaka Asako.

Table 1 Material properties for the HTC foam

	Manufacturer specifications
Effective thermal conductivity	
z-plane (20°C)	245 W/m K
z-plane (100°C)	165 W/m K
xy-plane (20°C)	70 W/m K
xy-plane (100°C)	Not available
Porosity	61%
Open porosity	95%
Pore diameter	350 μm
Emissivity	0.62

I/O modules, sampling rate, and uncertainty are summarized in Table 2.

Tests were completed over a range of conditions ($Ra=3\times10^6$ to 1.5×10^7). For each case investigated, the appropriate HTC foam geometric arrangement, aluminum finned pipe, or bare pipe was installed in the mounting system. The power supply to the heating cartridge was switched on, delivering approximately 0.5 W to the heater ($Ra\approx3\times10^6$). The apparatus was left running for approximately 2 h and allowed to reach thermal steady state (achieved when the mean surface temperature did not fluctuate more than ±0.1°C over a 5 min period). The data acquisition system was turned on and began sampling temperature, pressure, and power signals at 0.88 Hz. A routine in LABVIEW buffered the data (106 unique points) and performed appropriate data reductions and statistics before logging results in an excel spreadsheet. The LABVIEW application was stopped and I/O modules were turned off in order to reduce heat induced error in the FieldPoint hardware. The power supply to the cartridge heater was increased by approximately 0.5 W, and the apparatus was allowed to reach steady state (approximately 60 min). The LABVIEW application and I/O modules were turned back on and subsequent data were acquired. This procedure was repeated until a Rayleigh number of 1.5×10^7 was reached (~9 W).

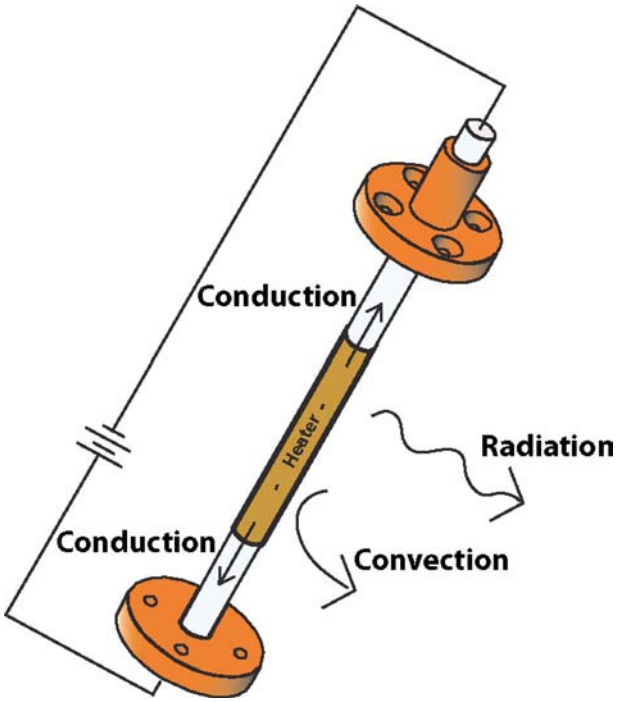

Fig. 2 Experimental apparatus and heat loss mechanisms

4 Heat Loss Estimation

Heat loss from the vertical pipe due to conduction through the Teflon mounts was estimated as follows. During no flow conditions an energy balance on the vertical pipe in Fig. 2 indicates that the heat input to the polished copper pipe is lost by three mechanisms (i.e., conduction, natural convection, and radiation). Since this study is interested in quantifying heat transferred by convection and radiation it is necessary to isolate the conduction term (i.e., heat loss). Therefore, small amounts of heat were supplied to

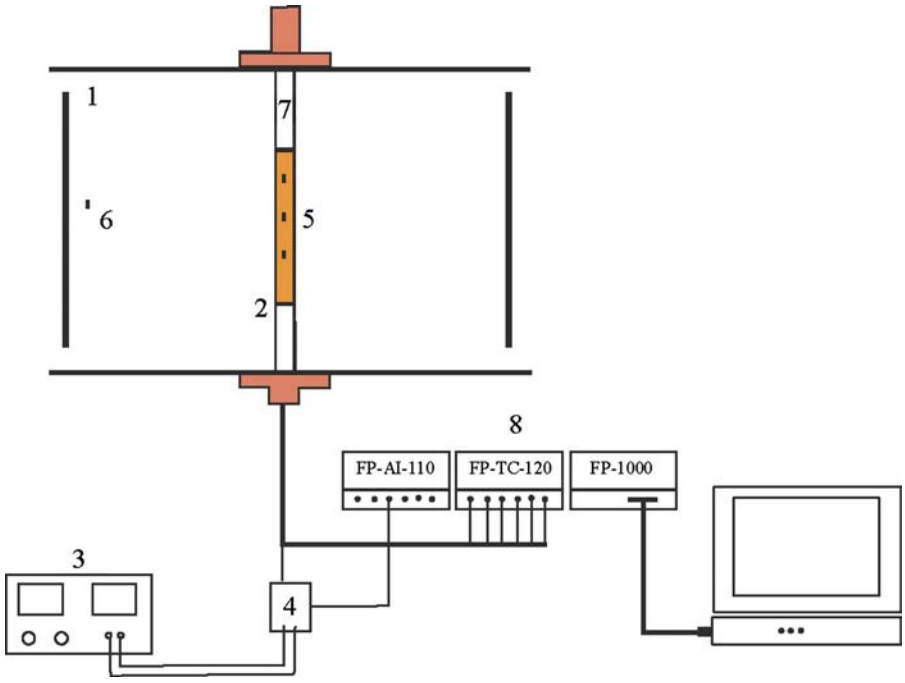

Fig. 1 Schematic layout of the vertical pipe and data acquisition system

Table 2 Data acquisition system

Measurement	Sensor	I/O module	Sample rate	Uncertainty
Mean surface temperature	Six type-K thermocouples (Omega TT-K-36-25)	FP-TC-120 (National Instruments)	0.88 Hz	±1.8°C (max) ±0.7°C (min)
Ambient temperature	One type-K thermocouple (Omega TT-K-20-25)	FP-TC-120 (National Instruments)	0.88 Hz	±0.5°C
Power	One dc signal rectifier	FP-AI-110 (National Instruments)	1.9 Hz	±0.2 W

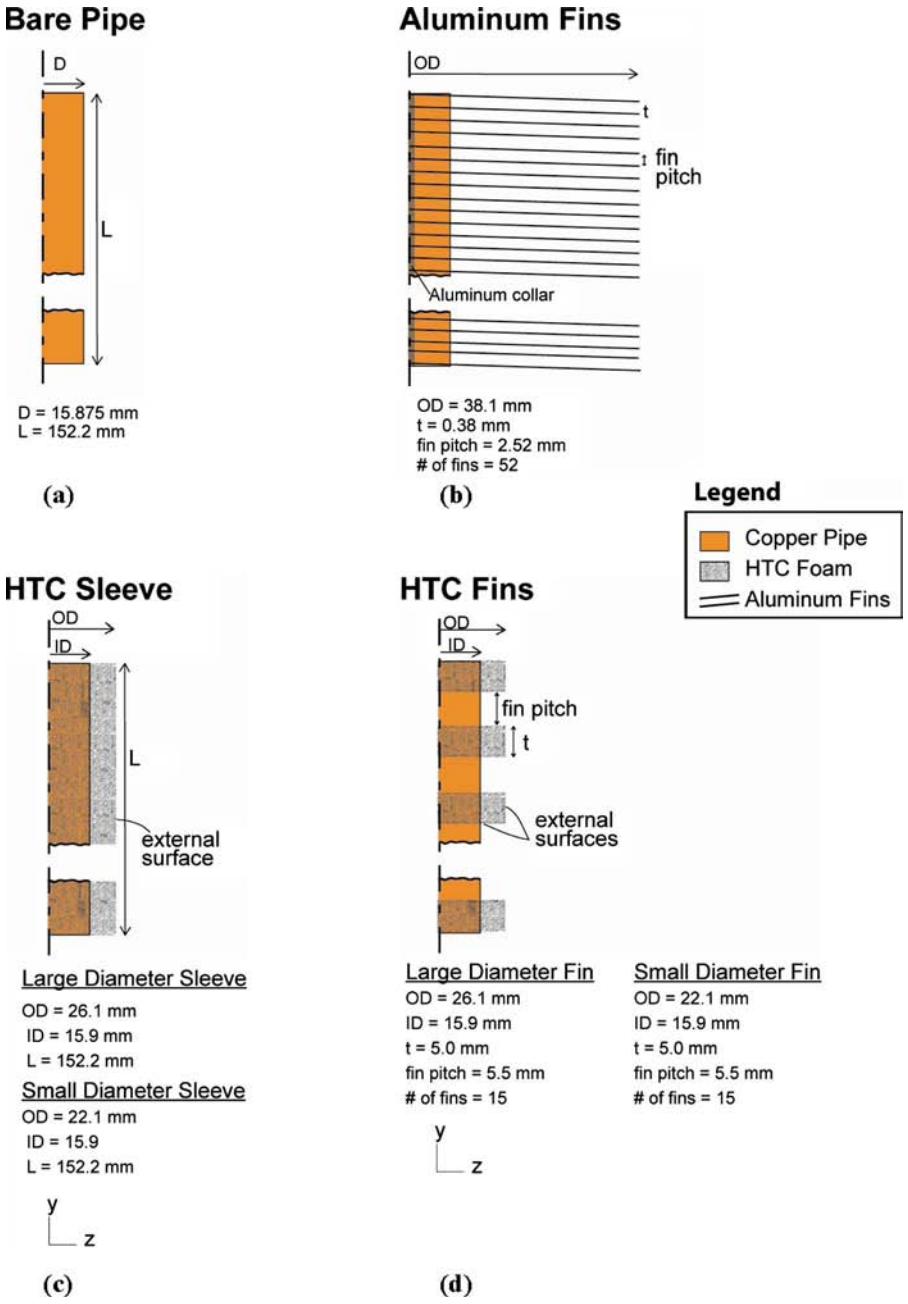

Fig. 3 (*a*)–(*d*) Geometric details of a bare copper pipe, aluminum fins, HTC sleeves, and HTC fins, respectively

the bare pipe and surface temperatures were measured. Natural convection was estimated using the empirical relation from Ref. [4] for a flat plate:

$$\bar{\mathrm{Nu}}_L = 0.68 + \frac{0.670\mathrm{Ra}_L^{1/4}}{\left[1 + \left(\frac{0.492}{\mathrm{Pr}}\right)^{9/16}\right]^{4/9}}$$

Heat transfer enhancement due to the pipe curvature was accounted for by applying the results from an investigation of laminar-free convection from the outer surface of a slender vertical cylinder [5]. This work provides a convenient expression to account for the transverse curvature influence of the pipe on heat transfer. Radiation from the pipe was determined from Ref. [6] using

$$Q_{\mathrm{rad}} = \sigma\varepsilon A(T_s^4 - T_\infty^4)$$

where copper surface emissivity is equal to 0.03. The difference between the heat supplied and natural convection plus radiation is the heat lost by conduction. Conduction heat losses from the bare copper pipe were plotted as a function of mean surface temperature and a least-squares fit obtained. The heat losses were then subtracted from the heat input during natural convection experiments at corresponding values of surface temperature.

Several different geometric arrangements were investigated in this experiment. Figure 3(*a*) presents the bare copper pipe. Figure 3(*c*) illustrates the dimensions of the large and small diameter HTC sleeves with the *z*-direction of the HTC foam indicated. Dimensions of the large and small diameter HTC fins are presented in Fig. 3(*d*) with *z*-direction indicated. An aluminum finned copper pipe was also investigated and its dimensions are presented in Fig. 3(*b*).

The copper pipe dimensions remained constant for all cases studied (i.e., $D=1.59$ cm, $L=15.22$ cm). For each of these cases the nondimensional parameter, Nusselt number, is calculated in relation to Rayleigh number. The mean Nusselt number is defined as

$$\bar{\mathrm{Nu}} = \frac{\bar{h}L}{k}$$

where L is the length of the copper pipe and k is the thermal conductivity of air at the film temperature. The mean heat transfer coefficient (h) is based on Newton's law of cooling.

$$\bar{h} = \frac{Q}{\pi DL(\overline{T}_s - T_\infty)}$$

For the sake of comparison between different cases the pipe outside diameter, D, will remain constant regardless of the material attached to the pipe surface. This calculation assumes isothermal surface temperature; uncertainty associated with this assumption is accounted for in the surface temperature error margin. Conduction losses are accounted for in the heat input value, Q. In order to evaluate the influence of the exposed surface area on Nusselt number a surface area coefficient, λ, is defined.

$$\lambda = \frac{\text{surface area}_{\text{porous layer}}}{\text{surface area}_{\text{bare pipe}}}$$

The Rayleigh number is calculated as

$$\mathrm{Ra}_L = \mathrm{Gr}_L\mathrm{Pr} = \frac{g\beta(T_s - T_\infty)L^3}{\nu\alpha}$$

where kinematic viscosity, υ, volumetric thermal expansion coefficient β, and thermal diffusivity α are evaluated at the film temperature. All primary variables (i.e., T_s, T_∞, and Q) are time averaged over a 2 min interval.

In order to verify results obtained with the methodology and apparatus described above, experimental results for Nusselt number from a bare pipe were compared with empirical and analytical predictions [4,7]. Experimental results illustrated in Fig. 4 show good agreement with empirical and analytical predictions over the range of Rayleigh numbers tested.

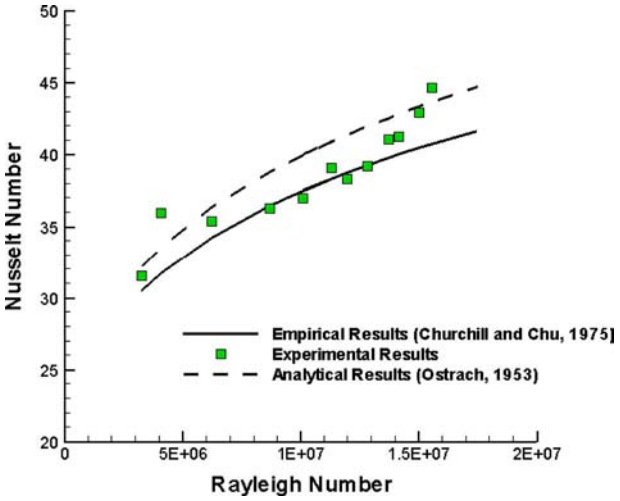

Fig. 4 Comparison of experimental and empirical natural convection results

5 Results and Discussion

The length-averaged surface temperature and mean Nusselt number versus Rayleigh number are presented in Figs. 5(*a*) and 5(*b*). No comparison between porous layer diameters is presented in Fig. 5(*a*) because all other surface temperature values fall on the same curve and no more useful information is gained. The relationship between surface temperature and Rayleigh number is presented in Fig. 5(*a*). It is observed that as the surface temperature increases the ratio of buoyancy forces to viscous forces increases. It follows that air flow rate and consequently Nu_L increase with increasing surface temperature and Rayleigh number. Figure 5(*b*) illustrates that Nu_L does indeed increase with Rayleigh number.

Part of the Nu_L increase observed in Fig. 5(*b*) can be explained by surface area coefficients presented in Table 3. The larger diameters result in more surface area, greater heat transfer rates, and a higher Nu_L. However, in the case of large diameter HTC sleeves, Fig. 5(*b*), a 2.5 times increase is observed for Nu_L relative to the bare pipe, while the corresponding increases in the surface area is only 1.64 times. This observation suggests that a heat transfer enhancement is achieved beyond that due to an increased surface area. This phenomenon can be explained as follows. First, air within the porous layer is not stagnant. Although there is high resistance to flow and air velocity is low, flow may be fast enough to have a noticeable effect on overall natural convection Nusselt number. Because of the tremendous surface area within the porous layer even small flow rates can be responsible for noticeable heat transfer under natural convection conditions. Second, the HTC sleeve offers a continuous surface for the development of flow in the vertical direction. Because the HTC foam is a good conductor, the surface temperature of the HTC sleeve remains relatively high and the air density gradient is allowed to develop along the continuous vertical surface, thus producing continuous air flow and good natural convection. Finally and most importantly, radiative heat transfer plays a very significant role in overall heat transfer for the HTC sleeve case. The surface characteristics are modified from a polished copper pipe ($\varepsilon=0.03$) to a dark porous layer ($\varepsilon=0.62$). This surface modification increases radiation from about

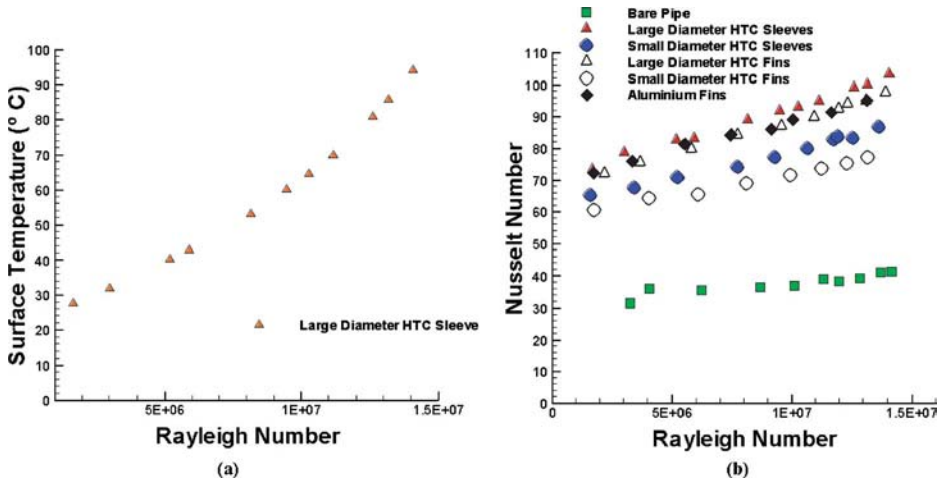

Fig. 5 (*a*) and (*b*) Variation of mean surface temperature (°C) and Nusselt number with Ra

3% of the total heat transfer rate to about 45% of the total heat transfer rate. The relative influence of radiation for each of the cases studied is presented in Table 4.

Interestingly, the increase in Nu_L was less than the increase in the surface area for the case of HTC fins in Fig. 5(*b*). For large diameter HTC fins, the increase in the surface area relative to the bare pipe was about 2.65, but the increase in Nu_L was only about 2.35 times. The failure of HTC fins to transfer heat from the pipe at a rate equivalent or greater than its increase in the surface area can be explained by two points. First, the momentum boundary layer induced by the temperature difference between the surface and ambient does not develop in the same manner as the bare pipe or HTC sleeve. The fins interrupt air flowing in the vertical direction and consequently reduce air velocity and heat transfer coefficient. Instead, much of the air circulation is restricted to the space between fins. Because these spaces are relatively small, the natural convection velocity is consequently much smaller than that expected for the bare pipe and HTC sleeve cases. Second, radiation from the HTC fins is less than that from HTC sleeves.

Table 3 Natural convection heat transfer enhancement and surface area ratios

	Heat transfer enhancement ratio (relative to the bare pipe)	λ
Bare pipe	1	1
Large HTC fins (15)	2.35	2.65
Small HTC fins (15)	1.85	1.93
Large HTC sleeve	2.50	1.64
Small HTC sleeve	2.10	1.40
Aluminum fins (52)	2.34	13.69

Table 4 Relative influence of radiation on total heat transfer for natural convection

	Radiation as percentage of total heat input (%)
Bare pipe	3
Large diameter HTC sleeve	45
Small diameter HTC sleeve	43
Large diameter HTC fins	35
Small diameter HTC fins	33
Aluminum fins	40

Figure 6 estimates radiation heat transfer rate for each of the cases studied. Fin geometry interrupts radiative heat transfer from the surface to the surroundings.

The aluminum finned pipe produces a Nusselt number well below that expected given its large surface area coefficient. This is likely due to its discontinuous surface. Each aluminum fin interrupts air flow in the vertical direction while the bulk of the surface area is exposed to air with very restricted circulation. Air flow between and perpendicular to the fins is low; thus the heat transfer coefficient is low. Also the surface emissivity coefficient of oxidized aluminum is about half of the value used for the HTC foam.

6 Uncertainty

The uncertainty associated with Nusselt numbers is summarized in Table 5. These values are based on the measurement uncertainty methodology published by Ref. [8]. Nusselt number uncertainty values are given for both high and low Rayleigh numbers and represent maximum and minimum errors. The uncertainties associated with Rayleigh numbers are 14.4% for low Ra and 2.3% at high Ra. The range of uncertainties produced by the equipment, methodology, and data reduction is reasonable for an

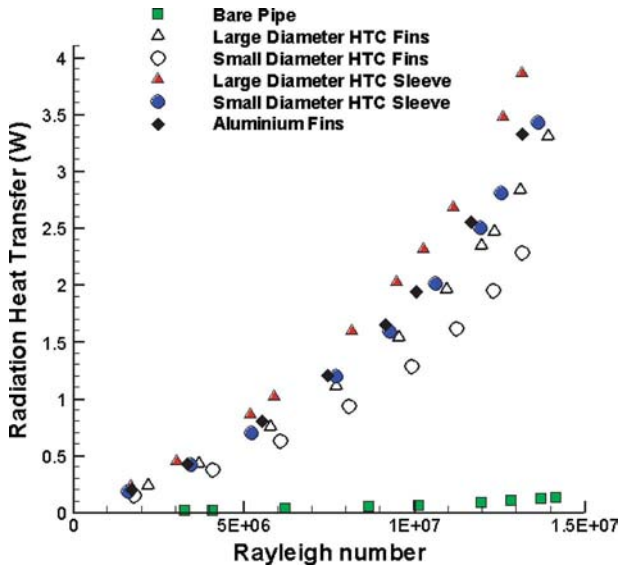

Fig. 6 Radiation heat transfer versus Rayleigh number

Table 5 Uncertainty associated with natural convection Nusselt numbers

	Nusselt uncertainty at low Rayleigh numbers (%)	Nusselt uncertainty at high Rayleigh numbers (%)
Large diameter HTC sleeve	13.3	3.5
Small diameter HTC sleeve	15.6	4.1
Large diameter HTC fins	13.1	3.8
Small diameter HTC fins	14.3	4.4
Aluminum fins	13.2	4.3
Bare pipe	9	6.3

experimental investigation. The maximum errors encountered for natural convection do not exceed 16% (with 95% confidence) of the measured values.

7 Conclusions

Test results for a bare pipe validated the methodology and assumptions employed during apparatus design and construction. Subsequent testing of HTC foam cases yielded results for variations in length-averaged surface temperature and mean Nusselt number natural convection conditions. HTC foam results were compared to corresponding results for aluminum fins, and the merits of each were discussed.

Several general conclusions can be made regarding the application of HTC foam layers in a natural convection environment.

- The Nusselt number increases as the diameter increases.
- The Nusselt number increases as the Rayleigh number increases.
- The influence of radiation on overall heat transfer rate is very important.

More specific conclusions can be made about each natural convection case studied.

- HTC sleeves produce more heat transfer enhancement than their surface area would indicate. This is due to the sleeve continuous surface, internal convection, and modified surface emissivity coefficient.
- HTC fins produce less heat transfer enhancement than their surface area would indicate. The discontinuous finned surface interrupts flow and reduces convective heat transfer.

The aluminum fins produce substantially less heat transfer enhancement than their surface area would indicate. Natural convection flow is severely interrupted by the finned surface. The rate of radiative heat transfer per unit surface area is much lower than HTC foam cases due to lower surface emissivity and fin geometry.

Given the natural convection experimental results obtained in this study, HTC sleeves are the most suitable heat transfer medium for natural convection applications.

Nomenclature

A_s = surface area
D = pipe outside diameter
Gr = Grashof number
g = gravity constant
$\bar{h}$ = mean convective heat transfer coefficient
k = thermal conductivity
L = pipe length
$\overline{\mathrm{Nu}}_L$ = mean Nusselt number for natural convection
OD = aluminum fin outside diameter
P = power
Pr = Prandtl number
Q = heat transfer rate
R = electrical resistance
Ra = Rayleigh number
$\bar{T}_s$ = length-averaged surface temperature
T_∞ = ambient temperature
V_s = supplied power voltage

Greek Symbols

α = thermal diffusivity
β = volumetric thermal expansion coefficient
ε = surface emissivity coefficient
λ = surface area ratio
υ = kinematic viscosity

References

[1] Vafai, K., and Kim, S., 1990, "Analysis of Surface Enhancement by Porous Substrate," ASME J. Heat Transfer, **112**, pp. 700–706.
[2] Angirasa, D., 2002, "Experimental Investigation of Forced Convection Heat Transfer Augmentation With Metallic Fibrous Materials," Int. J. Heat Mass Transfer, **45**, pp. 912–922.
[3] Gallego, N., and Klett, J., 2003, "Carbon Foams for Thermal Management," Carbon, **41**(7), pp. 1461–1466.
[4] Churchill, S., and Chu, H., 1975, "Correlating Equations for Laminar and Turbulent Free Convection From a Vertical Plate," Int. J. Heat Mass Transfer, **18**, pp. 1323–1329.
[5] Sparrow, E. M., and Gregg, J. L., 1956, "Laminar Free Convection From a Vertical Plate With Uniform Surface Heat Flux," Trans. ASME, **78**, pp. 435–440.
[6] Incropera, F., and DeWitt, D., 2002, *Introduction to Heat Transfer*, 4th ed., Wiley, New York.
[7] Ostrach, S., 1953, "An Analysis of Laminar Free Convection Flow and Heat Transfer About a Flat Plate Parallel to the Direction of the Generating Body Force," National Advisory Committee for Aeronautics, Report No. 1111.
[8] Abernethy, R., Benedict, R., and Dowdell, R., 1985, "ASME Measurement Uncertainty," ASME J. Fluids Eng., **107**, pp. 161–164.

Liquid Single-Phase Flow in an Array of Micro-Pin-Fins—Part II: Pressure Drop Characteristics

Weilin Qu[1]
e-mail: qu@hawaii.edu

Abel Siu-Ho

Department of Mechanical Engineering,
University of Hawaii at Manoa,
Honolulu, HI 96822

*This Technical Brief is Part II of a two-part study concerning water single-phase pressure drop and heat transfer in an array of staggered micro-pin-fins. This brief reports the pressure drop results. Both adiabatic and diabatic tests were conducted. Six previous friction factor correlations for low Reynolds number (Re <1000) flow in conventional and micro-pin-fin arrays were examined and found underpredicting the adiabatic data except the correlation by Short et al. (2002, "Performance of Pin Fin Cast Aluminum Coldwalls, Part 1: Friction Factor Correlation," J. Thermophys. Heat Transfer, **16**(3), pp. 389–396), which overpredicts the data. A new power-law type of correlation was developed, which showed good agreement with both adiabatic and diabatic data.* [DOI: 10.1115/1.2970082]

Keywords: micro-pin-fins, heat sink, liquid cooling, single phase, pressure drop, friction factor

1 Introduction

Liquid cooled micro-pin-fin heat sinks that utilize arrays of staggered or aligned micro-pin-fins as an internal heat transfer enhancement structure have recently emerged as a promising alternative to microchannel heat sinks [1–7]. The height-to-diameter ratio H_{fin}/d of the micro-pin-fins is in the intermediate range of 0.5–8, and flow is mostly in laminar or transitional regime with Reynolds number less than 1000. An accurate prediction of pressure drop in micro-pin-fin arrays is of paramount importance to practical implementation of the heat sinks due to the concern of excessive pressure loss.

A few published studies discussed single-phase pressure drop in micro-pin-fin arrays [1–7]. While some of the studies reported good agreement between predictions of previous conventional pin-fin correlations and the data [2–4], others found appreciable discrepancies [1,5–7]. Other relevant studies include those on pressure drop of low Reynolds number ($\text{Re}<1000$) flow in arrays of conventional intermediate pin-fins ($0.5 \le H_{\text{fin}}/d \le 8$) [8,9] and long pin-fins ($H_{\text{fin}}/d > 8$) [10–12] with diameters several millimeters and larger.

This Technical Brief is Part II of a two-part study that investigates water heat transfer and pressure drop in an array of staggered square micro-pin-fins. Heat transfer results were presented in Part I [13]. In this Technical Brief, pressure drop results for both adiabatic and diabatic water flows are reported, complemented by assessment of previous friction factor correlations and development of a new correlation.

2 Experimental Apparatus and Procedure

Detailed description of the experimental study can be found in Part I [13]. Only a brief overview is presented here. Figure 1 shows the construction of the test module that consists of a micro-pin-fin heat sink, a housing, a cover plate, and nine cartridge heaters. The heat sink had a platform (top) area of 3.38 cm (length) $\times$ 1.0 cm (width), which contained an array of 1950 staggered micro-pin-fins with a 200×200 μm^2 cross section ($W_{\text{fin}} \times L_{\text{fin}}$) by a 670 μm height (H_{fin}). Figure 2 shows a top view of the micro-pin-fin array together with key dimensions. Pressure drop across the heat sink was measured using a differential pressure transducer that was connected to the inlet and outlet deep plenums in the housing.

Two sets of tests were conducted: adiabatic tests without heat transfer and diabatic tests with heat transfer. Operating conditions and procedure for diabatic tests were described in detail in Part I [13]. For adiabatic tests, a water temperature of around 21 °C and six water mass flow rates $\dot{m}$, ranging from 0.611 g/s to 1.398 g/s, were tested. The corresponding maximum mass velocities $G_{\max}$ and Reynolds number Re ranged from 183 $\text{kg/m}^2\,\text{s}$ to 417 $\text{kg/m}^2\,\text{s}$ and from 37.9 to 85.8, respectively. The procedure for the adiabatic tests was set to be the same as that for the diabatic tests.

3 Results and Discussion

3.1 Adiabatic Pressure Drop. The measured ΔP is the sum of pressure drops across the inlet deep and shallow plenums, micro-pin-fin array, outlet shallow and deep plenums, as well as pressure losses and recoveries associated with the consecutive sections. Neglecting pressure drop in the plenums, ΔP_{fin} can be evaluated from

$$\Delta P_{\text{fin}} = \Delta P - (\Delta P_{c1} + \Delta P_{c2} + \Delta P_{e2} + \Delta P_{e1}) \tag{1}$$

where ΔP_{c1}, ΔP_{c2}, ΔP_{e2}, and ΔP_{e1} are calculated from [14]

$$\Delta P_{c1} = \frac{1}{2}\rho_f (u_{p2,\text{in}}^2 - u_{p1,\text{in}}^2) + \frac{K_{c1}}{2}\rho_f u_{p2,\text{in}}^2 \tag{2}$$

$$\Delta P_{c2} = \frac{1}{2}\rho_f (u_{\max}^2 - u_{p2,\text{in}}^2) + \frac{K_{c2}}{2}\rho_f u_{\max}^2 \tag{3}$$

$$\Delta P_{e2} = \frac{1}{2}\rho_f (u_{p2,\text{out}}^2 - u_{\max}^2) + \frac{K_{e2}}{2}\rho_f u_{\max}^2 \tag{4}$$

and

$$\Delta P_{e1} = \frac{1}{2}\rho_f (u_{p1,\text{out}}^2 - u_{p2,\text{out}}^2) + \frac{K_{e1}}{2}\rho_f u_{p2,\text{out}}^2 \tag{5}$$

The values of K_{c1}, K_{c2}, K_{e1}, and K_{e2} for the present test module geometry are evaluated in accordance with Ref. [14]. $\Delta P_{c1} + \Delta P_{c2} + \Delta P_{e2} + \Delta P_{e1}$ accounts for 0.7–1.1% of ΔP.

Once ΔP_{fin} is determined from Eq. (1), f_{fin} can be evaluated from

$$f_{\text{fin}} = \frac{\Delta P_{\text{fin}}}{N_L\left(\dfrac{\rho_f u_{\max}^2}{2}\right)} \tag{6}$$

Following the method developed by Kline and McClintock [15], the uncertainty in ΔP_{fin} is about 0.3% and the uncertainty in f_{fin} is about 9.9%. The variation of f_{fin} with Reynolds number Re is plotted in Fig. 3 on a log-log scale. Figure 3 shows that f_{fin} decreases with increasing Re in a fairly linear fashion, which indi-

[1]Corresponding author.

Contributed by the Heat Transfer Division of ASME for publication in the JOURNAL OF HEAT TRANSFER. Manuscript received September 11, 2007; final manuscript received May 1, 2008; published September 17, 2008. Review conducted by Yogendra Joshi. Paper presented at the 2007 ASME International Mechanical Engineering Congress (IMECE2007), Seattle, WA, November 10–16, 2007.

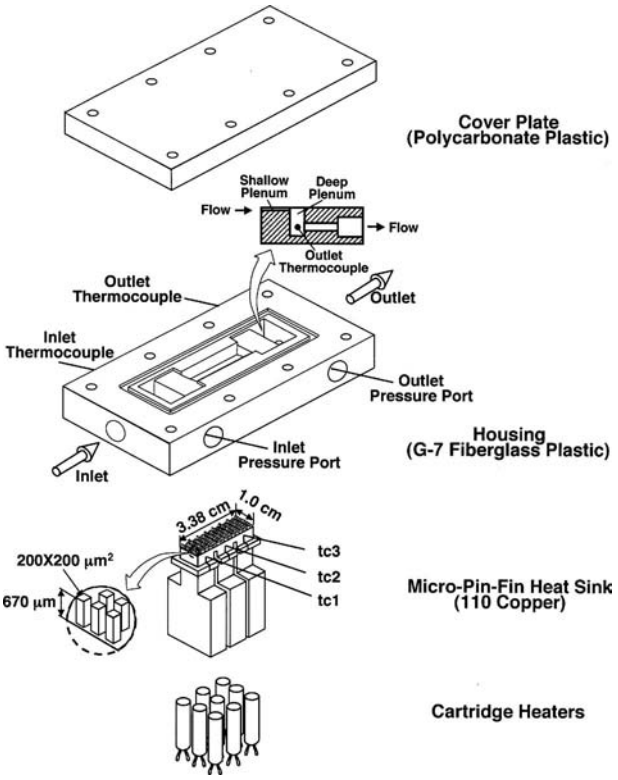

Fig. 1 Test module construction

cates a power law ($f_{\text{fin}} \propto \text{Re}^m$) relationship.

Six previous friction factor correlations for low Reynolds number ($\text{Re} < 1000$) flow in staggered pin-fin arrays are selected and listed in Table 1. Predictions of these correlations are plotted in Fig. 3 along with the adiabatic f_{fin} data for comparison. The mean absolute error (MAE) for each correlation is given in Table 1. Figure 3 shows all the correlations underpredicting the data by a large margin except correlation 3, which overpredicts the data.

A new power-law type of correlation is proposed through a linear regression of the adiabatic data as follows:

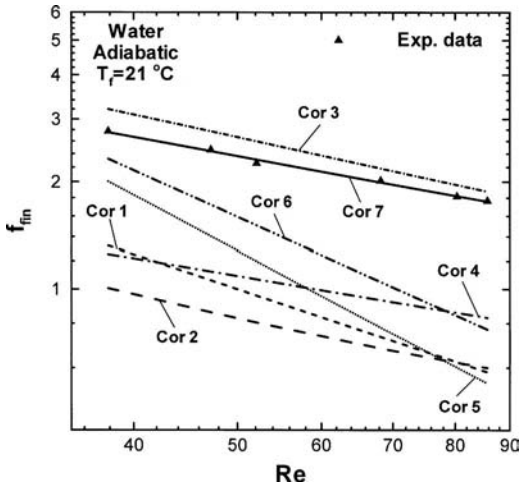

Fig. 3 Comparison of the fraction factor data with predictions of correlations for adiabatic tests

$$f_{\text{fin}} = 20.09\text{Re}^{-0.547} \tag{7}$$

The correlation is listed as correlation 7 in Table 1. The MAE value of the new correlation is 0.9%.

3.2 Diabatic Pressure Drop. The new correlation is applied to calculate the diabatic ΔP as follows:

$$\Delta P = \Delta P_{c1} + \Delta P_{c2} + \Delta P_{\text{fin}} + \Delta P_{e2} + \Delta P_{e1} \tag{8}$$

ΔP_{c1}, ΔP_{c2}, ΔP_{e2}, and ΔP_{e1} are evaluated by using Eqs. (2)–(5) with water properties evaluated at the corresponding T_{in} and T_{out}.

In order to better resolve the water property variation along the streamwise direction during diabatic tests, a segment-based approach is employed to evaluate ΔP_{fin}.

$$\Delta P_{\text{fin}} = \sum_{i=1}^{N_L} \Delta P_{\text{fin},i} = \sum_{i=1}^{N_L} \left[f_{\text{fin},i} \left(\frac{\mu_{f,i}}{\mu_{w,i}} \right)^{0.58} \frac{\rho_{f,i} u_{\max,i}^2}{2} \right] \tag{9}$$

where i indicates a segment in the streamwise direction that contains a row of micro-pin-fins as well as the corresponding portion of the top and bottom endwalls as shown in Fig. 2. All water properties in Eq. (9) except $\mu_{w,i}$ are evaluated based on $T_{f,i}$. As-

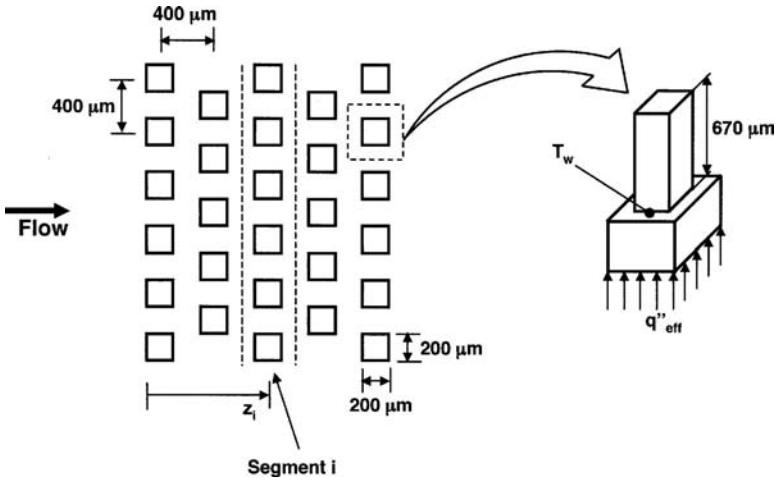

Fig. 2 Top view of the micro-pin-fin array and schematic of the streamwise segment

Table 1 Correlations for friction factor

Correlation	Pin-fin type	Reference	MAE (%)
1	Conventional long pin-fin	Gunter and Shaw [10]	60.6
2	Conventional long pin-fin	Gaddis and Gnielinski [12]	65.2
3	Conventional intermediate pin-fin	Short et al. [8]	10.9
4	Conventional intermediate pin-fin	Moores and Joshi [9]	53.6
5	Micro-pin-fin	Koşar et al. [1]	52.5
6	Micro-pin-fin	Prasher et al. [6]	39.7
7	Micro-pin-fin	Present study	0.9

suming a linear increase in water temperature along the streamwise direction, $T_{f,i}$ is determined from

$$T_{f,i} = T_{\text{in}} + (T_{\text{out}} - T_{\text{in}})\frac{z_i}{L} \tag{10}$$

The term $(\mu_{f,i}/\mu_{w,i})^{0.58}$ in Eq. (9) represents a property correction factor to account for the effect of fluid property variation within the segment due to heat transfer, and is introduced following the recommendation of Ref. [16]. $\mu_{w,i}$ is evaluated based on $T_{w,i}$, which can be calculated from the following energy balance equation for the segment:

$$q''_{\text{eff}}A_i = h_i(T_{w,i} - T_{f,i})[(A_i - N_T A_c) + \eta_{\text{fin}} N_T A_{\text{fin}}] \tag{11}$$

h_i represents the heat transfer coefficient in the segment and is evaluated using the following heat transfer correlation developed in Part I [13]:

$$\text{Nu}_i = 0.0285\ \text{Re}_i^{0.932}\ \text{Pr}_{f,i}^{1/3} \tag{12}$$

Figure 4 shows comparisons of all the diabatic ΔP data with the predictions of the new correlation (correlation 7). An excellent agreement is achieved with a MAE value of 6.9%.

4 Conclusions

This Technical Brief reports water single-phase pressure drop results in an array of staggered square micro-pin-fins. Key findings are as follows.

(1) Six previous friction factor correlations underpredicted the adiabatic data except the correlation by Short et al. [8], which overpredicted the data.
(2) A new power-law type of friction factor correlation was proposed base on the adiabatic data.
(3) The new correlation showed an excellent agreement with the diabatic data.

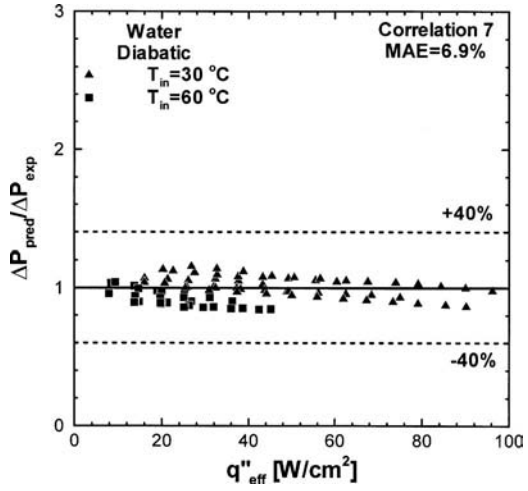

Fig. 4 Comparison of the measured diabatic pressure drop data with predictions of correlation 7

Acknowledgment

The authors are grateful for the support of the National Science Foundation (Award No. CBET07-30315). The micro-pin-fin heat sink test section was fabricated at the Laser-Assisted Multi-Scale Manufacturing Laboratory, University of Wisconsin-Madison. Professor Frank Pfefferkorn and Mr. Yongho Jeon's assistance in fabricating the heat sink test section was greatly appreciated.

Nomenclature

A_c = cross-sectional area of a micro-pin-fin
A_i = area of the segment base endwall
A_{fin} = wetted surface area of a single micro-pin-fin
d = diameter of the pin-fin
f_{fin} = friction factor in the micro-pin-fin array
$f_{\text{fin},i}$ = friction factor in segment i
$G_{\max}$ = maximum mass velocity
h_i = heat transfer coefficient in segment i
H_{fin} = height of a pin-fin
K_{c1}, K_{c2} = contraction loss coefficients
K_{e1}, K_{e2} = expansion recovery coefficients
L = length of the heat sink top platform area
m = exponent of the Reynolds number
$\dot{m}$ = total mass flow rate
N_L = total number of rows in the micro-pin-fin array
N_T = total number of micro-pin-fins in a segment
Nu = Nusselt number
ΔP = pressure drop across the heat sink
ΔP_{c1}, ΔP_{c2} = inlet contraction pressure losses
ΔP_{e1}, ΔP_{e2} = outlet expansion pressure recoveries
ΔP_{fin} = pressure drop across the micro-pin-fin array
Pr = Prandtl number
q''_{eff} = heat flux based on the heat sink top platform area
Re = Reynolds number based on d or d_e
$T_{f,i}$ = average water bulk temperature in segment i
T_{in} = measured inlet temperature
T_{out} = measured outlet temperature
$T_{w,i}$ = average micro-pin-fin base temperature in segment i
u = velocity
$u_{\max}$ = maximum velocity
z_i = streamwise location of the center of segment i

Greek Symbols

η_{fin} = fin efficiency
μ = viscosity
ρ = density

Subscripts

exp = experimental (measured)
f = liquid (water) bulk

i = a streamwise segment containing one row of micro-pin-fins
pred = predicted
$p1$ = deep plenum
$p2$ = shallow plenum
s = solid (copper)
w = pin-fin base

References

[1] Koşar, A., Mishra, C., and Peles, Y., 2005, "Laminar Flow Across a Bank of Low Aspect Ratio Micro Pin Fins," ASME J. Fluids Eng., **127**(3), pp. 419–430.

[2] Peles, Y., Koşar, A., Mishra, C., Kuo, C.-J., and Schneider, B., 2005, "Forced Convective Heat Transfer Across a Pin Fin Micro Heat Sink," Int. J. Heat Mass Transfer, **48**(17), pp. 3615–3627.

[3] Koşar, A., and Peles, Y., 2006, "Thermal-Hydraulic Performance of MEMS-Based Pin Fin Heat Sink," ASME J. Heat Transfer, **128**(2), pp. 121–131.

[4] Koşar, A., and Peles, Y., 2006, "Convective Flow of Refrigerant (R-123) Across a Bank of Micro Pin Fins," Int. J. Heat Mass Transfer, **49**(17–18), pp. 3142–3155.

[5] Koşar, A., Kuo, C., and Peles, Y., 2006, "Hydrofoil-Based Micro Pin Fin Heat Sink," ASME Paper No. IMECE2006-13257.

[6] Prasher, R. S., Dirner, J., Chang, J. Y., Myers, A., Chau, D., He, D., and Prstic, S., 2007, "Nusselt Number and Friction Factor of Staggered Arrays of Low Aspect Ratio Micro-Pin-Fins Under Cross Flow for Water as Fluid," ASME J. Heat Transfer, **129**(2), pp. 141–153.

[7] Siu-Ho, A., Qu, W., and Pfefferkorn, F., 2007, "Experimental Study of Pressure Drop and Heat Transfer in a Single-Phase Micro-Pin-Fin Heat Sink," ASME J. Electron. Packag., **129**(4), pp. 479–487.

[8] Short, B. E., Jr., Raad, P. E., and Price, D. C., 2002, "Performance of Pin Fin Cast Aluminum Coldwalls, Part 1: Friction Factor Correlation," J. Thermophys. Heat Transfer, **16**(3), pp. 389–396.

[9] Moores, K. A., and Joshi, Y. K., 2003, "Effect of Tip Clearance on the Thermal and Hydrodynamic Performance of a Shrouded Pin Fin Array," ASME J. Heat Transfer, **125**(6), pp. 999–1006.

[10] Gunter, A. Y., and Shaw, W. A., 1945, "A General Correlation of Friction Factor for Various Types of Surfaces in Crossflow," Trans. ASME, **67**, pp. 643–660.

[11] Zukauskas, A., 1972, "Heat Transfer From Tubes in Crossflow," *Advances in Heat Transfer*, Vol. 8, Academic, New York, pp. 93–160.

[12] Gaddis, E. S., and Gnielinski, V., 1985, "Pressure Drop in Cross Flow Across Tube Bundles," Int. Chem. Eng., **25**(1), pp. 1–14.

[13] Qu, W., and Siu-Ho, A., 2008, "Liquid Single-Phase Flow in an Array of Micro-Pin-Fins: Part-I Heat Transfer Characteristics," ASME J. Heat Transfer, **130**, p. 122402.

[14] Blevins, R. D., 1984, *Applied Fluid Dynamics Handbook*, Van Nostrand Reinhold, New York.

[15] Kline, S. J., and McClintock, F. A., 1953, "Describing Uncertainties in Single-Sample Experiments," Mech. Eng. (Am. Soc. Mech. Eng.), **75**(1), pp. 3–8.

[16] Kays, W. M., Crawford, M. E., and Weigand, B., 2005, *Convective Heat and Mass Transfer*, 4th ed., McGraw-Hill, New York.

Heat Exchanger Analysis Modified to Account for a Heat Source

Vinod Narayanan[1]
e-mail: vinod.narayanan@oregonstate.edu

Murty Kanury

Jeromy Jenks

Oregon State University,
204 Rogers Hall,
Corvallis, OR 97331-6001

A modified heat exchanger analysis is developed here that accounts for a heat source, which is assumed to be volumetrically uniform in the hot fluid. The motivation for this work arises from the analysis of an ammonia-water absorber heat exchanger where a heat-of-absorption source term arises in the solution side. Utility of the analysis in deducing the overall heat transfer coefficient from experimental measurements is demonstrated.
[DOI: 10.1115/1.2970063]

Keywords: heat exchanger, heat source term, heat of absorption, counter flow, overall heat transfer coefficient

1 Introduction

A modified heat exchanger analysis is presented for a steady parallel-plate counterflow heat exchanger that accounts for a uniformly distributed heat source in the hot fluid. This analysis is motivated by observations made in a recent experimental work [1] on a large-aspect-ratio absorber for use in an ammonia-water absorption refrigeration cycle. It was clear that although the solution in the absorber channel came into the counterflow heat exchanger at a temperature close to ambient, there were experimental conditions at which the exit temperature of this stream was higher than, or at the same temperature as, its inlet. This would tend to increase the average driving temperature differential between the two fluid streams, resulting in a U lower than that reported on the basis of just the inlet and exit temperatures of the fluid streams in the heat exchanger. In absorption literature, for example, Refs. [2,3], it is typical to report U values based only on the classical definition of ΔT_{lm}. Existing heat exchanger analyses, as they appear in heat exchanger books [4–8], to the best of the authors' knowledge, do not explicitly account for volumetric sources of thermal energy in the hot fluid stream. The present work aims to quantify the actual temperature differential that drives heat transfer in such a heat exchanger. A general analysis, applicable to any counterflow heat exchanger with a uniform heat source, is presented, followed by application of the analysis to an absorber.

2 Analysis

Figure 1 shows a schematic of a parallel-plate counterflow heat exchanger in which there is a volumetric heat source term in the hot-side fluid. For the purpose of this analysis, this source term is assumed to be uniform and constant over the length of the heat exchanger and is represented as a source strength rate per unit volume, $\dot{s}'''$. Although this source strength is expected to be a function of temperature and pressure, in the present analysis, source strength is considered invariant along the channel. This assumption can be later relaxed by invoking the absorption thermodynamics in which the dependency of the absorption rate on the local pressure and temperature is stipulated. Other standard assumptions that pertain to classical heat exchanger analysis hold good for this analysis as well: (1) There is no heat transfer between either the hot or cold stream and the surroundings, (2) axial conduction along the heat exchange surface is negligible, (3) fluid specific heats are constant, and (4) the overall heat transfer coefficient is constant.

An energy balance on a differential control volume on the hot fluid side shown in Fig. 1 can be expressed as

$$d\dot{s} = \dot{m}_h c_{ph} dT_h + d\dot{q}_h \tag{1}$$

An energy balance on the counterflowing cold fluid stream results in

$$d\dot{q}_c = -\dot{m}_c c_{pc} dT_c \tag{2}$$

A global energy balance over the entire length of the heat exchanger on the hot side can be obtained by integrating Eq. (1),

$$\dot{s} - \dot{q}_h = \dot{m}_h c_{ph}(T_{he} - T_{hi}) \tag{3}$$

Equation (3) shows the effect of a source on the hot fluid temperature change, namely, for $\dot{s} - \dot{q} \le 0$, $T_{he} \le T_{hi}$ and for $\dot{s} - \dot{q} \ge 0$, $T_{he} \ge T_{hi}$. Similarly Eq. (2) leads to the global energy balance on the cold stream,

$$\dot{q}_c = -\dot{m}_c c_{pc}(T_{ci} - T_{ce}) \tag{4}$$

That there is no heat exchange between the surroundings and either of the fluid streams is indicated by

$$d\dot{q}_h = d\dot{q}_c = d\dot{q} \tag{5}$$

The heat transfer rate between the two fluid streams across the heat exchange surface defines the overall heat transfer coefficient by

$$d\dot{q} = U(Wdx)(T_h - T_c) \tag{6}$$

Equations (1), (2), and (6) provide a system of three equations for three unknowns, $T_h(x)$, $T_c(x)$, and U, for any given set of heat capacity flow rates, uniform source strength distribution along the channel length, and dimensions of the heat exchanger. The pattern of variation of $(T_h - T_c)$ with the length, x, along the exchanger is indicative of the local driving potential for heat transfer. Combining Eqs. (1), (2), and (6), this pattern is described by

$$\frac{d(T_h - T_c)}{dx} = \frac{\dot{s}}{L\dot{m}_h c_{ph}} - UW(T_h - T_c)\left[\frac{1}{\dot{m}_h c_{ph}} - \frac{1}{\dot{m}_c c_{pc}}\right] \tag{7}$$

Solving with the boundary condition that at $x=0$, $T_h = T_{hi}$, and $T_c = T_{ce}$,

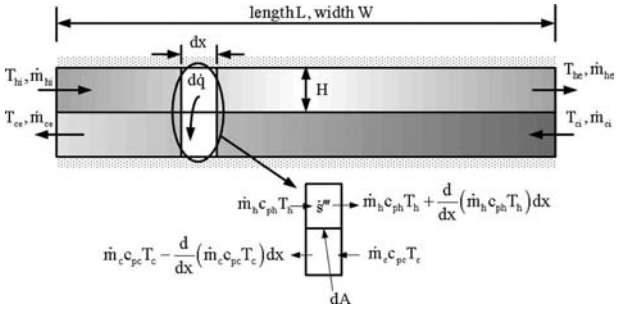

Fig. 1 Schematic of the heat exchanger showing the analysis control volume

[1]Corresponding author.

Contributed by the Heat Transfer Division of ASME for publication in the JOURNAL OF HEAT TRANSFER. Manuscript received July 27, 2007; final manuscript received April 24, 2008; published online September 19, 2008. Review conducted by S. A. Sherif. Paper presented at the 2007 ASME-JSME Thermal Engineering Conference and Summer Heat Transfer Conference (HT 2007), Vancouver, BC, Canada, July 8–12, 2007.

$$(T_h(x) - T_c(x)) = \frac{K_1}{K_2} + \left[(T_{hi} - T_{ce}) - \frac{K_1}{K_2} \right] \exp(-K_2 x) \tag{8}$$

where

$$K_1 = \frac{\dot{s}}{L \dot{m}_h c_{ph}} \tag{9a}$$

$$K_2 = UW \left[\frac{1}{\dot{m}_h c_{ph}} - \frac{1}{\dot{m}_c c_{pc}} \right] \tag{9b}$$

A relation for the total heat transfer rate can now be obtained by evaluating the temperature difference given by Eq. (8) at $x=L$ and replacing the heat capacity rates with the aid of Eqs. (3) and (4). The result is

$$\frac{\dot{q}}{UA}\left(1 - \left(\frac{\dot{s}}{\dot{q}}\right)\right) = \left\{ \frac{\left[(T_{hi} - T_{ce}) - (T_{he} - T_{ci}) + \left(\frac{\dot{s}}{\dot{q}}\right)(T_{ce} - T_{ci}) \right]}{\ln\left[\left((T_{hi} - T_{ce}) - \left(\frac{\dot{s}}{\dot{q}}\right)\left(\frac{\dot{q}}{UA}\right)\frac{1}{\left(1 - \frac{\dot{m}_h c_{ph}}{\dot{m}_c c_{pc}}\right)} \right) \Big/ \left((T_{he} - T_{ci}) - \left(\frac{\dot{s}}{\dot{q}}\right)\left(\frac{\dot{q}}{UA}\right)\frac{1}{\left(1 - \frac{\dot{m}_h c_{ph}}{\dot{m}_c c_{pc}}\right)} \right) \right]} \right\} \tag{10}$$

In the absence of a source term, the present result reduces to the traditional ΔT_{lm} definition of U. $\dot{q}/UA$ is a function of temperature differentials of the hot and cold fluid streams at the inlet and exit. The ratio of heat capacity flow rates then has no effect. However, with a nonzero source, $\dot{q}/UA$ is a function also of the ratios of the heat capacity flow rates, the ratio of the source rate to heat rate, and the temperature difference of the coolant side. In addition to the usual logarithmic nonlinearity associated with the traditional ΔT_{lm}, the heat transfer rate is also affected by the appearance of source term $\dot{s}$ in both the numerator and denominator of Eq. (10).

The overall heat transfer coefficient can be determined by rearranging Eq. (10) in the following implicit form:

$$U = \left(\frac{C_5}{C_1}\right) \ln\left[\left(\frac{C_2}{C_3}U - 1\right) \Big/ \left(\frac{C_4}{C_3}U - 1\right) \right] \tag{11}$$

where the quantities C_1, C_2, C_3, C_4, and C_5 are composed, as given below, of the experimentally measured heat transfer rate, source strength, temperatures, heat capacity flow rates, and the dimensions of the absorber,

$$C_1 = C_2 - C_4 + \frac{\dot{s}}{\dot{q}}(T_{ce} - T_{ci}) \tag{12a}$$

$$C_2 = (T_{hi} - T_{ce}) \tag{12b}$$

$$C_3 = \frac{\dot{s}}{A}\left(1 - \frac{\dot{m}_h c_{ph}}{\dot{m}_c c_{pc}}\right)^{-1} \tag{12c}$$

$$C_4 = (T_{he} - T_{ci}) \tag{12d}$$

and

$$C_5 = \frac{\dot{q} - \dot{s}}{A} \tag{12e}$$

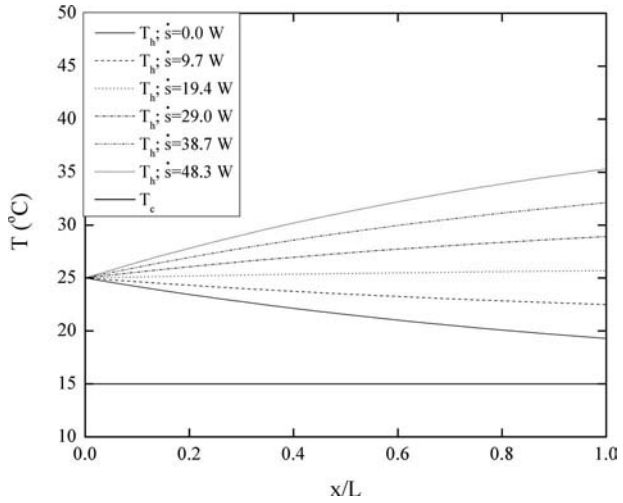

Fig. 2 Temperature distribution of the hot fluid along the heat exchanger with the variation in the source term. The cold fluid temperature is fixed at 15°C.

Figure 2 illustrates the temperature distribution for fixed values of the overall heat transfer coefficient of 1000 $\mathrm{W/m^2\,K}$, the hot stream inlet temperature of 25°C, and the cold stream inlet temperature of 15°C. To observe the trends of the hot fluid side more clearly, the cold fluid heat capacity rate is kept large such that $T_{ci}=T_{ce}$. Using the dimensions of the microchannel absorber heat exchanger from experiments [1], Eq. (8) leads to the x-dependency of the hot stream temperature, as shown in Fig. 2. The parameter on the curves is the source strength $\dot{s}$ in increments of 9.7 W. Whereas Eq. (3) shows that $T_{he} \geq T_{hi}$ for $\dot{s} - \dot{q} \geq 0$, Eq. (8) gives the local temperature difference between the fluid streams along the heat exchanger. The following observations can be made from Fig. 2: (a) The $\dot{s}=0$ W line in this figure corresponds identically to the distribution obtained using the traditional analysis obtained here from Eq. (8) by simply setting the source equal to zero. (b) For sufficiently large values of the source strength, the hot fluid temperature everywhere in the exchanger will be larger than its inlet temperature. (c) When $\dot{s}=\dot{q}$, Eq. (10) reduces to $T_{he}=T_{hi}$, and all the heat released in absorption is transferred to the cold fluid.

Corrections for the effect of heat release due to absorption come mainly in the additive source term and in ΔT_{lm} in Eq. (10). The fact that the heat transfer rate appears in this correction term in ΔT_{lm} makes Eq. (10) implicit in $\dot{q}$. However, if the heat capacity flow rate of the cooling fluid is large, this correction term becomes negligible. The more substantial correction comes in both the numerator and denominator of the log function argument, $(\dot{s}/\dot{q})(\dot{q}/(UA))/[1-(\dot{m}_h c_{ph}/\dot{m}_c c_{pc})]$.

As a case study, the above analysis was used to interpret data from a large-aspect-ratio absorber shown schematically in Fig.

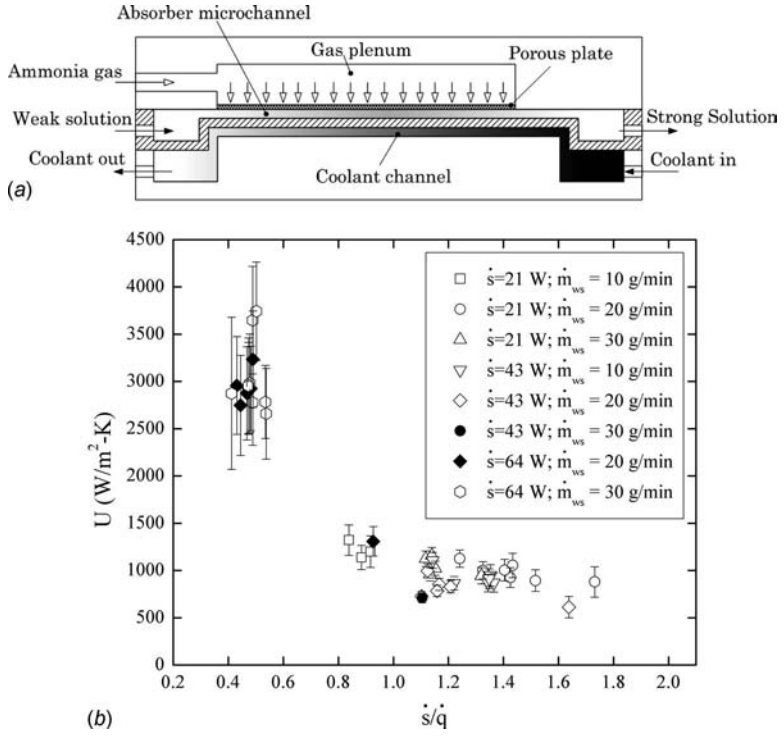

Fig. 3 Application of the modified *U* (Eq. (11)) to experimental observations on the constrained thin-film absorber heat exchanger: (*a*) schematic of the absorber configuration and (*b*) the overall heat transfer coefficient determined by using Eq. (11) and data from experiments

3(*a*). In this absorber, a weak solution of ammonia-water was constrained to flow in a microchannel, while ammonia vapor was bubbled through its top porous wall. A coolant that flows in a counterarrangement to the weak solution removed the heat of absorption that was released by the microchannel fluid. In order to visualize the effect of the heat of absorption on U, it is instructive to plot the variation of U with the ratio of the heat release rate of absorption, $\dot{s}$, to the heat removal rate, $\dot{q}$. A less than unity value of $\dot{s}/\dot{q}$ indicates that the heat transfer rate exceeds the source heat rate, whereas a value greater than unity indicates otherwise. Figure 3(*b*) is one such plot for the 150-μm-deep microchannel absorber for all weak solution and vapor flow rates. At $\dot{s}/\dot{q}<1$, high values in U are observed. However, at $\dot{s}/\dot{q}>1$, the decrement of U with the increase in $\dot{s}/\dot{q}$ is more gradual, and U tends to an almost constant value of about 900 $\mathrm{W/m^2\,K}$, indicating that heat transfer limitations begin to affect the absorber performance at $\dot{s}/\dot{q}>1$. A sequential perturbation technique [9] was used to determine the uncertainty in U based on Eq. (11). Uncertainties in constants C_1–C_5 were determined using Eqs. (12*a*)–(12*e*) based on the experimentally determined values of variables. The average uncertainty for U plotted in Fig. 3(*b*) was 12.5% with a 4.6% standard deviation in uncertainty values.

3 Conclusions

A modified heat exchanger analysis that accounts for the heat source within the hot fluid stream was presented. The resulting equations for the heat rate and the overall heat transfer coefficient (U) are implicit. Overall heat transfer coefficients were determined based on the modified equations for a microchannel absorber. Trends of the experimentally determined U indicate a high U value at low source to heat rate ratios, followed by an approach to a constant value at source to heat rate ratios larger than unity. Whereas the analysis presented here does not aid in the *design* of heat exchangers with a source term, it does present a method to *analyze* and interpret data from such heat exchangers.

Nomenclature

A = heat exchange area, $A=WL$ ($\mathrm{m^2}$)
c_p = specific heat at a constant pressure (J/kg K)
h = specific enthalpy of the fluid stream (J/kg)
H = height (depth) of the microchannel (m)
K_1 = parameter defined in Eq. (9*a*)
K_2 = parameter defined in Eq. (9*b*)
L = length of the microchannel (m)
$\dot{m}$ = mass flow rate (kg/s, g/min)
P = pressure (Pa)
$\dot{q}$ = heat rate (W)
$\dot{s}$ = source rate (W)
T = temperature (K)
U = overall heat transfer coefficient ($\mathrm{W/m^2\,K}$)
W = width of the microchannel (m)
X = mass concentration (%)

Greek

ΔT_{lm} = log-mean temperature difference (K)
ρ = density of the fluid

Subscripts

abs = absorber
c = cold fluid
e = exit of the microchannel
h = hot fluid
i = inlet of the microchannel
ss = strong solution
v = vapor (anhydrous ammonia gas)
ws = weak solution

References

[1] Jenks, J., and Narayanan, V., 2006, "An Experimental Study of Ammonia-Water Bubble Absorption in a Large Aspect Ratio Microchannel," ASME Paper No. IMECE2006-14036.

[2] Goel, N., and Goswami, D. Y., 2007, "Experimental Verification of a New Heat and Mass Transfer Enhancement Concept in a Microchannel Falling Film Absorber," ASME J. Heat Transfer, **129**, pp. 154–161.

[3] Lee, K. B., Chun, B. H., Lee, J. C., Lee, C. H., and Kim, S. H., 2002, "Experimental Analysis of Bubble Mode in a Plate-Type Absorber," Chem. Eng. Sci., **57**, pp. 1923–1929.

[4] Incropera, F. P., DeWitt, D. P., Bergman, T. L., and Lavine, A. S., 1988, *Fundamentals of Heat and Mass Transfer*, 6th ed., Wiley, New York.

[5] Holman, J. P., 2001, *Heat Transfer*, 9th ed., McGraw-Hill, New York.

[6] Kakac, S., and Liu, Q. H., 2002, *Heat Exchangers*, 2nd ed., CRC, Boca Raton, FL.

[7] Kays, W. M., and London, A. L., 1984, *Compact Heat Exchangers*, 3rd ed., McGraw-Hill, New York.

[8] Shah, R. K., and Seculik, D. P., 2003, *Fundamentals of Heat Exchanger Design*, Wiley, New York.

[9] Moffat, R. J., 1998, "Describing Uncertainties in Experimental Results," Exp. Therm. Fluid Sci., **1**, pp. 3–17.

Pressure Loss and Heat Transfer Characterization of a Cam-Shaped Cylinder at Different Orientations

A. Nouri-Borujerdi
Professor
School of Mechanical Engineering,
Sharif University of Technology,
Tehran, Iran
e-mail: anouri@sharif.edu

Arash M. Lavasani
Professor
Science and Research Branch,
Islamic Azad University,
Tehran, Iran
e-mail: a_lavasani@iauctb.ac.ir

Pressure drag coefficient and heat transfer are experimentally investigated around a single noncircular cylinder in cross-flow under angle of attack 0 deg $<\alpha<$ 360 deg and Reynolds number $1.5\times10^4<Re_{eq}<4.8\times10^4$ based on equivalent diameter of a circular cylinder. The results show that the trend of pressure drag coefficient against the angle of attack has a wavy shape but the wavy trend of the Nusselt number is smoother relative to the drag coefficient behavior. It is found that for $l/D_{eq}=0.4$ and over the whole range of the Reynolds number, the pressure drag coefficient has a minimum value of about $C_D=0.4$ at $\alpha=30$ deg, 180 deg, and 330 deg and a maximum value of about $C_D=0.9$ at $\alpha=90$ deg and 270 deg. The corresponding value of the mean Nusselt number to that of the equivalent circular tube is $1.05<\overline{Nu}_{cam}/\overline{Nu}_{cir}<1.08$ at $\alpha=90$ deg and 270 deg as well as $0.87<\overline{Nu}_{cam}/\overline{Nu}_{cir}<0.92$ at $\alpha=30$ deg and 180 deg.
[DOI: 10.1115/1.2969259]

Keywords: pressure drag, surface heat transfer, cam-shaped cylinder, heat exchangers

1 Introduction

In contrast to the circular tubes, which cause severe separation and large wake regions to produce high pressure drops, noncircular tubes of streamlined shapes offer high heat transfer and low hydraulic resistance and consequently require less pumping power.

Ota et al. [1,2] found that at $Re<10^4$ maximum and minimum mean heat transfer coefficients around an elliptic cylinder with a major axis parallel to the flow direction with axis ratios of 1:2 and 1:3 occurred in the range of 60 deg $<\alpha<$ 90 deg and 0 deg $<\alpha<$ 30 deg, respectively. The minimum mean heat transfer rate was higher than that of a circular tube with equal circumferential length. The drag coefficient was about 0.12 at $Re=4.8\times10^4$ and $\alpha=0$ deg and increased monotonically with α and reached 1.8 at $\alpha=90$ deg.

Ruth [3] measured pressure drop and heat transfer rate for a lenticular tube bundle in the range of $10^3<Re<5\times10^4$ with a transverse tube pitch-to-diameter ratio of 2. He found that the drag was reduced by 70% in comparison with a circular tube bundle.

Merker and Hanke [4] measured heat transfer and pressure drop along the shell-side of a tube bundle with oval-shaped tubes. They showed that heat exchangers with oval-shaped tubes have considerably smaller frontal areas on the shell-side in comparison with circular tubes in the range of $10^3<Re<5\times10^4$ based on the stream length.

Prasad et al. [5] reported heat transfer and pressure drop from an aerofoil NACA-0024 in cross-flow for $2\times10^4<Re<5\times10^4$ based on the equivalent diameter. They concluded that this shape gives higher values of Stanton number to pressure drop coefficient in comparison with a circular, lenticular, and oval tubes at $Re>2\times10^4$.

Badr et al. [6] numerically simulated the unsteady flow over an elliptic cylinder with a major axis parallel to the flow direction at different orientations. They obtained the total drag coefficient equal to 0.8 at $Re=3700$ and 0.9 at $Re=700$ with a length ratio of minor-to-major axis equal to 0.6. The form drag was 80–90% of the total drag. Compared with a circular tube, the drag coefficient was reduced between 10% and 20%.

Matos et al. [7] numerically and experimentally studied three dimensional of staggered finned circular and elliptic tubes at $Re_L=852$ and 1065, where subscript L is the swept length of a fixed volume. Circular and elliptic arrangements with the same flow obstruction cross-sectional area were compared on the basis of maximizing the total heat transfer. The results illustrate that the optimal elliptic tube arrangement exhibits higher heat transfer up to 19% in comparison with the optimal circular tube arrangement. The heat transfer gain and the relative total mass reduction of up to 32% show that the elliptical arrangement has a potential to deliver considerably higher global performance and lower cost.

Li et al. [8] numerically investigated the heat transfer enhancement of three streamlined polymer tubes with fins of lenticular and oval profiles. For $Bi<0.3$ and $2\times10^3<Re<2\times10^4$, the heat transfer of oval-shaped tubes was higher than that of the circular tubes. They showed that the teardrop tube had the highest efficiency in comparison with the lenticular and oval tubes.

Bouris et al. [9] carried out experiments and numerical simulations on a novel tube bundle heat exchanger with tube cross section that contained a parabolic shape in front and a semicircular one at the rear. The Reynolds number was in the range of $2.2\times10^3<Re<4.1\times10^3$ based on the diameter of the bottom circular section of the tube. Their results indicate a higher heat transfer level with 75% lower deposition rate and 40% lower pressure drop.

Moharana and Das [10] gave an improvement on the analysis of Li et al. [8]. They analyzed conduction through shaped tubes with a circular inner surface and a hydrodynamically shaped outer surface by two different techniques. These two techniques were a two-dimensional analysis as well as a one-dimensional approximate technique, which showed a closed agreement with the two-dimensional analysis.

Table 1 summarizes the results of the previous works concerning the pressure drag coefficient and the Nusselt number around a streamlined single tube or tube bundle. All these noncircular tubes have low pressure drag coefficient and high Nusselt number in comparison with circular tubes with the same circumferential length. Those tubes, which have cross-sectional area similar to a teardrop, have more efficiency than those of the oval and lenticular tubes with less deposition rate of suspension materials on the tube surface.

To give better understanding regarding the optimum shape for a noncircular tube in which high heat transfer and/or low drag can be achieved, this study has emphasized on cam-shaped tubes. This shape provides ease of manufacturing and varying flow pattern under different angles of attack in cross-flow.

Contributed by the Heat Transfer Division of ASME for publication in the JOURNAL OF HEAT TRANSFER. Manuscript received January 4, 2007; final manuscript received June 2, 2008; published online September 22, 2008. Review conducted by S. A. Sherif.

Table 1 Summary of some streamlined tube results in cross-flows

Ref.	Tube shape	10^{-3} Re	Remarks
[2]	Elliptic	8–79	$1.06 < \mathrm{Nu}_{\mathrm{ellip}}/\mathrm{Nu}_{\mathrm{cir}} < 1.67$ for $0 \le \alpha \le 90$ deg $0.12 < C_D < 1.8$ for 0 deg $< \alpha <$ 90 deg, $\mathrm{Re} = 4.8 \times 10^4$
[3]	Lenticular tube bundle	1–50	$\mathrm{Per}_{\mathrm{lenti}}/\mathrm{Per}_{\mathrm{cir}} \approx 1.2$ $(C_D)_{\mathrm{lenti}}/(C_D)_{\mathrm{cir}} \approx 0.3$[a]
[4]	Elliptic tube bundle	1–50	$(C_D)_{\mathrm{ellip}}/(C_D)_{\mathrm{cir}} \approx 0.05$
[5]	Aerofoil	20–50	$(\mathrm{St}/C_D)_{\mathrm{aerof}}/(\mathrm{St}/C_D)_{\mathrm{cir,ellip\ and\ lenti}} > 1$
[6]	Elliptic	<5	$0.8 < (C_D)_{\mathrm{ellip}}/(C_D)_{\mathrm{cir}} < 0.9$
[7]	Elliptic tube bundle	0.852 and 1.065	In optimal arrangement: $\dot{q}_{\mathrm{ellip}}/\dot{q}_{\mathrm{cir}} \approx 1.19$
[8]	Lenticular, teardrop and elliptic	2–20	$\eta_{\mathrm{tear}}/\eta_{\mathrm{lenti.and\ ellip}} > 1$ $\eta_{\mathrm{ellip}}/\eta_{\mathrm{cir}} > 1$ for $\mathrm{Bi} < 0.3$[b]
[9]	Parabolic tube bundle	2.2–4.1	$\dot{D}_{\mathrm{para}}/\dot{D}_{\mathrm{cir}} \approx 0.25$[c] $\Delta P_{\mathrm{para}}/\Delta P_{\mathrm{cir}} \approx 0.6$
Present work	Cam	15–48	$1.05 < \overline{\mathrm{Nu}}_{\mathrm{cam}}/\overline{\mathrm{Nu}}_{\mathrm{cir}} < 1.08$ at $\alpha = 90$ deg and 270 deg $0.87 < \overline{\mathrm{Nu}}_{\mathrm{cam}}/\overline{\mathrm{Nu}}_{\mathrm{cir}} < 0.92$ at $\alpha = 30$ deg and 180 deg $(\mathrm{St}/C_D)_{\mathrm{cam}} \approx 0.01$ at 30 deg $< \alpha <$ 150 deg

[a]per denotes performance.
[b]η denotes efficiency.
[c]$\dot{D}$ denotes deposition rate.

2 Experimental Setup

Three testing tubes made of a commercial copper plate with a thickness of 0.3 mm and a length of 12 cm were used (Fig. 1). These three tubes have identical diameters equal to $d = 1.2$ cm and $D = 2.2$ cm but with three different distances between their centers, $l = 1.1$ cm, 2.9 cm, and 6.6 cm. The surface of each tube is covered with 20 holes drilled at the middle length of the tube to measure the static pressure on its surface with 18 deg intervals. The angle of attack is measured between the flow direction and the major axis of the cam-shaped cylinder when it rotates clockwise about the center of its smaller circle. The frame blockage ratio varies from 0.1 to 0.12 at 0 deg $< \alpha <$ 90 deg. The frame is made of wood and the two ends of the tube are insulated by low thermal conductivity material. The heat loss by conduction from the two ends is estimated to be about 3.5% of the total heat transfer from the tube. Hence, no corrections are made for the frame effects upon the heat transfer and flow characteristics.

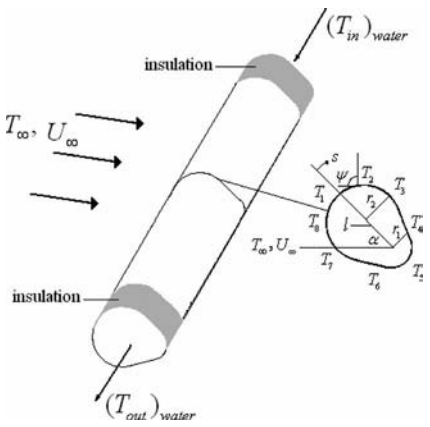

Fig. 1 Schematic of a cam-shaped tube and thermocouple location in cross-flow

Eight thermocouples were embedded and cemented on the surface around the cylinder where their positions are shown in the figure from T_1 to T_8. Two other thermocouples were used to measure the axial temperature. The mean surface temperature at the middle length and for fluid properties [11] was calculated. The average pressure drag coefficient was obtained by $C_D = \Sigma_{i=1}^{20} C_{p,i} \cos \psi_i \Delta S_i / D_{\mathrm{eq}}$ over the tube surface, where ψ_i is the angle between normal to the tube local surface and the free flow velocity (Fig. 1). ΔS_i represents a differential element of the tube perimeter belonging to each hole. The pressure drag and heat transfer coefficient uncertainties calculated are about 10.4–12.8% and 4.5–5.5% for 0 deg $< \alpha <$ 360 deg, respectively.

3 Results and Discussion

The effect of natural convection can be neglected because at the lowest velocity $\mathrm{Gr}/\mathrm{Re}^2 = 1.29 \times 10^{-4}$ is very small. The length scale in the Reynolds and Grashof numbers is based on an equivalent circular cylinder, $D_{\mathrm{eq}} = p/\pi$, whose circumferential length is equal to that of the cam-shaped cylinder. The equivalent diameters of three test cylinders are 2.47 cm, 3.57 cm, and 5.91 cm. Quarmby and Al-Fakhri [12] showed that for $L/D_{\mathrm{eq}} > 4$ this ratio has little effect on the heat transfer. To assess the accuracy of the experimental data, a single circular tube with a diameter of 2.47 cm and a length of 12.5 cm was tested before testing the cam-shaped tube and taking data process. This circular tube had the same perimeter length as the cam-shaped tube with $d = 1.2$ cm, $D = 2.2$ cm, and $l = 1.1$ cm. The experimental results show $0.73 < C_D < 0.75$ in the range of $1.9 \times 10^4 < \mathrm{Re}_{\mathrm{eq}} < 3.5 \times 10^4$ with a discrepancy 1–2% relative to the results of White [13], $C_D = 0.74$, for a circular tube.

In Figs. 2(*a*) and 2(*b*), the positive and negative values on the abscissa indicate the measured distance along the upper and lower parts of the cylinder surface, respectively. In Fig. 2(*a*), the trend of curves is similar for three values of $l/D_{\mathrm{eq}} = 0.4$, 0.8, and 1.1 and

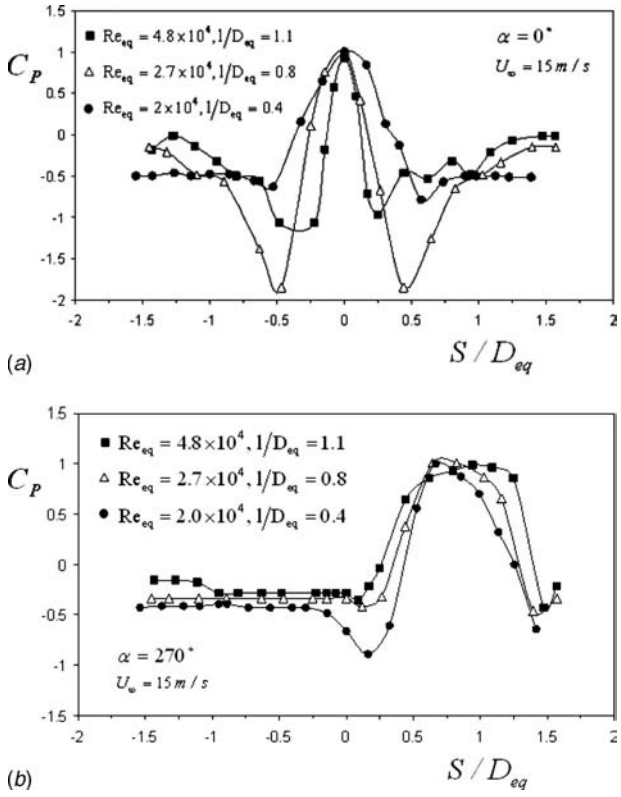

Fig. 2 (*a*) Pressure coefficient for three different l/D_{eq} and Reynolds number for $\alpha=0$ deg and (*b*) pressure coefficient for three different l/D_{eq} and Reynolds number for $\alpha=270$ deg

the discrepancy among them is limited in the range of $-0.5 < S/D_{eq} < 0.5$. This treatment will intensively continue in Fig. 2(*b*) for 270 deg. For $\alpha=0$ deg at $l/D_{eq}=0.4$, the flow separates at about $S/D_{eq}=\pm0.75$ and the pressure inside the separated flow region is constant. At $l/D_{eq}=0.8$ and 1.1 these points are at about $S/D_{eq}=\pm0.85$ and ±0.5 and reattach onto the surface at about $S/D_{eq}=1.3$ and 0.8, respectively. Then, the turbulent boundary layer develops downstream. Such a feature of pressure distribution around the surface causes to decrease the drag. As a result, the trend of the pressure coefficient is nearly similar to the one produced by the perfect fluid theory around a circular tube. By increasing more the angle of attack from $\alpha=0$ deg to 270 deg, the maximum pressure coefficient shifts toward the positive values of the abscissa (Fig. 2(*b*)).

In Fig. 3, the shape of all curves is almost the same and repeated every other 150 deg so that the overall relation between variables can be expressed by the least-squares curve fitting method as:

$$C_D = A + B\sin(C\alpha) \tag{1}$$

where A, B, and C are constants and their values are about 0.76, −0.42, and 2.4, respectively. In this figure the average drag coefficient of the cam-shaped tube with $l/D_{eq}=0.4$ and a circular cylinder [12] with the same circumference length of the cam-shaped tube have been compared. The maximum and minimum values of the average drag coefficient are about $C_D=0.9$ and $C_D=0.4$, respectively, and their occurrences are at different angles. The reason could be explained by external flow configuration, which involves the cam-shaped cylinder in cross-flow where the cylinder is under the angles of $\alpha=30$ deg, 90 deg, 180 deg, 270 deg, and 330 deg. At $\alpha=180$ deg under $2\times10^4 < \mathrm{Re} < 3.3\times10^4$, the laminar boundary layer is formed over the most part of the tube surface and separation is delayed, thereby reducing the extent of the

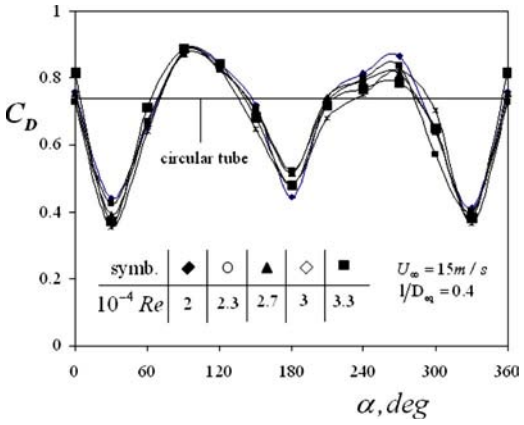

Fig. 3 Pressure drag coefficient of a cam-shaped and circular tubes versus angle of attack

wake region and the magnitude of the form drag. In other words, the pressure differential in the flow direction resulting from the formation of the wake is low compared with the boundary layer surface shear stress and causes a low pressure drag coefficient.

Figure 4 shows the effect of slenderness of the cam-shaped tube on the pressure drag coefficient against the angles of attack. It appears that the discrepancy of the drag coefficient between the cam-shaped tube and an equivalent circular tube increases monotonically as l/D_{eq} increases. For $l/D_{eq}=1.1$, the drag coefficient has a minimum value of $C_D=0.1$ at $\alpha=0$ deg and 180 deg.

Figure 5 represents the average Nusselt number around the circumference of the cam-shaped tube to the counterpart value in a circular tube with the same equivalent diameter. It is clear that the symmetry of the average Nusselt number distribution on the whole surface is approximately satisfactory for any Reynolds number at $\alpha=180$ deg. The maximum values of 1.05 and 1.08 occur at $\alpha=90$ deg and 270 deg, respectively. The minimum value of 0.87 occurs at $\alpha=180$ deg like the pressure drag coefficient in Fig. 3. The ratio of $\mathrm{Nu_{cam}/Nu_{cir}}$ over $0\ \mathrm{deg} \le \alpha \le 360$ deg may be equal or even less than 1 when the Reynolds number is below the critical one. This is probably due to a large wake formation below the critical Reynolds numbers over a large region of the cam-shaped tube. The critical Reynolds number is defined as a value over which $\mathrm{Nu_{cam}/Nu_{cir}} > 1$ and below which $\mathrm{Nu_{cam}/Nu_{cir}} \le 1$ for a certain value of the attack angle (here $\alpha=270$ deg).

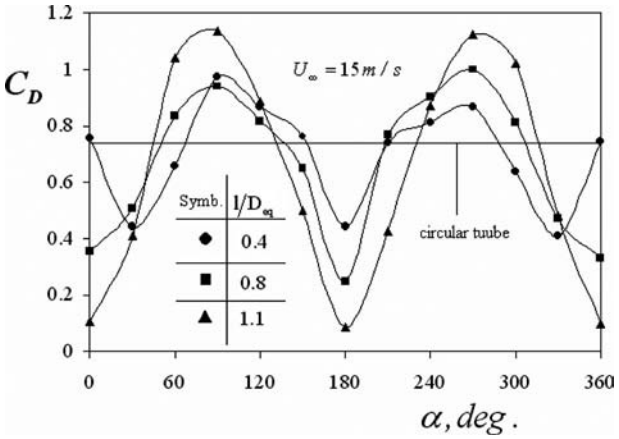

Fig. 4 Length to diameter ratio effects on the pressure drag coefficient of a cam-shaped tube

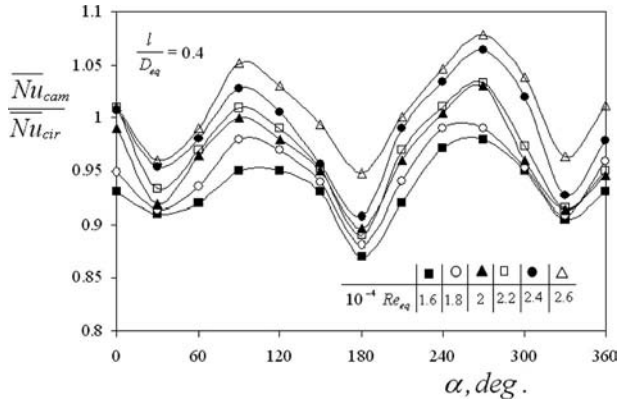

Fig. 5 The average Nusselt number ratio of the cam-shaped tube to an equivalent circular tube

4 Conclusions

This paper tries to experimentally demonstrate the advantage of using tubes with cam-shaped cross section in heat exchangers. The primary advantages of such a choice are reduced pressure drag and increased heat transfer coefficient.

The results show that the trends of the pressure drag coefficient and Nusselt number versus angle of attack have wavy shapes for all Reynolds numbers and repeated about every other 150 deg. For $l/D_{eq}=0.4$ over the whole range of the Reynolds number, the pressure drag coefficient has a minimum value of about $C_D=0.4$ at $\alpha=30$ deg, 180 deg, and 330 deg and a maximum value of about $C_D=0.9$ at $\alpha=90$ deg and 270 deg. The corresponding value of the mean Nusselt number to that of the equivalent circular tube is $1.05<\overline{\mathrm{Nu}}_{cam}/\overline{\mathrm{Nu}}_{cir}<1.08$ at $\alpha=90$ deg and 270 deg as well as $0.87<\overline{\mathrm{Nu}}_{cam}/\overline{\mathrm{Nu}}_{cir}<0.92$ at $\alpha=30$ deg and 180 deg.

Nomenclature

A, B, C = constants
Bi = Biot number, hD/k_w
C_D = pressure drag coefficient
C_p = pressure coefficient, $(P_i-P_\infty)/2\rho U_\infty^2$
d = small diameter
D = large diameter
g = gravity
Gr = Grashof number, $g\beta\Delta T D_{eq}^3/\alpha\nu$
h = heat transfer coefficient
L = cylinder length
Nu = Nusselt number, hD/k
P = pressure, circumferential length
Re = Reynolds number, $U_\infty D/\upsilon$
S = streamline coordinate
St = Stanton number, $h/\rho C_p U_\infty$
T = temperature
U = velocity

Greek Letters

α = angle of attack, thermal diffusivity
β = expansion coefficient
Δ = difference
ρ = density
ν = kinematic viscosity
ψ = hole angle

Superscript

- = mean

Subscripts

cam = cam-shaped tube
cir = circular tube
elip = elliptic tube
eq = equivalent
i = hole number, inlet
o = outlet
w = wall, water
∞ = freestream

References

[1] Ota, T., Aiba, S., Tsuruta, T., and Kaga, M., 1983, "Forced Convection Heat Transfer From an Elliptic Cylinder," Bull. JSME, **26**(212), pp. 262–267.
[2] Ota, T., and Nishiyama, H., 1984, "Heat Transfer and Flow Around an Elliptic Cylinder," Int. J. Heat Mass Transfer, **27**(10), pp. 1771–1779.
[3] Ruth, E. K., 1983, "Experiments on a Cross Flow Heat Exchanger With Tubes of Lenticular Shape," ASME J. Heat Transfer, **105**, pp. 571–575.
[4] Merker, G. P., and Hanke, H., 1986, "Heat Transfer and Pressure Drop Along the Shell-Side of Tube Banks Having Oval-Shaped Tubes," Int. J. Heat Mass Transfer, **29**(12), pp. 1903–1909.
[5] Prasad, B. V. S. S. S., Tawfek, A. A., and Rao, V. R. M., 1992, "Heat Transfer From Aerofoils in Cross-Flow," Int. J. Heat Mass Transfer, **19**, pp. 879–890.
[6] Badr, H. M., Dennis, S. C. R., and Kocabiyik, S., 2001, "Numerical Simulation of the Unsteady Flow Over an Elliptic Cylinder at Different Orientations," Int. J. Numer. Methods Fluids, **37**(8), pp. 905–931.
[7] Matos, R. S., Laursen, T. A., Vargas, J. V. C., and Bejan, A., 2004, "Three-Dimensional Optimization of Staggered Finned Circular and Elliptic Tubes in Forced Convection," Int. J. Therm. Sci., **43**, pp. 477–487.
[8] Li, Zhihua, Davidson, J. H., and Mantell, S. C., 2004, "Heat Transfer Enhancement Using Shaped Polymer Tubes: Fin Analysis," ASME J. Heat Transfer, **126**, pp. 211–218.
[9] Bouris, D., Konstantinidis, E., Balabani, S., Castiglia, D., and Bergeles, G., 2005, "Design of a Novel, Intensified Heat Exchanger for Reduced Fouling Rates," Int. J. Heat Mass Transfer, **48**, pp. 3817–3832.
[10] Moharana, M., and Das, P., 2008, "Heat Conduction Through Heat Exchanger Tubes of Noncircular Cross Section," ASME J. Heat Transfer, **130**(1), p. 011301.
[11] Ozisik, N. M., 1985, *Heat Transfer*, McGraw-Hill, New York.
[12] Quarmby, A., and Al-Fakhri, A. A. M., 1980, "Effect of Finite Length on Forced Convection Heat Transfer From Cylinders," Int. J. Heat Mass Transfer, **23**, pp. 463–469.
[13] White, F. M., 2005, *Fluid Mechanics*, McGraw-Hill, New York.

Heat Transfer in Mini/Microchannels With Combustion: A Simple Analysis for Application in Nonintrusive IR Diagnostics

Ananthanarayanan Veeraragavan

Christopher P. Cadou[1]
e-mail: cadou@eng.umd.edu

Department of Aerospace Engineering,
University of Maryland,
College Park, MD 20742

An analytical solution for the temperature distribution in 2D laminar reacting flow between closely spaced parallel plates is derived as part of a larger effort to develop a nonintrusive technique for measuring gas temperature distributions in millimeter and submillimeter scale channel flows. The results show that the exact solution, a Fourier series, which is a function of the Peclet number, is approximated by second and fourth order polynomial fits to an R^2 value of almost unity for both fits. The slopes of the temperature near the wall (heat fluxes) are captured to within 20% of the exact solution using a second order polynomial and to within 2% of the exact solution using a fourth order polynomial. The fits are used in a nonintrusive Fourier transform infrared spectroscopy technique and enable one to infer the temperature distribution along an absorbing gas column from the measured absorption spectrum. The technique is demonstrated in a silicon-walled microcombustor. [DOI: 10.1115/1.2969760]

Keywords: microscale combustion, temperature profiles, forced convective heat transfer, combustion diagnostics, in situ FTIR spectroscopy

Introduction

Interest in the development of miniaturized heat engines as battery replacements in handheld electronic devices [1,2] and as propulsion systems for micro-air vehicles (MAVs) [3] has motivated new investigations of heat transfer in small (millimeter and submillimeter scales) channels driven by exothermic chemical reaction in the gas phase. Analytical and numerical modeling efforts [4] have shown that temperature gradients are present and are important for understanding flame stabilization and quantifying thermal losses. However, the small scale has made it impossible to confirm these findings experimentally using conventional instrumentation. Recently, a technique that exploits silicon's transmissivity in the IR was used to make nonintrusive measurements of species concentration and temperature profiles in microcombustors [5]. In this work, the average gas temperature across the channel was determined by fitting a narrowband spectral model (EM2C) [6] to measure CO_2 absorption spectra. This technique can be extended to yield the temperature distribution along the channel provided that the functional form of the temperature distribution is known. Therefore, the objectives of this work are to develop an analytical solution for the transverse temperature profile in a laminar reacting flow between two parallel plates, to identify the functional form of the gas temperature distribution across the channel (i.e., in a direction perpendicular to the streamlines), to use this to infer the temperature profile across the channel from integrated absorption measurements in a real combustor, and to quantify the level of uncertainty introduced into the temperature measurement when the functional form of the temperature distribution across the channel is assumed a priori. To accomplish this, we treat this problem as an extension of the classical Graetzian problem [7], which is based on an energy balance between convective transport in the axial direction and heat conduction in the transverse direction. This problem has been extended in various ways over the years, but the extensions most pertinent to this work incorporate axial conduction in the gas [8,9].

1 Determination of the Temperature Profile Functional Form

1.1 Physical Formulation. The starting point for this analysis is the schematic of the simple microscale combustor illustrated in Fig. 1 that has been used to develop the nonintrusive diagnostic technique. It consists of two parallel plates separated by a distance $2d$ and a plenum from which premixed fuel and air enter the flow channel. The origin for the model problem is located at the flame front, and the flame is assumed to be far enough downstream in the channel that the plenum does not need to be considered. The boundary conditions are prescribed in the form of temperature values at the ends of the pre- and postflame regions.

1.2 Mathematical Formulation and Solution. The governing equation is the conservation of energy, which is given in a nondimensional form by Eq. (1).

$$\mathrm{Pe}\frac{\partial\theta}{\partial x^+} = \frac{\partial^2\theta}{\partial x^{+2}} + \frac{\partial^2\theta}{\partial y^{+2}} \tag{1}$$

The nondimensionalization is summarized below:

$$\theta = \frac{T - T_w}{T_f - T_w}, \quad x^+ = \frac{x}{d}, \quad y^+ = \frac{y}{d} \tag{2}$$

$$\mathrm{Pe} = \mathrm{Re}\,\mathrm{Pr} = \left(\frac{Ud}{\nu}\right)\left(\frac{\nu}{\alpha}\right) = \left(\frac{\rho UdCp}{k}\right) \tag{3}$$

In these equations, T_w is the wall temperature, T_f is the adiabatic flame temperature, d is the channel half width, Re is the Reynolds number, Pr is the Prandtl number, and Pe is the Peclet number, which is the ratio of convective to conductive heat transfer. The Pe number arises as a natural consequence of the nondimensionalization.

The boundary conditions in the transverse and axial directions are given in Eq. (4). The transverse boundary conditions arise from the planar symmetry and isothermal walls while the axial boundary conditions are that the flow temperature equals the wall temperature at the inlet and outlet.

$$\begin{aligned} &\theta(-\infty, y^+) = 0, \\ &\theta(0, y^+) = 1, \\ &\theta(\infty, y^+) = 0, \end{aligned} \qquad \left.\frac{\partial\theta}{\partial y^+}\right|_{y^+=0} = 0, \quad \theta(x^+, 1) = 0 \tag{4}$$

Equation (1) is solved using separation of variables leading to eigenfunction solutions of the form:

$$\theta(x^+_{\mathrm{preflame}}, y^+) = \sum_{n=0}^{\infty} A_n \exp\left(\frac{\mathrm{Pe} + \sqrt{\mathrm{Pe}^2 + 4\lambda_n^2}}{2} x^+_{\mathrm{preflame}}\right)\cos(\lambda_n y^+) \tag{5}$$

[1]Corresponding author.

Contributed by the Heat Transfer Division of ASME for publication in the JOURNAL OF HEAT TRANSFER. Manuscript received July 19, 2007; final manuscript received June 23, 2008; published online September 23, 2008. Review conducted by Walter W. Yuen.

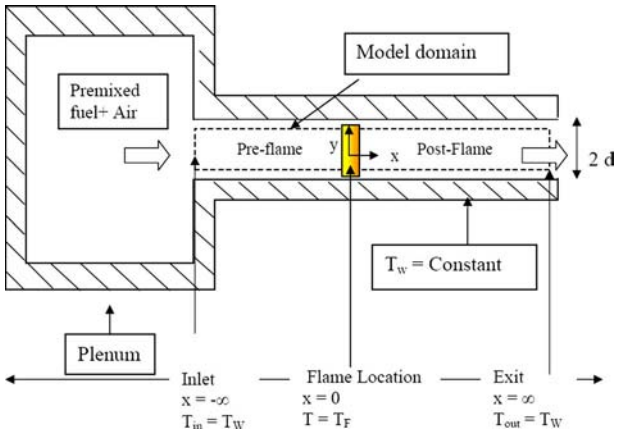

Fig. 1 Schematic of a microburner illustrating the domain associated with the analytical model

$$\theta(x^+_{\text{postflame}}, y^+) = \sum_{n=0}^{\infty} B_n \exp\left(\frac{\text{Pe} - \sqrt{\text{Pe}^2 + 4\lambda_n^2}}{2} x^+_{\text{postflame}}\right)\cos(\lambda_n y^+) \tag{6}$$

The eigenvalues and coefficients are given, respectively, by

$$\lambda_n = \frac{2n+1}{2}\pi$$

and

$$A_n = B_n = 2\int_0^1 \cos(\lambda_n y^+)dy = 2\frac{(-1)^n}{\lambda_n} \tag{7}$$

A more detailed discussion of the solution procedure and graphical representation of plots involving θ for large and low Pe limits can be found elsewhere [10].

The exponential behavior of the solution in the pre- and postflame regions is consistent with one-dimensional time-dependent solutions of the coupled energy and species equations [11] and with steady two-dimensional asymptotic solutions of the coupled energy and species equations [4]. Equations (6) and (7) approach zero as $x \to \pm\infty$ for the pre- and postflame regions as well as when y^+ equals 1. The constants A_n and B_n are evaluated using the boundary condition at the flame front (θ=1 at x^+=0). Computing the mean value of θ across the channel gives the following 1D expressions for temperature in the pre- and postflame regions.

$$\theta_m = \begin{cases} \displaystyle\sum_{n=0}^{\infty} \frac{2}{\lambda_n^2} \exp\left(\frac{\text{Pe} + \sqrt{\text{Pe}^2 + 4\lambda_n^2}}{2} x^+\right), & x^+ < 0 \text{ (preflame)} \\ \displaystyle\sum_{n=0}^{\infty} \frac{2}{\lambda_n^2} \exp\left(\frac{\text{Pe} - \sqrt{\text{Pe}^2 + 4\lambda_n^2}}{2} x^+\right), & x^+ \geqslant 0 \text{ (postflame)} \end{cases} \tag{8}$$

1.2.1 Large and Small Pe Number Limits. When the Peclet number is large, heat transfer in the transverse direction is less important than in the axial direction and two-dimensional effects become less important. This can also be shown explicitly by taking the limit of Eq. (8) as $\text{Pe} \gg \lambda_n$. It can be shown (using Parseval's equality condition [12]) that this simplifies to

$$\theta_m = \begin{cases} \exp(\text{Pe}\, x^+), & x^+ < 0 \quad \text{(preflame)} \\ 1, & x^+ \geqslant 0 \quad \text{(postflame)} \end{cases} \tag{9}$$

Equation (9) is identical to previous 1D solutions for freely propagating flames [13] where heat conduction in the transverse direction is neglected and the gas temperature is fixed by a balance between convective and conductive heat transports in the axial direction. Therefore, the 2D solution presented here is identical to the 1D solution in the limit of a large Pe. Similarly it can be shown that for very low Pe numbers:

$$\theta_m = \begin{cases} \dfrac{2}{\pi^2} \exp\left(\dfrac{\pi x^+}{2}\right)\Phi\left(e^{\pi x^+}, 2, \dfrac{1}{2}\right), & x^+ < 0 \quad \text{(preflame)} \\ \dfrac{2}{\pi^2} \exp\left(-\dfrac{\pi x^+}{2}\right)\Phi\left(e^{-\pi x^+}, 2, \dfrac{1}{2}\right), & x^+ \geqslant 0 \quad \text{(postflame)} \end{cases} \tag{10}$$

where Φ is the "Lerch transcendent" [14] defined as follows:

$$\Phi(z, s, a) = \sum_{k=0}^{\infty} \frac{z^k}{(a+k)^s} \tag{11}$$

Equation (11) shows that if the Peclet number is low enough (compared to the first eigenvalue λ_1), then the solution is independent of the Peclet number. Physically, this implies that the convective transport term in the energy equation is negligible compared to the axial and lateral conduction terms and the problem reduces to a balance between the heat conducted inside the gas and the heat conducted to (or from) the wall. Mathematically, the problem reduces to Laplace's equation.

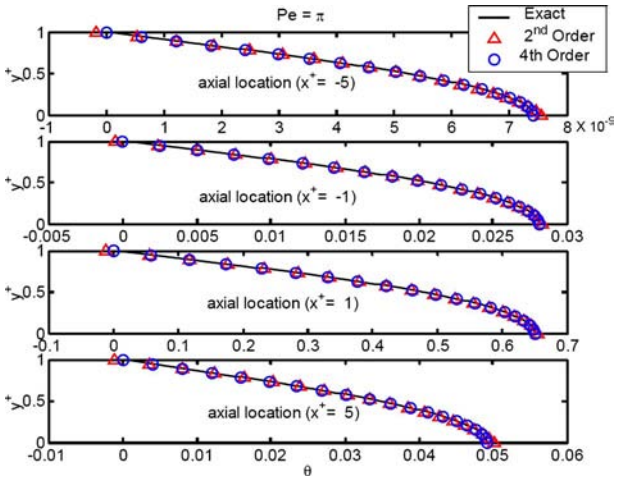

Fig. 2 Comparison of transverse temperature profiles at different axial locations computed from the exact solution (solid lines) and from polynomial fits (symbols) for Pe=π

1.3 Transverse Temperature Profiles. The analytical solution obtained above is compared to polynomial expansions in the vertical coordinate y that are often associated with solutions to problems with simple boundary conditions such as constant wall temperature or constant heat flux:

$$T(y) = A_0 + A_1 y + A_2 y^2 + \cdots + A_n y^n \tag{12}$$

Figure 2 shows the temperature profiles at four axial locations for Pe=π. The value π was chosen as it is the average of the first and second eigenvalues (usually the most significant) of the problem. The overall maximum mean deviations in temperature profiles between the model and the fit were found to be less than 4% for a second order fit and less than 0.5% for a fourth order fit. The slope at the wall (used to estimate heat exchange between wall and gas) was matched less accurately by the second order profile ($\approx$20% error) as compared to the fourth order profile ($\approx$2%). The $Y(y^+)$ function is a cosine function and therefore only involves even powers of y^+. Hence, polynomials with even powers are appropriate as fits, and the higher the order, the better the fit. However, the fourth order polynomial is already an excellent fit. Since the re-

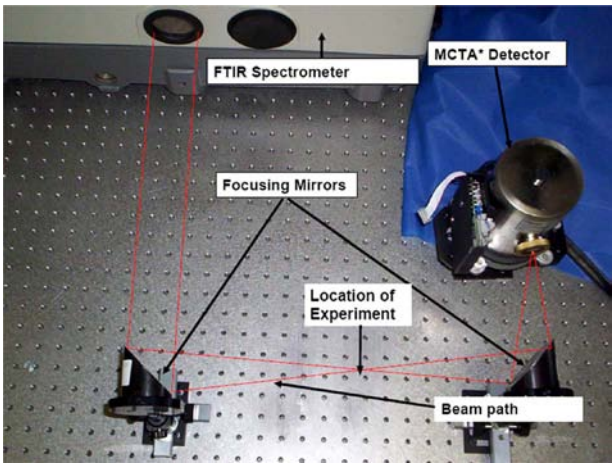

Fig. 3 Photograph illustrating optical path for the absorption measurements

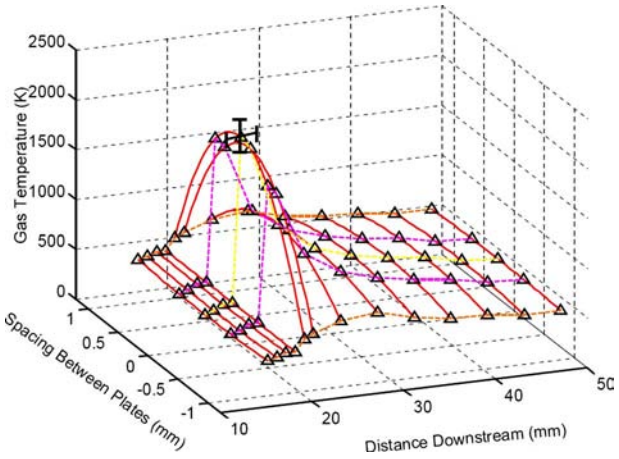

Fig. 4 Measured transverse temperature profiles at different axial positions in the channel

sults were found to be invariant with Pe number, the fitting procedure appears to be valid.

2 Application to Diagnostic Technique

2.1 Experimental Apparatus. The simulated microcombustor consists of two silicon plates attached to movable supports which allow the gap between the plates to be adjusted from 500 μm to 50 mm. Detailed descriptions of the burner may be found in Refs. [5,10]. Premixed methane and air are supplied to the plenum below the plates. The mixture is lit and a laminar flame is stabilized between the two plates initially by using a heat gun to heat the walls (silicon plates) of the combustor and then removing the heat gun.

Absorbance spectra of the flow between the plates are acquired using a Fourier transform infrared (FTIR) spectrometer and the external optical setup shown in Fig. 3. The IR beam exits the FTIR and is focused at a point midway between the silicon plates using an off axis parabolic mirror. A mask increases the spatial resolution of the measurement to 1 mm in the flow direction. The IR beam passes through the silicon walls (which are partially transmissive in the mid-IR region), is absorbed partially by species like CO_2 and CH_4 depending on whether we are interrogating the preflame or postflame regions, and is directed to the FTIR's MCTA* (mercury cadmium telluride A) detector using a second parabolic mirror. More detailed descriptions of the apparatus and the measurement procedures are available elsewhere [5,15].

2.2 Temperature Fitting Procedure. Gas temperature is determined by fitting the measured CO_2 absorption band to a statistical narrowband model (EM2C) [16] of the CO_2 band that is a function of temperature and concentration of CO_2. This has been shown to be the most accurate method for measuring gas temperature from absorption spectra [6]. Previous work assumed that the gas between the plates was at a single temperature and therefore used the gas temperature directly as the single fitting parameter. In this work, the coefficients of the polynomials used to represent the temperature profile become the fitting parameters. The fitting procedure uses a least-squares approach to minimize the difference between the measured and modeled absorption spectra. It is implemented using MATLAB's "lsqcurve" function.

2.2.1 Second Order Profile. Equation (13) shows the functional form of a second order temperature profile.

$$T(y) = a_2 y^2 + b_2 y + c_2 \tag{13}$$

In this expression, y varies from zero to $2d$, the channel width (2.15 mm in this experiment). Since the combustor is symmetric, it is reasonable to assume that the temperature profile is symmetric as well. In this case, it can be shown that

$$b_2 = -(2d)a_2 \tag{14}$$

Therefore, only two free parameters (a_2 and c_2) need to be adjusted in order to achieve the fit.

2.2.2 Fourth Order Profile. Equation (15) shows the functional form of a fourth order temperature profile:

$$T(y) = a_4 y^4 + b_4 y^3 + c_4 y^2 + d_4 y + e_4 \tag{15}$$

Again, symmetry conditions lead to the following relationships between the coefficients:

$$b_4 = \frac{-(2dc_4 + d_4)}{2d^2}$$

and

$$a_4 = \frac{(2dc_4 + d_4)}{(2d)^3} \tag{16}$$

Therefore, only three free parameters (c_4, d_4, and e_4) need to be adjusted in order to achieve the fit. However, the presence of the additional parameter makes achieving a good fit considerably more difficult than the second order case.

2.3 Uncertainty Estimation. The uncertainty in the measurement technique is estimated using the same methods developed in earlier work [5] except that the temperature profile is now included. The derivation is presented in the Appendix.

2.4 Experimental Results. Figure 4 shows a series of temperature measurements made over optical paths spaced at different downstream locations along the burner axis. These have been assembled to generate a 2D picture of the temperature distribution in the channel. The figure shows cool reactants entering the channel from the left and increasing in temperature slowly until they encounter the flame. The peak temperature occurs at the flame (located 20 mm from the inlet) and the products cool downstream of the flame as they lose heat to the channel walls. While uncertainty information is available at every point in the mesh, a single set of representative error bars is presented at the peak temperature in order to make the figure clearer.

Conclusions and Future Work

A simple model has been developed for gas-structure heat transfer in small channels where a combustion wave is present. Exact analytical solutions are obtained for the nondimensional temperature (θ) in terms of the nondimensional spatial coordinates

and the Peclet number. The results show that the solution approaches the one-dimensional solution in the limit of large Peclet numbers. Since the Peclet number is directly proportional to the size of the channel, this result indicates that two-dimensional effects should not be expected to play a strong role in macroscale channel flows. In the limit of small Peclet numbers, however, two-dimensional effects become dominant. While the exact solution for the temperature profile across the channel is a Fourier series, it is well approximated using either second or fourth order polynomials. This result enables one to make nonintrusive measurements of the two-dimensional temperature distribution in the gas by assembling a series of line-of-sight absorption measurements made at different downstream locations from the flame. Future work will couple this technique with measurements of the wall temperature to provide direct measurements of heat recirculation in microcombustors.

Nomenclature

d = channel half width
h = heat transfer coefficient
k = thermal conductivity of gas
x = dimensional axial coordinate
x^+ = nondimensional axial coordinate
y = dimensional transverse coordinate
y^+ = nondimensional transverse coordinate
C_p = specific heat capacity of gas
Nu = Nusselt number
Pe = Peclet number
Pr = Prandtl number
Re = Reynolds number
T = temperature
T_F = flame temperature
T_W = wall temperature
U = flow velocity
α = thermal diffusivity of gas
λ_n = eigenvalue
θ = nondimensional temperature
ρ = density of gas
ν = kinematic viscosity of gas

Appendix

Determining the uncertainty in the fitted temperature begins by considering the residual R_{sq} from the temperature fitting procedure. The uncertainty analysis presented here has been presented in detail in a previous paper by the authors [5], so the focus here will be on the incorporation of the temperature profile. The reference shows that R_{sq} of the difference between the absorbance measured by the instrument and that predicted by the EM2C program may be represented as:

$$R_{sq} = \sum_{i=1}^{N} \left\{ \pm \sigma_{rms} \mp \left[\left. \frac{\partial f_i}{\partial T} \right|_X \delta T + \left. \frac{\partial f_i}{\partial X} \right|_T \delta X \right] \right\}^2 \tag{A1}$$

where i is the ith spectral location, f is the EM2C function used to compute the absorbance as a function of gas temperature and concentration, and δX is the uncertainty in the gas mole fraction. The latter is treated as a known uncertainty in this analysis. The solution, derived from solving Eq. (A1) [5], is

$$\delta T = \frac{\sum_{i=1}^{N} \alpha_i \beta_i \pm \left\{ \left(\sum_{i=1}^{N} \alpha_i \beta_i \right)^2 - \left(\sum_{i=1}^{N} \beta_i^2 \right) \left(\sum_{i=1}^{N} \alpha_i^2 - R_{sq} \right) \right\}^{1/2}}{\sum_{i=1}^{N} \beta_i^2} \tag{A2}$$

where α and β are constants that can be computed using δ_{rms}, f, and δX.

$$\alpha_i = \sigma_{rms} - \left. \frac{\partial f_i}{\partial X} \right|_T \delta X \tag{A3}$$

and

$$\beta_{i,j} = \left. \frac{\partial f_i}{\partial T_j} \right|_X \tag{A4}$$

There are two solutions to Eq. (A2) and the larger is taken as the uncertainty in the temperature. The effect of the temperature profile choice is incorporated as follows: For a second order temperature profile, we have:

$$T(y_j) = a_2 y_j^2 + b_2 y_j + c_2 \tag{A5}$$

and

$$(j = 1{:}m), \quad y_j = \frac{w(j-1)}{m-1}$$

$$f = f(a_2, c_2, m, X) \tag{A6}$$

where m is the total number of discretizations adopted to fit the temperature profile between the two plates and w is the channel width. In the context of this paper, w corresponds to the channel width $2d$ in the analytical model. Therefore, $\beta_{i,j}$ can be expressed as:

$$\beta_{i,j} = \left. \frac{\partial f_i}{\partial T_j} \right|_X = \left. \frac{\partial f_i}{\partial a_2} \right|_X \frac{\partial a_2}{\partial T_j} + \left. \frac{\partial f_i}{\partial c_2} \right|_X \frac{\partial c_2}{\partial T_j} + \left. \frac{\partial f_i}{\partial m} \right|_X \frac{\partial m}{\partial T_j} \tag{A7}$$

The index i represents the wave number space over which the absorbance spectrum is collected, and the index j represents the location in the channel between the two plates at which the uncertainty is being computed. Direct differentiation of Eq. (A5) gives

$$\frac{\partial T_j}{\partial a_2} = (y_j^2 - w y_j) \tag{A8}$$

$$\frac{\partial T_j}{\partial c_2} = 1 \tag{A9}$$

$$\frac{\partial T_j}{\partial m} = a_2 (2y_j - w) \frac{\partial y_j}{\partial m} = -a_2 (2y_j - w) \frac{(j-1)w}{(m-1)^2} \tag{A10}$$

Substituting Eqs. (A8)–(A10) in Eq. (A7) and then into Eq. (A2) gives the uncertainty in temperature at different locations in the channel while accounting for the choice of the fitted temperature profile. The same procedure is applied for a fourth order fitting.

References

[1] Spadaccini, C. M., Zhang, X., Cadou, C. P., Miki, N., and Waitz, I. A., 2003, "Preliminary Development of Hydrocarbon-Fueled Catalytic Micro Combustor," Sens. Actuators, A, **103**(1–2), pp. 219–224.
[2] Fu, K., Knobloch, A. J., Martinez, F. C., Walther, D. C., Fernandez-Pello, C., Pisano, A. P., and Liepmann, D., 2001, "Design and Fabrication of a Silicon-Based MEMS Rotary Engine," ASME Paper No. IMECE2001/MEMS 23925.
[3] Cheung, W. S., and Tilston, J. R., 2001, "Testing of a Novel Propulsion System for Micro Air Vehicles," Proc. Inst. Mech. Eng., Part G, **215**, pp. 207–218.
[4] Daou, J., and Matalon, M., 2002, "Influence of Conductive Heat-Losses on the Propagation of Premixed Flames in Channels," Combust. Flame, **128**, pp. 321–339.
[5] Heatwole, S., Veeraragavan, A., Cadou, C. P., and Buckley, S. G., 2006, "In Situ Species and Temperature Measurements in a Millimeter-Scale Combustor," Microscale Thermophys. Eng., in press.
[6] Modest, M. F., and Bharadwaj, S. P., 2002, "Medium Resolution Transmission Measurements of CO_2 at High Temperature," J. Quant. Spectrosc. Radiat. Transf., **73**(2–5), pp. 329–338.
[7] Graetz, L., 1883, "Über die Wärmeleitus der fähigkeit von Flüssigkeiten," Ann. Phys. Chem., **18**, pp. 79–94
[8] Yin, X., and Bau, H., 1996, "The Conjugate Graetz Problem With Axial Conduction," ASME Trans. J. Heat Transfer, **118**, pp. 482–484.
[9] Lahjomri, J., and Oubarra, A., 1999, "Analytical Solution of the Graetz Prob-

lem With Axial Conduction," ASME Trans. J. Heat Transfer, **121**, pp. 1078–1083.
[10] Veeraragavan, A., 2006, "Heat Transfer Analysis for Improved In Situ Infrared Temperature Diagnostics in Microcombustors," M.S. thesis, University of Maryland, College Park.
[11] Maruta, K., Parc, J., Oh, K., Fujimori, T., Minaev, S., and Fursenko, R., 2004, "Characteristics of Microscale Combustion in a Narrow Heated Channel," Combust., Explos. Shock Waves, **40**(5), pp. 516–523.
[12] Strauss, W. A., 1992, *Partial Differential Equations: An Introduction*, Wiley, New York, p. 129.
[13] Williams, F., 1984, *Combustion Theory*, 2nd ed., Addison-Wesley, Reading, MA.
[14] Gradshteyn, I. S., and Ryzhik, I. M., 2000, "The Lerch Function $\Phi(z,s,v)$," *Tables of Integrals Series, and Products*, 6th ed. Academic, San Diego, CA, Sec. 9.55, p. 1029.
[15] Veeraragavan, A., Heatwole, S., Cadou, C., and Buckley, S., 2005, "Infrared Diagnostic Technique for Microcombustors," Paper No. AIAA-2005-938.
[16] Soufani, A., and Taine, J., 1999, "High Temperature Gas Radiative Property Parameters of Statistical Narrow-Band Model for H2O, CO2 and CO and Correlated K-model for H2O," Int. J. Heat Mass Transfer, **40**(4), pp. 987–991.

Thermal Management of Low Profile Electronic Equipment Using Radial Fans and Heat Sinks

Ed Walsh
e-mail: edmond.walsh@ul.ie

Pat Walsh
e-mail: pat.walsh@ul.ie

Ronan Grimes
e-mail: ronan.grimes@ul.ie

Vanessa Egan
e-mail: vanessa.egan@ul.ie

Stokes Institute,
University of Limerick,
Limerick, Ireland

There is an increasing need for low profile thermal management solutions for applications in the range of 5–10 W, targeted at portable electronic devices. This need is emerging due to enhanced power dissipation levels in portable electronics, such as mobile phones, portable gaming machines, and ultraportable personal computers. This work focuses on the optimization of such a solution within the constraints of the profile and footprint area. A number of fan geometries have been investigated where both the inlet and exit rotor angles are varied relative to the heat conducting fins on a heat sink. The ratio of the fan diameter to the heat sink fin length was also varied. The objective was to determine the optimal solution from a thermal management perspective within the defined constraints. The results show a good thermal performance and highlight the need to develop the heat sink and fan as an integrated thermal solution rather than in isolation as is the traditional methodology. An interesting finding is that the heat transfer scales are in line with turbulent rather than laminar correlations despite the low Reynolds number. It is also found that while increasing the pumping power generally improves the thermal performance, only small gains are achieved for relatively large pumping power increases. This is important in optimizing portable systems where reduced power consumption is a competitive advantage in the marketplace. [DOI: 10.1115/1.2977602]

Keywords: electronics cooling, low profile, portable electronics, radial fans and heat sinks, thermal management

Introduction

Performance and profile, or height, are two features that give companies a competitive advantage in the continuingly expanding portable electronics industry. Both of these features result in increased heat flux densities within electronic devices. It is generally accepted that unless technologies are developed to remove this heat at acceptable temperatures the future development of mobile technologies will suffer from both reliability and high surface temperatures. Using current passive cooling methodologies, which ultimately must rely on some form of natural convection, conduction, and radiation from the device surface to dissipate the heat, thermal management issues may become the primary constraint to the full implementation of advanced technologies. This is due to the high heat flux densities that will be required in portable electronic devices currently under development.

The thermal design of an electronic system is performed so that the system operates at a sufficiently low temperature to allow acceptable levels of reliability and performance. The choice of cooling methodology used to maintain this temperature varies from system to system and is dependent on a number of factors, which include the level of heat to be dissipated, the operating environment, the maximum allowable component temperatures, the available space, the cost, and the maintenance required. A fundamental challenge in the portable marketplace is the consumer demand for low profile devices. In desktop computers large scale heat sinks and fans may be used directly on the heat generating components as space is not a major concern, although it is becoming increasingly important. This technique can result in relatively high heat transfer coefficients from the chip surface, particularly if a fan is assembled with a heat sink and mounted on the heat source. Much work has been done in recent years to characterize and optimize the performance of fanned heat sinks [1–3]. However, these works have focused on large scale applications, with no effort to date focused on scales appropriate to handheld electronic devices. For low profile scales the design of cooling solutions becomes more difficult and new ideas and approaches should be considered. Examples of technologies under development for the thermal management of portable electronic devices are phase change materials [4], microheat pipes [5], and high conductivity materials. The focus of these technologies is on the heat spreading and transport within a device rather than the active removal of heat from the device. For example, the phase change materials store heat to be dissipated over time, while heat pipes and high conductivity materials only provide paths of reduced thermal resistance to the flow of heat within devices. Hence, heat is ultimately removed by passive techniques.

The use of forced convection technologies potentially integrated within low profile portable electronics has received much less attention despite the potential for higher heat flux densities and the potential compatibility with many of the existing heat spreading methodologies. When the advantages and disadvantages of the technologies discussed above are considered, forced convection air cooling may become a necessary part of the thermal management of future handheld devices to accommodate increased power dissipation levels. Integrated fans and heat sinks are relatively easy to implement, as they require no special packaging considerations. Air, the heat removal medium, is abundantly available, and is noncorrosive to the cooled equipment. Some studies have addressed piezoelectric based fans [6,7] but their low flow rate combined with the requirement for high voltages makes them unlikely competitors in the portable electronics marketplace. Recently, studies addressing the aerodynamic effects of geometrical scaling in both axial fans [8] and radial fans [9] have resulted in the development of low profile rotary fans for potential use in electronic cooling applications. The acoustics in such applications is also critical, and work by the same authors has demonstrated the limits to which existing scaling laws can be applied [10].

This paper addresses the integration of radial fans with heat sinks suitable to low profile portable electronics. The total thermal solution has a maximum height of 7 mm. A heat sink design with shaped fins was manufactured and tested, with features essentially scaled down from conventional macroscale heat sinks while also considering state of the art design philosophies [11]. It is shown that in low profile applications there is a need to consider the integrated heat sink and fan design as a complete thermal solution rather than in isolation as was also concluded by Walsh and Grimes [12] when addressing a single fan design with two heat sink geometries. The effect of the rotor inlet and exit angles relative to heat sink fin angles is shown to be important in achieving

Contributed by the Heat Transfer Division of ASME for publication in the JOURNAL OF HEAT TRANSFER. Manuscript received October 29, 2007; final manuscript received June 13, 2008; published online September 25, 2008. Review conducted by Yogendra Joshi. Paper presented at the 2007 ASME-JSME Thermal Engineering Conference and Summer Heat Transfer Conference (HT 2007), Vancouver, BC, Canada, July 8–12, 2007.

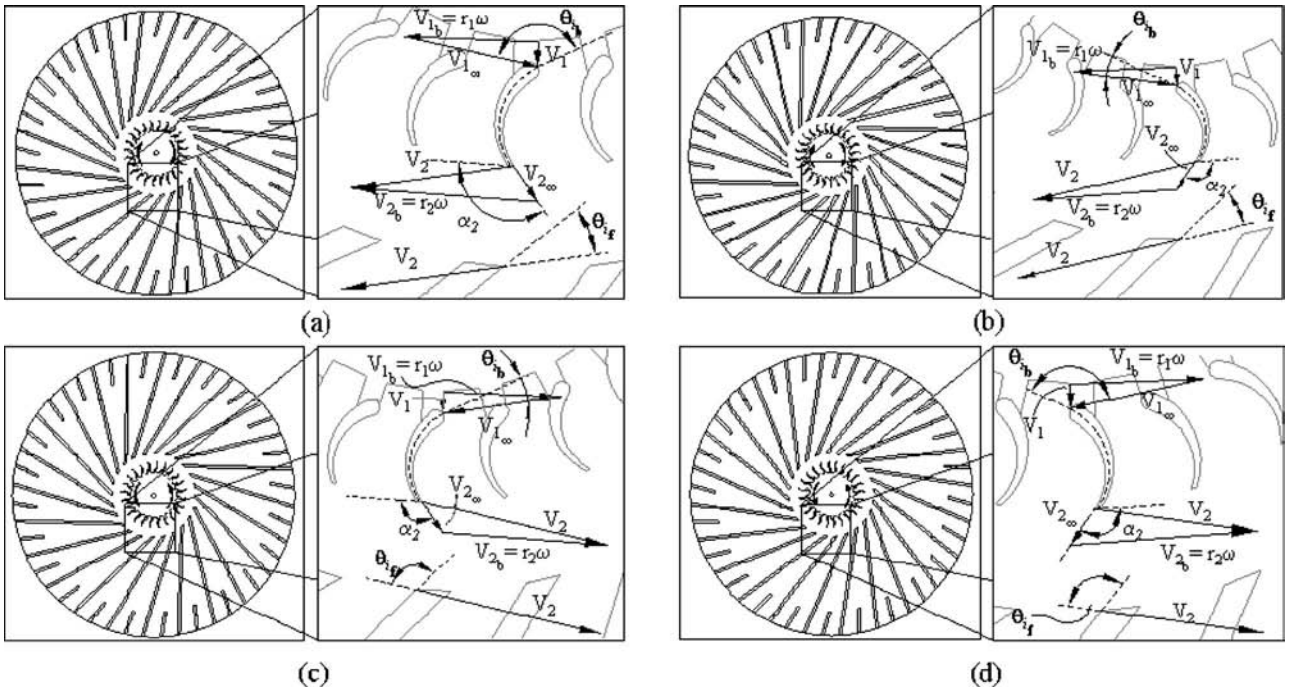

Fig. 1 Inlet and exit velocity triangles of tested configurations for the indicated blade in each image of the heat sink and rotors employed, the arrow over thick arrows represent the rotational direction in each case. N.B. Pictures or velocity triangles are not to scale and for visualization purposes only.

an efficient design, with a low incidence angle at the blade inlet and fin inlet providing the best thermal and aerodynamic performance. The effect of reducing the heat sink fin length with increasing the rotor diameter is investigated. It is found that the large pumping power due to the increased rotor diameter has a minimal impact on thermal resistance. Thereby highlighting the importance to resist the designers' desire to overcool handheld devices where power consumption is critical. It was found that the scaling parameters showed good agreement with classical turbulent laws rather than laminar ones despite a Reynolds number of less than 1000. Finally, it was found that the design of the inlet venting for the implementation of this thermal solution in portable electronics needs consideration from a thermal perspective.

Heat Sink and Fan Design

Two heat sink configurations were experimentally tested by Walsh and Grimes [12], where they found that the configuration with the nonradial fins outperformed the radial finned heat sink when a single rotor was operated as both forward and backward curved over a range of rotational speeds. They noted the improvement to be between 10% and 20% over the speed range of 5000–15,000 rpm. The current investigation builds on that work and focuses only on the tangential finned heat sink design. The investigation aims to examine a number of geometric parameters including the fan exit angle relative to the heat sink angle, rotor diameter, rotor blade designs and heat conducting fin lengths. Figure 1 shows representative velocity triangles at the inlet and exit from the rotor for various configurations considered in this work. These are not to scale and are used to aid understanding and explanation only. From this figure the various cases can be considered in terms of the angle of incidence of the fan inlet relative velocity vector $V_{1\infty}$ on the fan blade leading edge and the angle of incidence fan outlet absolute velocity vector $V_{2b\infty}$ on the heat sink fin leading edge. These two angles are labeled θ_{ib} and θ_{if}, respectively, in the velocity triangles in Figs. 2(*a*)–2(*d*). By changing the rotational direction of a given rotor design, the fan inlet incidence angle, θ_{ib}, is varied as illustrated in Fig. 1. Table 1 illustrates the resultant types of flow relative to the inlet and exit angles. Optima for each configuration were investigated by varying the exit flow angle while maintaining the inlet flow angle constant. This required the manufacture of new rotors for each test angle and the results for the eight rotor designs are presented in this paper. The two key features examined for each angle are the effects of the fan inlet incidence θ_{ib} and the effect of the blade angle α_2, and hence flow exit angle, causing an impingement on the heat transfer fins (large θ_{if}) or a relatively unobstructed flow due to the exit flow angle matching that of the heat transfer fins (small θ_{if}). Intuitively, one would expect that large values of θ_{ib} would result in the separation of flow at the blade leading edge, and hence a poor aerodynamic efficiency of the fan, and while one might expect a large value of θ_{if} to cause the separation at the inlet to the heat sink flow passages, it might also be expected that it would bring

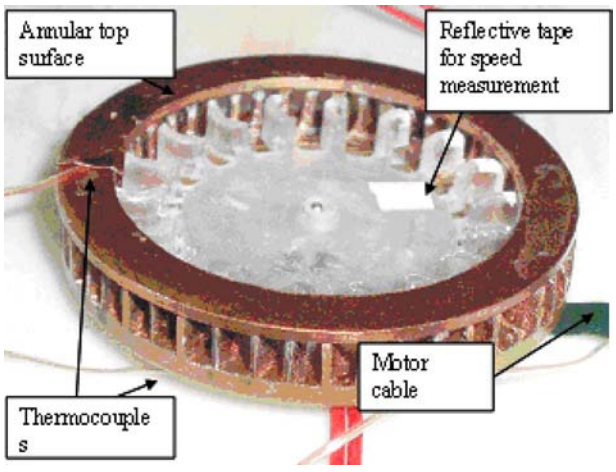

Fig. 2 Picture of experimental setup, this setup was placed within an enclosure for all results presented in this paper

Table 1 Summary of flow configurations tested for each exit flow angle

Case	Inlet flow angle design	Interaction with fins at the exit
A	Large fan inlet incidence angle, θ_{ib}	Small heat sink inlet incidence angle, θ_{if}
B	Small fan inlet incidence angle, θ_{ib}	Small heat sink inlet incidence angle, θ_{if}
C	Small fan inlet incidence angle, θ_{ib}	Large heat sink inlet incidence angle, θ_{if}, and therefore impingement on fins
D	Large fan inlet incidence angle, θ_{ib}	Large heat sink inlet incidence angle, θ_{if}, and therefore impingement on fins

about impingement levels of cooling, which could offset the negative aerodynamic consequences of the separation. So while configurations such as *D* were not expected to perform well, they are included as the flow field is complex, and at this low profile scale unexpected results may have emerged. For the part of this work where the flow angles and rotor angles were varied, the thickness of all fins was 0.5 mm, with fin lengths of 3.5 mm and 13.5 mm for the small and large scale fins, respectively, with an integrated 15 mm rotor.

In addition to varying the exit angle and relative flow angles, it is particularly interesting to consider the effect of the fin length and rotor diameter for the constant overall volume of the solution. For this section of the work the same heat sink was milled to fins starting at internal diameters of 16 mm, 25 mm, and 33 mm. Five rotors were manufactured with a constant height and diameters of 15 mm, 20 mm, 24 mm, 30 mm, and 32 mm. The rotor blade design was the one with the optimum thermal performance elucidated from the test cases in Table 1. The speed was monitored using an optical tachometer. The full set of experiments presented in this paper is detailed in Table 2.

Thermal Resistance Measurements. An annulus shaped thin film heater, available from Minco, was attached to the lower surfaces of each prototype to provide the heat source. The heater is supplied with a pressure sensitive acrylic adhesive of a thickness of 50 μm. This thermal barrier does not influence the experiment as the temperature measurement was on the heat sink surface, reflecting the focus on the heat sink design rather than on the package design. The experimental setup is illustrated in Figs. 2 and 3, where the thermal management solution represents the integrated fan and heat sink solutions. Flow enters axially and exits in a radial direction. An enclosure is necessary to isolate the measurement from any airflow in the larger room. The enclosure volume is several thousand times greater that of the thermal solution and hence its effect on the result is negligible. Thermocouples were set into drilled holes on the upper and lower surfaces of the heat sink, and its back was filled with epoxy. Such care is necessary when using standard thermocouples. For some tests miniature thermocouples were simply attached to the surface using an adhesive tape. This approach is sufficient when using miniature thermocouples with the two measurement approaches showing no measurable differences. A thermal paste was used to thermally connect the top plate to the heated heat sink by initially pressurizing the plate and then allowing its own weight to hold it in place. Good temperature uniformity was achieved with a maximum difference of 4 °C between the base and top of the heat sink at the lowest measured thermal resistance due to the reduced thermal contact area and the increased heat transfer coefficient. The temperature from the base of the heat sink, located no more than 3 mm from the heater was used in the results that follow, and hence the nonuniformity did not have a significant influence on the results. A third thermocouple was used to measure the ambient air temperature inside the enclosure. The measured voltage and current to the Minco thin film heaters were recorded and used to calculate the heat flux of the integrated fan and heat sink solutions. From these measurements, and the wetted surface area, the thermal performance of the solution can be presented in terms of the thermal resistance and Nusselt number given by

$$R_{\text{th}} = \frac{T_w - T_{\text{amb}}}{Q_{\text{measured}}} \tag{1}$$

$$\text{Nu} = \frac{hH}{k} \quad h = \frac{1}{R_{\text{th}}A} \tag{2}$$

The thermal resistance is a measure of the temperature increase per unit power dissipated in a device and is the quantity used to describe the heat sink performance.

Flow Rate Measurements. The flow rates through the heat sinks were measured using the measurement facility illustrated in Fig. 4, which shows a schematic of the full facility (left) and the configuration of the heat sink (right). Air enters the test facility through the orifice plate. The flow rate was calculated from the measured pressure drop across the orifice plate. The relationship between the flow rate and pressure drop was previously calibrated by Hanly et al. [9]. The air then passes through the pipe section and then through the straightening vanes to remove swirl. The air then passed through the auxiliary fan, which is used to overcome the pressure loss of the facility and to provide atmospheric inlet pressure conditions to the heat sink. Flow then passes through another set of straightening vanes. Once the air passed the second straightening vane it entered the fan inlet chamber. Three settling plates ensured uniform velocity in the air passing the fan inlet

Table 2 Range of experimental parameters experimentally tested

Fan diameter (mm)		15			20			24			28			30			32		
HS inner diameter (mm)		16	25	33	16	25	33	16	25	33	16	25	33	16	25	33	16	25	33
N (rpm)	1500			√			√			√			√			√			√
	3000			√			√			√			√			√			√
	4500			√			√			√			√			√			√
	6000			√			√			√			√			√			√
	7500	√[a]	√	√		√	√		√	√			√			√			√

[a]Note that for this operating condition, the blade angle of the fan was varied from 90 deg to 170 deg to determine the optimum blade angle, and the fan was operated in four different configurations, as described in Table 1.

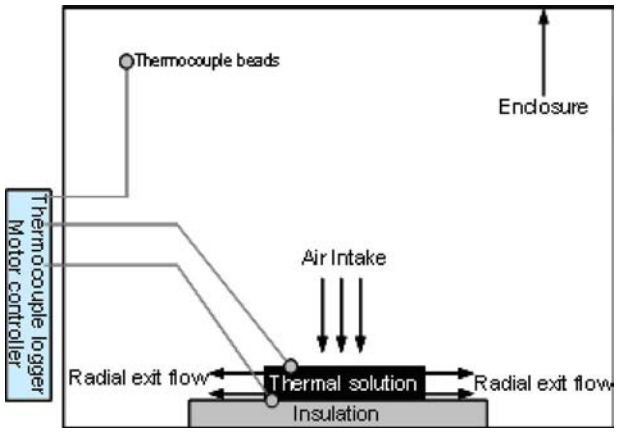

Fig. 3 Schematic of the experimental setup for thermal resistance measurements

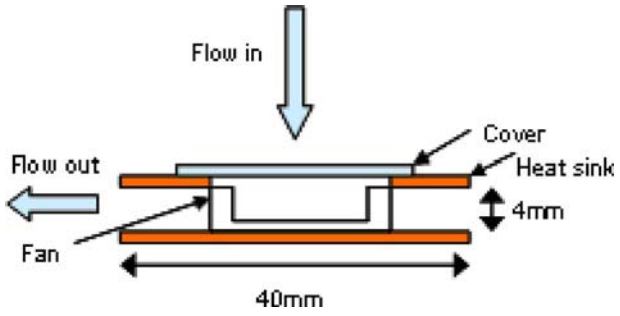

Fig. 5 Experimental setup for flow rate measurement (not to scale)

tappings. The differential static pressure across the heat sink was measured using these tappings. The fan and heat sink assembly to be tested were mounted on the fan fixture plate labeled 13 in Fig. 4. Three similar facilities are available, with different ranges of flow rate and pressure drop capabilities. For reference the flow rate for the 28 mm fan at 7500 rpm is 7.6×10^{-4} m^3/s.

Uncertainty Analysis. The uncertainty in the measurement of pressure, voltage, current, and temperature were estimated to be 0.5 Pa, 0.01 V, 0.01 A, and 0.5 K, respectively. Using these values the uncertainty in thermal resistance and relative volumetric flow rates were calculated using the method of Kline and McClintock [13]. This method uses Eq. (3) to determine the uncertainty in a given variable above and below the actual calculated value, where the uncertainty of the independent variables is known.

$$W_E = \sqrt{\left(\frac{\delta E}{\delta x_1}W_1\right)^2 + \left(\frac{\delta E}{\delta x_2}W_2\right)^2 + \cdots + \left(\frac{\delta E}{\delta x_n}W_n\right)^2} \quad (3)$$

The maximum uncertainty in the thermal resistance was less than 5% but was typically 3%. The uncertainty in thermal resistance was reduced when necessary by controlling the input power to the heater to ensure that all measurement had a heat sink base temperature of at least 20°C above ambient. The uncertainty in the relative volumetric flow rate was estimated to be 5%. However, the absolute error in the volumetric flow rate was substantially higher than the relative value with the calibration curve for the utilized orifice plate having a scatter of up to 10%, Quin [14]. The tachometer had a resolution of 1 rpm, but during experimentation the uncertainty in rotation speed was estimated to be approximately 50 rpm as fluctuations were observed in the measurement close to this level over the duration of the tests.

Inlet Venting for Implementation Within Portable Devices

It is anticipated that the proposed solution would draw air directly from the environment, but this air flow would not make direct contact with the electronic components. The heat would be transported to the heat transfer surfaces through conduction within the portable device. However, the exact embodiment of such a cooling solution in portable electronics has yet to be defined; one major concern is that of blockage due to the airflow through perforated plates to form inlet venting. This effect of blockage in close proximity to a solid wall was studied by Lin and Chou [15] for axial flow fans, and was found to have significant impact on both the flow rate and pressure rise. However, little work has been done on the effect of inlet venting designs on small scale fans, which would be necessary for the implementation of the active cooling solution.

To quantify the effect of the inlet perforated vent, a number of potential inlet cover designs were manufactured to elucidate their influence on the flow rate, the Reynolds number, and ultimately the Nusselt number. Figure 5 shows a schematic of the setup employed with the flow rate measurement facilities described above. The inlet design covers used are shown in Fig. 6 with *B*, *C*, *D*, and *E* representing covers with inlet holes of 1 mm, 2 mm, 3 mm, and 4 mm diameter, respectively. *F*, *G*, and *H* represent

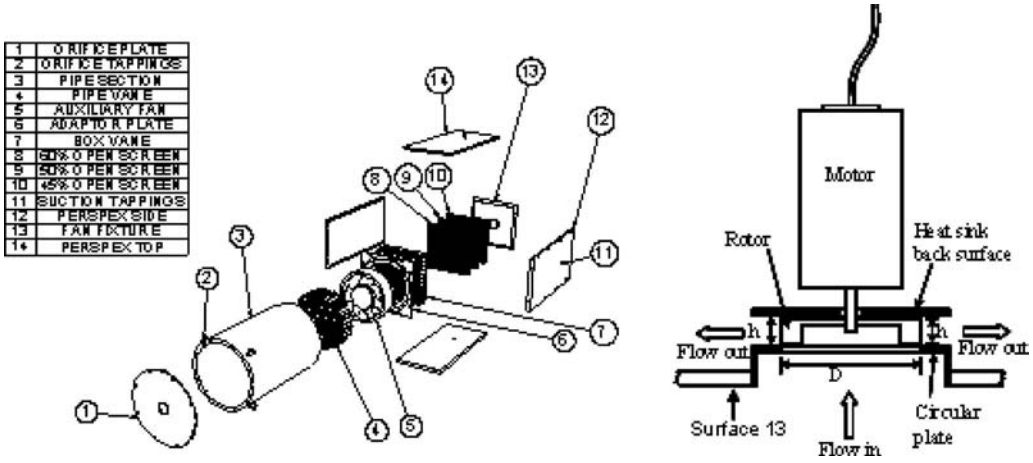

Fig. 4 (Left) Flow rate measurement facility for fans and the (right) thermal solution setup to measure the flow rate

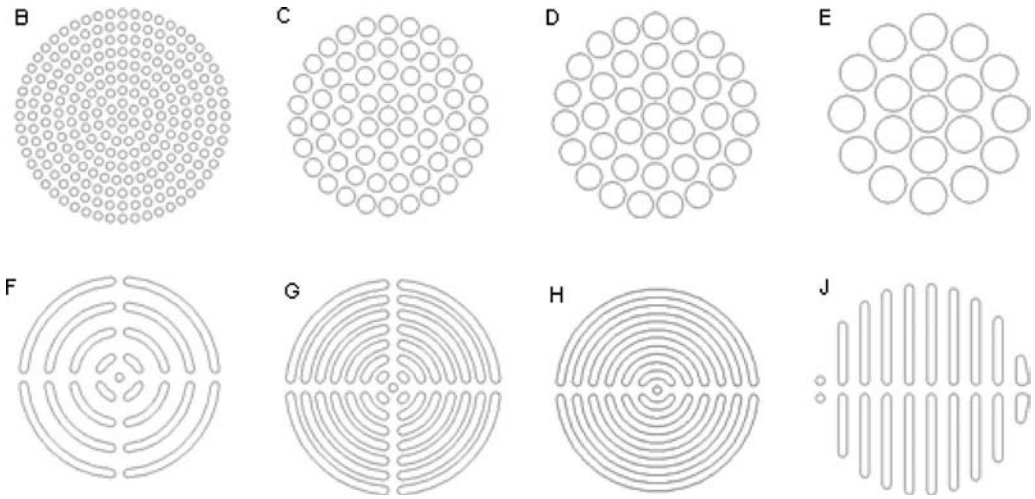

Fig. 6 Covers manufactured to investigate the effect of the cover design on flow rates for small scale fans

annular designs with different percentage open areas, while *J* represents a straight line design. All discs were made to have a 32 mm diameter and were placed over the inlet, as shown in Fig. 5. A gasket between the plates was used to ensure no leakage between the surfaces of the inlet vents and heat sink. A range of fan diameters and speeds were characterized. However, as the aim of this work is focused on the heat transfer data, to keep the paper succinct only one data set is presented. All other measurements showed similar trends. For this part of the work all tests were conducted in the absence of the finned heat sinks, with two flat plates 40 mm in diameter used in each, with the inlet orifice diameter equal to the fan outer diameter. The reason for this was to remove the influence of the fins and thereby make the results as general as possible, even beyond the current study.

Results and Discussion

Effect of Fan Blade Design. The main objective of this work is to determine the effect on the thermal resistance of varying the fin length and rotor diameter within a fixed volume. The initial study of the blade exit angle was aimed at identifying the optimum blade design philosophy and at examining the sensitivity to small changes in geometrical design on heat transfer. The inlet and exit angles from the rotor were varied to achieve this as per the labeling of Table 1. Figures 7 and 8 summarize the resultant relative flow rates and thermal resistances, respectively, for each flow angle tested, the error bands are calculated for each measurement point using the method of Kline and McClintock [13] described above. Firstly we will consider a single exit angle, 150 deg and relative performance between designs. Cases *A* and *B* have their exit angles aligned with the heat sink exit angle but with a large variation in the incidence angle. The relative inlet velocity is at a high incidence angle with the rotor blade in Case *A*. The result of this is a reduction in the aerodynamic efficiency of the blade design, where a large separation region can be expected to exist in the leading edge region due to the large adverse pressure gradient on the suction surface of the blade. The result is a dramatic reduction in the flow rate, ~40%, as corroborated by the results in Fig. 7. As would typically be expected the reduction in flow rate is also manifested in the thermal resistance measurements where the thermal resistance is seen to increase with the reduced flow rate. In summary, Case *B*, the low incidence angle clearly outperforms the high incidence angle as a design for thermal management solutions when the blade exit angle is aligned with the exit flow angle.

Addressing Cases *C* and *D* only, a similar result was evident when the blade exit angle formed an impingement region on the fin. Again it was found that a low incidence angle was the favorable design for a thermal management solution. Both of these results were as anticipated as large incidence angles result in separation regions near the leading edge of blades in classical turbomachinery design [16], effects that appear to be true in low profile blades considered in this work also.

Comparing Cases *B* and *C*, a reduction in flow rate is seen in Fig. 7 for the impingement cooling, Case *C*. This is typical of

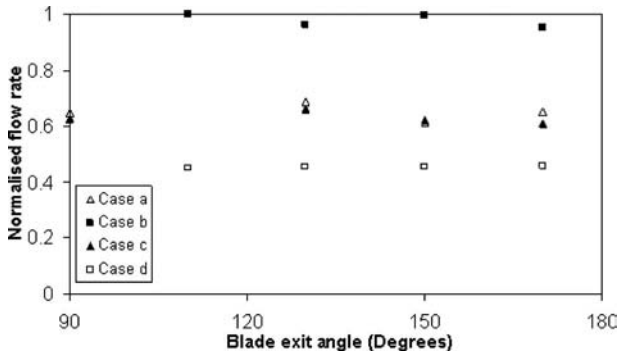

Fig. 7 Relative volumetric flow rate for the cases described in Table 1 for varying exit flow angles at 7500 rpm

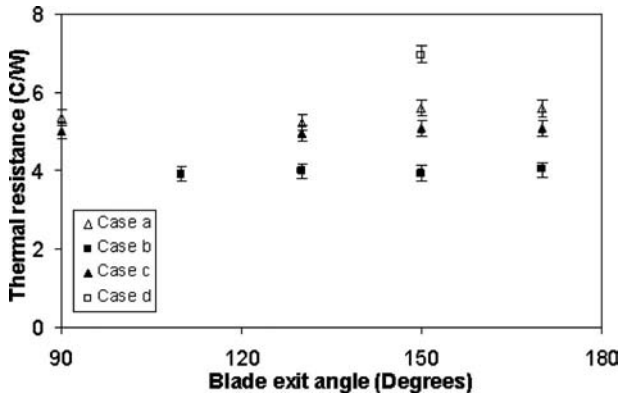

Fig. 8 Thermal resistance in °C/W for the cases described in Table 1 for varying exit flow angles at 7500 rpm

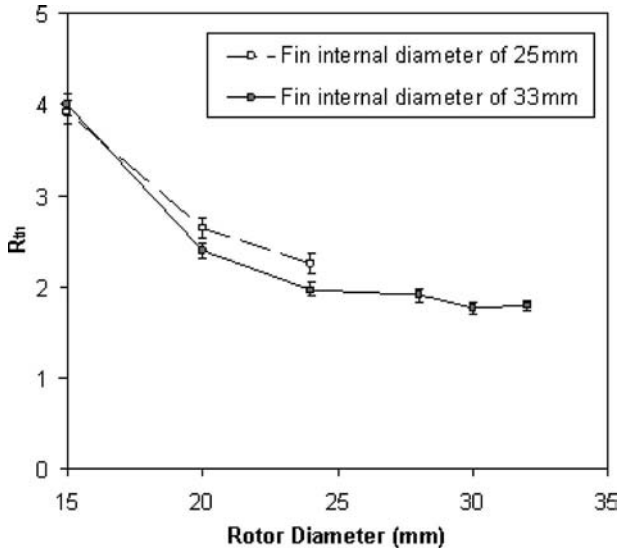

Fig. 9 Effect of varying the rotor diameter with a fixed internal fin diameter of 25 mm and 33 mm at a speed of 7500 rpm

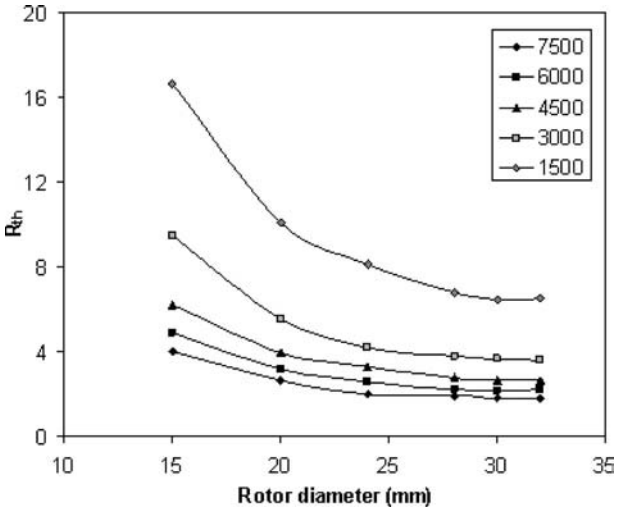

Fig. 10 Effect of the rotation speed on the thermal performance for different rotor diameters with the heat sink fin diameter starting at 33 mm

impingement cooling as it suffers from relatively large pressure drops resulting in a lower flow rate. The more important parameter is the thermal resistance, which is also decreased for the impingement type cooling of Case *C*. However, it is evident that an increase in flow rate of approximately 40% between Cases *C* and *B*, results in a reduction in thermal resistance of only 20% or so, Fig. 8. This illustrates that more of the fluid is heated in Case *C*, indicative of the higher heat transfer rates in the impingement type scenario, but these enhanced heat transfer rates are insufficient to overcome the drop in flow rate due to the increased pressure drop. Had such tests been performed for the unrealistic cases (although often presented in literature) of constant mass flow the impingement type flow of Case *C* would most likely have yielded the best performance. However, such a setup is practically unrealistic as any fan will decrease the flow rate when an increased pressure drop is introduced to the system. It can be concluded that, for a given volume and rotational speed, the best thermal resistance is achieved with Case *B* where the fan inlet incidence angle is low and the fan exit flow angle is matched to the heat sink fin angle.

An unexpected and interesting result is the insensitivity of both the flow rate and thermal resistance to the blade exit angle for each of the cases considered. Only a single measurement was done for Case *D* in thermal resistance as the thermal performance was poor and hence of no further interest. However, the same distribution can be expected with only minimal change in thermal resistance.

Effects of Fin Length and Rotor Diameter. As the thermal resistance was insensitive to the exit angle from the rotor, a fixed exit angle of 150 deg was chosen as a baseline to determine the effects of the rotor diameter on the thermal performance. The thermal resistance results are shown in Fig. 9 for two different fin lengths.

Considering first the results of the 15 mm rotor relative to those of Fig. 8 with the longer fin lengths, it is evident that the thermal performance is within the experimental uncertainty for the fin lengths starting at both 16 mm and 25 mm in diameter. In fact, the actual measured values differ by less than half of 1%. This presents the potential to remove material from the surface of the heat sink without suffering performance deterioration, which has positive manufacturing cost consequences. An added benefit is that the weight of the solution is reduced, which is always a critical component of portable devices. As expected a reduction in thermal resistance is noted with increasing the rotor diameter, although this reduction has a significant power consumption cost.

The fin length was then milled to a starting diameter of 33 mm. The results of this are also shown in Fig. 9 by closed square symbols. Again the 15 mm rotor's thermal performance is unchanged from the longer fin length experiments. However, for the larger diameter rotors an improvement in the thermal performance is observed for the shorter fin lengths. Increasing above 24 mm diameter it is interesting that only small decreases in thermal resistance are found; in fact, the 30 mm rotor measured a lower thermal resistance than the 32 mm rotor, albeit within the experimental uncertainty range. Again in terms of power requirements this has significant consequences as a rotor of 24 mm diameter requires only one-third the pumping power, using classical fan scaling laws, as a 32 mm rotor and achieves almost the same thermal performance. The measured power required to drive the motor and fan at 7500 rpm ranged between 50 mW and 300 mW for the 15 mm and 32 mm rotors, respectively. A useful measure of the effectiveness is a coefficient of performance, which could be the power dissipated by the heating element over the power required to drive the motor and fan. Using this measure and assuming that the heat sink is 20°C above ambient give coefficients of performance of 90 and 35 for the 15 mm and 32 mm rotors, respectively, and highlight the serious power cost of overcooling.

Since the almost constant thermal resistance is important in terms of portable devices, which are battery power constrained, it was decided to investigate the proposed design over a range of Reynolds numbers. This can be done simply by varying the rotational speed of the fans. The result of this is shown in Fig. 10 where almost identical trends are seen for variations in rotational speed. Over this speed range the classical fan theory predicts a five fold increase in the flow rate for a given fan diameter, the same scaling would apply to Reynolds numbers. It is noticeable that all the speeds produce similar characteristic curves with an almost constant thermal resistance value when the rotor diameter is above 28 mm.

To understand the performance of the proposed low profile thermal solution the Nusselt number based on the channel/fin height is plotted in Fig. 11 for the heat sink with the fin radius starting at 33 mm. The entire internal surface area wetted by the cooling fluid is used to calculate the heat transfer coefficient, and therefore the Nusselt number. Hence the wetted area varies with the rotor diameter, and includes the heat sink fins, upper and lower surfaces

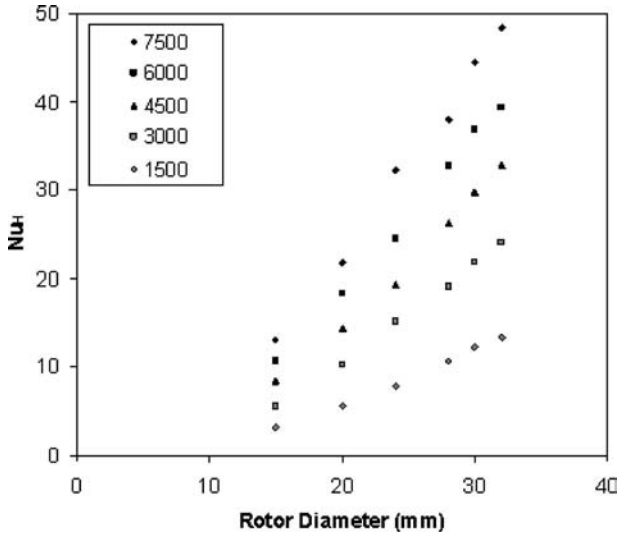

Fig. 11 Average heat transfer coefficient for the heat sink with the fin length starting at a radius of 33 mm

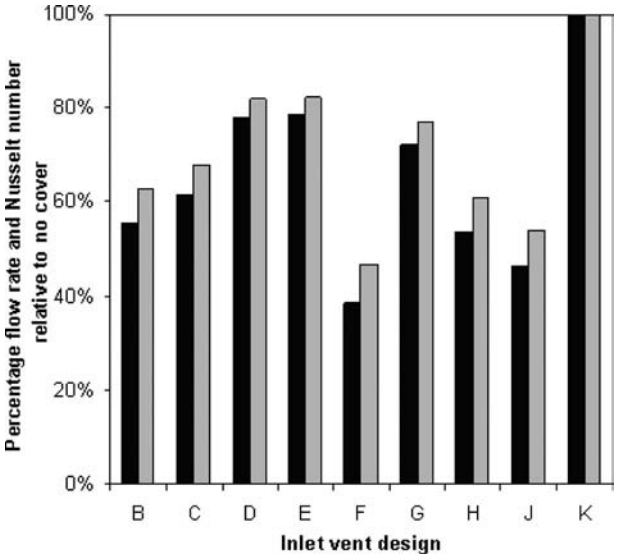

Fig. 13 Percentage flow rate and heat transfer relative to no cover; black and grey columns represent the flow rate and Nusselt number, respectively, and *K* refers to the case of no blockage

minus the fan area. The channel height was used in the calculation of the Nusselt number as it was a constant for all measurements. The use of either the hydraulic diameter or fin length, while intuitively more appropriate, did not collapse the data as effectively. A linear relationship between the Nusselt number and rotor diameter is evident with the proposed scaling, and this relationship could be exploited to develop an empirically based correlation to represent the Nusselt number as a function of rotor diameter and rotational speed.

Such a correlation approach lacks understanding of the basic heat transfer physics and makes comparison to existing literature somewhat difficult, hence a relationship of Nu as a function of the Reynolds number would be more appropriate. Channel and boundary layer flows yield the relationship of the Nusselt number proportional to the Reynolds number to the power of 0.5 and 0.8, for laminar and turbulent flows, respectively [17]. The Reynolds number for the flow considered is always less than 1000 based on the channel height and absolute exit velocity, and therefore can be expected to be laminar. Figure 12 shows the relationship between the Nusselt number and Reynolds number based on the tip speed and rotor diameter. This definition of the Reynolds number can be calculated without measurement and is available to any designer and hence its use here.

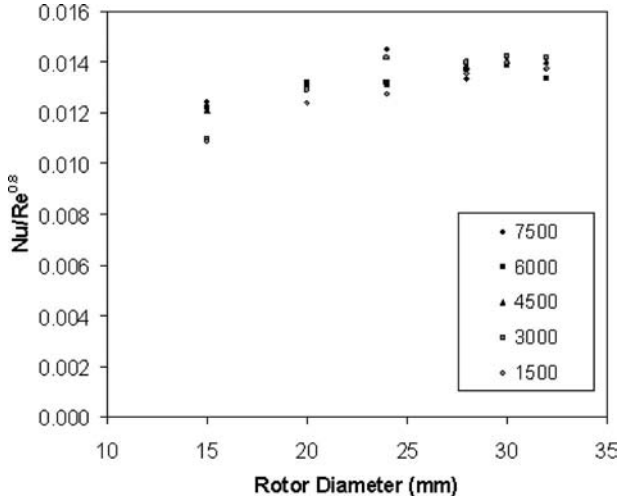

Fig. 12 Scaling of the Nusselt number and Reynolds number for a range of rotor diameters and speeds

Figure 12 demonstrates that the power of 0.8 collapses the data for each rotor diameter, when the rotational speed is varied. This scaling of 0.8 is representative of the turbulent rather than laminar heat transfer characteristics and suggests a nontypical flow within the heat sink design for the Reynolds numbers considered. An almost constant value, 0.014, is found for the rotor diameters of 24 mm and greater. Below 24 mm a significant reduction is found in this scaled value, the reason for this is unclear but some suggestions could be a change in fan law scaling at this reduced diameter, or the physics of heat transfer may have changed due to changes in the rotor to fin length ratio. Finally, attempts at collapsing the data from the heat sinks with different length fins were also attempted but were not successful. Here the flow rates will not scale with classical fan laws as the heat sink geometry is varied. The values were about 0.015 for the heat sink with an internal fin diameter of 25 mm and 0.012 for an internal fin diameter of 16 mm based on the same scaling as Fig. 12.

Influence of Inlet Vent Design. Although the influence of an inlet design is not directly relevant to the current work on heat transfer, for completeness it is useful to present the type of performance reductions to be expected from the integration of low profile thermal solutions within a device due to inlet vent design. Figure 13 shows the flow rates normalized at their maximum values for a single fan at a rotational speed of 7500 rpm. The maximum flow rate occurs when no cover is in place, *K*, with all inlet designs causing a reduction in the flow rate, up to about 60% for Design *F*. The effect of such a reduction on the heat transfer can be interpreted from the scaling found in Fig. 12, Nu proportional to the Reynolds number to the power of 0.8. For the cover designs investigated a reduction of up to 50% in the Nusselt number is therefore anticipated, for Cover *F*. The designs of *D*, *E*, and *G*, where good flow rates are achieved, are anticipated to result in decreases of about 20% in the Nusselt number and are good candidates for inlet cover designs in portable electronic devices.

Conclusions

The paper addressed the potential of a low profile thermal management solution for electronic portable devices. A number of

aerodynamic situations were tested experimentally to determine the thermal resistance achieved through impingement and aligned flow with the heat sink fins. The resultant data show two important points, a low incidence angle at the leading edge is important to achieved good thermal resistance, and the thermal resistance where the fan exit flow is aligned with the heat sink fins is superior to that where the fan exit flow impinges directly on the heat sink fins. Changes in the rotor exit blade angle proved to be only slightly sensitive to thermal resistance. Rotor diameter and fin length variation within a constant volume was examined and it was found that minimal reductions in thermal resistance were achieved despite large increases in pumping power. In portable devices power consumption is a key element of any design and this work highlights the importance of good designs in achieving energy efficient cooling systems.

From a more fundamental perspective the scaling parameters were found to be in better agreement with classical turbulent laws rather than laminar ones despite a Reynolds number of less than 1000. This suggests that the proposed thermal design demonstrates the favorable heat transfer characteristics of turbulent flows, which make it a promising design for low profile applications. Preliminary work on the inlet cover design demonstrated that this was not a hindrance to the implantation of active cooling in portable electronics.

Nomenclature

A = wetted area (m^2)
D = diameter (m)
E = given function
H = fin height (m)
M = meters (m)
N = rotational speed (rad s^{-1})
Nu = Nusselt number
Q = heat transfer (W)
R = radius of heat sinks (m)
Re = Reynolds number ($N D^2/\nu$)
R_{th} = thermal resistance (°C W^{-1})
rpm = revolutions per minute
T = temperature (K)
V = velocity (m/s)
W_E = uncertainty in the result
W_n = uncertainty in independent variables
h = heat transfer coefficient
k = thermal conductivity
x_n = independent variables
α = fan blade angle
ν = kinematic viscosity
θ = incidence angle

Subscripts

amb = ambient conditions
w = heat sink base wall
measured = measured conditions
1 = fan inlet conditions
2 = fan outlet conditions

References

[1] Loh, C. K., Nelson, D., and Chou, D. J., 2001, "Thermal Characterization of Fan-Heat Sink Systems in Miniature Axial Fan and Micro Blower Airflow," *Semiconductor Thermal Measurement and Management, Seventeenth Annual IEEE Symposium*, San Jose, CA, March 20–22.
[2] Noda, H., Ikeda, M., Kimura, Y., and Kawabata, K., 2005, "Development of High-Performance Heatsink 'Crimped Fin'," Furukawa Rev., **27**, pp. 14–19.
[3] Wirtz, R. A., and Zhong, N., 1998, "Methodology for Predicting Pin-Fin Fan-Sink Performance," *Proceedings of the InterSociety Conference on Thermal Phenomena*, NJ, May 27–30.
[4] Tan, F. L., and Tso, C. P., 2004, "Cooling of Mobile Electronic Devices Using Phase Change Materials," Appl. Therm. Eng., **24**(2–3), pp. 159–169.
[5] Launay, S., Sartre, V., and Lallemand, M., 2004, "Experimental Study on Silicon Micro-Heat Pipe Arrays," Appl. Therm. Eng., **24**(2–3), pp. 233–243.
[6] Acikalin, T., Sauciuc, I., and Garimella, S. V., 2005, "Piezoelectric Actuators for Low-Form-Factor Electronics Cooling," *Proceedings of InterPACK'05*, San Francisco, CA, July 17–22.
[7] Kimber, M., Garimella, S. V., and Raman, A., 2006, "Experimental Mapping of Local Heat Transfer Coefficients Under Multiple Piezoelectric Fans," ASME Paper No. IMECE2006-13922.
[8] Grimes, R., Walsh, E. J., Quin, D., and Davies, M., 2005, "The Effect of Geometric Scaling on Aerodynamic Performance," AIAA J., **43**(11), pp. 2293–2298.
[9] Walsh, E., Egan, V., Grimes, R., and Walsh, E., 2009, "Profile Scaling of Miniature Centrifugal Fans," Heat Transfer Eng., **30**, 1-2, pp. 130–137.
[10] Walsh, E. J., Walsh, P. A., Grimes, R., and Punch, J., 2008, "Acoustic Emissions From Active Cooling Solutions for Portable Devices," *Proceedings of ITHERM 2008*, Orlando, FL, May 28–31.
[11] Bejan, A., and Fautrelle, Y., 2003, "Constructal Multi-Scale Structure for Maximal Heat Transfer Density," Acta Mech., **163**(1–2), pp. 39–49.
[12] Walsh, E. J., and Grimes, R., 2007, "Low Profile Fan and Heat Sink Thermal Management Solution for Portable Applications," Int. J. Therm. Sci., **46**, pp. 1182–1190.
[13] Kline, S. J., and McClintock, F. A., 1953, "Describing Uncertainties in Single-Sample Experiments," Mech. Eng. (Am. Soc. Mech. Eng.), **75**, pp. 3–8.
[14] Quin, D., 2006, "Micro Scale Axial Flow Fans," Ph.D. thesis, University of Limerick, Limerick, Ireland.
[15] Lin, S.-C., and Chou, C., 2004, "Blockage Effect of Axial-Flow Fans Applied on Heat Sink Assembly," Appl. Therm. Eng., **24**, pp. 2375–2389.
[16] Buffum, D. H., Capece, V. R., King, A. J., and El-Aini, Y. M., 1998, "Oscillating Cascade Aerodynamics at Large Mean Incidence," ASME J. Turbomach., **120**(1), pp. 122–130.
[17] Bejan, A., 1984, *Convective Heat Transfer*, Wiley, New York.

Erratum: "Use of Streamwise Periodic Boundary Conditions for Problems in Heat and Mass Transfer" [Journal of Heat Transfer, 2007, 129(4), pp. 601–605]

S. B. Beale

The downstream condition may be written: $T(l,y,z)=c_1'T(l,y,z)+c_2'$, where $c_1'=1/c_1$ and $c_2'=-c_2/c_1$. Thus the source terms are $a_W[(c_1-1)T_W+c_2]$ at $i=1$ and $a_E[(c_1'-1)T_E+c_2']=a_E[(1-c_1)T_E-c_2]/c_1$ at $i=nx$. The latter is generally significant only at very low Reynolds numbers.

